Mathematical Problems in Engineering

Advanced Dynamics, Control and Management in Renewable Energy and Storage Systems 2021

Lead Guest Editor: Kai Wang
Guest Editors: Xiufeng Liu, Licheng Wang, Yaping Fu, Huajun Dong, and Jinyan Song

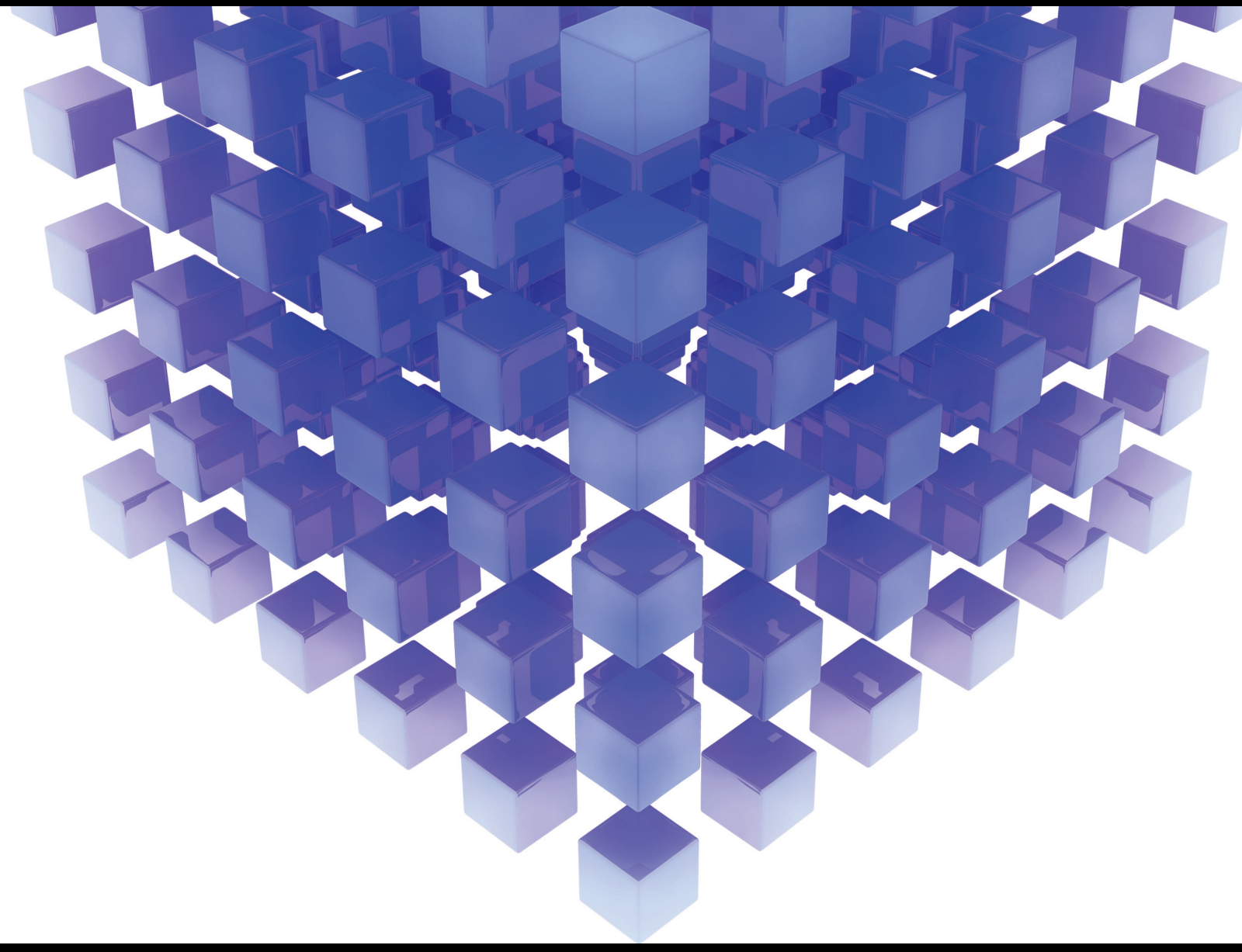

Advanced Dynamics, Control and Management in Renewable Energy and Storage Systems 2021

Mathematical Problems in Engineering

Advanced Dynamics, Control and Management in Renewable Energy and Storage Systems 2021

Lead Guest Editor: Kai Wang
Guest Editors: Xiufeng Liu, Licheng Wang, Yaping Fu, Huajun Dong, and Jinyan Song

Chief Editor

Academic Editors

Contents

Contents

Hindawi
Mathematical Problems in Engineering
Volume 2023, Article ID 9895041, 1 page
https://doi.org/10.1155/2023/9895041

Retraction

Retracted: Accelerated Iterative Learning Control for Linear Discrete Time Invariant Switched Systems

Mathematical Problems in Engineering

Received 18 July 2023; Accepted 18 July 2023; Published 19 July 2023

This article has been retracted by Hindawi following an investigation undertaken by the publisher [1]. This investigation has uncovered evidence of one or more of the following indicators of systematic manipulation of the publication process:

(1) Discrepancies in scope
(2) Discrepancies in the description of the research reported
(3) Discrepancies between the availability of data and the research described
(4) Inappropriate citations
(5) Incoherent, meaningless and/or irrelevant content included in the article
(6) Peer-review manipulation

The presence of these indicators undermines our confidence in the integrity of the article's content and we cannot, therefore, vouch for its reliability. Please note that this notice is intended solely to alert readers that the content of this article is unreliable. We have not investigated whether authors were aware of or involved in the systematic manipulation of the publication process.

Wiley and Hindawi regrets that the usual quality checks did not identify these issues before publication and have since put additional measures in place to safeguard research integrity.

We wish to credit our own Research Integrity and Research Publishing teams and anonymous and named external researchers and research integrity experts for contributing to this investigation.

The corresponding author, as the representative of all authors, has been given the opportunity to register their agreement or disagreement to this retraction. We have kept a record of any response received.

References

[1] Y. Wang, S. Riaz, Z. Bao, and W. Zhang, "Accelerated Iterative Learning Control for Linear Discrete Time Invariant Switched Systems," *Mathematical Problems in Engineering*, vol. 2022, Article ID 5738826, 10 pages, 2022.

Hindawi
Mathematical Problems in Engineering
Volume 2022, Article ID 2684983, 13 pages
https://doi.org/10.1155/2022/2684983

Research Article

Experimental and Numerical Research of Paved Microcrack Using Histogram Equalization for Detection and Segmentation

Asad Ullah,[1] **Zhaoyun Sun**,[1] **Hassan Elahi**,[2] **Farkhanda Afzal**,[3] **Amna Khatoon**,[1] **Nasir Sayed**,[4] **and Ishfaq Ahmad**[5]

[1]*Department of Information Engineering, Chang'an University, Xi'an 710064, China*
[2]*Department of Mechanical and Aerospace Engineering, Sapienza University of Rome, Rome, Italy*
[3]*Department of Humanities and Basic Sciences, MCS, National University of Sciences and Technology, Islamabad, Pakistan*
[4]*Department of Computer Science, Islamia College University, Peshawar, Pakistan*
[5]*School of Marine Science and Engineering, Northwestern Polytechnical University, 710072 Xi'an, China*

Correspondence should be addressed to Zhaoyun Sun; zhaoyunsun@126.com

Received 11 January 2022; Revised 5 April 2022; Accepted 3 May 2022; Published 21 June 2022

Academic Editor: Alessandro Rasulo

The paved cracks are one of the major concerns for scientists and engineers in road maintenance and damage evaluation study. Digital image processing applications have been applied in road surface inspection, classification, and decomposition of paved roads. This paper has tested and proposed the process to evaluate the road cracks and their possible solution as we know that the key issues for analysis are enhancement and segmentation of image along with edge detection to attain the promising results we have gained and discussed under the heading of simulations for the experimental and numerical of crack detection. Using MATLAB, we examine the various gray-level image using better techniques based on their computational capability. The method is based upon one of the histogram modification techniques, which is coupled with the segmentation method and the crack edge detection. At last, three feature methods are used, namely, Harris, MSERF, and SURF, to wind up our research.

1. Introduction

The maintenance of roads is an important aspect where the first step of maintenance is to identify road clutter and its documentation. Disaster troubles are defects that are visible on the road surface; appropriate assessments of roads will enable better opportunities for the allocation of resources and create better service conditions. Road surfaces such as cracks, disassembly, and surface deformation can be affected by various types of difficulties [1]. Image segmentation and feature extraction cannot be ignored in DIP [2]. Currently, there are different constraints in the investigation process, such as recording, analysis, and survey of data. [3–5]. Engineers have now realized the importance of this information to measure road quality [6]. Traditionally, pedestrian inspectors were used to collect road surface data as they walked or drove along the road to evaluate its difficulty, and then reports were generated; therefore, the entire process was time-consuming and costly. The entire job has to be done in fast-moving traffic, which makes it more difficult. This situation will jeopardize the safety of the members concerned [7]. There are various test methodologies used to check the quality of the road, such as ultrasonic testing, infrared detection, and image processing. There is also a method called WiseCrax, which uses infrared imaging to detect cracks [8]. With the passage of time, smarter, intelligent, and better methods are being developed to detect microcracks. These developments are still in progress and remarkable research is done on asphalt pavement progress [9]. The literature proposed a crack width detection method

for extracting crack images from road surface disturbances and calculating crack, an analysis method based on escaping images to break the walking image to improve the reliability of locking walking cracking [10].

The automatic real-time detection systems currently in use focus on low entry rates and soldering difficulties, but still, there is no precise algorithm for identification and classification perfectly [11]. Despite the fact that there are some automatic inspection systems currently in use, systems with surface-scan cameras have low differential distortion problems and the resolution of dynamically acquired images is not satisfactory [12]. Filtration is commonly done to reduce noise, and, in this process, median filtering is most commonly used for the detection of crack pretreatment techniques these days because the median filter is more sensitive than extreme values. Moore et al. [13] used the median filtering technique to improve road imaging. Median filtering can be explained in various ways, like salt-and-pepper and so on; it adds black-and-white pixels randomly in a grayscale image [14]. The segmentation method is selected due to the histogram modification technique. In this technique, the clip is continuously repeated. During each repetition, pixels are added in the background until there are only the remaining features. At this point, the threshold can be automatically determined to separate the distress feature from the background [15]. In the research, we introduce 4 segments, following the abstract. The first heading is about histogram equalization. The second heading is about the numerical model and its implementation. Then, we have result sections that verify the performed experiments, and at the end, we have to conclude our research under the conclusion and references. Below Figure 1 shows the standard algorithm flowchart for a random case.

2. Histogram Equalization Framework Design

2.1. Image Preprocessing. During the preprocessing, the recorded image data prevents errors associated with the geometry and brightness values of the pixels. Error correction techniques are used with mathematical models [16]; sometimes, due to the strict subimaging system and the lighting conditions, while capturing the images, the contrast and brightness of images obtained from conventional and digital cameras become low [17]. Therefore, enhancement of the image is being used widely for the extraction of features, analysis, and displaying of an image [18]. Figure 2 shows the processing flow of the image processing along with the communication directly with different segments. Figure 2 explains which segment is linked directly with the knowledge base and which is communicating indirectly with the base.

In the preprocessing section for the sake of better contrast between road and non-road pixels, mathematical morphology and the Gabor filter were proposed. Some of the images have no road pixels because that dataset is built through remote sensing [19]. It was used simultaneously in the algorithm in various studies [20–22].

This section is primarily focused on the initial processing shown in Figure 3 by applying the Gabor filter. The dataset was completed by me to obtain the automatic pavement detection through a vehicle. The pavement image data collection system consists of three parts. Figure 1 shows the system composition. The crack collection camera adopts the high-definition linear array CCD camera, which vertically illuminates the pavement surface image, and the corresponding line laser provides auxiliary lighting for the camera to store in the hard disk. Out of the acquired sample of images, cracked and uncracked images are gained, and the vehicle that has a speed limit of between 50 and 60 km/h was used. Multiple images have been analyzed and only a set of images were selected to be processed. The image set that has been used and analyzed has the following statistics shown in Table 1.

In Table 1, default parameters were used during capture and other steps like a transmission from the camera to the base station, and so on. A good number of scientists and researchers proposed different kinds of approaches (e.g., NSST, guided image filter, and structural-proper kernel histograms) [23]. Several researchers like Singh and Kaur have several methodologies for automatic road extraction [24]. They have presented image sources, advantages, and disadvantages, basic extraction algorithms, and statistics results. Image preprocessing is independent of transmission although being processed by image acquisition, capturing, storing, disposing of, and compressing.

2.2. Object Primary Attributes. The convolution in the algorithm is the calculation of the incident image, which would be explained in a later section. The physical meaning is to estimate the change of luminance in the image by calculating the weighted average of the pixel and the surrounding area and by removing change $L(x, y)$ and only retaining the $S(x, y)$ attributes. The objective of attribution is to identify regions between the grayscale and processed image (binarized image), such as shape, edges, and similarity coincidence. The spatial method is based on higher-order probability distribution or/and the correlation between pixels [25]. In local, the threshold adopts the value on each pixel to the local image characteristics. In this method, a different fixed point is selected for each pixel in the image [26].

2.3. Image Enhancement through Noise Filtering. Image enhancement is an important aspect of image processing [27]. For getting the required information, each specific character of an image will be emphasized. This is the actual purpose of the image enhancement because the information is not extracted by itself but is just emphasized. Here in the image recognition, the enhancement is observed in contrast, acuity, edge enhancement, pseudocoloring, filtering, and noise; it also enlarges the image to observe more keenly [28]. Out of several current image enhancement procedures, filtering techniques have become very prevalent over the years. It is considered appropriate for addressing the problem of noise removal and edge enhancement [29]. The

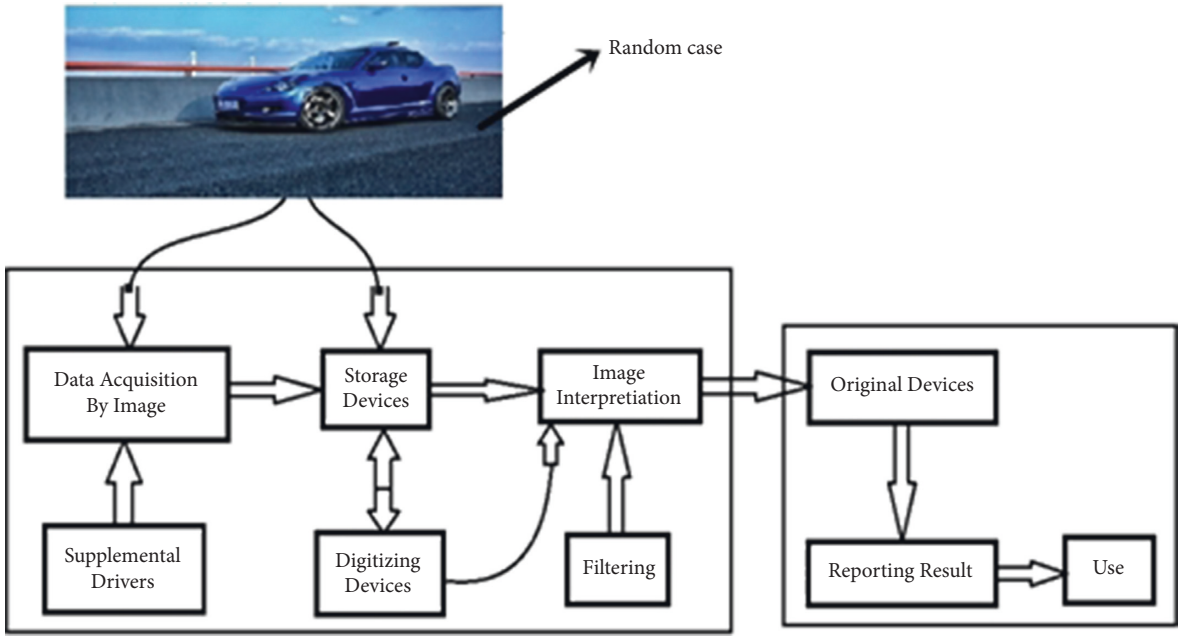

Figure 1: The standard procedure flowchart.

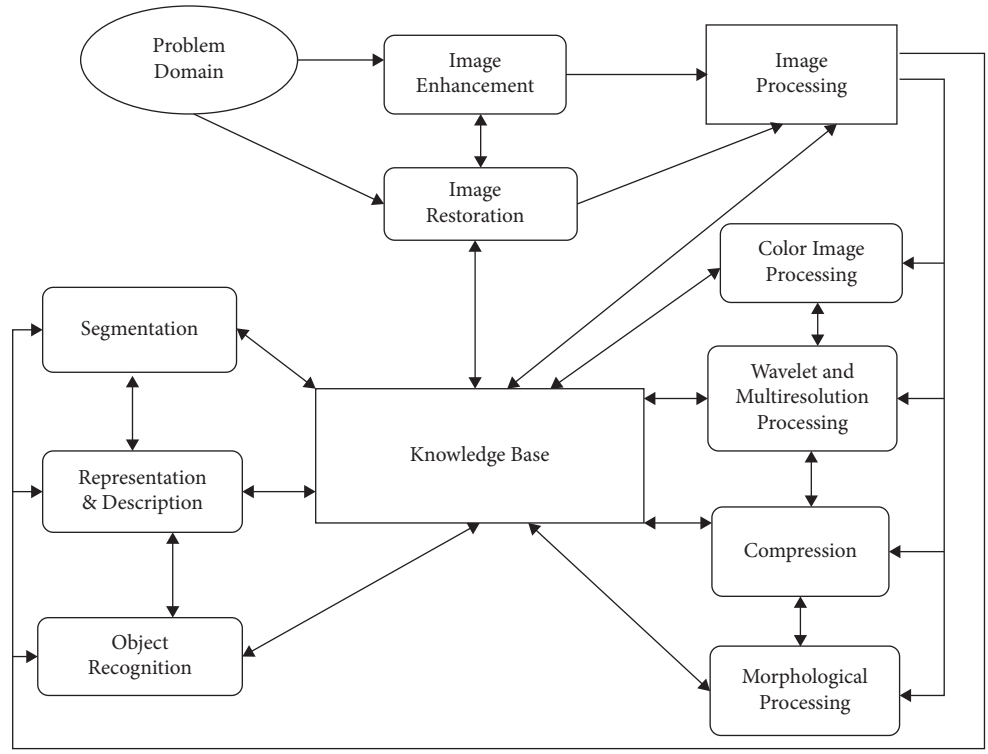

Figure 2: Converging methods for finding image attributes.

next portion is explained in Figure 4 for converging methods for bihistogram and edge enhanced equalization.

Figure 4 is showing the converging methods for bihistogram and edge enhanced equalization. In the mentioned flowchart, PLs are calculated for each subhistogram once histogram segmentation is completed to retain brightness. PLs of each subhistogram are calculated. After that, CDF is founded and the linear coefficient of GF of each pixel for the input image is also derived. To avoid overenhancement, histogram adjustment is done with the PLs. The CDF is next computed for each subhistogram, followed by the GF linear coefficients for each pixel of the input image. Finally, the edge-enhanced pictures are generated while noise amplification is suppressed using the linear coefficients and the

(a) (b)

Figure 3: Original preprocessed image by applying Gabor filter. (a) Original image. (b) After applying the Gabor filter.

Table 1: Generalized processing parameters.

Image no.	Size	Bytes	Class	Height	Width
1	$318 \times 307 \times 3$	292878	Unit 8	$2.48''$	$2.80''$

CDFs. Our proposed algorithm is unique because during histogram equalization we face brightness inconsistency, overenhancement, and undesired noise amplification, and to alleviate these shortcomings, we used GF and BHEPL.

The image processed here as a research experiment is homogeneous, not heterogeneous, so the level will be unchanged and remain constant. These image pixels are characterized as very narrow peaks to represent the histogram. Uniformity is the result of improper illumination on the scene. In the end, images are mixed and unable to understand easily because of the uncertainty of the human factor. It is due to one narrow gray level in the image; this has a wider range of gray minor levels. Jitprasithsiri suggested that median filtering is applied as a pavement image enhancement technique [30]. In common situations, the contrast stretching method is specifically designed. A vibrant network that is available for different stretching techniques has been developed to stretch a narrow range [31]. Different stretching techniques have been developed to stretch a narrow range in a dynamic network that is available [32]. Unwanted information from the image is filtered out through noise filtering. Most of these features are interactive and are also used to generate various types of sound from images. For common circumstances, the suited method is the contrast stretching method. Noise filtering declares all the unwanted information as noise and eliminates it from the image. Noise filtering can be used for generating various types of features from images and most of these features are interactive [33], as shown in Figure 5 below for original and filtered images after applying a noise filter.

In Figure 5, the original image and 5(b) are representing the adjusted image after applying the noise filter. Histograms are widely used for image enhancement, which reflects the image function. Image features can be modified by changing the histogram (e.g., equal histogram). The equation for a histogram is a nonlinear stretch that redistributes pixel values such that each value in the range has approximately the same number of pixels. The result is close to the average histogram. Therefore, the contrast at the peak increases, and the contrast at the tail decreases. In image enhancement, the proposed filter is the median filter because it reduces the noise very significantly. This noise reduction is a normal preprocessing step to improve subsequent processing results. Median filtering is very common in digital image processing because in some cases it maintains edges and so on [34]. The working way of the median filter is to replace every entry with the median value of the adjacent entry by the signal input of the entry.

2.4. Numerical Modelling and Implementation Algorithm. As it is known that every image is not uniform, some images will be brighter on the corners, but some will be on the edges. And maybe some images will be overall less bright [35]. So, enhancement is the best tool and usually, through this procedure, the contrast shoot at peak and tail got lessened. In the equalization, the pixel is redistributed in such a way that every point of the image approximately gets the same number of pixels in the given range. $I(x, y)$ is the true input image with the coordinate pixels. $n(x, y)$ is representing the noise image, which is added with the input function, and the image we gained can be represented by

$$\hat{I}(x, y) = I(x, y) + n(x, y). \quad (1)$$

The above mention set of parameters has two parts: the $I(x, y)$ part that is the initial image and the $n(x, y)$ part that is an unwanted signal representing noise. As that histogram modeling is used for continuous process function rather than a discrete function, the alternate means that on every pixel there is a certain value within the interval of 0 and 1. The function $f(x, y)$ represents the gray level input image with the coefficient of f and input pixel values on the

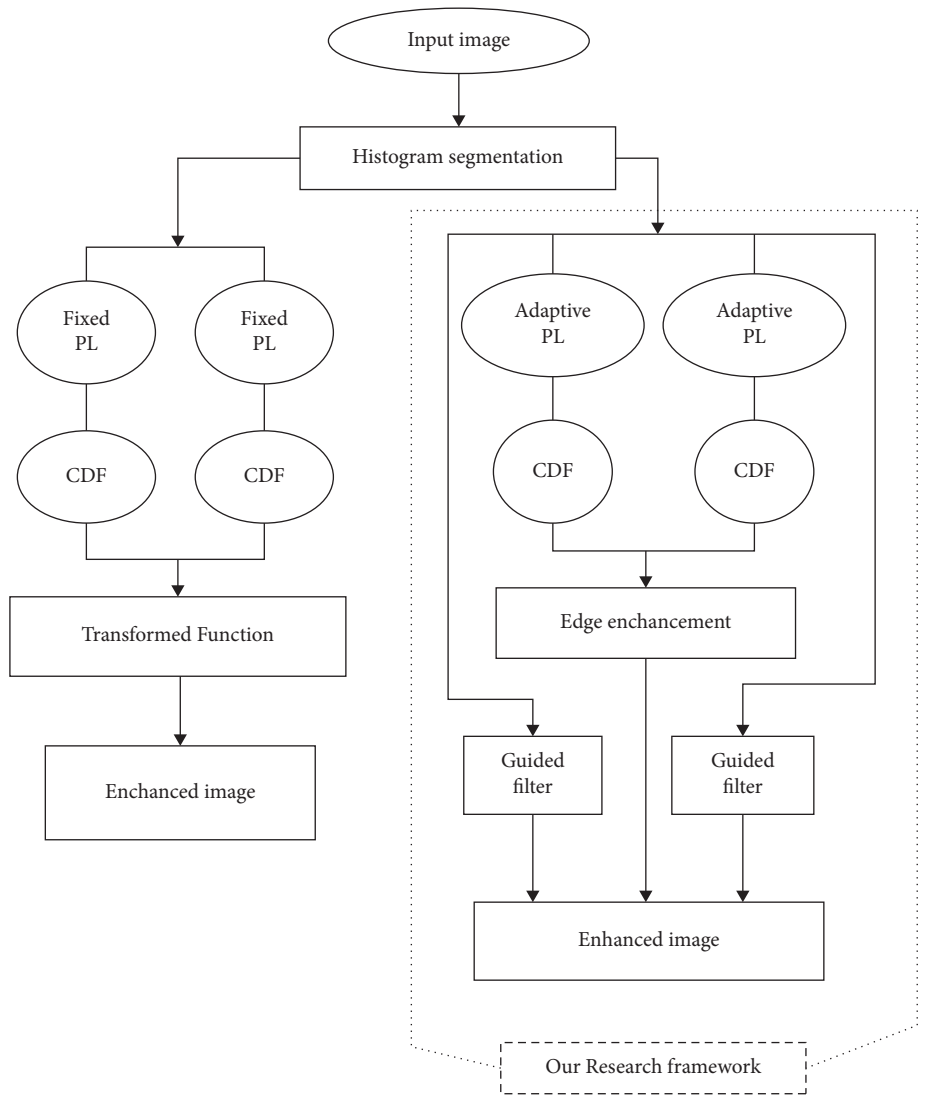

Figure 4: Converging methods for bihistogram and edge enhanced equalization.

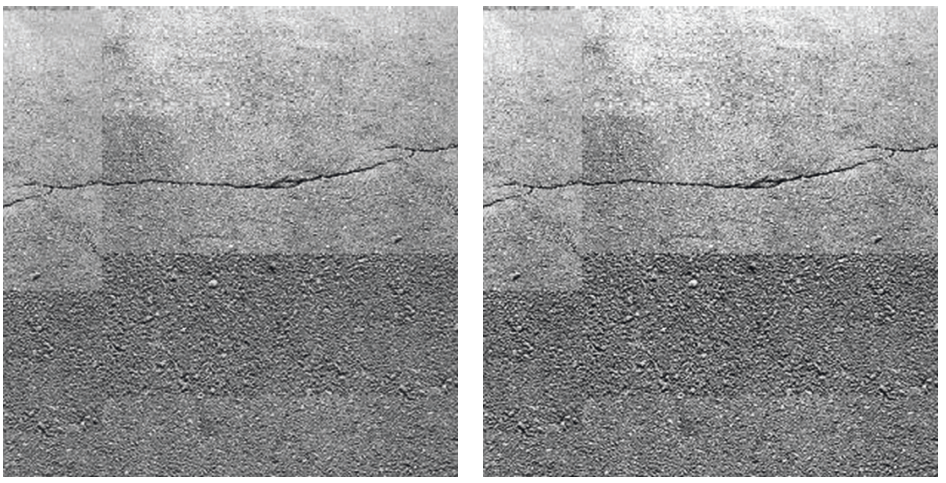

(a) (b)

Figure 5: Comparison view of the original image and a filtered image. (a) Original processed image. (b) Adjusted image by the noise filter.

coordinates (x, y). The processed image will be expressed by $s(x, y)$. So, mathematically, we can write it as follows.

$$f(x, y) = T[f(x, y)]. \tag{2}$$

In the above equation, $T[f(x, y)]$ represents the transfer function for the input image. The modified equation will be shown as $f(x, y)$ as $f(r)$, Then, the equation will be written as follows.

$$f(r) = T[f(r)], \tag{3}$$

where $f(r)$ is the input image and $T[f(r)]$ is the transfer function of the input image; basically the input is being shifted to output and it is shown mathematically as above in equation (3). As for histogram equalization, the density level is single and monotonically increased, so the overall equation is as follows.

$$U(x, y) = U(x, y). \tag{4}$$

In equation (4), the state of the image has been changed from A to B ($U_A \longrightarrow U_B$); in other words, the input is shifted to processed images with the transformation function. So, the region densities tense to the input side $U_A \longrightarrow U_A + dU_A$ and on outside $U_B \longrightarrow U_B + dU_B$. In terms of histogram equalization, it is shown as follows.

$$h_B(U_B) = \frac{h_A U_A}{dU_A}. \tag{5}$$

Now in terms of frequency, the overall equation will be like this, in which the left-hand side shows the frequency taken on the input image and the right-hand side shows the integral P_A within a limit from $i = 0$ from the maximum interval of U_A mentioned in the following equation.

$$fU_A = U_M \int_{i=0}^{U_A} P_A(u).du. \tag{6}$$

As $P_A u.du$ can be simply used as cumulative probability, equation (6) will be yielded into the following equation.

$$fU_A = U_M * F_A U_A. \tag{7}$$

For finding the inverse transfer function if S that is shown by processed image $T[r]$ is the transfer function of $[r]$, then the formula will be shown as $S = T[r]$ if it proved the condition of a single value and monotonically increased in the intensity level of $0 \le r \le 1$; then the transfer function will be converted into

$$r = T^{-1}[s], \tag{8}$$

where r is the gain of the inverse transform function of its input value. Thus, a comparison change g0 between u and v could be calculated by combining a pseudoinverse of H_V with H_u. This direct method is not adequate because it does not guarantee that in the end, g_0 will be the same or similar to v, specifically if the initial statement v = g(u) is not accurately right, that has to be expected in real situations. Therefore, the histogram of u and v is represented in the discrete case by the following governing equations.

$$h_{u,v}(i, j) = \frac{|\{x \in \Omega(u(x), v(x)) = (i, j)\}|}{\Omega}. \tag{9}$$

$$gk = g(\lambda_k). \tag{10}$$

$$E(g_k) = \sum_{x \in \Omega} (v(x) - gou(x))^2. \tag{11}$$

$$E(g_k) = \sum_{x \in \Omega} v(x)^2 = \sum_{k=1}^{N} \sum_{x \in \Omega_k} (gou(x))^2 - 2v(x)gou(x). \tag{12}$$

$$E(g_k) = \sum_{x \in \Omega} v(x)^2 + \sum_{k=1}^{N} |\Omega_k| g_k^2 - 2g_k \sum_{x \in \Omega_k} v(x). \tag{13}$$

$$E(g_k) = \sum_{x \in \Omega} v(x)^2 - \sum_{k=1}^{N} |\Omega_k| v_k^{-2} + \sum_{k=1}^{N} |\Omega_k| . (g_k - \overline{v}_k)^2. \tag{14}$$

$$E(g_k) \Rightarrow g_k = -\overline{v}_k. \tag{15}$$

In equation (9), u and v are the pixel values at point x. The point lies on i, j and the overall gain will be divided on sigma. In the above equation, there is a summation sign that sums up all the variables used in the image histogram with omega and gou composition. There is also limitation; for example, the minimum value of k is 1 to the maximum value of N. keep in mind that during summation x belongs to omega. The whole numerical sets mentioned above from (9) to (15) reflect the generalized solution methods for the histogram.

2.5. Image Segmentation through Iteration Point. In this part of image processing, every single image is divided into two main parts for segmentation: the background and the foreground. The endpoint or segmentation will stop when the goals are achieved by pointing or isolating the foreground from the image. The isolation processes of the foreground will lead us to the isolation of the background automatically. Achieving the automatic crack sealing of image processing, any researcher cannot ignore the importance of image segmentation [36]. In this part of image processing, the iteration point is used, and the image is having different segments explained under the subheadings.

2.6. Automatic Thresholding. The effective and reliable method is autothresholding, where the background noise is significantly minimized. Accomplish by utilizing a feedback

loop to optimize the thresholding value before converting the original grayscale image into binary. Because of the abundant research [37], a lot of methods for segmentation have been presented [38]. Two scientists, namely, Kaur and Singh, did their contribution to present different segmentation algorithms. They described the structural, stochastic, spectral, or hybrid techniques [39]. Thresholding is a technique that designates fixed point. If the image density on that specific point is less, then we consider that part of the image as black, but if the density of the picture is greater than the value of that fixed point, that part of the image is surely not black, so the alternate meaning is white. If X represents the fixed point and L_{ij} stands for density, then the white and black will be described as in equations (16) and (17).

$$Black \le L_{ij} \mathrm{X} L_{ij} \le White. \tag{16}$$

Simply put, the whole image is divided into two gray levels: one is for representing the foreground and the other is for background pixels.

$$S(x, y) = \int \begin{matrix} 0\, if\, g(x, y) \ge T(x, y) \\ 1\, if\, g(x, y) \le T(x, y). \end{matrix} \tag{17}$$

The general formula in equation (18) for $g(x, y)$ is the processed image that represents the grayscale of the pixel (x, y).

$$g(x, y) = T[f(x, y)]. \tag{18}$$

Equation (18) reflects the original image $f(x, y)$ enhancement by T and output gain is $g(x, y)$. As thresholding is a mapping of the binary set, the thresholding value will be at the coordinates, not a pixel, which is constant for every pixel of the image. Now, there are two ways if T defines the (x, y) on a certain field, this is known as template operation. But if T defines the (x, y) on each point, this is known as the point of operation [40]. As regards, the segmentation of the multireed solution image based on a graph-theoretic approach is used. Best thresholding can be improved through correlation, as it is known that the image might be the combination of different objects called heterogeneous images. We can find different objects and shapes like a kite, trees, wind, boy, and water in the same image. While considering the case of precise, accurate, and improved genetic algorithms, we divide the problem statement into two main classes under the umbrella of image segmentation.

(1) Parameter selection for the better result gained by the segmentation process.

(2) Involvement of region labeling of pixel-level segmentation.

In the above two mentioned algorithms, the first algorithm part is widely used because it requires the optimized parameters to be utilized. Besides this, there are so many other methods through which we can easily do the segmentation process. In the segmentation process, we have to divide the image into different segments through thresholding using different techniques like watershed techniques and iteration thresholding, and so on [41], in the iteration thresholding we use to find the minimum and maximum gray values to find the initial thresholding value, that is, $\mathrm{T}(i)$ for the functional variable in the following equation.

$$\mathrm{T}(i) = (Z_{max} + Z_{min})/2. \tag{19}$$

The above equation (19) shows the iteration thresholding mathematical equation in which $\mathrm{T}(i)$ shows the output gained as a result of iteration thresholding, where $Z_{\max}$ represents maximum gray value and $Z_{\min}$ represents minimum gray value. Table 2 illustrates the overall features of extraction methods.

2.7. Crack Detector Methods and Their Classification. Different algorithms are mentioned in Table 2 and three like MSER [42], Laplacian of Gaussian [43], unitary transforms [44], and various methods have been used by the researchers for image feature extraction [44] and the most convenient and reliable is Harris and Stephens detector [45] mentioned in Table 3. In the Harris detector, intensity will be changed for shift $[u, v]$ [46].

$$E(u, v) = \sum_{x,y} w(x, y)[I(x + u, y + v) - I(x, y)]^2. \tag{20}$$

In the above equation (20), the shifted intensity is shown by $I(x + u, y + v)$. In the abovementioned equation, the submission and x, y is noticed with the shifting intensity.

$$I(x + u, y + v). \tag{21}$$

$I(x, y)$. stands for the intensity of the specified pixels with the shift of u and v as shown in equation (21). In the following equation, the intensity of the specified pixel is subtracted from the shifted intensity pixel value.

$$I(x + u, y + v) - I(x, y). \tag{22}$$

Nearly constant patches will be close to the value of 0 and larger than zero for distinctive patches, which are identified already. So we need patches where $E(u, v)$ is larger to be started. The automatic clustering technique has been used by Porter and Canagarajah [47, 48] for the extraction of image features.

3. Simulations for the Experimental and Numerical Crack Detection

Every technique has its benefits and drawbacks. It is depending on the requirement of the research, resources, and desired output. Just like for noise filters, we can use different filters like low-pass filter, high-pass filter, or mean median [49].

3.1. Implemented Software. All the techniques and processes were done in the well-known software MATLAB because this software gives us the best environment for image processing simulation. Processing the images as the

Table 2: Feature extraction overall table.

Grey Scale subimage	Binary solid character	Outer contour	Vector
Template matching	Template matching		Template matching
Deformable template			Deformable template
Unitary transforms	Unitary transforms		Graph description
	Projection histogram	Contour profiles	Discrete features
Zoning	Zoning	Zoning	Zoning
Geometric moments	Geometric moments	Spline curve	
Zernike moments	Zernike moments	Fourier description	Fourier description

Table 3: Common crack detector methods and their classification table.

Feature detector	Edge	Corner	Blob
Canny	×		
Sobel	×		
Kayyali	×		
Harris and Stephens/Plessey/Shi-Tomasi	×	×	
SUSAN	×	×	
Shi and Tomasi		×	
Level curve curvature		×	
FAST		×	×
Laplacian of Gaussian		×	×
Difference of Gaussian		×	×
Determinant of Hessian		×	×
MSER			×
PCBR			×
Grey-level blobs			×

input after processing gaining the output is very easy and inexpensive with the Image Processing Toolbox [44]. One of the key points of using this software is the controlling features, as the control of input and the program can be stopped at every stage if needed [45]. This software is very approachable and friendly because while editing, we do not need to rewrite and run all the programs from the beginning as we do in other programming software like C or C++. So, with this, the researcher saved a lot of time and energy while achieving a better outcome than others like C or C++. For this experiment, NVIDIA GPU has been used, which speeds up the processing with no need to consume and is also suitable for using GUI (graphical user interface) to enable command control parameters. GPU is also essential for processing all the above techniques [46]. The device specification on which these experiments are performed is given in Table 4 below.

4. Description of the Experiment

For the experimental purpose here, the Dell laptop was used, with the Central Processing Unit of Core i7. The system model is 8565U having a 1.80 GHz and 1.99 GHz Intel processor. The useable RAM of 7.82 GB and the operating system of 64 bit. MATLAB 2015a is the best option for simulation and analysis of gained data that are images. Different images were captured from the camera with different specifications, but the processed image in MATLAB 2015a was having a size of $318 \times 307 \times 3$, which acquires a total size of 292878 bytes with unit 8.

5. Experimental Results and Analysis

The digital image constitutes every finite element with a particular location, worth, and value, which specifies the location known as an image element, pixel, or picture element [7]. So, in the image enhancement part, the brightness of the pixel is increased for a better understanding of machines or human visualization. In a classical way, histogram equalization of an image is analyzed independently from its contrast [4–29]. It comprises applying an extraordinary difference change that straightens the histogram. It can be done either identically or powers the repartition capacity to be as direct as could reasonably be expected. Histogram adjustment is not an appropriate answer for difference invariant image analysis. The mode of the neighbor is called the "window," that is, sliding, entering through the entry, exceeding the entire signal. For 1D signals, the most obvious window is just a few entries before and after, while for 2D or more dimensions, the more complex window pattern can be a "square" or "cross" pattern [50].

Figure 6 shows the origination of the experimental image that is taken from the camera as shown in Figure 6(b); its mathematical histogram is dragged while 6(c) is the graphical representation of the original image. Later in this research, it will be compared to the current research and previous literature.

While the image is visualized it becomes crystal clear that the background pixel varies from point to point. So, in the section of preprocessing, the uniformity tried has been observed by making the pixel uniform within a range. So, Figures 7(a) to 7(c) depict different stages and changes of approximate background and also its subtraction from original image 7(c), so that it can be added up and the variance of the pixel can be visualized and experienced. For creating an approximate background according to the composed algorithm, the morphological process is used with its suitable radius. For better visualization effect in Figure 7 in colored parametric surfaces, explain and sort out the study and study its mathematical functions in the region of the rectangle.

6. Adaptive Histogram Adjustment and Modification

In this part of the research, the subhistograms are adjusted and modified using histogram equalization [51]. For each subhistogram, segmentation is used. This method is effective for noise removal and better visual contrast.

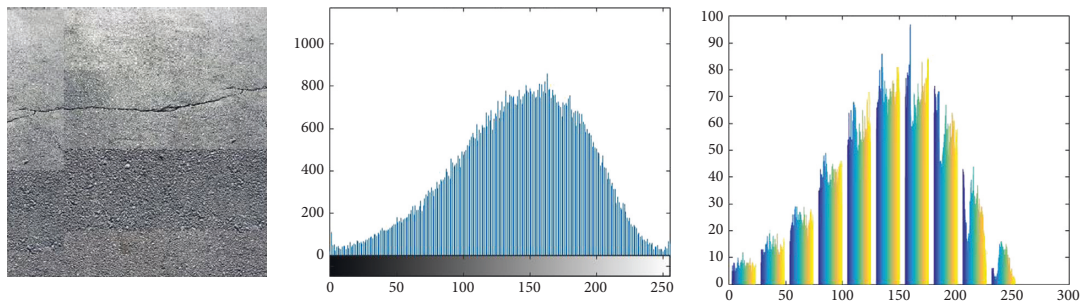

(a) (b) (c)

Figure 6: Original image histogram graphical representation. (a) Original image. (b) Original image histogram. (c) Original image graphical representation.

Table 4: Device specification.

Name	Specification
Device name	DESKTOP-G5S8E03
Processor	Intel® Core™ i7-8565U
CPU	1.80 GHz 1.99 GHz
Installed RAM	8.00 GB (7.80 GB useable)
Device ID	C1C9DA2A-6178-4297-9A17-A6CC8DC2D436
System type	64-bit operating system, x64-based processor
Pen and touch	No pen or touch input is available for this display
Product ID	Product ID 00330-80000-00000-AA020
Edition	Windows 11 Pro
Version	21H2
OS build	22000.434
Experience	Windows feature
Experience pack	1000.22000.434.0
Series	Intel Core i7
Socket	BGA1528
Features	Dual-channel DDR4 memory controller, hyperthreading, AVX, AVX2, quick sync, virtualization, AES-NI
GPU	Intel UHD graphics 620 (300–1150 MHz)

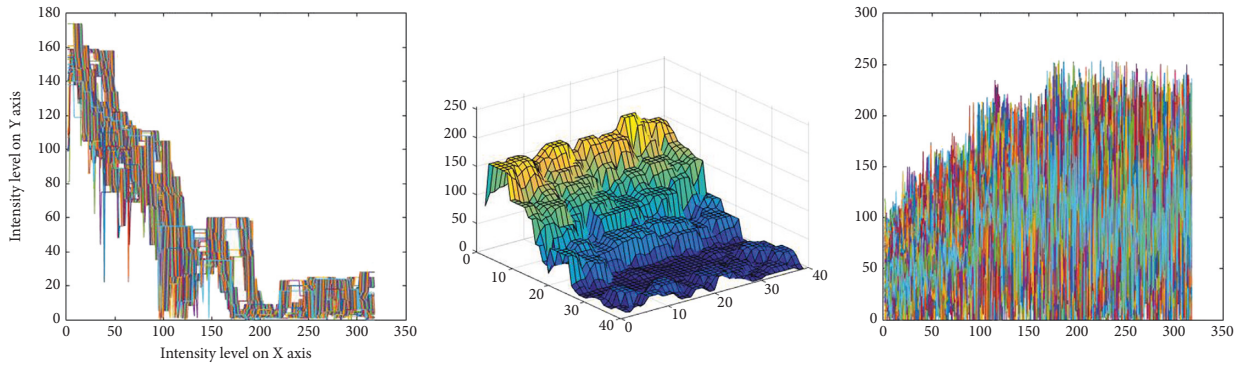

(a) (b) (c)

Figure 7: Graphical representation of the approximate background. (a) Approximate background. (b) Y-axis display in case. (c) Subtraction of approximate of reverse part from original image.

(1) Assume $A \times G$ is filtering (smoothing).

(2) $A \times (d-G)$ contains the high frequency.

(3) $A + lA \times (d-G) = A \times ((1+l) \quad d-lG) = A \times S(l)$ amplifies fine details in the image.

(4) The parameter l controls the quantity of amplification.

After propagating the approximate background and subtracting it from the original image, the output image has been adjusted and represented in Figure 8, in which 8(a) is showing adjusted image graphical representation, (8(b)) tells us about the adjusted image histogram, and 8(c) is the plotting representation of the adjusted image. The next processing step is the adaptation of the image that is proposed.

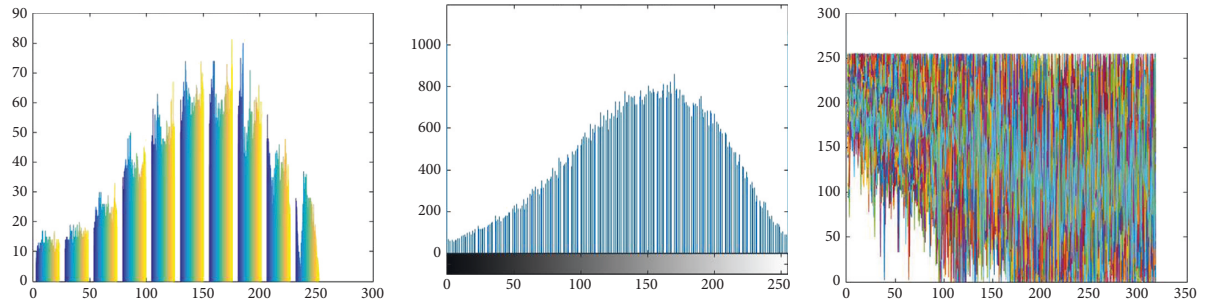

Figure 8: Graphical representation of the adjusted image. (a) Adjusted image graphical representation. (b) Adjusted image histogram. (c) Plotting representation of adjusted image.

Figure 9: Graphical representation of the adopted image. (a) Adapted histogram graphical representation. (b) Adapt histogram. (c) Adapted image histogram.

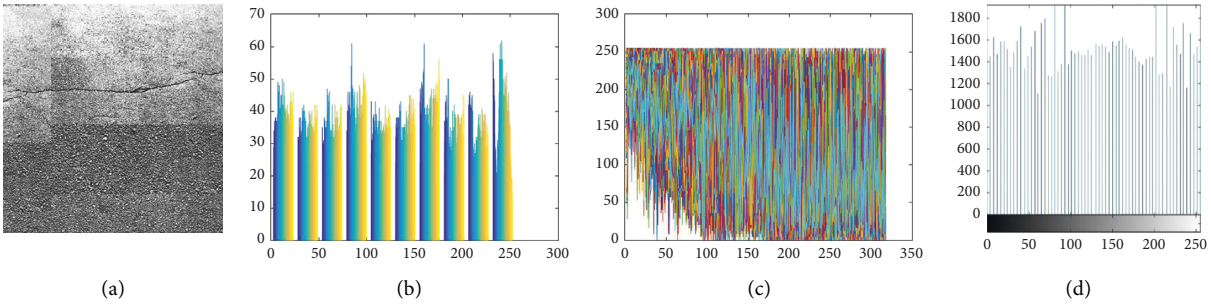

Figure 10: Equalized image histogram graphical representation. (a) Equalized image. (b) Histogram after equalization of image. (c) Plotting representation of equalized image. (d) Equalized image histogram.

Figures 9(a) to 9(c) are presenting adapted histogram graphical representation, adapt histogram, and adapted image histogram, respectively. While analyzing Figure 9above, it became very clear that the pixel is contrasted. After subtracting the approximate background, adjusting the image, and finally, the adopted image is gained. After it is compared, the huge difference is been noticed between pro and pre adapted image. The method application yields the processed image for us equalized histogram, as shown in Figure 10(d).

The output gain in Figure 10 of the whole histogram is shown and well explained in Figures 10(a) to 10(d). It reflects the final histogram that is distributed according to the pixel value. According to the image, the pixel value on every spot irrespective of center, upper, or lower side is almost the same as the pixel values are equalized and uniformly distributed shown in the above figures.

In Figure 11, the comparison between the different feature extractions like Harris, SURF, and MSERF is shown

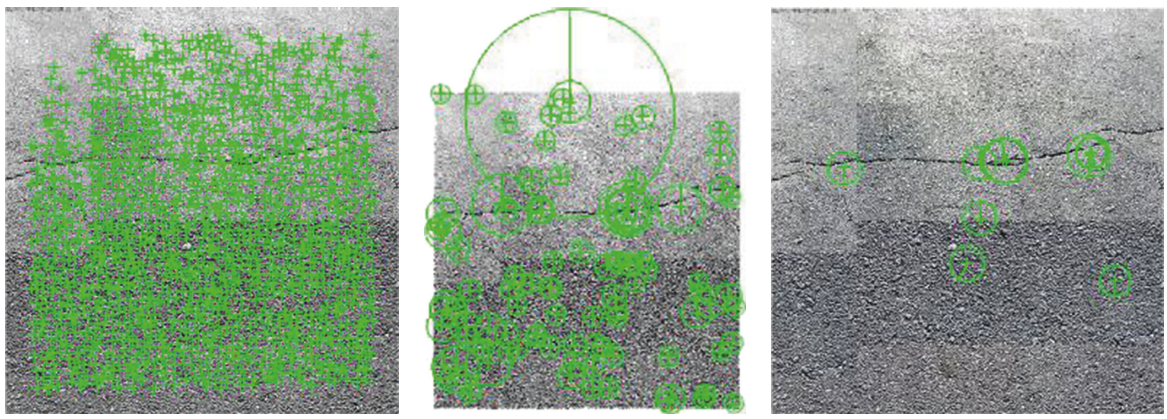

(a) (b) (c)

Figure 11: Features extracted comparison of different methods. (a) Harris features. (b) MSERF features. (c) SURF features.

as was already discussed in Table 3. It comprises an extraordinary difference change that straightens the histogram trend. It can be done either identically or powers the repartition capacity to be as direct as could reasonably be expected. For a few of the cases, the histogram adjustment may not be an appropriate answer for difference invariant image analysis [48]. A minor region of the image, either dark or bright, influenced the result of the histogram equalization. We observe the scenes of images with different angles and concentrations. That led us to become insensitive towards local contrast changes in scenes [52]. On the other hand, it is questioned that histogram equalization is unpredictable sometimes because it could deeply enlarge the noise amplitude in poorly contrasted regions [53], so they can produce unwanted noise textures. Histogram equalization cannot permit complete control of the noise application. It is risky if used as an input of the image analysis device.

7. Conclusions

This article provides an understandable explanation of different stages of digital image processing along with their implementation with the help of software through different variations. Initially, image processing is done, and processed images are enhanced using image enhancement. It validates the numerical and experimental model for the paved crack analysis through the software simulation for every stage and the degree of precision and improvements. The results lie in significant agreement compared with the existing models; they are also verified in the simulation result. In the implemented algorithms, it is found that the features are extracted in our very unique way. The results strongly support the conclusion that the noise parameters are effectively released with median filtering. Different feature extractors are used like Harris, MSERF, and SURF for features extraction. Regardless of the effectiveness and robustness of the executed techniques in MATLAB, there is some margin of improvement while studying crack detection for dynamic design. In the future, we can also implement using other algorithms and do a comparison with implemented algorithms.

Data Availability

The comparative and experimental data used to support the findings of this study are available from the corresponding author upon request.

Conflicts of Interest

There are no conflicts of interest regarding the publication of this paper.

References

[1] Y. Pan, X. Zhang, G. Cervone, and L. Yang, "Detection of asphalt pavement potholes and cracks based on the unmanned aerial vehicle multispectral imagery," *Ieee Journal of Selected Topics in Applied Earth Observations and Remote Sensing*, vol. 11, no. 10, pp. 3701–3712, 2018.

[2] S. Zhaoyun, L. Wei, and S. Aimin, "Automatic Detection System for Pavement Cracks Based on Digital Image," in *Proceedings of the 2010 Sixth International Conference on Natural Computation*, Yantai, China, Augest 2010.

[3] A. Ammouche, D. Breysse, H. Hornain, O. Didry, and J. Marchand, "New image analysis technique for the quantitative assessment of microcracks in cement-based materials," *Cement and Concrete Research*, 2000.

[4] A. Ammouche, J. Riss, D. Breysse, and J. Marchand, "Image analysis for the automated study of microcracks in concrete," *Cement and Concrete Composites*, vol. 23, no. 2-3, pp. 267–278, 2001.

[5] J. Tang and Y. Gu, "Automatic crack detection and segmetnation using a hybrid algorithm for road distress analysis," in *Proceedings - 2013 IEEE International Conference on Systems, Man, and Cybernetics, SMC*, Manchester, UK, October 2013.

[6] H. Oliveira and P. L. Correia, "Automatic crack detection on road imagery using anisotropic diffusion and region linkage," in *Proceedings of the European Signal Processing Conference*, Lisboa, Portugal, Augest2010.

[7] A. Jasim, H. Wang, G. Yesner, A. Safari, and A. Maher, "Optimized design of layered bridge transducer for piezoelectric energy harvesting from roadway," *Energy*, vol. 141, pp. 1133–1145, 2017.

[8] J. L. Groeger, P. Stephanos, P. Dorsey, and M. Chapman, "Implementation of Automated Network-Level Crack

Detection Processes in Maryland," *Transportation Research Record*, 2003.

[9] A. Di Graziano, V. Marchetta, and S. Cafiso, "Structural health monitoring of asphalt pavements using smart sensor networks: a comprehensive review," *Journal of Traffic and Transportation Engineering*, vol. 7, no. 5, pp. 639–651, 2020.

[10] W. Li, Z. Sun, X. Hao, X. Feng, and H. Zhao, "Measuring Method for Asphalt Pavement Texture Depth Based on Structured-Light Technology," *Advances in Transportation Studies*, vol. 36, 2015.

[11] R. Salini, B. Xu, and P. Paplauskas, "Pavement distress detection with picucha methodology for area-scan cameras and dark images," *Stavebni obzor-Civil Engineering Journal*, vol. 26, no. 1, pp. 34–45.

[12] A. Ullah, H. Elahi, Z. Sun, A. Khatoon, and I. Ahmad, "Comparative analysis of AlexNet, ResNet18 and SqueezeNet with diverse modification and arduous implementation," *Arabian Journal for Science and Engineering*, vol. 47, no. 2, pp. 2397–2417, 2021.

[13] J. E. Moore, S. Jitprasithsiri, and H. Lee, "Geographic Information System Technology and its Applications in Civil Engineering," *Civ. Eng. Syst.*, 1995.

[14] W. Li, R. Deng, Y. Zhang, Z. Sun, X. Hao, and J. Huyan, "Three-Dimensional Asphalt Pavement Crack Detection Based on Fruit Fly Optimisation Density Peak Clustering," *Mathematical Problems in Engineering.*vol. 2019, 2019.

[15] A. Vedrtnam, S. J. Pawar, and S. J. Pawar, "Laminated plate theories and fracture of laminated glass plate - a review," *'Engineering Fracture Mechanics*, vol. 186, pp. 316–330, 2017.

[16] J. Bauer, A. Sycev, and K. Blankenbach, *Image enhancement,"Handbook of Visual Display Technology*, Springer, Cham, 2016.

[17] G. Sayeed Ahmed, A. Algahtani, E. Mahmoud, and I. Badruddin, "Experimental Evaluation of Interfacial Surface Cracks in Friction Welded Dissimilar Metals through Image Segmentation Technique (IST)," *Materials (Basel)*, vol. 11, 2018.

[18] D. E. Ilea, P. F. Whelan, and P. Paplauskas, "Image segmentation based on the integration of colour–texture descriptors—a review," *Pattern Recognition*, vol. 44, no. 10–11, pp. 2479–2501, 2011.

[19] W. Wang, N. Yang, Y. Zhang, F. Wang, T. Cao, and P. Eklund, "A review of road extraction from remote sensing images," *Journal of Traffic and Transportation Engineering*, vol. 3, no. 3, pp. 271–282, 2016.

[20] S. Du, Y. Zhang, Z. Zou, S. Xu, X. He, and S. Chen, "Automatic building extraction from LiDAR data fusion of point and grid-based features," *ISPRS Journal of Photogrammetry and Remote Sensing*, 2017.

[21] R. Alshehhi, P. R. Marpu, W. L. Woon, and M. D. Mura, "Simultaneous extraction of roads and buildings in remote sensing imagery with convolutional neural networks," *ISPRS Journal of Photogrammetry and Remote Sensing*, vol. 130, pp. 139–149, 2017.

[22] R. Alshehhi and P. R. Marpu, "Hierarchical graph-based segmentation for extracting road networks from high-resolution satellite images," *ISPRS Journal of Photogrammetry and Remote Sensing*, vol. 126, pp. 245–260, 2017.

[23] Z. Qu, Y. Xing, and Y. Song, "An Image Enhancement Method Based on Non-subsampled Shearlet Transform and Directional Information Measurement," *Information*, vol. 9, no. 11, 2018.

[24] A. Kaur and C. Singh, "Contrast enhancement for cephalometric images using wavelet-based modified adaptive histogram equalization," *Applied Soft Computing*, vol. 51, pp. 180–191, 2017.

[25] Z. Wang, C. Zhang, Z. Pan et al., "Image segmentation approaches for weld pool monitoring during robotic arc welding," *Applied Sciences*, vol. 8, no. 12, p. 2445, 2018.

[26] R. Martín-Nieto, Á. García-Martín, J. Martínez, and J. SanMiguel, "Enhancing Multi-Camera People Detection by Online Automatic Parametrization Using Detection Transfer and Self-Correlation Maximization†," *Sensors*, vol. 18, no. (12), 2018.

[27] M. Song, H. Qu, G. Zhang, S. Tao, and G. Jin, "A variational model for sea image enhancement," *Remote Sensing*, vol. 10, no. 8, p. 1313, 2018.

[28] R. Sharma, A. Sharma, S. Kwon, and R. Booth, "Contrast enhancement methods in sodium MR imaging: a new emerging technique," *Journal of Biomedical Science and Engineering*, vol. 02, no. 06, pp. 445–457, 2009.

[29] J. Mun, Y. Jang, Y. Nam, and J. Kim, "Edge-enhancing bi-histogram equalisation using guided image filter," *Journal of Visual Communication and Image Representation*, vol. 58, pp. 688–700, 2019.

[30] M. Mangeruga, F. Bruno, M. Cozza, P. Agrafiotis, and D. Skarlatos, "Guidelines for underwater image enhancement based on benchmarking of different methods," *Remote Sensing*, vol. 10, no. 10, p. 1652, 2018.

[31] H. Vaishnav and H. Garg, "Image processing using xilinx system generator (XSG) in FPGA," *Ijrsi*, vol. II, no. Ix, pp. 119–125, 2015.

[32] R. F. Swati, A. A. Khan, and L. H. Wen, "Weight optimized main landing gears for UAV under impact loading for evaluation of explicit dynamics study," in *Proceedings of the Advanced Materials, Structures and Mechanical Engineering - Proceedings of the International Conference on Advanced Materials, Structures and Mechanical Engineering*, South-Korea, May2015.

[33] P. Murugeswari and D. Manimegalai, "Noise Reduction in Color Image Using Interval Type-2 Fuzzy Filter (IT2FF)," *International Journal of Engineering Science and Technology*, vol. 3, no. (2), 2011.

[34] H. Liu, W. Li, Y. Hou, and Z. Sun, "Aggregate grading composition analysis method based on 3D data," *Beijing Gongye Daxue Xuebao/Journal Beijing Univ. Technol.*vol. 43, no. 10, pp. 1521–1528, 2017.

[35] M. Zarie, H. Hajghassem, and A. Eslami Majd, "Contrast Enhancement Using Triple Dynamic Clipped Histogram Equalization Based on Mean or Median," *Optik (Stuttg)*, vol. 175, 2018.

[36] M. Gavilán, D. Balcones, M. Ocaña et al., "Adaptive road crack detection system by pavement classification," *Sensors*, vol. 11, no. 10, pp. 9628–9657, 2011.

[37] D. Kaur and Y. Kaur, "International Journal of Computer Science and Mobile Computing," *Various Image Segmentation Techniques: A Review*, vol. 3, no. 5, pp. 809–814, 2014.

[38] J. Verrelst, J. Rivera Caicedo, J. Vicent, P. Morcillo Pallarés, and J. Moreno, "Approximating empirical surface reflectance data through emulation: opportunities for synthetic scene generation," *Remote Sensing*, vol. 11, no. 2, p. 157, 2019.

[39] C. Singh and A. Kaur, "Fast computation of polar harmonic transforms," *Journal of Real-Time Image Processing*, vol. 10, no. 1, pp. 59–66, 2015.

[40] R. Firoz, M. S. Ali, M. N. U. Khan, M. K. Hossain, M. K. Islam, and M. Shahinuzzaman, "Medical image enhancement using morphological transformation," *Journal of Data Analysis and Information Processing*, vol. 04, no. 01, pp. 1–12, 2016.

[41] R. Salini, B. Xu, and P. Paplauskas, "Pavement distress detection with picucha methodology for area-scan cameras and dark images," *Stavební obzor - Civil Engineering Journal*, vol. 26, no. 1, pp. 34–45, 2017.

[42] J. Tang, "First international conference on artificial intelligence and cognitive computing," *Expert Systems With Applications*, vol. 38, pp. 19–22, 2009.

[43] A. Akagic, E. Buza, S. Omanovic, and A. Karabegovic, "Pavement crack detection using Otsu thresholding for image segmentation," in *Proceedings of the 2018 41st International Convention on Information and Communication Technology, Electronics and Microelectronics (MIPRO)*, vol. 815, no. c, pp. 9628–9657, Opatija, Croatia, May2018.

[44] A. K. Tiwari, V. Kanhangad, and R. B. Pachori, "Histogram Refinement for Texture Descriptor Based Image Retrieval," *Signal Process. Image Commun*, vol. 53, pp. 73–85, 2017.

[45] D. Frolova and D. Simakov, "Harris Corner Detector Slides Taken from," *Matching with Invariant Features*, 2004.

[46] B. Zhang and X. Liu, "Intelligent pavement damage monitoring research in China," *IEEE Access*, vol. 7, pp. 45891–45897, 2019.

[47] R. Porter and N. Canagarajah, "A Robust Automatic Clustering Scheme for Image Segmentation Using Wavelets," *IEEE Trans. Image Process*, vol. 5, pp. 662–665, 1996.

[48] R. Porter and N. Canagarajah, "Robust Rotation-Invariant Texture Classification: Wavelet, Gabor Filter and GMRF Based Schemes," *Vision, Image Signal Process*, IEE Proc.-, 1997.

[49] L. Su, L. Ma, N. Qin, D. Huang, and A. H. Kemp, "Fault diagnosis of high-speed train bogie by residual-squeeze net," *IEEE Transactions on Industrial Informatics*, vol. 15, no. 7, pp. 3856–3863, 2019.

[50] B. Yuan and M. Liu, "Power Histogram for circle Detection on Images," *Pattern Recognit*, vol. 48, no. (10), pp. 3268–3280, 2015.

[51] Z. Chen, X. Hao, and Z. Sun, "A modified bayes shrinkage in shearlet domain combined with p-Laplace anisotropic diffusion for image denoising," *ICIC Express Letters*, vol. 7, no. 10, pp. 2691–2696, 2013.

[52] Z. Xu, K. Yang, and Y. Li, "A physiologically-based adaptive three-Gaussian function model for image enhancement," *International Journal of Intelligence Science*, vol. 05, no. 02, pp. 72–79, 2015.

[53] G. Xuan, X. Li, and Y.-Q. Shi, "Minimum entropy and histogram-pair based JPEG image reversible data hiding," *Journal of Information Security and Applications*, vol. 45, pp. 1–9, 2019.

Hindawi
Mathematical Problems in Engineering
Volume 2022, Article ID 4251341, 8 pages
https://doi.org/10.1155/2022/4251341

Research Article

The Spatio-Temporal Variation of Isothermal Water Mass in Jiaozhou Bay

Dongfang Yang [1,2]

[1]*Accountancy School, Xijing University, Xi'an 710123, China*
[2]*North China Sea Environmental Monitoring Center, SOA, Qingdao 266033, China*

Correspondence should be addressed to Dongfang Yang; dfyang_dfyang@126.com

Received 18 February 2022; Accepted 5 May 2022; Published 11 June 2022

Academic Editor: Jinyan Song

According to the survey materials of the waters of Jiaozhou in April and August 1981, the author determined the variation range of temperature, location, and the variation process of isothermal water mass in the waters of Jiaozhou Bay. The results showed that in April, high-temperature water masses were formed in the coastal waters of Jiaozhou Bay from the northeast to the northwest, and the water temperature reached 12.82–13.70°C, where the length of the interval of seawater temperature change was 0.88°C. In August, the high-temperature water masses were formed in the coastal waters of Jiaozhou Bay from the northwest to the north with the high temperature within 27.32–27.37°C, where the length of the interval was 0.05°C. In April and August, the high-temperature water masses were formed in the northern coastal waters where the depth was 1.00–5.00 m. The heat of high-temperature water masses was sourced from solar radiation energy. In August and in the coastal waters near the estuary of Haibo River, high-temperature water masses were formed, with a high water temperature of 28.00–30.90°C. The high temperature of the Haibo River provided heat to the waters of Jiaozhou Bay. In April, a circular low-temperature water mass was formed in the central waters of the bay, and the water temperature reached a low temperature of 7.52–8.51°C, which indicated that the central waters of the bay still maintained the uniform low temperature in winter and formed a low-temperature water mass. Therefore, the innovation of this paper is to put forward the spatio-temporal variation of the isothermal water mass in Jiaozhou Bay, established the block diagram of temperature changes in the waters of Jiaozhou Bay in April and August, and further elaborated the characteristics of isothermal water masses. (1) At the same time change, both the high-temperature water mass and the low-temperature water mass have stability. (2) In different time changes, whether it is a high-temperature water mass with a relatively higher water temperature or a high-temperature water mass with a very high water temperature, the water mass is stable.

1. Introduction

The ocean occupies 71% of the Earth's surface area. At the same time, the heat capacity of seawater greatly exceeds the heat capacity of land and air. Therefore, the ocean plays a great role in climate regulation on the entire Earth [1–10] to study the isothermal water mass in the coastal waters and its variation process benefits to the sustainable development of marine ecosystems. According to the survey materials in 1981, the author determined the temperature ranges, position, and variation process of isothermal water mass in the waters of Jiaozhou Bay and obtained the heat sources in the waters of Jiaozhou Bay and spatio-temporal variation process of isothermal water masses, providing the scientific theoretical basis for the study of water temperature changes in Jiaozhou Bay. The results showed that in April, high-temperature water masses were formed in the coastal waters of Jiaozhou Bay from the northeast to the northwest, and the water temperature reached 12.82–13.70°C, where the length of the interval of seawater temperature change was 0.88°C. In August, the high-temperature water masses were formed in the coastal waters of Jiaozhou Bay from the northwest to the north with the high temperature within 27.32–27.37°C, where the length of the interval was 0.05°C. In April and August, the high-temperature water masses were formed in the northern coastal waters where the depth was 1.00–5.00 m. The heat of high-temperature water masses was sourced from solar radiation energy. In August and in the

coastal waters near the estuary of Haibo River, high-temperature water masses were formed, with a high water temperature of 28.00–30.90°C. The high temperature of Haibo River provided heat to the waters of Jiaozhou Bay. In April, a circular low-temperature water mass was formed in the central waters of the bay, and the water temperature reached a low temperature of 7.52–8.51°C, which indicated that the central waters of the bay still maintained the uniform low temperature in winter and formed a low-temperature water mass.

2. Survey Waters, Materials, and Methods

2.1. Natural Environment of Jiaozhou Bay. Jiaozhou Bay is located in the southern part of the Shandong Peninsula. Its geographical position is between 120°04′–120°23′E and 35°58′–36°18′N. It is bounded by the line connecting Tuan Island and Xuejia Island and is connected to the Yellow Sea. With an area of about 446 km^2 and an average water depth of about 7 m, it is a typical semienclosed bay. There are more than a dozen rivers entering the sea in Jiaozhou Bay, among which are the Dagu River, Yang River, the Haibo River, Licun River, and Loushan River in Qingdao City with larger runoff and sand content. These rivers are all seasonal rivers, and the river hydrological characteristics have obvious seasonal changes [11, 12].

2.2. Materials and Methods. The survey data of water temperature in the waters of Jiaozhou Bay in April and August 1981 used in this study are provided by the North Sea Monitoring Center of the State Oceanic Administration. In April, water samples are taken from 30 stations: A1, A2, A3, A4, A5, A6, A7, A8, B1, B2, B3, B4, B5, C1, C2, C3, C4, C5, C6, C7, C8, D1, D2, D3, D4, D5, D6, D7, D8, D9. In August, water samples are taken from 29 stations: A1, A2, A3, A4, A5, A6, A7, A8, B1, B3, B4, B5, C1, C2, C3, C4, C5, C6, C7, C8, D1, D2, D3, D4, D5, D6, D7, D8, D9 (Figure 1). Water samples were taken according to the water depth (surface and bottom layers were taken when the depth >10 m, and only the surface layer was taken when the depth <10 m) for investigation and sampling. The survey of water temperature in Jiaozhou Bay water body was carried out according to the national standard method, which was recorded in the national "Marine Monitoring Code" (1991) [13].

3. Results

3.1. The Definition of Yang Dongfang Water Mass and Isothermal Water Mass. The concept of water mass proposed by Yang Dongfang refers to a water body composed of a certain point or two points or multiple points, which have a certain common feature, which is called a water mass with a certain feature [14–18]. The definition of this water mass is proposed by the author to distinguish it from other concepts of water mass. It can be called the Yang Dongfang water mass. Yang Dongfang further proposed the concept of the isothermal water mass, which is defined as compared with the surrounding waters, a water body centered on a certain water area that has a relatively similar temperature. The water body of this water area is called Yang Dongfang isothermal water mass or isothermal water mass for short. For Yang Dongfang isothermal water mass, if the water temperature of the water mass is relatively high, it is called Yang Dongfang high-temperature water mass; if the water temperature of the water mass is relatively low, it is called Yang Dongfang low-temperature water mass; compared with other water temperatures, if the water temperature of the water mass is the median, it is called Yang Dongfang medium-temperature water mass [19–25].

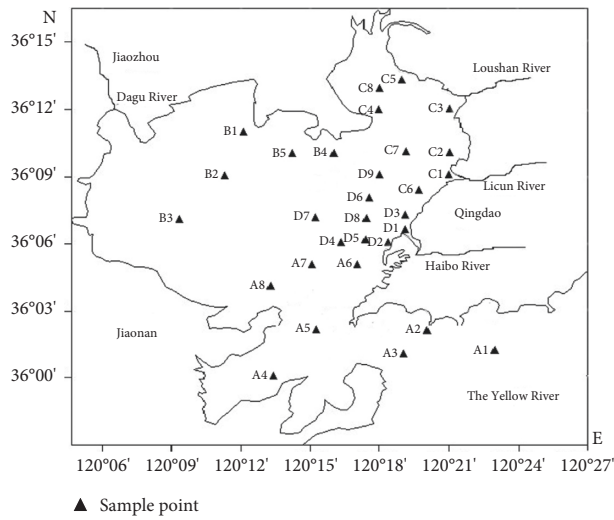

Figure 1: Investigation site of Jiaozhou Bay.

3.2. Yang DongFang High-Temperature Water Mass. In April, in the northeastern of Jiaozhou Bay, at station C3 in the coastal waters of the estuary of Loushan River and station C5 in the coastal waters, and at station B1 in the coastal waters of the northwest, that is, from the northeast along the northern coastal waters to the northwest, the water temperature reached [26–33] 12.82–13.70°C, and a high-temperature zone was formed with the northern coastal waters as the center. According to the definition of Yang Dongfang isothermal water mass, there was a high-temperature water mass in the waters of Jiaozhou Bay (Figure 2), located in the coastal waters from the northeast to the northwest. In this high-temperature water mass, the length of the interval of seawater temperature change was 0.88°C.

In August, at station B1 in the northwestern coastal waters and at station B4 in the northern coastal waters, that is, in the coastal waters from the northwest to the north, the water temperature reached a relatively high of 27.32–27.37°C, and a high-temperature zone was formed with the coastal waters from northwest to the north as the center. According to the definition of Yang DongFang isothermal water mass, there was a high-temperature water mass in the waters of Jiaozhou Bay (Figure 3), located in the coastal waters from northwest to the north. In this high-temperature water mass, the length of the interval of seawater temperature change was 0.05°C [34–40].

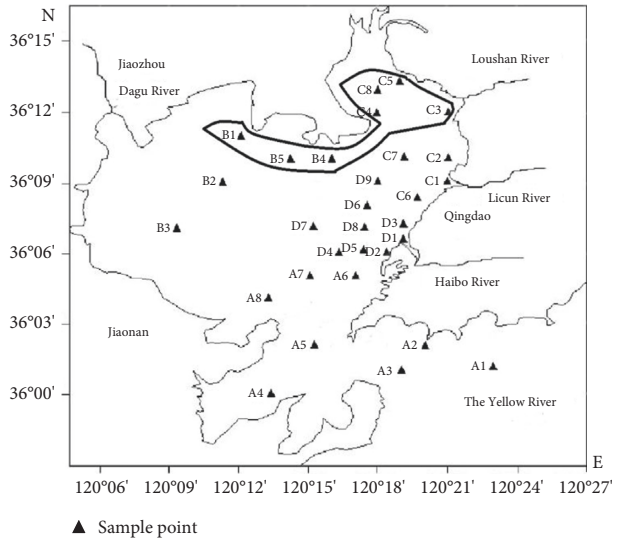

Figure 2: High-temperature water mass in the surface waters in April (°C).

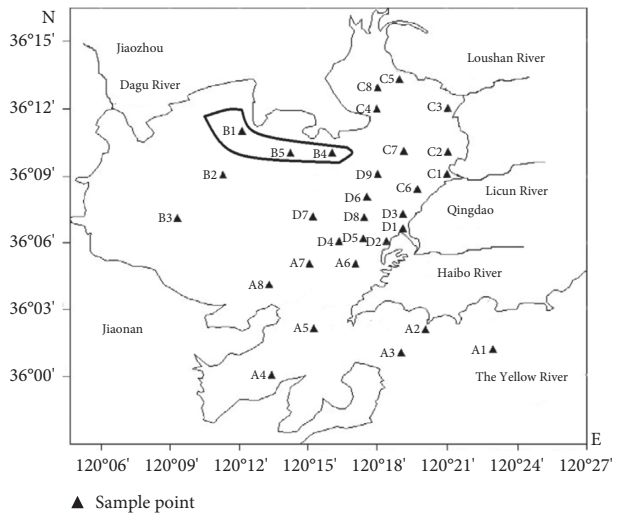

Figure 3: High-temperature water mass in the surface waters in August (°C).

In August, in the east of Jiaozhou Bay, at station D1 in the coastal waters of the estuary of Haibo River, the water temperature reached a relatively high of 30.90°C, and a high-temperature zone was formed with the coastal waters of the estuary of Haibo River as the center. According to the definition of Yang Dongfang isothermal water mass, there was a high-temperature water mass in the waters of Jiaozhou Bay (Figure 4), located in the coastal waters of the estuary of Haibo River. In this high-temperature water mass, the length of the interval of seawater temperature change was 2.90°C.

3.3. Yang Dongfang Low-Temperature Water Mass. In April, centering on station D7 in the central waters of the bay, covering stations A7 and D4 constituted a circular water area [41–45]. The water temperature reached a low temperature of 7.52–8.51°C, forming a low-temperature zone. In this way,

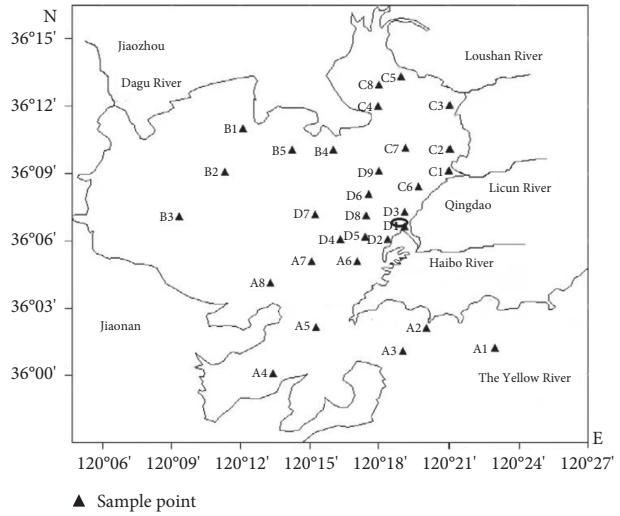

Figure 4: High-temperature water mass in the estuary of the river in Jiaozhou Bay in August 1981.

a closed-loop low-temperature zone appeared, the temperature of which was 7.52~8.51°C (Figure 5). According to the definition of Yang Dongfang isothermal water mass, there was a low-temperature water mass in the central waters of Jiaozhou Bay (Figure 5), located in the central waters of the bay. In this low-temperature water mass, the length of the interval of sea-water temperature change was 0.99°C.

4. Discussion

4.1. The Heat Sourced from Solar Radiation Energy. In April, a high-temperature water mass was formed in the coastal waters from the northeast to the northwest of Jiaozhou Bay [46–52]. In this high-temperature water mass, the water temperature reached a relatively high 12.82–13.70°C, and the length of the interval of water temperature change was 0.88°C. Moreover, this high-temperature water mass was in nearshore waters with a water depth of 1.00 to 5.00 meters.

In August, a high-temperature water mass was formed in the coastal waters from the northwest to the north of Jiaozhou Bay. In this high-temperature water mass, the water temperature reached a relatively high 27.32–27.37°C, and the length of the interval of water temperature change was 0.05°C. Moreover, this high-temperature water mass was in nearshore waters with a water depth of 2.00 to 5.00 meters.

The energy obtained by the Earth mainly comes from the sun. When seawater absorbs heat, short-wave radiation from the sun and long-wave radiation from the atmosphere bring heat to the sea. For the total solar radiation energy reaching the sea surface, coastal seawater can absorb up to 77.2% of the energy within one meter of the surface, and within 10 meters of the surface, the energy absorbed by the coastal seawater is as high as 99.6% [1]. In April and August, the high-temperature water masses were in the northern coastal waters of Jiaozhou Bay, with a water depth of 1.00 to 5.00 meters. Then, the heat source of the high-temperature water mass came from the total solar radiation energy, and the energy absorbed by the water body can reach more than

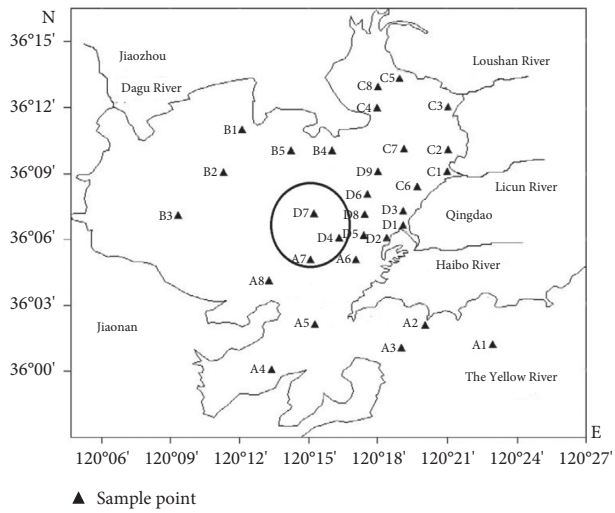

Figure 5: Low-temperature water mass in the central waters in April (°C).

80.0%. In this way, the heat source of the entire Jiaozhou Bay waters came from the northern coastal waters, and the northern coastal waters were heated by solar radiation energy.

4.2. Heat Source Input by River. In August, a high-temperature water mass was formed in the coastal waters of the estuary of Haibo River in the east of Jiaozhou Bay. In this high-temperature water mass, the water temperature reached a relatively high 28.00–30.90°C, and the length of the interval of water temperature change was 2.90°C. Moreover, this high-temperature water mass was in nearshore waters of the estuary of Haibo River with a water depth of 2.00 to 2.20 meters.

In August, solar radiation energy provided a lot of heat to the river. As the river flowed continuously, the total solar radiation heated up continuously. When the river reached the coastal waters of the estuary, the water temperature of the river was very high. When the river entered the coastal waters of the estuary, the water temperature reached the highest temperature of 30.90°C in the entire waters of Jiaozhou Bay. Therefore, in August, the river brought the high temperature to provide heat to the waters of Jiaozhou Bay.

4.3. The Formation Process of Low-Temperature Water Mass. In April, in the central water area of the bay, a circular water area was formed with this water area as the center, and a low-temperature water mass was formed. In this low-temperature water mass, the water temperature reached a low temperature of 7.52–8.51°C, and the length of the interval of seawater temperature change was 0.99°C. And this low-temperature water mass was in the central waters of the bay, with a water depth of 7.50–21.00 meters [47–50].

In winter, the entire sea area is controlled by the polar continental air mass, and strong northerly winds blow continuously over the sea. The seawater cools rapidly and evaporates strongly, with a strong vortex mix and convection mix, making the temperature from the sea surface to the seabed in many shallow water areas uniform [1]. With the end of winter and the advent of spring, the weather began to warm, and the total solar radiation energy began to gradually increase. As a result, in April, in the coastal waters of Jiaozhou Bay from the northeast to the northwest, where the water depth was 1.00 to 5.00 meters, it formed a high-temperature water mass. In the central waters of the bay, the water depth was 7.50–21.00 meters, and there was no heat source to provide heat to the central waters of the bay. In this way, the central waters of the bay still maintained the uniform low temperature in winter, forming a low-temperature water mass.

4.4. The Spatio-Temporal Variation of Isothermal Water Mass. The shape of the bay is like half a pot. In April, in the coastal waters of Jiaozhou Bay from the northeast to the northwest, the water depth was 1.00 to 5.00 meters. The solar radiation energy heated this water area, resulting in the rise of water temperature, 12.82–13.70°C, and forming a high-temperature water mass. The length of the interval of seawater temperature change was 0.88°C. It is like adding firewood to half a pot, and the temperature rises on the edge of the pot. The high-temperature water in the shallow water area cannot transfer heat to the central waters of the bay in time, and the water depth was 7.50–21.00 meters. In this way, there was no heat source to provide heat to the central waters of the bay. As a result, the central waters of the bay still maintained a uniform low temperature in winter, and the water temperature reached 7.52–8.51°C, forming a low-temperature water mass. The length of the interval of seawater temperature change was 0.99°C (Figure 6).

In August, solar radiation energy continued to heat this high-temperature water mass, causing the temperature of this high-temperature water mass to continue to rise, and the water temperature reached a higher 27.32–27.37°C. The length of the interval of seawater temperature change was 0.05°C. It is like adding firewood to half of the pot, and the temperature continues to rise on the edge of the pot. At the same time, the water temperature brought by the river at the estuary of the bay reached 30.90°C, which is the highest temperature in the entire waters of Jiaozhou Bay. As a result, in the coastal waters near the estuary of Haibo River, where the water depth was 2.00 to 2.20 meters, the high temperature of the river provided heat to the Jiaozhou Bay waters, resulting in the formation of high-temperature water mass in the coastal waters near the estuary of Haibo River, where the water temperature reached 28.00–30.90°C, and the length of the interval of seawater temperature change was 2.90°C. This is like sending a high-temperature stream of water to half of the pot, causing the edge of the pot to continue to rise in temperature. Moreover, in April, the low-temperature water mass formed in the central waters of the bay gradually turned into a medium-temperature water mass by August, and part of the heat of this water mass was transported to the outside of the bay. Here shows the variation process of the water mass in the center of the bay (Figure 7).

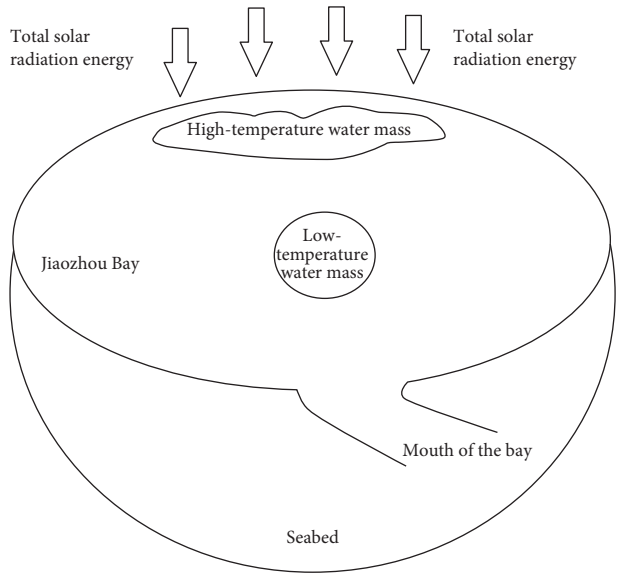

Figure 6: The block diagram of heat transfer of water temperature in April.

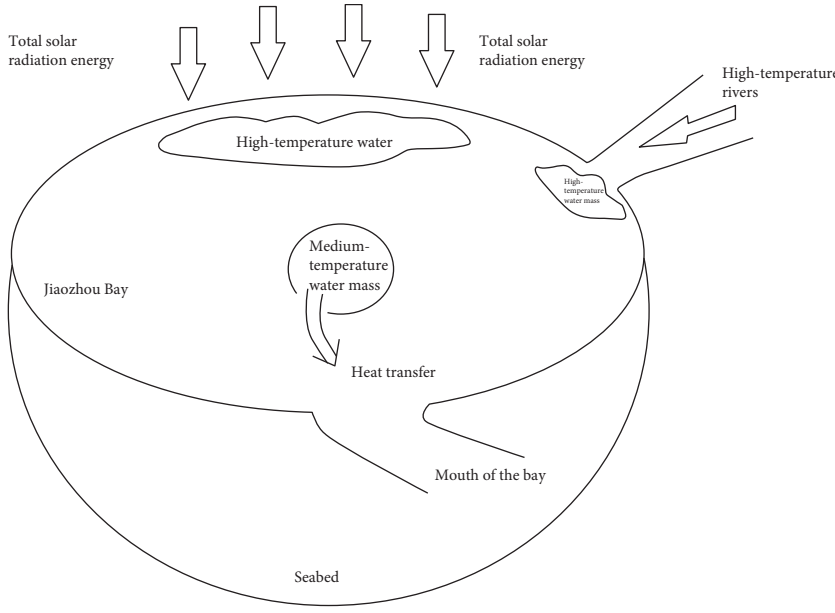

Figure 7: The block diagram of heat transfer of water temperature in August.

4.5. The Feature of Isothermal Water Mass. In April, the length of the interval of water temperature change in the high-temperature water mass was 0.88°C, which did not exceed 1.00°C. This showed that the high-temperature water mass was stable. The length of the interval of water temperature change of the low-temperature water mass was 0.99°C, which did not exceed 1.00°C, indicating that the low-temperature water mass was stable. Then, at the same time change, both the high-temperature water mass and the low-temperature water mass have stability.

In April, although the high-temperature water mass was very close to the low-temperature water mass, the water temperature of the high-temperature water mass was 12.82–13.70°C, and the water temperature of the low-temperature water mass was 7.52–8.51°C. It can be seen that the high-temperature water mass did not transfer the heat quickly to the low-temperature water mass.

In April, the water temperature of the high-temperature water mass reached a relatively high 12.82–13.70°C, and the length of the interval of water temperature change was 0.88°C, which did not exceed 1.00°C. This indicated that the high-temperature water mass with higher water temperature was stable. In August, in the high-temperature water mass, the water temperature reached a much higher 27.32~27.37°C, and the length of the interval of the water temperature change was 0.05°C, not exceeding 1.00°C. This showed that the high-temperature water mass with much higher water temperature was also stable. Then, in different

time changes, both the high-temperature water mass with high water temperature and the high-temperature water mass with much higher water temperature have stability.

5. Conclusion

In April, a high-temperature water mass was formed in the coastal waters from the northeast to the northwest of Jiaozhou Bay. In this high-temperature water mass, the water temperature reached a relatively high 12.82–13.70°C, and the length of the interval of water temperature change was 0.88°C. Moreover, this high-temperature water mass was in nearshore waters with a water depth of 1.00 to 5.00 meters. In August, a high-temperature water mass was formed in the coastal waters from the northwest to the north of Jiaozhou Bay. In this high-temperature water mass, the water temperature reached a relatively high 27.32–27.37°C, and the length of the interval of water temperature change was 0.05°C. Moreover, this high-temperature water mass was in nearshore waters with a water depth of 2.00 to 5.00 meters.

In April and August, the high-temperature water masses were in the northern coastal waters of Jiaozhou Bay, with a water depth of 1.00 to 5.00 meters. Then, the heat source of the high-temperature water mass came from the total solar radiation energy, and the energy absorbed by the water body can reach more than 80.0%. In this way, the heat source of the entire Jiaozhou Bay waters came from the northern coastal waters, and the northern coastal waters were heated by solar radiation energy.

In August, a high-temperature water mass was formed in the coastal waters of the estuary of Haibo River in the east of Jiaozhou Bay. In this high-temperature water mass, the water temperature reached a relatively high 28.00–30.90°C, and the length of the interval of water temperature change was 2.90°C. Moreover, this high-temperature water mass was in nearshore waters of the estuary of Haibo River with a water depth of 2.00 to 2.20 meters. With the high temperature, Haibo River supplied heat to the waters of Jiaozhou Bay.

In April, in the central water area of the bay, a circular water area was formed with this water area as the center, and a low-temperature water mass was formed. In this low-temperature water mass, the water temperature reached a low temperature of 7.52–8.51°C, and the length of the interval of seawater temperature change was 0.99°C. And this low-temperature water mass was in the central waters of the bay, with a water depth of 7.50–21.00 meters. There are no heat sources providing heat to the central waters of the bay. Thus, the central waters of the bay still maintained the uniform low temperature in winter and formed a low-temperature water mass.

In April, in the coastal waters of Jiaozhou Bay from the northeast to the northwest, the water depth was 1.00 to 5.00 meters. The solar radiation energy heated this water area, resulting in the rise of water temperature and forming a high-temperature water mass. However, the water with high temperature cannot transfer the heat immediately to the central waters of the bay. As a result, the central waters of the bay still maintained the uniform low temperature in winter and formed a low-temperature water mass. In August, solar radiation energy continued to heat this high-temperature water mass, causing the temperature of this high-temperature water mass to continue to rise. At the same time, in the coastal waters of the estuary of Haibo River, the river with high temperature supplied heat to the waters of Jiaozhou Bay, resulting in the formation of a high-temperature water mass in the coastal waters of the estuary of Haibo River. In addition, in April, the low-temperature water mass formed in the central waters of the bay gradually turned into a medium-temperature water mass by August, and part of the heat of this water mass was transported to the outside of the bay. Therefore, the author established the block diagram of the temperature changes in the waters of Jiaozhou Bay in April and August, presented the spatio-temporal variation process of isothermal water mass in Jiaozhou Bay, and elaborated the features of isothermal water mass: (1) in the same time change, both the high-temperature water mass and the low-temperature water mass have stability. (2) In different time changes, whether it is a high-temperature water mass with a relatively higher water temperature or a high-temperature water mass with a very high water temperature, the water mass is stable.

Data Availability

The data used to support the findings of this study are available from the corresponding author upon request.

Conflicts of Interest

The authors declare that they have no competing interests.

An earlier version of the paper has been presented at WCHBE 2021.

Acknowledgments

The authors thank WCHBE 2021 as an earlier version of it has been presented at the conference.

References

[1] J. Zeng, T. Zhang, W. Yang, Z. Ma, S. Li, and X. Zhang, "Karni period wet curtain: a review of climate-environment change and its effects on Marine ecology," *The Journal of Geology*, vol. 2022, no. 3, pp. 729–743, 2022.

[2] M. L. Zhou, "Marine meteorology," *Chinese World Window of the (Primary School)*, vol. 2022, no. 3, p. 79, 2022.

[3] X. Zhang, F. Zheng, L. I. Han, and D. Lu, "Multi-time scale variation characteristics and climate regulatory factors of global ocean heat wave," *Climatic and Environmental Research*, vol. 27, no. 1, pp. 170–182, 2021.

[4] L. Han and D. Lu, "Carbon neutral protection and development under the background of the rule of law of blue carbon path," *Journal of Northwest University for Nationalities (Philosophy and Social Sciences Edition)*, vol. 2022, no. 1, pp. 65–77, 2022.

[5] S. Hu, S. Li, H.-H. Sun, Y. G. Wang, and J. J. Luo, "Research progress and prospect of ocean heat wave," *Advances in Earth Science*, vol. 37, no. 1, pp. 51–64, 2021.

[6] H. Sun, Y. Wang, and J. Luo, "Effects of ocean data assimilation on seasonal and interannual climate prediction techniques and initial fields," *Journal of Tropical Oceans*, vol. 1-17, 2022.

[7] V. Veeramsetty, "Shapley value cooperative game theory-based locational marginal price computation for loss and emission reduction," *Protection and Control of Modern Power Systems*, vol. 6, no. 1, Article ID 33, 2021.

[8] B. Qiao and H. Deng, "Compensation and restoration schemes for climate and Ocean Change and case study of Marine ecological environment benefits," in *Proceedings of the China Environmental Science Society Proceedings of Science and Technology Annual Meeting*, vol. 2021, pp. 149–156, Xi'an, China, December 2021.

[9] Q. Wang, "The latest report shows that Marine protection is the key to climate policy," *Fisheries Information and Strategy*, vol. 36, no. 3, p. 233, 2020.

[10] Z. H. I. Cai, *Comparative Study on Atmospheric Forcing Caused by Marine Eddy in Different Latitudes of Northwest Pacific*, Nanjing Information Engineering University, Nanjing, China, 2021.

[11] D. F. Yang, Y. Chen, and Z. H. Gao, "Silicon limitation on primary production and its destiny in Jiaozhou Bay, China IV transect offshore the coast with estuaries," *Chinese Journal of Oceanology and Limnology*, vol. 23, no. 1, pp. 72–90, 2005.

[12] D. Yang, F. Wang, and Z. Gao, "Ecological phenomena of phytoplankton in Jiaozhou bay," *Marine Science*, vol. 28, no. 6, pp. 71–74, 2004.

[13] State Oceanic Administration, *The Specification for Marine Monitoring*, China Ocean Press, Beijing, China, 1991.

[14] K. Hong, "Typical underwater tunnels in the mainland of China and related tunneling technologies," *Engineering*, vol. 3, no. 6, pp. 871–879, 2017.

[15] Z. Cui, J. Dai, J. Sun, D. Li, L. Wang, and K. Wang, "Hybrid methods using neural network and Kalman filter for the state of charge estimation of lithium-ion battery," *Mathematical Problems in Engineering*, vol. 2022, Article ID 9616124, 10 pages, 2022.

[16] C. Liu, D. Li, L. Wang, L. Li, and K. Wang, "Strong robustness and high accuracy remaining useful life prediction on supercapacitors," *APL Materials*, vol. 10, no. 6, Article ID 158, 2022.

[17] Q. Li, D. Li, K. Zhao, L. Wang, and K. Wang, "State of health estimation of lithium-ion battery based on improved ant lion optimization and support vector regression," *Journal of Energy Storage*, vol. 50, Article ID 104215, 2022.

[18] L. Chen and Li Bo, "Study on vertical and horizontal section design of inclined shaft of Jiaozhou Bay Second subsea tunnel," *Geotechnical Foundation*, vol. 35, no. 6, pp. 708–711, 2021.

[19] R. Hu, Y. dou, Z. Liang et al., "Distribution characteristics and risk assessment of heavy metals in surface sediments of Jiaozhou Bay," *Marine Geological Frontier*, vol. 37, no. 11, pp. 11–21, 2021.

[20] C. Liu, Y. Zhang, J. Sun, Z. Cui, and K. Wang, "Stacked bidirectional LSTM RNN to evaluate the remaining useful life of supercapacitor," *International Journal of Energy Research*, vol. 46, no. 3, pp. 3034–3043, 2022.

[21] X. Lu, B. Zhao, and Y. Haiyang, "On the change and invariance of media deep integration from the perspective of "starfish invading Jiaozhou Bay"," *Media*, vol. 32, no. 21, pp. 80-81, 2021.

[22] Y. Zhou, Y. Wang, K. Wang et al., "Hybrid genetic algorithm method for efficient and robust evaluation of remaining useful life of supercapacitors," *Applied Energy*, vol. 260, Article ID 114169, 2020.

[23] C. Liu, Q. Li, and K. Wang, "State-of-charge estimation and remaining useful life prediction of supercapacitors," *Renewable and Sustainable Energy Reviews*, vol. 150, Article ID 111408, 2021.

[24] W. Zhou, H. Du, L. Kang et al., "Microstructure evolution and improved permeability of ceramic waste-based bricks," *Materials*, vol. 15, no. 3, p. 1130, 2022.

[25] Z. Yi, K. Zhao, J. Sun, L. Wang, K. Wang, and Y. Ma, "Prediction of the remaining useful life of supercapacitors," *Mathematical Problems in Engineering*, vol. 2022, Article ID 7620382, 7 pages, 2022.

[26] H. Yu, N. Wang, and K. Zhao, "Simultaneous unknown input and state estimation for the linear system with a rank-deficient distribution matrix," *Mathematical Problems in Engineering*, vol. 2021, Article ID 6693690, 11 pages, 2021.

[27] Z. Cui, L. Wang, Q. Li, and K. Wang, "A comprehensive review on the state of charge estimation for lithium-ion battery based on neural network," *International Journal of Energy Research*, vol. 46, no. 5, pp. 5423–5440, 2022.

[28] P. Shen, Y. Tang, L. Ying, Y. Tian, and L. Mengtan, "Correlation analysis between distribution of dinoflagellate cysts and environmental factors in surface sediments of Jiaozhou Bay," *Journal of Yantai University*, vol. 34, no. 4, pp. 392–399, 2021.

[29] Y. Zhou, D. Yu, X. Liu, Y. Qian, and G. Yingying, "Remote sensing inversion and diurnal variation of water transparency in Jiaozhou Bay based on Goci data," *Remote Sensing of Land and Rejsources*, vol. 33, no. 2, pp. 108–115, 2021.

[30] X. Liu, H. Wang, and B. Fuyu, "Why small "anecdotes" catch up with big news-reflections on the series of reports of "starfish flooding in Jiaozhou Bay"," *Young Journalist*, no. 11, pp. 34-35, 2021.

[31] X. Wang, *Simulation Study on the Effect of Tidal Cycle on the Release of Nitrogen, Phosphorus and DOM from Sediments in Dagu Estuary of Jiaozhou Bay*, Qingdao University, Qingdao, China, 2021.

[32] H. Xue and Q. Jiaozhou Bay, "Comprehensive bonded zone reform, enabling services and efficiency," *Institution and Administration*, vol. 24, no. 6, pp. 47-48, 2021.

[33] D. Li, L. Wang, C. Duan, Q. Li, and K. Wang, "Temperature prediction of lithium-ion batteries based on electrochemical impedance spectrum: a review," *International Journal of Energy Reseach*, 2022.

[34] X. Zeng and J. Xu, "Differences between willingness to receive compensation and willingness to pay based on Prospect Theory-a case study of land reclamation in Jiaozhou Bay," *Qingdao Resource Science*, vol. 43, no. 5, pp. 1025–1037, 2021.

[35] L. Xiaojiao, *Effects of Nitrogen and Phosphorus Nutrients on Phytoplankton Community Structure in Jiaozhou Bay*, Shanghai Ocean University, Shanghai, China, 2021.

[36] D. Feng, H. Du, H. Ran et al., "Antiferroelectric stability and energy storage properties of Co-doped $AgNbO_3$ ceramics," *Journal of Solid State Chemistry*, vol. 310, Article ID 123081, 2022.

[37] K. Wang, *Quantitative Analysis of Influencing Factors of Seabed Topographic Change, First Institute of Oceanography*, Ministry of Natural Resources, Peterborough, ON, USA, 2021.

[38] W. Li, "Application of fusion lane in Qingdao Jiaozhou bay tunnel toll station," *China Transportation Informatization*, vol. 124, no. S1, pp. 190-191, 2021.

[39] S. Liu and N. Chen, "Research Progress on biodiversity of phytoplankton and red tide species in Jiaozhou Bay," *Marine Science*, vol. 45, no. 4, pp. 170–188, 2021.

[40] L. Yang, D. Yu, Z. Gao, S. Dong, and Y. Zhou, "Remote sensing inversion of water transparency in Jiaozhou Bay based on sentinel-2," *Infrared and Laser Engineering*, vol. 50, no. 12, pp. 515–521, 2021.

[41] C. Yao, C. Zhang, S. Li, and H. Yang, "Distribution characteristics and ecological risk assessment of heavy metals in soil along the coast of Jiaozhou Bay," *Chinese Scientific Papers*, vol. 16, no. 1, pp. 112–120, 2021.

[42] X. Yang, W. Cui, M. Zhang, C. Chen, and Z. Yu, "A preliminary study on the ecology of Macrobenthos in Jiaozhou Bay," *Advances in Marine Science*, vol. 39, no. 1, pp. 89–101, 2021.

[43] H. Sun, J. Sun, K. Zhao, L. Wang, and K. Wang, "Data-driven ICA-Bi-LSTM combined lithium battery SOH estimation," *Mathematical Problems in Engineering*, vol. 2022, Article ID 9645892, 8 pages, 2022.

[44] L. Kang, H. Du, J. Deng, X. Jing, S. Zhang, and Y. Znang, "Synthesis and catalytic performance of a new V-doped CeO_2-supported alkali-activated-steel-slag-based photocatalyst," *Journal of Wuhan University of Technology-Materials Science Edition*, vol. 36, no. 2, pp. 209–214, 2021.

[45] F. Pan, H. Yuan, J. song et al., "Distribution characteristics and influencing factors of trace metals dissolved organic matter in seawater of Jiaozhou Bay," *Acta Oceanographica Sinica*, vol. 42, no. 12, pp. 1–13, 2020.

[46] Q. Wang, L. Qin, and B. Liu, "Research on performance evaluation index system of infrastructure projects-Taking Jiaozhou Bay Subsea Tunnel as an example," *Construction Technology*, vol. 53, no. 23, pp. 109-110, 2020.

[47] M. Luo, H. Li, K. Xiao, and H. Huang, "Purification evaluation of inorganic nitrogen and phosphorus in different types of wetlands in Jiaozhou Bay and Daya Bay," *Marine Environmental Science*, vol. 39, no. 6, pp. 860–866, 2020.

[48] D. Li, S. Li, S. Zhang, J. Sun, L. Wang, and K. Wang, "Aging state prediction for supercapacitors based on heuristic Kalman filter optimization extreme learning machine," *Energy*, vol. 250, Article ID 123773, 2022.

[49] S. Padhy and S. Panda, "Application of a simplified grey wolf optimization technique for adaptive fuzzy PID controller design for frequency regulation of a distributed power generation system," *Protection and Control of Modern Power Systems*, vol. 6, no. 1, Article ID 2, 2021.

[50] H. Xu, H. Du, L. Kang, Q. Cheng, D. Feng, and S. Xia, "Constructing straight pores and improving mechanical properties of GangueBased porous ceramics," *Journal of Renewable Materials*, vol. 9, no. 12, pp. 2129–2141, 2021.

[51] H. Ran, H. Du, C. Ma, Y. Zhao, D. Feng, and H. Xu, "Effects of A/B-site co-doping on microstructure and dielectric thermal stability of $AgNbO_3$ ceramics," *Science of Advanced Materials*, vol. 13, no. 5, pp. 741–747, 2021.

[52] C. Y. Ma, H. L. Du, J. Liu et al., "High-temperature stability of dielectric and energy-storage properties of weakly-coupled relaxor (1-x)$BaTiO_3$-xBi(Y1/3Ti1/2)O_3 ceramics," *Ceramics International*, vol. 47, no. 17, pp. 25029–25036, 2021.

Hindawi
Mathematical Problems in Engineering
Volume 2022, Article ID 1736931, 11 pages
https://doi.org/10.1155/2022/1736931

Research Article

Current Control of Permanent Magnet Synchronous Motors Using Improved Model Predictive Control

Muhammad Kashif Nawaz,[1] Manfeng Dou,[1] Saleem Riaz,[1] and Muhammad Usman Sardar[2]

[1]*Northwestern Polytechnical University, Xi'an, China*
[2]*Khawaja Fareed University of Engineering and Information Technology, Rahim Yar Khan, Pakistan*

Correspondence should be addressed to Muhammad Usman Sardar; muhammad.usman@kfueit.edu.pk

Received 27 December 2021; Accepted 13 May 2022; Published 1 June 2022

Academic Editor: Amin Jajarmi

Model predictive control (MPC) is a powerful tool for the control of permanent magnet synchronous motors. However, conventional MPC permits using a single voltage vector during one control interval. This results in higher current distortions and large torque ripples. Sensitivity to control parameters is another issue associated with conventional MPC. The duty cycle suggests using an active vector and a null vector during one sampling interval. The method needs excessive computational and prediction effort. Furthermore, a necessary zero vector as the second vector might not give the optimal results. To overcome the problems of computational burden, this paper proposes that a reference voltage vector can be calculated and used to determine the voltage vector to be used for the next interval. This reduces the computational effort to a minimum. Furthermore, it is proposed that the second vector can either be active or null. To overcome the problem of parameter dependence, an electromotive force is calculated on basis of previous values. Simulations have been carried out to verify the efficacy of the proposed method.

1. Introduction

Permanent magnet synchronous machines are recently grasping more attraction in industrial applications such as robots, electric vehicles, and numerical control machines due to several advantages in terms of high torque density, low volume, and efficiency over a wide speed range [1–7]. Among various control schemes for high-performance control of PMSM-based systems, field-oriented control (FOC) and direct torque control (DTC) [8–10] have developed as better control strategies. FOC has exhibited fast dynamic response and decent steady-state performance [11, 12]. Nevertheless, it demands fine-tuning of internal loop and axis transformation. Furthermore, FOC combined with space vector pulse width modulation (SVPWM) increases calculation process time. Direct torque control has emerged as another control strategy that uses measured current to estimate the magnetic flux and torque to calculate voltage command. It does not need the inner current loop and pulse width modulation [13]. DTC has a simple structure and achieves a very high quick response [14]. However, it is quite difficult to estimate the torque and magnetic flux precisely [15]. Also, it usually results in higher current harmonics and torque ripples with a variable switching pattern. Some research work has also been done in the field of iterative learning controller [16–18]. Several other modifications and improvements have been suggested in the literature to overcome FOC and DTC drawbacks [19–21].

In recent years, model predictive control, also known as MPC, has emerged as an improved alternative to previous techniques for control of PMSM as well as power converters [22–24]. MPC is an optimization-based methodology, and based on a system's internal model, it calculates control action for the next interval by minimizing the difference between the reference value and projected value. MPC has a simple control architecture with quick response and parameter robustness [22, 25–27]. As compared to FOC, MPC promises a quicker dynamic response. Compared to DTC,

vector selection for the next interval in MPC is comparatively more precise [24, 28]. Model predictive control can be used as a torque control or as a current control scheme. The former is called model predictive torque control (MPTC) [29–31], and the latter is known as model predictive current control (MPCC) scheme [32–38]. MPTC has shown improved enactments in terms of current harmonics and torque ripples compared to DTC [39–43]. However, for obtaining torque and flux values and tuning weighting factors, MPTC requires an observer or estimator.

MPCC is easy to implement due to the fact that the only control variable, that is, current, can be measured without an estimator or observer [35, 44]. Its fast response and the unpretentious principle have made it a promising strategy for high-performance current control of PMSM drive systems. MPCC is a current control strategy that can be implemented easily compared to MPTC, which requires an estimator or observer. Also, it does not require any weighing factor as the current is the only control variable. Therefore, MPCC provides a more straightforward solution as compared to MPTC.

Model predictive control depends on the system model for future prediction. Therefore, it needs an accurate representation of the system model. Some of the motor parameters such as motor inductance and resistance vary during the motor operation due to changing temperature. This results in a mismatch of these parameters, and the accurate representation of the system model is compromised. In order to overcome this problem, some methods have been implemented in the literature to minimize the dependence on motor parameters. A current difference technique is proposed in literature [45, 46] which is independent of system parameters. In order to make the system robust against system parameters, the study in [47] proposes an ultralocal technique that utilizes the inputs and outputs of the system only. To identify system parameters, the study in [48] suggests a recursive least square algorithm. Without the need for detailed system parameters, accurate prediction is possible. The back electromotive force (back emf) of the system can be evaluated based on previous emf values as suggested in the literature [32, 33].

Furthermore, in order to get the minimal cost function, conventional MPC has to predict as many current values as the inverter's switching states [40]. Usually, the MPC drive system is fed from a three-phase two-level voltage source inverter (2LVSI). It means there are a total of eight possible switching states, that is, six active vector states and two zero vector states. Consequently, the controller has to check for all eight states one by one. This complicates the situation for systems with a higher number of phases or when using a three-level inverter. Furthermore, the application of only one vector during one control interval fails to achieve minimum current error between the reference and the predicted value [41]. To overcome this difficulty, the idea of using more than one vector has been presented in the literature [39, 40]. The concept of the duty cycle has been presented in literature [36, 40, 41]. The basic concept is to utilize multiple voltage vectors during one control interval. The conventional duty-cycle method allows one active and a corresponding zero vector with less switching frequency during one control interval. Selection of the active vector is made by the tedious one-by-one check. The application of a zero vector decreases the error between predicted and reference values [49]. Even though this method significantly improves the steady-state performance of the concerned system, current error may be minimized by exploring the horizon for selecting a second vector rather than using a zero vector necessarily, which needs additional research [36].

In order to overcome the difficulties of the conventional model predictive control method, this paper has proposed some improvements. This paper uses an alpha-beta coordinate system for calculation in order to avoid dq-axes transformation. To reduce the dependence on system parameters, back emf can be calculated from previous emf values which are calculated from current values. An average of previous emf values can be used to calculate emf for the active control period. Secondly, an improvement in the duty-cycle approach has been proposed which focuses on generating a reference voltage vector for selecting the first optimal vector. The paper proposes that the active vector nearest to the reference voltage vector must be selected as the first vector. The second vector can either be an active voltage vector or a zero vector depending on which one generates the minimum cost function. A very simple but effective approach for duty calculation has been used which suggests that can be calculated from the cost functions of selected voltage vectors. The proposed method is compared with conventional MPC and conventional duty-cycle MPC. The effectiveness of the proposed method is confirmed by simulation results.

The paper is organized as follows: Section 2 covers the mathematical model of PMSM and its discrete model. The conventional model predictive control strategy is also covered in this section. Section 3 discusses the proposed MPC, which includes emf calculation, reference voltage generation, and selection of the first optimal vector and second vector. This section also discusses the duty calculation. Section 4 includes simulation verification of the proposed strategy by comparing results with conventional methods. Lastly, Section 5 presents the conclusion based on simulation results. References are added at the end of this paper.

2. Preliminaries

2.1. Mathematical Representation of PMSM. The following assumptions must be taken into consideration for a simplified analysis: magnetic hysteresis losses as well as eddy currents are very insignificant; hence, they can be neglected, clogging torque and magnetic saturation is negligible, and back emf is sinusoidal. In order to avoid tedious coordinate transformation, $\alpha\beta$-stationary axis is used in this paper. The model of a surface-mounted PMSM in stationary reference frame can be represented as

$$V_s = R_s i_s + L_s \frac{d(i_s)}{dt} + \frac{d(\psi_x)}{dt}, \tag{1}$$

where V_s (V) is the stator voltage, i_s (A) is the stator current, ψ_s (Wb) is the equivalent active flux, R_s (Ohm) is resistance, and L_s (H) is the inductance.

$$V_s = R_s i_s + L_s.\frac{d(i_s)}{dt} + e, \tag{2}$$

where e (V) represents back emf.

$$e = \left(\psi_f\right).e^{i\theta_e}, \tag{3}$$

where ψ_f is the permanent magnet flux linkages.

$$\frac{d(e)}{dt} = j\psi_f.\omega_r, \tag{4}$$

where ω_r (rad/s) is rotor speed.

$$T_e = \frac{3}{2}P.\left(\psi_x.i_s\right), \tag{5}$$

where T_e (Nm) is electromagnetic torque and P represents the number of poles.

2.2. Discrete-Time Model. For a sampling interval T_s, the voltages and calculated currents for the kth interval can be used to predict load currents for the next sampling interval.

By rearranging (2), we get

$$\frac{\mathrm{d}(i_s)}{\mathrm{d}t} = \frac{1}{L_s}\left(V_s - R_s i_s - e\right). \tag{6}$$

di/dt can be estimated as

$$\frac{\mathrm{d}(i_s(k))}{\mathrm{d}t} = \frac{i_s(k+1) - i_s(k)}{T_s}, \tag{7}$$

where T_s represents one control period.

Replacing in (6), and rearranging the equation, the predicted load current for the next interval can be represented as

$$i_s(k+1) = i_s(k) + \frac{T_s}{L_s}\left(V_s(k) - R_s i_s(k) - e(k)\right). \tag{8}$$

Estimation of *emf* requires a troublesome process. Theoretically, (2) can be used to approximate *emf*, but it is not as simple as it seems due to variations in machine parameters with increasing temperature and saturation. Therefore, the objective is to minimize the dependence on machine parameters [37].

The *emf* can also be approximated using an observer. Conversely, *emf* values are pretty low at a standstill or low speeds, making it difficult for the observer to estimate the *emf* effectively. Due to its computational time, an observer might estimate inaccurately during the transient intervals. Therefore, the following adjustments must be made in the theoretical model to estimate *emf* with the least dependence on machine parameters. The mechanical speed of the machine can be considered constant for a few control intervals as the machine time constant is much higher as compared to the electromagnetic time constant. Stator current $i_s(k)$ can be replaced by the following equation to represent its variation during one sampling interval:

$$i_s(k) = \frac{\left(i_s(k) + i_s(k-1)\right)}{2}. \tag{9}$$

By replacing these values in (8), *emf* can be estimated as

$$e_x(k-1) = V_s(k-1) - \frac{R_s}{2}\left(i_s(k) + i_s(k-1)\right) - \frac{L_s}{T_s}\left(i_s(k) - i_s(k-1)\right). \tag{10}$$

Similarly, for consecutive intervals,

$$\begin{aligned} e_x(k-2) &= V_s(k-2) - \frac{R_s}{2}\left(i_s(k-1) + i_s(k-2)\right) \\ &\quad - \frac{L_s}{T_s}\left(i_s(k-1) - i_s(k-2)\right), \\ e_x(k-3) &= V_s(k-3) - \frac{R_s}{2}\left(i_s(k-2) + i_s(k-3)\right) \\ &\quad - \frac{L_s}{T_s}\left(i_s(k-2) - i_s(k-3)\right). \end{aligned} \tag{11}$$

The back *emf* is considered constant for a few intervals as the *emf* frequency is significantly less as compared to the sampling frequency. Therefore, it is proposed that the *emf* value remains considerably consistent during a control interval [33]. However, it reduces the tolerance for variations in inductance. As stated in [50], taking the mean of two to four consecutive *emf* estimations increases the system's stability against varying inductance. The results show that the system shows stability against variations in the inductance values. Therefore, this paper proposes using two *emf* values from the previous consecutive intervals and taking the mean to estimate *emf* for the current interval.

$$e_x(k) = \frac{1}{2}e_x\left(e_x(k-1) + e_x(k-2)\right). \tag{12}$$

2.3. Model Predictive Control. The conventional MPC with single-vector selection and one-step delay compensation selects the optimum voltage vector from cost function minimization. The cost function is expressed as

$$\begin{aligned} C &= \left|i_s(\mathrm{ref}) - i_s(k+1)\right|, \\ \text{Subjected to } V_S &\in \left(V_1, V_2, \ldots, V_6\right), \end{aligned} \tag{13}$$

where i_s(ref) is the current reference is the stationary frame. As PMSM is fed by a two-level VSI, there are a total of eight switching states with six active and two zero voltage vectors. It means that the cost function has to be calculated for a total of seven times during each control interval. Additionally, the use of only one voltage vector during a single control interval results in enhanced current harmonic distortions and greater steady-state torque ripples.

3. Proposed MPC

The block diagram of the proposed MPC is represented in Figure 1. The tedious dq-axes transformation is avoided, and the $\alpha\beta$-coordinate system has been employed. The proposed

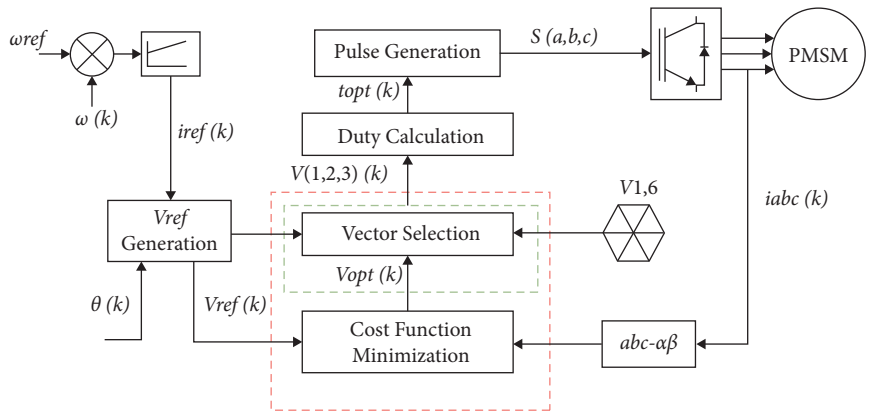

Figure 1: Block diagram of the proposed MPC strategy.

method is based on the fact that not all the switching state vectors are needed to predict and select the optimal control variable. A reference voltage vector can be used to predict future voltage vectors. Moreover, as utilizing a single voltage vector during one sampling interval might result in torque ripples, more than one nonzero voltage vector can be used through one control period. This paper suggests that the second vector can either be an active voltage vector or a zero vector depending on whichever produces the least cost function.

3.1. Reference Voltage Generation. The conventional MPC checks all the voltage vectors one by one to find the optimal vector. The ultimate goal is to minimize the current error in the cost function (14). Theoretically, it can be minimized to a zero value. Based on this statement, a reference voltage vector can be generated from (13) by replacing $i_s(k+1)$ with $i_s(\text{ref})$. A voltage reference vector is calculated from the current values of the present (k_{th}) control period.

$$V_k(\text{ref}) = \frac{1}{2}R_s\left(i_s(ref) + i_s(k)\right) + \frac{L_s}{T_s}\left(i_s(\text{ref}) - i_s(k)\right) + \left(\psi_f\right).e^{j\theta_e}. \tag{14}$$

3.2. Vector Selection. Once the reference voltage is generated, the next stage is to find the first optimal vector, which minimizes the cost function. A two-level VSI has six active and two zero vectors. Therefore, the inverter control plane can be divided into six equal segments, and the six active voltage vectors are located at the extremes of each segment. The angle information of reference voltage determines its location on the inverter control plane. The reference vector lies on one of the six sectors. The segment where reference voltage lies corresponds to the closest voltage vector on one of the sides of that segment as the optimal vector during the next control interval. For example, if the reference voltage vector lies in S_1, as shown in Figure 2, the closest voltage vector is V_1. Obviously, V_1 exhibits the least error towards reference voltage. Hence, it will generate the optimal vector for the next interval. The application of only the first voltage vector makes it the conventional duty-cycle MPC.

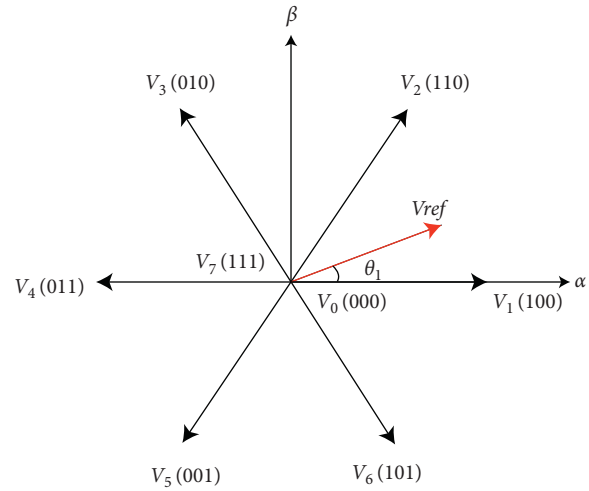

Figure 2: Voltage vectors' representation for a two-level VSI.

The reference voltage vector lies between two active vectors on the inverter plane. The one closest to the reference voltage ensures minimal error. This vector must be selected as the first voltage vector for the next control interval. The voltage vector on the other boundary of the same sector will be the one that will generate the minimum error among the remaining five active vectors as this is closest to the reference among those five. This method proposes that the second vector can either be this vector or a null vector. Taking the same example, the reference voltage lies in sector S_1. V_1 is already determined as the first vector. The second vector can either be V_2 or a null vector. The selection between these two candidates is based on which one generates the least error, that is, minimizing the cost function. If V_2 generates the lower cost function, it will be used as the second vector during the next interval; otherwise, a null vector will be selected. The method is handy in terms of lesser calculations. There is no need to check all the vectors one by one to search for optimal results. The first vector is selected instantly once the reference voltage is generated. A little calculation is needed when it comes to selecting a second vector. A cost function is generated only twice during one control period, and the one that minimizes the cost function will be the second vector.

Table 1: Control and motor parameters.

Parameter	Value
Stator resistance	0.2 Ω
Stator inductance	8.5 mH
Rated DC bus voltage	200 V
Inertia	0.0012 kg.m^2
Magnetic flux	0.24 Wb
Pole pairs	4
Rated current	9.4 A
Rated speed	2000 rpm
Rated load	7.15 Nm
Sampling period	50 μs

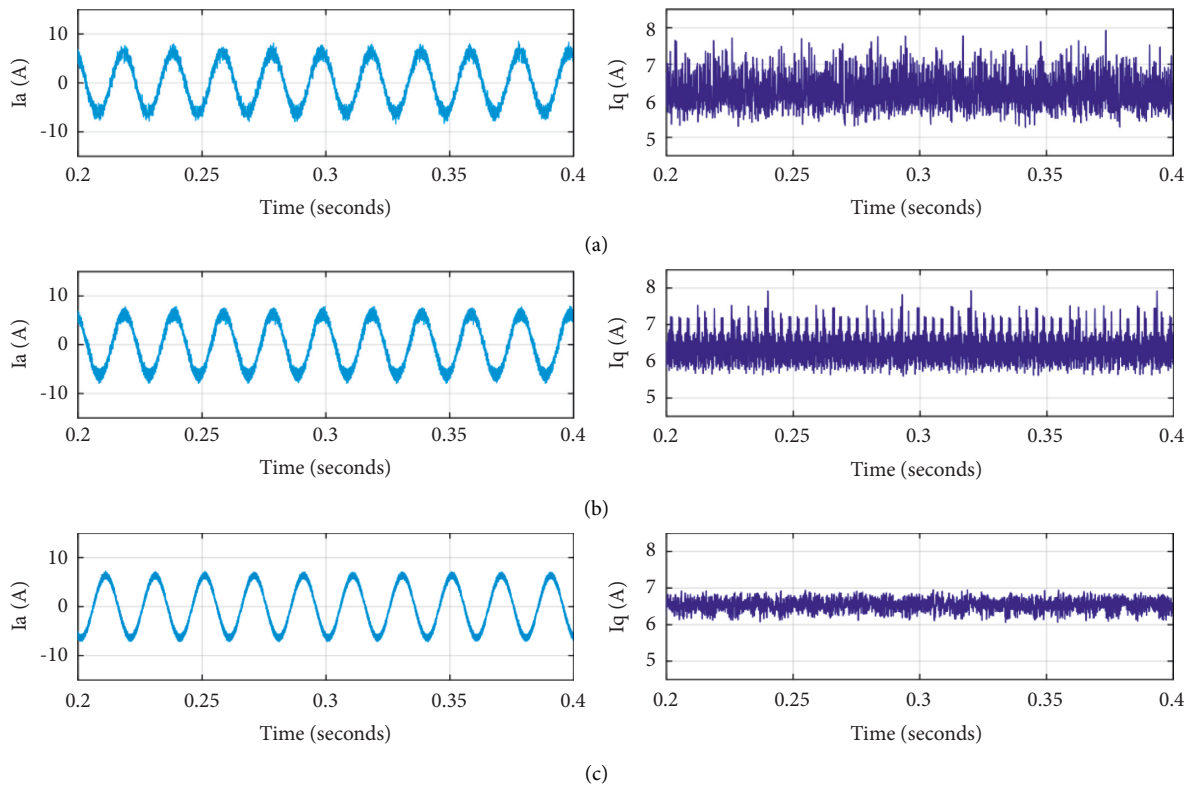

Figure 3: Steady-state response at 1500 rpm at constant load torque. (a) Conventional MPC, (b) conventional duty-cycle MPC, and (c) proposed MPC.

3.3. Duty Calculation. The best voltage vectors to be used in the next sampling interval are selected based on the angle of the reference voltage vector, that is, the location of the reference voltage vector. The voltage vectors nearer to the reference voltage vector will automatically generate the lowest cost function values. Hence, the burden to calculate the cost function of all vectors can be avoided. The duty calculation for the vectors involved for the next intervals is calculated on the basis of the fact that the action time of a vector is in inverse proportion to the cost function it produces. The higher the cost function, the lower will be the vector's action time.

The duty cycles for the selected vectors can be defined as

$$d_{Vx} = \frac{K}{C_{Vx}}, \tag{15}$$

where C_{Vx} represents the cost function of the corresponding voltage vector. K is a constant, and it can be derived as

$$K = \frac{1}{\sum_{x=1}^{n} (1/C_{Vx})}, \tag{16}$$

where $n = (1,2)$.

As two vectors are to be selected, their duty can be calculated as

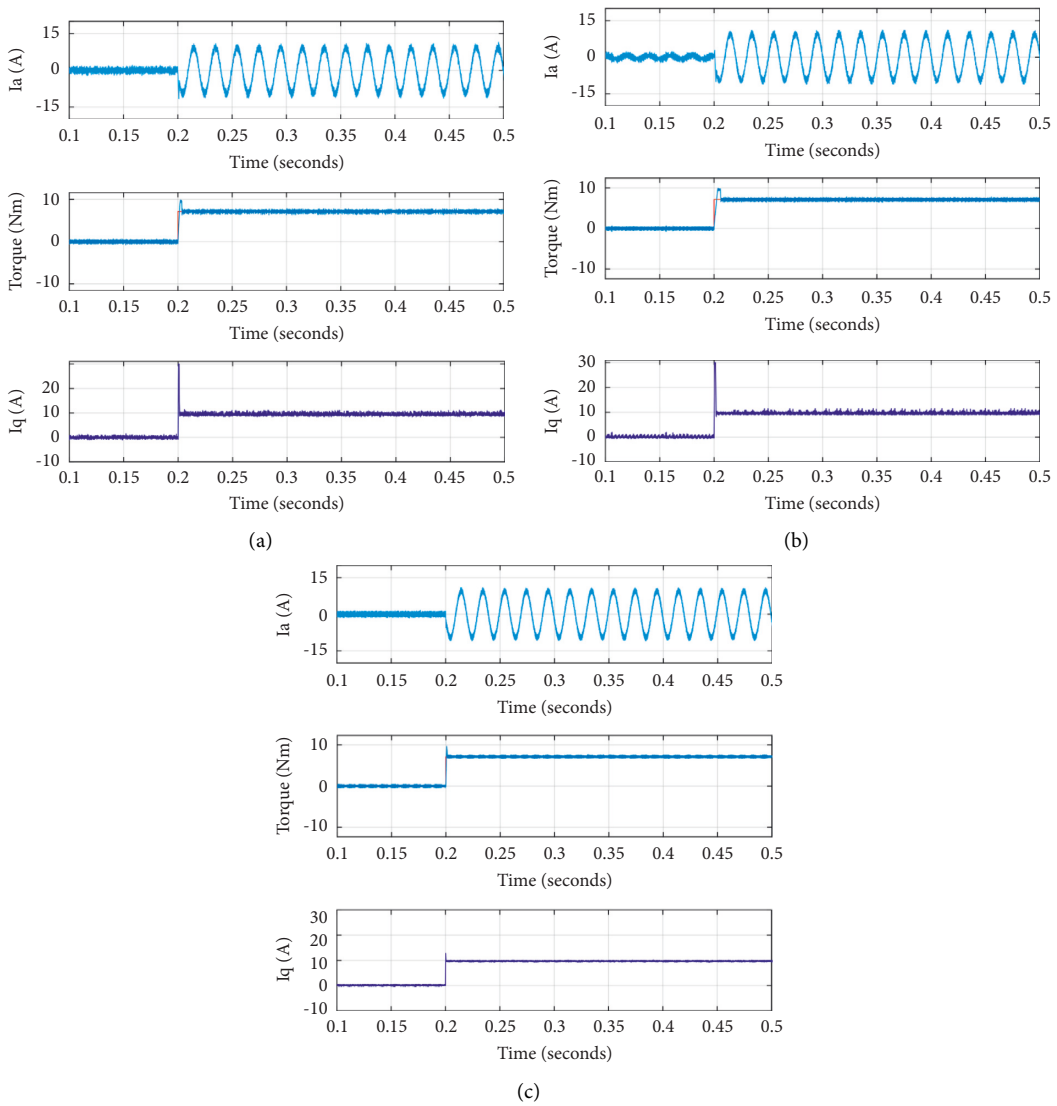

Figure 4: Steady-state response at 1500 rpm with sudden application of 100% load torque. (a) Conventional MPC, (b) conventional duty-cycle MPC, and (c) proposed MPC.

$$d_{V1} = \frac{K}{C_{V1}}, \qquad d_{V2} = \frac{K}{C_{V2}}, \tag{17}$$

where V_2 symbolizes either the adjacent active vector or the zero vector for the first method.

$$d_{V1} + d_{V2} = 1, \tag{18}$$

where C_{V1} and C_{V2} are cost functions of V_1 and V_2. K is a constant, and it can be expressed as

$$K = \frac{1}{(1/C_{V1}) + (1/C_{V2})}. \tag{19}$$

The above equations can be simplified as

$$d_{V1} = \frac{C_{V2}}{(C_{V1} + C_{V2})}, \qquad d_{V2} = \frac{C_{V1}}{(C_{V1} + C_{V2})}. \tag{20}$$

Or simply d_{V2} can be derived from (18).

$$d_{V2} = 1 - d_{V1}. \tag{21}$$

The final cost function can be expressed as

$$C = d_{V1}C_{V1} + d_{V2}C_{V2}. \tag{22}$$

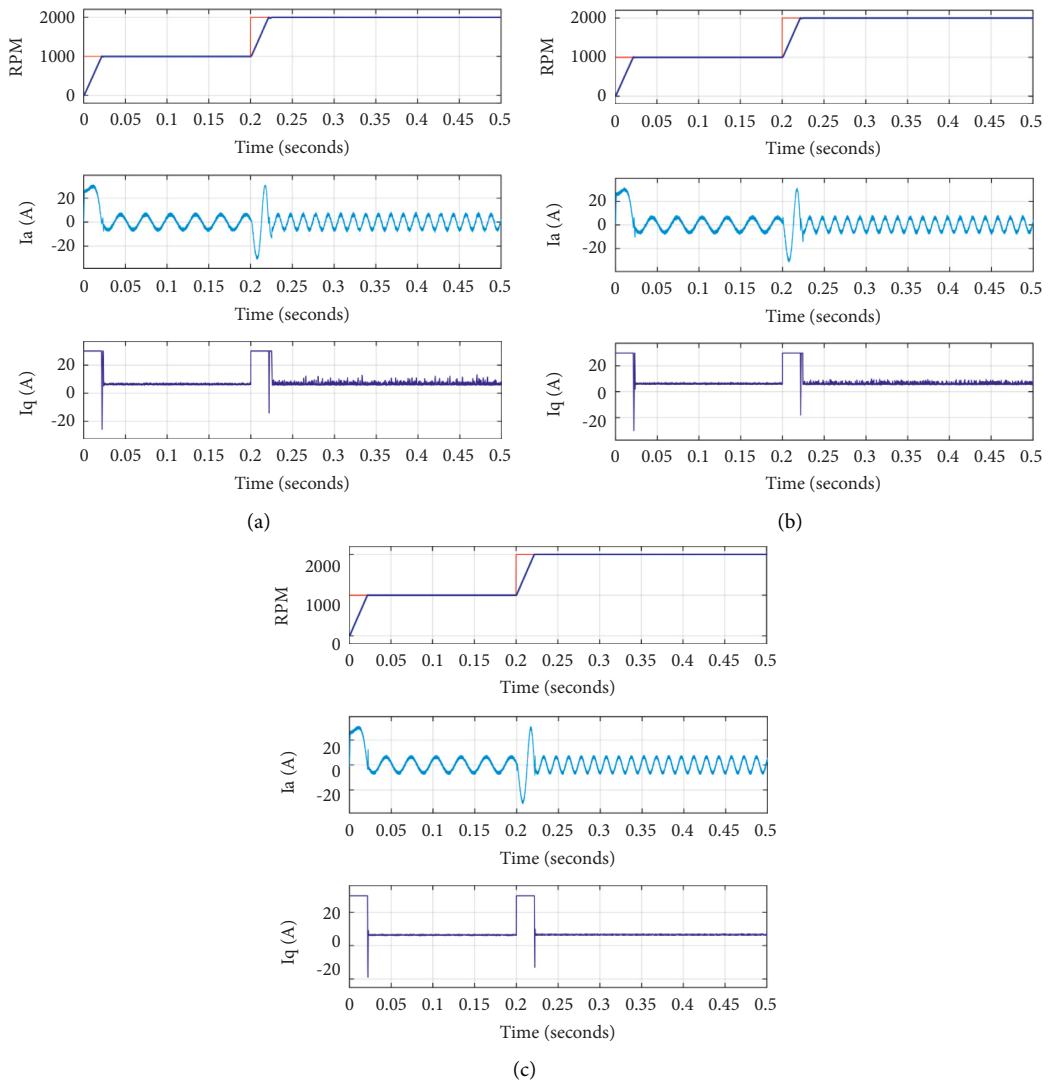

Figure 5: Dynamic speed maneuver response from standstill to 1000 rpm to 2000 rpm for (a) conventional MPC, (b) conventional duty-cycle MPC, and (c) proposed MPC.

4. Simulation Study

To explore the performance of PMSM considering the suggested control strategy, simulation work is carried out in MATLAB/Simulink environment. The nominal parameters of the PMSM used in the simulation work are shown in Table 1. The sampling frequency for simulations is kept at 20 kHz. The following assumptions have been taken into consideration: saturation in flux linkages is neglected, and emf is considered sinusoidal. The value of id is kept at zero. Simulation results of the proposed MPC strategy are compared with conventional MPC and conventional duty-cycle MPC strategy which considers one active and one null vector during a control interval.

The first test condition is the steady state in which the motor is running at 75% of nominal speed at 50% of constant rated load for a duration of 0.4 s. The simulation results are presented in Figure 3 which shows stator phase "a" current Ia (A) and q-axis Iq (A) for (a) conventional MPC, (b) conventional duty-cycle MPC, and (c) proposed MPC. It can be seen in Figure 3 that the q-axis current is showing much distortion for the conventional MPC method. These distortions are reduced for conventional duty-cycle MPC and further reduced for the proposed strategy.

Figure 4 shows simulation results for the case of changing load. The test condition is that the motor is running at 100% rated speed. The load torque is initially zero. Full load torque of 7.15 Nm is suddenly applied at 0.2 s. The motor speed reduces in small amounts, but a quick increase in electromagnetic torque causes the motor to regain its speed to the designated value of 1500 rpm momentarily. Figure 4(a) shows simulation results for conventional MPC, Figure 4(b) shows simulation results for conventional duty-cycle MPC, and Figure 4(c) shows simulation results for proposed MPC. The first channel in each part shows phase "a" current waveform. Load torque is shown in the second channel while the third channel shows the q-axis current. The motor response is almost similar in

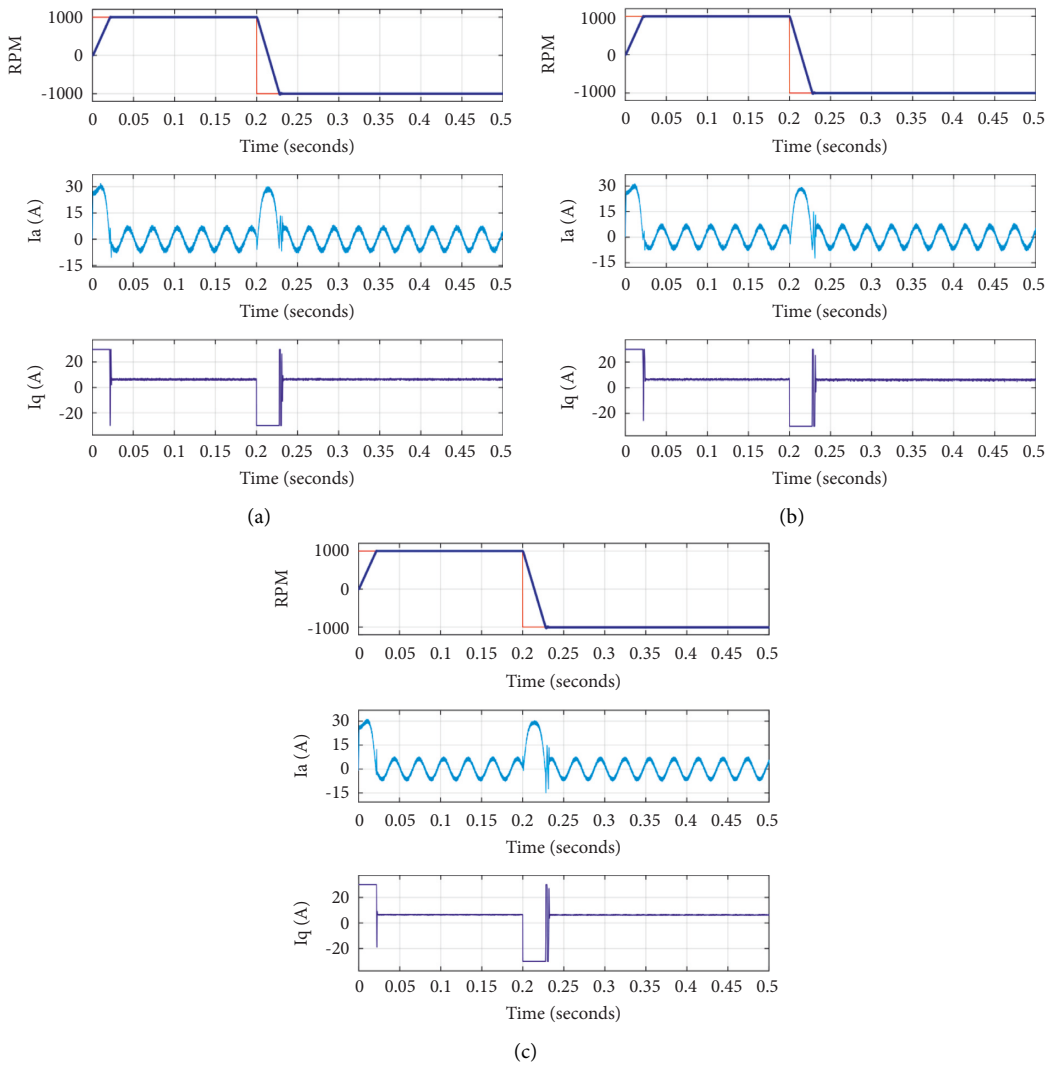

Figure 6: Dynamic speed maneuver response from 2000 rpm to -2000 rpm for (a) conventional MPC, (b) conventional duty-cycle MPC, and (c) proposed MPC.

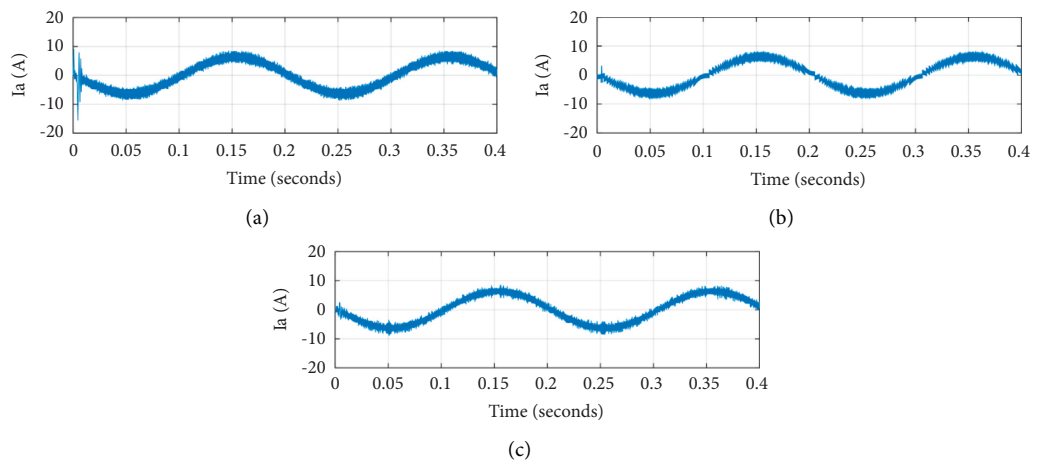

Figure 7: Steady-state response at low speed of 100 rpm for (a) conventional MPC, (b) conventional duty-cycle MPC, and (c) proposed MPC.

all these methods. However, as shown in the curves, the response in the proposed method has shown considerably improved steady-state performance in the form of reduced current harmonics and reduced torque ripples. The waveforms are smooth for the proposed MPC method.

The dynamic case scenario of accelerating the motor from zero speed to 50% of the rated speed at 0 s and then to 100% of the rated speed at 0.2 s is represented in Figure 5. A constant load torque of 3 Nm is applied during the whole simulation time. Figure 5(a) shows simulation results for conventional MPC, Figure 5(b) shows simulation results for conventional duty-cycle MPC, and Figure 5(c) shows simulation results for proposed MPC. The first channel in each part shows actual and reference speeds. The phase "a" current is shown in the second channel while the third channel shows the q-axis current. The conventional duty-cycle MPC shows more persistent results as compared to conventional MPC, but the problems of ripples and large current distortions are still present. The proposed MPC method has shown its effectiveness in reducing current distortions and also suppresses harmonics.

Next, the simulation results for motor speed reversal are represented in Figure 6. The motor is first accelerated to 1000 rpm, and then, at 0.2 s, the speed is reversed from 1000 rpm to -1000 rpm. The simulation results for conventional MPC, conventional duty-cycle MPC, and the proposed strategy are presented in Figure 6. It can be observed that the improved MPC strategy has effectively eliminated steady-state error completely. Furthermore, it has reduced the current distortion and torque ripple. Hence, the proposed scheme can ensure the dynamic performance of the control system.

Figure 7 shows stator phase "a" current for (a) conventional MPC, (b) conventional duty-cycle MPC, and (c) proposed MPC when the motor is operating at a low speed of 100 rpm. The proposed method has shown better results in terms of reduced current distortions.

5. Conclusion

In conventional MPC for motor control, the voltage vector that minimizes the cost function is selected and used for the next interval. The drawback of conventional MPC includes its dependence on system parameters for future predictions and the tedious process of checking all the voltage vectors one by one. The other problem is that conventional MPC utilizes only one voltage vector during one complete interval. This leads to higher steady-state torque ripples and more current distortions. The concept of the duty cycle adds an additional vector during one control interval. This paper proposes an approach to overcome these problems. In order to minimize the dependence on system parameters, the back emf can be calculated from the current values. This method further suggests that the second vector can also be an active vector. To overcome the computational burden, this paper proposes that instead of checking all the vector states one by one, the vectors for the next sampling interval can be directly selected by generating a reference voltage and checking its location on the voltage vector plane. Simulations have been carried out for the proposed method, and the results have been compared with conventional MPC and conventional duty-cycle MPC. The proposed method has shown promising results for the steady state as well as dynamic response.

Data Availability

The data are available and are mathematical-based simulations. The data can be provided upon request to the corresponding author.

Conflicts of Interest

The authors declare that they have no conflicts of interest.

References

[1] L. Corradini, E. Orietti, P. Mattavelli, and S. Saggini, "Digital hysteretic voltage-mode control for DC-DC converters based on asynchronous sampling," *IEEE Transactions on Power Electronics*, vol. 24, no. 1, pp. 201–211, 2009.

[2] R. Krishnan, *Electric Motor Drives: Modeling, Analysis, and Control*, Pearson, New York, NY, USA, 2001.

[3] M. Barcaro, E. Fornasiero, N. Bianchi, and S. Bolognani, "Design procedure of IPM motor drive for railway traction," in *Proceedings of the 2011 IEEE International Electric Machines & Drives Conference (IEMDC)*, pp. 983–988, IEEE, Niagara Falls, Canada, May 2011.

[4] A. Choudhury, P. Pillay, M. Amar, and S. S. Williamson, "Performance Comparison Study of Two and Three-Level Inverter for Electric Vehicle Application," in *Proceedings of the 2014 IEEE Transportation Electrification Conference and Expo (ITEC)*, pp. 1–6, IEEE, Dearborn, MI, USA, June 2014.

[5] Y. Zhang and J. Zhu, "Direct torque control of permanent magnet synchronous motor with reduced torque ripple and commutation frequency," *IEEE Transactions on Power Electronics*, vol. 26, no. 1, pp. 235–248, 2010.

[6] S. Riaz, H. Lin, and M. P. Akhter, "Design and implementation of an accelerated error convergence criterion for norm optimal iterative learning controller," *Electronics*, vol. 9, no. 11, p. 1766, 2020.

[7] S. Riaz, H. Lin, and H. Elahi, "A novel fast error convergence approach for an optimal iterative learning controller," *Integrated Ferroelectrics*, vol. 213, no. 1, pp. 103–115, 2021.

[8] Y. Inoue, S. Morimoto, and M. Sanada, "Comparative study of PMSM drive systems based on current control and direct torque control in flux-weakening control region," *IEEE Transactions on Industry Applications*, vol. 48, no. 6, pp. 2382–2389, 2012.

[9] I. Takahashi and T. Noguchi, "A new quick-response and high-efficiency control strategy of an induction motor," *IEEE Transactions on Industry Applications*, vol. IA-22, no. 5, pp. 820–827, 1986.

[10] Y. Hua, N. Wang, and K. Zhao, "Simultaneous unknown input and state estimation for the linear system with a rank-deficient distribution matrix," *Mathematical Problems in Engineering*, vol. 2021, pp. 1–11, 2021.

[11] D. W. Novotny and T. A. Lipo, *Vector Control and Dynamics of AC Drives*, Oxford University Press, Oxford, England, 1996.

[12] S. Riaz, H. Lin, M. Bilal Anwar, and H. Ali, "Design of PD-type second-order ILC law for PMSM servo position control," *Journal of Physics: Conference Series*, vol. 1707, no. 1, Article ID 012002, 2020.

[13] L. Lixin Tang, L. Limin Zhong, M. F. Rahman, and Y. Yuwen Hu, "A novel direct torque control for interior permanent-magnet synchronous machine drive with low ripple in torque and flux-a speed-sensorless approach," *IEEE Transactions on Industry Applications*, vol. 39, no. 6, pp. 1748–1756, 2003.

[14] J. S. Lee and R. D. Lorenz, "Deadbeat direct torque and flux control of IPMSM drives using a minimum time ramp trajectory method at voltage and current limits," *IEEE Transactions on Industry Applications*, vol. 50, no. 6, pp. 3795–3804, 2014.

[15] S. Riaz, H. Lin, F. Afzal, and A. Maqbool, "Design and implementation of novel LMI-based iterative learning robust nonlinear controller," *Complexity*, vol. 2021, Article ID 5577241, 13 pages, 2021.

[16] S. Riaz, H. Lin, M. Waqas, F. Afzal, K. Wang, and N. Saeed, "An accelerated error convergence design criterion and implementation of lebesgue-p norm ILC control topology for linear position control systems," *Mathematical Problems in Engineering*, vol. 2021, Article ID 5975158, 12 pages, 2021.

[17] S. Riaz, H. Lin, M. Mahsud, D. Afzal, A. Alsinai, and M. Cancan, "An improved fast error convergence topology for PDα-type fractional-order ILC," *Journal of Interdisciplinary Mathematics*, vol. 24, no. 7, pp. 2005–2019, 2021.

[18] C. Ma, H. Du, J. Liu et al., "High-temperature stability of dielectric and energy-storage properties of weakly-coupled relaxor (1-x)BaTiO3-xBi(Y1/3Ti1/2)O3 ceramics," *Ceramics International*, vol. 47, no. 17, pp. 25029–25036, 2021.

[19] Y. Jianguo Zhu and J. Zhu, "A novel duty cycle control strategy to reduce both torque and flux ripples for DTC of permanent magnet synchronous motor drives with switching frequency reduction," *IEEE Transactions on Power Electronics*, vol. 26, no. 10, pp. 3055–3067, 2011.

[20] A. Sivaprakasam and T. Manigandan, "A simple method to reduce torque ripple and mechanical vibration in direct torque controlled permanent magnet synchronous motor," *Journal of Vibroengineering*, vol. 15, no. 2, pp. 658–674, 2013.

[21] X. Feng, Q. li, and K. Wang, "Waste plastic triboelectric nanogenerators using recycled plastic bags for power generation," *ACS Applied Materials & Interfaces*, vol. 13, no. 1, pp. 400–410, 2020.

[22] J. Rodriguez and P. Cortes, *Predictive Control of Power Converters and Electrical Drives*, John Wiley & Sons, Hoboken, NJ, USA, 2012.

[23] S. Vazquez, J. I. Leon, L. G. Franquelo et al., "Model predictive control: a review of its applications in power electronics," *IEEE industrial electronics magazine*, vol. 8, no. 1, pp. 16–31, 2014.

[24] A. Linder and R. Kennel, "Model predictive control for electrical drives," in *Proceedings of the 2005 IEEE 36th Power Electronics Specialists Conference*, pp. 1793–1799, IEEE, Dresden, Germany, June 2005.

[25] V. Muzikova, T. Glasberger, V. Smidl, and Z. Peroutka, "Finite control set MPC with high frequency injections for sensorless position and speed estimation of a PMSM," in *Proceedings of the 2015 IEEE International Symposium on Predictive Control of Electrical Drives and Power Electronics (PRECEDE)*, pp. 9–14, IEEE, Valparaiso, Chile, October 2015.

[26] C. Liu, Q. Li, and K. Wang, "State-of-charge estimation and remaining useful life prediction of supercapacitors," *Renewable and Sustainable Energy Reviews*, vol. 150, Article ID 111408, 2021.

[27] H. Xu, H. Du, L. Kang, Q. Cheng, D. Feng, and S. Xia, "Constructing straight pores and improving mechanical properties of GangueBased porous ceramics," *Ceramics Art and Perception Journal of Renewable Materials*, vol. 9, no. 12, pp. 2129–2141, 2021.

[28] J. Rodriguez, M. P. Kazmierkowski, J. R. Espinoza et al., "State of the art of finite control set model predictive control in power electronics," *IEEE Transactions on Industrial Informatics*, vol. 9, no. 2, pp. 1003–1016, 2013.

[29] H. Peyrl, G. Papafotiou, and M. Morari, "Model Predictive Torque Control of a Switched Reluctance Motor," in *Proceedings of the 2009 IEEE International Conference on Industrial Technology*, pp. 1–6, IEEE, Churchill, Australia, February 2009.

[30] T. Geyer, G. A. Beccuti, G. Papafotiou, and M. Morari, "Model Predictive Direct Torque Control of Permanent Magnet Synchronous Motors," in *Proceedings of the 2010 IEEE Energy Conversion Congress and Exposition*, pp. 199–206, IEEE, Atlanta, GA, USA, September 2010.

[31] K. Wang, C. Liu, J. Sun et al., "State of charge estimation of composite energy storage systems with supercapacitors and lithium batteries," *Complexity*, vol. 2021, Article ID 8816250, 15 pages, 2021.

[32] Y. Zhang, S. Gao, and W. Xu, "An Improved Model Predictive Current Control of Permanent Magnet Synchronous Motor Drives," in *Proceedings of the 2016 IEEE Applied Power Electronics Conference and Exposition (APEC)*, pp. 2868–2874, IEEE, Long Beach, CA, USA, March 2016.

[33] Y. Zhang, D. Xu, J. Liu, S. Gao, and W. Xu, "Performance improvement of model-predictive current control of permanent magnet synchronous motor drives," *IEEE Transactions on Industry Applications*, vol. 53, no. 4, pp. 3683–3695, 2017.

[34] S. Tozawa, T. Zanma, K.-Z. Liu, Y. Aoki, and H. Yoshida, "Model predictive current control for PMSM considering trade-off between current ripple and number of switching operations," in *Proceedings of the 2015 10th Asian Control Conference (ASCC)*, pp. 1–6, IEEE, Kota Kinabalu, Malaysia, June 2015.

[35] H.-T. Hyung-Tae Moon, H.-S. Hyun-Soo Kim, and M.-J. Myung-Joong Youn, "A discrete-time predictive current control for PMSM," *IEEE Transactions on Power Electronics*, vol. 18, no. 1, pp. 464–472, 2003.

[36] P. Cortes, J. Rodriguez, D. E. Quevedo, and C. Silva, "Predictive current control strategy with imposed load current spectrum," *IEEE Transactions on Power Electronics*, vol. 23, no. 2, pp. 612–618, 2008.

[37] C. K. Lin, T. H. Liu, J. t. Yu, L. C. Fu, and C. F. Hsiao, "Model-free predictive current control for interior permanent-magnet synchronous motor drives based on current difference detection technique," *IEEE Transactions on Industrial Electronics*, vol. 61, no. 2, pp. 667–681, 2014.

[38] X. Feng, Y. Zhang, L. Kang et al., "Integrated energy storage system based on triboelectric nanogenerator in electronic devices," *Frontiers of Chemical Science and Engineering*, vol. 15, no. 2, pp. 238–250, 2021.

[39] Y. Wang, X. Wang, W. Xie et al., "Deadbeat model-predictive torque control with discrete space-vector modulation for PMSM drives," *IEEE Transactions on Industrial Electronics*, vol. 64, no. 5, pp. 3537–3547, 2017.

[40] Y. Xu, B. Zhang, and Q. Zhou, "A model predictive current control method of PMSM based on the simultaneous optimization of voltage vector and duty cycle," in *Proceedings of the 2016 IEEE 8th International Power Electronics and Motion Control Conference (IPEMC-ECCE Asia)*, pp. 881–884, IEEE, Kota Kinabalu, Malaysia, June 2016.

[41] A. M. Bozorgi, M. Farasat, and S. Jafarishiadeh, "Improved Model Predictive Current Control of Permanent Magnet Synchronous Machines with Fuzzy Based Duty Cycle Control," in *Proceedings of the 2016 IEEE Energy Conversion Congress and Exposition (ECCE)*, pp. 1–6, IEEE, Milwaukee, WI, USA, September 2016.

[42] Y. Zhang and X. Wei, "Torque ripple RMS minimization in model predictive torque control of PMSM drives," in *Proceedings of the 2013 International Conference on Electrical Machines and Systems (ICEMS)*, pp. 2183–2188, IEEE, Busan, Korea (South), October 2013.

[43] H. Ran, H. Du, C. Ma, Y. Zhao, D. Feng, and H. Xu, "Effects of A/B-site Co-doping on microstructure and dielectric thermal stability of AgNbO3 ceramics," *Science of Advanced Materials*, vol. 13, no. 5, pp. 741–747, 2021.

[44] L. Kang, H. Du, J. Deng, X. Jing, S. Zhang, and Y. Znang, "Synthesis and catalytic performance of a new V-doped CeO2-supported alkali-activated-steel-slag-based photocatalyst," *Journal of Wuhan University of Technology-Materials Science Edition*, vol. 36, no. 2, pp. 209–214, 2021.

[45] Y. Zhang, J. Jin, and L. Huang, "Model-Free predictive current control of PMSM drives based on extended state observer using ultralocal model," *IEEE Transactions on Industrial Electronics*, vol. 68, no. 2, pp. 993–1003, 2021.

[46] K. Yin, L. Gao, R. Chen, Z. Feng, and S. Liu, "Adaptive deadbeat predictive current control for PMSM with feed forward method," *IEEE Access*, vol. 9, pp. 101300–101310, 2021.

[47] X. Li, Y. Wang, X. Guo, X. Cui, S. Zhang, and Y. Li, "An improved model-free current predictive control method for SPMSM drives," *IEEE Access*, vol. 9, pp. 134672–134681, 2021.

[48] J. Rodriguez, R. Heydari, Z. Rafiee, H. A. Young, F. Flores-Bahamonde, and M. Shahparasti, "Model-Free predictive current control of a voltage source inverter," *IEEE Access*, vol. 8, pp. 211104–211114, 2020.

[49] Y. Yang, M. Fan, M. Xie, and Z. Zhu, "A fixed switching frequency model predictive control for t-type three-level three-phase grid-connected inverters," in *Proceedings of the 2017 12th IEEE Conference on Industrial Electronics and Applications (ICIEA)*, pp. 1137–1142, IEEE, Siem Reap, Cambodia, June 2017.

[50] W. Wang and X. Xi, "Current control method for PMSM with high dynamic performance," in *Proceedings of the 2013 International Electric Machines & Drives Conference*, pp. 1249–1254, IEEE, Chicago, IL, USA, May 2013.

Hindawi
Mathematical Problems in Engineering
Volume 2022, Article ID 9616124, 11 pages
https://doi.org/10.1155/2022/9616124

Review Article

Hybrid Methods Using Neural Network and Kalman Filter for the State of Charge Estimation of Lithium-Ion Battery

Zhenhua Cui,[1] **Jiyong Dai**,[2] **Jianrui Sun**,[2] **Dezhi Li**,[1] **Licheng Wang**,[3] **and Kai Wang**[1]

[1]*School of Electrical Engineering, Weihai Innovation Research Institute, Qingdao University, Qingdao 266000, China*
[2]*Shandong Wide Area Technology Co., Ltd, Dongying 257081, China*
[3]*School of Information Engineering, Zhejiang University of Technology, Hangzhou 310023, China*

Correspondence should be addressed to Kai Wang; wkwj888@163.com

Received 8 November 2021; Accepted 19 April 2022; Published 14 May 2022

Academic Editor: A. M. Bastos Pereira

With the increasing carbon emissions worldwide, lithium-ion batteries have become the main component of energy storage systems for clean energy due to their unique advantages. Accurate and reliable state-of-charge (SOC) estimation is a central factor in the widespread use of lithium-ion batteries. This review, therefore, examines the recent literature on estimating the SOC of lithium-ion batteries using the hybrid methods of neural networks combined with Kalman filtering (NN-KF), classifying the methods into Kalman filter-first and neural network-first methods. Then the hybrid methods are studied and discussed in terms of battery model, parameter identification, algorithm structure, implementation process, appropriate environment, advantages, disadvantages, and estimation errors. In addition, this review also gives corresponding recommendations for researchers in the battery field considering the existing problems.

1. Introduction

With the worldwide reduction of nonrenewable energy sources and carbon dioxide emissions, clean energy development has become an important theme [1–3]. Lithium-ion batteries are gradually regarded as the most natural green alternative to traditional fossil fuels for their high energy density, no memory effect [4], long life, and environmental protection [5]. Lithium-ion batteries are now widely used in electric vehicles, ships, and distributed energy storage systems. With the continuous development of the smart grid, the hybrid energy storage system consisting of lithium-ion batteries and supercapacitors has become an attractive option [6]. The continuous development of lithium-ion batteries also achieves emission peak and carbon neutrality goals.

In contrast to conventional fossil fuels, lithium-ion batteries also need a state parameter indicating the current remaining energy. Therefore, the state of charge (SOC) is proposed [7–9]. SOC is defined as the ratio of the current available capacity of the battery to the maximum available capacity. Consequently, accurate battery capacity estimation is crucial to estimate the SOC [10–12]. By clarifying the change in SOC, the abnormal charging capacity of the battery can be determined, ensuring the safe operation of the electric vehicle [13]. Meanwhile, the accurate estimation of the battery SOC is also the basis for managing lithium-ion batteries and understanding the battery status. However, SOC cannot be measured directly and can only be estimated based on the relationship between SOC and measurable variables [14, 15]. Consequently, it is essential to establish a reliable and accurate SOC estimation method [16].

More and more researchers are enthusiastic about estimating SOC using hybrid methods to improve the precision of SOC estimation. Achieving accurate SOC estimation in natural application environments remains a challenge due to the inconsistency of batteries in the pack [17]. The hybrid method combining neural network with Kalman filter (NN-KF) can solve the nonlinear relationship between battery SOC and other variables by using the self-learning ability and strong self-adaptability of neural

network (NN) [18–20] on the one hand. On the other hand, it is the ability to combine the fast convergence property of the Kalman filter to achieve a real-time estimation of SOC [21–23] and reduce the influence of noise on the results. This review classifies this hybrid method into Kalman filter-first method and the neural network-first method. It is promising to apply the NN-KF hybrid method into practice as an efficient method to obtain SOC estimates for lithium-ion batteries.

The remainder of this review is organized as follows: Section 2 describes the types and characteristics of lithium-ion battery models, the methodological flow of the Thevenin model parameter identification, and a detailed evaluation of all methods. A detailed and comprehensive introduction to the current framework and remarks of Kalman filter-first methods and neural network-first methods is presented in Section 3. Section 4 discusses the future direction from the perspective of the current situation. Conclusion is drawn in Section 5.

2. Modeling and Parameter Identification

SOC estimation of lithium-ion batteries requires high accuracy and reliability of the model, so it is essential to use a reasonable model and a suitable parameter identification method to simulate the battery characteristics.

2.1. Battery Model. Establishing a battery state-space model plays an essential role in the accurate estimation of SOC and directly affects the accuracy of the SOC estimation. To make the state model closer to the actual usage environment and meet the needs of combining neural network and Kalman filter, the battery model must be simple and compatible with the actual situation [24]. The standard battery models used in the research are the Thevenin and the neural network-based models. The following is a brief description of their characteristics.

Thevenin model has a simple structure, high accuracy, and strong robustness even in unknown cell environments. Figure 1(a) shows that it consists of an ideal voltage source U_{OC}, a series resistor R_0, and a capacitor-resistor (RC) network, where R_0 represents the battery's internal resistance, and R_1 and C_1 are the polarization resistance and polarization capacitance, respectively.

The number of RC networks is changeable, and its number represents the order of the Thevenin model. Figure 1(b) is the structural diagram of the second-order Thevenin model.

The complex dynamic characteristics and uncertain operating conditions make building a suitable battery model difficult. The results of SOC estimation under cold conditions were reported to be inadequate [25–29]. Accordingly, the Thevenin model is not perfect [30]. Other suitable battery models, such as the electrochemical-thermal degradation model [31], are still needed to describe the complex battery behavior at different ambient temperatures.

Neural network, a branch of artificial intelligence, has been widely used for predicting outcomes based on input data [32–35]. Compared with the Thevenin model, the neural network-based modeling method does not need to consider the electrochemical state inside the battery. However, it only needs to use the measurable parameters as inputs and establish a nonlinear relationship between the input data and the output data to construct the estimated battery SOC model through the self-learning capability [36].

2.2. Model Parameter Identification. Thevenin model parameters are susceptible to operating conditions such as SOC levels and ambient temperature. During the use of lithium-ion batteries, it is helpful to describe the electrochemical characteristics and improve the accuracy if the model parameters can be effectively identified. Meanwhile, the accurate identification of model parameters can facilitate the combination of Kalman filter and neural network to improve the accuracy of battery SOC estimation. The schematic diagram of the recognition process is depicted in Figure 2.

A large number of algorithms, including genetic algorithms (GA) [37], least squares (LA) [38], and hybrid pulse power characteristic (HPPC) test [39], have been used in recent years for parameter identification of Thevenin models.

Taking the first-order Thevenin model as an example, the unknown parameters are R_0, R_1, and C_1. According to Kirchhoff's law and analyzing the model, the following equations can be obtained:

$$\begin{cases} U_{OC} = U_L - U_R - U_1, \\ I_L = C_1 \dfrac{\mathrm{d}U_1}{\mathrm{d}t} + \dfrac{U_1}{R_1}. \end{cases} \tag{1}$$

The discrete equation is obtained according to equation (1), as shown in the following equation:

$$\begin{cases} \begin{bmatrix} \mathrm{SOC}_{k+1} \\ U_{1,k+1} \end{bmatrix} = \begin{bmatrix} 1 & 0 \\ 0 & e^{-(\triangle t/\tau)} \end{bmatrix} \begin{bmatrix} \mathrm{SOC}_k \\ U_{L,k+1} \end{bmatrix} + \begin{bmatrix} -\dfrac{\triangle t}{Q_N} \\ R_1\left(1 - e^{-(T/\tau)}\right) \end{bmatrix} I_{L,k}, \\ U_{L,k} = U_{OC,k} - R_{0,k} I_{L,k} + \begin{bmatrix} 0 \\ -1 \end{bmatrix}^T \begin{bmatrix} \mathrm{SOC}_k \\ U_{1,k} \end{bmatrix}. \end{cases} \tag{2}$$

In the above two equations, U_1 is the RC network voltage and U_L is the terminal voltage. Q_N is the rated capacity of the battery and I_L is the circuit current. $\triangle t$ is the sampling time interval, and τ is the time constant, $\tau = R_1 C_1$. k is the time parameter.

Yang et al. use GA for the first-order Thevenin model to identify the parameters [37]. GA is a global search method formed by simulating the genetics and evolution of organisms in their natural environment. However, it cannot use the feedback information in time, so the search speed is slow, and it is not good enough to solve the large-scale computation problem. In response to these problems, the

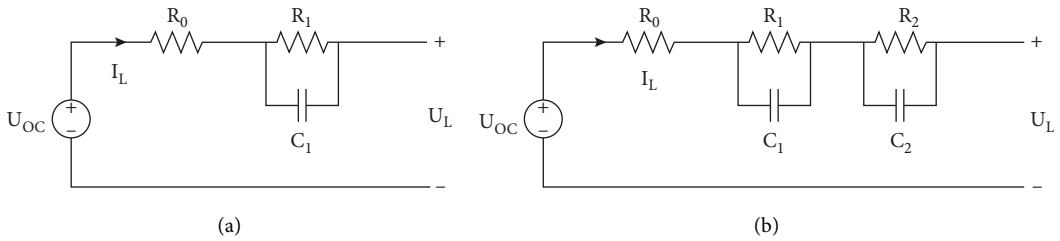

Figure 1: The structure of Thevenin models. (a) Thevenin equivalent circuit model. (b) Second-order Thevenin equivalent circuit model.

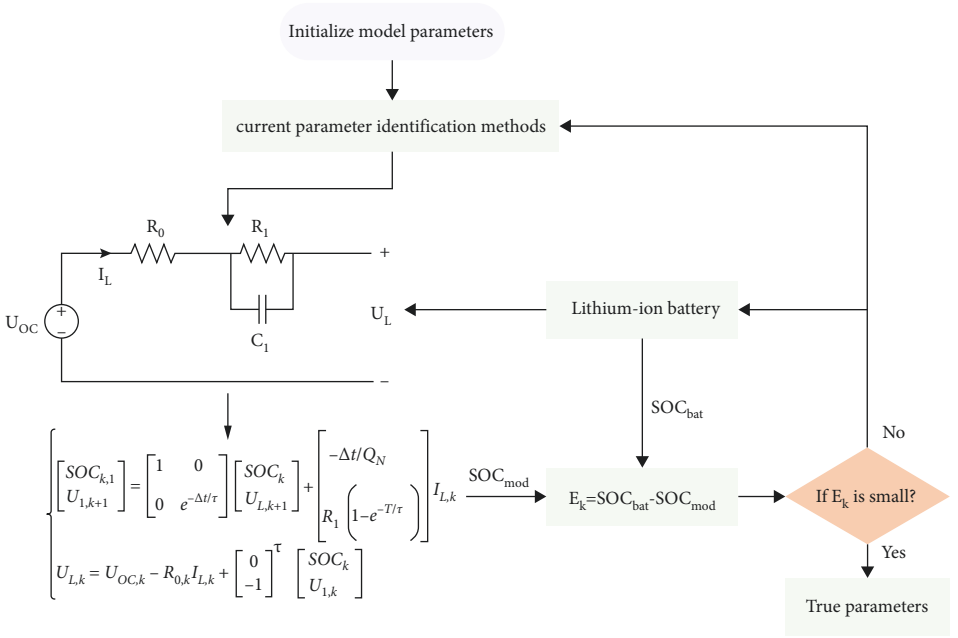

Figure 2: The process of battery parameter identification.

particle swarm optimization (PSO) algorithm is favored by many researchers because it is easier to implement and has lower computational complexity [40].

LA is also a standard method for the identification of battery model parameters. Thevenin battery model can be considered a linear system, identified by the parameter identification toolbox in Matlab/Simulink [41]. According to the parameter fitting function in the toolbox, parameter identification can be achieved using LA. The recursive least squares (RLS) method is proposed to make the algorithm relevant to the practical use environment. Compared to LS, it can extract model parameters in real time using new measurement data [42], significantly reducing the computational and storage effort. Recently, Li et al. performed discharge experiments on lithium-ion batteries and combined RLS to identify R_0, R_1, and C_1 in the battery model. The data from the voltage recovery stage makes it easier to obtain the model parameters to be identified with a high degree of accuracy [43].

The battery model is also affected by noise in the natural application environment. The RLS method is susceptible to noise, resulting in inaccurate identification of model parameters. The recursive total least squares (RTLS) [44], adaptive forgetting recursive total least squares (AF-RTLS) [45], and the Frisch scheme-based bias compensating recursive least squares (FBCRLS) [46] have been proposed to effectively suppress the model identification errors caused by noise, which provides more reliable SOC estimation.

A recursive least squares method with forgetting factors (FFRLS) is also applied to the parameter identification of the Thevenin model. FFRLS has faster convergence and better tracking performance with an increased forgetting factor λ [47]. In general, the smaller λ, the better the computational fit of the system, but the more significant the fluctuation. So, determining the λ value quickly is also an urgent problem to be solved.

HPPC tests can be used to determine the model parameters at different temperatures and different discharge rates. Li et al. (2021) conducted several experiments and finally created a table of battery parameters concerning temperature and discharge rate [39]. Experimental data from another part also verified the validity of the HPPC method. The appropriate methods for identifying battery parameters are summarized in Table 1.

Table 1: Methods for identifying battery model parameters.

Years	Methods	Advantages	Disadvantages
2019	GA [37]	Parallel and global search	Slow search speed
	LA [41]	Calculate the coefficients at one time	Offline
	RLS [42]	Process data in real-time	Taking up a lot of storage space
2020	FFRLS [47]	Better performance	Difficult to decide the value of λ
2021	RLS [43]	Conduct discharge experiments	Time-consuming
	HPPC [39]	Consider temperature and discharge rate	Tedious
	PSO [40]	Lower computational complexity	Easily fall into the local optimum

3. State-of-Charge Estimation

3.1. Kalman Filter-First Method. The basic idea of the Kalman filter-first method is that when the sensor obtains voltage, current, and temperature measurements from the battery, it can be iterated directly since various methods have previously determined the battery model parameters. The values needed by the neural network are then computed, and the final SOC estimation results are output by the neural network. The structure diagram is shown in Figure 3.

The Kalman filtering-first method is highly resistant to interference and suitable for SOC estimation in complex environments, while having high robustness. However, the method relies on an accurate battery model, and different battery models also require reasonable methods for parameter identification.

The traditional KF algorithm is proposed to solve the linear problem [48–50], while the lithium-ion battery can be considered a nonlinear system. Therefore, it is hardly used in the battery SOC estimation process. Several algorithms that can handle nonlinear systems, such as extended Kalman filter (EKF) and Unscented Kalman filter (UKF), are proposed.

The EKF linearizes nonlinear systems with Taylor series expansions, essentially a recursive algorithm. Xu et al. used EKF for the initial estimation of battery SOC and then used the estimated SOC value along with voltage and current as of the input to the long short-term memory (LSTM) network [47]. The model's performance was verified at −15°C, 0°C, and 25°C, respectively, and the mean absolute error (MAE) was less than 1%. The EKF-LSTM maintains high estimation accuracy even at very low ambient temperatures. Similarly, EKF can be combined with the back propagation neural network (BPNN) to estimate the battery SOC [51]. The EKF-BP algorithm is verified by dynamic stress test (DST), Beijing Bus Dynamic Stress Test (BBDST), and other complex working conditions. The estimated error is less than 1.10%.

Both the above algorithms are for individual lithium-ion batteries, while in practical applications, such as electric vehicles, the application of lithium-ion battery packs is much more. When estimating the battery pack SOC, it is not appropriate to consider it as a simple battery. The method discussed previously cannot be directly applied to a battery pack consisting of many batteries. Developing a simple, reliable, and effective SOC estimation method for battery packs is essential.

Dao et al. developed a smart battery management system (BMS) based on KF and NN to estimate the SOC of a lithium-ion battery pack, as shown in Figure 4. The battery pack temperature range is 19–42°C. The performance is better than ANN and KF alone by experimental evaluation on real battery packs with an error of less than 1% [52]. However, there are still some problems with this method. For example, the capacity balance between each battery in the pack is not considered in the application. The capacity decay of each battery varies during use, and the impact of capacity balance on BMS and battery pack SOC estimation needs to be considered.

EKF suffers from computational overload for complex nonlinear problems and generates linearity errors. UKF, proposed by Julier and Uhlmann in 1997 [53], uses lossless transformations to obtain the mean and covariance of individual probabilities, avoiding solving Jacobi matrices. By constructing an adaptive unscented Kalman filter (AUKF) algorithm based on the Thevenin model, Hosseininasab et al. presented a combined NN and AUKF method for SOC estimation [54]. Considering the initial offset, capacity error, and current sensor drift considering shunt thermal effects, the root-mean-square Error (RMSE) still reaches 0.954% at 25°C. The results of SOC estimation based on the Kalman filter-first method are summarized in Table 2.

3.2. Neural Network-First Method. The Kalman filter-first method can accommodate the initial error of the SOC and estimate the SOC effectively online. However, the high computational requirements and effective model parameterization need to be effectively addressed before practical application, which has limited the application of the method to some extent. In contrast, the neural network modeling approach can avoid the detailed study of lithium-ion battery models and parameter identification. A good battery SOC estimation algorithm can be built using only previous reliable data.

For the neural network method alone [55], the SOC estimation results highly depend on the dataset used. Once the data set differs significantly from the applied battery operating conditions, the error in the estimation results of the lithium-ion battery SOC can be substantial. The neural network-first method avoids this problem. Even if a less than perfect data set is used, the output of the NN can be corrected using the KF, and finally, an accurate battery SOC can be obtained.

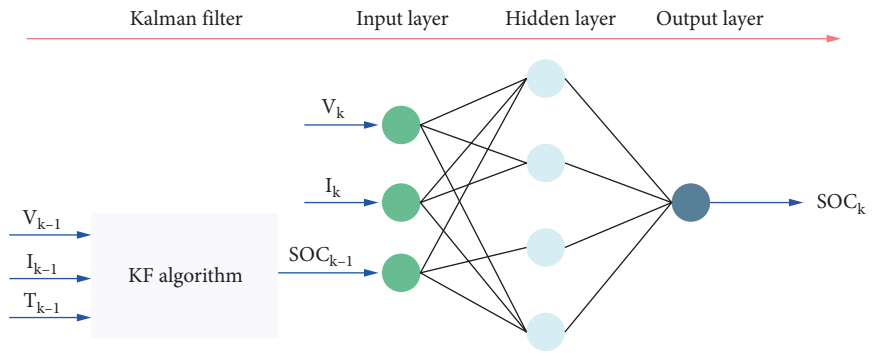

Figure 3: The structure diagram of the KF priority method.

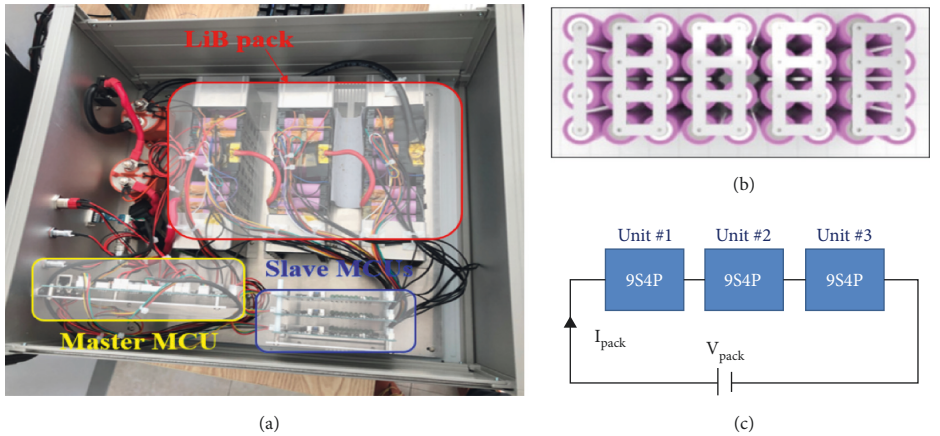

Figure 4: Configurations of the smart BMS and lithium-ion battery pack. Reproduced with permission from reference [23]. Copyright 2021, energies. (a) Smart BMS for experiment. (b) LiB unit configuration (9S4P). (c) LiB pack configuration with units.

Table 2: Kalman filter priority methods used for SOC estimation.

Years	Methods	Remarks	Temperature	SOC errors
2019	EKF-LSTM [47]	High accuracy at low temperatures	−15°C, 0°C, 25°C	MAE < 1%
2020	UKF-NN [54]	Easy to implement	25°C	RMSE = 0.954%
2021	EKF-BPNN [51]	Real-time estimation	Unspecified	<1.10%
	EKF-ANN [52]	Estimate SOC of the battery pack	19–42°C	<1%

The central idea of the neural network-first method is first to use the neural network to reveal the nonlinear relationship between SOC and measurable variables such as current, voltage, and temperature. The output of the NN is then smoothed using a KF algorithm to achieve accurate and stable SOC estimates.

3.2.1. Feed-Forward Neural Network. Feedforward neural network (FNN) is simple in structure and easy to train, which has become the most common method for SOC estimation of lithium-ion batteries [56–58].

Qin et al. used a nonlinear autoregressive neural network (NARXNN) to estimate the SOC of lithium-ion batteries and then applied UKF to reduce the error [59]. Compared with the battery SOC estimation results based on NARXNN alone, the error is reduced by about 1% at 0°C. Since each estimate uses data from a single sampling point and does not consider the dynamic chemistry of the battery, the estimation accuracy of this method is usually not very high.

The polarization characteristics of the battery can be used as a new input to the FNN to describe the dynamic chemistry of the battery accurately. One way to consider polarization is to increase the NN input data from a single sample point to multiple sample points [60], which requires selecting a suitable time constant. The method for selecting the time constant is designed as shown in Figure 5, where τ represents the time constant and $r(x, y)$ represents the correlation coefficient. Chen et al. (2019) designed a neural network-first battery SOC estimation method based on an improved FNN model and EKF algorithm [61]. The SOC estimation error can be kept to less than 2% even with inaccurate initial SOC value, inaccurate initial capacity, and low temperature (−10°C, 0°C, and 10°C). This method is more suitable for complex electric vehicle application environments.

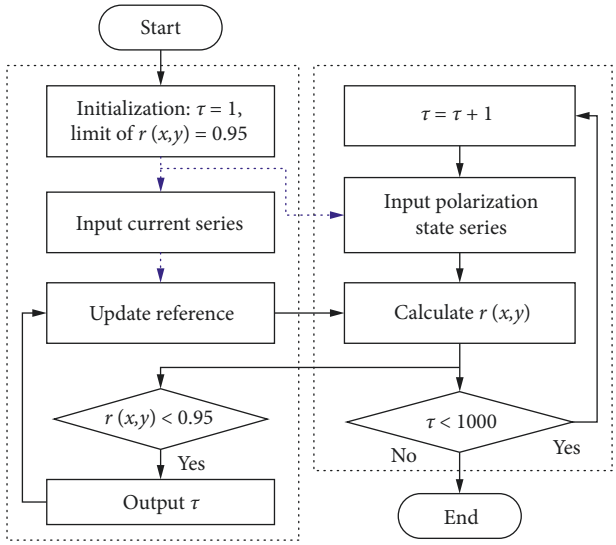

Figure 5: The selection process of time constants. Reproduced with permission from reference [29]. Copyright 2019, Elsevier.

The terminal voltage can be used as the output of the neural network. Meanwhile, the SOC is considered as an internal state, which is indirectly estimated through the feedback error of the voltage [62]. This indirect method has the advantage of uncertainty enhancement and feedback compensation. The effect of temperature on SOC, however, is not considered. Table 3 lists the above studies.

3.2.2. Deep Learning. In recent years, deep learning algorithms have attracted the attention of researchers in the field of battery state estimation because of their ability to automatically extract features and their good generalization performance [63]. Deep learning algorithms are also increasingly introduced into the SOC estimation of lithium-ion batteries.

Deep belief network (DBN) can be combined with KF. The DBN can extract the relationship between battery SOC and input parameters with its strong nonlinear fitting ability. The KF eliminates measurement noise and improves SOC estimation accuracy [64]. The framework of the proposed model is shown in Figure 6. The RMSE of the SOC estimation by DST is lower than 0.7%. This hybrid is suitable for estimating the SOC of lithium-ion batteries under dynamic conditions.

LSTM network can handle time-series data considering the time dependence of SOC estimation. Yang et al. (2020) used a stepwise search algorithm to determine the hyperparameters of the LSTM network and further reduce the estimation error by UKF [65]. The results show that the RMSE of the LSTM-UKF method is 1.1%, which is better than other FNN methods. In addition, the method has excellent generalization ability to the temperature at 0–50°C, and more reliable SOC estimation results can be obtained at temperatures without training data.

The commonly used LSTM network is a "many-to-many" structure, as shown in Figure 7. The output at moment $t+1$ is related to the input information at moment $t+1$ and moment t. The results in earlier information have little to no impact on the current output, making it impossible to take full advantage of the past information.

To address this problem, Tian et al. (2020) proposed a "many-to-one" structure of the LSTM network [66]. This framework introduced an adaptive cubature Kalman filter (ACKF) algorithm that maximizes the impact of the above measurements on current SOC estimates and further extended the applicability of the neural network-first method. High estimation accuracy was achieved in the temperature range of 10 to 50°C. This LSTM-ACKF method avoids finding the optimal hyperparameters in the training phase of the LSTM network, which is very difficult. Only a rough selection in the training phase is needed, and then a more accurate SOC estimation result can be obtained using ACKF.

To accurately estimate the SOC for lithium-ion battery packs, a combination of LSTM and improved square root cubature Kalman filter (SRCKF) is proposed [67]. To address the inconsistency of batteries among packs, Shu et al. designed an iterative rule for LSTM-SRCKF using the smoothing method with the maximum and minimum SOC values in the packs as features. The method could converge quickly to the reference value even at sub-zero temperatures, with RMSE less than 0.4%. This method still has not considered aging problems such as battery capacity decay.

By combining different neural networks, the advantages of each can be retained, which improves the estimation efficiency and applicability. One-dimensional convolutional units can be combined with the gated recurrent unit (GRU) to form a new deep neural network (DNN), as shown in Figure 8. The DNN used 10 minutes of data as input for fast and accurate SOC estimation across the entire battery SOC range [68].

The KF algorithm is introduced to enhance the robustness of the neural network. The DNN-KF method can quickly adapt to batteries with different aging states, and the RMSE can be less than 3.146%. The deep learning-based SOC estimation methods are summarized in Table 4.

Table 3: SOC errors of those estimation methods.

Years	Methods	Remarks	Temperature	SOC errors
2019	NARXNN-UKF [59]	Ignoring dynamic properties	0°C, 25°C, 45°C	<3.55%
	FNN-EKF [61]	Introducing the new input	−10°C, 0°C, 10°C	<2%
2020	RBFNN-UKF [62]	Indirect method to estimate SOC	Unspecified	Unspecified

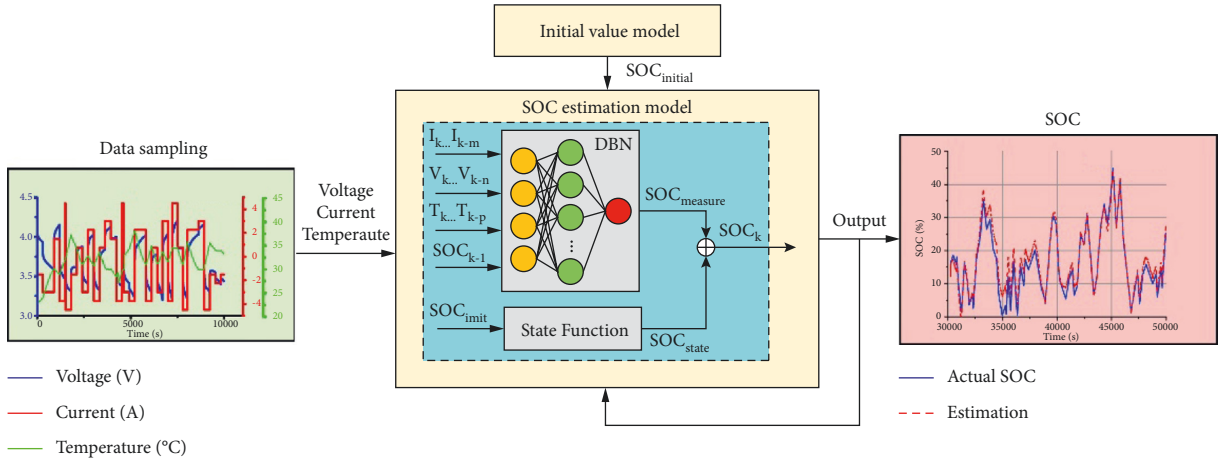

Figure 6: The framework of the proposed model based on DBN-KF. Reproduced with permission from Ref 32. Copyright 2019, Elsevier.

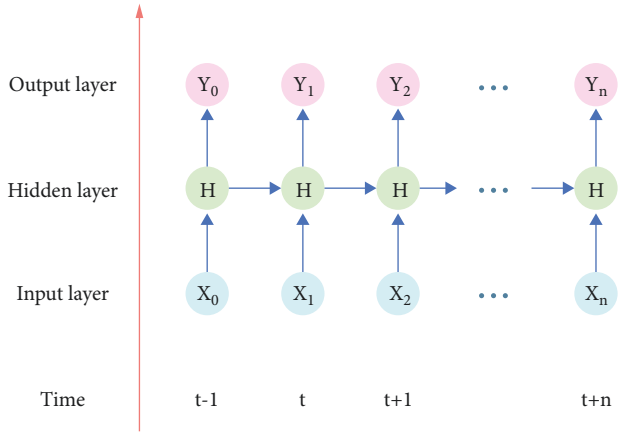

Figure 7: Basic LSTM architecture.

4. Discussion

From the above experimental results, the NN-KF hybrid method to estimate the SOC of lithium-ion battery is accurate. However, there are still some problems that need to be investigated.

(1) The problem of SOC estimation for lithium-ion battery packs has still not been effectively addressed. Battery capacity and SOC imbalance in packs are widespread problems [69]. As a result, developing an NN-KF hybrid method considering the capacity balance of lithium-ion batteries is necessary to improve battery safety and extend the applicability of SOC estimation methods.

(2) In subsequent studies, the use of transfer learning to improve the generalization ability of the hybrid method can be considered so that the method can be generalized to SOC estimation of other types of lithium batteries. After transfer learning, the hybrid method can be quickly adapted to various situations.

(3) Expand the types of the NN-KF hybrid methods through the mutual hybrid of different neural networks and Kalman filters. Analyzing the effects of different combinations on the SOC estimation and finding a more suitable hybrid method might be the following research priorities.

(4) Noise disturbance is still a pressing problem for the Kalman filter-first method. Therefore, an effective method is needed to improve the accuracy of model parameter identification and SOC estimation in the whole life cycle of the battery under noise disturbance.

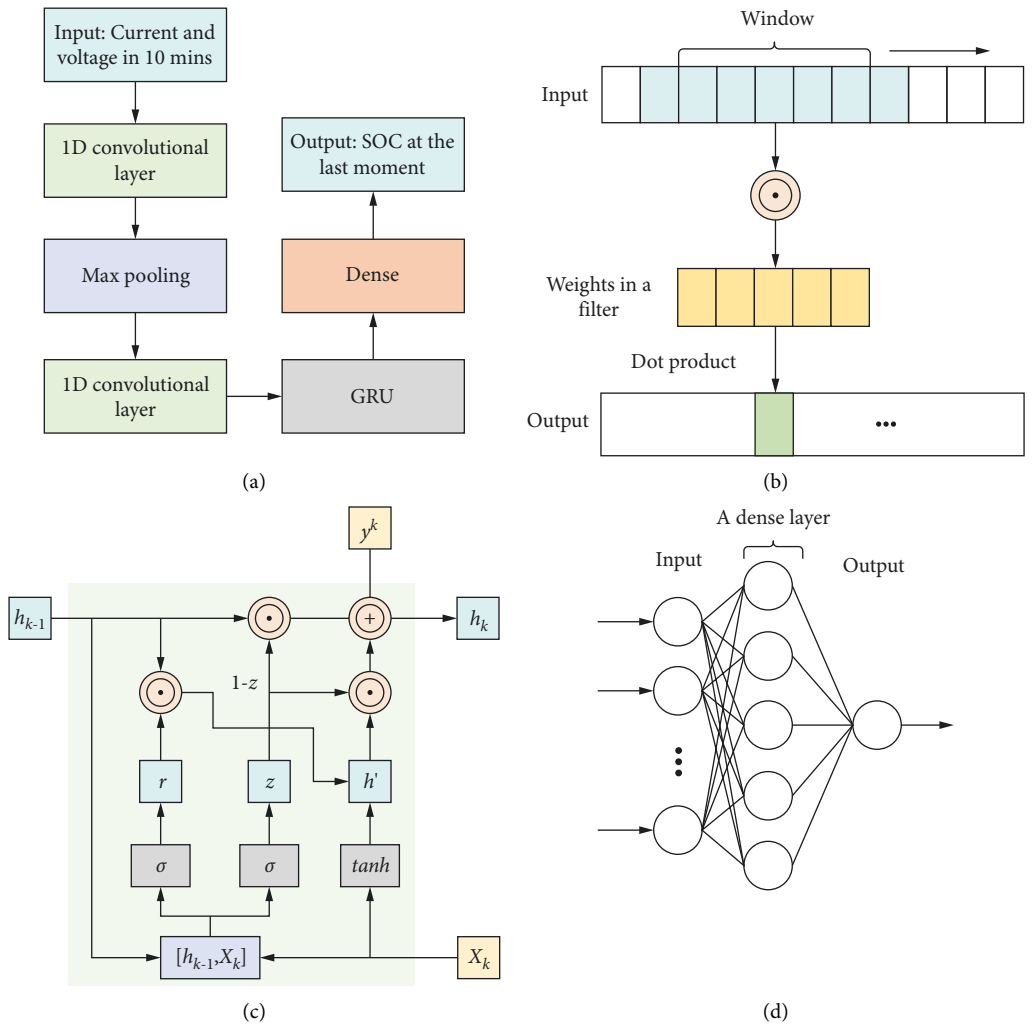

Figure 8: Schematic diagrams of (a) the developed DNN, (b) a 1D convolutional unit, (c) a GRU, and (d) dense layers. Reproduced with permission from reference [36]. Copyright 2021, Elsevier.

Table 4: Deep learning frameworks used for SOC estimation.

Years	Methods	Remarks	Temperature	SOC errors
2019	DBN-KF [64]	Better for dynamic conditions	22°C to 45°C	RMSE <0.7%
2020	LSTM-UKF [65]	Excellent generalization to temperature	0°C to 50°C	RMSE <1.1%
	LSTM-ACKF [66]	Making the most of past information	10°C to 50°C	RMSE <2.2%
2021	LSTM-SRCKF [67]	New iteration rules designed	−20°C to 0°C	RMSE <0.4%
	DNN-KF [68]	Short input time required	Unspecified	RMSE <3.15%

(5) The SOC estimation results are sensitive to temperature changes. In the future, it is essential to improve the stability of SOC estimation methods in more extreme environments. Furthermore, the ambient temperature does not directly reflect the chemical properties inside the battery. The surface temperature of the battery can be used as an input variable for the hybrid method.

(6) SOC needs to be predicted without interruption during the battery life. Therefore, it is essential to ensure that the SOC is accurately estimated even during the continuous aging of the battery. Few hybrid methods consider this problem. Future work is to integrate state of health (SOH) and remaining useful life (RUL) as aging parameters into the NN-KF hybrid method, adapting to different degrees of dynamic characteristics and aging states of the battery.

5. Conclusion

This review analyzes the SOC estimation of lithium-ion batteries based on the NN-KF hybrid method. First, the battery model is introduced, and the parameter

identification methods and procedures are discussed to prepare for SOC estimation. Then, the Kalman filter-first method and the neural network-first method are introduced, and the remarks of each method. Finally, the future development direction is proposed with the actual existing problems.

Lithium-ion batteries' chemical reactions and aging mechanisms are very complex, making it challenging to describe them with a specific model. The existing model parameter identification methods all have their advantages and disadvantages. None of them perfectly matches the natural application environment, which means that most Kalman filter-first methods can only achieve good estimation performance in simulated environments. Of course, the advantages of small computation and short estimation time of Kalman filter-first methods are challenging to be possessed by neural network-first methods. Future research focuses on making the SOC estimation results of NN-KF hybrid methods more accurate, applying these methods to practical application environments, and achieving real-time estimation.

In conclusion, this review makes a significant contribution to the accurate estimation of the SOC and help to expand the use of lithium-ion batteries. The widespread use of lithium-ion batteries can promote energy conservation, carbon dioxide emission reduction, and environmental protection, contributing to emission peak and carbon neutrality goals. This review can also provide a valuable overview and recommendations for researchers in the battery field.

Conflicts of Interest

The authors declare no conflicts of interest.

Acknowledgments

This work was supported by the Youth Fund of Shandong Province Natural Science Foundation (No. ZR2020QE212), Key Projects of Shandong Province Natural Science Foundation (No. ZR2020KF020), the Guangdong Provincial Key Lab of Green Chemical Product Technology (GC202111), Zhejiang Province Natural Science Foundation (No. LY22E070007), and National Natural Science Foundation of China (No. 52007170).

References

[1] H. L. Sun, J. R. Sun, K. Zhao, L. C. Wang, and K. Wang, "Data-driven ICA-Bi-LSTM combined lithium battery SOH estimation," *Mathematical Problems in Engineering*, vol. 20228 pages, Article ID 9645892, 2022.

[2] Z. Cui, L. Wang, Q. Li, and K. Wang, "A comprehensive review on the state of charge estimation for lithium-ion battery based on neural network," *International Journal of Energy Research*, vol. 46, no. 5, pp. 5423–5440, 2022.

[3] K. Yin, L. Wang, Q. Deng et al., "Femtosecond laser thermal accumulation-triggered micro-/nanostructures with patternable and controllable wettability towards liquid manipulating," *Nano-Micro Letters*, vol. 14, p. 97, 2022.

[4] D. Feng, H. Du, H. Ran et al., "Antiferroelectric stability and energy storage properties of Co-doped AgNbO3 ceramics," *Journal of Solid State Chemistry*, vol. 310, Article ID 123081, 2022.

[5] Z. Yi, K. Zhao, J. Sun, L. Wang, K. Wang, and Y. Ma, "Prediction of the remaining useful life of supercapacitors," *Mathematical Problems in Engineering*, vol. 2022, Article ID 7620382, 2022.

[6] L. Zhang, X. Hu, Z. Wang et al., "Hybrid electrochemical energy storage systems: an overview for smart grid and electrified vehicle applications," *Renewable and Sustainable Energy Reviews*, vol. 139, Article ID 110581, 2021.

[7] D. Z. Li, W. C. Wang, C. X. Duan, Q. Li, and L. Wang, "Temperature prediction of lithium-ion batteries based on electrochemical impedance spectrum: a review," *International Journal of Energy Research*, 2022.

[8] C. Liu, Q. Li, and K. Wang, "State-of-charge estimation and remaining useful life prediction of supercapacitors," *Renewable and Sustainable Energy Reviews*, vol. 150, Article ID 111408, 2021.

[9] K. Wang, C. Liu, J. Sun et al., "State of charge estimation of composite energy storage systems with supercapacitors and lithium batteries," *Complexity*, vol. 2021, pp. 1–15, 2021.

[10] J. He, Z. Wei, X. Bian, and F. Yan, "State-of-Health estimation of lithium-ion batteries using incremental capacity analysis based on voltage-capacity model," *IEEE Transactions on Transportation Electrification*, vol. 6, no. 2, pp. 417–426, 2020.

[11] H. Ruan, H. He, Z. Wei, Z. Quan, and Y. Li, "State of health estimation of lithium-ion battery based on constant-voltage charging reconstruction," *IEEE Journal of Emerging and Selected Topics in Power Electronics*, p. 1, 2021.

[12] X. Bian, Z. Wei, J. He, F. Yan, and L. Liu, "A novel model-based voltage construction method for robust state-of-health estimation of lithium-ion batteries," *IEEE Transactions on Industrial Electronics*, vol. 68, no. 12, Article ID 12173, 2021.

[13] Z. Wang, C. Song, L. Zhang, Y. Zhao, P. Liu, and D. G. Dorrell, "A data-driven method for battery charging capacity abnormality diagnosis in electric vehicle applications," *IEEE Transactions on Transportation Electrification*, vol. 8, no. 1, 2021, https://doi.org/10.1109/TTE.2021.3117841.

[14] K. Wang, W. Wang, L. Wang, and L. Li, "An improved SOC control strategy for electric vehicle hybrid energy storage systems," *Energies*, vol. 13, no. 20, p. 5297, 2020.

[15] W. Kai, F. Xiao, J. Pang, R. Jun, C. Duan, and L. Li, "State of charge (SOC) estimation of lithium-ion battery based on adaptive square root unscented kalman filter," *International Journal of Electrochemical Science*, vol. 15, no. 9, pp. 9499–9516, 2020.

[16] K. A. Severson, P. M. Attia, N. Jin et al., "Data-driven prediction of battery cycle life before capacity degradation," *Nature Energy*, vol. 4, no. 5, pp. 383–391, 2019.

[17] C. She, L. Zhang, Z. Wang, F. Sun, P. Liu, and C. Song, "Battery state of health estimation based on incremental capacity analysis method: synthesizing from cell-level test to real-world application," *IEEE Journal of Emerging and Selected Topics in Power Electronics*, p. 1, 2021.

[18] E. Chemali, P. J. Kollmeyer, M. Preindl, R. Ahmed, and A. Emadi, "Long short-term memory networks for accurate state-of-charge estimation of Li-ion batteries," *IEEE Transactions on Industrial Electronics*, vol. 65, no. 8, pp. 6730–6739, 2018.

[19] H. Ran, H. Du, C. Ma, Y. Zhao, D. Feng, and H. Xu, "Effects of A/B-site Co-doping on microstructure and dielectric thermal

stability of AgNbO3 ceramics," *Science of Advanced Materials*, vol. 13, no. 5, pp. 741–747, 2021.

[20] J. Zhao, F. Li, Z. Wang, P. Dong, G. Xia, and K. Wang, "Flexible PVDF nanogenerator-driven motion sensors for human body motion energy tracking and monitoring," *Journal of Materials Science: Materials in Electronics*, vol. 32, no. 11, pp. 14715–14727, 2021.

[21] G. L. Plett, "Extended Kalman filtering for battery management systems of LiPB-based HEV battery packs," *Journal of Power Sources*, vol. 134, no. 2, pp. 277–292, 2004.

[22] X. Feng, Q. Li, and K. Wang, "Waste plastic triboelectric nanogenerators using recycled plastic bags for power generation," *ACS Applied Materials & Interfaces*, vol. 13, no. 1, pp. 400–410, 2021.

[23] C. Liu, Y. Zhang, J. Sun, Z. Cui, and K. Wang, "Stacked bidirectional LSTM RNN to evaluate the remaining useful life of supercapacitor," *International Journal of Energy Research*, vol. 46, no. 3, pp. 3034–3043, 2022.

[24] Z. Wei, J. Zhao, H. He, G. Ding, H. Cui, and L. Liu, "Future smart battery and management: advanced sensing from external to embedded multi-dimensional measurement," *Journal of Power Sources*, vol. 489, Article ID 229462, 2021.

[25] V. P. Sakthivel and P. D. Sathya, "Single and multi-area multi-fuel economic dispatch using a fuzzified squirrel search algorithm," *Protection and Control of Modern Power Systems*, vol. 6, no. 1, p. 11, 2021.

[26] R. Xiong, J. Tian, W. Shen, and F. Sun, "A novel fractional order model for state of charge estimation in lithium ion batteries," *IEEE Transactions on Vehicular Technology*, vol. 68, no. 5, pp. 4130–4139, 2019.

[27] W. Wang, J. Pang, J. Su et al., "Applications of Nanogenerators for Biomedical Engineering and Healthcare Systems," *InfoMat*, vol. 4, no. 2, Article ID e12262, 2022.

[28] D. Yuan, C. Zhang, S. Tang et al., "Ferric ion-ascorbic acid complex catalyzed calcium peroxide for organic wastewater treatment: optimized by response surface method," *Chinese Chemical Letters*, vol. 32, no. 11, pp. 3387–3392, 2021.

[29] H. Xu, H. Du, L. Kang, Q. Cheng, D. Feng, and S. Xia, "Constructing straight pores and improving mechanical properties of Gangue-Based porous ceramics," *Journal of Renewable Materials*, vol. 9, no. 12, pp. 2129–2141, 2021.

[30] J. Hu, H. He, Z. Wei, and Y. Li, "Disturbance-immune and aging-robust internal short circuit diagnostic for lithium-ion battery," *IEEE Transactions on Industrial Electronics*, vol. 69, no. 2, pp. 1988–1999, 2022.

[31] Y. Li, Z. Wei, B. Xiong, and D. M. Vilathgamuwa, "Adaptive ensemble-based electrochemical-thermal-degradation state estimation of lithium-ion batteries," *IEEE Transactions on Industrial Electronics*, vol. 69, 2021.

[32] D. Z. Li, S. Li, S. Zhang, J. R. Sun, L. C. Wang, and K. Wang, "Aging state prediction for supercapacitors based on heuristic Kalman filter optimization extreme learning machine," *Energy*, vol. 250, Article ID 123773, 2022.

[33] Y. Liu, L. Zhang, J. Jiang, S. Wei, S. Liu, and W. Zhang, "A data-driven learning-based continuous-time estimation and simulation method for energy efficiency and coulombic efficiency of lithium ion batteries," *Energies*, vol. 10, no. 5, p. 597, 2017.

[34] C. Ma, H. Du, J. Liu et al., "High-temperature stability of dielectric and energy-storage properties of weakly-coupled relaxor (1-x)BaTiO3-xBi(Y1/3Ti1/2)O3 ceramics," *Ceramics International*, vol. 47, no. 17, Article ID 25029, 2021.

[35] L. Kang, H. Du, J. Deng, X. Jing, S. Zhang, and Y. Znang, "Synthesis and catalytic performance of a new V-doped CeO2-supported alkali-activated-steel-slag-based photocatalyst," *Journal of Wuhan University of Technology-Materials Science Edition*, vol. 36, no. 2, pp. 209–214, 2021.

[36] B. H. M. Sadeghi, "A BP-neural network predictor model for plastic injection molding process," *Journal of Materials Processing Technology*, vol. 103, no. 3, pp. 411–416, 2000.

[37] Q. Li, D. Li, K. Zhao, L. Wang, and K. Wang, "State of health estimation of lithium-ion battery based on improved ant lion optimization and support vector regression," *Journal of Energy Storage*, vol. 50, Article ID 104215, 2022.

[38] V. H. Duong, H. A. Bastawrous, K. C. Lim, K. W. See, P. Zhang, and S. X. Dou, "SOC Estimation for LiFePO4 Battery in EVs Using Recursive Least-Squares with Multiple Adaptive Forgetting Factors," in *Proceedings of the 2014 International Conference On Connected Vehicles And Expo (ICCVE)*, pp. 520-521, Vienna, Austria, November 2014.

[39] Y. Li, G. Xu, B. Xu, and Y. Zhang, "A novel fusion model for battery online state of charge (SOC) estimation," *International Journal of Electrochemical Science*, vol. 16, no. 1, Article ID 151050, 2021.

[40] X. Bian, Z. Wei, J. He, F. Yan, and L. Liu, "A two-step parameter optimization method for low-order model-based state-of-charge estimation," *IEEE Transactions on Transportation Electrification*, vol. 7, no. 2, pp. 399–409, 2021.

[41] Z. Wu, M. Shang, D. Shen, and S. Qi, "SOC estimation for batteries using MS-AUKF and neural network," *Journal of Renewable and Sustainable Energy*, vol. 11, no. 2, Article ID 024103, 2019.

[42] X. Li, Z. Wang, and L. Zhang, "Co-estimation of capacity and state-of-charge for lithium-ion batteries in electric vehicles," *Energy*, vol. 174, pp. 33–44, 2019.

[43] J. Li, J. Zhang, and S. Zhang, "Lithium battery SOC estimation based on ABP-EKF algorithm," *Journal of Chongqing Jiaotong University. Natural Science*, vol. 40, no. 3, pp. 125–140, 2021.

[44] Z. Wei, C. Zou, F. Leng, B. H. Soong, and K.-J. Tseng, "Online model identification and state-of-charge estimate for lithium-ion battery with a recursive total least squares-based observer," *IEEE Transactions on Industrial Electronics*, vol. 65, no. 2, pp. 1336–1346, 2018.

[45] Z. Wei, J. Zhao, R. Xiong, G. Dong, J. Pou, and K. J. Tseng, "Online estimation of power capacity with noise effect attenuation for lithium-ion battery," *IEEE Transactions on Industrial Electronics*, vol. 66, no. 7, pp. 5724–5735, 2019.

[46] Z. Wei, S. Meng, B. Xiong, D. Ji, and K. J. Tseng, "Enhanced online model identification and state of charge estimation for lithium-ion battery with a FBCRLS based observer," *Applied Energy*, vol. 181, pp. 332–341, 2016.

[47] S. Padhy and S. Panda, "Application of a simplified Grey Wolf optimization technique for adaptive fuzzy PID controller design for frequency regulation of a distributed power generation system," *Protection and Control of Modern Power Systems*, vol. 6, no. 1, p. 2, 2021.

[48] X. Feng, Y. Zhang, L. Kang et al., "Integrated energy storage system based on triboelectric nanogenerator in electronic devices," *Frontiers of Chemical Science and Engineering*, vol. 15, no. 2, pp. 238–250, 2020.

[49] C. Bu, F. Li, K. Yin, J. Pang, L. Wang, and K. Wang, "Research progress and prospect of triboelectric nanogenerators as self-powered human body sensors," *ACS Applied Electronic Materials*, vol. 2, no. 4, pp. 863–878, 2020.

[50] Y. Hua, N. Wang, and K. Zhao, "Simultaneous unknown input and state estimation for the linear system with a rank-deficient distribution matrix," *Mathematical Problems in Engineering*, vol. 2021, Article ID 6693690, 11 pages, 2021.

[51] Y. Zhou, Y. Wang, K. Wang et al., "Hybrid genetic algorithm method for efficient and robust evaluation of remaining useful life of supercapacitors," *Applied Energy*, vol. 260, Article ID 114169, 2020.

[52] V. Q. Dao, M.-C. Dinh, C. S. Kim et al., "Design of an effective state of charge estimation method for a lithium-ion battery pack using extended kalman filter and artificial neural network," *Energies*, vol. 14, no. 9, p. 2634, 2021.

[53] S. J. Julier and J. K. Uhlmann, "New extension of the Kalman filter to nonlinear systems," in *Signal processing, sensor fusion, and target recognition VI*vol. 3068, , pp. 182–193, International Society for Optics and Photonics, 1997.

[54] S. Hosseininasab, Z. Wan, T. Bender, G. Vagnoni, and L. Bauer, "State-of-Charge Estimation of Lithium-Ion Battery Based on a Combined Method of Neural Network and Unscented Kalman filter," in *Proceedings of the 2020 IEEE Vehicle Power and Propulsion Conference (VPPC)*, Gijon, Spain, December 2020.

[55] G. Xia, Y. Huang, F. Li et al., "A thermally flexible and multisite tactile sensor for remote 3D dynamic sensing imaging," *Frontiers of Chemical Science and Engineering*, vol. 14, no. 6, pp. 1039–1051, 2020.

[56] C. Bian, H. He, and S. Yang, "Stacked bidirectional long short-term memory networks for state-of-charge estimation of lithium-ion batteries," *Energy*, vol. 191, Article ID 116538, 2020.

[57] C. Duan, Y. Yu, J. Li et al., "Recent advances in the synthesis of monolithic metal-organic frameworks," *Science China Materials*, vol. 64, no. 6, pp. 1305–1319, 2021.

[58] W. Zhou, H. Du, L. Kang et al., "Microstructure evolution and improved permeability of ceramic waste-based bricks," *Materials*, vol. 15, no. 3, p. 1130, 2022.

[59] X. Qin, M. Gao, Z. He, and Y. Liu, "State of Charge Estimation for Lithium-Ion Batteries Based on NARX Neural Network and UKF," in *Proceedings of the 2019 IEEE 17th International Conference On Industrial Informatics (INDIN)*, pp. 1706–1711, Helsinki, Finland, July 2019.

[60] Y. Wang, D. Yang, X. Zhang, and Z. Chen, "Probability based remaining capacity estimation using data-driven and neural network model," *Journal of Power Sources*, vol. 315, pp. 199–208, 2016.

[61] C. Chen, R. Xiong, R. Yang, W. Shen, and F. Sun, "State-of-charge estimation of lithium-ion battery using an improved neural network model and extended Kalman filter," *Journal of Cleaner Production*, vol. 234, pp. 1153–1164, 2019.

[62] W. Sun, Y. Qiu, L. Sun, and Q. Hua, "Neural network-based learning and estimation of battery state-of-charge: a comparison study between direct and indirect methodology," *International Journal of Energy Research*, vol. 44, no. 13, Article ID 10307, 2020.

[63] S. Shen, M. Sadoughi, M. Li, Z. Wang, and C. Hu, "Deep convolutional neural networks with ensemble learning and transfer learning for capacity estimation of lithium-ion batteries," *Applied Energy*, vol. 260, Article ID 114296, 2020.

[64] D. Liu, L. Li, Y. Song, L. Wu, and Y. Peng, "Hybrid state of charge estimation for lithium-ion battery under dynamic operating conditions," *International Journal of Electrical Power & Energy Systems*, vol. 110, pp. 48–61, 2019.

[65] F. Yang, S. Zhang, W. Li, and Q. Miao, "State-of-charge estimation of lithium-ion batteries using LSTM and UKF," *Energy*, vol. 201, Article ID 117664, 2020.

[66] Y. Tian, R. Lai, X. Li, L. Xiang, and J. Tian, "A combined method for state-of-charge estimation for lithium-ion batteries using a long short-term memory network and an adaptive cubature Kalman filter," *Applied Energy*, vol. 265, Article ID 114789, 2020.

[67] X. Shu, G. Li, Y. Zhang, S. Shen, Z. Chen, and Y. Liu, "Stage of charge estimation of lithium-ion battery packs based on improved cubature kalman filter with long short-term memory model," *IEEE Transactions on Transportation Electrification*, vol. 7, no. 3, pp. 1271–1284, 2021.

[68] J. Tian, R. Xiong, W. Shen, and J. Lu, "State-of-charge estimation of LiFePO4 batteries in electric vehicles: a deep-learning enabled approach," *Applied Energy*, vol. 291, Article ID 116812, 2021.

[69] C. Jian and A. Emadi, "A new battery/UltraCapacitor hybrid energy storage system for electric, hybrid, and plug-in hybrid electric vehicles," *IEEE Transactions on Power Electronics*, vol. 27, no. 1, pp. 122–132, 2012.

Hindawi
Mathematical Problems in Engineering
Volume 2022, Article ID 7620382, 8 pages
https://doi.org/10.1155/2022/7620382

Review Article

Prediction of the Remaining Useful Life of Supercapacitors

Zhenxiao Yi,[1,2] **Kun Zhao**,[3] **Jianrui Sun**,[3] **Licheng Wang**,[4] **Kai Wang**,[2] **and Yongzhi Ma**[1]

[1]*College of Mechanical and Electrical Engineering, Qingdao University, Qingdao 266000, China*
[2]*School of Electrical Engineering, Weihai Innovation Research Institute, Qingdao University, Qingdao 266000, China*
[3]*Shandong Wide Area Technology Co., Ltd, Dongying 257081, China*
[4]*School of Information Engineering, Zhejiang University of Technology, Hangzhou 310023, China*

Correspondence should be addressed to Kai Wang; wkwj888@163.com and Yongzhi Ma; hiking@126.com

Received 25 January 2022; Revised 1 March 2022; Accepted 10 April 2022; Published 11 May 2022

Academic Editor: Ali Ahmadian

As a new type of energy-storage device, supercapacitors are widely used in various energy storage fields because of their advantages such as fast charging and discharging, high power density, wide operating temperature range, and long cycle life. However, the degradation and failure of supercapacitors in large-scale applications will adversely affect the operation of the whole system. To maximize the efficiency of supercapacitors without damaging the equipment and to ensure timely replacement before reaching the end of their useful life, it is critical to accurately predict the remaining useful life of supercapacitors. This paper presents a comprehensive review of model-based and data-driven approaches to predict the remaining useful life of supercapacitors, introduces the characteristics of the various methods, and foresees future trends, with the expectation of providing a reference for further research in this field.

1. Introduction

With the rapid development of the global economy, the living standard of human beings has been improving, and the consumption of resources has been further increased. For example, the massive burning of coal will also produce numerous solid wastes [1], the generation and discharge of industrial wastewater and cause serious water pollution [2], and the problems of energy crisis and environmental pollution are becoming more and more serious [3, 4]. In this context, the concept of green environmental protection, energy-saving, and low carbon has gradually become popular. Tens of thousands of plastics produced by humans have caused immeasurable harm to the environment, while energy consumption is becoming more and more serious, and a study has proposed a triboelectric nanogenerator (TENG) based entirely on waste plastic bags [5]. In addition, a study has formed high-efficiency photovoltaic cells based on PdSe2 [6]. Some studies combine energy storage elements with material directions in an attempt to develop efficient and low-cost energy-consuming devices [7–12].

In addition, new high-performance, low carbon, and green energy storage power systems are a key approach to improve this situation [13]. Similarly, energy-storage power systems have a wide range of applications in biomedical and medical devices and motion sensors [14, 15]. Energy storage systems also have unique advantages in industrial, military, transportation, and power fields [16–18]. Lithium batteries [19, 20] and capacitors play an important role in new energy-storage power systems, where capacitors are mainly classified as dielectric energy storage capacitors and widely studied supercapacitors [21]. To solve the problem that electrical conductivity and cycle life cannot meet the requirements of applications, various types of metal-organic frameworks (MOFs) materials [22] have been tried to be used in supercapacitors and metal cells to explore their electrochemical energy storage mechanisms, stability of electrode materials, charge transfer pathways, mass transfer, and electrochemical reactions. Dielectric energy storage

capacitors are mainly lead-free energy storage ceramics [23], which have a certain potential for application due to their higher effective energy storage density compared to conventional linear dielectrics. Lead-free energy storage ceramics are both environmentally friendly and less dense than lead-based materials because they are lead-free materials, which facilitates lightweight in applications [24]. Supercapacitors (SCs), as a new type of energy storage device, have the advantages of fast charging and discharging, high power density, wide operating temperature range, long cycle life, and high reliability [25].

At this stage, ultracapacitors are widely used in standby or emergency power, alone or mixed with batteries as peak power, as well as in control systems, communication fields, hybrid electric vehicles, and smart grids. Meanwhile, a study has proposed an optimized power distribution method for hybrid energy-storage systems for electric vehicles (EVs) [26]. The hybrid energy storage system (HESS) uses two isolated soft-switched symmetrical half-bridge bidirectional converters connected to a battery and a supercapacitor (SC) as a protection structure for the composite structure. It helps to improve energy utilization and reduce the battery aging effect.

However, since an energy storage system consisting of ultracapacitors is a complex nonlinear system, degradation and failure of individual ultracapacitors in an application will adversely affect the operation of the entire system. Therefore, accurate prediction of the remaining useful life (RUL) of ultracapacitors is crucial to improve the reliability of energy storage systems and effectively reduce the occurrence of failures.

The mainstream methods are mainly model-based and data-driven approaches. The model-based approaches consider the battery loading conditions, material properties, and degradation mechanisms, mainly including equivalent circuit models, electrochemical models, and empirical degradation models [27, 28]. However, the principles of model-based approaches are complex and vulnerable to external factors, making it difficult to build stable models. Notably, data-driven methods do not require complex modeling and internal mechanism analysis, are highly flexible and scalable, and have been widely used in recent years [29].

This paper reviews model-based and data-driven approaches to predict the remaining useful life of supercapacitors and analyzes the characteristics and problems of each approach as well as future research trends.

2. Operating Principle and Aging Mechanism

2.1. Operating Principle. According to the energy-storage mechanism, supercapacitors are divided into double-layer capacitors and Faraday capacitors. The double-layer capacitor uses carbon material as an electrode to store electrical energy by electrostatic effect, and the physical reaction occurs and the process is reversible. The energy storage is achieved by the potential difference between the two solid electrodes due to the adsorption of positive and negative ions on the surface between the solid electrode and the electrolyte, respectively. During charging, the anions and cations in the electrolyte gather on the surfaces of the two solid electrodes under the effect of charge gravity on the solid electrodes; during discharging, the anions and cations leave the surfaces of the solid electrodes and return to the electrolyte body, while the stored charge is released through an external circuit. The changes in the supercapacitor before and after charging are shown in Figure 1.

When a Faraday capacitor is charged, the ions in the electrolyte diffuse into the solution under the action of the applied electric field to the electrode/solution interface and then enter the electrode surface-active oxide through the electrochemical reaction at the interface; if the electrode material is an oxide with a large specific surface area, a considerable number of such electrochemical reactions take place and a large amount of charge is stored in the electrode. When discharging, these ions that enter the oxide are returned to the electrolyte, while the stored charge is released through the external circuit. Thus, it is able to supply power to the load.

Therefore, electrode materials and electrolytes can have a huge impact on the electrochemistry of supercapacitors and are also important factors in the aging of supercapacitors.

2.2. Aging Mechanism. The study of the aging mechanism of supercapacitors is important for the accurate prediction of the remaining service life of supercapacitors.

Supercapacitors consist of electrodes, electrolyte, diaphragm, and fluid collector, so the aging characteristics of supercapacitors usually refer to case damage, electrolyte decomposition, and electrode degradation [30]. In practical applications, their service life is also influenced by external stresses. For example, voltage, current, and temperature are the main factors affecting the aging of supercapacitors. Water decomposition of supercapacitors generates a certain amount of air pressure inside the case, which may damage the case with long-term use or in extreme cases. In the temperature range, high temperatures will promote the chemical activity of activated carbon electrodes and accelerate their aging. The capacitance value of supercapacitors is directly proportional to the specific surface area of the electrode material, so changes in the electrode material often cause a decrease in the specific surface area and thus the capacity of supercapacitors [31]. The by-products of aging of supercapacitors and polymers will result in a smaller pore structure on the electrode surface, and impurities from electrolyte decomposition reduce the ability of ions to reach the cavities, leading to an increase in the equivalent series resistance (ESR). This affects the normal embedding and deembedding of ions and makes the performance of the supercapacitor degraded.

In addition, during the preparation of electrode materials, a small number of impurities as well as oxygen-containing functional groups, remain on the electrode surface, which can lead to a faster decrease in capacitance value of supercapacitors in the early stages of aging [32].

Under the influence of these aging factors, the RUL of supercapacitors gradually degrades along a certain nonlinear

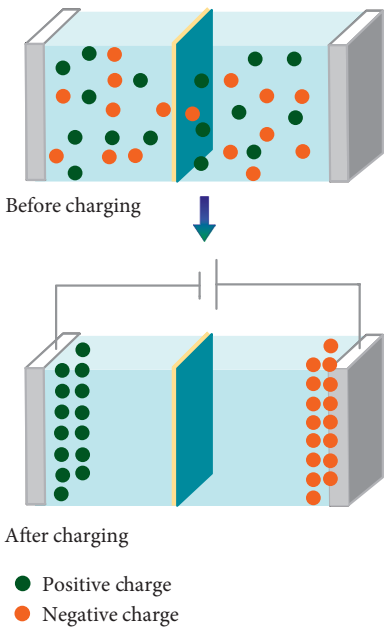

Figure 1: Principle of operation of supercapacitors.

curve until it reaches the critical allowable use range [33]. Therefore, it is important to accurately predict the RUL of supercapacitors to ensure the safety and reliability of their operation.

3. Model-Based Prediction Methods

The model-based prediction method is an effective way to evaluate the lifetime of supercapacitor devices by building an equivalent circuit model based on the electrical performance or energy storage principle of the supercapacitor. The equivalent circuit model uses a parametric RC (capacitor-resistor) network to model the electrical behavior of the supercapacitor, and usually uses ordinary differential equations with simplicity and ease of implementation in the model formulation.

The study conducted by Liu et al. [34] can fit the parameters of the power function model better based on the decay trajectory of supercapacitor capacitance and extrapolate the failure life model which conforms to the Weibull distribution. The validation results of the life model show that the relative error decreases as the number of cycles increases, and the cycle life of supercapacitors can be better predicted by choosing the appropriate number of cycles. In the literature [35], a prediction model of supercapacitor capacity decay including temperature, current intensity, and cycle number factors was established based on the classical Arrhenius model through the performance decay law exhibited by supercapacitors under different charging and discharging currents and temperature conditions. The validation results show that the fitted results are in good agreement with the actual decay data, and most of the relative errors are within 3%. In the literature [36], an online estimation scheme based on particle filtering (PF) is proposed to estimate the state of health (SOH) of SC by combining the electrical equivalent circuit model (ECM) and thermal model and to monitor the SOH of SC by estimating the equivalent series resistance (ESR) and device capacity in real-time.

Based on this, a supercapacitor RUL prediction model considering aging conditions such as temperature and voltage was proposed in the literature [37]. Experiments conducted under different aging conditions found that the method can predict the capacitance and resistance as well as the RUL under different initial conditions well in addition to considering voltage and temperature, an improved reliability model was proposed in the literature [38], which simulates the voltage, temperature, and humidity levels to which the supercapacitor is exposed during operation under actual operating conditions, further improving the prediction accuracy of the model.

Model-based prediction methods usually combine different models and filtering methods to achieve data tracking and prediction of the remaining lifetime of supercapacitors. However, model-based prediction methods are very complex and difficult to implement due to the complexity of supercapacitors.

4. Data-Driven Forecasting Methods

Compared with model-based methods, data-based methods do not require complex mathematical models to simulate the internal aging mechanism of supercapacitors. They are methods to predict the trends of device parameters during the aging process mainly based on historical data of supercapacitor aging process and state data, such as artificial neural networks and fuzzy logic.

A simple recurrent neural network (SIM RNN) was proposed in the literature [39] for supercapacitor lifetime prediction, but SIM RNN has the disadvantage of long-term dependent learning. If the information is stored for too long, the gradient will disappear and the SIM RNN cannot continue to learn. Zhao et al. [40] proposed a lifetime prediction method based on long short-term memory neural network (LSTM RNN), which used the Dropout algorithm to prevent overfitting and optimized the neural network using Adam's algorithm. The input of the neural network is the measurement data under different operating conditions that are divided into training and prediction sets, and the root mean square error (RMSE) of the prediction results is about 0.0261. The life prediction of offline data has a mean absolute error (MAE) of about 0.0338, which proves the applicability of the algorithm. The gated recurrent unit (GRU) structure is simpler than the LSTM. The advantage of the GRU is that it is a simpler simple model with fewer parameters, and GRU is more likely to converge. However, the LSTM RNN has better performance when the data set is larger [41]. Therefore, the long-short memory neural network is very suitable for the prediction of the remaining lifetime of supercapacitors.

Zhou et al. [42] proposed an algorithm combining a long short-term memory neural network and a hybrid genetic algorithm, whose structure is shown in Figure 2. The sequential quadratic programming is used as a kind of local

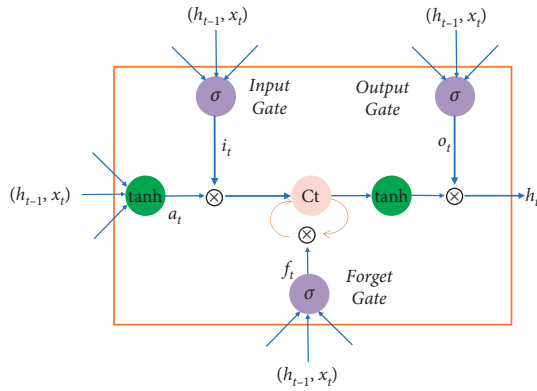

FIGURE 2: A structural diagram of the long short-term memory, a type of neural network. Here, a gate component is embedded to process the memorizing and forgetting and input as well as output inside such active memory [42]. Reproduced with permission. Copyright 2020, applied energy.

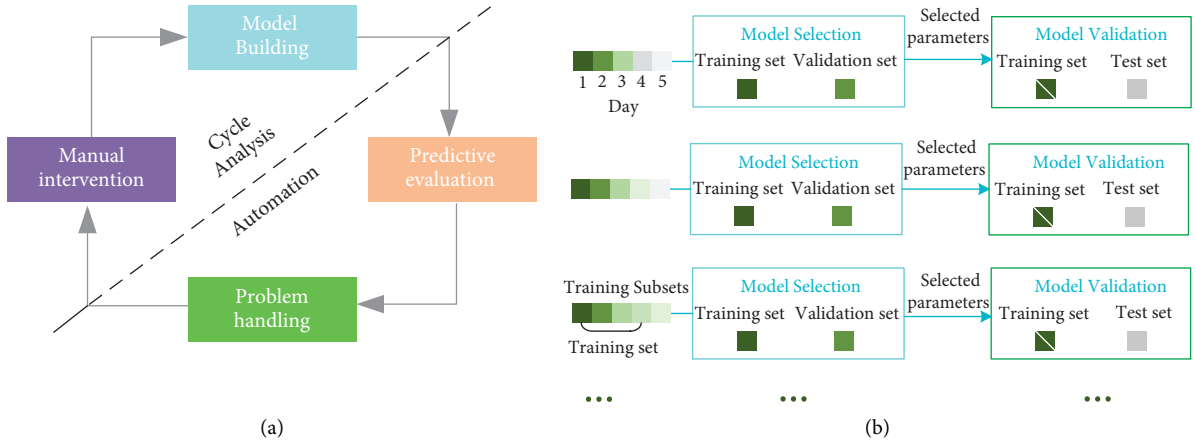

FIGURE 3: (a) Flowchart of the prophet model. (b) Schematic diagram of the forward chain method [44]. Reproduced with permission. Copyright 2021, Chinese Journal of electrical engineering.

search operator of the genetic algorithm, which enhances its global search capability and enables it to search the local optimal solution quickly by the exit probability and the number of hidden layer units. This prediction method can estimate the remaining lifetime of supercapacitors in steady-state charging mode well, and also works well for supercapacitors with dynamic operation cycles.

The study by Liu et al. [43] uses a stacked bidirectional long- and short-term memory recurrent neural network model, which adds a reverse recurrent layer with t-time and subsequent time values in the input sequence to the traditional long- and short-term memory recurrent neural network. Among them, the stacked network can ensure sufficient capacity space. When the number of hidden layers is 2, the predicted RMSE and MAE are 0.0275 and 0.0241, respectively, indicating that the network has better performance. A method for predicting the life of supercapacitor modules based on the monitoring data of buses under actual service conditions is proposed in the literature [44]. The qualified memory least squares method is used for parameter identification of service condition data to obtain the resistance and capacitance values with time-series and seasonal characteristics, and then, the RUL is predicted based on this method using the Prophet algorithm. The forward chain method is also introduced to validate the results, which is better than the cross-validation method in machine learning that ignores the time-series characteristics of the time-series data. The running time of Prophet is only about 20% of the running time of LSTM RNN, and the prediction accuracy is higher and the time required is shorter for data with periodic and seasonal characteristics, provided that the model remains unchanged and the same prediction accuracy is obtained. The structure diagram of Prophet and the flow chart of the forward chain method are shown in Figure 3.

Haris et al. [45] proposed a new deep learning algorithm, deep belief network (DBN) combined with Bayesian Optimization and HyperBand (BOHB), with the structure shown in Figure 4, for predicting the RUL at the early stage of supercapacitor degradation. Compared with previous studies, the development time of the RUL prediction model was reduced by 54%, largely saving the time required to collect and measure supercapacitor cycle data, and the proposed model has good accuracy and robustness.

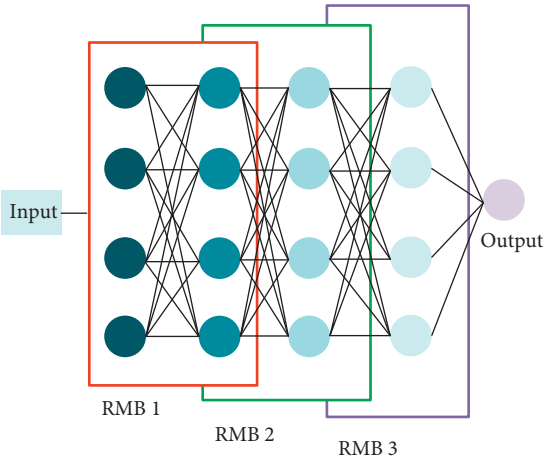

Figure 4: Deep belief network structure diagram [45]. Reproduced with permission. Copyright 2021, applied energy.

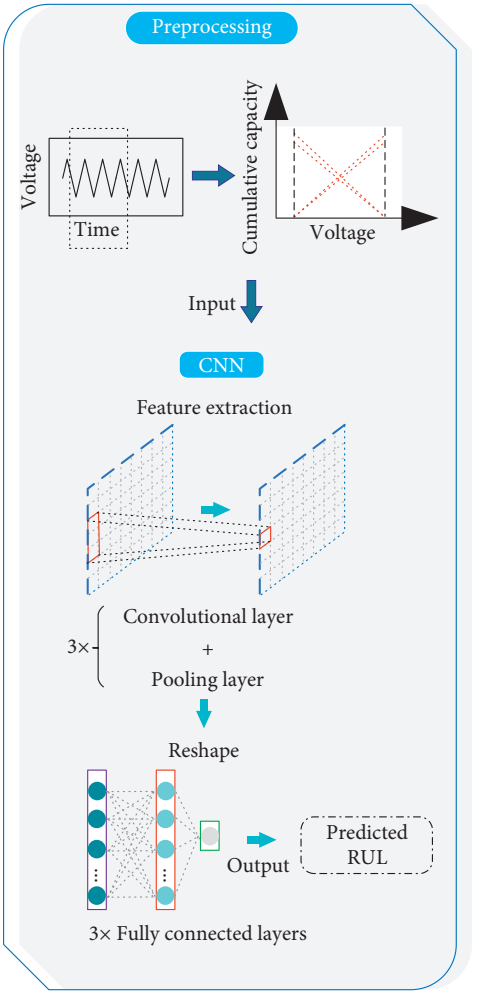

Figure 5: Framework of the proposed CNN [47]. Reproduced with permission. Copyright 2022, applied energy.

Ren et al. [46] presented a neural network-based RUL prediction method for supercapacitors that does not strongly depend on the data distribution and is less dependent on the correlation between variables and features, and the proposed model is suitable for data sets with a wide training distribution and has an accurate early diagnosis and prediction capability for the performance of complex supply chain systems. The testing error is less than 10.9%, and this error can be further adjusted by the dataset.

The above methods enable a significant reduction in the length of the input cycle, but they still require a large amount of data for their extraction. Since manually produced features inevitably lose aging information, the accuracy of prediction results is limited. In addition, manual feature extraction is cumbersome because it requires domain-specific knowledge and a long processing time. An end-to-end RUL prediction method based on convolutional neural networks (CNNs) is proposed in the literature [47]. The method has higher accuracy while requiring significantly fewer input data. Also, the method effectively reduces the need for data and improves prediction accuracy, which helps in the diagnosis and prediction of supercapacitors. The framework of the proposed CNN is shown in Figure 5.

Using a data-driven approach that does not require physical modeling of the component and is designed to simulate the relationship between measurement data and component degradation, it can effectively predict energy storage lifetime and discharge behavior without the need for detailed studies of internal chemical changes and side reaction disturbances.

5. Conclusion

Supercapacitors are widely used in many fields because of their advantages such as high power density, fast charging and discharging speed, and wide operating temperature range. Since the supercapacitors storage system is composed of a set of basic units, the inconsistent parameters of each unit, uneven charging voltage, and the difference in internal temperature in large-scale applications will lead to the degradation of its performance and the aging of the device. Therefore, accurate prediction of the remaining service life of supercapacitors can effectively reduce the occurrence of failures and accidents. Currently, there are mainly model-based and data-driven prediction methods. Due to the complexity of supercapacitors, model-based prediction methods are complicated to implement. The data-based approach does not require complex mathematical models to simulate the internal aging mechanism of supercapacitors, and combined with artificial neural networks can have better prediction accuracy and efficiency, which is the focus of future research. However, since the method relies only on relevant historical data to complete the prediction, the quality of the assessment depends heavily on the accuracy of the historical data. Because of the long lifetime of supercapacitors, it takes longer to collect cycle life data, which will increase the possibility of noise pollution and affect the prediction results. Also, the difficulty of obtaining high-precision historical data is a technical problem that needs to be broken in the process of achieving accurate evaluation. Combining with transfer learning techniques to reduce the reliance on data will be a future research trend.

Conflicts of Interest

The authors declare no competing interests.

Acknowledgments

This work was supported by the Youth Fund of Shandong Province Natural Science Foundation (no. ZR2020QE212), Key Projects of Shandong Province Natural Science Foundation (no. ZR2020KF020), Shandong Province Natural Science Foundation (no. ZR2020MF083), Shandong Province Natural Science Foundation (no. ZR2020MF068), Zhejiang Province Natural Science Foundation (no. LY22E070007), and National Natural Science Foundation of China (no. 52007170).

References

[1] H. Xu, H. Du, L. Kang, Q. Cheng, D. Feng, and S. Xia, "Constructing straight pores and improving mechanical properties of GangueBased porous ceramics," *Journal of Renewable Materials*, vol. 9, no. 12, pp. 2129–2141, 2021.

[2] D. Yuan, C. Zhang, S. Tang et al., "Ferric ion-ascorbic acid complex catalyzed calcium peroxide for organic wastewater treatment: optimized by response surface method," *Chinese Chemical Letters*, vol. 32, no. 11, pp. 3387–3392, 2021.

[3] Q. Li, D. Li, K. Zhao, L. Wang, and K. Wang, "State of health estimation of lithium-ion battery based on improved ant lion optimization and support vector regression," *Journal of Energy Storage*, vol. 50, Article ID 104215, 2022.

[4] L. Kang, H. Du, J. Deng, X. Jing, S. Zhang, and Y. Znang, "Synthesis and catalytic performance of a new V-doped CeO2-supported alkali-activated-steel-slag-based photocatalyst," *Journal of Wuhan University of Technology-Materials Science Edition*, vol. 36, no. 2, pp. 209–214, 2021.

[5] X. Feng, Q. Li, and K. Wang, "Waste plastic triboelectric nanogenerators using recycled plastic bags for power generation," *ACS Applied Materials & Interfaces*, vol. 13, no. 1, pp. 400–410, 2021.

[6] Y. Wang, J. Pang, Q. Cheng et al., "Applications of 2D-layered palladium diselenide and its van der Waals heterostructures in electronics and optoelectronics," *Nano-Micro Letters*, vol. 13, no. 1, p. 143, 2021.

[7] S. Padhy and S. Panda, "Application of a simplified Grey Wolf optimization technique for adaptive fuzzy PID controller design for frequency regulation of a distributed power generation system," *Protection and Control of Modern Power Systems*, vol. 6, no. 1, Article ID 2, 2021.

[8] K. Yin, J. Wu, Q. Deng et al., "Tailoring micro/nanostructured porous polytetrafluoroethylene surfaces for dual-reversible transition of wettability and transmittance," *Chemical Engineering Journal*, vol. 434, Article ID 134756, 2022.

[9] D. Z. Li, W. C. Wang, C. X. Duan, Q. Li, and L. Wang, "Temperature prediction of lithium-ion batteries based on electrochemical impedance spectrum: a review," *International Journal of Energy Research*, 2022.

[10] X. Feng, Y. Zhang, L. Kang et al., "Integrated energy storage system based on triboelectric nanogenerator in electronic devices," *Frontiers of Chemical Science and Engineering*, vol. 15, no. 2, pp. þ238–250, 2021.

[11] C. Duan, K. Liang, Z. Zhang et al., "Recent advances in the synthesis of nanoscale hierarchically porous metal-organic frameworks," *Nano Materials Science*, pp. 1–10, 2022.

[12] X. X. Wang, G. F. Yu, J. Zhang, M. Yu, S. Ramakrishna, and Y. Z. Long, "Conductive polymer ultrafine fibers via electrospinning: preparation, physical properties and applications," *Progress in Materials Science*, vol. 115, Article ID 100704, 2021.

[13] Y. Zhou, Y. Huang, J. Pang, and K. Wang, "Remaining useful life prediction for supercapacitor based on long short-term memory neural network," *Journal of Power Sources*, vol. 440, Article ID 227149, 2019.

[14] W. L. Wang, J. B. Pang, J. Su et al., "Applications of nanogenerators for biomedical engineering and healthcare systems," *Infomat*, vol. 4, no. 2, Article ID e12262, 2022.

[15] W. Zhou, H. Du, L. Kang et al., "Microstructure evolution and improved permeability of ceramic waste-based bricks," *Materials*, vol. 15, no. 3, p. 1130, 2022.

[16] H. L. Sun, J. R. Sun, K. Zhao, L. C. Wang, and K. Wang, "Data-driven ICA-Bi-LSTM combined lithium battery SOH estimation," *Mathematical Problems in Engineering*, vol. 2022, Article ID 9645892, 2022.

[17] S. Zhang, J. Pang, Y. Li et al., "Emerging Internet of Things driven carbon nanotubes-based devices," *Nano Research*, 2022.

[18] Z. Cui, J. Dai, J. Sun, D. Li, L. Wang, and K. Wang, "Hybrid methods using neural network and Kalman filter for the state of charge estimation of lithium-ion battery," *Mathematical Problems in Engineering*, vol. 2022, Article ID 9616124, 2022.

[19] Z. Cui, L. Wang, Q. Li, and K. Wang, "A comprehensive review on the state of charge estimation for lithium-ion battery based on neural network," *International Journal of Energy Research*, vol. 46, no. 5, pp. 5423–5440, 2022.

[20] D. Feng, H. Du, H. Ran et al., "Antiferroelectric stability and energy storage properties of Co-doped AgNbO3 ceramics," *Journal of Solid State Chemistry*, vol. 310, Article ID 123081, 2022.

[21] K. Wang, C. L. Liu, J. R. Sun et al., "State of charge estimation of composite energy storage systems with supercapacitors and lithium batteries," *Complexity*, vol. 2021, Article ID 8816250, 2021.

[22] C. Duan, K. Liang, J. Lin et al., "Application of hierarchically porous metal-organic frameworks in heterogeneous catalysis: a review," *Science China Materials*, vol. 65, no. 2, pp. 298–320, 2022.

[23] C. Y. Ma, H. L. Du, J. Liu et al., "High-temperature stability of dielectric and energy-storage properties of weakly-coupled relaxor (1-x)BaTiO3-xBi(Y1/3Ti1/2)O3 ceramics," *Ceramics International*, vol. 47, no. 17, pp. 25029–25036, 2021.

[24] H. Ran, H. Du, C. Ma, Y. Zhao, D. Feng, and H. Xu, "Effects of A/B-site co-doping on microstructure and dielectric thermal stability of AgNbO3 ceramics," *Science of Advanced Materials*, vol. 13, no. 5, pp. 741–747, 2021.

[25] C. Liu, Q. Li, and K. Wang, "State-of-charge estimation and remaining useful life prediction of supercapacitors," *Renewable and Sustainable Energy Reviews*, vol. 150, Article ID 111408, 2021.

[26] V. P. Sakthivel and P. D. Sathya, "Single and multi-area multi-fuel economic dispatch using a fuzzified squirrel search algorithm," *Protection and Control of Modern Power Systems*, vol. 6, no. 1, Article ID 11, 2021.

[27] X. Li, J. Su, Z. Li et al., "Revealing interfacial space charge storage of Li+/Na+/K+ by operando magnetometry," *Science Bulletin*, 2022.

[28] Y. Hua, N. Wang, K. Zhao, and J. Song, "Simultaneous unknown input and state estimation for the linear system with a rank-deficient distribution matrix," *Mathematical Problems in Engineering*, vol. 2021, Article ID 6693690, 11 pages, 2021.

[29] X. Li, Z. Shang, F. Peng, L. Li, Y. Zhao, and Z. Liu, "Increment-oriented online power distribution strategy for multi-stack proton exchange membrane fuel cell systems aimed at collaborative performance enhancement," *Journal of Power Sources*, vol. 512, Article ID 230512, 2021.

[30] M. Lucu, E. Martinez-Laserna, I. Gandiaga, and H. Camblong, "A critical review on self-adaptive Li-ion battery ageing models," *Journal of Power Sources*, vol. 401, pp. 85–101, 2018.

[31] M. L. He, K. Fic, E. Frackowiak, P. Novak, and E. J. Berg, "Towards more durable electrochemical capacitors by elucidating the ageing mechanisms under different testing procedures," *Chemelectrochem*, vol. 6, no. 2, pp. 566–573, 2018.

[32] E. H. El Brouji, O. Briat, J. M. Vinassa, N. Bertrand, and E. Woirgard, "Impact of calendar life and cycling ageing on supercapacitor performance," *IEEE Transactions on Vehicular Technology*, vol. 58, no. 8, pp. 3917–3929, 2009.

[33] C. Wu, C. Zhu, and Y. Ge, "A new fault diagnosis and prognosis technology for high-power lithium-ion battery," *IEEE Transactions on Plasma Science*, vol. 45, no. 7, pp. 1533–1538, 2017.

[34] H. Z. Liu, X. C. Xu, and X. J. Lu, "Prediction of cycle life of supercapacitors," *Battery*, vol. 48, no. 3, pp. 159–162, 2018.

[35] X. C. Xu, H. Z. Liu, X. J. Lu, and Y. Zhao, "Research on capacity life prediction model of supercapacitor," *Powder Technology*, vol. 43, no. 2, pp. 270–272+282, 2019.

[36] P. Saha and M. Khanra, "Online estimation of state-of-charge, state-of-health and temperature of supercapacitor," *IEEE International Symposium on Circuits and Systems*, vol. 2020, Article ID 20765103, 2020.

[37] A. El Mejdoubi, H. Chaoui, J. Sabor, and H. Gualous, "Remaining useful life prognosis of supercapacitors under temperature and voltage aging conditions," *IEEE Transactions on Industrial Electronics*, vol. 65, no. 5, pp. 4357–4367, 2018.

[38] B. Radej and G. Beges, "An enhanced model for reliability prediction of a supercapacitor's lifetime: developing an improved reliability model," *IEEE Industrial Electronics Magazine*, vol. 13, no. 3, pp. 26–34, 2019.

[39] D. Z. Li, S. Li, B. Zhang, J. R. Sun, L. C. Wang, and K. Wang, "Aging state prediction for supercapacitors based on heuristic kalman filter optimization extreme learning machine," *Energy*, vol. 250, Article ID 123773, 2022.

[40] J. C. Zhao, F. J. Li, Z. L. Wang, P. Dong, G. T. Xia, and K. Wang, "Flexible PVDF nanogenerator-driven motion sensors for human body motion energy tracking and monitoring," *Journal of Materials Science: Materials in Electronics*, vol. 32, no. 11, pp. 14715–14727, 2021.

[41] T. Ergen and S. S. Kozat, "Efficient online learning algorithms based on LSTM neural networks," *IEEE Transactions on Neural Networks and Learning Systems*, vol. 29, no. 8, pp. 1–12, 2017.

[42] Y. Zhou, Y. Wang, K. Wang et al., "Hybrid genetic algorithm method for efficient and robust evaluation of remaining useful life of supercapacitors," *Applied Energy*, vol. 260, Article ID 114169, 2020.

[43] C. Liu, Y. Zhang, J. Sun, Z. Cui, and K. Wang, "Stacked bidirectional LSTM RNN to evaluate the remaining useful life of supercapacitor," *International Journal of Energy Research*, vol. 46, no. 3, pp. 3034–3043, 2022.

[44] W. T. Zhang, Li Wei, M. D. Yan, and X. T. Bai, "Research on the life prediction method of supercapacitor modules for off-road service conditions," *Chinese Journal of Electrical Engineering*, vol. 41, no. S1, pp. 286–293, 2021.

[45] M. Haris, M. N. Hasan, and S. Qin, "Early and robust remaining useful life prediction of supercapacitors using BOHB optimized Deep Belief Network," *Applied Energy*, vol. 286, Article ID 116541, 2021.

[46] J. Ren, X. Lin, J. Liu et al., "Engineering early prediction of supercapacitors' cycle life using neural networks," *Materials Today Energy*, vol. 18, Article ID 100537, 2020.

[47] C. Wang, R. Xiong, J. Tian, J. Lu, and C. Zhang, "Rapid ultracapacitor life prediction with a convolutional neural network," *Applied Energy*, vol. 305, Article ID 117819, 2022.

Hindawi
Mathematical Problems in Engineering
Volume 2022, Article ID 2779623, 11 pages
https://doi.org/10.1155/2022/2779623

Research Article

Security-Based Asynchronous Control for Discrete-Time Markov Switching Power Systems *

Weifeng Xu,[1] Bin Yu,[1] Liguo Weng ,[1] and Jianguo Zhou[2]

[1]*State Grid Hangzhou Xiaoshan Power Supply Company, Hangzhou 311200, China*
[2]*Zhejiang Zhongxin Power Engineering Construction Co., Ltd, Hangzhou 311200, China*

Correspondence should be addressed to Liguo Weng; wlgzxdj@163.com

Received 14 December 2021; Accepted 14 March 2022; Published 5 May 2022

Academic Editor: Licheng Wang

This paper addresses the asynchronous control problem for power systems subject to abrupt variations and cyber-attacks. In the sequel, the transient faults of circuit breakers can be described as the Markov process. In light of these situations, the power systems are transmitted to discrete-time Markov switching systems. Meanwhile, the deception attacks with time-varying delays in dispatchers are regulated by a Markov process. The controller and dispatcher are mode-dependent and their modes are nonsynchronous with those of power systems, which are modeled by the hidden Markov models. On the basis of the deception attacks, sufficient conditions are presented to guarantee the stochastic mean-square stability of the closed-loop dynamic. Finally, the proposed control design strategy is testified via a simulation result.

1. Introduction

As a type of complex nonlinear system, power systems have gained considerable interest due to their spontaneous oscillation characters and high penetration [1–3]. Over the past decades, many significant methods have been devoted to power systems, such as state estimation [4–8]. For the purpose of stabilizing interconnected power systems, many efforts have been devoted to exploring the mismatch between load demand and total power generation. Following this character, many techniques are forwarded to maintain the frequency balance including the load frequency control, state feedback control [9–11]. Therefore, how to keep the frequency deviation of power systems within a certain range remains a hot topic. For instance, to overcome the low/zero inertia, stability has been studied for power systems with fluctuation and intermittency in [12]. In [13], the load frequency control technique has been utilized to balance the power exchanges among different areas. In [14], the network-induced time delay has been considered in supplying high-quality electric energy. In [15], the fuzzy-dependent power system stabilizer with uncertain factors has been investigated.

In reality, owing to many unexpected factors such as component faults, external disturbances, and unknown attacks, the power systems always experience random variations in parameters/structures, which lead to the resulting operation changes and performance degeneration [16, 17]. Markov switching is identified as an effective tool in modeling the aforementioned conditions [18]. Note that Markov switching is ubiquitous, which has been applied in many physical situations, such as tunnel-diode-circuit-model and complex networks [18–20]. However, to our knowledge, little attention has been given to Markov switching power systems (MSPSs) except for [21–23]. In [21], the random switching of power systems can be modeled as MSPSs. Lately, the continuous-time interconnected multiarea MSPSs with load frequency control are considered in [22]. In [23], the discrete-time MSPSs are studied with a hidden Markov model. Nevertheless, in contrast with the fruitful achievements of power systems, MSPSs have not gained suitable attention.

On the other hand, many valuable results have been reported on the networked power systems subjected to many network-induced factors, such as communication delays, packet losses, quantization effects, and event-triggered

protocols [24–26]. By comparison, potential cyber-attacks may destroy the stability of power systems via a shared communication network. In light of the different attack ways, cyber-attacks can be summarized into three categories: denial-of-service [27], repeat attack [28, 29], and deception attacks [30–33]. In more detail, the former aims at destroying the channel of signal exchange, and repeat attacks inject historic data into the network affect the performance, while deception attacks attempt to inject false data into the communication network to destroy the data trustworthiness. On the basis of these cyber-attacks, the conventional control law becomes untrusted. It is of significance to be concerned with cyber-attacks. Among these cyber-attacks, deception attacks are common in practice. For instance, in [34], the unified power systems against random-occurring deception attacks have been studied. In [35], on the basis of credibility, the multiarea power systems with deception attacks have been well concerned. Nevertheless, the security issues of power systems with regard to cyber-attacks have not been adequately explored, such as random occurring deception attacks with time-varying delays, not to mention power systems against Markov switching.

Through expounds of the above discussion, this work shall consider the nonsynchronous controller design issue for MSPSs with cyber-attacks. The main contributions are listed below: (1) a generalized MSPS is established, which covers asynchronous dispatcher, asynchronous controller, and deception attacks, simultaneously. (2) Deception attacks with time-varying delays are taken into consideration. The probability of each time-varying delay is different, and random-occurring deception attacks are described by a sequence of stochastic variables induced by a new Markov process. (3) A more general scenario is that the asynchronous phenomena among system mode, controller mode, and dispatcher mode are well revealed and the hidden Markov model technique is applied. Finally, the effectiveness of the gained methodology is verified via an illustrated example.

Notations: the notations in this paper is standard. $\mathbb{N}$ symbols the set of all non-negative integers. diag$\{\cdots\}$ means a block-diagonal matrix. $\mathbf{He}\{\mathscr{Z}\} = \mathscr{Z} + \mathscr{Z}^{\top}$. $\|\cdot\|$ implies the Euclidean norm of a vector. $\mathbb{R}^n$ signifies the n dimensional real space. $\mathscr{E}\{\cdot\}$ represents the mathematical expectation. $*$ describes the symmetric term.

2. Problem Formulations

As sketched in Figure 1, a type of single-machine infinite bus (SMIB) through tie line is explored in the current study. From the SMIB, we can observe the dynamic behavior of large interconnected power systems. Following this trend, the basic components of SMIB power systems (SMIBPSs) are expressed in Figure 2. Accordingly, the following formula can be established:

$$\begin{cases} \dot{\delta} = \omega_0 \omega, \\ \dot{\omega} = \dfrac{\mathfrak{T}_m - \mathfrak{T}_e}{\mathfrak{M}}, \\ \mathfrak{T}_{do}{}' \dot{\mathfrak{E}}_q{}' = \mathfrak{E}_{fd} - \dfrac{x_d + x_e}{x_d' + x_e} \mathfrak{E}_q{}' + \dfrac{x_d + x_d'}{x_d' + x_e} \mathfrak{V} \cos(\delta), \\ \mathfrak{T}_E \dot{\mathfrak{E}}_{fd} = \mathfrak{K}_E \mathfrak{E}_{ref} - \mathfrak{K}_E \mathfrak{V}_t + \mathfrak{K}_E u - \mathfrak{E}_{fd}, \end{cases} \tag{1}$$

where δ, ω, E_q', and E_{fd} refer to the generator angle, generator speed, q-axis voltage, and generator voltage, respectively. Meanwhile, other physical meanings are summarized in Table 1.

In view of the aforementioned observation, the fourth-order state-space model of SMIBPS is formulated as

$$\dot{x}(t) = Ax(t) + Bu(t), \tag{2}$$

where

$$x(t) = \begin{bmatrix} \Delta\delta \\ \Delta\omega \\ \Delta\mathfrak{E}_q{}' \\ \Delta\mathfrak{E}_{fd} \end{bmatrix},$$

$$A = \begin{bmatrix} 0 & \omega_0 & 0 & 0 \\ -\dfrac{k_1}{\mathfrak{M}} & 0 & -\dfrac{k_2}{\mathfrak{M}} & 0 \\ -\dfrac{k_4}{\mathfrak{T}_{\mathrm{do}}{}'} & 0 & -\dfrac{1}{k_3 \mathfrak{T}_{\mathrm{do}}{}'} & -\dfrac{1}{\mathfrak{T}_{\mathrm{do}}{}'} \\ -\dfrac{k_5 k_E}{\mathfrak{T}_E} & 0 & -\dfrac{k_6 k_E}{\mathfrak{T}_E} & -\dfrac{1}{\mathfrak{T}_E} \end{bmatrix}, \tag{3}$$

$$B = \begin{bmatrix} 0 \\ 0 \\ 0 \\ \dfrac{k_E}{\mathfrak{T}_E} \end{bmatrix}.$$

Similar to the work of [10], $\mathfrak{Q}$ and $\mathfrak{P}$, respectively, represent the reactive and real power loading, whose functions are presented by the parameters $k_l (l = 1, \ldots, 6)$.

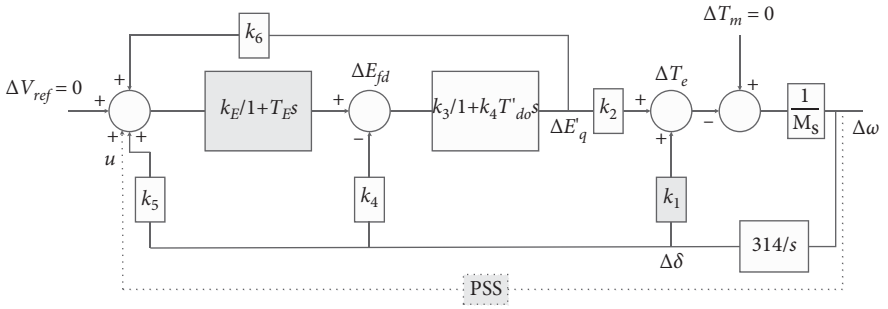

Figure 1: Signal model of SMIBPSs.

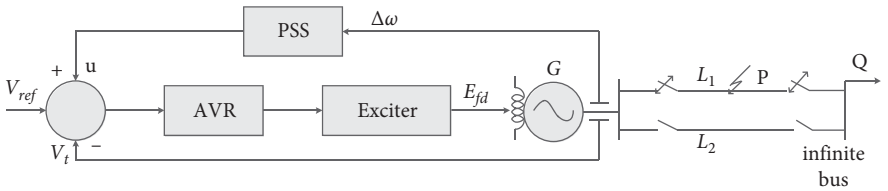

Figure 2: Basic components of SMIBPSs with faults.

Table 1: The parameters of power systems.

x'_d	Generator d-axis transient reactance
x_d, x_q	$d-q$ axis synchronous reactance
$\mathfrak{T}_e, \mathfrak{T}_m$	Electrical, mechanical torque
$k_E, \mathfrak{T}_E$	Exciter gain and time constant
$\mathfrak{V}$	Infinite busbar voltage
$\mathfrak{V}_t$	Terminal voltage
$\mathfrak{P}, \mathfrak{Q}$	Real and reactive power loadings
$\mathfrak{M}$	Inertia coefficient
$\mathfrak{T}_{\mathrm{do}}{}'$	Open circuit d-axis transient time constant
u	Stabilizing signal
x_e	External reactance
Δw	Speed deviation
$k_1, \ldots, k_6$	Linearized model constants of the synchronous machine

More specifically, the values of parameters in Table 1 are given by $x_q = 1.55$pu, $x_d = 1.6$pu, $x'_d = 0.32$pu, $\mathfrak{T}'_{\mathrm{do}} = 6$s, $\mathfrak{M} = 10$s, $x_e = 0.4$pu, $\omega_0 = 50\pi$rad/s, $\mathfrak{T}_E = 0.05$s, $k_E = 50$, and $\mathfrak{L}_l = 0.8\,(l = 1, 2)$.

By resorting to a discretization period T, the discrete-time SMIBPS (2) can be established as

$$x(k+1) = Ax(k) + Bu(k), \tag{4}$$

where $A = e^{\mathrm{AT}}$ and $B = \int_0^T e^{At} B \mathrm{d}t$.

In light of the unreliability of the network medium, the abrupt variations of SMIBPS cannot be avoided. To model the variation of SMIBPS in a suitable way, a stochastic variable $\sigma(k)$ takes values within a space $\mathscr{M} = \{1, \ldots, \mathscr{M}\}$, is presented to depict the Markov switching SMIBPSs as follows:

$$x(k+1) = A_{\sigma(k)} x(k) + B_{\sigma(k)} u(k),\ k = 0, 1, \ldots, \tag{5}$$

where $\sigma(k)$ refers to a Markov chain, whose transition probability matrix (TPM) $\Pi = [\pi_{mn}]_{\mathscr{M}\times\mathscr{M}}$ is inferred as

$$\pi_{mn} = \Pr\{\sigma(k+1) = n \mid \sigma(k) m\}, \tag{6}$$

where $0 \le \pi_{mn} \le 1$ and $\sum_{n=1}^{\mathscr{M}} \pi_{mn} = 1$ for all $m, n \in \mathscr{M} = \{1, 2, \ldots, \mathscr{M}\}$.

Notice that the data are transmitted to controllers via an unencrypted communication network, which is always being attacked on the sensor-to-controller channels. It is well-known that deception attacks are commonly encountered, which launch some deception signals to destroy the information authenticity of $x(k)$. Thus, as depicted in Figure 1, we consider the random occurring deception attacks in power systems, which damage/destroy the performance to the data integrity. Therefore, the real system information is modeled as

$$\overline{x}(k) = x(k) + \alpha_{\varepsilon(k)}(k)\zeta(k), \tag{7}$$

where $\zeta(k) = -x(k) + f(x(k - \tau_{\varepsilon(k)}(k)))$. $\tau_{\varepsilon(k)}(k)$ stand for the jump-mode-dependent time-varying delay of deception attacks, and $\tau_{\varepsilon(k)}(k) \in [\tau_1, \tau_2]$. τ_1 and τ_2 are two constants, which satisfies $0 \le \tau_1 \le {}_2$. $f(x(k)) = [f(x_1(k - \tau_{\varepsilon(k)}(k)))$ $, f(x_2(k - \tau_{\varepsilon(k)}(k))), \ldots, f(x_n(k - \tau_{\varepsilon(k)}(k)))]^{\top}$ being the nonlinear function of deception attacks subject to random occurring time-varying delays. $\alpha_{\varepsilon(k)}(k)$ implies the Bernoulli variable, in which $\alpha_{\varepsilon(k)}(k) = 1$ and $\alpha_{\varepsilon(k)}(k) = 0$ signify the transmission channel with and without attack. It yields

$$\begin{aligned} \mathscr{E}\left\{\alpha_{\varepsilon(k)}(k) = 1\right\} &= \overline{\alpha}_{\varepsilon(k)}, \mathscr{E}\left\{\alpha_{\varepsilon(k)}(k) = 0\right\} \\ &= 1 - \overline{\alpha}_{\varepsilon(k)}, \\ \mathscr{E}\left\{\left(\alpha_{\varepsilon(k)}(k) - \overline{\alpha}_{\varepsilon(k)}\right)^2\right\} &= \overline{\alpha}_{\varepsilon(k)}\left(1 - \overline{\alpha}_{\varepsilon(k)}\right) \\ &= \widehat{\alpha}^2_{\varepsilon(k)}. \end{aligned} \tag{8}$$

In particularly, $\varepsilon(k)$ is a Markov process having values over a set $\mathscr{S} = \{1, \ldots, \mathscr{S}\}$, whose TPM $\Omega = [\psi_{\mathrm{ms}}]_{\mathscr{M}\mathrm{s}}$ with

$$\psi_{\mathrm{ms}} = \Pr\{\varepsilon(k) = s|\sigma(k) = m\}, \tag{9}$$

where $0 \le \psi_{ms} \le 1$ and $\sum_{s=1}^{\mathcal{S}} \psi_{\mathrm{ms}} = 1$ for any $m \in \mathcal{M}$ and $s \in \mathcal{S}$.

Accordingly, the actual system information can be reformulated as

$$\overline{x}(k) = \left(1 - \alpha_{\varepsilon(k)}(k)\right)x(k) + \alpha_{\varepsilon(k)}(k) f\left(x\left(k - \tau_{\varepsilon(k)}(k)\right)\right). \tag{10}$$

Remark 1. In contrast to the reporting literature with mode-independent deception attacks [30–33], the deception attacks have the Markov behavior, and the attack indication scalar $\alpha_{\varepsilon(k)}(k)$ is presented to describe the dynamic behavior. Meanwhile, in the current study, time-varying delays against Markov behavior are considered in the deception attacks, which covers the existing deception attacks as special cases [30–33].

Assumption 1. (see [36]). The embedded function $f(x(k - \tau_{\varepsilon(k)}(k)))$, which is adopted to restrain deception attacks with random occurring time-varying delays, satisfies the following condition:

$$\left\| f\left(x\left(k - \tau_{\varepsilon(k)}(k)\right)\right)\right\|^2 \le \left\| Qx\left(k - \tau_{\varepsilon(k)}(k)\right)\right\|^2, \tag{11}$$

where Q indicates a known matrix implying an upper bound of embedded function $f(x(k - \tau_{\varepsilon(k)}(k)))$.

It is noteworthy that the resulting mode information determines the controller design and effects the performance. With respect to the mode information that cannot be observed when an attack occurs, in the current study, an asynchronous controller was developed as follows:

$$u(k) = K_{\theta(k)}\overline{x}(k), \tag{12}$$

where $K_{\theta(k)}$ being the controller gains. Stochastic variable $\theta(k)$ implies a Markov chain having values in a space $\mathcal{D} = \{1, 2, \ldots, \mathcal{D}\}$, whose TPM $\Xi = [\varphi_{md}]_{\mathcal{M}\mathrm{D}}$ with

$$\varphi_{md} = \Pr\{\theta(k) = d|\sigma(k) = m\}, \tag{13}$$

where $0 \le \varphi_{md} \le 1$ and $\sum_{d=1}^{\mathcal{D}} \varphi_{md} = 1$ for any $m \in \mathcal{M}$ and $d \in \mathcal{D}$.

Let $\sigma(k) = m \in \mathcal{M}$, $\varepsilon(k) = s \in \mathcal{S}$, and $\theta(k) = d \in \mathcal{D}$, combining (5), (10), and (12), we have

$$\begin{aligned} x(k+1) = {} & \mathcal{A}_{msd}x(k) + \overline{\alpha}_s B_m K_d f\left(x\left(k - \tau_s(k)\right)\right) \\ & + \left(\alpha_s(k) - \overline{\alpha}_s\right)B_m K_d\left(-x(k) + f\left(x\left(k - \tau_s(k)\right)\right)\right), \end{aligned} \tag{14}$$

where $\mathcal{A}_{msd} = A + (1 - \overline{\alpha}_s)B_m K_d$.

Remark 2. Actually, the mode information of the SMIBPSs is difficult to achieve due to many factors, including higher costs and time-wasting. In order to describe the dynamic behavior of random occurring deception attacks and control laws, the hidden Markov models are adopted to model these asynchronous phenomena. More specifically, we get the two-independent conditional probabilities as follows:

$$\begin{aligned} & \Pr\{\varepsilon(k) = s, \theta(k) = d|\sigma(k) = m\} \\ & = \Pr\{\varepsilon(k) = s|\sigma(k) = m\} \times \Pr\{\theta(k) = d|\sigma(k) = m\} \\ & = \psi_{ms}\varphi_{md}. \end{aligned} \tag{15}$$

For the convenience of presentation, the following definition is recalled:

Definition 1. (see [37]). The closed-loop dynamic (14) is stochastically mean-square stable (SMSS), if under any initial condition $\alpha(t_0)$, $\varphi(t_0) \in \mathcal{L}$, and $\upsilon(t_0) \in \mathcal{M}$, such that

$$\mathcal{E}\left\{\sum_{0}^{\infty} \|x(k)\|^2 | x\left(k_0\right), \sigma\left(k_0\right)\right\} < \infty. \tag{16}$$

3. Main Results

In the current section, the SMSS criteria for the closed-loop dynamic (14) and controller design method will be established in Theorem 1 and Theorem 2, respectively.

Theorem 1. *For given scalars $\tau_2 \ge \tau_1 \ge 0$, and $\overline{\alpha}_s (s \in \mathcal{S})$., and gain matrix K_d, the closed-loop dynamic (14) is SMSS, if there exist matrices $P_m > 0 (m \in \mathcal{M})$, $R > 0$, such that for any $(m, n \in \mathcal{M}, s \in \mathcal{S}, d \in \mathcal{D})$,*

$$\sum_{s=1}^{\mathcal{S}} \psi_{ms} \sum_{d=1}^{\mathcal{D}} \varphi_{md} U_{msd}^{-1} < P_m^{-1}, \tag{17}$$

$$\widehat{\Sigma}_{msd} = \Upsilon_{msd}^1 + \Upsilon_{msd}^{2\top} \mathrm{P}_m \Upsilon_{msd}^2 + \widehat{\alpha}_s^2 \Upsilon_{msd}^{3\top} \mathrm{P}_m \Upsilon_{msd}^3 < 0, \tag{18}$$

where

$$\begin{aligned} \Upsilon_{msd}^1 &= \mathrm{diag}\left\{-U_{msd}^{-1} + (\tau_2 - \tau_1 + 1)R, -R + \overline{\alpha}_s Q^\top Q, -\overline{\alpha}_s I\right\}, \\ \Upsilon_{msd}^2 &= \left[A_m + \left(1 - \overline{\alpha}_s\right)B_m K_d 0 \overline{\alpha}_s B_m K_d\right], \\ \Upsilon_{msd}^3 &= \left[-B_m K_d 0 B_m K_d\right]. \end{aligned} \tag{19}$$

Proof. Let us construct the following Lyapunov functional:

$$V(x(k), \sigma(k)) = \sum_{\iota=1}^{3} V_\iota(\alpha(t), \varphi(t), \upsilon(t)), \tag{20}$$

where

$$\begin{aligned} V_1(x(k), \sigma(k)) &= x^\top(k) P_{\sigma(k)}^{-1} x(k), \\ V_2(x(k), \sigma(k)) &= \sum_{\delta=k-\tau_s(k)}^{k-1} x^\top(\delta) R x(\delta), \\ V_3(x(k), \sigma(k)) &= \sum_{l=-\tau_2+2}^{-\tau_1+1} \sum_{\delta=k+l-1}^{k-1} x^\top(\delta) R x(\delta). \end{aligned} \tag{21}$$

Calculating the derivation of $V(x(k), \sigma(k))$ along the trajectories (14), yields

$$\begin{aligned}\mathscr{E}\{\Delta V(k)\} &= \mathscr{E}\{V(x(k+1),\sigma(k+1)=n)|x(k),\sigma(k)=m\} - V(x(k),\sigma(k))\\ &= \mathscr{E}\{x^{\top}(k+1)\mathrm{P}_m x(k+1)\} - x^{\top}(k)P_m^{-1}x(k)\\ &= \left[\mathscr{A}_{msd}x(k) + \overline{\alpha}_s B_m K_d f(k-\tau_s(k))\right]^{\top}\sum_{s=1}^{\mathscr{S}}\psi_{ms}\sum_{d}^{\mathscr{D}}\varphi_{md}\mathrm{P}_m\\ &\quad\times\left[\mathscr{A}_{msd}x(k) + \overline{\alpha}_s B_m K_d f(k-\tau_s(k))\right]\\ &\quad+\widehat{\alpha}_s^2\left[B_m K_d(-x(k)+f(k-\tau_s(k)))\right]^{\top}\sum_{s=1}^{\mathscr{S}}\psi_{ms}\sum_{d}^{\mathscr{D}}\varphi_{md}\mathrm{P}_m\\ &\quad\times\left[B_m K_d(-x(k)+f(k-\tau_s(k)))\right] - x^{\top}(k)P_m^{-1}x(k).\end{aligned} \tag{22}$$

$$\begin{aligned}\mathscr{E}\{\Delta V_2(k)\} &= \mathscr{E}\{V_2(x(k+1),\sigma(k+1))\} - V_2(x(k),\sigma(k))\\ &\le x^{\top}(k)Rx(k) - x^{\top}(k-\tau_s(k))Rx(k-\tau_s(k)) + \sum_{k+1-\tau_2}^{k-\tau_1}x^{\top}(\delta)Rx(\delta).\end{aligned} \tag{23}$$

$$\begin{aligned}\mathscr{E}\{\Delta V_3(k)\} &= \mathscr{E}\{V_3(x(k+1),\sigma(k+1))\} - V_3(x(k),\sigma(k))\\ &\le (\tau_2-\tau_1)x^{\top}(k)Rx(k) - \sum_{k+1-\tau_2}^{k-\tau_1}x^{\top}(\delta)Rx(\delta).\end{aligned} \tag{24}$$

Recalling Assumption 1, the following formula can be acquired:

$$\begin{aligned}&-\overline{\alpha}_s x^{\top}(k-\tau_s(k))Q^{\top}Qx(k-\tau_s(k))\\ &\quad+\overline{\alpha}_s f^{\top}(k-\tau_s(k))f(k-\tau_s(k))\le 0.\end{aligned} \tag{25}$$

If follows from (20)–(25), it can be obtained that

$$\begin{aligned}\mathscr{E}\{\Delta V(k)\} &= \mathscr{E}\{\Delta V_1(k)\} + \mathscr{E}\{\Delta V_2(k)\} + \mathscr{E}\{\Delta V_3(k)\}\\ &= \mathscr{E}\left\{\eta^{\top}(k)\sum_{s=1}^{\mathscr{S}}\psi_{ms}\sum_{d=1}^{\mathscr{D}}\varphi_{md}\widehat{\Sigma}_{msd}\eta(k) - x^{\top}(k)P_m^{-1}x(k)\right\}\\ &\le \mathscr{E}\left\{\eta^{\top}(k)\sum_{s=1}^{\mathscr{S}}\psi_{ms}\sum_{d=1}^{\mathscr{D}}\varphi_{md}\overline{\Sigma}_{msd}\eta(k) - x^{\top}(k)P_m^{-1}x(k)\right\}\\ &= \mathscr{E}\left\{x^{\top}(k)\left(\sum_{s=1}^{\mathscr{S}}\psi_{ms}\sum_{d=1}^{\mathscr{D}}\varphi_{md}U_{msd}^{-1} - P_m^{-1}\right)x(k)\right\},\end{aligned} \tag{26}$$

where $\eta^{\top}(k) = [x^{\top}(k)x^{\top}(k-\tau_s(k))f^{\top}(x(k-\tau_s(k)))]$, $\overline{\Sigma}_{\mathrm{msd}} = \mathrm{diag}\{U_{msd}^{-1},0,0\}$.

In light of condition (17), the above inequality equivalents to

$$\mathscr{E}\{\Delta V(k)\} \le -\lambda_{\min}(-\overline{\Sigma}_{msd})\eta^{\top}(k)\eta(k) \le -\upsilon x^{\top}(k)x(k), \tag{27}$$

where $\upsilon = \inf\{\lambda_{\min}(-\overline{\Sigma}_{msd})\}$. Obviously, it yielded $\mathscr{E}\{\Delta V(k)\} < 0$, which means

$$\begin{aligned}\mathscr{E}\left\{\sum_{k=0}^{\infty}\|x(k)\|^2\right\} &\le \frac{1}{\upsilon}\{\mathscr{E}V(x(0),\sigma(0))\} - \mathscr{E}\{V(x(\infty),\sigma(\infty))\}\\ &\le \frac{1}{\upsilon}\mathscr{E}\{V(x(0),\sigma(0))\} < \infty.\end{aligned} \tag{28}$$

Based on Definition 1, the closed-loop dynamic (14) achieves SMSS, which completes the proof.□ □

Theorem 2. *For given scalars $\tau_2 \ge \tau_1 \ge 0$, and $\overline{\alpha}_s\,(s\in\mathscr{S})$, and gain matrix $\overline{K}_d$, the closed-loop dynamic (14) is SMSS, if there exist matrices $P_m > 0\,(m\in\mathscr{M})$., $U_{msd} > 0\,(m,n\in\mathscr{M}, s\in\mathscr{S}, d\in\mathscr{D})$., $\overline{R} > 0$, and matrix $Y_d\,(d\in\mathscr{D})$ such that for any $(m,n\in\mathscr{M}, s\in\mathscr{S}, d\in\mathscr{D})$,*

$$\begin{bmatrix}-P_m & \Phi_{msd}\\ * & \mathrm{diag}\{-U_{m11},\ldots,-U_{msd},\ldots-U_{m\mathrm{SD}}\}\end{bmatrix} < 0, \tag{29}$$

where

$$\begin{aligned}\Phi_{msd} &= \left[\sqrt{\psi_{m1}\varphi_{m1}}\,P_m\cdots\sqrt{\psi_{ms}\varphi_{md}}\,P_m\cdots\sqrt{\psi_{m\mathscr{S}}\varphi_{m\mathscr{D}}}\,P_m\right],\\ \overrightarrow{\Upsilon}_{msd}^{1} &= \mathrm{diag}\{U_{msd} - \mathbf{sym}\{Y_d\} + (\tau_2-\tau_1+1)\overline{R}_d,\\ &\quad -\overline{R}_d, \overline{\alpha}_s(I - \mathbf{sym}\{Y_d\})\},\\ \overrightarrow{\Upsilon}_{msd}^{2} &= \left[\varpi_m\overrightarrow{\Upsilon}_{msd}^{2,1\top}\varpi_m\overrightarrow{\Upsilon}_{msd}^{2,2\top}\overrightarrow{\Upsilon}_{msd}^{2,3}\right],\\ \overrightarrow{\Upsilon}^{3} &= \mathrm{diag}\{\Upsilon^{3,1},\Upsilon^{3,1},-I\},\\ \overrightarrow{\Upsilon}_{msd}^{2,1} &= [A_m Y_d + (1-\overline{\alpha}_s)B_m\overline{K}_d 0\overline{\alpha}_s B_m\overline{K}_d],\\ \overrightarrow{\Upsilon}_{msd}^{2,2} &= [-B_m\overline{K}_d 0 B_m\overline{K}_d],\\ \overrightarrow{\Upsilon}_{msd}^{2,3} &= [0\sqrt{\alpha_s}QY_d 0]^{\top},\\ \varpi_m &= [\sqrt{\pi_{m1}}\,I\sqrt{\pi_{m2}}\,I\cdots\sqrt{\pi_{m\mathscr{M}}}\,I],\\ \Upsilon^{3,1} &= \mathrm{diag}\{-P_1,-P_2,\ldots,-P_{\mathscr{M}}\}.\end{aligned} \tag{30}$$

Furthermore, the controller gains are achieved as

$$K_d = \overline{K}_d Y_d^{-1}, \quad \forall d \in \mathscr{D}. \tag{31}$$

Proof. Firstly, premultiplying and postmultiplying the condition (29) by term $\mathrm{diag}\{P_m^{-1}, I, \ldots, I\}$ and its transpose, we can get that

$$\begin{bmatrix} -P_m^{-1} & \overline{\Phi}_{msd} \\ * & \mathrm{diag}\{-U_{m11}, \ldots, -U_{msd}, \cdots - U_{m\mathrm{SD}}\} \end{bmatrix} < 0, \tag{32}$$

where

$$\overline{\Phi}_{msd} = \left[\sqrt{\psi_{m1}\varphi_{m1}}\, I \cdots \sqrt{\psi_{ms}\varphi_{md}}\, I \cdots \sqrt{\psi_{m\mathscr{S}}\varphi_{m\mathscr{D}}}\, I\right]. \tag{33}$$

According to Schur complement, one can derive (33) is equivalent to (17).

Next, by means of Schur complement, it can be easily obtained from (17)as follows:

$$\begin{bmatrix} \overline{\Upsilon}_{msd}^1 & \varpi_m \Upsilon_{msd}^2 \\ * & \overrightarrow{\Upsilon}^3 \end{bmatrix} < 0, \tag{34}$$

where

$$\begin{aligned} \overline{\Upsilon}_{msd}^1 &= \mathrm{diag}\left\{-U_{msd}^{-1} + (\tau_2 - \tau_1 + 1)R, -R, -\overline{\alpha}_s I\right\}, \\ &\quad \left[\varpi_m \Upsilon_{msd}^{2\top} \varpi_m \Upsilon_{msd}^{3\top} \Upsilon_{msd}^4\right], \\ \overline{\Upsilon}_{msd}^2 &= \Upsilon_{msd}^4 \\ &= \left[\sqrt{\alpha_s}\, Q00\right]^\top. \end{aligned} \tag{35}$$

Premultiplying and postmultiplying (35) by $\mathrm{diag}\{Y_d, Y_d, Y_d, I, I, \ldots, I\}$ and its transpose, respectively. It yields

$$\begin{bmatrix} \widehat{\Upsilon}_{msd}^1 & \widehat{\Upsilon}_{msd}^2 \\ * & \overrightarrow{\Upsilon}_m^3 \end{bmatrix} < 0, \tag{36}$$

where

$$\begin{aligned} \widehat{\Upsilon}_{msd}^1 &= \mathrm{diag}\left\{-Y_d U_{msd}^{-1} Y_d^\top + (\tau_2 - \tau_1 + 1)\overline{R}_d, -\overline{R}_d, -Y_d \overline{\alpha}_s Y_d^\top\right\}, \\ \widehat{\Upsilon}_{msd}^2 &= \left[\varpi_m \widehat{\Upsilon}_{msd}^{2,1\top} \varpi_m \widehat{\Upsilon}_{msd}^{2,2\top} \overrightarrow{\Upsilon}_{msd}^{2,3}\right], \\ \widehat{\Upsilon}_{msd}^{2,1} &= \left[A_m Y_d + (1 - \overline{\alpha}_s) B_m K_d Y_d 0 \overline{\alpha}_s B_m K_d Y_d\right], \\ \widehat{\Upsilon}_{msd}^{2,2} &= \left[-B_m K_d Y_d 0 B_m K_d Y_d\right], \\ \overline{R}_d &= Y_d R Y_d^\top. \end{aligned} \tag{37}$$

On the other hand, with respect to $U_{msd} > 0$, it can be derived that

$$(U_{msd} - Y_d) U_{msd}^{-1} (U_{msd} - Y_d)^\top \geq 0, \tag{38}$$

which equivalents to

$$U_{msd} - \mathbf{sym}\{Y\}_d \geq -Y_d U_{msd}^{-1} Y_d^\top. \tag{39}$$

Similarly, in light of $\overline{\alpha}_s \geq 0$, one can also obtain

$$\overline{\alpha}_s (I - \mathbf{sym}\{Y_d\}) \geq -Y_d (\overline{\alpha}_s I) Y_d^\top. \tag{40}$$

Substituting (40) and (41) into (37) and utilizing Schur complement, (30) can be guaranteed. This completes the proof.

4. Numerical Examples

In the current section, to evaluate the efficiency of the attained methodology, the off-on jumping of circuit breakers subject to Markov switching that is associated with two modes, similar to [9, 11], the parameters are listed as follows:

For Mode $m = 1$

$$A_1 = \begin{bmatrix} 0.9833 & 9.368 & -0.01264 & -1.833 \times 10^{-5} \\ -3.529 \times 10^{-3} & 0.9833 & -2.655 \times 10^{-3} & -5.542 \times 10^{-6} \\ 6.39 \times 10^{-3} & -2.936 \times 10^{-2} & 0.955 & 3.681 \times 10^{-3} \\ -0.2263 & -1.253 & -11.31 & 0.5231 \end{bmatrix},$$
$$B_1 = \left[-1.417 \times 10^{-4} - 5.836 \times 10^{-5} 6.133 \times 10^{-2} 22.27\right]^\top. \tag{41}$$

For Mode $m = 2$

$$A_2 = \begin{bmatrix} 0.9866 & 9.378 & -8.638 \times 10^{-3} & -1.253 \times 10^{-5} \\ -2.837 \times 10^{-3} & 0.9866 & -1.812 \times 10^{-3} & -3.878 \times 10^{-6} \\ 2.054 \times 10^{-3} & -1.243 \times 10^{-2} & 0.9443 & 3.67 \times 10^{-3} \\ -0.6894 & 3.545 & -16.25 & 0.5118 \end{bmatrix},$$
$$B_2 = \left[-9.692 \times 10^{-5} - 3.99 \times 10^{-5} 6.123 \times 10^{-2} 22.15\right]^\top. \tag{42}$$

As stated in [11], a Markov chain is adopted to describe the fault switching in power lines, the transition probabilities are illustrated in Table 2. From which, it is clear that $\Pi = \begin{bmatrix} -0.07 & 0.93 \\ -0.2 & 0.8 \end{bmatrix}$.

Furthermore, the condition TPM Ω with two modes and condition TPM Ξ with three modes are selected as

$$\Omega = \begin{bmatrix} 0.4 & 0.6 \\ 0.5 & 0.5 \end{bmatrix}, \quad \Xi = \begin{bmatrix} 0.1 & 0.4 & 0.5 \\ 0.6 & 0.2 & 0.2 \end{bmatrix}. \tag{43}$$

Meanwhile, choosing $\alpha_1 = 0.5$, $\alpha_2 = 0.2$, $\tau_1 = 1$, and $\tau_2 = 2$. The embedded function of deception attacks is chosen as

$$f\left(x\left(k - \tau_{\varepsilon(k)}(k)\right)\right) = \begin{bmatrix} -\tanh\left(\varrho_1 x_1\left(k - \tau_{\varepsilon(k)}(k)\right)\right) \\ -\tanh\left(\varrho_2 x_1\left(k - \tau_{\varepsilon(k)}(k)\right)\right) \\ -\tanh\left(\varrho_3 x_1\left(k - \tau_{\varepsilon(k)}(k)\right)\right) \\ -\tanh\left(\varrho_4 x_1\left(k - \tau_{\varepsilon(k)}(k)\right)\right) \end{bmatrix}, \tag{44}$$

with $\varrho_1 = 10^{-4}$, $\varrho_2 = 5 * 10^{-4}$, $\varrho_3 = 2 * 10^{-4}$, and $\varrho_4 = 3 * 10^{-4}$. From which, we get the upper bound $Q = 10^{-4} \times \{1, 5, 2, 3\}$. On the basis of conditions in Theorem 2, the controller gains can be computed as

$$\begin{aligned} K_1 &= [\,-0.0546 \;\; 2.0486 \;\; 0.0083 \;\; -0.0010\,], \\ K_2 &= [\,-0.0492 \;\; 1.7493 \;\; 0.0296 \;\; -0.0013\,], \\ K_3 &= [\,-0.0482 \;\; 1.6955 \;\; 0.0334 \;\; -0.0013\,]. \end{aligned} \tag{45}$$

The simulations are plotted in Figure 3, which presents the uncontrolled curves of $x(k)$. The evolution of system mode $\sigma(k)$, dispatcher mode $\varepsilon(k)$, and controller mode $\theta(k)$ are depicted in Figure 4. The random occurring deception attacks and evolution of time-varying delays $\tau_\varepsilon(k)$ are described in Figures 5 and 6, respectively. Under the aforementioned control gains, the state trajectories of the closed-loop dynamic (14) is displayed in Figure 7, and the control input $u(k)$ is exhibited in Figure 8. It can be seen from Figure 8 that the developed methodology works well.

Meanwhile, when $\mathscr{M} = \mathscr{S} = \mathscr{D} = \{2\}$ and TPMs $\Pi = \Omega = \Xi = \begin{bmatrix} -0.07 & 0.93 \\ -0.2 & 0.8 \end{bmatrix}$, the asynchronous controller degrades into the synchronous case. Similarly, the controller gains can be acquired as

$$\begin{aligned} K_1 &= [\,-0.0082 \;\; 0.3773 \;\; 0.0391 \;\; -0.0044\,], \\ K_2 &= [\,-0.0459 \;\; 1.9166 \;\; -0.0047 \;\; -0.0006\,]. \end{aligned} \tag{46}$$

On the basis of the abovementioned controller gains, the state trajectories of closed-loop dynamic (14) are plotted in

Table 2: The transition probabilities.

System reliability	Mode 1	Mode 2
Model 1 (maximum)	0.826	0.174
Model 2 (minimum)	0.00116	0.99884

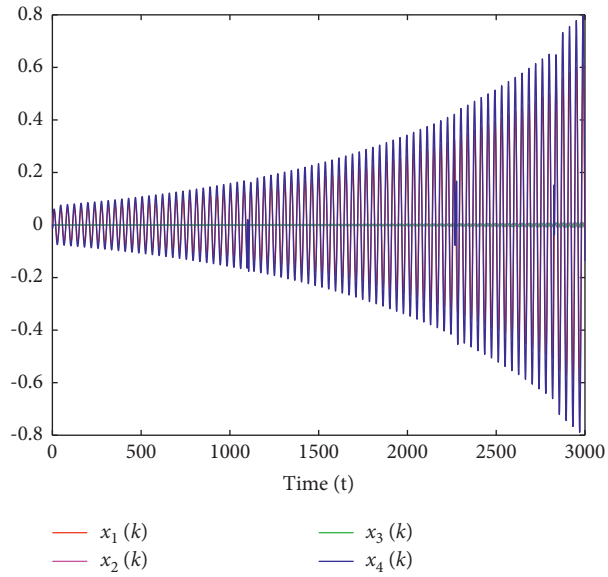

Figure 3: State trajectories of open-loop dynamic (14).

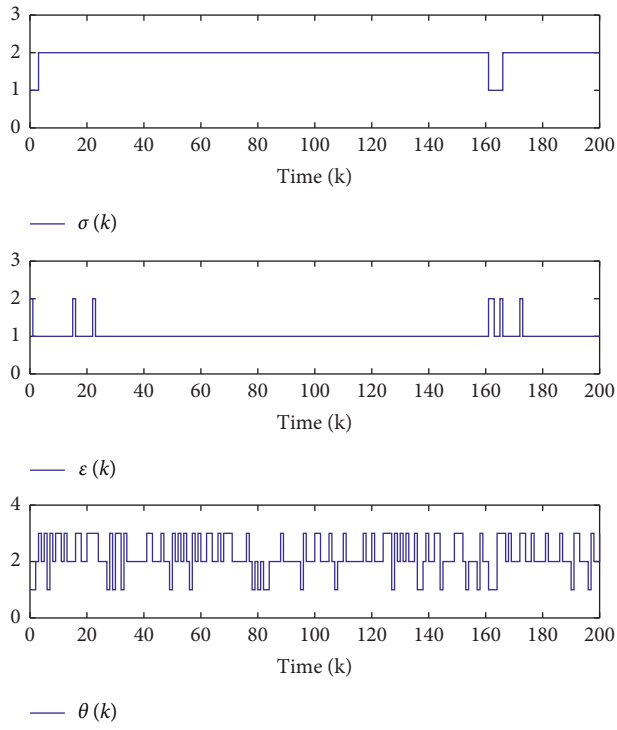

Figure 4: Evolution of modes.

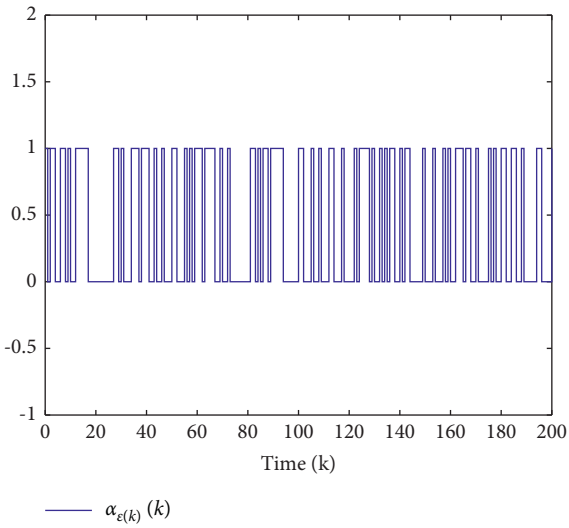

Figure 5: Evolution of $\alpha_{\varepsilon(k)}(k)$.

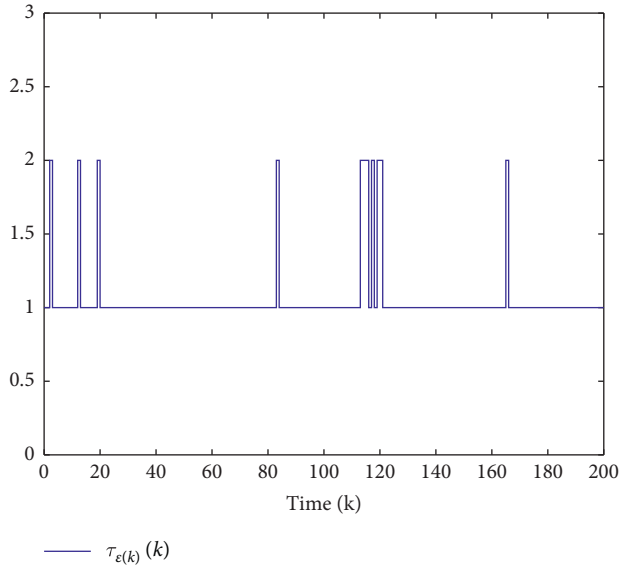

Figure 6: Evolution of time-varying delay.

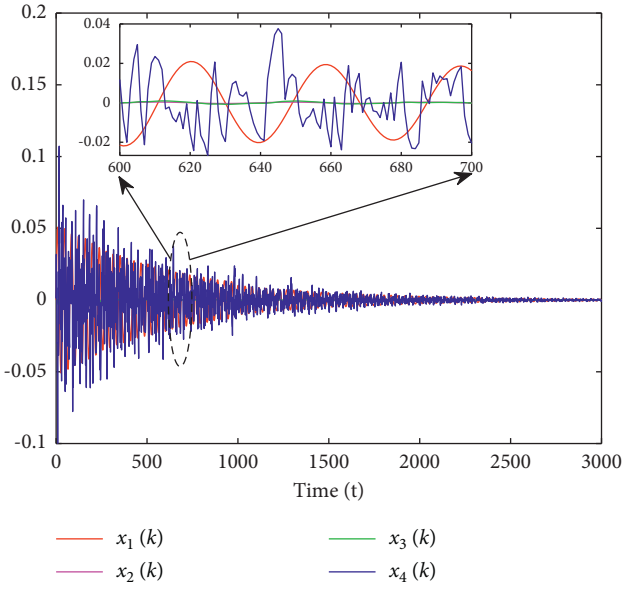

Figure 7: State trajectories of closed-loop dynamic (14).

Figure 9 and the control input $u(k)$ is shown in Figure 10. Clearly, it can be seen from Figures 9 and 10 that the ideal control situation (synchronous control) can achieve better performance.

On the other hand, to further verify the impact of the deception attacks, let $\alpha_{\varepsilon(k)}(k) = 0$, which signifies no deception attacks occur. Similarly, by solving the conditions of Theorem 2, the corresponding gains can be calculated as

$$\begin{aligned} K_1 &= [\,-0.0571 \quad 1.8693 \quad 0.3956 \quad -0.0407\,], \\ K_2 &= [\,-0.0598 \quad 1.9824 \quad 0.3964 \quad -0.0453\,], \\ K_3 &= [\,-0.0597 \quad 2.0021 \quad 0.3918 \quad -0.0458\,]. \end{aligned} \tag{47}$$

Under the aforementioned control gains, the state trajectories of the closed-loop dynamic (14) are displayed in Figure 11 and the control input $u(k)$ is exhibited in

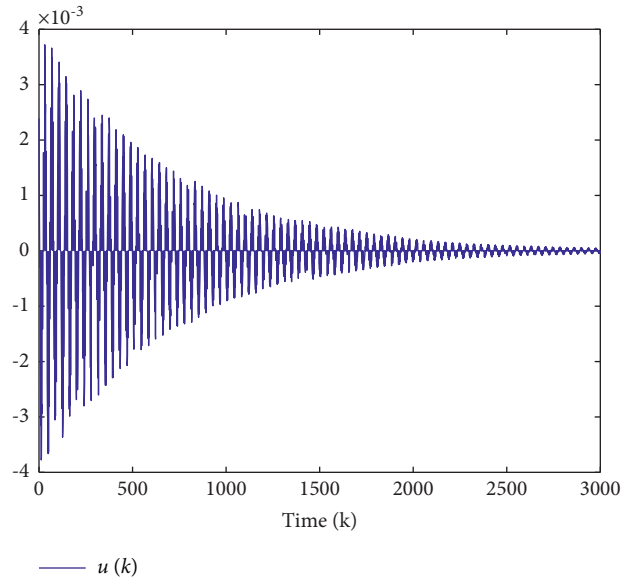

Figure 8: Curve of control input with deception attacks.

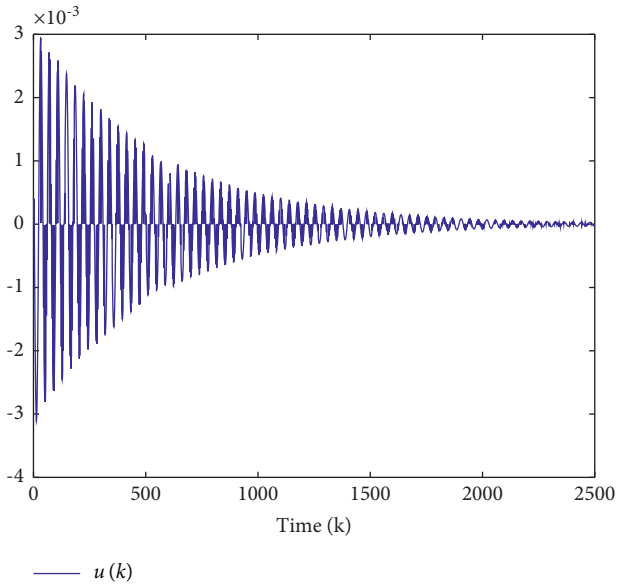

Figure 10: Curve of synchronous control input.

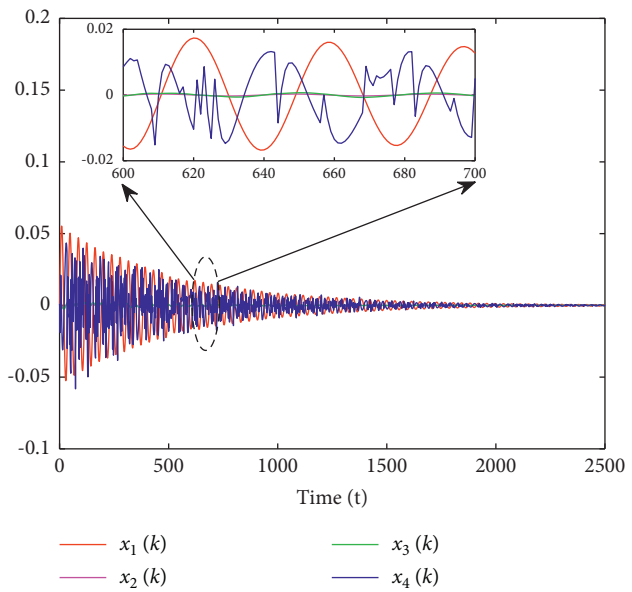

Figure 9: State trajectories of synchronous closed-loop dynamic (14).

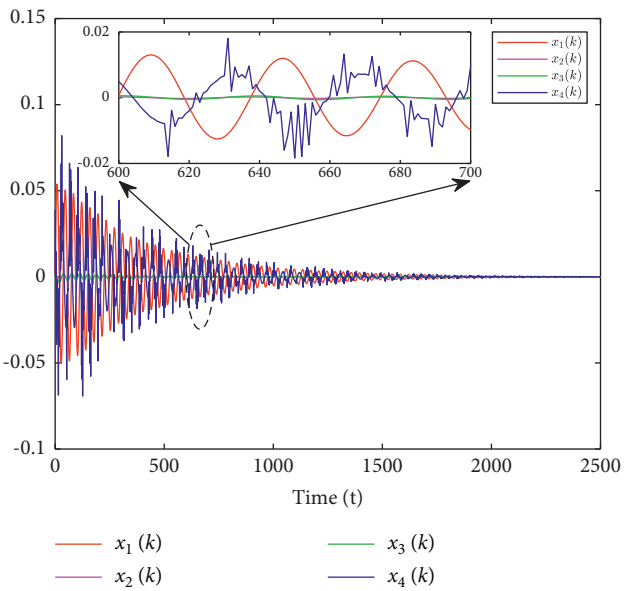

Figure 11: State trajectories of closed-loop dynamic (14) without deception attacks.

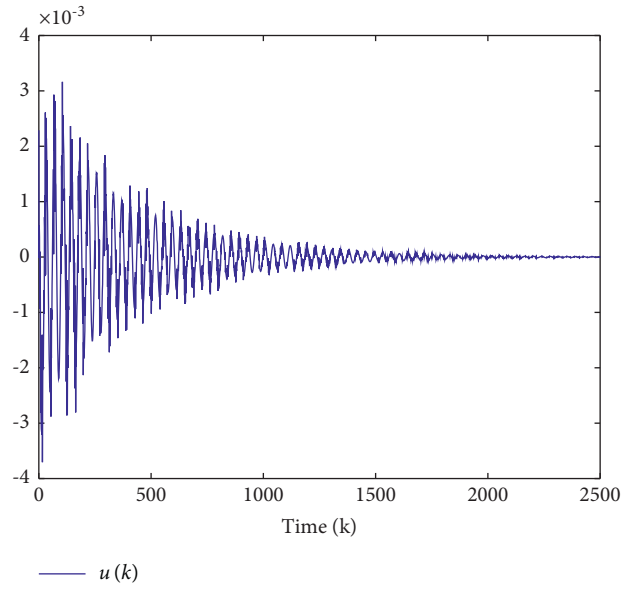

Figure 12: Curve of control input without deception attacks.

Figure 12. From the figures, it is clear that a better performance can be achieved without considering the deception attacks. From which, one concludes that deception attacks degrade the dynamic performance to a certain extent.

5. Conclusion

The problem of power systems being subject to abrupt variations and cyber-attacks has been addressed in the current study. Two hidden Markov models are expressed to characterize the asynchronous phenomena among system mode, dispatcher mode, and controller mode. Furthermore, unlike the existing cyber-attacks, the deception attacks with time-varying delays are regulated by a Markov process. Based on the Lyapunov theory, sufficient conditions are presented to guarantee the stochastic mean-square stability of the closed-loop dynamic. Finally, the proposed control design strategy is testified via a simulation result.

Data Availability

All the data are included within this manuscript.

Conflicts of Interest

The authors declare that they have no conflicts of interest.

References

[1] W. Kai, F. Xiao, P. Jinbo, R. Jun, D. Chongxiong, and L. Liwei, "State of charge (soc) estimation of lithium-ion battery based on adaptive square root unscented kalman filter," *International Journal of Electrochemical Science*, vol. 15, no. 9, pp. 9499–9516, 2020.

[2] K. Wang, W. Wang, L. Wang, and L. Li, "An improved soc control strategy for electric vehicle hybrid energy storage systems," *Energies*, vol. 13, no. 20, p. 5297, 2020.

[3] X. Feng, Q. Li, and K. Wang, "Waste plastic triboelectric nanogenerators using recycled plastic bags for power generation," *ACS Applied Materials & Interfaces*, vol. 13, no. 1, pp. 400–410, 2020.

[4] Y. Hua, N. Wang, and K. Zhao, "Simultaneous unknown input and state estimation for the linear system with a rank-deficient distribution matrix," *Mathematical Problems in Engineering*, vol. 2021, Article ID 6693690, 11 pages, 2021.

[5] K. Wang, C. Liu, J. Sun et al., "State of charge estimation of composite energy storage systems with supercapacitors and lithium batteries," *Complexity*, vol. 2021, Article ID 8816250, 15 pages, 2021.

[6] C. Liu, Q. Li, and K. Wang, "State-of-charge estimation and remaining useful life prediction of supercapacitors," *Renewable and Sustainable Energy Reviews*, vol. 150, Article ID 111408, 2021.

[7] C. Liu, Y. Zhang, J. Sun, Z. Cui, and K. Wang, "Stacked bidirectional lstm rnn to evaluate the remaining useful life of supercapacitor," *International Journal of Energy Research*, vol. 46, no. 3, 2022.

[8] Z. Cui, L. Wang, Q. Li, and K. Wang, "A comprehensive review on the state of charge estimation for lithium-ion battery based on neural network," *International Journal of Energy Research*, vol. 46, no. 5, 2022.

[9] V. Ugrinovskii and H. R. Pota, "Decentralized control of power systems via robust control of uncertain Markov jump parameter systems," *International Journal of Control*, vol. 78, no. 9, pp. 662–677, 2005.

[10] P. Kundur, "Power system stability," *Power system stability and control*, vol. 10, pp. 7–1, 2007.

[11] F. A. El-Sheikhi, H. M. Soliman, R. Ahshan, and E. Hossain, "Regional pole placers of power systems under random failures/repair Markov jumps," *Energies*, vol. 14, no. 7, p. 1989, 2021.

[12] K. Dehghanpour and S. Afsharnia, "Electrical demand side contribution to frequency control in power systems: a review on technical aspects," *Renewable and Sustainable Energy Reviews*, vol. 41, pp. 1267–1276, 2015.

[13] H. Shayeghi, H. A. Shayanfar, and A. Jalili, "Load frequency control strategies: a state-of-the-art survey for the researcher," *Energy Conversion and Management*, vol. 50, no. 2, pp. 344–353, 2009.

[14] C.-K. Zhang, L. Jiang, Q. H. Wu, Y. He, and M. Wu, "Delay-dependent robust load frequency control for time delay power systems," *IEEE Transactions on Power Systems*, vol. 28, no. 3, pp. 2192–2201, 2013.

[15] H. Shokouhandeh and M. Jazaeri, "Robust design of fuzzy-based power system stabiliser considering uncertainties of loading conditions and transmission line parameters," *IET Generation, Transmission & Distribution*, vol. 13, no. 19, pp. 4287–4300, 2019.

[16] T. Yang, Y. Zhang, W. Li, and A. Y. Zomaya, "Decentralized networked load frequency control in interconnected power systems based on stochastic jump system theory," *IEEE Transactions on Smart Grid*, vol. 11, no. 5, pp. 4427–4439, 2020.

[17] J. Cheng, J. H. Park, and Z.-G. Wu, "A hidden Markov model based control for periodic systems subject to singular perturbations," *Systems & Control Letters*, vol. 157, Article ID 105059, 2021.

[18] Y. Wang, H. Pu, P. Shi, C. K. Ahn, and J. Luo, "Sliding mode control for singularly perturbed Markov jump descriptor systems with nonlinear perturbation," *Automatica*, vol. 127, Article ID 109515, 2021.

[19] J. Cheng, L. Liang, J. H. Park, H. Yan, and K. Li, "A dynamic event-triggered approach to state estimation for switched memristive neural networks with nonhomogeneous sojourn probabilities," *IEEE Transactions on Circuits and Systems I: Regular Papers*, vol. 68, no. 12, pp. 4924–4934, 2021.

[20] J. Cheng, Y. Wang, J. H. Park, J. Cao, and K. Shi, "Static output feedback quantized control for fuzzy Markovian switching singularly perturbed systems with deception attacks," *IEEE Transactions on Fuzzy Systems*, vol. 30, no. 4, pp. 1036–1047, 2022.

[21] A. Ameli, A. Hooshyar, A. H. Yazdavar, E. F. El-Saadany, and A. Youssef, "Attack detection for load frequency control systems using stochastic unknown input estimators," *IEEE Transactions on Information Forensics and Security*, vol. 13, no. 10, pp. 2575–2590, 2018.

[22] A. Kazemy and M. Hajatipour, "Event-triggered load frequency control of Markovian jump interconnected power systems under denial-of-service attacks," *International Journal of Electrical Power & Energy Systems*, vol. 133, Article ID 107250, 2021.

[23] S. Kuppusamy, Y. H. Joo, and H. S. Kim, "Asynchronous control for discrete-time hidden Markov jump power systems," *IEEE Transactions on Cybernetics*, 2021.

[24] M. Chi, X.-L. Wang, Y. Dou, and Z.-W. Liu, "Intermittent Sampled Data Control for Time-Varying Formation-Containment of the Multiagent System With/without Time Delay," *Complexity*, vol. 2021, Article ID 9971855, 9 pages, 2021.

[25] J. Cheng, J. J. H. Park, Z. G. Wu, and H. Yan, "Ultimate Boundedness Control for Networked Singularly Perturbed Systems with Deception Attacks: A Markovian Communication Protocol Approach," *IEEE Transactions on Network Science and Engineering*, vol. 9, no. 2, pp. 445–456, 2022.

[26] W. Zhou, J. Fu, H. Yan, X. Du, Y. Wang, and H. Zhou, "Event-triggered approximate optimal path-following control for unmanned surface vehicles with state constraints," *IEEE Transactions on Neural Networks and Learning Systems*, pp. 1–15, 2021.

[27] D. Zhang, Z. Ye, G. Feng, and H. Li, "Intelligent event-based fuzzy dynamic positioning control of nonlinear unmanned marine vehicles under dos attack," *IEEE Transactions on Cybernetics*, pp. 1–14, 2021.

[28] E. I. Bilis, W. Kröger, and C. Cen Nan, "Performance of electric power systems under physical malicious attacks," *IEEE Systems Journal*, vol. 7, no. 4, pp. 854–865, 2013.

[29] Z. Ye, D. Zhang, Z.-G. Wu, and H. Yan, "A3c-based intelligent event-triggering control of networked nonlinear unmanned marine vehicles subject to hybrid attacks," *IEEE Transactions on Intelligent Transportation Systems*, pp. 1–14, 2021.

[30] D. Ding, Z. Wang, D. W. C. Ho, and G. Wei, "Distributed recursive filtering for stochastic systems under uniform quantizations and deception attacks through sensor networks," *Automatica*, vol. 78, pp. 231–240, 2017.

[31] Y. Wu, J. Cheng, X. Zhou, J. Cao, and M. Luo, "Asynchronous filtering for nonhomogeneous Markov jumping systems with deception attacks," *Applied Mathematics and Computation*, vol. 394, Article ID 125790, 2021.

[32] S. Huo and F. Li, "Hidden Markov model-based control for networked fuzzy Markov jump systems against randomly occurring multichannel attacks," *International Journal of Robust and Nonlinear Control*, vol. 31, no. 5, pp. 1657–1673, 2021.

[33] Y. Xu, Z.-G. Wu, and J. Sun, "Security-based passivity analysis of Markov jump systems via asynchronous triggering control," *IEEE Transactions on Cybernetics*, pp. 1–10, 2021.

[34] E. Tian and C. Peng, "Memory-Based event-triggering H ∞ load frequency control for power systems under deception attacks," *IEEE Transactions on Cybernetics*, vol. 50, no. 11, pp. 4610–4618, 2020.

[35] Z. Hu, S. Liu, W. Luo, and L. Wu, "Credibility-based secure distributed load frequency control for power systems under false data injection attacks," *IET Generation, Transmission & Distribution*, vol. 14, no. 17, pp. 3498–3507, 2020.

[36] J. Liu, L. Wei, X. Xie, E. Tian, and S. Fei, "Quantized stabilization for T-S fuzzy systems with hybrid-triggered mechanism and stochastic cyber-attacks," *IEEE Transactions on Fuzzy Systems*, vol. 26, no. 6, pp. 3820–3834, 2018.

[37] Z. Xu, Z.-G. Wu, H. Su, P. Shi, and H. Que, "Energy-to-peak filtering of semi-markov jump systems with mismatched modes," *IEEE Transactions on Automatic Control*, vol. 65, no. 10, pp. 4356–4361, 2019.

Hindawi
Mathematical Problems in Engineering
Volume 2022, Article ID 4710868, 12 pages
https://doi.org/10.1155/2022/4710868

Research Article

Long-Term Bidding Scheduling of a Price-Maker Cascade Hydropower Station Based on Supply Function Equilibrium

Gang Liu,[1,2] Guangwen Ma,[1,2] Weibin Huang ,[1,2] and Shijun Chen[1,2]

[1]*College of Water Resource and Hydropower, Sichuan University, Chengdu 610065, Sichuan, China*
[2]*State Key Laboratory of Hydraulics and Mountain River Engineering, Sichuan University, Chengdu 610065, Sichuan, China*

Correspondence should be addressed to Weibin Huang; huangweibin@scu.edu.cn

Received 20 August 2021; Revised 9 October 2021; Accepted 22 March 2022; Published 16 April 2022

Academic Editor: Kai Wang

How cascade hydropower stations (CHSs) play the electricity market game is regarded as an important issue. The majority of the work to date has focused on short-term horizons and several simplifications in the hydropower system. If future prices are expected to be higher than the current price, CHSs with large reservoirs allow the bidder to postpone energy production for a longer time scale, such as several months or more, which generally matches with the regulation period of the reservoir. Rejecting the assumption of simplifying the hydropower system (ASHS), the long-term bidding strategy of CHSs is discussed for a price-maker based on the supply function equilibrium (SFE). This study considers multiple price-makers, time-coupling, and the characteristics of the hydropower system, with significant challenges. The difference from the conventional model is that the long-term optimal scheduling model of CHSs is added. Moreover, a new methodology is proposed, the equilibrium curve of the uniform clearing price (UCP) is introduced, and the Nash equilibrium solutions are solved based on the nonlinear complementarity approach. In a simulated electricity market, the result can validate the feasibility of the model and adopted methodology and the rationality of the results by taking certain CHSs with multireservoir as an example. The negative influence of ASHS is analyzed, which shows that the characteristics of the hydropower system should be fully considered in the long-term bidding research. Future study aspects are also considered, which are presented as the key issues such as market assumptions and randomness.

1. Introduction

As the new round of power system reform in China is developed, market participants are faced with a series of large-scale, highly complex, and nonlinear multiperson decision-making problems. In an electricity market, independent power producers (IPPs) exercise market power by adopting certain strategic behaviors to earn greater profit. Researchers focus on the investigation of the bidding strategy in the short-term or day-ahead electricity market to explore the bidding strategy of IPPs in the electricity market. The currently available methods include (1) a method to forecast the market clearing price [1–4]; (2) a method based on risk management [5, 6]; (3) a method to forecast and estimate the strategies of competitors [7]; and (4) a method based on game theory. Much research has been conducted on the first method, which is applicable to IPPs as the price-taker. In the electricity market, which is a typical oligopoly, the method based on game theory confers more theoretical advantages compared with other methods, so it is applicable to IPPs as the price-maker. The equilibrium models of oligopolistic competition based on game theory include the Cournot equilibrium model [8–10], Bertrand equilibrium model [11], Stackelberg equilibrium model [12, 13], and SFE model [14–18]. Among them, the SFE model is akin to the bid-based pool (BBP) mode as is mainly used in the electricity market, so it is extensively studied. The strategic bidding problem for price-maker agents based on the equilibrium model is usually formulated as a bilevel optimization problem, which is in turn transformed into a mixed nonlinear complementarity problem (NCP) by applying Karush–Kuhn–Tucker (KKT) complementarity conditions,

known as mathematical programming with equilibrium constraints (MPECs). There have been many solution methods, such as interior point method with penalty term [14, 19], heuristics and iterative procedures [15, 20, 21], and the nonlinear complementarity approach [8, 22–27]. At present, there has been much research into this topic [8, 14–24, 28]. However, most of them are applied in the electricity market with only thermoelectric systems and are based on the market-wide equilibrium at a certain point in time. Such scheduling decisions are generally decoupled in time.

A pattern of cascade hydropower systems with the basin development company as the main body has been formed in China, in which CHSs have become important participants in the competition in the electricity market. Since the reservoir has the ability to store water (energy), it can be decided whether to generate in the present or store water for future use, which makes the operation of CHSs coupled in time. CHSs allow the bidder to postpone energy production through reservoir regulation if future prices are expected to be higher than the current price. Furthermore, the interconnection between the CHSs makes the operation coupled in space. This means that the bidding strategy should consider the characteristics of the hydropower system, making strategic bidding among cascade hydropower companies a large-scale multiperiod bilevel optimization. The strategic bidding problem solution is therefore more subtle.

For the issue of bidding for hydropower and thermal power based on the game theory, the dynamics of the hydropower station bidding game were considered [29]. A bilevel optimization problem to electricity generation scheduling in the wholesale market environment is proposed [30]. The numerical example of a 15 bus energy power system with thermal and hydropower plants is used to test the applicability of the approaches. The coalitional strategy, forms, and coalitional conditions of CHSs were studied based on coalitional game theory [31]. Moreover, it is supposed that the output of hydropower stations is a quadratic function of inflows and storage capacity. The equilibrium of a Cournot game between multiple firms that each possesses a mixture of hydropower and thermal generation resources was studied [8]. A price-taking fringe was introduced as a new element, and a mixed linear complementarity model was established. A test case with 21 scenarios (i.e., three months and seven load levels) is proposed to analyze the equilibrium characteristics under different market structures, which is still the equilibrium at a single point in time. Moreover, the model simplified the hydroelectric system with the maximum and minimum output parameters.

The above-mentioned research mainly studied the bidding equilibrium at a single point in time and has made simplified assumptions, but all ignored the time coupling of hydropower systems, which is necessary for practical applications. A multiyear model of strategic hydroscheduling was examined through the use of a stochastic dynamic programming recursion technique [32]. A dual dynamic programming approach to the numerical solution for a medium-term optimal hydroschedule was used [33], and the submodels at each stage are Cournot duopolies. But the model only considers a single price-maker hydropower company. Based on a review of the methodology adopted for solving the problems of single-period and multiperiod stochastic strategic bidding scenarios, a new methodology for long-term strategic bidding of a price-maker hydropower-based company was proposed [34]. The proposed approach considers the uncertainty of inflow and the interconnection between the CHSs. A deterministic residual demand curve (RDC) and a piecewise linear approximation of the expected future benefit function were proposed. The model is solved based on stochastic dual dynamic programming; however, the model discussed in the present work considers a single price-maker company and follows a quantity-only bid approach, which is a particular case of a more general market equilibrium model. Several reservoirs are not aggregated into one "equivalent reservoir", but the production coefficients of hydropower stations were assumed to be constant. The midterm stochastic mixed-integer linear programming model for a price-maker hydroproducer with pumped storage in the day-ahead market was proposed [7]. A yearly stochastic self-scheduling model is presented because there is only one price-maker. The proposed approach considers the modification of the RDC based on pumped storage characteristics and a three-stage scenario tree with 90 scenarios to simulate uncertainty in inflow and demand load. But similar to most models, the output is considered a linear function of inflow.

Although these studies have considered time-coupling of CHSs, they are not a market-wide equilibrium model, but a single-firm profit-maximization model that focuses on the self-scheduling of price-maker. The short-term bidding strategy for hydropower stations based on a static game was studied [35], but by assigning weights to each generator, the multiobjective programming problem was transformed into a single-objective optimization problem to be solved approximately. An equilibrium model to determine the price and quantity of strategic bids was studied in a day-ahead electricity market, with predominantly hydropower stations [20]. A new solution method is proposed, which replaces the MPEC complementary condition with the strong dual condition and solves the competition between several leaders through a step-by-step iterative process, which we expect to be a Nash equilibrium. Two price-makers are considered, and each company has multiple thermal power and CHSs, but the output is still calculated with a constant production coefficient. There have been many reports based on market-wide equilibrium, the vast majority of which focused on short-term horizons.

All the aforementioned research simplifies the hydropower system: first, the production coefficient and the available head of water at each hydropower plant are assumed to be constant, which will make the total amount of electricity for the same amount of water constant. However, in actual operation, because of the same amount of water, different operation modes have different total electricity, so it is often necessary to ensure maximum power generation by optimizing the operation of the reservoir. This is mainly

because the production coefficient is a nonlinear factor, which is related to the available head of water, discharge flow, and other factors; especially in the long-term operation, the range of variation in the available head is larger, as is the variation in production coefficient. This assumption will lead to significant discrepancies in model output data. At the same time, the difference between electricity quantity and actual power generation will bring various risks. In the period of low water level, because the actual water head is far less than the fixed water head, the actual hydropower generation is lower than expected, and there are performance risks. In the period of high water level, because the actual water head is much larger than the fixed water head and the actual power generation is higher than the expectation, abandoned water will occur. Second, the model aggregates several hydropower stations into one "equivalent hydropower station", which is a numerical accumulation. Each hydropower station is isolated from the others. The model does not consider various characteristics such as upstream and downstream hydraulic connectivity and interval inflow between CHSs, which is quite different from the actual situation.

Hence, based on the aforementioned comments, the main aims of the paper are to (1) build a long-term strategic bidding model of CHSs based on the linear supply function equilibrium (LSFE). This model considers time-coupling, so it is multiperiod. It also considers the market-wide equilibrium resulting from the competition between multiple price-makers on the quantity and price of electricity in an electricity market with multiple types of generation sources; (2) reject ASHS, be full considered the characteristics of the hydropower system, such as changes in water head, the water balance, overflow or surplus water flow, upstream and downstream hydraulic connection and interval inflow, and make a comparative analysis; (3) propose a solution methodology and introduce the equilibrium curve of the UCP.

2. Model Description and Formulation

Strategic bidding for price-maker agents is usually formulated as a bilevel optimization problem for the electricity market, in which the internal layer corresponds to the minimization of the power purchase cost of the independent system operator (ISO) under the mechanism of a UCP; the external layer represents the maximizing the profits to all bidders. The inner layer problem can be modeled by a competitive equilibrium model. The BBP mode is still the most widely used transaction mode in the actual electricity market, and the competition of power producers is more akin to the competition of supply function. Each power producers submit an incremental supply function to ISO to quote. This paper adopts the LSFE model to simulate an electricity market. In terms of long-term bidding games among hydropower generators, a multiperiod dimension is added due to hydraulic and electric connections between periods. Moreover, due to changes in inflows and outputs in different periods, the market equilibrium of the internal layer also varies synchronously, so the model is more complex.

2.1. Market Clearing Model. In the electricity market with UCP, ISO determines the power purchase plan and the UCP according to the objective of minimizing power purchase cost based on the predicted future load curve. It is supposed that there are n strategic IPPs in an electricity market, and the game between these IPPs is a static noncooperative game with complete information. It is supposed that, without considering transmission constraints and network losses, only constraints on the outputs of generator units and electricity price in the electricity market are considered; thus, the model for market clearing in the period t is given by

$$\text{Min} \sum_{i=1}^{n} P_{it} \cdot q_{it}, \tag{1}$$

$$\begin{aligned} \text{s.t.} \sum_{i=1}^{n} q_{it} &= D(t, P_t) \\ &= L_t - \delta_t P_t, \end{aligned} \tag{2}$$

$$q_{i,\min} \le q_{it} \le q_{i,\max}, \tag{3}$$

$$p_{\min} \le P_t \le p_{\max}, \tag{4}$$

$$q_{\text{it}} \ge 0, \tag{5}$$

where q_{it} and P_{it} denote the output and bidding price of the IPP i in period t; $D(t, P_t)$ denotes the demand function for power load in period t; L_t represents the predicted value of load demand in the period t as obtained by ISO prediction; δ_t $(\delta_t \ge 0)$ represents the price elasticity coefficient of the load demand; P_t refers to the market electricity price in period t; $q_{i,\min}$ and $q_{i,\max}$ denote the min and max output of the IPP i in period t; $p_{\min}$ and $p_{\max}$ denote the price floor and price cap of the electricity market.

It is supposed that IPP i makes a tender offer to ISO based on LSFE so $P_{\text{it}} = \beta_{\text{it}} q_{\text{it}} + \gamma_{\text{it}}$, in which $\beta_{\text{it}} \ge 0$. β_{it} and γ_{it} are parameters pertaining to linear supply function of the IPP i in the period t. Generally, the parameter β_{it} is defined as the decision variable of the strategy used by IPPs.

2.2. Profit Maximization Model. According to the principles of microeconomics, all parties in the game aim to maximize their own benefit; that is, they are expected to maximize their own profit by calculating their own bidding functions; therefore, the long-term decision model for any IPP based on profit maximization is expressed as follows:

$$\max \pi_i = \max \sum_{t=1}^{T} \left(P_t \cdot q_{\text{it}} - c_i q_{\text{it}}\right), \tag{6}$$

where π_i denotes the amount (in CNY) of annual profitability through IPP i (other parameters are as defined above). It is supposed that IPP i features a linear function of variable

operation cost: $c_i = a_i q_{\mathrm{it}} + b_i$, in which a_i and b_i are parameters pertaining to the variable cost.

Based on equations (1) to (5) and equation (6) for n IPPs, the long-term bidding game of IPPs is formed.

2.3. Profit Maximization Model for CHSs. In terms of multiple periods and stations, CHSs present a close hydraulic connection; the same water use for power generation corresponds to multiple different combinations of outputs, and the market equilibrium also varies. It is therefore necessary to ensure the overall equilibrium of the market in multiple periods within the operating period during the long-term bidding game. Equation (6) is transformed into equations (7) to (15).

The long-term optimal operation model for CHSs based on profit maximization is given by

$$\mathrm{Max}\,\pi_i = \mathrm{Max}\sum_{t=1}^{T}\left(\left(P_t - b_i\right)\cdot A_{ij}\cdot Q_{ij,t}\cdot H_{ij,t}\cdot M_t\right). \quad (7)$$

The constraint on the water balance is

$$V_{ij,t+1} = V_{ij,t} + \left(R_{ij,t} - Q_{ij,t} - S_{ij,t}\right)\cdot \Delta t, \quad \forall t \in T. \quad (8)$$

The constraint on water storage in reservoirs is

$$V_{ij,t,\min} \le V_{ij,t} \le V_{ij,t,\max}, \quad \forall t \in T. \quad (9)$$

The constraint on discharge flow from reservoirs is

$$Q_{ij,t,\min} \le Q_{ij,t} \le Q_{ij,t,\max}, \quad \forall t \in T, \quad (10)$$

$$S_{ij,t} \ge 0, \quad \forall t \in T. \quad (11)$$

The constraint on the output of a station is

$$N_{ij,t} = A_{ij}\cdot Q_{ij,t}\cdot H_{ij,t}, \quad (12)$$

$$N_{ij,\min} \le N_{ij,t} \le N_{ij,\max}, \quad \forall t \in T. \quad (13)$$

The constraint on the total output of CHSs is

$$\sum_{i}^{k}\sum_{j}^{m} q_{ij,t} \le L_{t\max}. \quad (14)$$

The constraint on the electricity price is

$$P_{\min} \le P_t \le P_{\max}. \quad (15)$$

Nonnegative constraint: all the above variables are nonnegative (≥0).where A_{ij} denotes the output factor of the j^{th} hydropower station of the IPP i; Q_{ijt} and $H_{ij,t}$ separately refer to the discharge flow (m^3/s) and the mean average net head of water (m) during power generation at the hydropower station in period t; M_t is the duration (in hours) of period t; T denotes the total number of periods within the operating period (if that lasts for one year and the calculation is undertaken on a monthly basis, then $T = 12$); $V_{ij,t}$ refers to the initial water storage (m^3) of the reservoirs; $R_{ij,t}$ and $S_{ij,t}$ represent reservoir inflow (m^3/s) and surplus water flow (m^3/s) to the hydropower station in period t, respectively; Δt is the duration (s) of the calculation period; $V_{ij,t,\min}$, $V_{ij,t,\max}$, $Q_{ij,t,\min}$, and $Q_{ij,t,\max}$ represent the minimum and maximum water storages (m^3) of reservoirs as well as the minimum discharge flow (m^3/s) and the allowable maximum discharge flow (m^3/s) of the hydropower station in period t, respectively; $N_{ij,\min}$ and $N_{ij,\max}$ separately denote the minimum operating output and the rated installed capacity (MW) of the hydropower station; $N_{ij,t}$ and $L_{t\max}$ denote the output (MW) of the hydropower station in period t and the maximum adjustable load of the electricity market in period t, respectively. If the total output of these CHSs exceeds the adjustable load demand of the market, surplus water is generated; $P_{\min}$ and $P_{\max}$ separately refer to the lowest and the highest electricity prices in the electricity market, with $i = 1, 2, \ldots, k$; $j = 1, 2, \ldots, m_i$.

Moreover, three conversion formulae for the water level of reservoirs with storage capacity, tail water level at a hydropower station with a certain discharge flow, and the water level for a given available head of water are as follows:

$$L_{ij,t}^{\mathrm{up}} = f_{ij}\left(V_{ij,t}\right), \quad (16)$$

$$L_{ij,t}^{\mathrm{down}} = f_{ij}'\left(Q_{ij,t} + S_{ij,t}\right), \quad (17)$$

$$H_{ij,t} = L_{ij,t}^{\mathrm{up}} - L_{ij,t}^{\mathrm{down}} - \Delta H_{ij}, \quad (18)$$

where $L_{ij,t}^{\mathrm{up}}$, $f_{ij}(\cdot)$, $L_{ij,t}^{\mathrm{down}}$, and $f_{ij}'(.)$ refer to the water level (m) of reservoirs of the j^{th} hydropower station of IPP i in period t, the water level–storage capacity curve of the station, the tailwater level (m) of the station in period t, and the nonlinear relationship between the tailwater level and the discharge flow in the lower reaches of the station, respectively; ΔH_{ij} represents the head loss (m) during power generation at the hydropower station, with $\Delta H_{ij} > 0$.

It can be seen from equation (8) and equations (16) to (18) that the storage capacity and head of water are both an implicit function of flows for power generation. Assuming that $H_{ij,t} = x_{ij}(Q_{ij,t}$ and $V_{ij,t} = y_{ij}(Q_{ij,t})$, the decision variable of the bidding strategy for CHSs is shifted from outputs to flows for power generation.

2.4. Multiperiod Bilevel Optimization Problem. Equations (1) to (5), equation (6) for n-k thermal power plants, and equations (7) to (18) for k CHSs constitute a long-term bidding strategy model of price-maker CHSs based on the LSFE equilibrium, which is a multiperiod bilayer optimization problem. The bidding strategy of each IPP is related to the strategy of its competitors. In order to achieve Nash equilibrium, it is not allowed to solve the bidding strategy of each IPP separately but must solve the bidding strategy problems of all IPPs simultaneously.

3. Proposed Methodology

The model involves many different types of IPPs, with many equality or inequality constraints, taking the form of implicit functions for multiple variables. Therefore, the equilibrium problem of large-scale electricity market is sophisticated

mathematical programs. Together with the requirement for overall equilibrium for multiple hydropower stations in multiple periods among CHSs, the model is difficult to solve. It is necessary to optimize and decompose the model as described below:

3.1. Time Decoupling and Time Coupling. For thermal power, wind power, and solar photovoltaic power stations as well as run-of-the-river hydropower stations (or hydropower stations with a regulation capacity less than the duration of the chosen time period), the outputs in different time periods are independent. This means that the bids made at one given period had no effect on the following periods; that is, the problem was decoupled in time. The maximization of the long-term profits means profit maximization in each period.

As previously mentioned, a time-coupling characteristic is inherent to the problem of CHSs because of the existence of water reservoirs, which enable them to transfer available energy from one period to subsequent ones. So the profit maximization at each period is time coupled.

3.2. Price-Takers and Price-Makers. For generator units (such as run-of-the-river hydropower stations, wind power, and solar photovoltaic power stations) with a constant and low marginal cost, it is common to apply a low bidding price to realize the possible maximum output to guarantee consumption and reduce the risk of surplus water, surplus wind, and surplus photovoltaic power in the long-term schedule. These units are price-takers: it can be thought that competition occurs on the basis of the adjustable load on the system excluding outputs from the aforementioned generator units [8, 36]; that is, a bidding game occurs between hydropower stations with regulation capacity and thermal power plants as price-makers.

3.3. The Effect of Output Regulation of CHSs on the UCP. The short-term bidding strategy and long-term bidding strategy of CHSs are different. Due to the existence of the reservoir, CHSs can be scheduled according to the bidding result in the day-ahead market, without abandoning water or performing the contract risk. It can become the marginal unit and participate in the bidding game like a thermal power unit to reach the market equilibrium. However, the long-term bidding strategy is more complicated because of the seasonality of the inflow and the limited regulation ability of the reservoir, as well as the full and empty periods of the reservoir. In general, the marginal cost of hydropower station is constant and low, and the loss of profit from abandoning water often exceeds the gain from higher electricity prices. Therefore, it is assumed that CHSs are generally not taken as marginal units to determine directly the price, but as units below the marginal unit to indirectly affect the price by regulating the output of unit during the long-term bidding game.

The mechanism of influence is described as follows: it is supposed that the equilibrium curve of the UCP is given by $P = B(L)$, and the corresponding UCP of the load L_a of the system is expressed as $P_a = B(L_a)$. If the output of CHSs (located below the marginal units) is increased by ΔN ($\Delta N = L_a - L_b$), which is equivalent to the adjustable load on the system being reduced from L_a to L_b, the UCP is given by $P_b = B(L_b)$, and thus, the electricity price decreases. On the contrary, if the output of the CHSs decreases by ΔL, implying that the adjustable load on the system increases by ΔL and the electricity price increases, as shown in Figure 1. On this basis, the functional relationship between the electricity price and the output (load) when CHSs participate in the long-term game of the electricity market is established thus.

$$P_t = B\left(L_t' + \Delta N\right), \tag{19}$$

where L_t' denote the adjustable load of the system after excluding output from stations of price-takers in period t.

Hence, when the equilibrium curve of UCP is known, the different electricity prices corresponding to different outputs of CHSs can be solved, and the correlations of the inflow, output, load, and electricity price can be established, and it is possible to transform the problem of the long-term bidding game of CHSs based on LFSE into a long-term optimal operation problem of CHSs in the case that the electricity price changes with the output.

Based on the characteristics whereby CHSs are permitted to change the UCP by regulating outputs, the electricity market bidding is divided into two parts. The first part is the bidding between thermal power plants, as price-maker. The second part is the bidding between CHSs and all thermal power plants. In this way, a bilevel optimization problem is divided into two independent problems to be solved step-by-step, thus decreasing the complexity of the problem and difficulty of calculation. The first step is to calculate the equilibrium curve of the UCP excluding CHSs; the second step is to solve the long-term optimal operation problem of CHSs based on the equilibrium solution curve.

3.4. The Equilibrium Curve of the UCP Excluding CHSs. The bidding game of the electricity market without CHSs is usually the strategic bidding problem of thermal power as the price-makers. This is a one-period, bilevel optimization problem, and the scheduling decision is decoupled in time. Based on the static game of complete information, the equilibrium solution of the quantity of the bidding parties and the UCP can be obtained by specifying the load demand. According to different load demands, the equilibrium curve of the UCP at each period can be obtained. When the number and installed capacity of thermal power units, as the price-makers, change with factors such as the new units put into operation, maintenance, shutdown, and decommissioning, the equilibrium curve of UCP will change. The influence of these factors should be considered in each period of long-term bidding scheduling.

The market equilibrium solution excluding CHSs, including the equilibrium solution of the UCP, can be derived by solving equations (1) to (5) and equation (6) for $n - k$ IPPs. Therefore, the equilibrium curve of UCP describing the relationship between load demand and UCP equilibrium

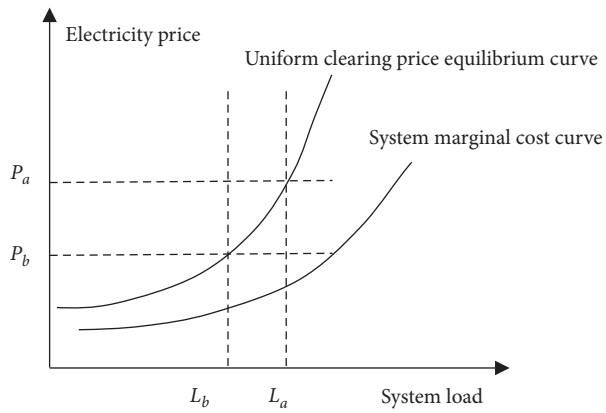

Figure 1: The effect of output regulation of CHSs on the UCP.

solution can be derived. The calculation is conducted by using a nonlinear complementarity approach and the improved Levenberg–Marquardt algorithm [32, 37–39].

3.4.1. Nonlinear Complementarity Approach. By applying the KTT complementarity condition of each participant, this bilayer optimization problem is transformed into a mixed NCP. There are many ways to solve the mixed NCP. In theory, the heuristic iterative algorithm cannot guarantee that the solution obtained by convergence is the Nash equilibrium solution, and the convergence of the algorithm cannot be guaranteed either. Direct solution methods are mainly aimed at the linear complementarity problem (LCP), and corresponding commercial LCP software packages are used to solve it [8, 25]. When the model becomes more complex and NCP occurs, the interior point method and the nonlinear complementarity approach are usually used [22]. The interior point method requires the initial value and iteration value to be in the positive octant, and additional conditions are required. Compared with other methods, the nonlinear complementarity approach is chosen because of its advantages in the following aspects: reduction of the difficulty of solution, more convenient calculation, and wider applicability and is more suitable for solving large-scale and complex equilibrium problems [26].

By introducing the generalized Lagrange multiplier, the equivalent KKT complementarity conditions for profit maximization of IPPs are obtained, and then, the KTT complementarity condition of each IPPs is transformed into a group of nonlinear algebraic equations by using the nonlinear complementary function $\psi(a,b) = a + b - \sqrt{a^2 + b^2}$. Thus, multiple MPECs are transformed into multiple ordinary nonlinear programming problems with standard constraint qualification [27].

3.4.2. The Improved Levenberg–Marquardt Algorithm. The nonlinear complementary function is nondifferentiable and nonsmooth at the origin (0, 0), which leads to the nonexistence of its gradient. When solving the above equations, semismooth algorithms should be used. Compared with other algorithms, the improved Levenberg–Marquardt algorithm considers the search direction of the Newton method and gradient method at the same time, and the algorithm has better stability performance and faster convergence speed, which is more suitable for solving large-scale NCP problems.

Definition 1. Let g: $R^n \longrightarrow R$ is a function under the local Lipschitzian condition and D_g is the set of all differentiable points of g, then the subdifferential $\partial_B g(x)$ of g is defined as follows:

$$\partial_B g(x) = \left\{ h \in R^{n\times 1} | h = \lim_{x^k \in D_g, x^k \longrightarrow x} \nabla g\left(x^k\right) \right\}, \tag{20}$$

where $\nabla g(x^k)$ is the gradient of g at a differentiable point x^k. If g is differentiable at point x, then $\partial_B g(x)$ is equal to $\nabla g(x)$. The convex closure of $\partial_B g(x)$ is the generalized gradient.

The main calculation steps are as follows.

Step 1. Initialize parameters, set the computational precision ε, and the initial point x^0.

Step 2. Calculate the search direction Δx^k.

Select any $H^k \in \partial_B E(x^k)$ and solve for Δx^k according to the following equation:

$$\left(\left(H^k\right)^T H^k + \sigma^k I\right)\Delta x^k = -\left(H^k\right)^T E\left(x^k\right) + r^k, \tag{21}$$

where σ^k is the algorithm parameter, and $\sigma^k \geq 0$; r^k is a variable vector whose norm is small enough.

Step 3. Calculate the iteration step size h^k.

In this paper, the iterative step size is determined by minimizing the merit function using the line search method.

$h^k = 2^{-i}$, $i \in \{0, 1, 2, \ldots, n\}$, and i take the minimum value satisfying the following equation:

$$\Phi\left(x^k + 2^{-i}\Delta x^k\right) \leq \Phi\left(x^k\right) + \beta 2^{-i} \nabla \Phi^T\left(x^k\right)\Delta x^k, \tag{22}$$

where the merit function $\Phi(x) = 1/2E(x)^T E(x)$, and $\beta \in (0, 0.5)$.

Step 4. Variable iteration.

Iterate according to the following formula:

$$x^{k+1} = x^k + h^k \Delta x^k, \tag{23}$$

Step 5. Iteration termination criterion.

When $\|\nabla \Phi(x^k)\| \leq \varepsilon$, meeting the accuracy requirements, the iteration ends.

3.5. Long-Term Bidding Problem of CHSs: The Improved POA. Compared with other optimization algorithms, the POA is chosen because of its advantages in the following aspects: reduction of the calculation of dimensions, faster convergence speed, less parameter adjustment, and excellent practicality [40]. The POA has been improved several times and successfully applied to reservoir scheduling [41–43].

The essence of the POA is to decompose a multistate decision problem into a series of two-stage subproblems. Firstly, the variables of other stages are fixed, and the decision variables of the selected two-stage are searched for optimization and then optimized stage by stage. The optimization result of this round is taken as the initial condition of the next round of optimization, and a new round of optimization is started until the convergence condition is satisfied.

The improved POA proposed in this paper mainly has the following two improvements:

(1) Variable step size search: Considering the accuracy and time of searching for the optimal solution, a larger step length is adopted at the beginning of searching for the optimal solution, and the step size is gradually reduced according to the level of iteration accuracy until the global optimal solution is found.

(2) Consider market constraints, namely cascade total output constraints and price constraints: In each two-stage optimization process, it is necessary to judge whether the total output of the steps exceeds the adjustable load of the system, and water must be abandoned if the total output exceeds the adjustable load of the system. To judge whether the electricity price derived from the equilibrium curve of the UCP exceeds the price cap or the price floor of the electricity market, the maximum and minimum allowable values will be taken if the price exceeds the price cap or the price floor.

4. Case Study

4.1. Description of the Case Study. We simulate the competitive behavior of a regional electricity market with multiple types of generation resources. The total installed capacity of the electricity market is 7,900 MW, of which 25.6% are hydropower stations with regulating capacity, namely A1 hydropower station and A2 hydropower station, both belonging to the same IPP, and is the price-maker. Six thermal power stations, including five coal units and one gas-fired one, belong to different IPPs and are all the price-makers. Run-of-the-river hydropower station group, wind farms group, and photovoltaic power station group are composed of many different IPPs, and they are all price-takers. The installed capacities of the regional electricity market and their main parameters are listed in Table 1.

IPP A manages two hydropower stations with reservoirs, which lie on the upper and lower reaches of the same river basin. Hydropower station A1 has an incomplete annual regulating capacity, with the dead water level of 540 m and the normal water level of 600 m; hydropower station A2 also has an incomplete seasonal regulation capacity, with the dead water level of 370 m and the normal water level of 380 m. This is a multireservoir joint optimal operation problem. Monthly inflow was selected from the data of typical normal flow year in the river basin; the operating period started at the beginning of June and ran to the end of the following May, and the calculation was conducted on a monthly basis. The initial and final water levels of the operating period were both set as the respective dead water levels.

The system loads and the adjustable loads of the system are different from month to month, as shown in Figure 2. The adjustable load of the system is the system load minus the output of power stations of price-takers such as run-of-the-river hydropower station group, wind farms group, and photovoltaic power station group. Assuming that during the operating period, all IPPs in the electricity market participate in the market competition every month, and the installed capacity, number of competitors, and operation cost parameters are the same, and the same equilibrium curve of the UCP excluding CHSs is adopted every month.

4.2. Case Study Results. According to the model for SFE consisting of equations (1) to (5) and (6) for $n-k$ thermal power plants, the equilibrium curve of the UCP excluding CHSs is deduced by using the nonlinear complementarity approach and the improved Levenberg–Marquardt algorithm; that is,

$$P_t = B\left(L_t'\right) = 0.000014155L_t'^2 + 0.01839L_t' + 260.35, \quad L_t' \geq 0. \tag{24}$$

According to equations (7) to (18) and (24), the result of the long-term bidding game of CHSs based on SFE was calculated by using the improved POA, as shown in Table 2, Figures 3, and 4. For the convenience of comparison, the bidding game was conducted based on the optimal operation result obtained by using the objective functions of maximizing annual power generation (Figure 5).

As shown in Figure 5, when the objective function is to maximize the annual power generation, the CHSs scheduling process is as follows: for the leading reservoir A1, the highest operating water level, that is, the normal water level, will be maintained from the beginning of October to the end of April of the following year. In May, the water level of the reservoir A1 will be decreased and fell to the dead level at the end of May. From the beginning of June to the end of September, the water level of the reservoir A1 will be raised from the dead water level to the normal water level. The maximum annual power generation of the CHSs can be achieved through the above long-term operation schedule that keeps the water level as high as possible.

If ASHS is accepted and a fixed production coefficient of the CHSs is adopted, the power generation cannot be optimized. When the inflow is fixed, the power generation is fixed. In this case, the annual power generation of the CHSs that accept ASHS is 11.41% less than those that reject ASHS, and the deviation ratio of monthly output ranges from -18.3% to 1.1%. Moreover, since it is maintained at a high water level most of the time, the monthly output after accepting ASHS is generally lower than that reject ASHS, and the higher the average water level, the greater the deviation ratio. Only the monthly output in June was 1.1%

Table 1: Installed capacities of the regional electricity market and their main parameters.

Power station	Installed capacity (MW)	Maximum output (MW)	Minimum output (MW)	a_i	b_i
Hydropower station A1	1,386	1,386	0	0	60
Hydropower station A2	640	640	0	0	60
Coal-fired unit 1	1,000	1,000	100	0.102	179
Coal-fired unit 2	1,000	1,000	100	0.104	185.3
Coal-fired unit 3	600	600	50	0.208	191.6
Coal-fired unit 4	600	600	50	0.212	196.2
Coal-fired unit 5	300	300	50	0.432	206.7
Gas-fired unit 6	600	600	50	0.448	268.6
Run-of-the-river hydropower station group	1,200	1,200	0	0	50
Wind farm group	214	214	0	0	30
Photovoltaic power station group	360	360	0	0	20
Sum	7,900				

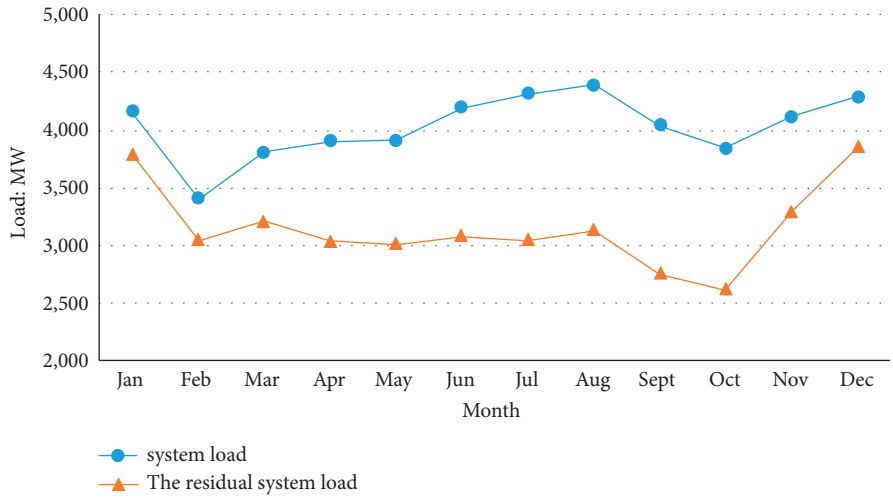

Figure 2: The curve of the system loads and the adjustable system loads.

Table 2: Result of the long-term bidding game of CHSs based on SFE.

Time period	Hydropower station A1		Hydropower station A2		Average output of CHSs (MW)	UCP (CNY/MW·h)	Hydro generation of CHSs (MW·h)	Profit of CHSs ($\times 10^6$ CNY)
	Inflow (m^3/s)	Water level at the end of the period (m)	Interval inflow (m^3/s)	Water level at the end of the period (m)				
May	331.5	540	9.6	370	1,138.1	344.74	846,765	291.91
June	383.1	540.01	11.1	380	847.3	371.85	610,060	226.85
July	910.9	599.82	26.2	380	1,696.7	310.82	1,262,362	392.37
August	726.4	597.88	20.9	380	1,975.6	300.44	1,469,837	441.6
September	776.6	599.99	22.4	379.99	2,026.0	281.38	1,458,704	410.45
October	641.8	600	18.5	380	1,785.9	285.41	1,328,728	379.24
November	288.4	600	8.3	380	828.4	392.05	596,426	233.83
December	221.2	600	6.4	379.99	640.5	465.21	476,556	221.7
January	198.9	600	5.7	380	577.4	465.84	429,610	200.13
February	186.7	597.44	5.4	380	581.6	391.76	390,868	153.13
March	193.1	600	5.6	379.99	522.1	411.86	388,433	159.98
April	184.7	575.82	5.3	380	831.4	370.13	598,589	221.55
Sum							9,856,938	3,332.74

higher than that of reject ASHS, which was caused by the lowest average water level in June.

However, when the CHSs participate in the electricity market game as price-maker, the long-term optimal operation scheme of the CHSs will be fundamentally changed, and if the assumption of the simplified hydropower system is accepted, it will also bring large losses and risks in the long-term bidding game of CHSs.

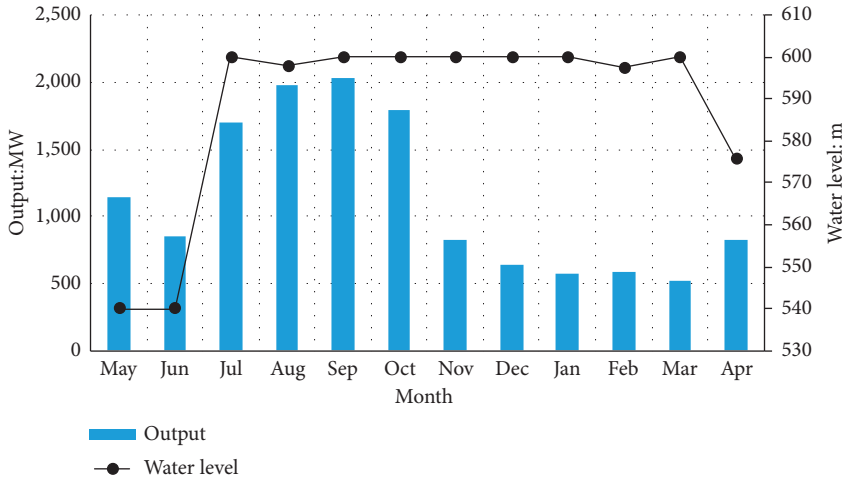

Figure 3: Output and water level based on SFE.

As shown in Table 2 and Figure 3, the CHSs scheduling process is as follows: the amount of power generation of the CHSs is determined by the inflow, and the dead water level of the reservoir A1 will be maintained in June, so as to reserve water storage capacity for subsequent flood mitigation and ensure that the monthly UCP in the flood season is relatively average, because if the discharge flow in the subsequent months of the flood season is too large, the UCP will be too low, and the profit of CHSs will decrease instead. At the end of September, the water level of the reservoir A1 will be raised to the normal water level. From the beginning of October to the end of January of the following year, the water level of the reservoir A1 will be kept at the normal water level. From the beginning of April to the end of May, the water level of the reservoir A1 gradually decreased from the normal water level to the dead water level. From February to March and from August to September, there is a process in which the water level of the reservoir A1 is first decreased and then increased, in order to obtain an optimal value in the multiperiod equilibrium.

In summer, the system load is the highest in the year, especially in July and August, but this is also the high-flow season for hydropower, which means more hydropower available output and the lowest UCP of the year. Wind power and photovoltaic outputs are greatly affected especially on rainy days. At this time, the energy structure of the grid is dominated by hydropower.

In winter, the system load is higher in the year, only lower than the load in summer, except in February. At this time, the inflow of hydropower is reduced month by month due to the decline of rainfall and the decrease in temperature, which means that the hydropower available output is also gradually reduced. Although the output of wind power and photovoltaic power is more than that in summer, the complementary influence is limited, and these factors ultimately result in the highest UCP of the year. Affected by the Chinese New Year, the system load in February was the lowest in the year. Due to the decline in demand, the UCP also decreased.

The negative correlation between the UCP and the output of CHSs shows that the UCP changes dynamically with variations in the output of CHSs and the system load in the market game, as shown in Figures 2 and 4. It can be seen that this bidding model based on SFE can better respond to the demand imposed by the electricity market and more effectively participate in electricity market competition, thus realizing an overall equilibrium across multiple periods.

If ASHS is accepted, compared with rejecting ASHS, the annual power generation and profit will be reduced by 10.8% and 13.8%, and the deviation ratio of monthly output will range from -46.8% to 22.5%, which is a large deviation. Therefore, if IPPs use the model results that accept ASHS to bid, it will bring significant economic losses and performance risks.

As shown in Figure 6, during the period from July to April of the following year, the reservoir is operating at a high water level, and the deviation of monthly output is negative; that is, the actual available output is higher than the model result. This means that in order to reduce profit losses and abandon water, it is necessary to sell unscheduled power generation that exceeds the model results in the short-term electricity market. This will further lower the UCP in the short-term market. The superposition of the two will bring about a greater loss of profit. At the same time, due to the higher expected electricity price, there is a risk of bid failure.

In May and June, the reservoir is operating at a low water level, and the deviation of the monthly output is positive; that is, the actual available output is lower than the model result. This means not only to sell the power generation in the long-term market at a lower price but also to purchase the power generation in the short-term market at a higher price to fulfill the contract.

Therefore, in the long-term bidding, the impact of various main factors of the hydropower system should be fully considered, such as changes in water head, the water balance, overflow or surplus water flow, upstream and downstream hydraulic connection, and interval inflow. This will make the model more realistic and the model results more reasonable and more accurate.

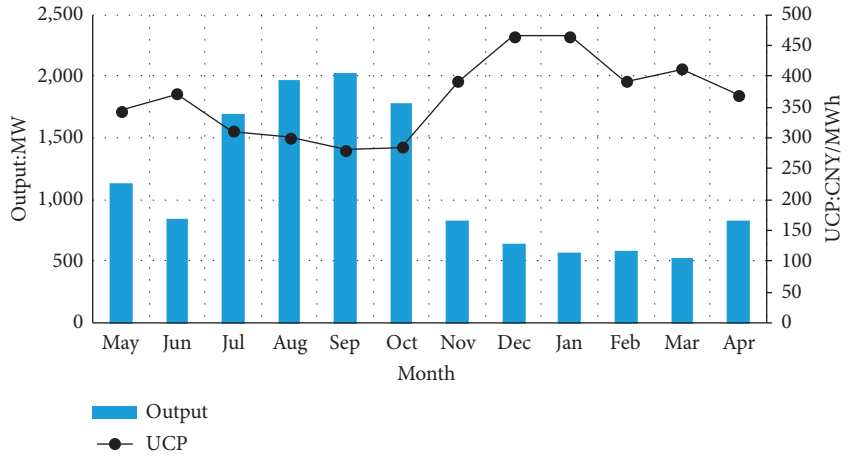

Figure 4: UCP and output based on SFE.

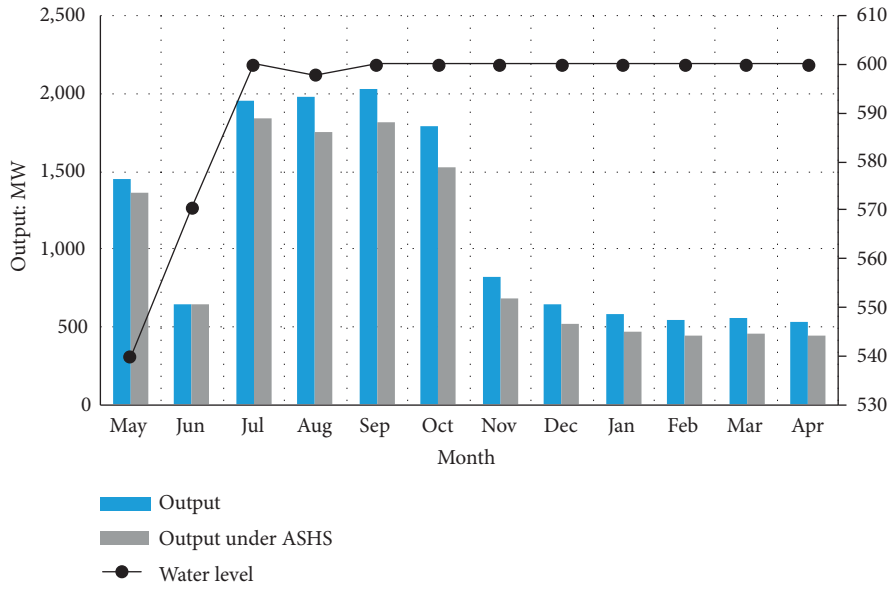

Figure 5: Influence of output under ASHS based on maximizing power generation.

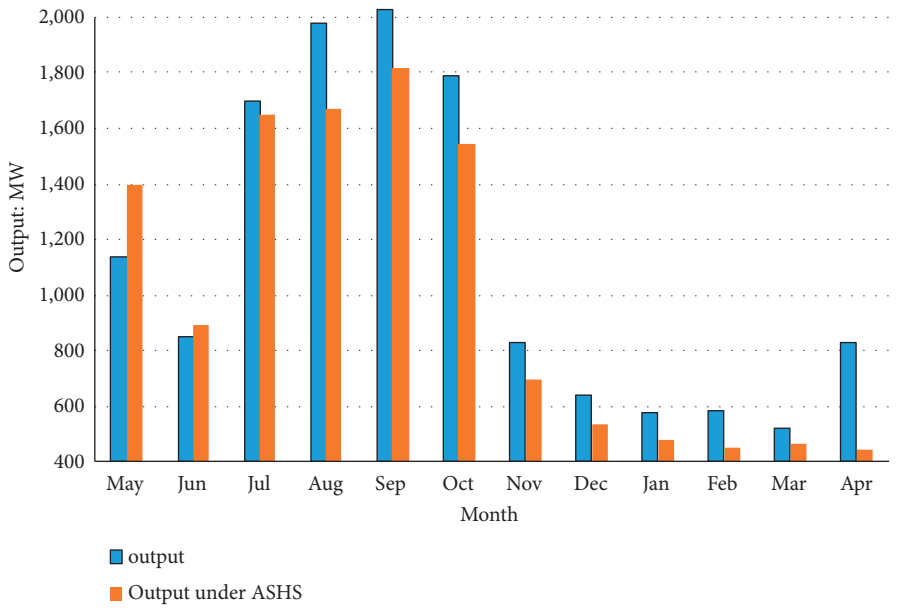

Figure 6: Influence of output under ASHS based on SFE.

5. Conclusions

The long-term bidding of CHSs as price-maker was explored based on game theory and the model for SFE, which made the market-wide equilibrium from a certain point in time to a certain longer time range. Through analysis of the major deviations and risks brought about by ASHS, it was shown that the characteristics of the hydropower system should be fully considered in the long-term bidding. The model was more complicated than the conventional model because it rejected ASHS and considered multiple price-makers, time coupling, and the characteristics of the hydropower system. The correlation among inflows, outputs, loads, and UCPs was established for CHSs through the model. In this paper, based on the characteristics of hydropower, thermal power, and other conventional types of power stations, a new methodology was proposed, the equilibrium curve of the UCP was introduced, and the market-wide equilibrium during the dispatching period was solved based on the nonlinear complementarity approach. Finally, the feasibility of the model and methodology and the rationality of the results are confirmed by way of a practical case study.

In terms of future work, we highlight three possible areas of investigation: the first is to consider more hydropower companies as price-makers. The second extension is to consider stochastic inflows, and the stochasticity of inflows is an important consideration in the operation of hydro-resources. Finally, the third relates to market-related assumptions. The present study was conducted on the assumption of noncooperative behavior with complete information: in reality, market information is generally incompletely asymmetric, and participants also tend to collude and form alliances.

Data Availability

The data that support the findings of this study are available on request from the corresponding author. The data are not publicly available due to reasons related to commercial confidentiality.

Conflicts of Interest

The authors declare that they have no conflicts of interest.

Authors' Contributions

Gang Liu conducted the main research tasks and wrote the manuscript; Guangwen Ma contributed with comments and advice throughout the development of the manuscript. Shijun Chen contributed to the research material; Weibin Huang supervised and checked the research. All authors have read and agreed to the submitted version of the manuscript.

Acknowledgments

This work was supported by the National Key R & D Plan (2016YFC0402205 & 2016YFC0402208).

References

[1] Preeti and R. Jain, "Bidding strategy for deregulated power markets," *Carpathian Journal of Electronic and Computer Engineering*, vol. 9, no. 1, pp. 8–16, 2016.

[2] L. Fan, J. Wang, R. Jiang, and Y. Guan, "Min-max regret bidding strategy for thermal generator considering price uncertainty," *IEEE Transactions on Power Systems*, vol. 29, no. 5, pp. 2169–2179, 2014.

[3] B. Xu, P.-A. Zhong, B. Du et al., "Analysis of a stochastic programming model for optimal hydropower system operation under a deregulated electricity market by considering forecasting uncertainty," *Water*, vol. 10, no. 7, 885 pages, 2018.

[4] J. Lu, B.-x. Liu, Y. b. Wang, C.-T. Cheng, and F. Chen, "Research on optimal dispatching of cascade reservoirs based on electricity price prediction under the Environment of Electric Power Market," *World environmental and water resources congress*, pp. 120–129, 2018.

[5] G. Liu, S. Chen, and F.-li Jiang, "Short-term power generation risk dispatching of hydropower stations based on the multivariate GARCH-VaR," *Water Resources and Power*, vol. 36, pp. 71–74, 2018.

[6] W. Wu, D. Qian, C. Pan et al., "Short-term optimal operation of power generators taking uncertainties into account," *IOP Conference Series: Earth and Environmental Science*, vol. 227, no. 3, 032038 pages, 2019.

[7] C. G. Baslis and A. G. Bakirtzis, "Mid-term stochastic scheduling of a price-maker hydro producer with pumped storage," *IEEE Transactions on Power Systems*, vol. 26, no. 4, pp. 1856–1865, 2011.

[8] J. Bushnell, "A mixed complementarity model of hydrothermal electricity competition in the western United States," *Operations Research*, vol. 51, no. 1, pp. 80–93, 2003.

[9] Y. Zhang, C. Gu, X. Yan, and F. Li, "Cournot oligopoly game-based local energy trading considering renewable energy uncertainty costs," *Renewable Energy*, vol. 159, pp. 1117–1127, 2020.

[10] J. Vuelvas and F. Ruiz, "A novel incentive-based demand response model for Cournot competition in electricity markets," *Energy Systems*, vol. 10, no. 1, pp. 95–112, 2019.

[11] N. Aizenberg and N. Voropai, "Price setting in the retail electricity market under the Bertrand competition," *Procedia Computer Science*, vol. 122, pp. 649–656, 2017.

[12] H. Wu, X. Liu, B. Ye, and B. Xu, "Optimal dispatch and bidding strategy of a virtual power plant based on a Stackelberg game," *IET Generation, Transmission & Distribution*, vol. 14, no. 4, pp. 552–563, 2020.

[13] E. G. Tsimopoulos and M. C. Georgiadis, "Optimal strategic offerings for a conventional producer in jointly cleared energy and balancing markets under high penetration of wind power production," *Applied Energy*, vol. 244, pp. 16–35, 2019.

[14] A. G. Petoussis, X.-P. Zhang, S. G. Petoussis, and K. R. Godfrey, "Parameterization of linear supply functions in nonlinear AC electricity market equilibrium models-Part I: literature review and equilibrium algorithm," *IEEE Transactions on Power Systems*, vol. 28, no. 2, pp. 650–658, 2013.

[15] T. Niknam, S. Sharifinia, and R. Azizipanah-Abarghooee, "A new enhanced bat-inspired algorithm for finding linear supply function equilibrium of GENCOs in the competitive electricity market," *Energy Conversion and Management*, vol. 76, pp. 1015–1028, 2013.

[16] M. Banaei, M. Oloomi Buygi, and H. Raouf Sheybani, "Supply function Nash equilibrium of joint day-ahead electricity

markets and forward contracts," *International Journal of Electrical Power & Energy Systems*, vol. 113, pp. 104–116, 2019.

[17] M. Banaei, M. Oloomi-Buygi, and S.-M. Zabetian-Hosseini, "Strategic gaming of wind power producers joined with thermal units in electricity markets," *Renewable Energy*, vol. 115, pp. 1067–1074, 2018.

[18] D. Langary, N. Sadati, A. M. Ranjbar, and A. Mohammad Ranjbar, "Direct approach in computing robust Nash strategies for generating companies in electricity markets," *International Journal of Electrical Power & Energy Systems*, vol. 54, no. 1, pp. 442–453, 2014.

[19] A. G. Petoussis, X.-P. Zhang, S. G. Petoussis, and K. R. Godfrey, "Parameterization of linear supply functions in nonlinear AC electricity market equilibrium models-Part II: case studies," *IEEE Transactions on Power Systems*, vol. 28, no. 2, pp. 659–668, 2013.

[20] M. P. Cruz, E. C. Finardi, V. L. de Matos, and J. P. Luna, "Strategic bidding for price-maker producers in predominantly hydroelectric systems," *Electric Power Systems Research*, vol. 140, pp. 435–444, 2016.

[21] M. Shivaie and M. T. Ameli, "An environmental/techno-economic approach for bidding strategy in security-constrained electricity markets by a bi-level harmony search algorithm," *Renewable Energy*, vol. 83, pp. 881–896, 2015.

[22] B. F. Hobbs, C. B. Metzler, and J.-S. Pang, "Strategic gaming analysis for electric power systems: an MPEC approach," *IEEE Transactions on Power Systems*, vol. 15, no. 2, pp. 638–645, 2000.

[23] X. An, S. Zhang, X. Li, and D. Du, "Two-stage joint equilibrium model of electricity market with tradable green certificates," *Transactions of the Institute of Measurement and Control*, vol. 41, no. 6, pp. 1615–1626, 2019.

[24] Q. M. Bui and H. C. Elman, "Semi-smooth Newton methods for nonlinear complementarity formulation of compositional two-phase flow in porous media," *Journal of Computational Physics*, vol. 407109163 pages, 2020.

[25] G. Wang, J. Yu, and S. Li, "An MPCC formulation and its smooth solution algorithm for continuous network design problem," *Promet - Traffic & Transportation*, vol. 29, no. 6, pp. 569–580, 2017.

[26] Y.-p. Zhang, T. Xiao-jiao, and F. Wu, "Study on semi-smooth Newton optimal power flow algorithm based on nonlinear complementarity problem function," *Proceedings of the Chinese Society for Electrical Engineering*, vol. 24, no. 9, pp. 130–135, 2004.

[27] M. de Lujan Latorre and S. Granville, "The stackelberg equilibrium applied to AC power systems - a non-interior point algorithm," *IEEE Transactions on Power Systems*, vol. 18, no. 2, pp. 611–618, 2003.

[28] A. Natalya and K. Marina, "Microeconomic models of strategic interactions and their applications to wholesale electricity market (Bi-level Programming, Optimization Methods, and Applications to Economics)," *International Journal of Biomedical Soft Computing and Human Sciences: The Official Journal of the Biomedical Fuzzy Systems Association*, vol. 18, no. 1, pp. 9–14, 2017.

[29] M. Homayoun-Far, A. Ganji, D. Khalili, and J. Harris, "Two solution methods for dynamic game in reservoir operation," *Advances in Water Resources*, vol. 33, no. 7, pp. 752–761, 2010.

[30] I. A. Nechaev and S. I. Palamarchuk, "Generation scheduling based on two-level optimization problem," *International Journal of Energy Optimization and Engineering*, vol. 3, no. 1, pp. 1–11, 2014.

[31] H. Song, C. Yue, S. Han, and J. Li, "Coalitional game modeling and simulation of power producer's strategy behavior in electricity markets," *International Journal of Digital Content Technology and its Applications*, vol. 16, pp. 256–264, 2012.

[32] R. Kelman, L. A. N. Barroso, and M. V. F. Pereira, "Market power assessment and mitigation in hydrothermal systems," *IEEE Transactions on Power Systems*, vol. 16, no. 3, pp. 354–359, 2001.

[33] T. J. Scott and E. G. Read, "Modelling hydro reservoir operation in a deregulated electricity market," *International Transactions in Operational Research*, vol. 3, no. 3–4, pp. 243–253, 1996.

[34] B. C. Flach, L. A. Barroso, and M. V. F. Pereira, "Long-term optimal allocation of hydro generation for a price-maker company in a competitive market: latest developments and a stochastic dual dynamic programming approach," *IET Generation, Transmission & Distribution*, vol. 4, no. 2, pp. 299–314, 2010.

[35] S. Wu, *Research on Bidding Strategies for Competitive Hydropower Generators Based on Game Theory*, Sichuan University, Sichuan, China, 2006.

[36] X.-dong Zhang and Bo Gao, "Simulation of areal spot market based on supply function equilibrium model," *Power System Technology*, vol. 29, pp. 80–84, 2005.

[37] T. De Luca, F. Facchinei, and C. Kanzow, "A theoretical and NumericalComparison of some semismooth algorithms for complementarity problems," *Computational Optimization and Applications*, vol. 16, no. 2, pp. 173–205, 2000.

[38] L. Song and Y. Gao, "A smoothing Levenberg-Marquardt method for nonlinear complementarity problems," *Numerical Algorithms*, vol. 79, no. 4, pp. 1305–1321, 2018.

[39] X. Zhu and G.-H. Lin, "Improved convergence results for a modified Levenberg-Marquardt method for nonlinear equations and applications in MPCC," *Optimization Methods and Software*, vol. 31, no. 4, pp. 791–804, 2016.

[40] J. Yi, J. W. Labadie, and S. Stitt, "Dynamic optimal unit commitment and loading in hydropower systems," *Journal of Water Resources Planning and Management*, vol. 129, no. 5, pp. 388–398, 2003.

[41] S. Chen, S. Yan, W. Huang, Y. Hu, and G. Ma, "A method for optimal floodgate operation in cascade reservoirs," *Proceedings of the Institution of Civil Engineers - Water Management*, vol. 170, no. 2, pp. 81–92, 2017.

[42] M.i Xie, J. Zhou, C. Li, and S. Zhu, "Long-term generation scheduling of Xiluodu and Xiangjiaba cascade hydro plants considering monthly streamflow forecasting error," *Energy Conversion and Management*, vol. 105, pp. 368–376, 2015.

[43] Ali Thaeer Hammid and I. Omar, "Awad and Mohd Herwan Sulaiman etc., a Review of Optimization Algorithms in Solving Hydro Generation Scheduling Problems," *Energies*, vol. 13, no. 11, 2020.

Hindawi
Mathematical Problems in Engineering
Volume 2022, Article ID 1643807, 11 pages
https://doi.org/10.1155/2022/1643807

Research Article

Predicting Spare Parts Inventory of Hydropower Stations and Substations Based on Combined Model

Zhenguo Ma,[1] Bing Tang,[1] Keqi Zhang,[1] Yuming Huang,[1] Danyi Cao,[1] Jiaohong Luo,[1] and Jianyong Zhang[2]

[1]*Changzhou Power Supply Branch, State Grid Jiangsu Electric Power Co., Ltd., Nanjing, Jiangsu 213022, China*
[2]*College of Science, Hohai University, Changzhou, Jiangsu 213022, China*

Correspondence should be addressed to Jianyong Zhang; hohaizhangjy@hhu.edu.cn

Received 23 December 2021; Accepted 4 March 2022; Published 7 April 2022

Academic Editor: Jinyan Song

In this paper, a combined model is proposed to predict spare parts inventory in accordance with equipment characteristics and defect elimination records. Fourier series is employed to process the periodicity of the data, autoregressive moving average (ARMA) is used to deal with the linear autocorrelation of the data, and backpropagation (BP) neural network is used to settle the nonlinearity of the data. The prediction results, comparisons, and error analyses show that the combined model is accurate and meets the practical requirements. The combined model not only fully utilizes the information contained in the data but also provides a reasonable decision basis for the procurement of spare parts, making the inventory in a safe state and saving holding costs.

1. Introduction

As an important part of the power grid, the stable operation of hydroelectric power stations and substations is of great significance to the safety of the power grid [1, 2]. To ensure the stable operation of the system, the inventory of equipment spare parts needs to be in a safety status. When the quantity of inventory is insufficient, it cannot guarantee the system's demand for spare parts and the timely elimination of defects, and when the quantity of inventory is too much, it will occupy too much storage space and capital.

Effective inventory forecasting not only ensures stable system operation but also reduces inventory costs and improves capital utilization of enterprises. There are a large number of research results on inventory forecasting, the forecasting objects are distributed in different industries such as supply chain, supply side, and demand side, and the forecasting methods are often focused on single-quantity model or improved single-quantity model [3].

There have been many research results for forecasting the spare parts demand for hydropower stations and substations. In these studies, scholars have gradually shifted from research on the management and optimization of inventories to that on inventory forecasting. Inventory management is receiving more and more attention as a condition for sustainable production. From the point of view of analytical techniques, researches on inventory management are focused on descriptive analytics, as well as on predictive and prescriptive analytics [4]. These applications and studies could be developed as an optimal resource allocation method that helps the inventory managers and engineers to optimize their inventory policy. For some power equipment, the long service life often leads to an excessive intermittent demand for spare parts, which is a challenge for inventory control, and to solve this problem, a regular review inventory control system is theoretically considered to be an optimal approach [5]. In [4, 5], the authors did not make full use of the information contained in the data. With the improvement of data mining techniques, many studies started to use machine learning [6], deep learning [7], and classification methods [4, 8] to make simple predictions about the inventory, and these predictions bring benefits to the actual inventory management such as improving the reliability of the system, decreasing

the failure rate of the equipment, and reducing the cost of operation and maintenance.

The application of artificial intelligence technology in spare parts inventory forecasting technology has significantly improved the accuracy of forecasting results. Ding [9] proposed an algorithmic model based on the modified BP neural network for grid material demand forecasting. The author simply improved the BP model to improve convergence. Similar studies based on artificial intelligence methods are machine learning [6, 10], deep learning [7], and so forth.

Qualitative forecasting models such as the expert meeting method [11] and the Delphi method [12] rely too much on experience and expert scoring, for short-term predictions of large data volumes are not valid, so their applicability and reliability are relatively poor. Quantitative models focus on mathematical models that use historical data or factor variables to forecast demand and apply certain mathematical methods to reveal the regular links between relevant variables, which have a high degree of objectivity. The conventional quantitative forecasting models are the autoregressive moving average (ARMA) model [13, 14], regression analysis [15, 16], and gray forecasting model [17].

Although fruitful results have been achieved based on these quantitative models, we have to consider the following three aspects. The first one is prediction accuracy. Any forecasting models have their limitations, which originate from the model itself or the data. For example, the ARMA model is suitable for time series with linear relationships and does not predict well for data with nonlinear relationships. While data often have multiple characteristics such as linear relationships, nonlinear relationships, and periodic characteristics at the same time, and if a single forecasting model is adopted, it will inevitably reduce the forecasting accuracy. An effective way to solve this kind of problem is to combine multiple models. Study [18] showed that when combining two single forecasting methods, its error was reduced by 7.2%, and when the combination of methods was increased to five, its error was reduced by 16.3%. Using an appropriate combination of forecasting models can overcome the limitations of a single model and improve the accuracy and diversify the forecasting risk as much as possible [19–21]. Researchers [19] used the recursive least square method combined with the 2RC model to obtain the best prediction of the state of charge of lithium batteries. However, in literature [20, 21], researchers considered fewer influencing factors. When the influencing factors are added, it will increase the difficulty of the study. The second one is that any prediction should be considered from a practical point of view. For solving practical problems, it is also necessary to start from the actual problem of the enterprise; for example, in power companies, the prediction value of spare parts must be slightly higher than the real value to prevent the failure of protection devices caused by insufficient spare parts when an unexpected event occurs, resulting in a power failure. The third point is that many factors affect inventory, such as internal and external factors. In this paper, we consider the inventory problem under 10 factors in a comprehensive manner, which is shown in Section 4.1. The proposed combined prediction model based on the above three aspects is the main innovation of this paper.

At present, power enterprises like DH Hydropower Station and JC Power Supply Company stockpile spare parts using the agreed inventory procurement [22]. This form of procurement relies on experience to speculate on the approximate demand rather than some theoretical model, such as the minimum life-cycle cost (LCC) [23] for spare parts for the next year. It has the disadvantage of insufficient spare parts inventory caused by both internal and external factors, which often leads to insufficient spare parts inventory and the need for temporary procurement. There is also overpurchase of certain spare parts, which causes inventory backlog and increases the cost of holding materials, thus taking up a lot of capital and storage space.

Based on the above reasons, this paper proposes a combined model to predict the inventory for the DH Hydropower Station excitation unit and substation relay protection equipment in JC Power Supply Company. To the best of our knowledge, no literature combines Fourier series, ARMA, and BP neural network to study inventory prediction, and there is no literature that uses this kind of mixed model to design a prediction scheme for inventory materials in Hydropower Station and substations. Moreover, the mixed model developed in this paper has a high prediction accuracy compared with the models developed by using the ARMA method alone and combining ARMA and BP neural network, and the model validity is good because the RMSE and MAE of the mixed model given in this paper are smallest. The first part is about the current status of research on the issue. The second part is about the related works, including the principle of Fourier series form of sequence, ARMA model, and BP neural network. In the third section, we put forward a combined model based on the Fourier series, ARMA, and BP neural network for inventory. The fourth part is the simulation of the real case and comparisons, and the last section is about the conclusions and a brief perspective of the future work.

2. Related Works

2.1. Fourier Series of Time Series. When analyzing defect elimination records, we find that the spare parts have a certain periodicity in usage; for example, during the rainy season, the usage of certain spare parts is higher than usual. To make the prediction more accurate, the periodic characteristics of the data need to be extracted using the Fourier series [24].

Let the sequence $x_1, x_2, \ldots, x_n$, which can be considered as a point in an n-dimensional space coordinate system, form a set of bases for any n-dimensional orthogonal vectors for a given n-dimensional space. Thus, the sequence $\{x_t, \quad t = 1, 2, \ldots, n\}$ can be represented by a linear combination of orthogonal trigonometric functions as

$$y(t) = \sum_{k=0}^{[m/2]} \left(a_k \cos \frac{2k\pi t}{m} + a_k \sin \frac{2k\pi t}{m} \right) + \varepsilon_t. \tag{1}$$

Equation (1) means that the Fourier series form of the sequence $\{x_t\}$ is $\{y_t\}$. The coefficients a_k, b_k can be calculated by the following equation:

$$a_k = \begin{cases} \dfrac{1}{m}\sum_{i=1}^{m} x_i \cos\dfrac{2k\pi t}{m}, & k = 0 \text{ or } k = \dfrac{m}{2}, \text{m is even number}, \\ \dfrac{2}{m}\sum_{i=1}^{m} x_i \cos\dfrac{2k\pi t}{m}, & k = 1, 2, \ldots, \dfrac{m-1}{2}, \end{cases}$$

$$b_k = \frac{2}{m}\sum_{i=1}^{m} x_i \sin\frac{2k\pi t}{m}, k = 0, 1, 2, \ldots, \frac{m-1}{2}, \tag{2}$$

where $\varepsilon_t = y_t - x_t \sim N(0, \sigma_\varepsilon^2)$. y_t is data with certain seasonal periodicity characteristics, and the periodicity can be adjusted by adjusting the value of parameter m.

2.2. ARMA Model. ARMA model is a relatively mature forecasting model for studying linear time series, which requires time series data to be stationary to build the model, and has certain requirements on the magnitude of the data. Its model expression is

$$\begin{cases} y_t = \phi_1 y_{t-1} + \cdots \phi_p y_{t-p} + u_t + \theta_1 u_{t-1} + \cdots + \theta_q u_{t-q}, \\ \phi_p \neq 0, \theta_q \neq 0, \\ E(u_t) = 0, \mathrm{Var}(u_t) = \sigma_u^2, E(u_t u_s) = 0, s \neq t, \\ E(y_s u_t) = 0, \forall s < t, \end{cases} \tag{3}$$

where y_t is the time series, p is the autoregressive order, q is the moving average order, and $\phi_i (i = 1, \ldots p)$, $\theta_j (j = 1, \ldots q)$ is the coefficient to be determined. u_t is the error.

The stationarity of the data is an important prerequisite for ARMA, and it can be verified by the Augmented Dickey-Fuller (ADF) test [25]. If the data are not stationary, stationary processing can be performed by using the n th-order difference method with the following equation:

$$\begin{aligned} \Delta^n y_t &= \sum_{i=0}^{n} (-1)^{n-i} C_n^i y_{t+i} \\ &= \sum_{i=0}^{n} (-1)^{n-i} C_n^i y_{t+n-i}. \end{aligned} \tag{4}$$

To obtain the best prediction model, the Akaike information criterion (AIC) [26–28] can be used to determine the parameters p and q of the model. Different AIC values can be obtained when fitting the data by selecting different p and q.

$$\mathrm{AIC} = -2 \ln \widehat{\sigma}_t^2(p, q) + \frac{2(p+q)}{N}, \tag{5}$$

where $\widehat{\sigma}_t^2(p, q)$ is the variance of residuals and ARMA (p, q) is considered the best prediction model when AIC has the smallest value.

2.3. BP Neural Network Model. The learning process of the BP neural network consists of two processes: forward propagation of signal and backward propagation of error. By continuously adjusting the value of network weights, the final output of the network is made as close as possible to the desired output for training purposes. Therefore, it can capture the nonlinear features and trends in it well when dealing with time series and thus is widely used for time series prediction. It is composed of an input layer, an output layer, and one or more hidden layers, each of which consists of several neurons, and the individual neurons of adjacent layers are fully connected. Figure 1 shows a typical multilayer neural network.

The input vector is $\boldsymbol{y} = (y_1, y_2, \ldots, y_m)$, the output vector is $\mathbf{Y} = (Y_1, Y_2, \ldots, Y_n)$, and the input of each neuron in the l th hidden layer is $\mathrm{h}^{(l)} = (h_1^{(l)}, h_2^{(l)}, \ldots, h_t^{(l)})$, where t is the number of neurons in the l th layer. Let $w_{ij}^{(l)}$ be the connection weight between the neuron from the j th neuron in the $(l-1)$ th layer and the i th neuron in the l th layer and $b_i^{(l)}$ be the bias of the i th neuron in the l th layer. Then,

$$\mathrm{net}_i^{(l)} = \sum_{j=1}^{t-1} w_{ij}^{(l)} h_j^{(l-1)} + b_i^{(l)}, \tag{6}$$

where $h_i^{(l)} = f(\mathrm{net}_i^{(l)})$, where $\mathrm{net}_i^{(l)}$ is the output of the i th neuron in l th layer and $f(\cdot)$ is the neuronal activation function. Usually a nonlinear activation function is used in multilayer neural networks.

To ensure the prediction accuracy of the BP neural network, the loss function is defined as follows:

$$lf(k) = \sqrt{\frac{1}{n}\sum_{i=1}^{n} \left[x_a(i) - x_{pk}(i)\right]^2}, \tag{7}$$

where x_{pk} denotes the predicted value of the BP model after the k th round of training. The function $lf(k)$ means the root mean square error of the true value x_a and x_{pk}. A smaller

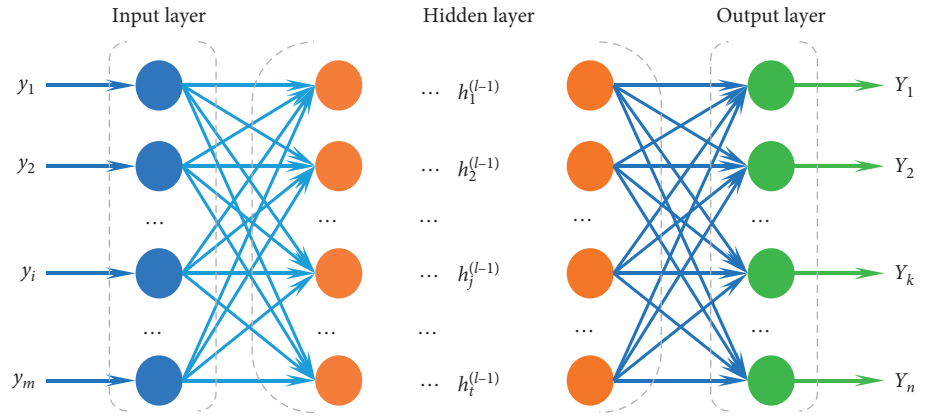

Figure 1: Multilayer BP neural network diagram.

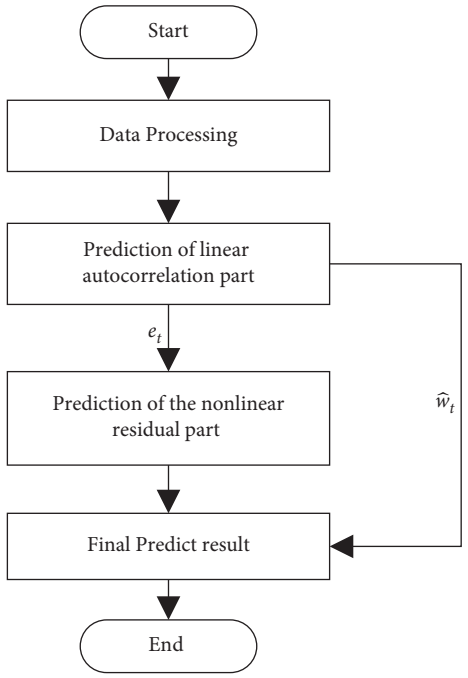

Figure 2: The flowchart of the combined model.

$lf(k)$ indicates adequate training and more accurate prediction.

3. Combined Model

For the time series $\{x_t\}$, in this paper, it not only reflects periodicity but also reflects certain linear autocorrelation and nonlinear nature of the residuals. To make the prediction accurate, in this section, we construct a combined model to forecast the data. The idea of the model is shown in Figure 2.

3.1. Data Processing. For a given time series data $\{x_t\}$, firstly, it can be transformed into a time series $\{w_t\}$ with periodic properties by using the Fourier series of the time series in equation (1) and then verify the smoothness of the data to predict the autocorrelation part of the series. The data processing in this study is shown in Algorithm 1.

3.2. Prediction of Linear Autocorrelation. For the smooth time series $\{w_t\}$ with periodic characteristics, the ARMA model is used to get $\{\widehat{w}_t\}$, and $\{\widehat{w}_t\}$ is the predicted result of the linear autocorrelation of the time series. The residual $\{e_t\}$ is also calculated, which is the input of the prediction of the nonlinear residual. The linear autocorrelation prediction process is shown in Algorithm 2.

3.3. Prediction of Nonlinear Autocorrelation. In this section, we are going to construct BP neural network model to forecast the residuals, and the main steps are shown in Algorithm 3.

3.4. Combined Model. Taking together Algorithms 1–3, we can generate a combined model to computer the predicted results $\{\widehat{X}_t\}$ for the time series $\{x_t\}$. The details are listed in Algorithm 4.

Note: [1]the case of first-order difference.

4. Experiment, Results, and Comparisons

4.1. Experimental Data. The spare parts in this paper are the liquid crystal display (LCD), the central processing unit (CPU), and DC220V Power Supply (DCPS), which are installed in the excitation system of hydroelectric generating units and substation relay protection equipment. They have the following features:

A wide variety and distribution and high value and integration

It is difficult to obtain monitoring data, and the operation and maintenance (O&M) process requires a lot of manpower. It has a long procurement cycle

Service life is influenced by environmental factors and human factors

The data from the defect elimination records stored in DH Hydropower Station and JC Power Supply Company contain 10 field variables: Component Name, Installation Date, Manufacturer, Damage Date, Design Life, Temperature, Humidity, Installation Location, Interval, and O&M (Operation and Maintenance) Shift, where Design Life is a

Input: $\{x_t\}$
Step1. Get $\{y_t\}$ from $\{x_t\}$ by equation (1)
Step2. ADF test
  if $\{y_t\}$ is stationary, then
    $w_t \leftarrow y_t$
  else
    $w_t \leftarrow y_t - y_{t-1}$
  end
Output: $\{w_t\}$

Algorithm 1: Data processing.

Input: $\{w_t\}$
Step1. Calculate p and q for ARMA (p, q)
  for $p = 0$ to M % M is a positive integer
    for $q = 0$ to K % K is a positive integer
      $\mathrm{AIC}(p, q) = -2ln\widehat{\sigma}_t^2(p, q) + 2(p, q)/N$
    end
  end
  if AIC is minimum
  output p, q
Step2. Forecast the time series $\{w_t\}$ using ARMA (p, q).
Step3. Get $\{\widehat{w}_t\}$ % prediction values
Step4. $e_t = w_t - \widehat{w}_t$ % residuals
Output: $\{\widehat{w}_t\}$ and $\{e_t\}$

Algorithm 2: Prediction of a linear autocorrelation.

Input: $\{e_t\}$
Step1. Configure BP neural network
Step2. Construct the training set $\{(i, e_i), \quad i = 1, 2, \ldots, n\}$
Step3. Train BP model
  While $|lf(k+1) - lf(k)| > \epsilon$ or $lf(\cdot) > \alpha$
    Train BP model
    Determine the BP model
Step4. Get predicted values of the residuals $\{\widehat{e}_t\}$
Output: $\{\widehat{e}_t\}$

Algorithm 3: Prediction of the nonlinear residual.

Input: $\{x_t\}$
Step1. Get $\{w_t\}$ by Algorithm 1
Step2. Obtain $\{\widehat{w}_t\}$ and $\{e_t\}$ via Algorithm 2
Step3. Calculate $\{\widehat{e}_t\}$ by Algorithm 3
Step4. Compute $\{\widehat{X}_t\}$:
  if $\{x_t\}$ is smoothing, then
    $\widehat{X}_t = \widehat{e}_t + \widehat{w}_t$
  else
    $\widehat{X}_t = \widehat{e}_t + \widehat{w}_t + \widehat{x}_{t-1}{}^1$
  End
Output: $\{\widehat{X}_t\}$

Algorithm 4: Combined model.

Table 1: Parameters of the ARMA model.

Equipment	AIC	p	q
LCD	322.213	1	1
CPU	370.750	2	1
DCPS	403.561	1	0

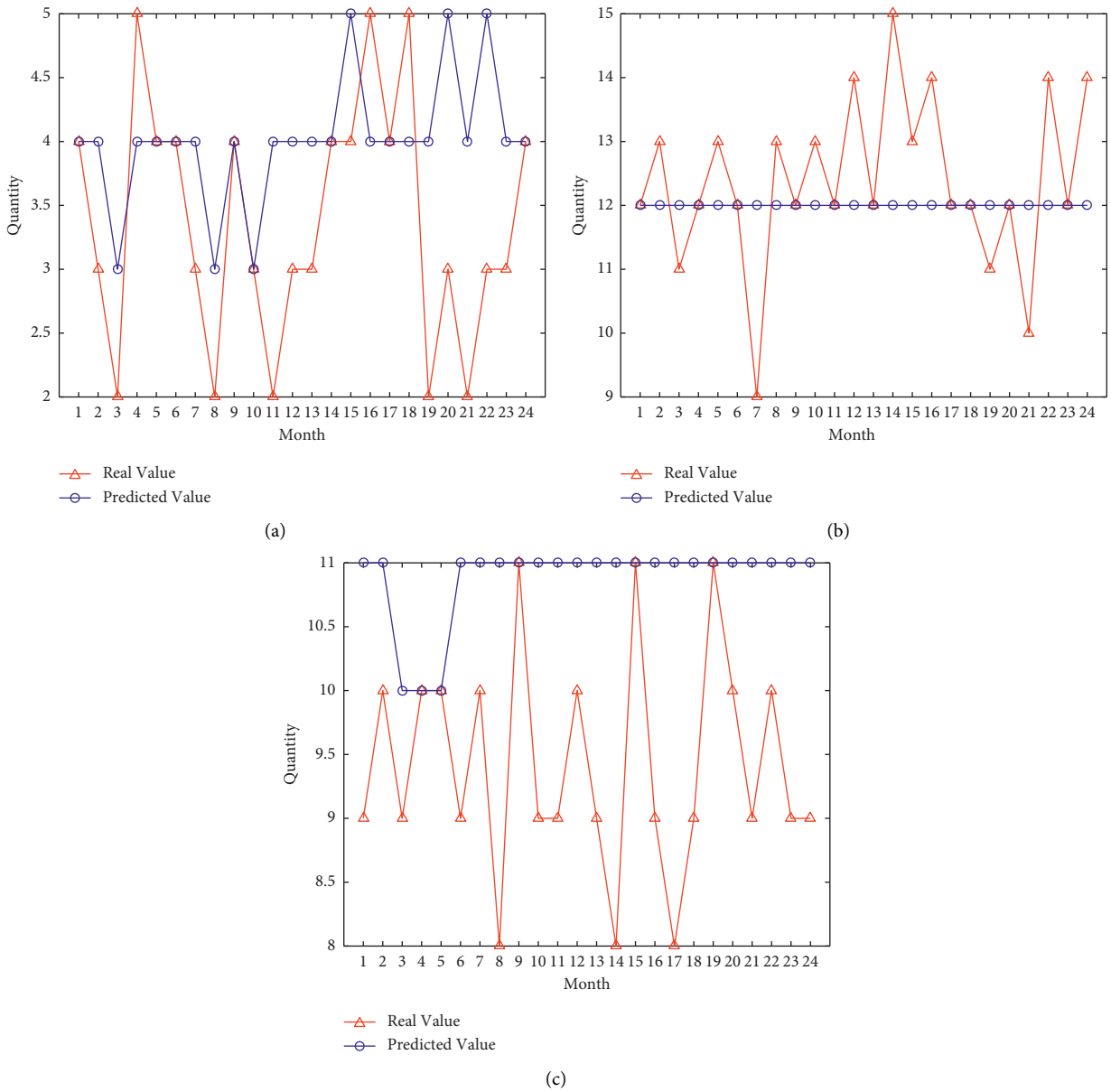

Figure 3: Prediction values based on the ARMA model. (a) Prediction values for LCD based on ARMA (1, 1). (b) Prediction values for CPU based on ARMA (2, 1). (c) Prediction values for DCPS based on ARMA (1, 0).

numeric variable, Installation Date and Damage Date are temporal variables, and the others are textual variables.

The overall trend in the annual usage of a certain relay protection equipment is smooth, and we can consider the data as a time series. Each year, in the case of high temperature and high humidity or low temperature and high humidity, the use of spare parts will increase; that is, the data will reflect a certain periodicity. At the same time, the service life of the equipment, that is, Damage Date minus Installation Date, will be affected by the working conditions. Therefore, the data will reflect a certain nonlinear characteristic.

4.2. Inventory Prediction Based on ARMA Only. In this section, only the ARMA model is used to forecast three kinds of components. We can find that all data are stationary after

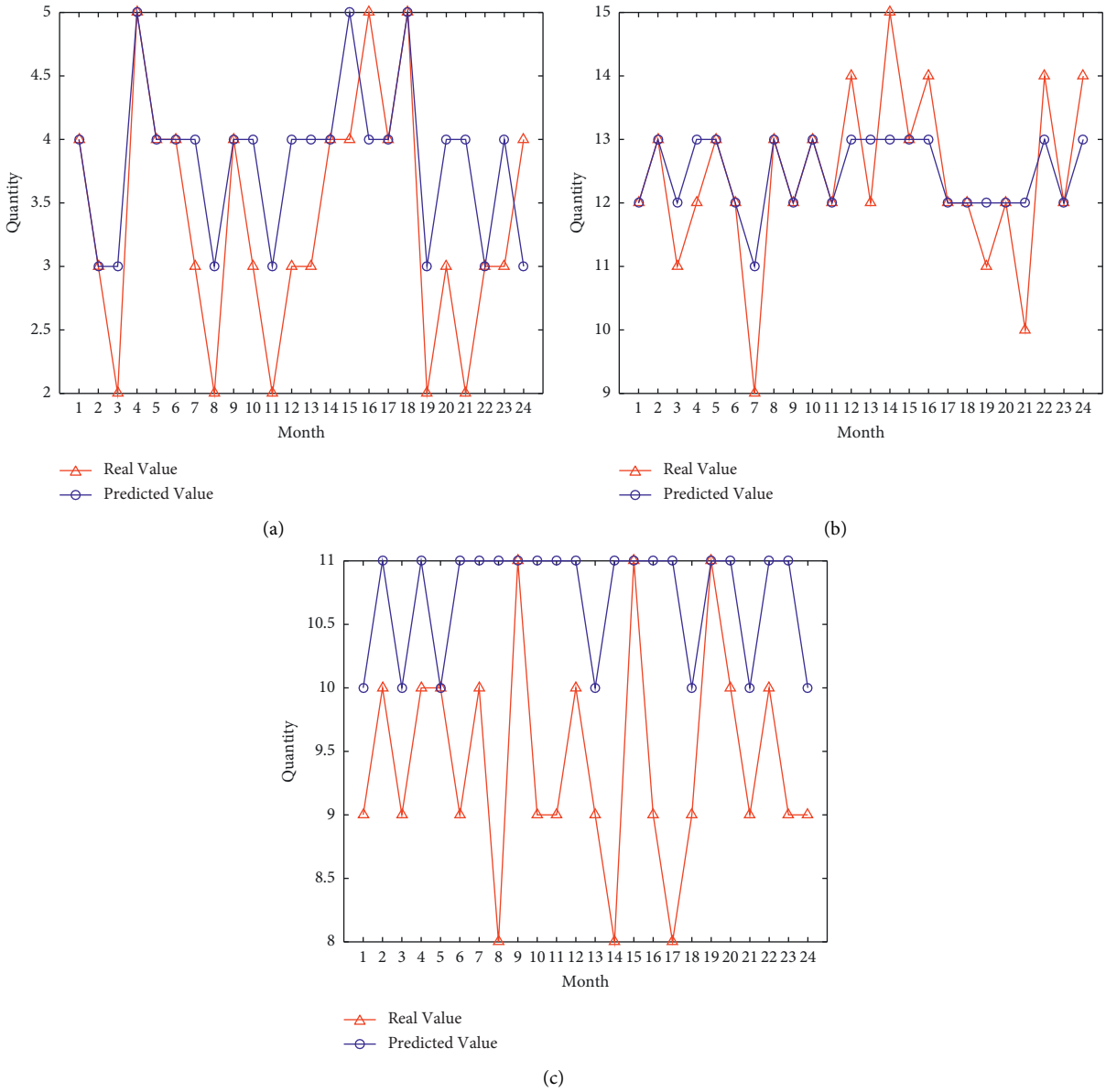

Figure 4: Prediction values based on the ARMA model and BP neural network. (a) Prediction values for LCD based on the ARMA (1, 1) +BP. (b) Prediction values for CPU based on the ARMA (2, 1) +BP. (c) Prediction values for DCPS based on the ARMA (1, 0) +BP.

testing by the ADF method. The parameters p and q are determined according to AIC in (5), the details are listed in Table 1, and the forecast results are shown in Figure 3.

From Figure 3, we can conclude that the predicted values match too poorly with the true values. This indicates that the data have a weak linear autocorrelation, especially for the data of CPU and DCPS. But the ARMA model can only deal with data with linear relationships by nature; therefore, it can be concluded that the prediction based on this model only is invalid.

4.3. Inventory Prediction Based on ARMA and BP. To deal with the nonlinear relationships in the data, a BP neural network model is added to the ARMA model. The settings of the parameters in the ARMA model are shown in Table 1.

In the BP neural network, the input and output layers have one node each, and three hidden layers include a fully connected layer containing 10 nodes, a discarded layer with a discard rate of 20%, and a fully connected layer with 15 nodes, respectively. Training termination conditions $\varepsilon = 0.001$, $\alpha = 0.05$. To avoid the gradient explosion and gradient disappearance problems in BP neural networks, simplify the computation process and improve the computation speed, and the activation function that we adopt in this paper is the Rectified Linear Unit (ReLU) [29, 30]:

$$f(x) = \max\{0, x\}. \tag{8}$$

The predicted values for LCD, CPU, and DCPS based on the ARMA model and the BP neural network are shown in Figure 4.

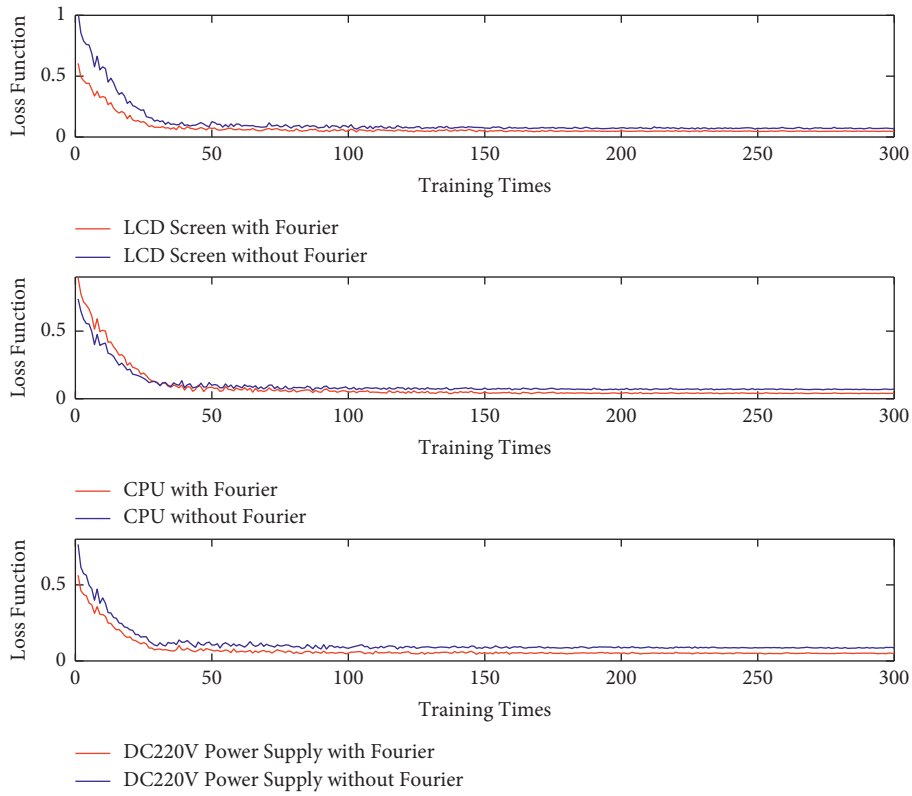

Figure 5: The relationship between loss function and training times.

Table 2: Parameters of the ARMA model.

Equipment	AIC	p	q
LCD	327.925	1	4
CPU	395.599	1	3
DCPS	400.587	2	1

Comparing Figures 3 and 4, we can see that the degree of agreement of the predicted values based on the ARMA model and BP neural network is higher than the ARMA model's, which indicates that there is indeed a nonlinear relationship in the data.

At the same time, it can be seen from Figure 4 that the results are not bad for LCD, but for CPU, there are more cases where the predicted values are lower than the true values, and for DCPS, throughout the forecast curve, there are several cases where peaks and valleys occur at the same time point, resulting to a large difference in predictions, which is due to the fact that the ARMA and BP neural network model have not fully explored the information of the data.

4.4. Inventory Prediction Based on the Combined Model. According to the experience of operation and maintenance, in periods of high temperature and humidity, or low temperature and humidity, the demand for spare parts is higher, and the data reflect a certain periodicity. Figure 5 is the description of the loss function of the BP neural network versus the training time. The smaller the loss function values are, the more accurate the neural network model is and the better the prediction result is. In Figure 5, we conclude that the data after the Fourier series extraction of features will make the BP neural network have smaller loss function values.

In this section, we are going to implement a combined model to forecast the number of spare parts. We set $n = 48$ for the Fourier series in Algorithm 1. In Algorithm 2, we recalculate the AIC of ARMA, the values of p and q are obtained and shown in Table 2, and in Algorithm 3, we adopt the same BP neural network used in Section 4.3. The prediction results are shown in Figure 6.

As can be seen from Figure 6, the predicted and true values of the three devices are in good agreement with the trend of change. Moreover, the predicted values are all slightly greater than or equal to the true values. Such prediction results are in line with the safety requirements of hydropower stations and substations for spare parts, and this prediction model is more advantageous for the stability of the system. Comparing Figures 3–6, we can draw a conclusion that the periodical and nonlinear features in the data play a major role.

Through the comparison of predicted results, the combined model we constructed in Section 3 is the best one for this type of predicting problem.

4.5. Error Analyses. To further illustrate the validity of the combined model, we conduct error analysis for the three prediction models in this paper. The corresponding root means square error (RMSE) and means absolute error (MAE) under the three methods are discussed, which are calculated as follows:

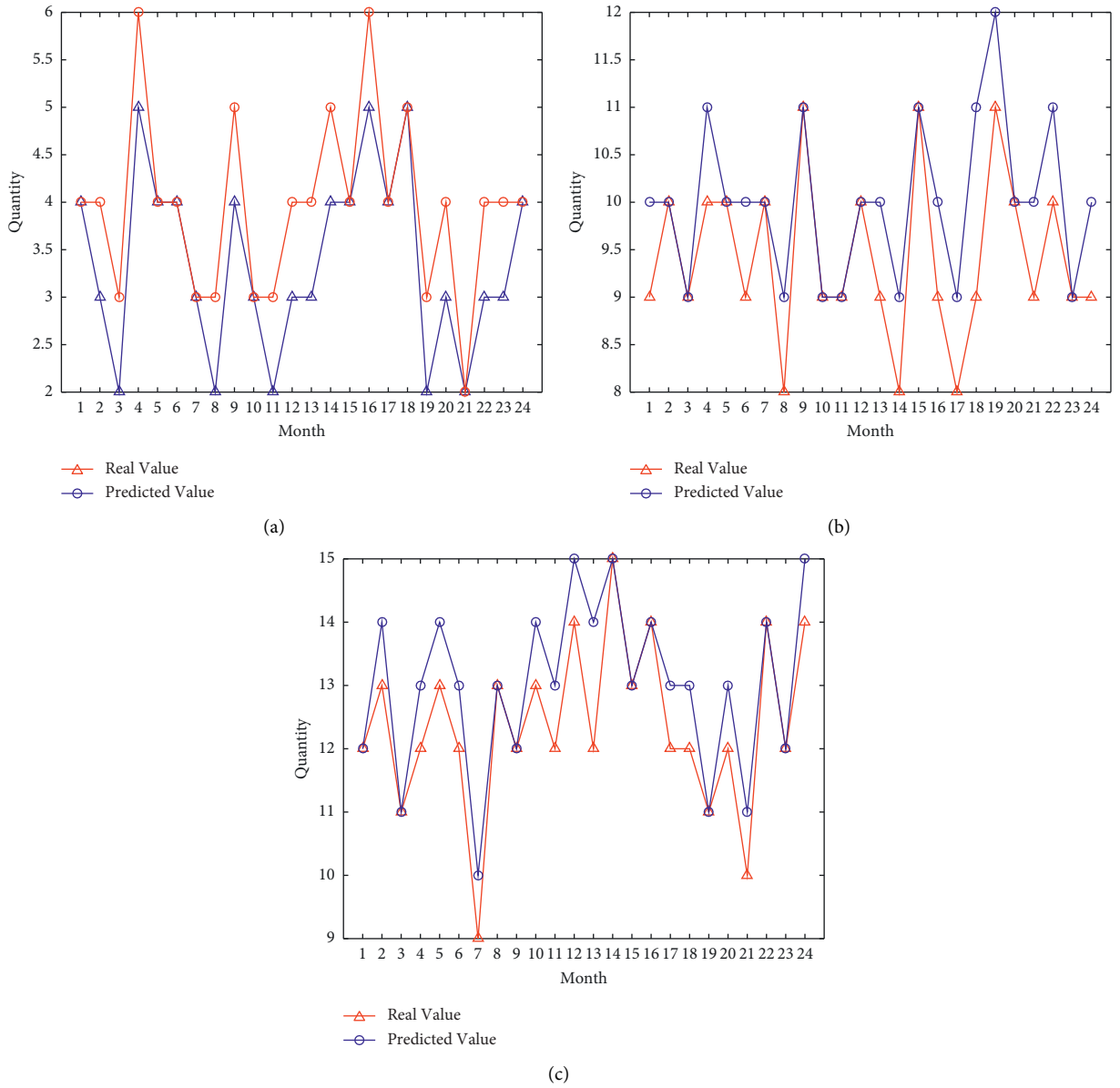

Figure 6: Predicted values based on the combined model for: (a) LCD, ARMA (1, 4); (b) CPU, ARMA (1, 3); (c) DCPS, ARMA (2, 1).

Table 3: RMSE and MAE of three prediction methods.

Equipment	RMSE			MAE		
	ARMA	ARMA + BP	Combined model	ARMA	ARMA + BP	Combined model
LCD	1.1365	0.8416	0.6770	0.8751	0.6251	0.4583
CPU	1.3693	0.9128	0.7905	0.9583	0.5833	0.5416
DCPS	1.7440	1.5679	1.1902	1.4583	1.2916	0.9167

$$\text{RMSE} = \sqrt{\frac{1}{n}\sum_{i=1}^{n}\left[x_a(i) - x_p(i)\right]^2}, \quad \text{MAE} = \frac{1}{n}\sum_{i=1}^{n}\left|x_a(i) - x_p(i)\right|, \tag{9}$$

where x_p and x_a denote the predicted and true values, respectively. If the RMSE and MAE of a certain algorithm are smaller, it means that the algorithm is more effective. The RMSEs and MAEs of the three prediction models are shown in Table 3.

From Table 3, it is known that the RMSE and MAE based on the combined model are both minimal, which further illustrates the effectiveness of the combined model.

5. Conclusions and Prospect

According to the prediction results and their comparison, the data of defect elimination records have certain periodic characteristics, linear autocorrelation, and nonlinear relationship, so extraction of the periodic characteristics via the Fourier series is a key step. The ARMA model does its work in processing the linear autocorrelation, and this is the main part of the forecasting results. The BP neural network model fully exploits the nonlinear relationship of the data, and its purpose is to improve the prediction accuracy. Three different methods take full advantage of their respective strengths and make the combined model perform well.

The combined model was used in inventory forecasting for three different devices at the same time, and all of them demonstrated good forecasting results, which indicate that this model has some strong portability and stability. The analysis of the forecasting results also shows that the model has some advantages over the single model or two models in forecasting.

The combined model used in this paper embodies three practical applications: the first is the accurate calculation, high portability, and stability; the second is to improve inventory management capability and save inventory cost and storage space; the third is the ideas in this paper that can be generalized to another field, such as the primary equipment of power system.

For electric power enterprises, the problem of predicting inventory of equipment without monitoring devices has a high practical value, and subsequent research efforts can add more influencing factors, such as product batches, idle time, and extreme weather conditions, but data on these influencing factors are currently unavailable. Under the many factors, we can reconstruct the prediction model and choose the remaining useful life (RUL) [31, 32] of the equipment as the main influence variable while considering the life-cycle costing (LCC) [23, 33] of the equipment to achieve a more accurate prediction of the equipment inventory, which is more conducive to the operation and maintenance of relay protection equipment, as well as reducing inventory expenditures.

Data Availability

All data included in this study are available upon request with the corresponding author.

Conflicts of Interest

The authors declare no conflicts of interest.

Acknowledgments

The authors are very grateful to Professor Binwu Zhang from the Institute of Intelligent Optimization and Control of Hohai University for their enthusiastic guidance and constructive suggestions. This work was supported by the Science and Technology Project of State Grid Corporation Limited (SGJSCZ00KJJS2100747) and in part by the National Nature Science Foundation of China (NSFC) under Grant no. 52077058.

References

[1] L. Zhu, D. J. Hill, and C. Lu, "Intelligent short-term voltage stability assessment via spatial attention rectified RNN learning," *IEEE Transactions on Industrial Informatics*, vol. 17, no. 10, pp. 7005–7016, 2021.

[2] H. Y. Su and H. H. Hong, "An intelligent data-driven learning approach to enhance online probabilistic voltage stability margin prediction," *IEEE Transactions on Power Systems*, vol. 36, no. 4, pp. 3790–3793, 2021.

[3] N. Kourentzes, J. R. Trapero, and D. K. Barrow, "Optimising forecasting models for inventory planning," *International Journal of Production Economics*, vol. 225, Article ID 107597, 2020.

[4] S. Zhang, K. Huang, and Y. Yuan, "Spare parts inventory management: a literature review," *Sustainability*, vol. 13, no. 5, p. 2460, 2021.

[5] M. Guajardo, M. Rönnqvist, A. M. Halvorsen, and S. I. Kallevik, "Inventory management of spare parts in an energy company," *Journal of the Operational Research Society*, vol. 66, no. 2, pp. 331–341, 2015.

[6] A. Kantasa-Ard, M. Nouiri, A. Bekrar, A. Ait el Cadi, and Y. Sallez, "Machine learning for demand forecasting in the physical internet: a case study of agricultural products in Thailand," *International Journal of Production Research*, vol. 59, no. 24, pp. 7491–7515, 2021.

[7] S. Punia, K. Nikolopoulos, S. P. Singh, J. K. Madaan, and K. Litsiou, "Deep learning with long short-term memory networks and random forests for demand forecasting in multi-channel retail," *International Journal of Production Research*, vol. 58, no. 16, pp. 4964–4979, 2020.

[8] K. Kovacs, F. Ansari, and W. Sihn, "A modified Weibull model for service life prediction and spare parts forecast in heat treatment industry," *Procedia Manufacturing*, vol. 54, pp. 172–177, 2021.

[9] H. Ding, W. Wang, L. Wan, and J. Luo, "Research on material demand prediction of power network based on BP neural network," *Computer Technology and Development*, vol. 29, pp. 138–142, 2019.

[10] T. Gunda, S. Hackett, L. Kraus et al., "A machine learning evaluation of maintenance records for common failure modes in PV inverters," *IEEE Access*, vol. 8, pp. 211610–211620, 2020.

[11] A. Chaudhuri, H. A. Gerlich, J. Jayaram et al., "Selecting spare parts suitable for additive manufacturing: a design science approach," *Production Planning & Control*, vol. 32, no. 8, pp. 670–687, 2021.

[12] E. E. Ameyaw, Y. Hu, M. Shan, A. P. C. Chan, and Y. Le, "Application of Delphi method in construction engineering and management research: a quantitative perspective," *Journal of Civil Engineering and Management*, vol. 22, no. 8, pp. 991–1000, 2016.

[13] Y. Wang, D. Wang, and Y. Tang, "Clustered hybrid wind power prediction model based on ARMA, PSO-SVM, and clustering methods," *IEEE Access*, vol. 8, pp. 17071–17079, 2020.

[14] F. Granata and F. Di Nunno, "Artificial intelligence models for prediction of the tide level in venice," *Stochastic Environmental Research and Risk Assessment*, pp. 1–12, Springer, New York, NY, USA, 2021.

[15] S. Jomnonkwao, S. Uttra, and V. Ratanavaraha, "Forecasting road traffic deaths in Thailand: applications of time-series, curve estimation, multiple linear regression, and path analysis models," *Sustainability*, vol. 12, no. 1, p. 395, 2020.

[16] W.-J. Niu, Z.-K. Feng, B.-F. Feng, Y.-W. Min, C.-T. Cheng, and J.-Z. Zhou, "Comparison of multiple linear regression, artificial neural network, extreme learning machine, and support vector machine in deriving operation rule of hydropower reservoir," *Water*, vol. 11, no. 1, p. 88, 2019.

[17] S. Ding, K. W. Hipel, and Y.-g. Dang, "Forecasting China's electricity consumption using a new grey prediction model," *Energy*, vol. 149, pp. 314–328, 2018.

[18] S. Makridakis, E. Spiliotis, and V. Assimakopoulos, "The M4 competition: 100,000 time series and 61 forecasting methods," *International Journal of Forecasting*, vol. 36, no. 1, pp. 54–74, 2020.

[19] K. Wang, C. Liu, J. Sun et al., "State of charge estimation of composite energy storage systems with supercapacitors and lithium batteries," *Complexity*, vol. 2021, Article ID 8816250, 2021.

[20] P. Jiang, Z. Liu, X. Niu, and L. Zhang, "A combined forecasting system based on statistical method, artificial neural networks, and deep learning methods for short-term wind speed forecasting," *Energy*, vol. 217, Article ID 119361, 2021.

[21] J. Wang, Q. Li, and B. Zeng, "Multi-layer cooperative combined forecasting system for short-term wind speed forecasting," *Sustainable Energy Technologies and Assessments*, vol. 43, Article ID 100946, 2021.

[22] Z. Bi and L. Wang, "Prediction method of grid material demand," *North China Electric Power*, vol. 10, pp. 26–30, 2015.

[23] S.-I. Gustafsson, "Optimal use of solar collectors for residential buildings," *International Journal of Energy Research*, vol. 25, no. 11, pp. 993–1004, 2001.

[24] I. A. Iwok and G. M. Udoh, "A comparative study between the ARIMA- Fourier model and the wavelet," *American Journal of Scientific and Industrial Research*, vol. 7, pp. 137–144, 2016.

[25] O. S. Yaya, A. E. Ogbonna, F. Furuoka, and L. A. Gil-Alana, "A new unit root test for unemployment hysteresis based on the autoregressive neural network∗," *Oxford Bulletin of Economics & Statistics*, vol. 83, no. 4, pp. 960–981, 2021.

[26] A. Khalid and A. I. Sarwat, "Unified univariate-neural network models for lithium-ion battery state-of-charge forecasting using minimized akaike information criterion algorithm," *IEEE Access*, vol. 9, pp. 39154–39170, 2021.

[27] M. Ingdal, R. Johnsen, and D. A. Harrington, "The Akaike information criterion in weighted regression of immittance data," *Electrochimica Acta*, vol. 317, pp. 648–653, 2019.

[28] T. DelSole and M. K. Tippett, "Correcting the corrected AIC," *Statistics & Probability Letters*, vol. 173, Article ID 109064, 2021.

[29] B. Liu and Y. Liang, "Optimal function approximation with ReLU neural networks," *Neurocomputing*, vol. 435, pp. 216–227, 2021.

[30] D. R. Harvey, "RELU special issue: editorial reflections," *Journal of Agricultural Economics*, vol. 57, no. 2, pp. 329–336, 2006.

[31] C. Liu, Q. Li, and K. Wang, "State-of-charge estimation and remaining useful life prediction of supercapacitors," *Renewable and Sustainable Energy Reviews*, vol. 150, Article ID 111408, 2021.

[32] C. Liu, Y. Zhang, J. Sun, Z. Cui, and K. Wang, "Stacked bidirectional LSTM RNN to evaluate the remaining useful life of supercapacitor," *International Journal of Energy Research*, vol. 46, no. 3, pp. 3034–3043, 2021.

[33] R. T. Fauzi, P. Lavoie, A. Tanguy, and B. Amor, "Life cycle assessment and life cycle costing of multistorey building: attributional and consequential perspectives," *Building and Environment*, vol. 197, Article ID 107836, 2021.

Hindawi
Mathematical Problems in Engineering
Volume 2022, Article ID 6872799, 12 pages
https://doi.org/10.1155/2022/6872799

Research Article

Research on Combined Frequency Regulation Control Method of Wind Storage with Storage System Optimized Intervals Considered

Yulu Ma[1] **and Peng Yu**[1,2]

[1]*School of Electrical and Electronic Engineering, Shandong University of Technology, Zibo 255000, China*
[2]*State Grid Shandong Electric Power Research Institute, Jinan 250000, China*

Correspondence should be addressed to Yulu Ma; 19504010494@stumail.sdut.edu.cn

Received 28 January 2022; Accepted 22 February 2022; Published 5 April 2022

Academic Editor: Kai Wang

To solve the insufficient frequency regulation capacity and inertia of the power system caused by the increase of grid-connected wind capacity, a combined wind-storage frequency regulation control strategy considering the optimized intervals of the energy storage system is proposed. This article selects the joint frequency regulation of wind turbine overspeed control and energy storage virtual synchronous control, and virtual synchronous control is used as the upper-level control of the entire wind-storage system. In the process of frequency modulation, the output power of wind turbine and energy storage is reasonably distributed through the upper control. On this basis, to ensure the long-term and stable operation of energy storage, the state of charge (SOC) partition principle of energy storage is set up, which is divided into different areas according to the size of the SOC, and the output of the energy storage device is adjusted according to the divided regions. The results of simulation analysis and verification show that the proposed strategy provides additional frequency regulation capacity and inertia during the frequency variation and greatly improves the frequency stability. Besides, the SOC zoning principle ensures the stable operation of the energy storage.

1. Introduction

With the national "30.60" dual carbon goal, clean energy recycled, such as solar, wind, thermal, and kinetic energy, has gradually attracted attention [1]. Therefore, new energy power generation represented by wind power generation has developed rapidly. Wind power generation usually does not have inertial response and frequency regulation capabilities, and it cannot participate in frequency adjustment when the frequency of the power system changes [2]. As the penetration rate of wind power generation in the power system continues to increase, the capacity and output of conventional thermal power units in the power grid are remarkably compressed, reducing the inertia and reserve capacity of the system [3]. It is necessary to extensively increase the frequency regulation resources of the power grid and enhance the safe operation level of the power grid under the increasing penetration rate of renewable energy. According to GB/T19963-2011 "Technical Regulations for Wind Farm Access to Power System," wind farms should follow the DL/T104 criteria and have the ability to participate in power system frequency regulation, peak regulation, and backup [4].

With the rapid development of energy storage, there are many types of energy storage, including battery, supercapacitors, flywheel energy storage, and compressed air energy storage. At present, there are some new energy storage materials [5] and devices, such as integrated energy storage systems based on triboelectric nanogenerator [6–8], magnesium-decorated carbon nitride (g-C3N4) [9], and inorganic dielectric materials [10]. In summary, the current development of energy storage is rapid. The energy storage system has precise, fast, and flexible power response capabilities [11], and it is suitable for joint deployment with wind

farms. On the one hand, energy storage participates in wind power peak adjustment. It can reduce wind curtailment and improve the level of wind power consumption. On the other hand, it enhances the controllability of wind farm output through real-time charge and discharges power control. It can actively contribute to power grid frequency regulation. Also, it provides a solid guarantee for the construction of safe and stable operation of a new power system with energy as the main object [12]. The joint frequency regulation of wind-storage systems requires a fast and real-time response to the power grid frequency anomalies, which poses a challenge to the real-time joint operation control method of wind farms and energy storage systems. Considering the maximum energy capture capabilities of wind turbines, associated power response capabilities, and the safe and effective operation of energy storage systems has been a prevalent concern in problem solving in recent years and is a critical issue that requires an urgent solution.

For the joint frequency regulation control of wind power generation and energy storage, Miao et al. [13] proposed the combined energy storage with the frequency regulation strategy of wind power to cater to the slow response of wind turbine pitch angle according to the fast response of energy storage. However, the combined wind and storage system cannot provide additional inertia but additional power during frequency regulation. Yan et al. [14] proposed a strategy for energy storage compensating system inertia. The energy storage is linked in parallel to the wind farm's outlet to compensate for the wind farm's inertia dynamically. The energy storage can output additional inertia and capacity during frequency regulation. However, it dramatically increases the configuration requirements for energy storage because the wind turbine does not participate in frequency regulation.

There are power and electricity limitations when energy storage participates in frequency regulation. At present, the monitoring of energy storage SOC has been very accurate [15, 16]. Therefore, it is necessary to reasonably allocate the power and set its charging and discharging strategy according to the SOC of energy storage, which ensures the safe operation of the energy storage system. Liu et al. [17] proposed a wind-storage coordinated frequency regulation control strategy, which considered the power distribution between the wind turbine and the energy storage when the wind-storage combined frequency regulation. However, they did not consider the SOC of the energy storage during frequency regulation, which may cause overcharge and overdischarge of energy storage. In order to ensure the safe operation of energy storage, Liu et al. [18] reviewed the remaining useful life prediction and state-of-charge estimation of supercapacitors. Aiming at the problem of SOC during frequency regulation of energy storage, some authors [19, 20] proposed the upper and lower limits of the energy storage SOC during frequency regulation to avoid overcharge and overdischarge of energy storage. However, it does not consider the problem of energy storage SOC recovery when the system is in a steady state. It will be unfavorable for energy storage to participate in the subsequent frequency regulation if SOC is too high or too low after frequency regulation.

A combined frequency regulation control method for wind power generation and energy storage with the safe operation of an energy storage system is proposed in this article. The wind turbine adopts overspeed control, and the energy storage uses virtual synchronization control. The entire wind-storage combined system has the same frequency regulation characteristics as the conventional synchronous generator. According to the definition of energy storage virtual synchronization, it is used as the upper-level control of the wind-storage combined system as a whole. It provides extra inertia and frequency regulation reserve capacity when the frequency changes, which can effectively improve the frequency stability of the system and reasonably distribute the output of wind turbine and energy storage during frequency regulation through the upper layer control. Therefore, the energy storage SOC is divided into distinct frequency regulation areas, early warning areas, and forbidden areas. The energy storage stops working in prohibited areas. The safe operation level of the energy storage system is improved by dynamically adjusting the frequency regulation coefficient control of the energy storage system when it is in the early warning area. Moreover, the SOC recovery of the energy storage in a steady state is considered, which ensures the long-term operation of the energy storage system. Besides, the feasibility and effectiveness of the wind-storage combined frequency regulation control method considering the safe operation of energy storage is verified by simulation.

2. Wind Turbine and Energy Storage Frequency Regulation Control Strategy

2.1. Wind Turbine Overspeed Load Reduction Control. The output of the wind turbine is related to the pitch angle, rotor speed, wind speed, and other factors. The output characteristics of the wind turbine are as follows:

$$P_{\mathrm{m}} = \frac{1}{2} C_{\mathrm{p}}(\lambda, \beta) p \pi R^2 v^3, \tag{1}$$

where C_{p} is the wind energy utilization coefficient, v is the wind speed, R is the blade radius, ω is the rotational angular velocity of the blade, and β is the blade pitch angle. In order to facilitate the analysis of the characteristics, the tip speed ratio λ is defined, that is, the ratio of the tip speed to the wind speed. There is a relation between the power coefficient Cp, the pitch angle β, and the tip speed ratio λ, which is given as follows:

$$\begin{cases} C_p(\lambda, \beta) = 0.22\left(\dfrac{116}{\lambda_i} - 0.46\beta - 5\right)^{e^{-12.5/\lambda_i}}, \\ \lambda_i = \dfrac{1}{1/(\lambda + 0.08\beta) - 0.035/\left(1 + \beta^3\right)}, \\ \lambda = \dfrac{\omega R}{v}. \end{cases} \tag{2}$$

The normal operation of wind power generation usually adopts the maximum power point tracking (MPPT) control

strategy, which cannot address additional spare capacity to participate in the adjustment of the power system frequency, which makes the power system stability problem more serious. Suppose the wind turbine adopts the method of tracking the suboptimal power during operation and reserves a part of the reserve capacity. In that case, the wind turbine can participate in the frequency adjustment of the power system. Reservation strategies for wind turbine spare capacity include pitch angle control and overspeed control [21]. The response speed of the pitch angle control is slow, and the frequent change of the pitch angle will seriously affect the service life of the wind turbine. Therefore, the wind turbine adopts overspeed control in this study.

The overspeed control makes the wind turbine run under suboptimal power by controlling the size of the rotational speed. It can set aside a part of the spare capacity to participate in the frequency adjustment. The principle of wind turbine overspeed control is shown in Figure 1.

In Figure 1, line A is the power curve under the MPPT operating state, and line B is the power curve under overspeed control. When the wind turbine runs in the form of A, the wind turbine produce outputs the maximum power is P_a, and the rotational speed is ω_a. The wind turbine rotates to ω_b through the overspeed and load reduction control. The wind turbine output power is P_b, which can set aside a part of the spare capacity to participate in system frequency adjustment. The power of load shedding is given as follows:

$$\Delta P_0 = d\%P = P_a - P_b, \tag{3}$$

where ΔP_0 is the power reserved by the wind turbine, and $d\%$ is the load shedding rate. Wind turbines participate in grid frequency regulation by reserving reserve capacity, which reduces the installed energy storage capacity of wind farms. The control strategy of wind turbine overspeed load reduction and frequency regulation is shown in Figure 2.

In Figure 2, K_w is the set frequency regulation coefficient of the wind turbine, and ΔP_W is the power emitted by the wind turbine during frequency regulation.

2.2. Virtual Synchronization Control Strategy of Energy Storage System. The traditional generator realizes frequency adjustment through inertial response and primary frequency regulation when the power system's frequency changes. The change of the power system frequency is related to the system inertia, and the power system inertia can be expressed as the property of changing the frequency change by the kinetic energy stored in the rotor of the synchronous generator. When the frequency changes, the equation of motion of the synchronous motor rotor is given as

$$\begin{cases} \Delta P = J\dfrac{d\omega}{dt}, \\ f = \dfrac{\omega}{2\pi}, \end{cases} \tag{4}$$

where ΔP is the difference between mechanical and electromagnetic power, J is the moment of inertia, ω is the rotor angular velocity, and f is the system frequency.

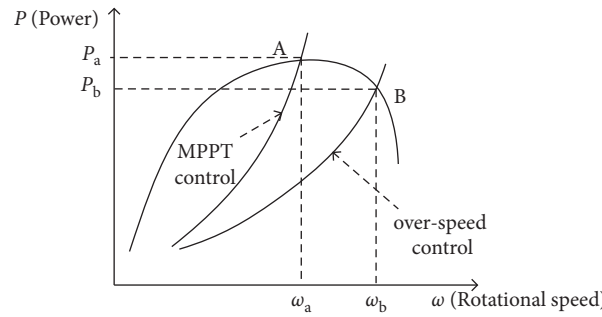

Figure 1: Overspeed load reduction control.

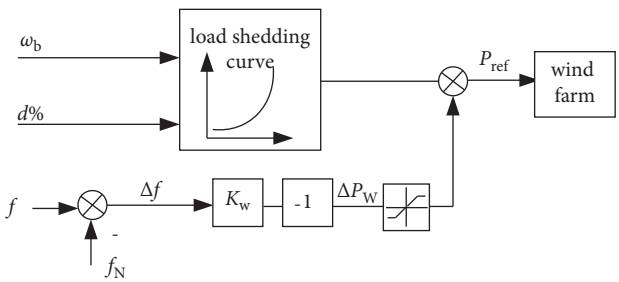

Figure 2: Wind turbine overspeed load reduction and frequency regulation strategy.

With the rapid development of energy storage, energy storage participates in the system's frequency regulation, and it provides a solid guarantee for the safe and stable operation of the system [22]. The virtual synchronous control of energy storage simulates the characteristics of traditional generators by adding virtual inertia and virtual droop coefficient to the energy storage control strategy [23]. It can provide additional capacity and inertia to slow down the rate of frequency drop when the frequency changes. The frequency regulation control strategy is shown in Figure 3.

The power generated by the energy storage system during frequency regulation is given as

$$\Delta P_{S1} = -K_d\Delta f - J_d\frac{df}{dt}, \tag{5}$$

where K_d is the virtual droop coefficient, J_d is the virtual inertia coefficient, and ΔP_{s1} is the output power.

3. Combined Frequency Regulation Control Strategy of Wind Power Generation and Energy Storage under the Optimal Operation of Energy Storage

3.1. Frequency Regulation Control Strategy of Wind-Storage Combined System. A combined frequency regulation control strategy for wind power generation and energy storage is proposed for solving the insufficient inertial capacity and frequency regulation capacity in high renewable energy penetration power grids. The structure of the wind power generation and energy storage combined system is shown in Figure 4.

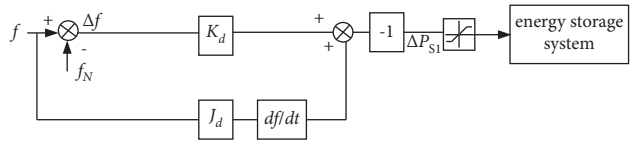

Figure 3: Virtual synchronization control strategy of energy storage system.

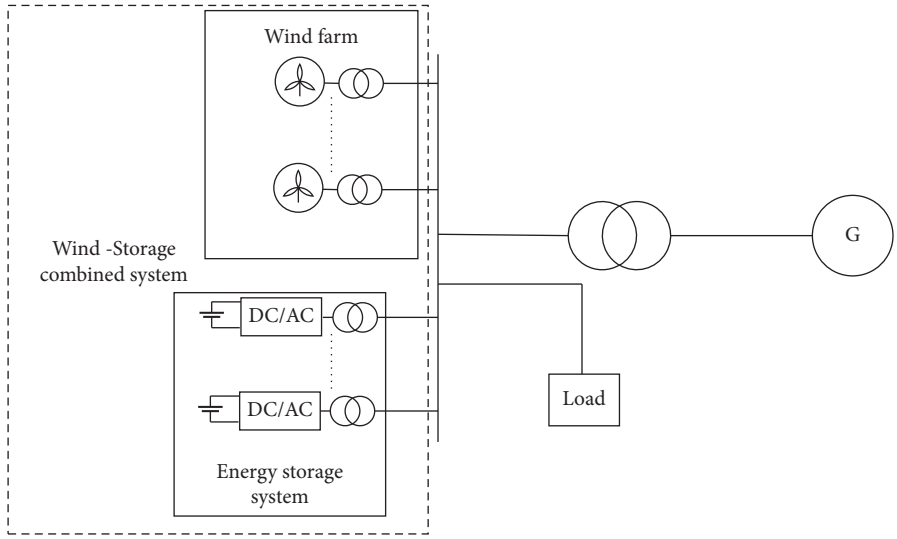

Figure 4: Combined system of wind power generation and energy storage.

It can be seen from Figure 4 that the combined wind power generation and energy storage system is mainly composed of doubly-fed wind turbines, energy storage systems, loads, and grid-equivalent frequency-modulated synchronous generators. The energy storage system is configured at the grid connection point of the wind farm. Compared with the configuration on the DC side of the turbines, the first-level energy exchange is reduced, the economy is better, and it is easy to control centrally [24]. Wind power generation and energy storage provide output power to the grid through their respective converters in a combined wind power generation and energy storage system. The wind turbine and energy storage simultaneously adjust and respond to grid frequency anomalies when the grid frequency changes.

The slow response cannot fully exert the frequency regulation capability of wind turbines, although the strategy of wind turbines improves the effectiveness of frequency regulation [25]. The energy storage system has the characteristics, such as being fast, flexible, and stable, in frequency regulation. A certain amount of energy storage is arranged in the wind farm to assist the wind turbine in participating in the frequency regulation. Only relying on energy storage to undertake the task of frequency regulation of wind farms in the process of frequency regulation will inevitably lead to large energy storage capacity, high cost, and poor economic benefits for wind farms. Therefore, combining the energy storage and the wind turbine is necessary to participate in the frequency regulation and achieve complementary advantages. Wind farms will better participate in system frequency regulation.

For a power system with n traditional synchronous motors, the equivalent inertia constant H_{sys} [26] is given as follows:

$$H_{sys} = \frac{\sum_{i=1}^{n} H_i S_i}{S_{sys}}, \tag{6}$$

where S_{sys} is the total capacity of the system and H_i and S_i are the inertia constant and capacity of the i-th traditional synchronous motor. According to formula (6), the capacity of the traditional synchronous motor decreases, the equivalent inertia of the system decreases as the installed capacity of the wind turbines in the system increases. The relationship between the equivalent inertia constant of the power system and the initial frequency change rate can be deduced as follows:

$$\frac{2H_{sys}}{f_N}\frac{df}{dt} = \frac{\Delta P}{S_{sys}}, \tag{7}$$

where f_{N} is the rated frequency.

The joint frequency regulation of wind power generation and energy storage is usually controlled separately by the wind turbine and energy storage. In this article, according to the definition of virtual synchronous control of energy storage, the virtual synchronous control as the upper-level control of the entire wind power generation and energy storage system due to the difference in response time between the wind turbine and the energy storage, it may cause frequency oscillation. It is used to calculate the power required by the entire wind power generation and energy storage combined system during frequency adjustment. It

then distributes it to the wind turbine and energy storage in real time. The combined frequency regulation strategy of wind power generation and energy storage is shown in Figure 5:

According to Figure 5, the combined frequency regulation control of wind power generation and energy storage includes wind power generation and energy storage combined system layer, wind farm layer, and energy storage system layer. The upper control adopts virtual droop and virtual inertia control by taking the entire wind-storage joint frequency modulation as a system. The whole of the wind-storage combined system has the same frequency regulation characteristics as the traditional generator set. It can provide additional inertia to delay the transient frequency change and provide additional capacity to participate in the frequency regulation of the power system. The deviation coefficient of the wind turbine can simulate the primary frequency regulation ability of the synchronous generator, but it does not have the ability of the inertial response. The output power of the energy storage is the difference between the frequency regulation power output by the upper-level control and the power output by the primary frequency regulation of the wind turbine. Therefore, the energy storage can provide the inertia adjustment part and the shortage of the frequency regulation capacity of the wind turbine.

The expression of the output power required for the frequency regulation of the combined wind power generation and energy storage system is as follows:

$$\Delta P_{W+S} = -K \cdot \Delta f + \left(-K_J \frac{df}{dt}\right), \tag{8}$$

$$\Delta P_W = -K_w \Delta f, \tag{9}$$

$$\Delta P_S = K_2 \left(\Delta P_{W+S} - \Delta P_W\right), \tag{10}$$

where ΔP_{W+S} is the power generated by wind power generation and energy storage during frequency regulation; K and K_J are the virtual droop coefficient and virtual inertia coefficient of the entire wind power generation and energy storage system; K_2 is the energy storage constraints frequency regulation factor.

The upper-level control of the wind power generation and energy storage system adopts virtual synchronous control. The inertia constant H_{W+S} of the joint system as a whole can be deduced as

$$H_{W+S} = \frac{f_N}{2} * K_J. \tag{11}$$

By adding virtual inertia, the total equivalent inertia constant H_{sys} of the system can be expressed as

$$H_{sys} = \frac{\sum_{i=1}^{n} H_i S_i + \sum H_{W+S} S_{W+S}}{S_{sys}}, \tag{12}$$

where S_{W+S} is the rated capacity of the combined wind power generation and energy storage system. According to the above equation, it can be seen that the equivalent inertia of the entire power system can be provided by adding virtual inertia to the whole wind power generation and energy storage system.

In order to ensure the superiority of the frequency regulation of the wind-storage combined system in the process of frequency regulation, the wind-storage integrated approach needs to generate additional power when the system frequency decreases. At this time, the frequency regulation coefficient of the wind farm is increased so that the wind turbine can provide more power and improve the utilization rate of wind energy. The combined system of wind power generation and energy storage needs to reduce the output power when the frequency increases. At this time, the adjustment coefficient of the wind farm is reduced, and the energy storage system absorbs extra power as much as possible to avoid the low utilization rate of wind energy. The power allocation flow chart of the wind-storage combined system is as follow:

According to Figure 6, the wind power generation and energy storage combined system layer respond first when the frequency fluctuation of the system crosses the dead zone. When the frequency changes, it calculates the power required by the wind power generation and energy storage combined system. If the load shedding power of the wind turbine is greater than the power required for droop control in the wind-storage combined system when the frequency decreases, in that case, the output power of the wind turbine is the same as the power required for the droop control of the wind-storage combined system. The energy storage provides the power needed for inertia response. Assuming that the output power required for the wind-storage combined system is greater than that provided by the wind turbine, the energy storage provides additional power at this time. When the frequency rises, if the power required to be reduced by the wind-storage combined system is greater than the power that the energy storage can absorb, the excess power will be absorbed by the wind turbine. If the power required to be reduced by the wind-storage combined system is less than the power that the energy storage can absorb, the wind turbine will not work at this time.

3.2. The Principle of Energy Storage Optimization Operation Interval Partition. The combined system of wind power generation and energy storage needs to consider the SOC constraint of energy storage in the actual operation [27]. The output power is related to the frequency change because the energy storage uses virtual synchronous control when it participates in frequency regulation. The SOC may exceed the limit during the frequency regulation process if the energy storage is always in the state of charging and discharging. The service life of the energy storage will be affected when the SOC is too large or too small. Simultaneously, the energy storage causes the SOC to be too high or too low after frequency regulation, which is not conducive to the energy storage for the following frequency

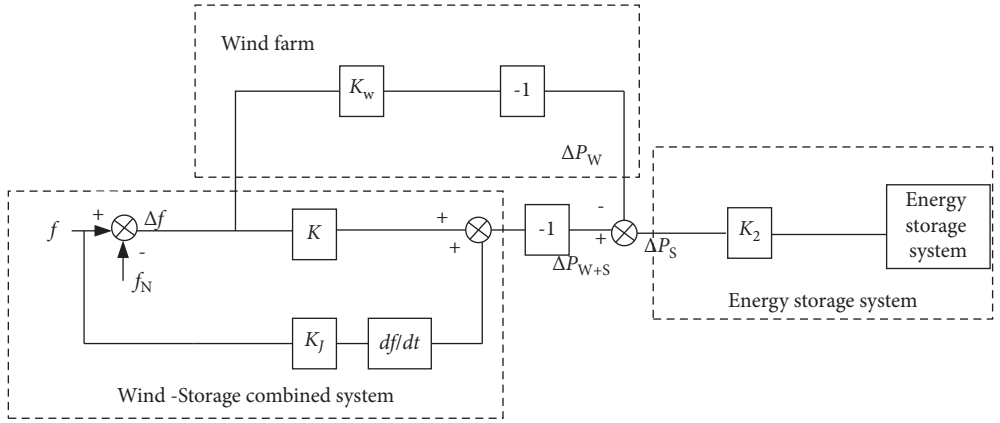

Figure 5: Combined frequency regulation strategy of wind power generation and energy storage.

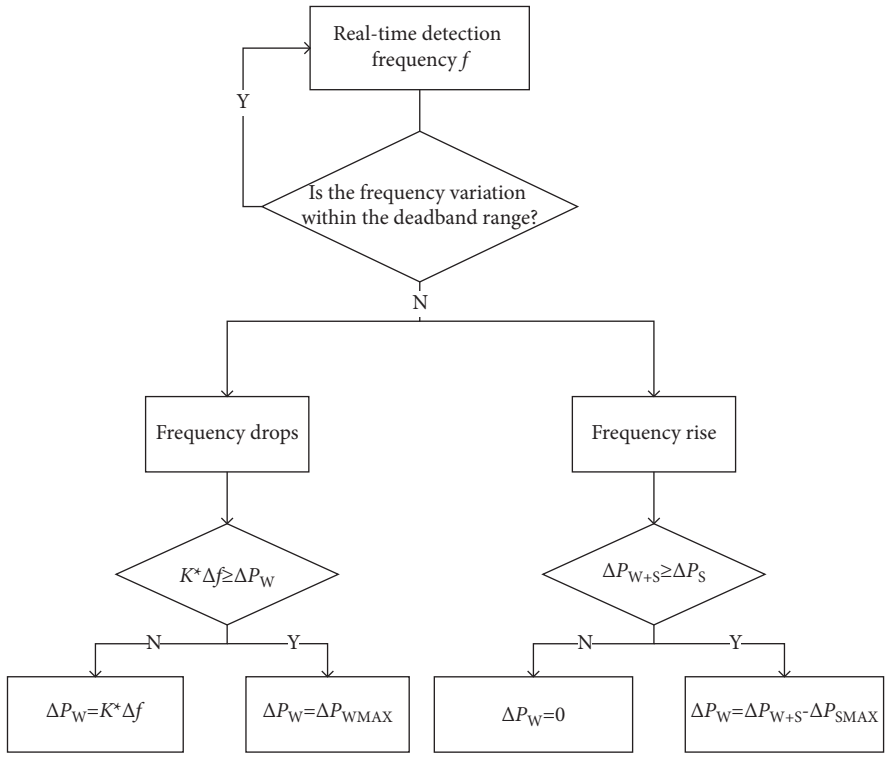

Figure 6: Power distribution flow chart.

regulation. To cope with this problem, we set the SOC partition principle according to the state of the energy storage SOC and the system's operating condition. In the frequency regulation state, the dead zone of the energy storage charge and discharge is set. The energy storage SOC is restored to the set range in the nonfrequency regulation state to ensure the safe operation of the energy storage. The specific SOC partition principle is shown in Figure 7.

The battery management system (BMS) is used to measure the size of the SOC of the energy storage system online. To prevent the overcharge or over-discharge of the energy storage, the normal area, early warning area, and forbidden area are set during the frequency regulation period. Energy storage provides an early warning of insufficient capacity during discharging when SOC ≤20%, and it does not discharge when SOC ≤10%. Energy storage raises a capacity overshoot warning during charging when SOC ≥80%. Charging is prohibited when SOC >90%. Normal charging and discharging of energy storage and wind power will participate in grid frequency regulation when 20% <SOC <80%. It is easy to cause insufficient absorption or output power during frequency regulation to avoid the SOC of energy storage being too large or too small before frequency adjustment. Therefore, 30% ≤SOC ≤70% is set as the

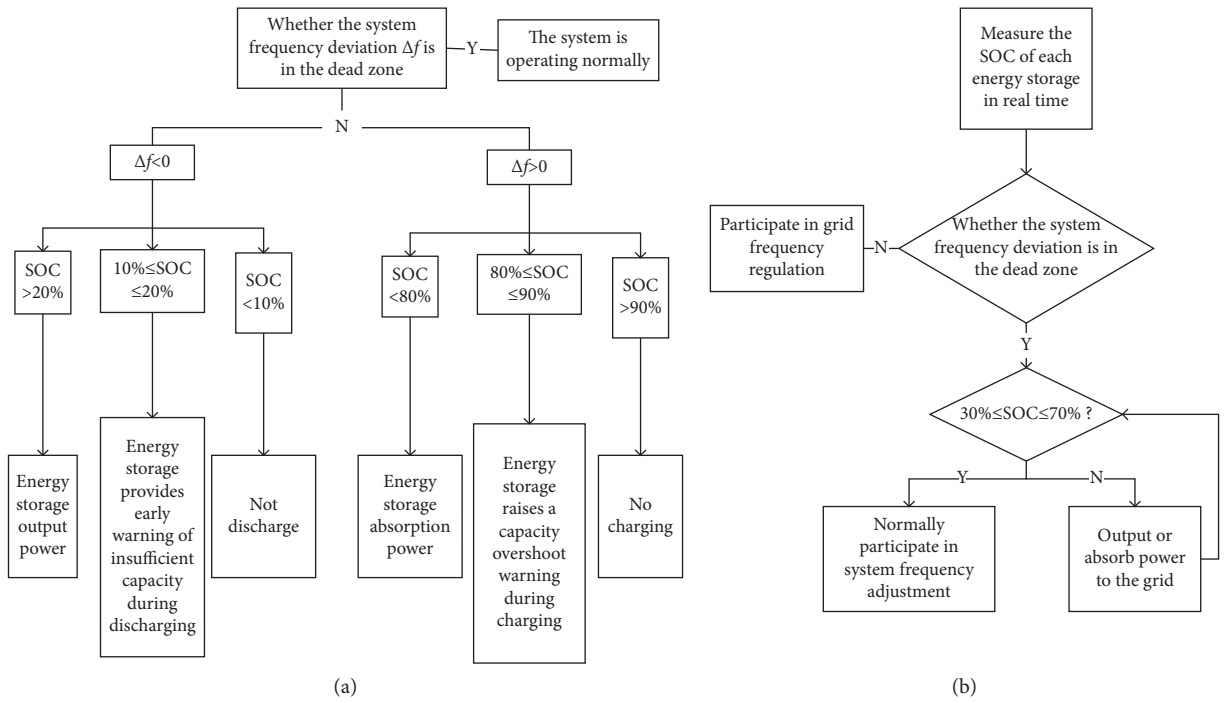

Figure 7: Energy storage participates in frequency regulation SOC partition. (a) Frequency adjustment period. (b) Nonfrequency regulation period.

safety range of the nonfrequency regulation period of energy storage. During the nonfrequency regulation period, the energy storage will send power to the grid at this time until the SOC drops to 70% if the SOC is too large. The power will be absorbed from the grid until the SOC reaches 30% when the SOC is too small. The energy storage absorbs/outputs 1 MW of power to the grid when the energy storage is set in the nonfrequency regulation period and not within the specified interval. The energy storage SOC can always be within the set range, thereby ensuring energy storage's safe and efficient operation.

To ensure the safety of energy storage during frequency regulation, combined with the set energy storage SOC division principle, when the energy storage provides an early warning of insufficient capacity or capacity overshoot, the frequency regulation coefficient is dynamically adjusted, thereby controlling the output power of the energy storage.

The logistic function combined with the partition principle is used in this article to control the frequency regulation coefficient of the energy storage system due to the value of the logistic function increasing exponentially in the initial stage with reasonable continuity. It gives full play to the frequency regulation capability of the energy storage system and maintains the stability of the SOC. The adaptive adjustment frequency regulation coefficient is shown in Figure 8.

The self-adaptive frequency regulation coefficient of the energy storage running in the discharge state is given as

$$K_2 = \begin{cases} 0, SOC(t) < 10\%, \\ \dfrac{0.02e^{10\left(SOC(t)-SOC_{\min}\right)/\left(20\%-SOC_{\min}\right)/2}}{1+0.02\left(e^{10\left(SOC(t)-SOC_{\min}\right)/\left(20\%-SOC_{\min}\right)/2}-1\right)}, 10\% \le SOC(t) \le 20\%, \\ 1, SOC(t) > 20\%. \end{cases} \tag{13}$$

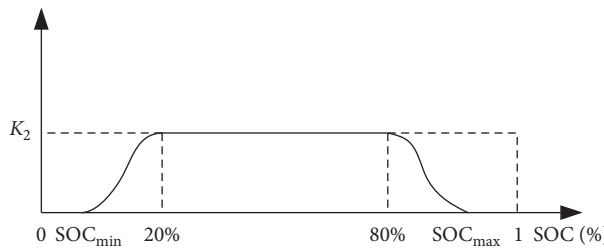

Figure 8: Energy storage adaptive frequency regulation coefficient.

The self-adaptive frequency regulation coefficient of the energy storage running in the charging state is given as

$$K_2 = \begin{cases} 1, SOC(t) < 80\%, \\ \dfrac{0.02e^{10\left(SOC_{max} - SOC(t)\right)/\left(SOC_{max} - 80\%\right)/2}}{1 + 0.02\left(e^{10\left(SOC_{max} - SOC(t)\right)/\left(SOC_{max} - 80\%\right)/2} - 1\right)}, 80\% \le SOC(t) \le 90\%, \\ 0, SOC(t) > 90\%, \end{cases} \tag{14}$$

where $SOC_{min} = 10\%$, $SOC_{max} = 90\%$. When SOC <10% or SOC >90%, the energy storage exits frequency regulation. The safe operation of the energy storage is ensured by dynamically modifying the frequency regulation coefficient of the energy storage.

4. Simulation Experiment Analysis

Aiming at the joint frequency regulation strategy of wind power generation and energy storage proposed in this article, we consider the optimal operating range of the energy storage system and a simulation model of the wind-storage combined system shown in Figure 5, which is built in Matlab/Simulink software to verify the feasibility of its control technology. The equivalent simulated grid capacity is 200 MVA, the initial load power is 120 MW, and the rated power of the wind farm is 50 MW and consists of 25 double-fed wind turbines with the power of 2 MW. The wind farm operates at a fixed wind speed, regardless of wind speed fluctuations. The wind farm reserves a capacity of 5 MW, and the adjustment coefficient K_w of the wind farm is 20 MW/Hz during normal operation. The rated power of the energy storage system is 5 MW, the rated frequency f of the system is 50 Hz, the frequency regulation coefficient K_d of the combined wind power generation and energy storage system is 20 MW/Hz, and the equivalent inertia time constant is 5 s.

4.1. Simulation Analysis on the Effectiveness of Combined Frequency Regulation Strategy for Wind Power Generation and Energy Storage. We increased the load by 20 MW at 6 S to verify the effectiveness of the wind-storage joint frequency regulation strategy presented in this study. Figures 9 and 10 show the frequency change, wind power generation, and energy storage output power, respectively.

According to Figures 9 and 10, the lowest frequency is 49.66 Hz when wind power and energy storage do not participate in frequency regulation. The lowest frequency of wind turbines alone is 49.75 Hz, which decreases the frequency drop compared with wind power and energy storage without frequency regulation. The lowest frequency is 49.76 Hz under the combined frequency regulation strategy of wind power generation and energy storage. It can provide certain inertia and delay the rate of frequency drop due to the virtual synchronous control adopted by the upper-level control of the combined frequency regulation of wind power generation and energy storage. According to the set power distribution, the power required for the combined frequency regulation of wind power and energy storage is less than the output power of the wind farm. The energy storage provides additional power needed for an inertial response during the initial phase of the frequency change to slow down the rate of frequency drop while the wind farm provides additional power.

We set that the load is reduced by 20 MW at 6 S. Figures 11 and 12 show the frequency change, wind power generation, and energy storage output power, respectively.

According to Figures 11 and 12, wind power generation and energy storage do not participate in frequency regulation. When the load is reduced, the peak frequency rises 50.34 Hz. Wind turbines' peak independent frequency regulation is 50.25 Hz, and the peak of combined frequency regulation of wind power generation and energy storage is 50.24 Hz. Moreover, the rate of frequency rise is delayed. According to the set power distribution principle, the power required by the entire wind-storage combined frequency regulation system is less than the output power of the energy storage. At this time,

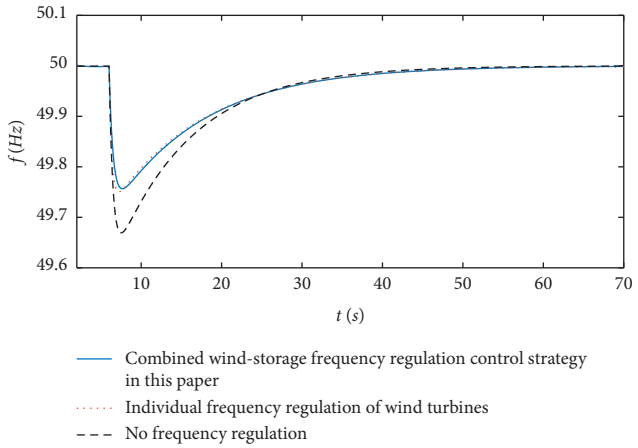

Figure 9: Comparison of frequency changes.

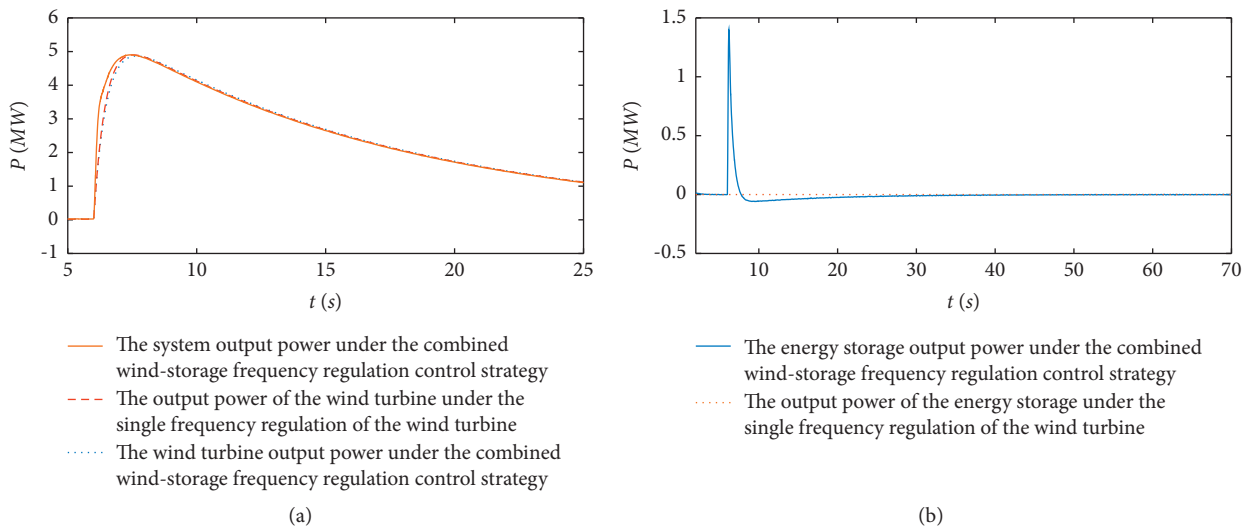

Figure 10: Output power of wind turbine and energy storage. (a) Wind turbine frequency regulation output power. (b) Energy storage frequency regulation output power.

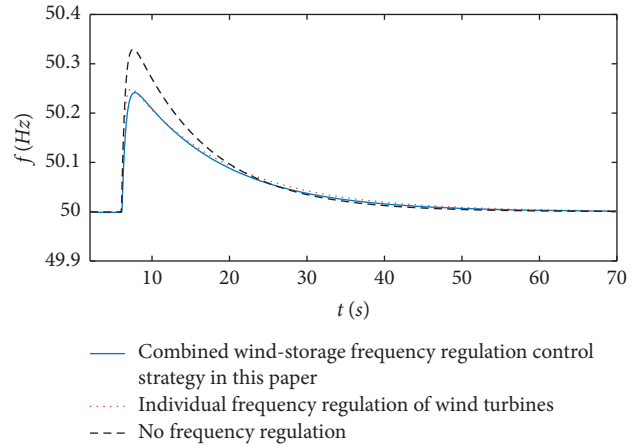

Figure 11: Comparison of frequency changes.

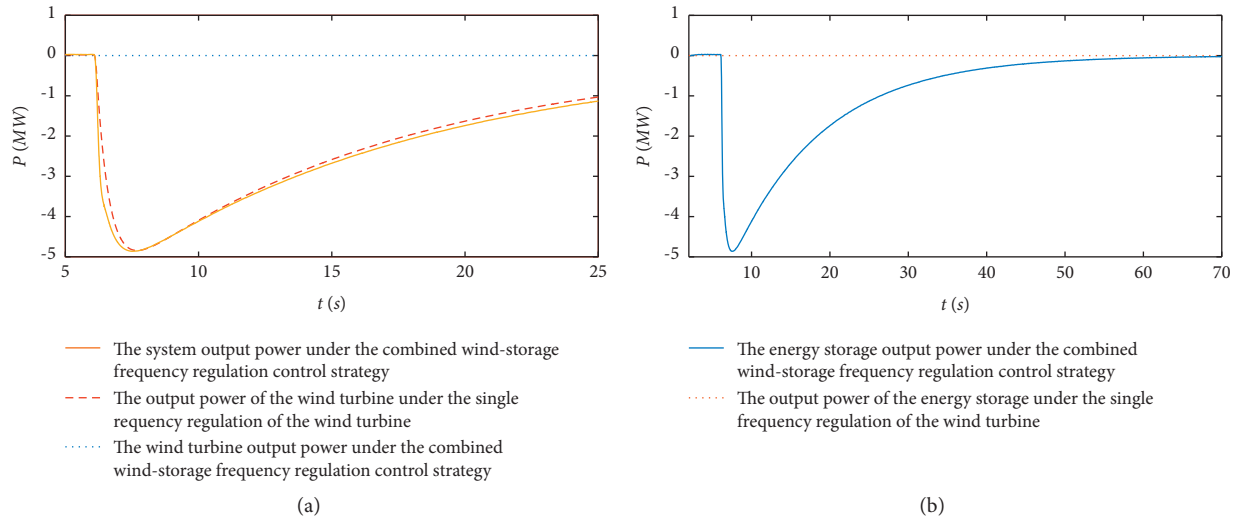

Figure 12: Wind turbine and energy storage output power. (a) Wind turbine frequency regulation output power. (b) Energy storage frequency regulation output power.

the power required for frequency regulation is all issued by the energy storage, and the wind turbine does not perform frequency regulation. The wind turbine will continue to reduce the power, and the wind energy utilization rate is too low when wind turbines participate in frequency regulation alone.

4.2. Simulation Analysis on the Effectiveness of Frequency Regulation Strategy considering Energy Storage Optimization Operating Range. The effectiveness of the wind-storage combined frequency regulation strategy in the energy storage optimal operating range is verified. We set the initial SOC of the energy storage to 70%. When the system reduces the load of 20 MW at 6 s, the energy storage system's output power and SOC changes are shown in Figures 13 and 14.

It can be seen from Figures 13 and 14 that when the frequency increases, the energy storage will absorb the power, and the SOC of the energy storage will increase at this time. After considering the energy storage constraint range, the frequency regulation coefficient is fixed. Also, the energy storage system automatically exits the frequency adjustment when the energy storage SOC rises to 90% during the frequency regulation process, which avoids the further decline of the energy storage SOC. Suppose the adaptive droop coefficient control is considered. In that case, the absorbed power of the energy storage is reduced when the SOC of the energy storage rises to the early warning range, thereby avoiding the withdrawal of the energy storage during frequency regulation, further ensuring the safe operation of the energy storage. The energy storage provides output power to the grid when the system frequency returns to stability. The energy storage stops absorbing power until the energy storage SOC rises to the set area. The energy storage SOC is always kept within a safe range and ensures the safe operation of the energy storage. However, the energy storage does not consider the constraint range that continues to provide output power during frequency regulation. So that the energy storage SOC rises to an excessively high state, and

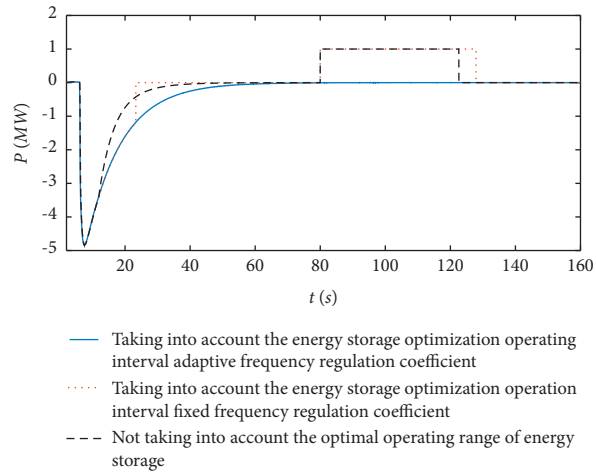

Figure 13: Comparison of energy storage output power under different strategies.

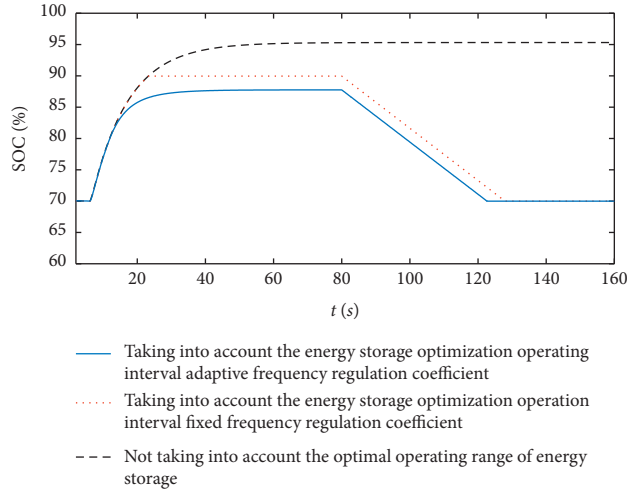

Figure 14: Comparison of SOC changes under different strategies.

the SOC will not recover in the steady state, resulting in the energy storage SOC remaining at an overly high level. In this state, it is not conducive to the stable operation of energy storage.

In general, the combined frequency regulation control strategy of wind power generation and energy storage considering the optimal operation range of energy storage can provide the required reserve capacity and inertia when the frequency fluctuates, and it effectively improves the frequency stability of the power system. At the same time, it not only avoids the overcharge and overdischarge of energy storage in the frequency regulation state but also ensures that the energy storage can always be located in a safe range after considering the constraint range of energy storage. Thus, the safe operation of the energy storage system in the wind-storage combined system is guaranteed.

5. Conclusion

The thesis sentence proposes a unique combined frequency regulation control method for wind power generation and energy storage that considers the optimal operating range of energy storage. The wind-storage combination is achieved using the overspeed control of the fan itself and the virtual synchronous control of the energy storage. The control has the advantages of overspeed control and virtual synchronous control. It can provide additional inertia and reserve capacity for the system during frequency adjustment and effectively improve the system frequency variation characteristics by setting the upper-level control of the wind-storage combined system to reasonably distribute the frequency regulation power. At the same time, the optimal operating range and partition principle of the energy storage SOC is considered in the energy storage control. The energy storage is regulated according to the divided intervals, which avoids the phenomenon that the SOC of the energy storage exceeds the limit during frequency regulation and controls the energy storage. It ensures the safe operation of the energy storage system due to the energy storage SOC always being within a safe range. Thereby, the sustainability and effectiveness of the wind-storage combined frequency regulation system have been improved.

Data Availability

The (all data) data used to support the findings of this study are included within the article.

Conflicts of Interest

The authors declare that they have no conflicts of interest.

References

[1] J. C. Zhao, F. J. Li, Z. L. Wang, P. Dong, G. Xia, and K. Wang, "Flexible PVDF nanogenerator-driven motion sensors for human body motion energy tracking and monitoring[J]," *Journal of Materials Science: Materials in Electronics*, vol. 32, no. 11, pp. 14715–14727, 2021.

[2] X. S. Tang, F. F. Miao, Z. P. Qi, and H. He, "Survey on frequency control of wind power[J]," *Proceedings of the Chinese Society of Electrical Engineering*, vol. 34, no. 25, pp. 4304–4314, 2014.

[3] X. Xu, X. . Lu, and T. Zhou, "Grid risk assessment based on the improved severity model considering the influence of secondary system [J]," *Electric Power Engineering Technology*, vol. 40, no. 02, pp. 205–211+219, 2021.

[4] GB/T 19963-2011, *Technical Regulations for Wind Farm Access to Power System [S]*, China Standard Press, Beijing, 2011.

[5] G. T. Xia, Y. N. Huang, F. J. Li et al., "A thermally flexible and multi-site tactile sensor for remote 3D dynamic sensing imaging[J]," *Frontiers of Chemical Science and Engineering*, vol. 14, no. 6, p. 13, 2020.

[6] X. Feng, Y. Zhang, L. Kang et al., "Integrated energy storage system based on triboelectric nanogenerator in electronic devices[J]," *Frontiers of Chemical Science and Engineering*, vol. 15, pp. 238–250, 2020.

[7] X. Feng, Q. Li, and K. Wang, "Waste plastic triboelectric nanogenerators using recycled plastic bags for power generation[J]," *ACS Applied Materials & Interfaces*, vol. 13, no. 1, pp. 400–410, 2020.

[8] C. Bu, F. Li, K. Yin, J. Pang, L. Wang, and K. Wang, "Research progress and prospect of triboelectric nanogenerators as self-powered human body sensors," *ACS Applied Electronic Materials*, vol. 2, no. 4, pp. 863–878, 2020.

[9] P. Gao, J. W. Li, J. Zhang, and G. Wang, "Computational exploration of magnesium-decorated carbon nitride (g-C3N4) monolayer as advanced energy storage materials[J]," *International Journal of Hydrogen Energy*, vol. 46, no. 4, pp. 21739–21747, 2021.

[10] J. H. Du, Y. Li, and N. N. Sun, "Energy storage behavior of inorganic dielectric materials [J/OL]," *Journal of the Chinese Ceramic Society*, pp. 1–17, 2022.

[11] Q. Y. Jiang and Y. Z. Gong, "Review of wind power integration control with energy storage technology [J]," *Power System Technology*, vol. 39, no. 12, pp. 3360–3368, 2015.

[12] H. F. Fan, Z. P. Yu, and W. L. Liu, "A demand assessment approach of energy storage for participating in fast frequency regulation of power system [J]," *Electric Power Engineering Technology*, vol. 38, no. 02, pp. 18–24, 2019.

[13] F. F. Miao, X. S. Tang, and Z. P. Qi, "Capacity optimization of energy storage participating to wind plant primary frequency regulation[J]," *Advanced Technology of Electrical Engineering and Energy*, vol. 35, no. 04, pp. 23–29, 2016.

[14] G. G. Yan, Y. B. Wang, and C. Zhong, "Frequency control strategy for wind storage combined system[J]," *Electric Power Construction*, vol. 37, no. 12, pp. 55–60, 2016.

[15] M. Zhang, K. Wang, and Y. T. Zhou, "Online state of charge estimation of lithium-ion cells using particle filter-based hybrid filtering approach[J]," *Complexity*, vol. 2020, 2020.

[16] Y. Hua, N. Wang, and K. Zhao, "Simultaneous unknown input and state estimation for the linear system with a rank-deficient distribution matrix," *Mathematical Problems in Engineering*, vol. 2021, no. 12, pp. 1–11, 2021.

[17] H. Liu, J. Ge, and Y. Gong, "Optimization scheme selection of wind farm participation in grid primary frequency regulation and study of wind-storage coordination control strategy[J]," *Journal of Global Energy Interconnection*, vol. 2, no. 01, pp. 44–52, 2019.

[18] C. Liu, Q. Li, and K. Wang, "State-of-charge estimation and remaining useful life prediction of supercapacitors," *Renewable and Sustainable Energy Reviews*, vol. 150, no. 2, p. 111408, 2021.

[19] X. W. Yan, S. Cui, and W. F. Chang, "Primary frequency regulation control strategy of doubly-fed induction generator considering supercapacitor SOC feedback adaptive adjustment[J]," *Transactions of China Electrotechnical Society*, vol. 36, no. 05, pp. 1027–1039, 2021.

[20] L. B. Yu, P. Kou, and Y. T. Feng, "Analysis on impact of virtual inertia control of DFIG-based wind turbine on electromechanical oscillation of power system[J]," *Automation of Electric Power Systems*, vol. 43, no. 12, pp. 36–43, 2019.

[21] Y. D. Si, *Study on Effect and Control of DFIG Connection to System Frequency [D]*, , 2020.

[22] X. R. Li, T. Deng, and J. Y. Huang, "Adaptive control strategy for energy storage batteries to participate in rapid frequency regulation of power grids [J]," *High Voltage Technology*, vol. 43, no. 07, pp. 2362–2369, 2017.

[23] Q. F. Yang, C. Q. Wang, and J. H. Wei, "Capacity allocation of energy storage system for improving grid inertia and primary frequency regulation [J]," *Electric Power Construction*, vol. 41, no. 10, pp. 116–124, 2020.

[24] S. G. Wang, B. M. Ge, and D. Q. Bi, "Control strategies of grid-connected wind farm based on virtual synchronous generator [J]," *Power System Protection & Control*, vol. 39, no. 21, pp. 49–54, 2011.

[25] J. H. Fu, H. F. Chen, and H. Zhao, "Review on frequency regulation technology with high wind power penetration [J]," *China Electric Power*, vol. 54, no. 01, pp. 104–115, 2021.

[26] P. Kundur, *Power System Stability and Control [M]*, pp. 128–136, McGraw-Hill Professional, New York, 1994.

[27] H. F. Chen, C. Y. Zhang, and Y. Y. Miao, "Virtual synchronous generator system with battery SOC feedback control [J]," *Electric Power Engineering Technology*, vol. 37, no. 04, pp. 90–96, 2018.

Hindawi
Mathematical Problems in Engineering
Volume 2022, Article ID 6150753, 11 pages
https://doi.org/10.1155/2022/6150753

Research Article

Synergetic Control Strategy of Front-End Speed Regulation Wind Turbine (FESRWT) for Fault Ride through

Xiaoqing Li,[1,2] **Haiying Dong**,[1,3] **Jun Liu**,[2] **Xiaojun Lin**,[2] **and Zhiqiang Sun**[4]

[1]*School of Automation and Electrical Engineering, Lanzhou Jiaotong University, Lanzhou 730070, China*
[2]*Lanzhou Institute of Technology, Lanzhou 730050, China*
[3]*School of New Energy and Power Engineering, Lanzhou Jiaotong University, Lanzhou 730070, China*
[4]*Institute of Railway Technology, Lanzhou Jiaotong University, Lanzhou 730000, China*

Correspondence should be addressed to Xiaoqing Li; xqli0910@163.com and Haiying Dong; hydong@mail.lzjtu.cn

Received 11 November 2021; Accepted 14 February 2022; Published 31 March 2022

Academic Editor: Licheng Wang

A synergetic control method is proposed to improve the fault ride through capability of front-end speed regulation wind turbine (FESRWT). In case of three-phase short-circuit fault and single-phase grounding fault, this method can accelerate the attenuation of stator flux transient component and restrain the fluctuation of rotor speed, make generator produce large reactive power which will provide more reactive power support for power grid, and improve the fault ride through capability of FESRWT. By dynamic analysis of the proposed algorithm, the large range stability constraint condition satisfying the fault ride through is obtained, and the parameter range satisfying the condition is solved by Monte Carlo method. Taking 2 MW FESRWT as an example, the control strategy is verified and analyzed. Simulation results show that the proposed method can improve the fault ride through performance of FESRWT.

1. Introduction

In recent years, wind power, as the renewable energy with the best large-scale development conditions and commercial development prospects, has developed rapidly. The capacity of single units and the total installed capacity have increased rapidly. The average annual coverage of wind power has increased year by year. However, the access of wind power has made power system more complicated, and the contradiction with the standard of "high efficiency, reliability, safety and grid friendly" becomes increasingly prominent [1,2]. Power departments and relevant authoritative companies in many countries around the world have formulated technical regulations for wind farms access to power system. It is required that wind farm can support the voltage of system connection point under normal working conditions, alleviate the interference caused by wind speed change to voltage fluctuation, and ensure that the voltage of wind farm connection point is always in a stable state. When the power system accident or disturbance causes voltage sags at the connection point, the wind turbine can ensure continuous operation without off-grid within a certain voltage sag range and time range [3–5]. Research on the fault ride through capability of wind turbines has become a hot issue in the field of wind power research.

At present, there are many literature on low voltage ride through (LVRT) capability of doubly fed induction generator (DFIG) and permanent magnet direct drive wind turbine, but there are few research on FESRWT. Aiming at the LVRT problem of FESRWT, reference [6] determined the control structure of the unit based on the characteristics of FESRWT. The pitch control with LVRT function based on gray prediction model, the variable universe fuzzy control of hydraulic speed control system based on multigroup genetic algorithm, and the predictive fuzzy PID control of brushless excitation system based on gray model were, respectively, proposed. The LVRT control of the unit was realized through the control of three subsystems. At the same time, the dynamic reactive power support ability of FESRWT was discussed. Reference [7] proposed a LVRT control method

based on the robust control of excitation system. The nonlinear controlled object is feedback linearized by constructing an extended state observer. The angle of attack deviation, angular velocity deviation, active power deviation, and terminal voltage deviation were selected as state variables, and a robust controller for excitation system was designed. The effectiveness of control algorithm was verified by simulation. Reference [8] carried out a simulation based on the operating characteristics of a 2.0 MW FESRWT, combined with actual parameters, and analyzed the dynamic response capability of generator's LVRT when a short-circuit fault occurs in power grid. Reference [9] compared and analyzed the LVRT capability of wind farms with FESRWTs and wind farms with DFIGs, as well as their impact on transient stability of power grid. The transient stability of different fault points was studied. The LVRT characteristics of FESRWT have been studied in the above references and some achievements have been achieved, but the high voltage ride through (HVRT) performance of wind turbine and the large-scale stability analysis of the system have not been involved.

The synergetic control theory was proposed by Russian scholar A. Kolesnikov. It could reduce the order of the closed-loop system, simplify the design of the controller, and make the controlled system have good steady state and dynamic performance, as well as strong robustness [10–13]. At present, the research on synergetic control strategy of wind turbine is attracting more and more attention. Reference [14] designed a synergetic controller for permanent magnet direct drive wind turbine and verified the LVRT performance. Reference [15] proposed a synergetic control strategy of DFIG and verified the LVRT performance of the proposed control strategy through simulation. Reference [16] proposed a synergistic control algorithm, system stability constraints, and optimization method of control parameters for DFIG that could improve DFIG's HVRT and LVRT capability.

Based on the above-mentioned references, this paper firstly establishes the mathematical model of FESRWT. Then the synergistic control algorithm is used to realize the fault ride through of FESRWT. The dynamic analysis of proposed algorithm is carried out, and the large-scale stability constraint conditions satisfying the fault ride through are given. The Monte Carlo method is used to solve the parameters that meet the conditions. Finally, based on the actual operation data of FESRWT, the proposed control strategy is verified and compared with existing control strategy.

2. FESRWT Mathematical Model and Transient Current Analysis

The structure of FESRWT is shown in Figure 1. Its components include wind wheel, speed-increasing gear box, hydraulic speed converter, and Electrically Excited Synchronous Generator (EESG). The electric energy generated by the unit is merged into power grid through transformer.

2.1. Mathematical Modeling of EESG. The 5th-order practical mathematical model of EESG is as follows [17]:

(1) Stator voltage equation:

$$\begin{aligned} u_d &= E_d' + X_q'' i_q - i_d r_a, \\ u_q &= E_q'' - X_d'' i_d - i_q r_a. \end{aligned} \tag{1}$$

(2) Voltage equation of rotor f winding:

$$T_{d0}' \frac{dE_q'}{dt} = E_f + \frac{X_d - X_d''}{X_d'' - X_d'} E_q' + \frac{X_d' - X_d}{X_d'' - X_d'} E_q''. \tag{2}$$

(3) Voltage equation of rotor D winding:

$$T_{d0}'' \frac{dE_q''}{dt} = -E_q'' + E_q' + (X_d'' - X_d') i_d. \tag{3}$$

(4) Voltage equation of rotor Q winding:

$$T_{q0}'' \frac{dE_d''}{dt} = -E_d'' + (X_q - X_q'') i_q. \tag{4}$$

(5) Rotor motion equation:

$$\begin{aligned} 2H \frac{d\omega}{dt} &= P_m - P_e - D(\omega - 1), \\ \frac{d\delta}{dt} &= \omega - 1, \end{aligned} \tag{5}$$

where u_d is the stator d-axis voltage, u_q is the stator q-axis voltage, i_d is the d-axis current, i_q is the q-axis current, r_a is the stator A-phase winding resistance, E_q' is the motor q-axis transient electromotive force, E_d' is the motor d-axis transient electromotive force, E_q'' is the q-axis supertransient electromotive force, E_d'' is the d-axis supertransient electromotive force, E_f is the stator excitation electromotive force, X_q is the q-axis synchronous reactance, X_q'' is the q-axis supertransient reactance, X_d is the d-axis synchronous reactance, X_d' is the d-axis transient reactance, X_d'' is the d-axis supertransient reactance, T_{d0}' is the d-axis open-circuit transient time, T_{d0}'' is the d-axis open-circuit supertransient time, T_{q0}'' is the q-axis open-circuit supertransient time, H is the unit inertia time constant, ω is the electrical angular velocity, P_m is the mechanical power, and P_e is the electromagnetic power. The previously mentioned parameters are all unit values using X_{ad} as the base value, D is the constant damping coefficient, δ is the angle of the q-axis leading the real axis of the synchronous coordinate system, and the unit is rad.

Under the conditions of ignoring the voltage sag caused by resistance of stator winding and omitting the flux linkage generated by damping winding current, the above parameters meet the following relationship [18] :

$$U_q = E_q' - I_d X_d'. \tag{6}$$

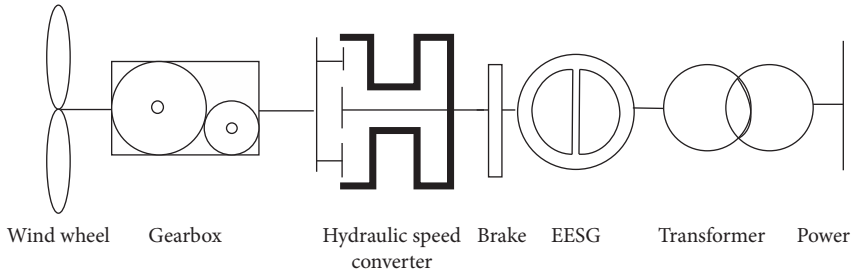

Figure 1: Structure diagram of FESRWT.

2.2. Transient Characteristic Analysis of EESG during Power Grid Voltage Sag.

(1) Transient characteristics of EESG When the generator is suddenly short circuited, the current of each stator winding will include fundamental frequency component, frequency doubling component, and DC component. After reaching the steady state, the DC component and the double frequency component in stator current will attenuate from its initial value to zero; and the fundamental frequency component will attenuate to the steady state value [19]. Similarly, the rotor winding also contains DC component and AC component with the same frequency. After introducing the attenuation factor, the d-axis and q-axis components of stator current are

$$i_d = \frac{E_{q[0]}}{x_d} + \left(\frac{E_{qo}''}{x_d''} - \frac{E_{q[0]}'}{x'}\right)\exp\left(-\frac{t}{T_d''}\right) + \left(\frac{E_{q[0]}'}{x_d'} - \frac{E_{q[0]}'}{x_d}\right)\exp\left(-\frac{t}{T_d'}\right) - \frac{V_{[0]}}{x_q''}\exp\left(-\frac{t}{T_a}\right)\cos(wt + \delta_o),$$
$$i_q = -\frac{E_{do}''}{x_q''}\exp\left(-\frac{t}{T_q''}\right) + \frac{V_{[0]}}{x_q''}\exp\left(-\frac{t}{T_a}\right)\sin(wt + \delta_o). \tag{7}$$

After transformation, the A-phase current of stator is

$$\begin{aligned} i_a = {} & -\frac{E_{q[0]}}{x_d}\cos(wt + \alpha_0) - \left(\frac{E_{qo}''}{x_d''} - \frac{E_{q[0]}'}{x_d'}\right)\exp \\ & \cdot\left(-\frac{t}{T_q''}\right)\cos(wt + \alpha_0) \\ & -\left(\frac{E_{q[0]}'}{x_d'} - \frac{E_{q[0]}}{x_d}\right)\exp\left(-\frac{t}{T_d'}\right)\cos(wt + \alpha_0) \\ & -\frac{E_{q0}''}{x_q''}\exp\left(-\frac{t}{T_q''}\right)\sin(wt + \alpha_0) \\ & +\frac{V_{[0]}}{2}\left(\frac{1}{x_d''} + \frac{1}{x_q''}\right)\exp\left(-\frac{t}{T_a}\right)\cos(\delta - \alpha_0) \\ & +\frac{V_{[0]}}{2}\left(\frac{1}{x_d''} + \frac{1}{x_q''}\right)\exp\left(-\frac{t}{T_a}\right)\cos(2wt + \delta + \alpha_0). \end{aligned} \tag{8}$$

The current in rotor winding is

$$\begin{aligned} i_f = {} & i_{f[0]} + \left[\frac{x_{ad}x_{\sigma D}V_{[0]}\cos\delta_0}{\left(x_f x_D - x_d^2\right)x_d'} - \frac{(x_d - x_d')V_{[0]}\cos\delta_0}{x_{ad}x_d'}\right]\exp \\ & \cdot\left(-\frac{t}{T_d''}\right) \\ & +\frac{(x_d - x_d)V_{[0]}\cos\delta_0}{x_{ad}x_d'}\exp\left(-\frac{t}{T_d'}\right) \\ & -\frac{x_{ad}x_{\sigma D}V_{[0]}}{\left(x_f x_D - x_{ad}^2\right)x_d''}\exp\left(-\frac{t}{T_a}\right)\cos(wt + \delta_0). \end{aligned} \tag{9}$$

In the above equation, x_f is the armature reaction reactance between longitudinal axis windings, x_{ad} and x_{aq} are the reactances of d-axis and q-axis of the rotor, x_D and x_Q represent the reactances of D and Q damping windings, $x_{\sigma D}$ is the leakage reactance of D damping winding, and $E_{q[0]}$ and $V_{[0]}$ are the instantaneous no-load potential and terminal voltage before short circuit.

(2) Based on the above analysis, taking three-phase symmetrical short-circuit and single-phase grounding fault of power grid as examples, the transient characteristics of EESG are simulated and analyzed. As shown in Figures 2 and 3, the simulation waveforms are A-phase current of stator, d-axis component of stator current, q-axis component

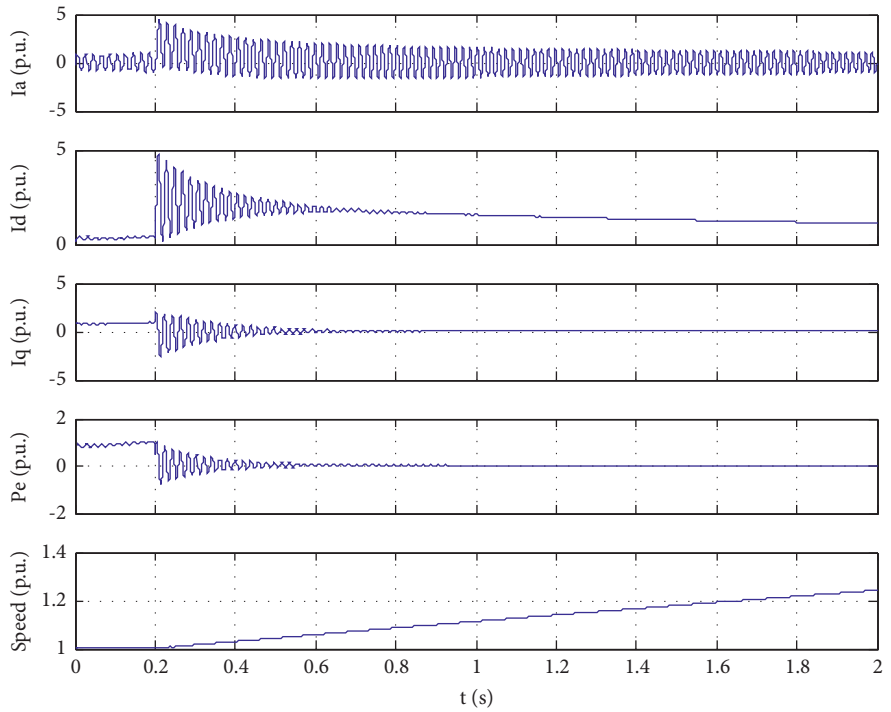

Figure 2: Transient simulation results of EESG in case of three-phase short-circuit fault.

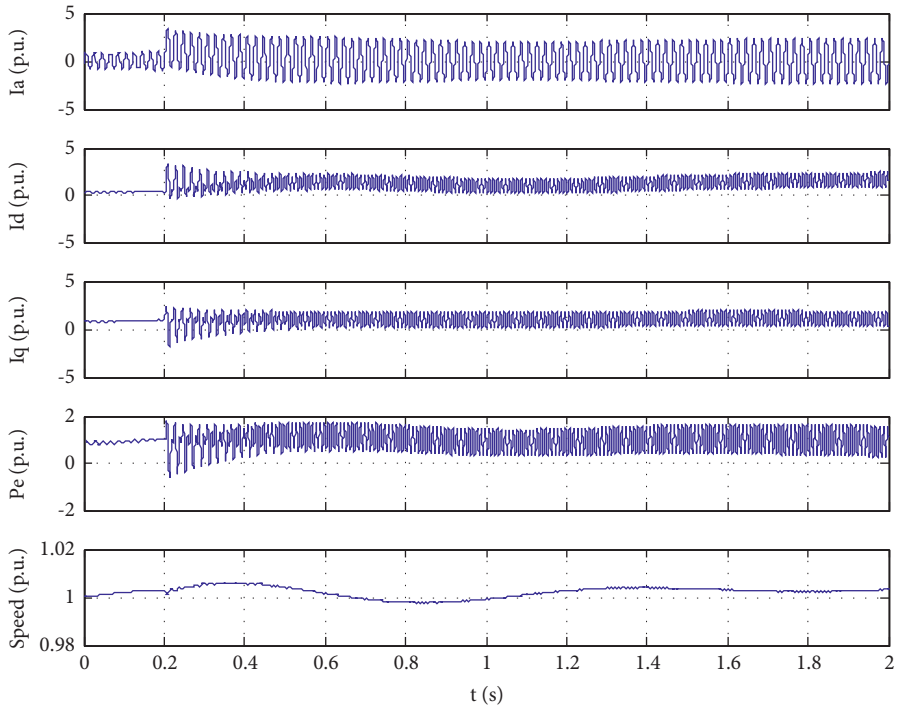

Figure 3: Transient simulation results of EESG in case of single-phase grounding fault.

of stator current, active power output of generator, and rotor speed in sequence. Under the normal operation of FESRWT, the active power delivered by generator to power grid is equal to the mechanical power input by wind turbine, and the current in stator winding is a symmetrical, positive-sequence three-phase current. When a three-phase symmetrical short-circuit fault occurs in grid, it can be seen from Figure 2 that the mechanical power input by wind turbine remains unchanged, while the power delivered by generator to grid decreases; at this time, large excess power is generated, the rotor speed

increases, and there is a large short-circuit current in generator stator winding. When a single-phase grounding fault occurs in power grid, it can be seen from Figure 3 that the stator current contains a large number of harmonic components, and the transient oscillation of EESG is large during the fault.

3. Synergetic Control Strategy

By taking advantage of the system's own nonlinearity and the self-organization ability of open system far from the equilibrium state, the synergetic control can stably converge to the manifold and ensure the global asymptotic stability of high-dimensional nonlinear system through manifold. Therefore, in the case of power grid failure, according to the transient characteristics of EESG, the synergetic control strategy of excitation system is designed to make the generator work in the overexcitation state for forced excitation, so as to increase the excitation current, prevent the generator voltage from falling, and transmit a large amount of reactive power to the power grid to maintain the stability of system and realize the fault ride through control of FESRWT.

3.1. Synergetic Control Theory. Synergetic control is a state space method proposed by Russian scholars. The design of controller can be divided into three steps: defining macro variables, defining manifolds, and obtaining control laws [20, 21].

Suppose that there is an N-dimensional nonlinear system as follows:

$$\frac{dx}{dt} = f(x, d, t), \tag{10}$$

where x is the state vector of system, d is the control vector of system, and t is time. Macro variables should be defined according to control objectives and dynamic performance indicators of system, and specific state variables should be contained, taking macro variable $\psi = \psi(x)$. In general, a linear combination of state variables can be simply selected. For systems with multiple control outputs, the same number of macro variables needs to be defined. The system manifold is constructed as $\psi(x) = 0$. According to the macro variable, the control law of system is solved by the manifold, so that the system converges from any initial state in finite time and remains on the manifold and approaches the equilibrium point of controlled system along the manifold.

The following equation is generally used to solve the control law:

$$T\frac{d\psi}{dt} + \psi = 0, \tag{11}$$

where T is a time constant, and $T > 0$. T determines the time when the macro variable converges to $\psi(x) = 0$. On the premise of system stability, the smaller T is, the faster the dynamic response of system is. The control variable d can be obtained from equation (11). Through d, the system converges from initial state to manifold $\psi(x) = 0$ to ensure that the system operates at the equilibrium point. Because the nonlinear model of system is used in the process of solving the control law, the obtained control law can not only maintain stability at each operating point but also make the system have better dynamic characteristics.

3.2. Synergetic Control Strategy of FESRWT. The control objective of synergetic excitation controller is to obtain appropriate control law E_f, so that, after the grid voltage sags, the generator terminal voltage and rotor speed can be maintained at set values, and the power oscillation of system can be suppressed. Combined with the mathematical model of EESG, the macro variable can be selected as linear combination of generator terminal voltage and rotor angular speed deviation, as shown in the following formula:

$$\psi = (U_{\text{sref}} - U_s) + k1(w_{\text{ref}} - w), \tag{12}$$

where U_{sref} and ω_{ref} are reference values of generator terminal voltage and rotor angular velocity, respectively, and k_1 is the coefficient, which defines the proportional relationship between generator terminal voltage deviation and rotor angular velocity deviation. The goal of synergetic control is to make the system converge to manifold $\psi(x) = 0$ after grid voltage sags and finally reach the equilibrium point along the manifold. By substituting formula (2), formula (5), formula (6), and formula (12) into formula (11), the control law of the synergetic excitation controller can be obtained:

$$\begin{aligned} E_f &= -\frac{X_d - X_d''}{X_d'' - X_d'}E_q' - \frac{X_d' - X_d}{X_d'' - X_d'}E_q'' \\ &\quad + \frac{\psi T_{d0}' U_s}{TU_q} - \frac{k_1 T_{d0}' U_s \dot{\omega}}{U_q} - \frac{T_{d0}' U_d \dot{U}_d}{U_q} + \dot{I}_d X_d' T_{d0}' \\ &= -\frac{X_d - X_d''}{X_d'' - X_d'}E_q' - \frac{X_d' - X_d}{X_d'' - X_d'}E_q'' \\ &\quad + \frac{((U_{\text{sref}} - U_s) + k_1(\omega_{\text{ref}} - \omega))T_{d0}' U_s}{TU_q} \\ &\quad - \frac{k_1 T_{d0}' U_s}{2HU_q}(P_m - P_e - D(\omega - 1)) \\ &\quad - \frac{T_{d0}' U_d \dot{U}_d}{U_q} + \dot{I}_d X_d' T_{d0}'. \end{aligned} \tag{13}$$

4. Stability Analysis of Synergetic Controller

Although the structure of synergetic control algorithm can be determined by formula (13), appropriate control parameters should be selected to make the unit meet requirements of system in normal and fault conditions of power grid. Selecting reasonable control parameters to keep the disturbed system stable is a high-dimensional and strong nonlinear problem, it is very difficult to select control parameters by experience, and the system cannot be guaranteed to have good dynamic response characteristics [22, 23].

For FESRWT, it is necessary to not only ensure good operation under normal grid voltage but also have a certain fault ride through capability. Therefore, the normal operating state of FESRWT needs to be located in the gradually stable attraction domain of fault ride through state.

In the analysis of dynamic system problems, the fault ride through stability analysis of FESRWT belongs to large-scale stability analysis. The Lyapunov direct method can be used to determine the stability of FESRWT and solve the range of parameters that satisfy fault ride through stability. Selecting the appropriate Lyapunov function is the key to judge the stability of system and solve the range of control parameters [24].

According to formulas (1)–(6), formula (13) takes the state variable $x = [U_s, E_q', E_q'', E_d'', \omega, \delta]^T$. Then, the mathematical model of FESRWT can be expressed by the following formula:

$$\dot{x} = A\mathbf{x} + BI + U, \tag{14}$$

where

$$A = \begin{bmatrix} \frac{-1}{T} & 0 & 0 & 0 & \frac{k_1 D - k_1}{2H} & 0 \\ 0 & \frac{X_d - X_d''}{T_{d0}'(X_d'' - X_d')} & \frac{X_d' - X_d}{T_{d0}'(X_d'' - X_d')} & 0 & 0 & 0 \\ 0 & \frac{1}{T_{d0}''} & \frac{-1}{T_{d0}''} & 0 & 0 & 0 \\ 0 & 0 & 0 & \frac{-1}{T_{d0}''} & 0 & 0 \\ 0 & 0 & 0 & 0 & \frac{-D}{2H} & 0 \\ 0 & 0 & 0 & 0 & 1 & 0 \end{bmatrix}, \tag{15}$$

$$B = \begin{bmatrix} 0 & 0 \\ 0 & 0 \\ \frac{(X_d'' - X_d')}{T_{d0}''} & 0 \\ 0 & \frac{(X_q - X_q'')}{T_{q0}''} \\ 0 & 0 \\ 0 & 0 \end{bmatrix},$$

$$U = \begin{bmatrix} \frac{U_{\text{sref}} + k_1 \omega_{\text{ref}}}{T} - \frac{k_1 (P_m - P_e + D)}{2H} & \frac{E_f}{T_{d0}'} & 0 & 0 & \frac{P_m - P_e + D}{2H} & -1 \end{bmatrix}^T.$$

Let the Lyapunov function be

$$\begin{aligned} v(x) &= x^T P x, \\ \dot{v}(x) &= x^T (-Q) x. \end{aligned} \tag{16}$$

Taking $Q = I$, the P matrix is determined by formula (16).

$$A^T P + PA = -I. \tag{17}$$

According to the relevant theorem of Lyapunov's second method, when FESRWT satisfies $v(x,t) > 0$ and $\dot{v}(x,t) < 0$, it can be judged that FESRWT is asymptotically stable in the neighborhood of this operating point.

Due to the large number of state variables in FESRWT, it is difficult to solve the range of control parameters by analytical method to make it meet the conditions of large-scale asymptotic stability. Therefore, the Monte Carlo method is used to obtain the range of control parameters. Monte Carlo method is also called computer stochastic simulation method. The principle is to understand a system through a large number of random samples and then obtain the value to be calculated.

Let H be a matrix composed of control parameters; that is, $H = [h_1, h_2, \ldots, h_n]$; and divide each element in H into intervals; that is, $h_i \in (a_i, b_i)$, $i = 1, 2, \ldots, n$, and $a_i < b_i$. Monte Carlo points are taken in n-dimensional state space region formed by h_i, and different H is got. The value range of the control parameters satisfying control requirements can be solved by screening the points through numerical calculation.

Taking $H = [T, k_1]$, according to the method of constructing Lyapunov function above, the state equation of FESRWT is substituted into formula (16) to obtain matrix P. The positive characterization of P is tested by Sylvester's criterion. The stable control parameter range of system is to satisfy the parameter range where A is a positive definite matrix. The solution can be obtained: $T \in (0.005, 1)$ and $k_1 \in (-120, -20)$. It should be noted that the range of parameters obtained is relatively conservative.

5. Simulation Verification

In order to verify the effectiveness of proposed synergetic control strategy, a 2 MW FESRWT simulation model was built by Matlab/Simulink software. The simulation experiment of fault ride through control is carried out in the cases of three-phase symmetrical short circuit and single-phase grounding short circuit. The basic parameters of FESRWT are shown in Table 1. Due to the short simulation time, it can be assumed that wind speed is constant during the fault period, and the wind speed is taken as 12.5 m/s.

5.1. Analysis of Fault Ride through Characteristics When Three-Phase Symmetrical Short-Circuit Fault Occurs. The wind farm adopts the unit wiring method of "wind turbine-box-type substation." 35 kV overhead lines are used to connect the box-type substations in each group. 35 kV cable is used to connect the high-voltage side of the box-type transformer to the 35 kV overhead line. There are 2 overhead lines to 110 kV boost substation in wind farm. Suppose that, at $t = 0.3$ s, a three-phase symmetrical short-circuit fault occurs on the high voltage side of transformer on one circuit of the transmission line, and the voltage sags to 20% of the rated voltage, lasting 625 ms; when $t = 0.925$ s, the fault is removed and the double circuit is resumed. Simulation waveform using synergetic control strategy is shown in Figure 4.

Table 1: Simulation parameters table.

Parameter	Value
S (MW)	2
U_{sref} (V)	690
n (rpm)	1500
r_a (pu)	0.0074
X_d (pu)	1.97
X_d' (pu)	0.15
X_d'' (pu)	0.125
X_q (pu)	0.823
$X_{q'}''$ (pu)	0.186
T_{d0}' (s)	2.757
T_{d0}'' (s)	0.013
T_{q0}'' (s)	0.212
H (Pu)	0.14
D (Pu)	0.02056

The technical regulations of wind farm access to the power system require that when the voltage at the grid connection point sags to 20% of nominal voltage, the wind turbine in the wind farm shall ensure the continuous operation of 625 ms without off-grid. When the voltage of wind farm connection point can be restored to 90% of nominal voltage within 2 s after falling, the wind turbines in wind farm are guaranteed not to be off-grid and run continuously. It can be seen from Figures 4(a)–(f) that the synergetic control strategy adopted in this paper can make wind turbines meet the requirements of grid connection. In [7], the robust control strategy was used to carry out the simulation under the above working conditions. Compared with the robust control strategy, the average value of reactive current during the fault period increases from 1.9pu to 3.07pu, and the generator sends out large reactive power, which can provide more reactive power support to the power grid and is more conducive to the voltage recovery of the power grid. The active power transition time of the generator is reduced from 1.9s to 1.6s, and the oscillation amplitude is small. The maximum speed of the generator is reduced from 1.06pu to 1.017pu. It can be seen that the synergetic control strategy can restore FESRWT to normal operation state more quickly and provide reactive power support to power grid in time after the three-phase symmetrical short-circuit fault is cleared.

5.2. Analysis of Fault Ride through Characteristics under Single-Phase Grounding Fault. Suppose that, at $t = 0.3$ s, a single-phase grounding fault occurs on a loop of the transmission line on the high voltage side of the transformer, the voltage sags to 40% of rated voltage, and the fault is removed at $t = 0.925$ s. The simulation waveform of synergetic control strategy is shown in Figure 5. It can be seen from Figures 5(a)–5(f) that the synergetic control strategy adopted in this paper can make wind turbines meet the requirements of grid connection. Reference [7] used a robust control strategy to carry out the simulation under the above conditions. Compared with robust control strategy, although the short-circuit current in three-phase winding of

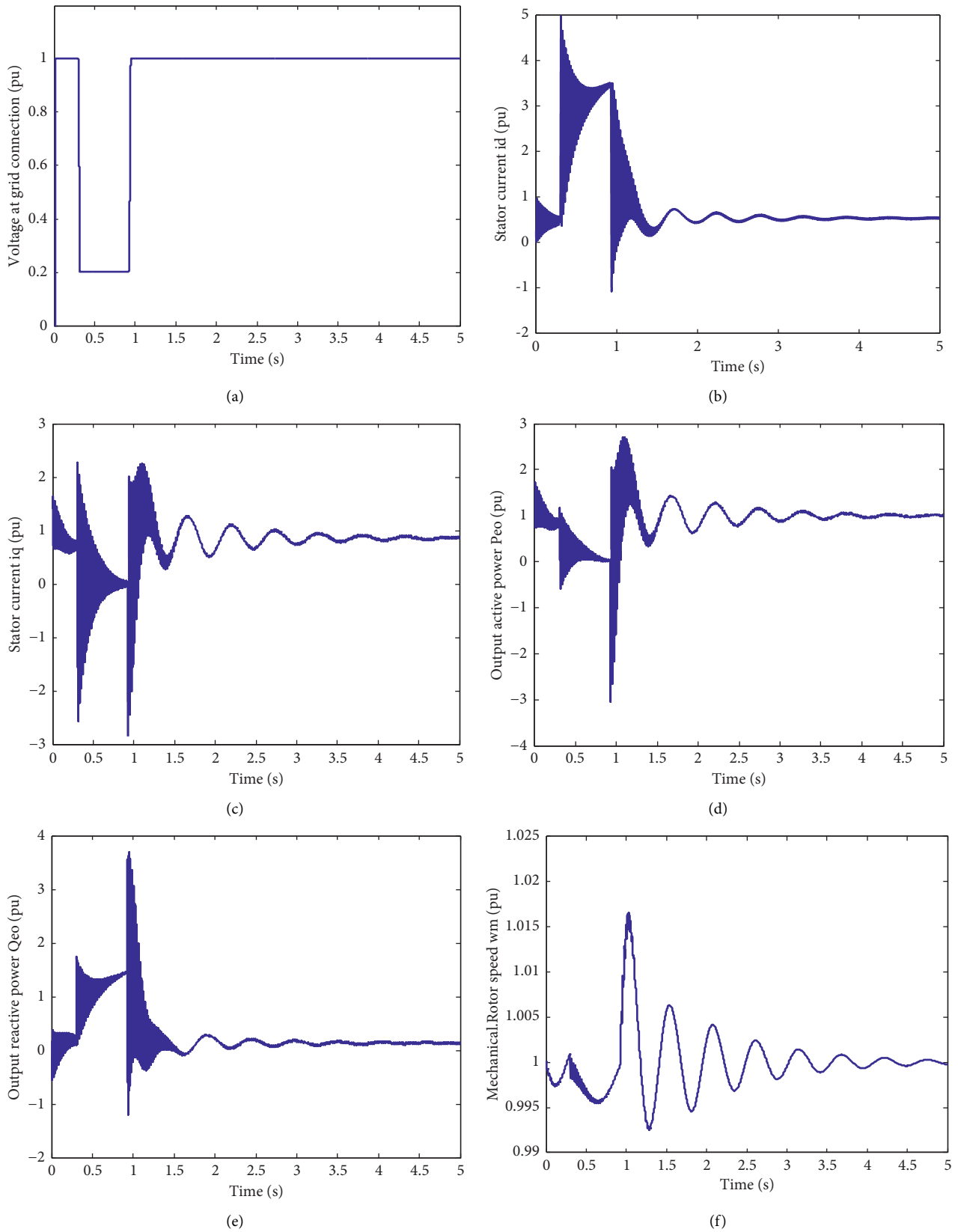

Figure 4: Fault ride through characteristics of FESRWT under three-phase symmetrical short-circuit fault. (a) Voltage at grid connection. (b) d-axis component of stator current. (c) q-axis component of stator current. (d) Output active power. (e) Output reactive power. (f) Mechanical rotor speed.

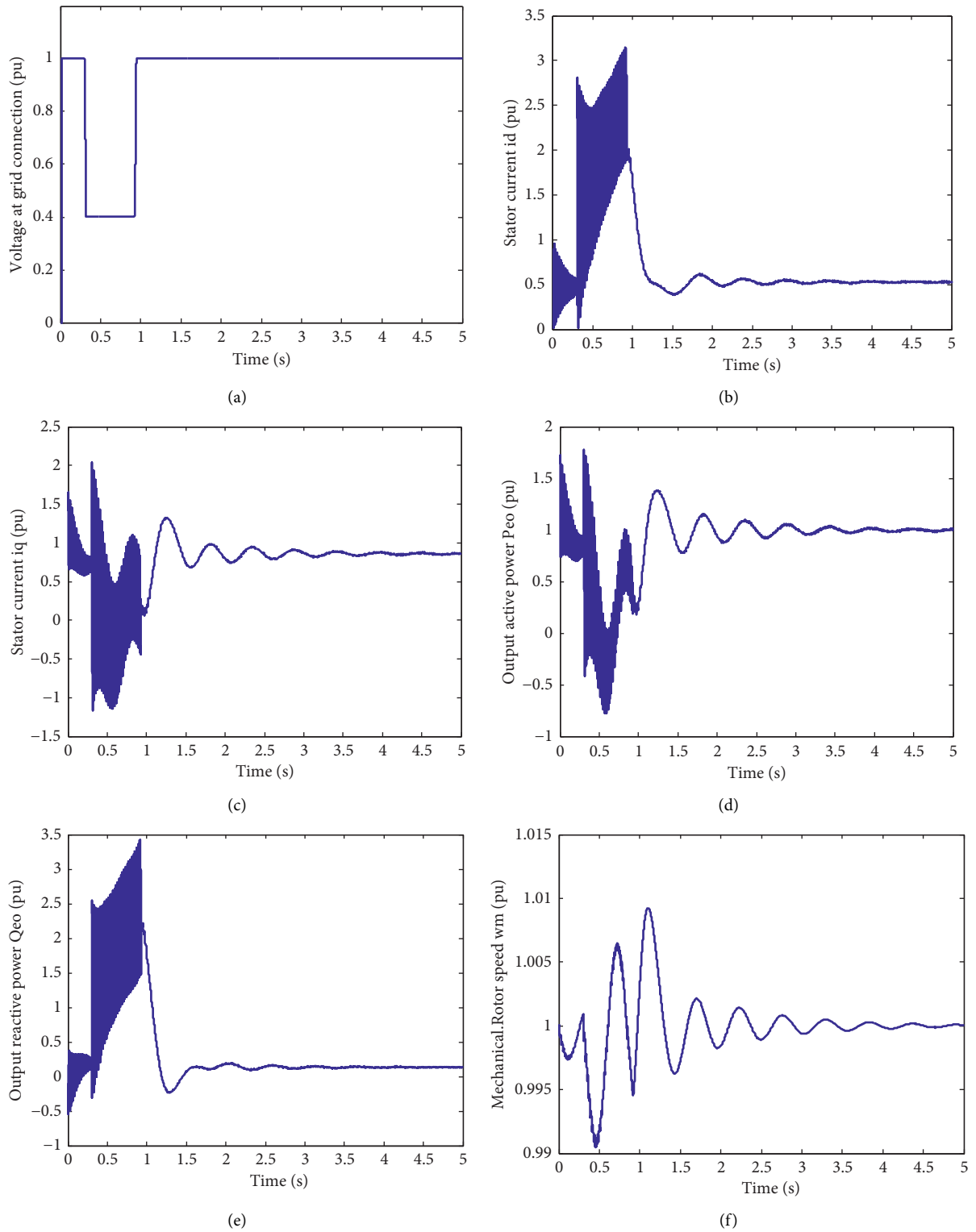

Figure 5: Continued.

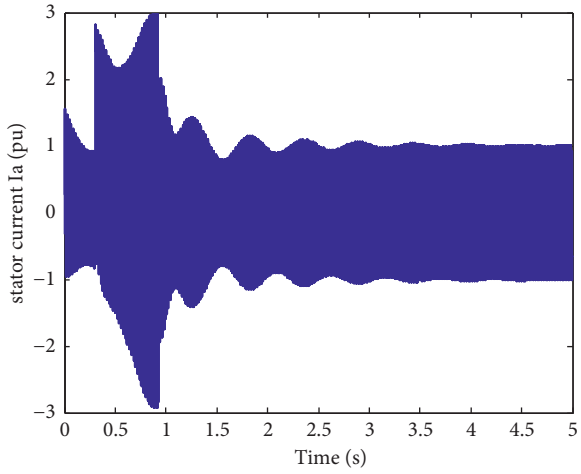

(g)

Figure 5: Fault ride through characteristics of FESRWT during single-phase ground fault. (a) Voltage at grid connection. (b) d-axis component of stator current. (c) q-axis component of stator current. (d) Output active power. (e) Output reactive power. (f) Mechanical rotor speed. (g) Stator current Ia.

stator increases, the oscillation amplitude and transition time of active power generated by the generator and rotor speed are shortened. The generated reactive power is greatly increased. It is realized that wind turbines can operate without off-grid when a single-phase grounding short-circuit fault occurs.

6. Conclusion

Combined with the characteristics of FESRWT, this paper analyzes the transient characteristics of d-axis and q-axis components of stator current, active power, reactive power, and rotor speed of EESG in case of power grid fault, and a fault ride through method for the synergetic control of excitation system is proposed. The simulation verification is carried out in the case of three-phase symmetrical short circuit and single-phase grounding short circuit, respectively. The simulation results show that the synergetic control strategy proposed in this paper can greatly increase the fault ride through capability of FESRWT, and the control effect is better than that of the robust control method used in the existing reference.

This paper mainly studies the fault ride through control of FESRWT and has achieved certain results, but there are still some problems that have not been deeply understood and studied, which need to be considered and improved: (1) more detailed analysis and more accurate modeling of the excitation system of synchronous generator and (2) further optimization of synergetic control parameters.

Data Availability

The project research is in progress. The data used in the paper involves the key technologies of the project. In order to maintain competitiveness, the data used will not be disclosed temporarily.

Conflicts of Interest

The authors declare that they have no conflicts of interest.

Acknowledgments

This work was funded by the "Qizhi" Talent Cultivation Project of Lanzhou Institute of Technology (Grant no. 2020QZ-07), the "Kaiwu" Innovation Team Support Project of Lanzhou Institute of Technology (Grant no. 2018KW-04), Innovation Capability Improvement Project of Colleges and Universities In Gansu Pro. (Grant no. 2020A-142), and the Young Scholars Science Foundation of Lanzhou Jiaotong University (Grant no. 2021026).

References

[1] Z. Lingzhi, C. Ning, and H. Hualing, "Key problems and solutions of wind power accommodation," *Automation of Electric Power Systems*, vol. 35, no. 22, pp. 29–35, 2011.

[2] Z. Yingli, Y. Tinglu, X. Yaozhong, H. Feng, and F. Gaofeng, "Problems and measures of power grid accommodating large scale wind power," *Proceedings of the CSEE*, vol. 30, no. 25, pp. 1–9, 2010.

[3] W. Wei, S. Mingdong, and Z. Xiaodong, "Analysis of low voltage ride through technology of doubly fed wind turbine," *Automation of Electric Power Systems*, vol. 31, no. 23, pp. 84–89, 2007.

[4] C. Ruifa, Z. Wu, T. Xiangcun, and G. Shuixiu, "Analysis on low voltage ride-through techniques for wind turbines using doubly-fed induction generator," *Power System Technology*, vol. 33, no. 9, pp. 72–77, 2009.

[5] H. Jiabing and H. Yikang, "Low voltage ride through operation and control of doubly fed induction generator wind turbines," *Automation of Electric Power Systems*, vol. 32, no. 2, pp. 94–97, 2008.

[6] W. Zhanhong, *Research on Low Voltage Ride through Control of Front-End Speed Controlled Wind Turbines*, M.S. thesis,

Dept. Electron. Eng., Lanzhou Jiaotong Univ., Lanzhou, China, 2014.

[7] C. Ningning, D. Haiying, L. Xiaoqing, and L. Hongwei, "Analysis of low voltage ride through technology of doubly fed wind turbine," *Journal of Power System And Automation*, vol. 31, no. 6, pp. 43–49, 2019.

[8] W. Junwei, "Low voltage ride through performance analysis of hydraulic torque converter synchronous wind turbine," *Electric Drive Automation*, vol. 38, no. 3, pp. 1–8, 2016.

[9] H. Amin, *Research on `the Influences of Integration of Wind Farm on Regional Power Grid Stability Containing Front-End Speed Controlled Wind Turbines*, M.S. thesis, Dept. Electron. Eng., Lanzhou Jiaotong Univ., Lanzhou, China, 2016.

[10] Z. Ping, *A Dissertation Submitted in Partial Fulfillment of the Requirements for the Degree of Doctor of Philosophy in Engineering*, Ph.D. dissertation, Dept. Electron. Eng., Huazhong University of Science & Technology, Wuhan, China, 2013.

[11] W. Licheng, Y. Ruifeng, B. Feifei, S. Tapan, and W. Kai, "A distributed inter-phase coordination algorithm for voltage control with unbalanced PV integration in LV system," *IEEE Transactions on Sustainable Energy*, vol. 11, no. 4, pp. 2687–2697, 2020.

[12] W. Licheng, Y. Ruifeng, B. Feifei, and S. Tapan Kumar, "Real-time coordinated voltage control of PV inverters and energy storage for weak networks with high PV penetration," *IEEE Transactions on Power Systems*, vol. 33, no. 3, pp. 3383–3395, 2018.

[13] H. Yu, W. Na, and Z. Keyou, "Simultaneous unknown input and state estimation for the linear system with a rank-deficient distribution matrix," *Mathematical Problems in Engineering*, vol. 2021, no. 12, 11 pages, Article ID 6693690, 2021.

[14] Z. Anwen, *Research on Cooperative Control of Offshore Wind Power System*, M.S. thesis, Dept. Electron. Eng., Nanjing Normal Univ., Nanjing, China, 2018.

[15] D. Jean, G. Kenné, and E. M. Nfah, "Design of nonlinear synergetic controller for transient stabilization enhancement of DFIG in multimachine wind power systems," *Energy Procedia*, vol. 9, no. 3, pp. 93–125, 2016.

[16] Z. Yongzan, S. Ningsai, L. Meilin, and L. Hongwei, "Research on doubly-fed induction generators synergetic control strategy and stability technology for high/low voltage ride through," *Power System Technology*, vol. 45, no. 1, pp. 39–48, 2021.

[17] N. Yixin, *Theory and Analysis of Dynamic Power System*pp. 1–59, Tsinghua University Press, Beijing, China, 1st edition, 2002.

[18] L. Qiagn, M. Shengwei, and S. Yuanzhang, *Nonlinear Control of Power System*, pp. 213–224, Tsinghua University Press, 2nded, Beijing, China, 2008.

[19] Y. Qun, *Matlab/Simulink Power System Modeling and Simulation*pp. 108–115, Machinery Industry Press, Beijing, China, 1st edition, 2011.

[20] N. Mingzhe, *Research on Asynchronous Motor Control Strategy Based on Cooperative Theory*, M. S. thesis, Dept. Electron. Eng., Southwest Jiaotong Univ., Chengdu, China, 2017.

[21] A. Ardjal, M. Bettayeb, R. Mansouri et al., "Nonlinear synergetic control approach for dc-link voltage regulator of wind turbine DFIG connected to the grid," in *Proceedings of the 2018 5th International Conference on Renewable Energy: Generation and Applications (ICREGA)*, Al Ain, United Arab Emirates, February 2018.

[22] L. Chunli, L. Qiang, and W. Kai, "State-of-charge estimation and remaining useful life prediction of supercapacitors," *Renewable and Sustainable Energy Reviews*, vol. 150, Article ID 111408, 2021.

[23] W. Kai, L. Chunli, S. Jianrui et al., "State of charge estimation of composite energy storage systems with supercapacitors and lithium batteries," *Complexity*, vol. 2021, Article ID 8816250, 15 pages, 2021.

[24] X. Keming, *Fundamentals of Modern Control Theory*, Beijing University of Technology Press, Beijing, China, 1st edition, 2000.

Hindawi
Mathematical Problems in Engineering
Volume 2022, Article ID 9645892, 8 pages
https://doi.org/10.1155/2022/9645892

Research Article

Data-Driven ICA-Bi-LSTM-Combined Lithium Battery SOH Estimation

Hanlei Sun,[1] **Jianrui Sun**,[2] **Kun Zhao**,[2] **Licheng Wang**,[3] **and Kai Wang**[1]

[1]*School of Electrical Engineering, Weihai Innovation Research Institute, Qingdao University, Qingdao 266000, China*
[2]*Shandong Wide Area Technology Co., Ltd., Dongying 257081, China*
[3]*School of Information Engineering, Zhejiang University of Technology, Hangzhou 310023, China*

Correspondence should be addressed to Kai Wang; wkwj888@163.com

Received 14 January 2022; Revised 26 February 2022; Accepted 9 March 2022; Published 28 March 2022

Academic Editor: Mohammad Yaghoub Abdollahzadeh Jamalabadi

Lithium battery state of health (SOH) is a key parameter to characterize the actual battery life. SOH cannot be directly measured. In order to further improve the accuracy of SOH estimation of lithium batteries, a model combining incremental capacity analysis (ICA) and bidirectional long- and short-term memory (Bi-LSTM) neural networks based on health characteristic parameters is proposed to predict the SOH of lithium-ion batteries. First, the health characteristic parameters are initially selected from the lithium battery charging curve, and the health characteristics are extracted by the Pearson correlation coefficient, including the charging time of constant current, charging time of constant voltage, voltage change rate from 300 s to 1000 s, 200s of voltage per cycle at a time. Second, ICA was used to deeply mine the deep associations related to SOH and the peaks of IC curves and their corresponding voltages were extracted as additional inputs to the model. Then, Bi-LSTM is used to form a combined SOH estimation model through adaptive weighting factors. Finally, the verification is based on the 5th battery parameters of the NASA lithium battery data set. The experimental results show that the proposed combined model reduces the mean square error by 55.17%, 49.28%, and 41.47%, respectively, compared with single models such as BP neural network (BPNN), LSTM, and gated recurrent neural network (GRU).

1. Introduction

With the increasingly serious energy crisis and environmental problems [1–3], the demand for energy is increasing [4]. In order to reduce carbon emissions and fossil energy consumption [5], various industries are actively promoting the development of the energy and power industry [6], such as lithium-ion batteries [7] and supercapacitors [8, 9]. Lithium-ion batteries have become the preferred battery type for electric vehicles, mobile phones, power grids, and other application scenarios due to their high energy density [10], high output voltage, no memory effect, low self-discharge rate, and long service life [11]. However, the aging phenomenon of Li-ion batteries is inevitable, and battery degradation is a complex combination of internal reactions and external environment [12, 13]. The most significant process of external performance is the reduction of battery capacity [14]. As an indicator of battery deterioration, SOH is a key indicator to characterize battery aging. It is generally believed that when SOH is reduced to 70%, the battery reaches the end of its life [15]. Its SOH is not clearly defined [16]. It is generally believed that the SOH of a lithium-ion battery can be calculated by the ratio of the current maximum capacity to the initial capacity. The mathematical formula is as follows:

$$SOH = \frac{C_t}{C_0}. \tag{1}$$

SOH cannot be directly obtained through measurement equipment [17]. Therefore, how to accurately evaluate the battery aging of real vehicles under complex and variable operating conditions has become a core step in battery management [18]. At present, the prediction methods of lithium-ion batteries mainly include model-driven methods

and data-driven methods. The model-driven method is mainly based on the complex internal physical model of the lithium-ion battery [19], which is partially established based on experience and is transformed into a mathematical problem, and the degradation process of the lithium-ion battery is represented by the method of learning modeling [20], such as the Kalman filter method [21] and particle filter method [22]. For example, Wang et al. used the Kalman filter to estimate the SOC of lithium-ion battery energy system [23], Gholizade-Narm and Charkhgard used a square-root unscented Kalman filter to estimate the SOC of lithium-ion batteries [24]. Hua et al. solved simultaneous unknown input and state estimation for the linear system with a rank-deficient distribution matrix using specific recursive steps of the corresponding filters [25, 26].

With the advent of the era of big data, thanks to the powerful computing power and robustness of computers, data-driven machine learning (ML) [27] and deep learning (DL) have increasingly become important tools. For example, Cui et al. reviewed the use of deep learning for real-time prediction of SOC of lithium-ion batteries [28], such as artificial neural network (ANN) [29] and support vector machine (SVM) [30]. For example, Liu et al. used the SVM model to predict the state of health of lithium-ion batteries [31], LSTM, etc. Zhou et al. used LSTM to predict the remaining useful life of supercapacitors [32]. Data-driven machine learning methods have the following characteristics:

(1) There is no need to know too much about the internal mechanism of the target, and it is necessary to extract features that are highly correlated with the results.

(2) General ML and DL need a large amount of data as support. As a method that does not require the establishment of an internal mechanism model, a small amount of data alone cannot support ML for accurate model establishment.

(3) The quality of data is generally considered to be the reason that hinders ML from further improving the prediction accuracy. Due to unavoidable factors in actual measurement, the data are full of noise, which will seriously limit the offline training of ML models.

Among various data-driven methods, neural networks have received extensive attention in the field of battery life prediction due to their advantages of deeply mining nonlinear relationships between data. Among them, the long short-term memory network solves the gradient disappearance and gradient explosion problems of the recurrent neural network (RNN) itself and has achieved relatively good results in the field of battery life prediction, but the generalization ability of the data-driven method of a single model is limited. At the same time, its accuracy and robustness are still not high.

In order to further improve the SOH prediction accuracy of lithium-ion batteries, this study proposes a combined estimation method of ICA-Bi-LSTM based on ICA. Firstly, the health characteristic parameters are extracted from the voltage, current, and time of the battery charging stage by using the Pearson correlation coefficient. Then, the local features of the input parameters are extracted by ICA [16], the local features are transferred to LSTM in a time-series manner, and the ICA-Bi-LSTM fusion model is constructed to deeply mine the potential relationship between healthy features and SOH. The multimodel combined prediction model is constructed by adaptive weights to achieve accurate prediction of lithium battery SOH.

2. Battery Data and Health Feature Extraction

2.1. Battery Data Source. This study uses the NASA lithium battery data set to study the state of health of the battery [33]. Based on the parameters of the 5th, 6th, 7th, and 18th batteries, the influence of battery aging on the internal parameters of the battery at room temperature and 24°C was observed. The main parameters include charging voltage, charging current, and charging time. The charging process of these four sets of batteries includes two stages: constant current charging and constant voltage charging, that is, first charging in the constant current mode of 1.5 A until the rated voltage of 4.2 V is reached and then charging in the constant voltage charge mode until the current drops to 20 mA. The charging voltage and charging current curves of the battery are shown in Figure 1.

2.2. Health Feature Extraction. Among the four groups of batteries in the NASA battery data set, since only one current maximum capacity value is given for each charge-discharge cycle, the extraction of the health features in this study is performed in units of each cycle. On this basis, with B0005 as the example, a lithium-ion battery reaches the end of its life after a total of 166 cycles.

As the aging degree of the battery increases, the maximum capacity of the battery will inevitably decrease. Correspondingly, the constant current charging mode time will decrease and the constant voltage charging time will gradually increase. The temperature of the battery is also an important measure, but since this dataset does not give rigorous battery internal temperature and lacks correlation with capacity fading, temperature features are not collected. In addition, the electrochemical reaction rate and the change of the internal resistance of the battery are considered important indicators to reflect the SOH of the battery, but these two items are not considered due to the lack of measurement devices in practical applications and their poor applicability.

Therefore, the health features to be extracted in this study include constant current charging time T_{im}, constant voltage charging time T_{Vm}, voltage change rate ΔV_t from 300 s to 1000 s, and voltage V_{200} at 200 s.

In order to quantify the degree of correlation between the health features proposed above and the SOH of lithium-ion batteries, the statistical Pearson correlation coefficient was used to calculate the correlation coefficient between each feature and the SOH. Its calculation formula and calculation results are shown in the following formula (Table 1):

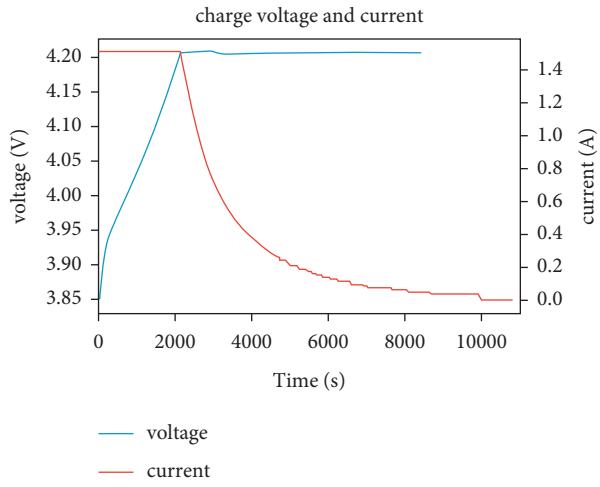

Figure 1: Charge voltage and current.

$$\rho_{xy} = \frac{C_{ov}(X,Y)}{\sqrt{D(X)}\sqrt{D(Y)}} = \frac{E((X-EX)(Y-EY))}{\sqrt{D(X)}\sqrt{D(Y)}}. \quad (2)$$

Among them, E is the mathematical expectation, D is the variance, and the root of D is the standard deviation, $E((X-EX)(Y-EY))$ is called the covariance of random variables X and Y and the difference between the two variables. The quotient of covariance and standard deviation is called the correlation coefficient ρ_{xy} of random variables X and Y.

The larger the absolute value of the Pearson correlation coefficient is, the higher the correlation between the two is. If the correlation coefficient is greater than 0, it means that the feature is positively correlated with the current capacity of the battery and vice versa. The characteristics with the correlation coefficient are greater than 0.95, that is, the charging duration T_{im} of the constant current and the voltage V_{200} at the 200 s time are selected as the input parameters for the SOH prediction of the lithium-ion battery.

3. Incremental Capacity Analysis

ICA deeply excavated and quantitatively analyzed the relationship between the voltage and the capacity of the lithium-ion battery during the charging and discharging process [34]. During the charging process of a lithium-ion battery, the open-circuit voltage (OCV) has a relatively level section during the rising process. In this section, as the charged power increases, the internal voltage of the battery changes slowly, which is called a voltage plateau. This is because the internal chemical reaction of the lithium-ion battery reaches a relatively balanced state during the charging and discharging process. As the number of cycles increases, the voltage plateau gradually shifts upward. As a unique electrochemical phenomenon of lithium-ion batteries, the change of the voltage plateau is very gentle and the amplitude is small, which is not conducive to quantitative analysis. ICA is shown by the following formulas:

Table 1: Pearson correlation coefficient results.

Health indicators	T_{im}	T_{Vm}	ΔV_t	V_{200}
Pearson coefficient	0.959363	−0.354834	0.419258	−0.973505

$$\frac{dQ}{dV} = \frac{Q_t - Q_{t-1}}{V_t - V_{t-1}}, \quad (3)$$

$$Q_t = \int_0^t I\, dt. \quad (4)$$

Among them, Q_t is the electricity at time t, V_t is the voltage at time t, and I_t is the current at time t.

Through the conversion of the above formula, the flat area on the voltage platform curve is converted into the peak point on the capacity increment (IC) curve, that is, the maximum point of the slope of the QV curve, so that the change of the voltage platform can be intuitively reflected, and intuitively, the relationship between the external characteristics of the battery and the chemical reaction characteristics inside the battery is used to predict the battery SOH.

Since the NASA data set does not give the real-time capacity change value of each cycle, in the constant current charging mode, since the current is almost unchanged, the time difference is used to replace the capacity change as shown in the following formulas:

$$\Delta Q = I_t t_t - I_{t-1} t_{t-1} = I\left(t_t - t_{t-1}\right), \quad (5)$$

$$\frac{dQ}{dV} = \frac{t_0 - t_1}{V_t - V_{t-1}}.I. \quad (6)$$

Among them, I is the current constant 1.5 A of the constant current mode.

The grey curve in Figure 2 is the IC curve directly drawn from the original sampling data. It can be seen that the curve is noisy, and the basic characteristics of the curve cannot be directly identified, so the curve needs to be denoised. The Savitzky–Gola (S–G) filter is used here, which is a filtering method based on local polynomial least-squares fitting in the time domain. The biggest feature of this filter is that it can ensure that the shape and width of the signal remain unchanged while filtering out noise improving the smoothness of the curve, and reducing the interference of noise. It varies with the selected window width and can meet different occasions on demand.

After filtering, as shown in the red curve in Figure 2, the curve becomes smooth after noise reduction, and there are three obvious peak points. The last two points can be regarded as a peak point due to the characteristics of the selected lithium-ion battery. Voltage plateau characteristics are converted to IC curves. In this way, the relationship between the external characteristics of the battery and its internal electrochemical characteristics can be established more intuitively.

As shown in Figure 3, the number in the legend represents the number of cycles. It can be seen that with the continuous progress of the cycle, the peak value of the IC curve gradually decreases, and the voltage value corresponding to the peak

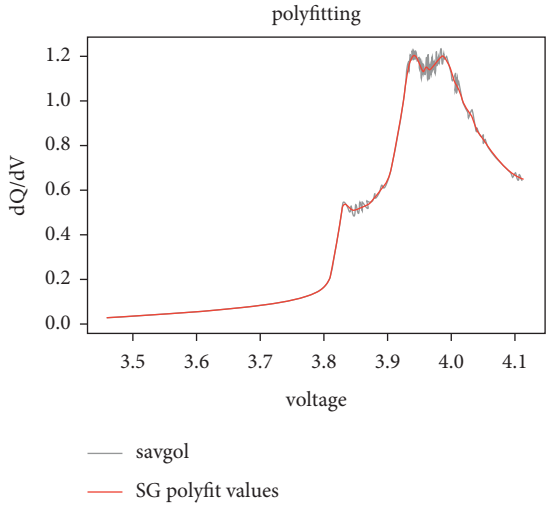

Figure 2: Comparison of IC curve before and after filtering.

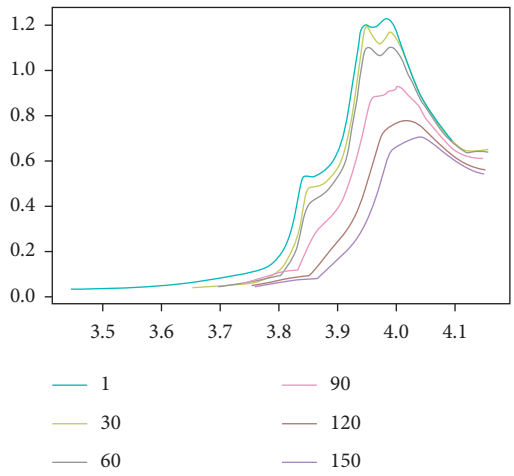

Figure 3: IC curve shift with peak.

point gradually increases. This is because the chemical reaction inside the battery changes due to factors such as active material and lithium-ion loss, resulting in an increase in internal resistance and making the voltage plateau cheaper. Therefore, the change of the peak position and peak amplitude on the IC curve can reflect the process of the decline of the state of health of the battery during the cycle, so as to estimate the SOH of the battery (Table 2).

4. Bi-LSTM Model

LSTM is a type of RNN, which is an improvement over a simple RNN. The parameter learning of the RNN cycle can be learned through the back-propagation algorithm over time, that is, the error is passed forward step by step according to the reverse order of time. When the input sequence is relatively long, the gradient explosion or gradient disappearance problem will occur, which is also called the long-term dependency problem. To address this issue, gating mechanisms are introduced to improve recurrent neural networks, namely, LSTM and GRU.

Table 2: Correlation analysis of IC curve characteristics.

Health indicators	dQ/dV_max	dQ/dV_voltage
Pearson coefficient	0.992277	−0.966454

Figure 4 shows the detailed internal structure of LSTM, in which LSTM has three special network structures called "gates" [35]. The overall combined LSTM structure can more effectively determine the forgetting or retention of information, specifically, as follows:

Forgetting Gate (f_t). The forgetting gate will jointly decide which part of the memory needs to be forgotten according to the current input x_t, the state C_{t-1} at the last moment, and the output h_{t-1} at the last moment. The mathematical formula is as follows:

$$f_t = \sigma_g\left(W_f x_t + U h_{t-1} + b_f\right). \tag{7}$$

Among them, W_f represents the input matrix of the forget gate at the current moment, U represents the output matrix of the previous moment, b_f represents the bias unit, and σ_g represents the sigmoid activation function.

Input Gate (i_t). After the work of the forget gate is over, some information is deleted and the input gate determines which memories will enter the current state C_t according to x_t, C_{t-1}, h_{t-1}. The mathematical formula is as follows:

$$i_t = \sigma_g\left(W_i x_t + U h_{t-1} + b_i\right). \tag{8}$$

Output Gate (o_t): After the new state C_t is calculated, the output of the current moment is generated through the output gate according to x_t, C_{t-1}, h_{t-1}. The mathematical formula is as follows:

$$o_t = \sigma_g\left(W_o x_t + U h_{t-1} + b_o\right). \tag{9}$$

So far, the current state C_t and output h_t can be obtained through the overall structure of LSTM. The mathematical formula is as follows:

$$\begin{aligned} C_t &= f_t {}^* C_{t-1} + i_t {}^* \sigma_c\left(W_c + U h_{t-1} + b_c\right), \\ h_t &= o_t {}^* \sigma_c\left(C_t\right). \end{aligned} \tag{10}$$

Among them, σ_c represents the tanh activation function and $*$ represents the star multiplication, which is the point-to-point multiplication between matrices.

Based on LSTM, Bi-LSTM is a variant that performs better in many tasks. Since LSTM is particularly dependent on order or time, disrupting the time step or reversing the time step will completely change the features that LSTM extracts from the learned column, Therefore, Bi-LSTM takes advantage of the sensitivity of LSTM to sequence order and combines two ordinary LSTMs of positive and negative time series to form a bidirectional LSTM network. This makes it possible to deeply mine the correlation between the characteristics of Li-ion batteries and their SOH from two sequence directions. Bi-LSTM can capture the information that may be ignored by the one-way network.

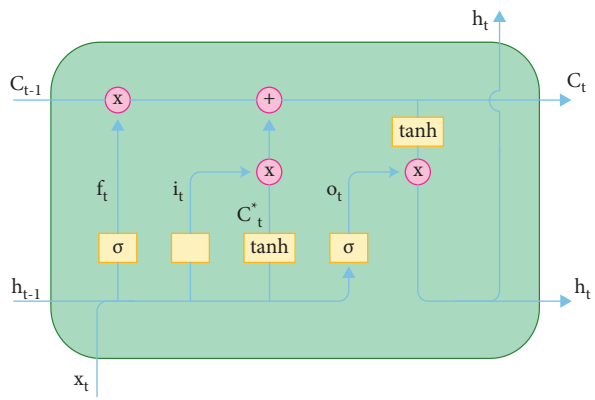

Figure 4: LSTM structure.

5. Li-Ion Battery SOH Estimation

5.1. Data Processing. In the process of measuring and collecting battery data, due to the influence of noise from uncontrollable factors such as environmental measurement equipment, the measured data will inevitably have abnormal values. Therefore, in order to improve the accuracy of the proposed combined model, the Boxplot method is used to select abnormal data to further improve the potential correlation of the data [36]. Among them, the outliers are determined by quartile and interquartile range, and the data less than $Q_1 - 1.5I_{QR}$ and greater than $Q_3 + 1.5I_{QR}$ are set as abnormal data, as shown in the following formula:

$$\left(D_{low}, D_{high}\right) = \left(Q_1 - 1.5I_{QR}, Q_3 + 1.5I_{QR}\right). \tag{11}$$

Among them, D_{low} and D_{high} are the lower and upper boundaries of abnormal data, respectively, Q_1 and Q_3 are the first and third quantiles of battery data, respectively, and I_{QR} is the interquartile range. Using this formula, combined with the above method of determining outliers, delete abnormal data to improve data quality.

In the deep learning algorithm, the dimensions of each battery health feature are different [34], which will lead to a surge in the calculation amount and gradient explosion in the fitting process [35]. In order to improve the convergence speed and model accuracy of the model, Z-score standardization is adopted. The mean and standard deviation of the original data were used to standardize the data [37]. The processed data conform to the standard normal distribution, that is, the mean is 0 and the standard deviation is 1, as shown in the following formula:

$$y = \frac{x - \mu}{\sigma}. \tag{12}$$

Among them, x and y correspond to the data before and after normalization, μ represents the mean of the original data, and σ represents the standard deviation of the original data. The processed data are all distributed around 0, the magnitude of the data decreases rapidly, and the values are relatively close, which is more conducive to the progress of deep learning.

5.2. SOH Estimation Method. The overall estimation process of SOH is shown in Figure 5. First, the abnormal data of the battery charging voltage, charging current, and battery charging and discharging time are screened and eliminated; meanwhile, the IC curve is extracted for capacity increment analysis, and relevant features are extracted. At the same time, the health feature parameters are extracted by the Pearson correlation coefficient and normalized. Then, all the normalized lithium-ion battery features are used as input to the Bi-LSTM network for model fitting, and the output results are added first through the adaptive weight module to finally realize the SOH estimation.

5.3. Case Analysis. In order to verify the feasibility of the proposed ICA-Bi-LSTM combination model for improving the SOH estimation accuracy of lithium-ion batteries, the B0005 battery data set of the NSA data set was used as the simulation data. The B5 battery was cycled 166 times, and the first 140 cycles of the battery were used. The periodic data are used as the training set, and the last 21 groups are used as the test set (5 of which have been proposed as garbage data). The parameters of Bi-LSTM are set as follows: the time step of the input layer is 1, the data dimension is 4, the number of neurons in the hidden layer is 64, the maximum number of training is 175, dropout is added as a regularization method, and its parameters are set to 0.2. In the comparison experimental group, L1 and L2 are added to BPNN as regularization methods, and the parameters are set to 0.1. LSTM and GRU also add a Dropout layer as a Regularization method, and the parameter is also 0.2. Finally, for all the methods mentioned above, the neural network learning rate is set to 0.001 [36]. In the python simulation environment, BP neural network, LSTM, GRU, and ICA-Bi-LSTM are used to predict the SOH of lithium-ion batteries, and the results are shown in Figure 6. The error of the training set is the mean square error (MSE) between the predicted value of the battery capacity and the actual value, as shown in the following formula:

$$MSE = \frac{1}{M}\sum_{m=1}^{M}\left(y_m - y_0\right)^2. \tag{13}$$

From the analysis and comparison in Figure 6, it can be seen that after the learning and training of the above four algorithms, compared with the traditional BPNN, LSTM, and GRU, the combined model of multidepth mining features such as ICA-Bi-LSTM and bidirectional LSTM has quite high accuracy, and it has a strong generalization ability for the test set. Although the minimum value of MSE does not have much advantage compared to the minimum value of other models, its smooth error like a straight line makes the model very good in practical engineering applications. In terms of stability and refitting speed, the advantages of bidirectional LSTM are highlighted in that compared with other models, it can complete the fast fitting process while ensuring considerable accuracy, and both fitting efficiency and fitting accuracy have been exactly guaranteed.

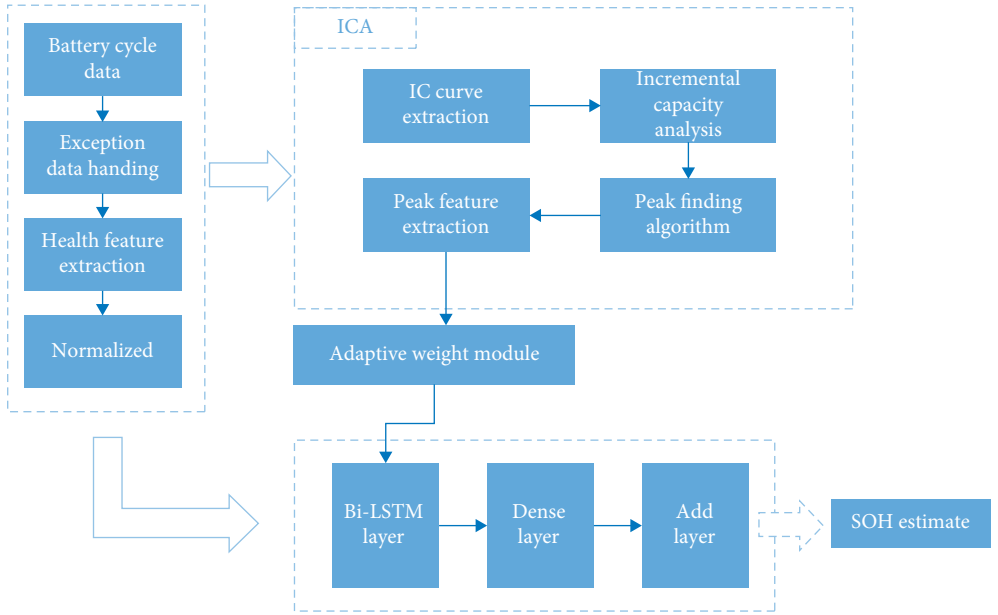

Figure 5: ICA-Bi-LSTM model construction process.

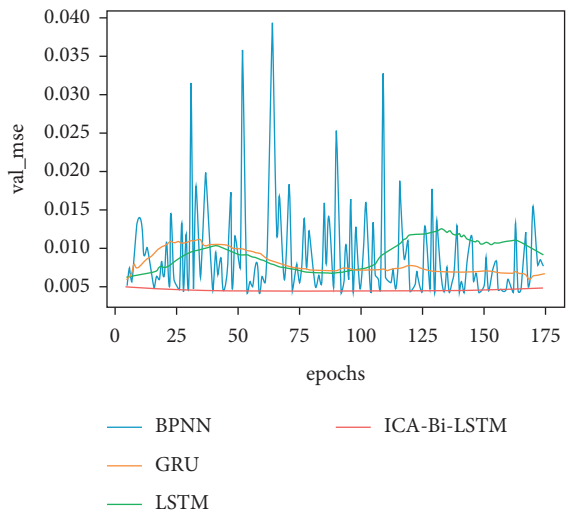

Figure 6: Comparison of multimodel test set prediction results.

Table 3: Comparison of multimodel test set prediction results.

Model	BPNN	LSTM	GRU	ICA-Bi-LSTM
Average Train_MSE	0.0092094	0.0085493	0.0073294	0.0032103
Average Train_MSE + regularize	0.0087362	0.0080372	0.0076837	0.0029074
Average VAL_MSE	0.0159374	0.0103984	0.0079732	0.0050012
Average VAL_MSE + regularize	0.0101514	0.0089733	0.0077760	0.0045510

From Table 3, we can quantify the average MSE of the training set and the average MSE of the validation set in the SOH prediction process of lithium-ion batteries for the four models. The fitting phenomenon is mainly caused by the scale of the data. After comprehensively considering the training set and the validation set MSE, ICA-Bi-LSTM still has significant advantages. Compared with the BPNN model, the accuracy of the ICA-Bi-LSTM model is improved by 55.17%, the accuracy of the LSTM model is increased by 49.28%, and the accuracy of the GRU model is increased by 41.47%. Therefore, through the comparative analysis, it can be seen that the prediction method of ICA-Bi-LSTM mentioned by the knowledge has higher prediction efficiency and accuracy.

Data Availability

The data used to support the findings of this study are available from the corresponding author upon request.

Conflicts of Interest

The authors declare that they have no conflicts of interest.

Authors' Contributions

H. S. performed most of the experiments and conceived the project. K. W. and Y. Z. supervised the work. All the authors contributed to the writing of the manuscript.

Acknowledgments

This work was supported by the Youth Fund of Shandong Natural Science Foundation (no. ZR2020QE212), Key Projects of Shandong Natural Science Foundation (no. ZR2020KF020), Shandong Natural Science Foundation (no. ZR201911140024), Shandong Natural Science Foundation (no. ZR2020MF068), and National Natural Science Foundation of China (no. 52007170).

References

[1] D. Yuan, C. Zhang, S. Tang et al., "Ferric ion-ascorbic acid complex catalyzed calcium peroxide for organic wastewater treatment: o," *Chinese Chemical Letters*, vol. 32, no. 11, pp. 3387–3392, 2021.

[2] X.-X. Wang, G.-F. Yu, J. Zhang, M. Yu, S. Ramakrishna, and Y.-Z. Long, "Conductive polymer ultrafine fibers via electrospinning: p," *Progress in Materials Science*, vol. 115, p. 100704, 2021.

[3] Y. Fu, Y. Hou, Z. Wang, X. Wu, K. Gao, and L. Wang, "Distributed scheduling problems in intelligent manufacturing systems," *Tsinghua Science and Technology*, vol. 26, no. 5, pp. 625–645, 2021.

[4] H. Xu, H. Du, L. Kang, Q. Cheng, D. Feng, and S. Xia, "Constructing straight pores and improving mechanical properties of GangueBased porous ceramics," *Journal of Renewable Materials*, vol. 9, no. 12, pp. 2129–2141, 2021.

[5] L. Kang, H. Du, J. Deng, X. Jing, S. Zhang, and Y. Znang, "Synthesis and catalytic performance of a new V-doped CeO2-supported ap," *Journal of Wuhan University of Technology-Materials Science Edition*, vol. 36, no. 2, pp. 209–214, 2021.

[6] W. L. Wang, J. B. Pang, J. Su et al., "Applications of nanogenerators for biomedical engineering and healthcare systems [J]," *Infomat*, vol. 4, no. 2, p. e12262, 2022.

[7] K. Wang, W. Wang, L. Wang, and L. Li, "An improved SOC control strategy for electric vehicle hybrid energy storage systems," *Energies*, vol. 13, no. 20, p. 5297, 2020.

[8] C. Liu, Y. Zhang, J. Sun, Z. Cui, and K. Wang, "Stacked bidirectional LSTM RNN to evaluate the remaining useful life of supercapacitor," *International Journal of Energy Research*, vol. 46, no. 3, pp. 3034–3043, 2022.

[9] Y. Zhou, Y. Wang, K. Wang et al., "Hybrid genetic algorithm method for efficient and robust evaluation of remaining useful life of supercapacitors," *Applied Energy*, vol. 260, p. 114169, 2020.

[10] X. Feng, Q. Li, and K. Wang, "Waste ptn using recycled plastic bags for power generation," *ACS Applied Materials & Interfaces*, vol. 13, no. 1, pp. 400–410, 2021.

[11] J. Li, H. Meng, Z. Pi, B. Wang, and B. Lv, "Application status and development trends of the lithium pprimary batteries[J]," *Chinese Journal of Power Sources*, vol. 42, no. 5, pp. 725–727, 2018.

[12] H. Ran, H. Du, C. Ma, Y. Zhao, D. Feng, and H. Xu, "Effects of A/B-site Co-doping on microstructure and dielectric thermal stability of AgNbO3," *Science of Advanced Materials*, vol. 13, no. 5, pp. 741–747, 2021.

[13] D. Z. Li, L. C. Wang, C. X. Duan, Q. Li, and L. Wang, "Temperature prediction of lithium-ion batteries based on electrochemical impedance spectrum: a review," *International Journal of Energy Research*, Article ID. 17349022, 2022.

[14] C. Y. Ma, H. L. Du, J. Liu et al., "High-temperature stability of dielectric and energy-storage properties of weakly-coupled relaxor (1-x)$BaTiO_3$-xBi(Y1/3Ti1/2)O_3 ceramics[J]," *Ceramics International*, vol. 47, no. 17, pp. 25029–25036, 2021.

[15] J. C. Zhao, F. J. Li, Z. L. Wang, P. Dong, G. T. Xia, and K. Wang, "Flexible PVDF nanogenerator-driven motion sensors for human body motion energy tracking and monitoring[J]," *Journal of Materials Science: Materials in Electronics*, vol. 32, no. 11, pp. 14715–14727, 2021.

[16] J. Tian, R. Xiong, and Q. Yu, "Fractional-order model-based incremental capacity analysis for degradation state recognition of lithium-ion batteries," *IEEE Transactions on Industrial Electronics*, vol. 66, no. 2, pp. 1576–1584, 2019.

[17] F. Zhang, Z. Li, Q. Xia et al., "Li-ionic control of magnetism through spin capacitance and conversion," *Matter*, vol. 4, no. 11, pp. 3605–3620, 2021.

[18] Y. Fu, H. Wang, G. Tian, Z. Li, and H. Hu, "Two-agent stochastic flow shop deteriorating scheduling via a hybrid multi-objective evolutionary algorithm," *Journal of Intelligent Manufacturing*, vol. 30, no. 5, pp. 2257–2272, 2019.

[19] C. Duan, K. Liang, Z. Zhang et al., "Recent advances in the synthesis of nanoscale hierarchically porous metal–organic frameworks [J]," *Nano Materials Science*, pp. 1–10, 2022.

[20] C. Duan, K. Liang, J. Lin et al., "Application of hierarchically porous metal-organic frameworks in heterogeneous catalysis: a review," *Science China Materials*, vol. 65, no. 2, pp. 298–320, 2022.

[21] D. Z. Li, S. Li, B. Zhang, J. R. Sun, L. C. Wang, and K. Wang, "Aging state prediction for supercapacitors based on heuristic kalman filter optimization extreme learning machine," *Energy*, vol. 250, Article ID 123773, 2022.

[22] R. Xiong, Y. Zhang, H. He, X. Zhou, and M. G. Pecht, "A double-scale, particle-filtering, energy state prediction algorithm for lithium-ion batteries," *IEEE Transactions on Industrial Electronics*, vol. 65, no. 2, pp. 1526–1538, 2018.

[23] K. Wang, C. L. Liu, J. R. Sun et al., "State of charge estimation of composite energy storage systems with supercapacitors and lithium batteries," *Complexity*, vol. 2021, p. 8816250, 2021.

[24] H. Gholizade-Narm and M. Charkhgard, "Lithium-ion battery state of charge estimation based on square-root unscented kalman filter[J]," *IET Power Electronics*, vol. 6, no. 9, pp. 1833–1841, 2013.

[25] Y. Hua, N. Wang, K. Zhao, and J. Song, "Simultaneous Unknown input and state estimation for the linear system with a rank-deficient distribution matrix[J]," *Mathematical Problems in Engineering*, vol. 2021, p. 6693690, 2021.

[26] M. Zhang, K. Wang, and Y. T. Zhou, "Online state of charge estimation of lithium-ion cells using particle filter-based

hybrid filtering approach[J]," *Complexity*, vol. 2020, p. 8231243, 2020.

[27] Y. Fu, M. Zhou, X. Guo, and L. Qi, "Scheduling dual-objective stochastic hybrid flow shop with deteriorating jobs via Bi-population evolutionary algorithm," *IEEE Transactions on Systems, Man, and Cybernetics: Systems*, vol. 50, no. 12, pp. 5037–5048, 2020.

[28] Z. H. Cui, L. C. Wang, Q. Li, and K. Wang, "A comprehensive review on the state of charge estimation for lithium-ion battery based on neural network[J]," *International Journal of Energy Research*, vol. 46, no. 5, pp. 5423–5440, 2022.

[29] A. G. Kashkooli, H. Fathiannasab, Z. Mao, and Z. Chen, "Application of artificial intelligence to state-of-charge and state-of-health estimation of calendar-aged lithium-ion pouch cells," *Journal of the Electrochemical Society*, vol. 166, no. 4, pp. A605–A615, 2019.

[30] J. C. Alvarez Anton, P. J. Garcia Nieto, C. Blanco Viejo, and J. A. Vilan Vilan, "Support vector machines used to estimate the battery state of charge," *IEEE Transactions on Power Electronics*, vol. 28, no. 12, pp. 5919–5926, 2013.

[31] C. Liu, Q. Li, and K. Wang, "State-of-charge estimation and remaining useful life prediction of supercapacitors," *Renewable and Sustainable Energy Reviews*, vol. 150, p. 111408, 2021.

[32] Y. Zhou, Y. Huang, J. Pang, and K. Wang, "Remaining useful life prediction for supercapacitor based on long short-term memory neural network," *Journal of Power Sources*, vol. 440, p. 227149, 2019.

[33] X. Tang, C. Zou, K. Yao et al., "A fast estimation algorithm for lithium-ion battery state of health," *Journal of Power Sources*, vol. 396, pp. 453–458, 2018.

[34] X. Li, C. Yuan, and Z. Wang, "State of health estimation for Li-ion battery via partial incremental capacity analysis based on support vector regression," *Energy*, vol. 203, p. 117852, 2020.

[35] K. Park, Y. Choi, W. J. Choi, H.-Y. Ryu, and H. Kim, "LSTM-based battery remaining useful life prediction with multi-channel charging profiles," *IEEE Access*, vol. 8, pp. 20786–20798, 2020.

[36] M. B. Adam, B. I. Babura, and K. Gopal, "Range-box plotting relating to discrete distribution," *Matematika*, vol. 34, no. 2, pp. 187–204, 2018.

[37] Q. Li, D. Li, K. Zhao, L. Wang, and K. Wang, "State of health estimation of lithium-ion battery based on improved ant lion optimization and support vector regression," *Journal of Energy Storage*, vol. 50, p. 104215, 2022.

Hindawi
Mathematical Problems in Engineering
Volume 2022, Article ID 8998922, 16 pages
https://doi.org/10.1155/2022/8998922

Research Article

Modeling of Strong Wind-Sand Dielectric Streamer Discharge

Yongqiang Kang, Zhipeng Shi, and Shuaibing Li

School of New Energy & Power Engineering, Lanzhou Jiaotong University, Lanzhou, China

Correspondence should be addressed to Shuaibing Li; shuaibingli@mail.lzjtu.cn

Received 21 January 2022; Accepted 9 February 2022; Published 8 March 2022

Academic Editor: Licheng Wang

Due to the complex and harsh climate environment in Northwest China, the external insulation of power lines and high-speed train are exposed to strong wind-sand environment all year round, which brings severe challenges to the external insulation design and protection of the electric systems. Based on the theories of streamer discharge, the plate-plate electrode was taken as the analysis object, and a theoretical physical model of the strong wind-sand dielectric discharge is established. In this model, the analytical expressions of electron ionization coefficient and positive ion generation coefficient in a wind-sand environment are deduced considering the combined effects of the airflow velocity, the distortion of the electric field caused by sand particles, and the electrons captured by sand particles in the discharge process; furthermore, the streamer breakdown criterion in wind-sand environment is proposed. Research results can provide an important theoretical basis for the quantitative calculation of the breakdown voltage and the external insulation protection in a strong wind-sand environment.

1. Introduction

In recent years, the power system has developed rapidly, which is the energy foundation support for the stable and rapid development of the country [1, 2]. However, the external insulation of transmission lines in Northwest China is exposed to the sandstorm environment for a long time, which is easy to cause abnormal flashover of the outdoor insulators and pose a serious threat to the safety and reliability of the external insulation for the northwest power grid [3, 4]. In addition, the strong wind-sand environment caused by the high-speed train from Lanzhou to Xinjiang running in the northwest region of China is the key factor to induce the abnormal breakdown or flashover of the external insulation of the train, which poses a serious threat to the safe operation of the train [5–7]. Therefore, the investigations of gas discharge characteristics and dielectric breakdown model in strong wind-sand environment are of great significance for external insulation design, insulation coordination, and insulation protection of the electric system.

Recently, researchers have performed a lot of research on gas discharge characteristics in wind-sand or airflow environment. In the area of air gap breakdown in wind-sand environment, He et al. [8] found that the breakdown voltage of the plate-plate gap in a wind-sand environment is related to the wind speed, gap distance, and sand concentration. Under the condition of pure airflow, the breakdown voltage increases with the increase of wind speed. At fixed wind speed, the breakdown voltage decreases with the increase of sand concentration, but the breakdown voltage-gap distance curve is lower than that under pure airflow. The simulation results show that the distortion of the local electric field caused by sand particles reduces the breakdown voltage. For the discharge of the needle-plate gap and in a wind-sand environment, [9] found that, with the increase of wind speed, the change trend of breakdown voltage in needle-plate gap increases first and then decreases. The experimental results of [10] showed that the breakdown voltage of rod-rod gaps decreases with increasing wind speed in both wind-sand and pure airflow environments, and the variation trends of the breakdown voltage with wind speed are the same under these two conditions. Ai Arainy et al. [11–14] also found that the breakdown voltage of rod-rod and rod-plate gaps in a sand dust environment is related to the gap distance, polarity of the impulse voltage, shape of the electrodes, and size of the sand particles. The above research

shows that the influence of wind and sand dust on gap breakdown voltage is closely related to electrode structure, voltage type, airflow velocity, sand dust concentration, and sand particles size. Besides, the distortion of the local electric field caused by sand particles is an important factor affecting gap discharge characteristics.

In the area of insulation flashover in a wind-sand and airflow environment, Sima et al. [15] studied the effects of wind speed, charge deposited on sand, and sand quality in flashover process. The results show that the flashover voltage of insulators increases with the increase of wind speed, and the flashover voltage in wind-and-sand condition is lower than that in wind-and-no-sand condition. The distortion of the electric field caused by sand particles is the main reason for this phenomenon. Some researchers have also studied the influence of wind speed on flashover path and discharge patterns of insulators in a wind-sand environment [16, 17]. Additionally, charged sand dust will also have an important impact on insulator flashover process. Yu et al. [18] found that charged sand particles will lead to the decrease of insulator flashover voltage, and the decrease degree increases obviously with the increase of charge amount of sand particles.

In the area of gas-solid or gas-liquid two-phase discharge, Marquard et al. [19] found that the influence of particles on corona discharge is related to the particle concentration. When the particle concentration is high, the corona starting voltage increases and the corona current decreases. By studying the corona discharge current density of gas-solid two-phase medium with micron particles, Xu et al. [20, 21] concluded that particles reduce the corona current, and, with the decrease of particle size, its influence on the corona current is more significant; that is, the smaller size of particles and higher concentration particles are easier to restrain the discharge process. The experimental results of Yao et al. [22] also show that the size of particles under DC voltage plays a decisive role in the breakdown voltage and the choice of breakdown path of two-phase mixture. Li et al. [23] carried out numerical simulation of rod-plate gap streamer discharge in 50~50% SF_6/N_2 gas mixtures based on ETG-FCT method and extended ETG scheme to gas discharge problems. Based on the above research results, it can be concluded that the main factor affecting the discharge of solid/liquid particles is the serious distortion of the local electric field in the mixture. Therefore, solving the local electric field in the mixture has become an important content to analyse its influence on the discharge process. In this regard, Ye et al. [24–26] have proposed the calculation methods of local electric field in the mixture such as dipole-enhanced model and displaced dipole model and presented a dielectric breakdown model for static gas-solid two-phase mixture, but the model did not consider the influence of airflow on discharge. Kang et al. [27–29] found that the flowing gases have a significant impact on the discharge process. The frequent collision between gas molecules and electrons or ions causes the change of discharge path and space charge, and the gas discharge model in the flowing gases environment was established. Guo et al. [30] improved a two-dimensional numerical model by considering the effect of wind velocity and wind direction on the movement of the corona charges. However, the dielectric breakdown process in strong wind-sand environment is the comprehensive effects of airflow and sand particles. How to obtain the correlation between the discharge parameters and the comprehensive effects of airflow or sand dust is the key to establish the dielectric breakdown model of strong wind-sand environment.

In this work, on the basis of streamer discharge theory, we attempt to present a theoretical model of strong wind-sand dielectric discharge considering the combined effects of airflow and sand particles on the discharge process, and the breakdown criterion for strong wind-sand dielectric discharge is obtained, which can realize the quantitative calculation and effective prediction of the breakdown voltage in a strong wind-sand environment.

2. Model of Strong Wind-Sand Dielectric Streamer Discharge

2.1. Basic Preconditions. Compared with Townsend's discharge theory, streamer discharge theory is more suitable for higher *pd* value conditions and considers the significant role of space charge in the discharge process, which is more suitable for the construction of discharge model under the strong wind-sand condition. According to the streamer discharge theory, establishing the relationship between airflow or sand particle and ionization coefficient and space charge (positive ion generation coefficient) is the key to establish the model of strong wind-sand dielectric discharge based on the streamer discharge theory.

First, in order to describe the effect of airflow or sand particles on discharge process, we put forward the basic preconditions for the modeling of strong wind-sand dielectric discharge. Previous studies have shown that the deflection of discharge path, the blowing away of some electrons and ions, the change in gas density, distorting the electric field, and the capture of charge caused by sand particles are the main factors affecting dielectric discharge process in strong wind-sand environment. Therefore, the basic preconditions for the effects of airflow or sand particles on discharge process are presented as follows [27, 31]:

(1) The discharge path deflects an angle along the gas flow direction, that is, the motion path of electrons and ions participating in the discharge deflects an angle along the gas flow direction

(2) Some electrons and ions are blown away by the gas flow, including the electrons and ions completely blown away and deviated from the main discharge path

(3) Gas is a compressible fluid; that is, the gas density decreases with the increase of gas flow velocity

(4) The sand particles are spheres of the same size and are evenly distributed in the electrode space

(5) An equivalent electric field is used instead of the original electric field to consider the interaction among sand particles

(6) During the discharge process, the sand particles capture some electrons or ions for charging

Based on the above six preconditions, streamer discharge in strong wind-sand environment with horizontal airflow velocity and short gap in uniform electric field can be described as a physical process shown in Figure 1.

In order to explain clearly the modeling thinking of this paper, the modeling process of strong wind-sand dielectric streamer discharge is shown in Figure 2.

The parameters defined in this paper are shown in Table 1.

2.2. Calculation of Electron Ionization Coefficient and Positive Ion Generation Coefficient. On the basis of the above preconditions, the Townsend ionization coefficient and positive ion generation coefficient will be solved step by step from the four following aspects.

2.2.1. Local Electric Field of Sand Particles. The local electric field near one sand particle is not only affected by the self-polarization of the sand particles but also affected by other sand particles. For the interaction between sand particles, the dipole-enhanced model is used to calculate the local electric field around sand particles [24, 25]. At this time, it can be considered that the sand is in an equivalent electric field E_{0c}, and the configuration diagram of the equivalent electric field is shown in Figure 3.

The equivalent electric field E_{0c} can be calculated as

$$E_{0c} = \frac{E}{1 - \left[\left(\varepsilon_i - \varepsilon_e\right)/\left(\varepsilon_i + 2\varepsilon_e\right)\right](2R/h)^3}, \tag{1}$$

where ε_i is the permittivity of the sand particles, ε_e is the permittivity of the environment, R is the radius of the sand particles, E is the applied electric field, and h is the distance between sand particles.

By solving the Laplace equation in the spherical coordinate system, it can be obtained that the external electric field E_{out} of sand particles caused by the equivalent electric field is

$$\begin{aligned} E_{\text{out}} = {} & r_0\left(E_{0c}\cos\theta + \frac{\varepsilon_i - \varepsilon_e}{\varepsilon_i + 2\varepsilon_e}\frac{2E_{0c}R^3\cos\theta}{r^3}\right) \\ & + \theta_0\left(-E_{0c}\sin\theta + \frac{\varepsilon_i - \varepsilon_e}{\varepsilon_i + 2\varepsilon_e}\frac{E_{0c}R^3\sin\theta}{r^3}\right). \end{aligned} \tag{2}$$

According to (2), we can obtain the maximum electric field on the surface of one sand particle as follows:

$$E_{\max}{}' = \frac{3\varepsilon_i}{\varepsilon_i + 2\varepsilon_e}E_{0c}. \tag{3}$$

In addition, when the sand captures the electrons or ions, it will further affect the local electric field distribution. In order to calculate the local electric field after the sand is charged, we first assume that the saturation charge (i.e., the maximum charge) captured by every sand particle and the amount of saturated charge captured by the sand particles are related to the charging process of the sand particles. When the electric field generated by the charged sand particles is equal to the maximum electric field on the surface of sand particle caused by the equivalent electric field, the amount of charge captured by the sand particle reaches saturation [32]. At this time, the charging process of sand particles ends, and the saturated charging balance relationship of sand particles can be characterized by the following formula:

$$\frac{3\varepsilon_i}{\varepsilon_i + 2\varepsilon_e}E_{0c} = \frac{q_0}{4\pi\varepsilon_e R^2}, \tag{4}$$

where q_0 is the saturation charge of sand particles.

Solving (4), the saturation charge of sand particles is derived as

$$q_0 = \frac{12\pi\varepsilon_i\varepsilon_e R^2 E}{\varepsilon_i + 2\varepsilon_e - (2R/h)^3\left(\varepsilon_i - \varepsilon_e\right)}. \tag{5}$$

In practice, if the charge coefficient of the sand particles is expressed by f, the charge captured by sand particles is $q = fq_0$. According to the field charging model [32], we have

$$f = \frac{t}{t + \tau}, \tag{6}$$

where t is the charging time, with $t = 2R/v_e$, and τ is charge time constant, with $\tau = 4\varepsilon_e E_{0c}/J$, wherein J is the electron current density and $J = nev_e$, with n being the number density of electrons before the sand particle is charged and e is the absolute value of the charge carried by the electron. v_e is the drift velocity of electrons.

Substitute J into τ and expand it:

$$\begin{aligned} \tau &= \frac{4\varepsilon_e E_{0c}}{J} \\ &= \frac{4\varepsilon_e E_{0c}}{nev_e} \\ &= \frac{4\varepsilon_e E_{0c}}{neK_e E_{0c}} \\ &= \frac{4\varepsilon_e}{K_e ne}, \end{aligned} \tag{7}$$

where K_e is the electron mobility, $K_e = v_e/E_{0c}$.

Substituting (7) into (6), we can obtain

$$\begin{aligned} f &= \frac{t}{t + \tau} \\ &= \frac{neR}{neR + 2\varepsilon_e E_{0c}}. \end{aligned} \tag{8}$$

Therefore, the charge q can be calculated as

$$\begin{aligned} q &= fq_0 \\ &= \frac{neR}{neR + 2\varepsilon_e E_{0c}}\frac{12\pi\varepsilon_i\varepsilon_e R^2 E_{0c}}{\varepsilon_i + 2\varepsilon_e}. \end{aligned} \tag{9}$$

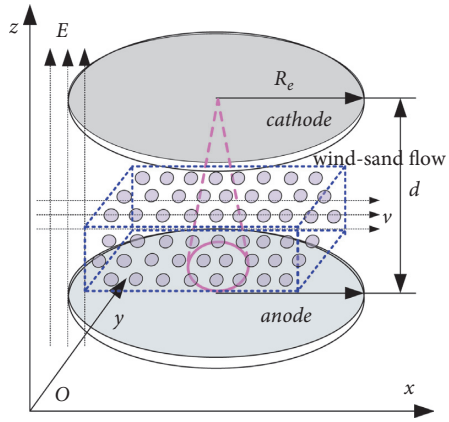

Figure 1: Streamer discharge in uniform field under strong wind-sand environment.

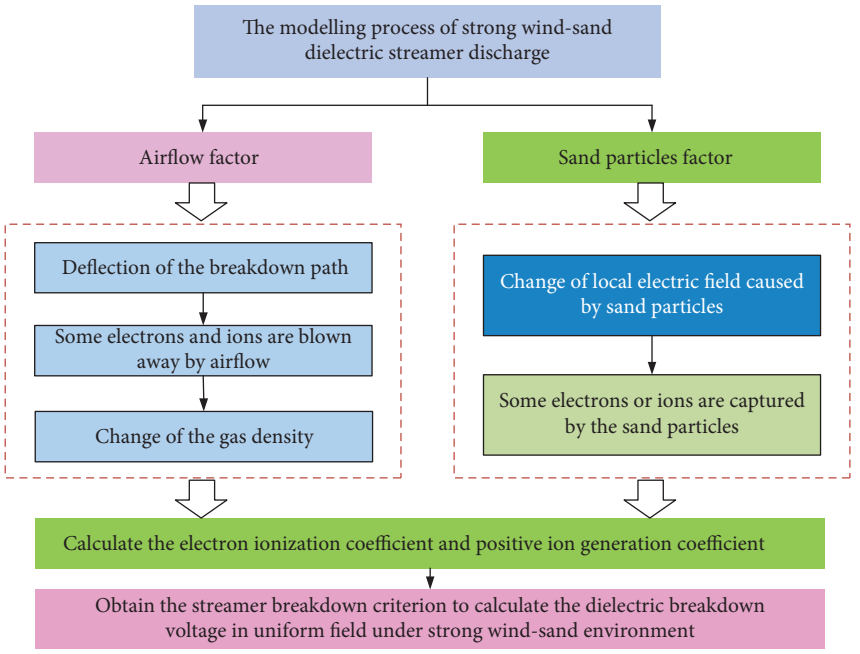

Figure 2: Modeling flow chart of strong wind-sand dielectric streamer discharge.

Table 1: The parameters defined in this paper.

Parameters	Unit symbol	Meaning	Value
E	V/m	Applied electric field	
R_e	m	Electrode radius	
d	m	Gap distance	
v_e	m/s	Electron velocity	
v	m/s	Gas flow velocity	
θ	°	Deflection angle	
K_e	$m^2/(V{\cdot}s)$	Electron mobility	
$\overline{\lambda e}$	m	Mean electron free path	
e	C	Electronic charge	1.6×10^{-19}
V_i	V	Atomic ionization potential	
α	cm^{-1}	Townsend's first ionization coefficient	
t	s	Time	
μ		Blowing away factor	
ρ	kg/m^3	Gas density	
ρ_0	kg/m^3	Static gas density	
γ_a		Specific heat ratio	

Table 1: Continued.

Parameters	Unit symbol	Meaning	Value
p	Pa	Gas pressure	
Ma		Mach's number	
s	m/s	Speed of sound	
d_m	m	Effective molecule diameter	
N_A	mol^{-1}	Avogadro's number	6.02×10^{-23}
M		Relative molecular weight	
γ_e		Cathode ionization coefficient	
ε_i		Permittivity of the sand particles	
ε_e		Permittivity of the environment	
R	μm	Radius of sand particles	
q	C	Charge of sand particles	
q_0	C	Saturation charge of sand particles	
h	m	Distance between sand particles	
f		Charge coefficient of sand particles	
τ		Constant of charging time	
i		Electron current density	
n		Electron number	
m		Number of sand particles parallel to the electric field direction	
c		Attractive parameter of sand particles	
U	V	Breakdown voltage	
E_r	V/m	Space charge field	
r	m	Electron diffusion radius	
x_E	m	Electric field distance	
g		Electron collision energy loss coefficient	0.025
ε_0	F/m	Permittivity of the vacuum	8.85×10^{-12}
K		Electric field scale factor	1

According to (9), it can be obtained that the charged electric field E_q generated on the surface of sand particles after charging is

$$E_q = \frac{q}{4\pi\varepsilon_e R^2}. \tag{10}$$

The maximum electric field E''_{max} on the surface of the charged sand particles consists of the charged electric field E_q on the surface of the sand particles and the maximum electric field E'_{max} on the surface of the sand particles, which can be calculated as

$$\begin{aligned} E''_{max} &= E'_{max} + E_q \\ &= (1+f)\frac{3\varepsilon_i}{\varepsilon_i + 2\varepsilon_e}E_{0c} \\ &= \left(1 + \frac{neR}{neR + \varepsilon_e E_{0c}}\right)\frac{3\varepsilon_i}{\varepsilon_i + 2\varepsilon_e}E_{0c}. \end{aligned} \tag{11}$$

2.2.2. Deflection of the Breakdown Path. In the discharge process of the strong wind-sand dielectric, charged particles obtain electric field acceleration in the direction of electric field; that is, the charged particles obtain a drift velocity. At the same time, charged particles are frequently collided by neutral molecules in the direction of airflow to obtain another horizontal velocity, namely, airflow velocity. Therefore, under the combined action of electric field force and horizontal collision force, the average moving path of charged particles will deflect an angle along the airflow direction, which will affect the ionization coefficient. For the specific influence process, please refer to the results previously published in our article in [27].

Combined with the change of spatial electric field in wind-sand environment and considering the path deflection effect of charged particles, Townsend's first ionization coefficient in wind-sand environment is deduced as

$$\alpha_a = \frac{1}{\overline{\lambda}_e \cos\{\arctan(v/K_e E_{0c})\}} \exp\left\{-\frac{V_i}{E_{0c}\overline{\lambda}_e \cos\{\arctan(v/K_e E_{0c})\}}\right\}, \tag{12}$$

where θ is the deflection angle of electron moving path along the horizontal direction, v is the gas flow velocity, K_e is the electron mobility, $\overline{\lambda}_e$ is the electron mean free path, and V_i is the ionization potential.

2.2.3. Some Electrons and Ions Are Blown Away by Airflow. Due to frequent collisions between neutral molecules and electrons and ions in the direction of airflow, some electrons and ions involved in discharge will be blown away or deviated from the path of main discharge by airflow, which will affect the discharge process. Please refer to the article in [27] for the specific impact process. Combined with the spatial electric field change of wind-sand environment and comprehensively considering the discharge path deflection and blowing away effects, Townsend's first ionization coefficient in wind-sand environment can be deduced as

$$\alpha_{ab} = \exp\left(-\mu_1 \rho \frac{v}{E_{0c}}\right)\alpha_a, \tag{13}$$

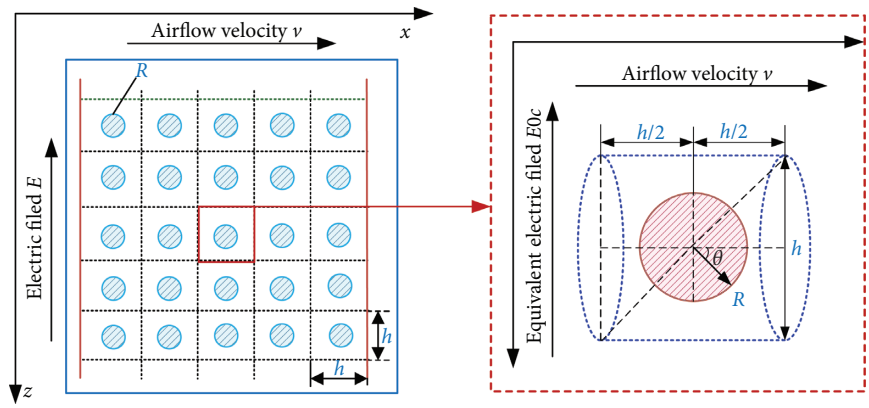

Figure 3: Diagram of equivalent electric field of sand particles.

where μ_1 is the electron blowing away coefficient and ρ is the gas density.

In the process of streamer discharge, the generation and development of positive ions have an important influence on the process of streamer discharge. In static air, the number of electrons generated by collision ionization per unit distance of electron moving is equal to the number of ions; that is, the positive ion generation coefficient is equal to the electron ionization coefficient. However, in wind-sand environment, in addition to considering the change of electron ionization coefficient, the blowing away effect of positive ions needs to be considered. For this purpose, the positive ion generation coefficient in wind-sand environment is defined as the number of positive ions generated by collision ionization per unit distance of electrons moving along the direction of electric field and not blown away by airflow. According to literature [27] and (13), the positive ion generation coefficient in wind-sand environment can be calculated as

$$\alpha_i = \exp\left(-\mu_2\rho\frac{v}{E_{0c}}\right)\alpha_{ab}, \tag{14}$$

where μ_2 is the positive ion blowing away coefficient.

2.2.4. Change of the Gas Density. Based on the previous research [27], the relationship between the mean electron free path and the airflow velocity can be deduced as follows:

$$\overline{\lambda}_e = \frac{4M}{\pi {d_m}^2 N_A \rho_0 \left\{1 + \gamma_a - 1/2\,(v/s)^2\right\}^{-1/\gamma_a - 1}}, \tag{15}$$

where γ_a is the specific heat ratio of a gas, Mach's number $\mathrm{Ma} = v/s$, s is the speed of sound, d_m is the effective molecular diameter, N_A is Avogadro's number, M is the relative molecular weight, and parameter ρ_0 represents the corresponding value at a stationary point, which is taken as the reference value.

Therefore, Townsend's ionization coefficient considering the spatial electric field of sand particles, the deflection of discharge path, the blowing away of some electrons and ions, and the change of gas density can be calculated as

$$\alpha = A(v, E_{0c})\exp\left(-\frac{\mu_1\rho v + B(v, E_{0c})}{E_{0c}}\right), \tag{16}$$

where

$$A(v, E_{0c}) = \frac{1}{\overline{\lambda}_e \cos\{\arctan(v/K_e E_{0c})\}},$$
$$B(v, E_{0c}) = A(v, E_{0c})V. \tag{17}$$

At this time, the positive ion generation coefficient is calculated as

$$\alpha_i' = A(v, E_{0c})\exp\left(-\frac{\mu\rho v + B(v, E_{0c})}{E_{0c}}\right), \tag{18}$$

where $\mu = \mu_1 + \mu_2$.

2.2.5. Some Electrons or Ions Are Captured by the Sand Particles. In the process of gas discharge in strong wind-sand environment, in addition to considering the above four factors, the electrons or ions will be captured by sand particles for charging in the process of migration along the electric field direction, resulting in the reduction of the number of electrons or ions. At the same time, the electric field generated by the charged sand particles will further distort the local electric field and affect the ionization process.

In order to analyse this process, it is assumed that the sand particles are spherical and evenly distributed in the gap space, the radius of sand particles is R, the permittivity of sand particles is ε_i, the ambient permittivity is ε_e, the streamer discharge is filamentous channel discharge, and the channel path is mostly gap sand path. It is assumed that the sand particles are evenly distributed on this discharge channel path. With every sand particle as the centre, the electrode space is divided into multiple cube units with the same volume. The length of each unit is h, the volume is h^3, the cross-sectional area of the cube unit is $S = h^2$, and the volume of spherical sand particles is $4\pi R^3/3$; then the volume fraction of sand particles is $V_p = (4\ \pi R^3/3)/h^3$ (i.e., the volume of sand particles in unit space volume).

Each equivalent unit is shown in Figure 4, where EFGH is the unit area (GH length is h), and ABCD is the influence area of sand particles for local electric field (BD length is $2d_0$). Under the action of the local electric field force, electrons will be attracted by the electric field from the EG surface into the AB surface and then move from the AB surface to the $O'KO$ surface. Except that some electrons are captured by sand particles, other electrons continue to through the sand particles and participate in the discharge. In region EABG, the electrons do not enter the influence range of the local electric field of sand particles, and the ionization in this region is only affected by the equivalent electric field E_{0c}. In region $AO'KOB$, the electrons are affected by the local electric field of the uncharged sand particles. The ionization in this region needs to consider the effect of the distorting electric field of the sand particles, and it is assumed that the number of electrons reaching surface $O'KO$ is approximately equal to the number of electrons generated by the average electric field along the axis of region $ABA'B'$ on surface $A'B'$. In region $O'MO\,DC$, the sand particles have been charged, and the electrons will be affected by the local electric field of the charged sand particles. For ionization in this region, the role of the charged electric field caused by charged sand particles needs to be further considered, and it is assumed that the number of electrons from surface $O'MO$ to CD surface is approximately equal to the number of electrons generated by the average electric field along the axis of region $C\,DC'D'$ on CD surface. We assume that the ionization coefficient in the left half of area ABCD is α', that in the right half of area ABCD is α'', and that outside of area ABCD is α.

From the above analysis, it can be seen that the area ABEG and area CDFH outside area ABCD are not affected by sand particles, and the ionization coefficient in this area can be calculated as

$$\alpha = A\left(v, E_{0c}\right)\exp\left(-\frac{\mu_1\rho v + B\left(v, E_{0c}\right)}{E_{0c}}\right). \tag{19}$$

In this region, the positive ion generation coefficient is

$$\alpha_i' = A\left(v, E_{0c}\right)\exp\left(-\frac{\mu\rho v + B\left(v, E_{0c}\right)}{E_{0c}}\right). \tag{20}$$

When electrons enter the AB surface, they will be affected by the local electric field of sand particles. According to the dipole-enhanced model [24], taking $\theta = 0$, we can get that the external electric field of the sand sphere is

$$E_{out} = \left(E_{0c} + \frac{\varepsilon_i - \varepsilon_e}{\varepsilon_i + 2\varepsilon_e}\frac{2E_{0c}R^3}{r^3}\right). \tag{21}$$

From (21), it can be obtained that the average electric field in region $ABA'B'$ is

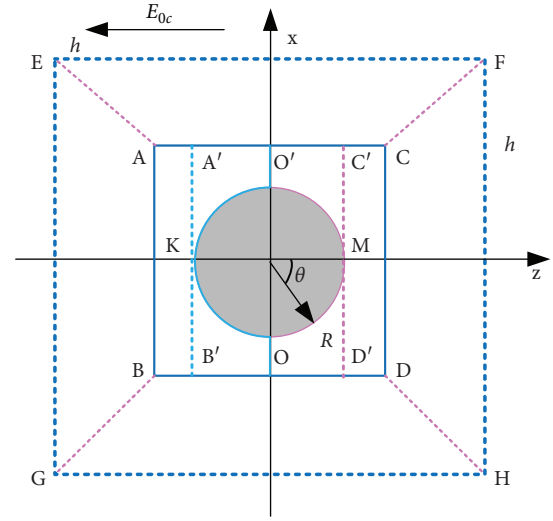

Figure 4: Diagram of sand particles unit in equivalent field E_{0c}.

$$\begin{aligned}\overline{E}_1 &= \frac{\int_R^{d_0} E_{\text{out}}dr}{d_0 - R} \\ &= \frac{\int_R^{d_0}\left(E_{0c} + \varepsilon_i - \varepsilon_e/\varepsilon_i + 2\varepsilon_e 2E_{0c}R^3/r^3\right)dr}{d_0 - R}.\end{aligned} \tag{22}$$

Let $k = \varepsilon_i - \varepsilon_e/\varepsilon_i + 2\varepsilon_e$; according to Figure 3, we can derive

$$\begin{aligned}\int_R^{d_0}\left(E_{0c} + k\frac{2E_{0c}R^3}{r^3}\right)dr &= E_{0c}\left(d_0 - R\right) + 2kE_{0c}R^3\int_R^{d_0}\frac{1}{r^3}dr \\ &= \left(d_0 - R - \frac{kR\left(R^2 - {d_0}^2\right)}{{d_0}^2}\right)E_{0c}.\end{aligned} \tag{23}$$

We then substitute (23) into (22) and derive

$$\overline{E}_1 = \left(1 + \frac{kR\left(R + d_0\right)}{{d_0}^2}\right)E_{0c}. \tag{24}$$

Thus, the ionization coefficient in the region $ABA'B'$ can be calculated as

$$\begin{aligned}\alpha' &= A\left(v, \overline{E}_1\right)\exp\left(-\mu_1\rho\frac{v}{\overline{E}_1}\right)\exp\left(-\frac{B\left(v, \overline{E}_1\right)}{\overline{E}_1}\right) \\ &= \alpha\exp\left(\frac{kR\left(R + d_0\right)\left(B\left(v, E_{0c}\right) + \mu_1\rho v\right)}{\left({d_0}^2 + kR\left(R + d_0\right)\right)E_{0c}}\right).\end{aligned} \tag{25}$$

In this region, the positive ion generation coefficient is

$$\alpha_i' = A\left(v, \overline{E}_1\right)\exp\left(-\mu\rho\frac{v}{\overline{E}_1}\right)\exp\left(-\frac{B\left(v, \overline{E}_1\right)}{\overline{E}_1}\right) = \alpha\exp\left(\frac{kR\left(R+d_0\right)\left(B\left(v, E_{0c}\right)+\mu\rho v\right)}{\left(d_0{}^2 + kR\left(R+d_0\right)\right)E_{0c}}\right). \tag{26}$$

The number of electrons produced by initial electrons n_0 moving from the EG plane to the curved surface $O'KO$ can be calculated as follows.

According to equation (28), the average ionization coefficient in the region $EGOO'$ is

$$\overline{\alpha}_1 = \alpha\left(1-\frac{2d_0}{h}\right)+\alpha'\frac{2\left(d_0-R\right)}{h} = \alpha\left[1-\frac{2d_0}{h}+\frac{2\left(d_0-R\right)}{h}\exp\left(\frac{kR\left(R+d_0\right)\left(B\left(v, E_{0c}\right)+\mu_1\rho v\right)}{\left(d_0{}^2 + kR\left(R+d_0\right)\right)E_{0c}}\right)\right]. \tag{27}$$

The positive ion generation coefficient in region $EGOO'$ is

$$\overline{\alpha}_{i1} = \alpha_i'\left[1-\frac{2d_0}{h}+\frac{2\left(d_0-R\right)}{h}\exp\left(\frac{kR\left(R+d_0\right)\left(B\left(v, E_{0c}\right)+\mu\rho v\right)}{\left(d_0{}^2 + kR\left(R+d_0\right)\right)E_{0c}}\right)\right]. \tag{28}$$

After the sand particles are charged, the average electric field in region $C'D'C\ D$ is

$$\overline{E}_2 = \frac{\int_R^{d_0}\left(E_{out}+E_q'\right)dr}{d_0-R} = \overline{E}_1 + \frac{\int_R^{d_0} q/4\pi\varepsilon_e r^2 dr}{d_0-R} = \left(1+\frac{kR\left(R+d_0\right)}{d_0{}^2}+\frac{3f\varepsilon_i R}{\left(\varepsilon_i+2\varepsilon_e\right)d_0}\right)E_{0c}. \tag{29}$$

According to (28), the average ionization coefficient in region $C'D'C\ D$ is

$$\alpha'' = A\left(v, \overline{E}_2\right)\exp\left(-\mu_1\rho\frac{v}{\overline{E}_2}\right)\exp\left(-\frac{B\left(v, \overline{E}_2\right)}{\overline{E}_2}\right) = \alpha\exp\left(\frac{\left(kRd_0\left(R+d_0\right)\left(\varepsilon_i+2\varepsilon_e\right)+3f\varepsilon_i R d_0{}^2\right)\left(B\left(v, E_{0c}\right)+\mu_1\rho v\right)}{\left(d_0{}^3\left(\varepsilon_i+2\varepsilon_e\right)+kRd_0\left(R+d_0\right)\left(\varepsilon_i+2\varepsilon_e\right)+3f\varepsilon_i R d_0{}^2\right)E_{0c}}\right). \tag{30}$$

It can be seen that the positive ion generation coefficient in this region is

$$\alpha'' = A\left(v, \overline{E}_2\right)\exp\left(-\mu_1\rho\frac{v}{\overline{E}_2}\right)\exp\left(-\frac{B\left(v, \overline{E}_2\right)}{\overline{E}_2}\right) = \alpha\exp\left(\frac{\left(kRd_0\left(R+d_0\right)\left(\varepsilon_i+2\varepsilon_e\right)+3f\varepsilon_i R d_0{}^2\right)\left(B\left(v, E_{0c}\right)+\mu_1\rho v\right)}{\left(d_0{}^3\left(\varepsilon_i+2\varepsilon_e\right)+kRd_0\left(R+d_0\right)\left(\varepsilon_i+2\varepsilon_e\right)+3f\varepsilon_i R d_0{}^2\right)E_{0c}}\right). \tag{31}$$

The number of electrons produced by initial electrons n_0 moving from the curved surface $O'MO$ to the FH plane can be calculated as

$$n_R = n_L\exp\left[\alpha\left(\frac{h}{2}-d_0\right)+\alpha''\left(d_0-R\right)\right] = n_L\exp\left[\frac{h}{2}\left(\alpha\left(1-\frac{2d_0}{h}\right)+\alpha''\frac{2\left(d_0-R\right)}{h}\right)\right]. \tag{32}$$

According to (32), the average ionization coefficient in region $FHOO'$ is

$$\begin{aligned}\overline{\alpha}_2 &= \alpha\left(1-\frac{2d_0}{h}\right)+\alpha''\frac{2(d_0-R)}{h}\\ &= \alpha\left[1-\frac{2d_0}{h}+\frac{2(d_0-R)}{h}\times\exp\left(\frac{\left(kRd_0(R+d_0)(\varepsilon_i+2\varepsilon_e)+3f\varepsilon_iR{d_0}^2\right)(B(v,E_{0c})+\mu_1\rho v)}{\left({d_0}^3(\varepsilon_i+2\varepsilon_e)+kRd_0(R+d_0)(\varepsilon_i+2\varepsilon_e)+3f\varepsilon_iR{d_0}^2\right)E_{0c}}\right)\right].\end{aligned} \tag{33}$$

The average positive ion generation coefficient in this region is

$$\overline{\alpha}_{i2} = \alpha_i'\left[1-\frac{2d_0}{h}+\frac{2(d_0-R)}{h}\times\exp\left(\frac{\left(kRd_0(R+d_0)(\varepsilon_i+2\varepsilon_e)+3f\varepsilon_iR{d_0}^2\right)(B(v,E_{0c})+\mu\rho v)}{\left({d_0}^3(\varepsilon_i+2\varepsilon_e)+kRd_0(R+d_0)(\varepsilon_i+2\varepsilon_e)+3f\varepsilon_iR{d_0}^2\right)E_{0c}}\right)\right]. \tag{34}$$

Thus, the total number of electrons generated by the initial electron n_0 moving from the EG plane to the FH plane is

$$\begin{aligned}n_R &= n_L\exp\left[\alpha\left(\frac{h}{2}-d_0\right)+\alpha''(d_0-R)\right]\\ &= n_L\exp\left[\frac{h}{2}\left(\alpha\left(1-\frac{2d_0}{h}\right)+\alpha''\frac{2(d_0-R)}{h}\right)\right]\\ &= n_0\exp\left[h\left(\alpha\left(1-\frac{2d_0}{h}\right)+\frac{(d_0-R)}{h}(\alpha'+\alpha'')\right)\right].\end{aligned} \tag{35}$$

According to (35), the average ionization coefficient under strong wind-sand environment can be derived as

$$\begin{aligned}\overline{\alpha} = \alpha\Bigg\{1-\frac{2d_0}{h}+\frac{(d_0-R)}{h}\Bigg[&\exp\left(\frac{kR(R+d_0)(\mu_1\rho v+B(v,E_{0c}))}{\left({d_0}^2+kR(R+d_0)\right)E_{0c}}\right)\\ &+\exp\left(\frac{\left(kRd_0(R+d_0)(\varepsilon_i+2\varepsilon_e)+3f\varepsilon_iR{d_0}^2\right)(B(v,E_{0c})+\mu_1\rho v)}{\left({d_0}^3(\varepsilon_i+2\varepsilon_e)+kRd_0(R+d_0)(\varepsilon_i+2\varepsilon_e)+3f\varepsilon_iR{d_0}^2\right)E_{0c}}\right)\Bigg]\Bigg\}.\end{aligned} \tag{36}$$

Then the average positive ion generation coefficient under strong wind-sand environment can be calculated as

$$\begin{aligned}\overline{\alpha}_i = \alpha_i'\Bigg\{1-\frac{2d_0}{h}+\frac{(d_0-R)}{h}\Bigg[&\exp\left(\frac{kR(R+d_0)(\mu\rho v+B(v,E_{0c}))}{\left({d_0}^2+kR(R+d_0)\right)E_{0c}}\right)\\ &+\exp\left(\frac{\left(kRd_0(R+d_0)(\varepsilon_i+2\varepsilon_e)+3f\varepsilon_iR{d_0}^2\right)(B(v,E_{0c})+\mu\rho v)}{\left({d_0}^3(\varepsilon_i+2\varepsilon_e)+kRd_0(R+d_0)(\varepsilon_i+2\varepsilon_e)+3f\varepsilon_iR{d_0}^2\right)E_{0c}}\right)\Bigg]\Bigg\}.\end{aligned} \tag{37}$$

From equation (28), we can find that $\overline{\alpha}$, $\overline{\alpha}_1$, and $\overline{\alpha}_2$ satisfy $\overline{\alpha} = (\overline{\alpha}_1 + \overline{\alpha}_2)$, and $\overline{\alpha}_i$, $\overline{\alpha}_{i1}$, and $\overline{\alpha}_{i2}$ satisfy $\overline{\alpha}_i = (\overline{\alpha}_{i1} + \overline{\alpha}_{i2})$, which can be further simplified as

$$\overline{\alpha} = 2A(v, E_{0c})\frac{(d_0 - R)}{h}\exp\left\{-(\mu\rho v + B(v, E_{0c})) \times \frac{\left(1 + kR(R + d_0)/d_0^2\right)^2 + 3f\varepsilon_i R/(\varepsilon_i + 2\varepsilon_e)d_0 \times kR(R + d_0)/d_0^2}{2\left(1 + kR(R + d_0)/d_0^2\right)\left(1 + kR(R + d_0)/d_0^2 + 3f\varepsilon_i R/(\varepsilon_i + 2\varepsilon_e)d_0\right)E_{0c}}\right\}. \tag{38}$$

The general form of (38) with ionization coefficient can be rewritten as

$$\overline{\alpha} = A'\exp\left(-\frac{B'}{E}\right), \tag{39}$$

where

$$A' = 2A(v, E_{0c})\frac{d_0 - R}{h}. \tag{40}$$

And

$$B' = (\mu_1\rho v + B(v, E_{0c}))\left[1 - \frac{\varepsilon_i - \varepsilon_e}{\varepsilon_i + 2\varepsilon_e}\left(\frac{2R}{h}\right)^3\right] \times \frac{\left(1 + kR(R + d_0)/d_0^2\right)^2 + 3f\varepsilon_i R/(\varepsilon_i + 2\varepsilon_e)d_0 \times kR(R + d_0)/d_0^2}{2\left(1 + kR(R + d_0)/d_0^2\right)\left(1 + kR(R + d_0)/d_0^2 + 3f\varepsilon_i R/(\varepsilon_i + 2\varepsilon_e)d_0\right)}. \tag{41}$$

The general form of positive ion generation coefficient can be written as

$$\overline{\alpha}_i = A'\exp\left(-\frac{B_i'}{E}\right), \tag{42}$$

where

$$B_i' = (\mu\rho v + B(v, E_{0c}))\left[1 - \frac{\varepsilon_i - \varepsilon_e}{\varepsilon_i + 2\varepsilon_e}\left(\frac{2R}{h}\right)^3\right] \times \frac{\left(1 + kR(R + d_0)/d_0^2\right)^2 + 3f\varepsilon_i R/(\varepsilon_i + 2\varepsilon_e)d_0 \times kR(R + d_0)/d_0^2}{2\left(1 + kR(R + d_0)/d_0^2\right)\left(1 + kR(R + d_0)/d_0^2 + 3f\varepsilon_i R/(\varepsilon_i + 2\varepsilon_e)d_0\right)}. \tag{43}$$

So far, the general forms of electron ionization coefficient and positive ion generation coefficient in strong wind-sand environment have been solved.

2.3. Streamer Breakdown Criteria. On the basis of streamer discharge theory, combined with the calculation results of electron ionization coefficient and positive ion generation coefficient, we attempt to establish the analytical solution of streamer breakdown criterion to quantitatively calculate the dielectric breakdown voltage in uniform field in strong wind-sand environment.

Assuming that the number of initial electrons in the cathode is n_0 and the number of sand particles along the radial direction of the streamer discharge circuit is m, the total number of electrons generated by the initial electrons moving from the cathode to the anode along the electric field direction can be calculated as

$$\begin{aligned} n_{em} &= n_0\exp(\overline{\alpha}d) - \frac{q}{e}\exp(\overline{\alpha}mh) - \frac{q}{e}\exp(\overline{\alpha}(m-1)h) - \frac{q}{e}\exp(\overline{\alpha}(m-2)h) - \cdots - \frac{q}{e}\exp(\overline{\alpha}h) \\ &= n_0\exp(\overline{\alpha}d) - \frac{q}{e}\frac{\exp(\overline{\alpha}(h+d)) - \exp(\overline{\alpha}h)}{\exp(\overline{\alpha}h) - 1}. \end{aligned} \tag{44}$$

From (44), the following equation is defined:

$$\frac{q}{e}\frac{\exp(\overline{\alpha}(h+d))-\exp(\overline{\alpha}h)}{\exp(\overline{\alpha}h)-1}=\gamma n_0\exp(\overline{\alpha}d), \tag{45}$$

where γ is a constant, which takes a value between (0, 1).

Let $\exp(\overline{\alpha}h)=x$. Solving (45) results in

$$\frac{q}{e}\frac{\exp(\overline{\alpha}(h+d))-\exp(\overline{\alpha}h)}{\exp(\overline{\alpha}h)-1}=\gamma n_0\left(\frac{\gamma}{\gamma-cf}\right)^m, \tag{46}$$

where $c=q_0/n_0$ e, $f=q/q_0$.

Substituting (46) into (44), the total number of electrons reaching the anode is calculated as

$$n_{em}=n_0\exp(\overline{\alpha}d)-\gamma n_0\left(\frac{\gamma}{\gamma-cf}\right)^m. \tag{47}$$

Based on the streamer theory [33], the space charge field formed by positive ions is calculated. Assuming that the ion set at the head of the electron avalanche is spherical, the positive ion density in the spherical ion set is

$$\begin{aligned} n' &= \frac{n_{em}\overline{\alpha}_i \mathrm{d}x}{\pi r^2 \mathrm{d}x} \\ &= \frac{n_{em}\overline{\alpha}_i}{\pi r^2}. \end{aligned} \tag{48}$$

Then the space charge field formed by positive ions can be calculated as

$$\begin{aligned} E_{\mathrm{r}} &= \frac{en'}{4\pi\varepsilon_0 r^2}\left(\frac{4}{3}\pi r^3\right) \\ &= \frac{e\overline{\alpha}_i n_{em}}{3\pi\varepsilon_0 r}, \end{aligned} \tag{49}$$

where E_{r} is the space charge field and r is the electron diffusion radius.

In the process of dielectric discharge under strong wind-sand environment, electrons are affected by the horizontal collision force of gas molecules and the electric field force. The ratio of mean electron velocity $\overline{v}_e$ to electron drift velocity $\overline{v}_E$ in the electric field direction is equal to the ratio of mean electron free path $\overline{\lambda}_e$ to electron free path $\overline{\lambda}_E$ in the electric field direction, so we can obtain

$$\frac{\overline{v}_e}{\overline{v}_E}=\frac{\overline{\lambda}_e}{\overline{\lambda}_E}. \tag{50}$$

According to [33], energy eEx obtained by an electron in a uniform field is equal to the energy lost by the collision between an electron and a gas molecule. Thus, we have

$$eE\overline{\lambda}_e=g\frac{\overline{v}_e}{\overline{v}_E}\frac{1}{2}m_e{v_e}^2. \tag{51}$$

The mean electron free path is given by

$$\overline{\lambda}_e=\frac{1}{0.815}\frac{m_e}{e}\overline{v}_e K_e, \tag{52}$$

where g is the electron collision energy loss coefficient, K_e is the electron mobility, v_e is the electron random velocity, and m_e is the electron mass.

Combining (46) and (47), we can get

$$\frac{v_e}{\overline{v}_E}=\sqrt{\frac{2.45}{g}}. \tag{53}$$

Assuming that v_e is submitted to Maxwell velocity distribution, we can obtain

$$\frac{\overline{v}_e}{\overline{v}_E}=1.44\sqrt{\frac{1}{g}}. \tag{54}$$

Substituting (49) into (46), let $1/2m_e{v_e}^2=eV$, and we can get

$$\frac{V}{E}=\frac{\overline{\lambda}_e}{1.44\sqrt{g}}. \tag{55}$$

Therefore, the electron diffusion radius can be calculated as

$$\begin{aligned} r &= \sqrt{\frac{2Vx_E}{E}} \\ &= \sqrt{\frac{2\overline{\lambda}_e x_E}{1.5\sqrt{g}}}. \end{aligned} \tag{56}$$

Substituting (56) into (49), we can obtain the space charge field as follows:

$$E_{\mathrm{r}}=\frac{e\overline{\alpha}_i\left(n_0\exp(\overline{\alpha}d)-\gamma n_0\left(\gamma/(\gamma-cf)\right)^m\right)\sqrt{1.5\sqrt{g}}}{3\pi\varepsilon_0\sqrt{2\overline{\lambda}_e x_{\mathrm{E}}}}. \tag{57}$$

Substitute the empirical value $g=0.025$ and let $n_0=1, e=1.6\times10^{-6}$, and $\varepsilon_0=8.85\times10^{-12}$; (57) can be written as

$$E_{\mathrm{r}}=6.6\times10^{-10}\frac{\overline{\alpha}_i\left(\exp(\overline{\alpha}d)-\gamma\left(\gamma/\gamma-cf\right)^m\right)}{\sqrt{\overline{\lambda}_e x_{\mathrm{E}}}}. \tag{58}$$

According to the streamer discharge theory, when the space charge field E_{r} and the external equivalent electric field E_{0c} are of the same order of magnitude, the streamer will be formed. Therefore, the streamer breakdown criterion can be expressed as

$$E_{\mathrm{r}}=KE_{0\mathrm{c}}, \tag{59}$$

where K is the scale factor.

Substituting (58) into (59), we can get

$$\overline{\alpha}x_{\mathrm{E}}=\ln\left(3.11\times10^{-4}\frac{KE_{0\mathrm{c}}\sqrt{\overline{\lambda}_e x_{\mathrm{E}}}}{\overline{\alpha}_i}+\gamma\left(\frac{\gamma}{\gamma-cf}\right)^m\right). \tag{60}$$

Then substituting (39) and (42) into (60), we can obtain

$$A'\exp\left(-\frac{B'}{E}\right)x_{\mathrm{E}} = \ln\left(3.11\times10^{-4}\frac{KE_{0c}\sqrt{\overline{\lambda}_e x_{\mathrm{E}}}}{A'\exp\left(-B_i'/E\right)} + \gamma\left(\frac{\gamma}{\gamma - cf}\right)^m\right). \tag{61}$$

In the above equation, x_{E} represents the spatial distance required for streamer formation.

We now substitute U/d for E in (61), and then the streamer breakdown criterion under uniform field in strong wind-sand environment can be deduced as

$$A'\exp\left(-\frac{\mathrm{d}B'}{U}\right)d = \ln\left(3.11\times10^{-4}\frac{KE_{0c}\sqrt{\overline{\lambda}_e d}}{A'\exp\left(-dB_i'/U\right)} + \gamma\left(\frac{\gamma}{\gamma - cf}\right)^m\right). \tag{62}$$

So far, the analytical form of streamer breakdown criterion in uniform field under strong wind-sand environment has been obtained as in (62), the breakdown voltage is taken as the implicit function of airflow and sand particles related parameters in strong wind-sand environment, and its corresponding relationship can be solved by numerical method.

3. Simulation and Discussion

The proposed physical model is calculated to obtain the variation characteristic curve of breakdown voltage with various parameters of airflow and sand through simulation. For air, we let the initial air density $\rho_0 = 1.205\,\mathrm{kg/m^3}$, the permittivity of the environment medium $\varepsilon_e = 1$, $\gamma_a = 1.4$, the mean free path of air molecules $\lambda_{\mathrm{m}} = 1.03\times10^{-7}\mathrm{m}$, ionization potential $V_i = 15$, the speed of sound $s = 340\,\mathrm{m/s}$, gap distance $d = 0.01\,\mathrm{m}$, the electron blowing away coefficient $\mu_1 = 15$, and the positive ions blowing away coefficient $\mu_2 = 15000$. For sand particles, we let the permittivity of the sand particles $\varepsilon_i = 6$; f is the charging coefficient of sand particles, which is the ratio of the real charge q captured by sand particles to the saturation charge q_0 of sand particles, and its range of value is within [0, 1]. Let the attraction coefficient of sand particle $c = 0.06$ and the capture coefficient of sand particle $\gamma = 0.1$; R is the radius of sand particles; the average size range of sand particles used in simulation is within [0, 200] μm (referring to the operation environment of Lanzhou-Xinjiang Railway, the actual size distribution of sand particles in the surrounding environment of Lanzhou-Xinjiang Railway is within [0, 200] μm); h represents the length of each unit of the discharge gap, which is taken to be within [0, d]; $m = d/h$, indicating the number of sand particles in the discharge gap, which can reflect the concentration of sand particle; $2R/h$ represents the ratio of sand diameter to unit length in each unit of discharge gap, which can reflect the size of sand volume fraction V_{p}, which is taken to be within [0,1]. According to the values and ranges of the above parameters, the model is simulated and calculated to obtain the relationship curve of dielectric breakdown voltage with airflow velocity under different parameters in strong wind-sand environment. The calculation results are shown in Figures 5–7.

Figure 5 shows the variation curves of dielectric breakdown voltage with airflow velocity under different sand particle size R when the airflow velocity increases from 0 m/s to 300 m/s, the gap distance $d = 0.01\,\mathrm{m}$, the charging coefficient $f = 1$ (i.e., saturated charging), and the number of sand particles $m = 20$. It can be seen from Figure 4 that when the condition is in the pure airflow environment, the breakdown criterion obtained from equation (62) will transform into the streamer breakdown criterion in the pure airflow environment. The breakdown voltage gradually decreases with the increase of airflow velocity. The calculation results are consistent with the experimental results of our previous articles [27, 28]. When the charging coefficient f, gap distance d, and parameter m (that can represent sand concentration) remain unchanged, the breakdown voltage increases with the decrease of sand particle size R. For example, when $R = 50\,\mu$m, the breakdown voltage is about 22 kV/cm at the airflow speed $v = 30\,\mathrm{m/s}$, while when R is 100 μm, 150 μm, and 200 μm, the breakdown voltage is about 17 kV/cm, 15 kV/cm, and 11 kV/cm, respectively, at the same airflow speed, which is, respectively, about 77%, 68%, and 50% of the breakdown voltage value at $R = 50\,\mu$m. These results show that when m is fixed (the sand concentration remains unchanged), the sand particle size has a significant impact on the dielectric breakdown voltage in wind-sand environment, and the breakdown voltage decreases with the increase of sand particle size. The variation trend of breakdown voltage with sand particle size shows a trend similar to that in the experimental results obtained by relevant scholars in [34, 35]. The effect of sand particles on gap discharge is mainly the combined effect of the local electric field and the capture of charge. It can be seen from the simulation results that the breakdown voltage of large-size sand particles is lower than that of small-size sand particles; that is, the comprehensive impact of small-size sand particles on the breakdown voltage in strong wind-sand environment is weaker than that of large-size sand particles. The main reason for this result is that small-size sand particles have less impact on the local electric field (including before and after charging) than large-size sand particles. The impact of small-size sand particles on the breakdown voltage through the local electric field is weaker than that through the capture of charge. Therefore, the charge capture of sand particles

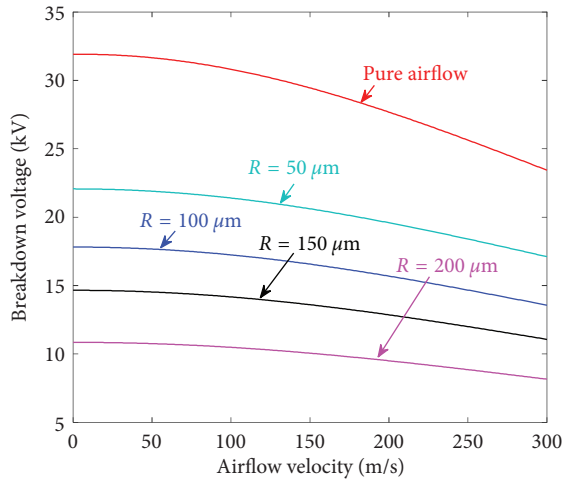

Figure 5: Relationship between breakdown voltage and airflow velocity in different sand particles sizes ($f = 1$, $m = 20$).

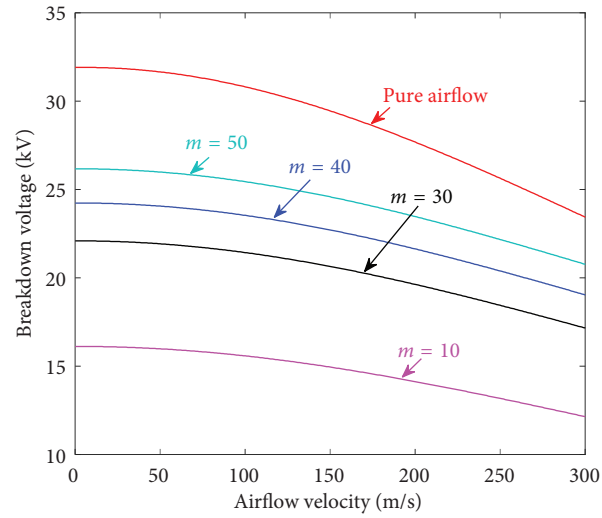

Figure 6: Relationship between breakdown voltage and airflow velocity in different sand particles concentration ($(f) = 1$, $2(R)/(h) = 0.3$).

plays a dominant role in small-size sand particles case. The large-size sand is just the opposite; that is, the impact of large-size sand particles on the breakdown voltage through local electric field is stronger than that through capture of charge. Therefore, the distortion of local electric field caused by sand particles plays a dominant role in large-size sand particles case.

Figure 6 shows the variation curves of dielectric breakdown voltage under different m (sand concentration) when the airflow velocity increases from 0 m/s to 300 m/s, the gap distance $d = 0.01$ m, the charging coefficient $f = 1$ (i.e., saturated charging), and the volume fraction $2R/h = 0.3$. As can be seen from Figure 5, when the volume fraction of sand particles $2R/h$ remains unchanged, the breakdown voltage increases with the increase of sand concentration m. When $m = 50$, the breakdown voltage is about 26 kV/cm at the airflow speed $v = 30$ m/s, while when m is 40, 30, and 10, the breakdown voltage is about 24 kV/cm, 22 kV/cm, and 17 kV/cm, respectively, at the same airflow speed, which is, respectively, about 92%, 84%, and 65% of the breakdown voltage value at $m = 50$. These results show that when the volume fraction is fixed, the sand concentration also has a significant effect on the dielectric breakdown voltage in wind-sand environment. The effect of sand concentration on the dielectric breakdown voltage is the combined effect of the local electric field of charged particles and the capture of charge. It can be seen from the simulation results that when the volume fraction remains unchanged, the dielectric breakdown voltage in high-concentration sand particles case is higher than that in low-concentration sand particles case; that is, the comprehensive impact of high-concentration sand particles on the breakdown voltage in strong wind-sand environment is stronger than that of low-concentration sand particles. The main reason for this result is that, with the increase of sand concentration, the size of sand particle decreases in the same proportion when the volume fraction remains unchanged, which can be seen from equations (1), (3), and (11). At this time, the equivalent electric field and the maximum electric field remain unchanged, but the maximum charged electric field or local electric field of charged sand particles decreases, which will reduce the local ionization coefficient of sand and suppress the occurrence of discharge. In addition, although the reduction of sand particle size decreases the charging capture capacity of a single sand particle, the increase of sand concentration rapidly increases the number of sand particles, which increases the overall charging capture capacity of sand particles, reduces the total number of discharge effective electrons, and then suppresses the development of discharge. Therefore, when the volume fraction remains unchanged, the increase of sand concentration also reduces sand particles size, which decreases the local electric field of charged sand particles and increases the overall amount of charge captured by sand particles. This comprehensive effect jointly suppresses the development of discharge and increases the breakdown voltage. Therefore, the breakdown voltage in wind-sand environment with high-concentration and small-size sand particles is much higher than that with low-concentration and large-size sand particles; that is to say, the sand dust environment with high-concentration and small-size sand particles makes it more difficult to form streamer discharge and has stronger discharge suppression action and higher breakdown voltage, which is in good agreement with the experimental results of relevant scholars in [22, 36].

Figure 7 shows the variation curves of dielectric breakdown voltage under different charging coefficient f when the airflow velocity increases from 0 m/s to 300 m/s, the gap distance $d = 0.01$ m, the number of sand particles $m = 20$, and the volume fraction $2R/h = 0.2$. As can be seen from Figure 6 that the breakdown voltage increases with the increase of the charging coefficient f, which is similar to the change trend of literature [31], f only reflects the amplitude of the breakdown voltage and does not affect the change trend of the breakdown voltage with the airflow velocity. The change trend of the breakdown voltage with the airflow velocity is basically the same under different f values. When $f = 1$, the breakdown voltage is about 22 kV/cm at the airflow

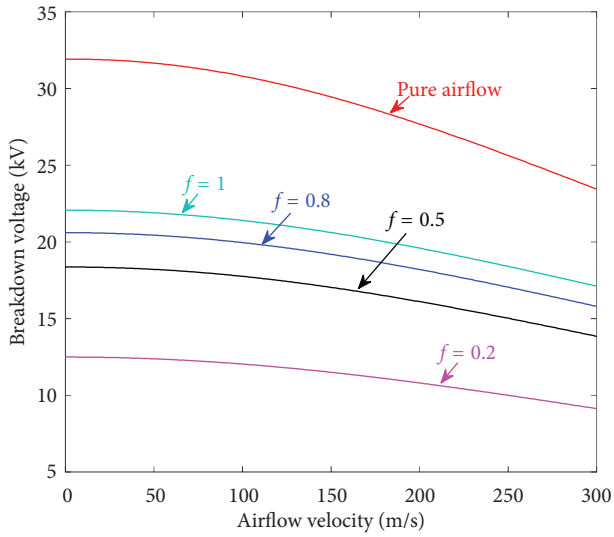

Figure 7: Relationship between breakdown voltage and airflow velocity in different charge coefficient ($m = 20$, $2R/h = 0.2$)

speed $v = 30$ m/s, while when f is 0.8, 0.5, and 0.2, the breakdown voltage is about 20 kV/cm, 18 kV/cm, and 12 kV/cm, respectively, at the same airflow speed, which is, respectively, about 91%, 82%, and 55% of the breakdown voltage value at $f = 1$. These results show that when the sand volume fraction and concentration remain unchanged, the dielectric breakdown voltage in wind-sand conditions is affected by the charging coefficient. The influence of the charging coefficient on the dielectric breakdown voltage is mainly reflected in the comprehensive influence of the local electric field caused by charged sand particles and the amount of captured charge in the discharge space. When the sand charging coefficient increases, the captured charge by sand particles increases and the local electric field increases, which results in the increase of ionization coefficient and promotes discharge. At the same time, with the increase of sand charging coefficient, the number of electrons captured by sand particles also increases, which will reduce the total number of effective electrons and inhibit the discharge. It can be seen from the calculation results that the larger the charging coefficient, the higher the breakdown voltage; that is to say, the increase of sand charging coefficient has a stronger impact on the increase of breakdown voltage caused by the decrease of number of effective electrons than the decrease of breakdown voltage caused by the increase of local electric field caused by charged sand particles.

The above discussion shows that the dielectric breakdown voltage in strong wind-sand environment is significantly different from that in static environment. The breakdown voltage is comprehensively affected by the airflow velocity v, sand particle size R, sand particle concentration m, and sand charging coefficient f.

4. Conclusion

In this work, based on streamer discharge theory, we presented a physical model of wind-sand dielectric streamer discharge by analysing the influence of airflow and sand particles on discharge process in strong wind-sand environment. Six factors that influence the streamer discharge process are considered: the deflection of the major discharge path, the blowing away of some electrons and ions, the decline in gas density, the distortion of the electric field caused by sand particles, the capture of the electrons, and the electric field formed by charged sand particles. The analytical solutions of electron ionization coefficient and positive ion generation coefficient are obtained, and the dielectric breakdown criterion is proposed. The analytical form of the presented model can be used to quantitatively calculate the dielectric breakdown voltage in strong wind-sand environment. The following conclusions are drawn:

(1) The variation trend of breakdown voltage with airflow velocity is in good agreement between strong wind-sand environment and pure airflow environment. The breakdown voltage decreases with the increase of airflow velocity, and the variation curve of breakdown voltage with airflow velocity under wind-sand condition is lower than that under pure airflow condition. Airflow is the main factor affecting the variation trend of breakdown voltage, and sand particles will reduce the amplitude of breakdown voltage, which is related to the sand particle size, concentration, and charging coefficient.

(2) When the sand concentration is constant, the dielectric breakdown voltage increases with the decrease of sand particle size. The effect of sand particle size on dielectric breakdown voltage is the comprehensive effect of the local electric field and the capture of charge. When sand particle size is small, the capture of charge is the dominant factor, which results in the fact that the comprehensive effect is to inhibit discharge and increase the breakdown voltage. When sand particle size is large, the distortion of local electric field caused by sand particles is the dominant factor, which results in the fact that the comprehensive effect is to promote the discharge and reduce the breakdown voltage.

(3) When the sand volume fraction remains unchanged, the dielectric breakdown voltage increases with the increase of sand concentration; that is, the breakdown voltage is higher at high-concentration and small-size sand particle. At this time, the influence of sand particles on the dielectric breakdown voltage is the combined effect of the local electric field of charged sand particles and the capture of charge. At high-concentration and small-size sand particles, the electric field generated by charged sand particles decreases, and the overall amount of charge captured by sand particles increases, both of which inhibit the discharge and make the breakdown voltage increase. Therefore, in wind-sand environment, the breakdown voltage with high-concentration and small-size sand particles is higher; that is, the high-concentration and small-size sand particle can restrain the development of streamer discharge in strong wind-sand environment.

(4) The dielectric breakdown voltage in wind-sand environment increases with the increase of sand charging coefficient. The influence of sand charging coefficient on dielectric breakdown voltage is the comprehensive effect of the local electric field of charged sand particles and the amount of captured charge. When the charging coefficient is small, the electric field generated by charged sand particles is the dominant factor, and the comprehensive effect is to promote discharge and reduce the breakdown voltage. When the charging coefficient is large, the amount of captured charge is the dominant factor, and the comprehensive effect is to restrain the development of discharge and increase the breakdown voltage.

(5) The presented streamer discharge model and corresponding breakdown criteria can be applied to realize the quantitative analysis and calculation of dielectric breakdown voltage in the wind-sand environment. This paper extends the classical streamer discharge theory for static gases to the gas-solid two-phase flow environment. The proposed model in this paper can provide a theoretical reference for the design and protection of external insulation in gas-solid two-phase flow environment.

Data Availability

The data used to support the findings of this study are included within the article.

Conflicts of Interest

The authors declare that they have no conflicts of interest.

Acknowledgments

The authors are grateful to the supporting programs of the http://dxNational Natural Science Foundation of China (nos. 52067014 and 52167018), the Young Doctor Foundation of JYT. GANSU. GOV.CN (no. 2021QB-060), and the Young Science Research Foundation of Lanzhou Jiaotong University (nos. 2020013 and 2019029).

References

[1] Y. Hua, N. Wang, and K. Zhao, "Simultaneous unknown input and state estimation for the linear system with a rank-deficient distribution matrix," *Mathematical Problems in Engineering*, vol. 2021, Article ID 6693690, 2021.

[2] H. Liu, Q. Li, and K. Wang, "State-of-charge estimation and remaining useful life prediction of supercapacitors," *Renewable and Sustainable Energy Reviews*, vol. 150, Article ID 11408, 2021.

[3] H. Deng, Y. Li, W. Cai et al., "Status and prospect on technical research of power transmission in desert areas," *High Voltage Engineering*, vol. 43, no. 12, pp. 15–21, 2017.

[4] J. Yang, *Characteristics of the Dust Storms in the Northern China and its Relationship to Natural Factors over the Period 1960 to 2007*, Lanzhou University, China, 2015.

[5] K. Zhang, J. Qu, Y. Yu et al., "Progress of research on wind-blown sand prevention and control of railways in China," *Advances in Earth Science*, vol. 34, no. 06, pp. 573–583, 2019.

[6] Y. Xiao and G. Zhang, "Study on weatherability technology of EMUs on lanzhou-xinjiang railway," *Railway Locomotive & Car*, vol. 34, no. 04, pp. 90–93, 2014.

[7] G. Wu, C. Chi, and X. Zhang, "Research progress of roof insulator used for high-speed train," *Southern Power System Technology*, vol. 10, no. 03, pp. 71–78, 2016.

[8] B. He, G. Zhang, B. Chen et al., "Simulation experimental study on the influence of dust environment on the discharge characteristics of plate to plate electrode air gap," *Science in China*, vol. 40, no. 03, pp. 296–302, 2010.

[9] X. Zhang, X. Yin, Y. Kang, G. Cao, S. Peng, and G. Wu, "Breakdown voltage of needle-plate Air gaps in high-speed sand environment," *High Voltage Engineering*, vol. 44, no. 12, pp. 3973–3979, 2018.

[10] W. Sima, L. Wu, and Q. Yang, "Effect of sand dust environment on external insulation of electrical power system," *High Voltage Engineering*, vol. 34, no. 01, pp. 16–20, 2008.

[11] A. A. Al-Arainy, N. H. Malik, and M. I. Qureshi, "Influence of sand/dust contamination on the breakdown of asymmetrical air gap under lightning impulses," *IEEE Transactions on Dielectrics and Electrical Insulation*, vol. 27, no. 02, pp. 193–206, 1992.

[12] A. A. Al-Arainy, N. H. Malik, and M. I. Qureshi, "Influence of desert pollution on the lightning impulse breakdown voltages of rod to plane air gaps," *IEEE Transactions on Dielectrics and Electrical Insulation*, vol. 6, no. 01, pp. 421–428, 1991.

[13] M. I. Qureshi, N. H. Malik, and A. A. Al-Arainy, "Performance of protective rod gaps for medium voltage networks in the presence of dust particles under lightning impulses," *IEEE Transactions on Dielectrics and Electrical Insulation*, vol. 14, no. 04, pp. 1311–1316, 1999.

[14] M. I. Qureshi, N. H. Malik, and A. A. Al-Arainy, "Performance of rod-rod gaps in the presence of dust particles under standard switching impulses," *IEEE Transactions on Dielectrics and Electrical Insulation*, vol. 8, no. 03, pp. 1045–1051, 1993.

[15] W. Sima, H. Cheng, and Q. Yang, "AC Flashover performance and mechanism of insulator in wind sand environment," *High Voltage Engineering*, vol. 34, no. 04, pp. 834–840, 2011.

[16] J. Gen, B. Jia, Z. Xu, and P. Wang, "Flashover characteristics of insulators in strong wind environment," *High Voltage Engineering*, vol. 37, no. 01, pp. 227–233, 2011.

[17] X. Liu, C. Gao, X. Deng, L. Cao, and X. Chen, "Influence of high-speed airflow on surface discharge characteristics of insulator," *Transactions of China Electrotechnical Society*, vol. 25, no. 12, pp. 16–21, 2010.

[18] X. Yu, G. Wu, X. Zhang, Y. Kang, Y. Liu, and Y. Wang, "Flashover characteristics of epoxy resin insulator in high-speed charged sand environment," *High Voltage Engineering*, vol. 45, no. 01, pp. 144–151, 2019.

[19] A. Marquard, J. Meyer, and G. Kasper, "Influence of corona Quenching on Charging and Collection of Nanoparticles," in *Proceedings of the International society for electrostatic precipitation conference (ISESP)*, pp. 1–11, 2007.

[20] H. Xu, Z. He, J. Bai, J. Zhou, C. Yang, and J. Li, "Experiment study on direct current corona discharge in two-phase mixture of gas and solid," *High Voltage Engineering*, vol. 32, no. 02, pp. 42–45, 2007.

[21] X. Meng, J. Zhu, and H. Zhang, "The characteristics of current density distribution during corona charging processes of different particulates," *Journal of Physics D: Applied Physics*, vol. 41, no. 17, Article ID 172007, 2008.

[22] W. Yao, Z. He, H. Deng et al., "Effects of macroparticle sizes on two-phase mixture discharge under DC voltage," *Proceedings of the CSEE*, vol. 32, no. 13, pp. 144–151, 2012.
[23] M. Li, F. Wang, F. Zhao et al., "Numerical simulation of rod-plate gap streamer discharge in SF_6/N_2 gas mixtures based on ETG-FCT method," *Mathematical Problems in Engineering*, vol. 2015, Article ID 9853439, 2015.
[24] Q. Ye, J. Li, and J. Zhang, "A dipole-enhanced approximation for a dielectric mixture," *Journal of Electrostatics*, vol. 61, no. 2, pp. 99–106, 2004.
[25] C. Yang, J. Li, and Q. Ye, "A generalized dipole-enhanced approximation for a dielectric mixture," *Electromagnetics*, vol. 26, no. 06, pp. 473–483, 2006.
[26] Q. Ye, J. Li, and C. Yang, "A displaced dipole model for spheres in a nonuniform field," *Journal of Electrostatics*, vol. 56, pp. 1–18, 2002.
[27] Y. Kang, G. Wu, X. Zhang et al., "Modeling of flowing gas discharge – Part I," *IEEE Transactions on Dielectrics and Electrical Insulation*, vol. 26, no. 04, pp. 1048–1055, 2019.
[28] Y. Kang, G. Wu, X. Zhang et al., "Verification and analysis of flowing gas discharge – Part II," *IEEE Transactions on Dielectrics and Electrical Insulation*, vol. 26, no. 04, pp. 1056–1064, 2019.
[29] Y. Kang, G. Wu, C. Chi et al., "Breakdown characteristics and mechanisms of short needle-plate air gap in high-speed airflow," *IEEE Transactions on Plasma Science*, vol. 45, no. 09, pp. 2406–2415, 2017.
[30] X. Guo, Q. Zhang, and J. Zhang, "Improvement of corona discharge model and its application on simulating corona discharge in the presence of wind," *Mathematical Problems in Engineering*, vol. 2017, Article ID 9853439, 2017.
[31] Q. Ye, J. Li, and Z. Xie, "Analytical model of the breakdown mechanism in a two-phase mixture," *Journal of Physics D: Applied Physics*, vol. 37, no. 24, pp. 3373–3382, 2004.
[32] L. Wang, N. C. Pereira, and Y. T. Hung, *Air Pollution Control Engineering*, pp. 3373–3382, Tsinghua University Press, Beijing, China, 2000.
[33] J. M. Meek, "A theory of spark discharge," *Physical Review*, vol. 57, no. 8, pp. 722–728, 1940.
[34] H. Deng, Z. He, J. Ma, Y. Xu, L. Zhu, and R. Guo, "Effect of large sand dust particles on discharge development in sand dust weather," *High Voltage Engineering*, vol. 36, no. 05, pp. 1246–1251, 2010.
[35] X. Yu, *Flashover Characteristics of Roof Insulator in High-Speed Charged Sand Environment*, Southwest Jiaotong University, Chengdu, China, 2018.
[36] W. Yao, Z. He, H. Deng, J. Li, and J. Ma, "Experimental investigation of two-phase mixture discharges under DC voltage from effects of macro-particle sizes," *IEEE Transactions on Plasma Science*, vol. 39, no. 03, pp. 856–864, 2011.

Hindawi
Mathematical Problems in Engineering
Volume 2022, Article ID 2050821, 13 pages
https://doi.org/10.1155/2022/2050821

Research Article

The Impact of Critical Flutter Velocity in Composite Wind Turbine Blade with Prebend Condition

H. S. Sunil Kumar,[1] **K. R. Jagadeesh**,[2] **R. B. Anand**,[3] **T. Rangaswamy**,[4] **Srikanth Salyan**,[5] **Jenoris Muthiya Solomon**,[6] **Joshuva Arockia Dhanraj**,[7] **and Joshua Stephen Chellakumar Isaac Joshua Ramesh Lalvani**[8]

[1]*Department of Mechanical Engineering, D.A.C.G. (Govt.) Polytechnic, Chikmagalur 577101, India*
[2]*Department of Mechanical Engineering, Smt L.V. (Govt.) Polytechnic, Hassan 573201, India*
[3]*Department of Mechanical Engineering, National Institute of Technology, Tiruchirappalli 620015, India*
[4]*Departments of Mechanical Engineering, Government Engineering College, Hassan 573201, India*
[5]*Department of Aeronautical Engineering, Dayananda Sagar College of Engineering, Bangalore 560111, India*
[6]*Department of Automobile Engineering, Dayananda Sagar College of Engineering, Bangalore 560111, India*
[7]*Centre for Automation and Robotics (ANRO), Department of Mechanical Engineering, Hindustan Institute of Technology and Science, Chennai 603103, India*
[8]*Faculty of Mechanical Engineering, ArbaMinch Institute of Technology, ArbaMinch University, ArbaMinch, Ethiopia*

Correspondence should be addressed to H. S. Sunil Kumar; sunil.kumar.slvp@gmail.com

Received 24 November 2021; Revised 6 January 2022; Accepted 28 January 2022; Published 2 March 2022

Academic Editor: Jinyan Song

The present work focuses on the effect of flutter in prebend 100 m horizontal axis wind turbine blade (HAWT) within the stability limits. The study was carried out with an advanced beam model for idyllic structure in a DU-97-W-300 cross-sectional area. A Galerkin type of approach has been applied to derive the equations, and the analysis was performed using a standard FEA code which involves the PK method and double lattice method for calculating flutter solution and aerodynamic loads respectively. The results reveal the significance of inducing prebending to improve the stability of the blade structures, and hence, the flutter velocity has moved from 11 m/s to 23 m/s. Furthermore, the output highlights the effect of prebending on the structural stability and also the flutter limit was found to be lengthened.

1. Introduction

The tremendous increase in energy demand and the factors affecting environmental degradation due to production of energy has resulted in dependence on clean energy resources. Among various resources wind energy has outperformed its counterparts for reliable source for renewable energy resources and vast amount of research and implementation is on rise in the recent decades. The design optimization of wind turbine and blades is essential to extract more energy to meet increasing energy demand which results in study of increasing in blade size while exposing them to high load conditions; at the same time wind blades should be flexible and slender. Because of such slenderness issues there are multiple phenomena which tend to make the blades unstable. Figure 1 and Figure 2 illustrate the wind turbine blade with prebend configuration and prebend blade terminology.

The preliminary sciences of such instabilities like aeroelasticity, flutter instability, and relative factors have been clearly explained in [2]. The structural stability and its mathematical relation with the boundary and load conditions have been derived in [3] while, various types of dynamic instabilities and relations are detailed in [4]. The flutter instability has been found to be capable of becoming a prime design driver for future wind turbine blades and

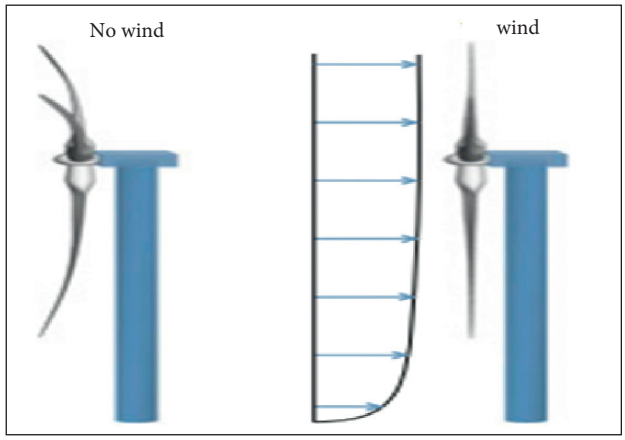

Figure 1: Wind turbine blade with prebend configuration [1].

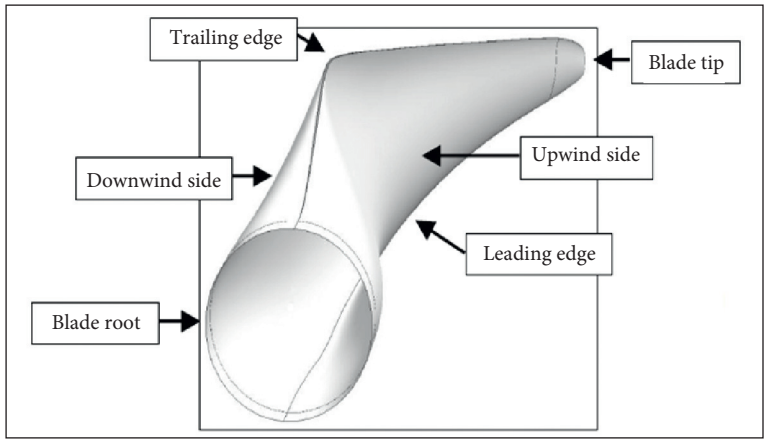

Figure 2: Prebend blade terminology.

thus has emerged as an area of research, where researchers and scientists have come up with several methods to detect, control, and eliminate such instabilities. The flutter instability is considered more important as it is much difficult to detect when compared to resonance. One such method for enhancing the stability is what is called prebending of the blade structure. To tackle such issues without sacrificing the expectations of energy output, prebending of the blade structures is performed to reduce blade weight, improve overall energy generation capacity per annum, and increase tip deflection to a certain extent. The aim of this work is to investigate the wind turbine with prebend condition and its flutter velocity. The preliminary studies investigate the aeroelastic behaviour of blade structures revealing that the flutter limit of a blade depends upon natural frequencies of torsional as well as flapwise direction of a blade [5]. Further, studies on the influence of system parameters and its uncertainties for the wind turbine blades on onset of flutter suggest that structural randomness can make the blade more unstable by decreasing the critical speed for fluttering below the operational speed designated for the wind turbine [6]. After detecting the occurrence of flutter instability, researchers moved further to find optimum methods which show the closeness in approximation using reliability evaluation methods [7]. As further studies kept revealing more and more flutter control parameters, the analysis techniques gained more correctness and reliability [8]. The aeroelastic stability in a wind turbine is presented by another simplified method using Eigen value approach [9] and linear aerostatic turbine model [10] to find the critical frequency of three-bladed rotor arrangements. Similarly, [11, 12] study the fluttering of two-dimensional as well as three-dimensional nonlinear cyclic oscillations and its effect on aeroelastic instabilities. An approach to flutter analysis study by nonlinear damping for aerofoil using equivalent linearization [10] and Range Kutta method [13] for various tip speed ratio is reported in literature.

The above analysis investigated the structural instability and flutter analysis of large wind turbine blades; there aroused a necessity to induce structural modification techniques and study their effect on the blade reliability and longer life under the desired operating conditions. Among such modifications, prebending is one where the blade is bent towards aerodynamic pressure to ensure interference margins with the tower. Although this technique has provoked more difficulties in transportation and storage, the studies show that this method has overall impact in the performance and reliability of the structure. Prebending

being an effective technique has also increased the complexity of design and evaluation as the induced bend has an impact on length of the blade and on angle of attack, thereby affecting the aerodynamic load. Generally, a coupled aerodynamic-structural iterative analysis will predict the aerodynamic loading and structural response in a better way. Paper [14] has conducted a parametric study on a swept blade for a power output of 750 kW wind turbine along with modification in design conditions. Papers [15, 16] investigated the flutter speed for wind turbines with two different types of straight and swept blades. Paper [17] has established several methods for predicting the prebend shape of the wind turbine blades such as when the blades are straightened into their design configuration when they are subjected to both wind and inertial loads. Paper [1] studied the comparison of multiple prebend positions and performed an optimization analysis based on multiobjective particle swarm optimization algorithm (MOPSO) to study the optimized design of blade in order to perform well in reliability, cost, energy efficiency, and stability. The frequency along with deflection change in the geometry with respect to backward sweep is presented in [18]. References [19, 20] made investigations and concluded that backward swept shapes also help in load alleviation without greatly increasing blade root torsion and life-time equivalent fatigue moment. Mehrvarz [21] addressed a Timoshenko beam's asymptotic stability with respect to the effect of piezoelectric actuators. Sahoo [22] compared numerical results computed using MATLAB with experimental data for higher order model of a composite layered shell structure. Meanwhile, Nahavandian [23] investigated the linear stability of thixotropic fluid obeying Moore model using a temporal stability analysis with infinitesimally small perturbations. Fakhraei [24] studied chaotic behaviour of a ground oscillating system by modeling a full nonlinear seven-degree freedom system with an addition of freedom for passengers in one degree. Lobitz [25] studied 3.5 MW turbine blades and concluded that the natural frequencies are subjected to change because of torsional and bending stiffness changes in blades. Meng [26] investigated the flutter frequency as well as critical speed for NREL 5 MW turbine blade for coupling of first torsional and second flapwise modes (instead of the third). Owens et al. [27] developed BLAST, an aerostatic stability design tool, which is an extension of the NASTRAN for flutter analysis for the study with better flutter trends, and studied the impact of composite blade to study the start of instability in blade in two different blades (Wind PACT of 1.5 MW and SNL 100–00 blade). The flutter onset was detected at 13.05 rpm and 40.6 rpm for the SNL 100–00 blades and Wind PACT, respectively. Jonkman et al. [28] developed a design tool called HAWCStab stability tool to study the properties of the blade by using eigenvalue analysis and linearization of nonlinear aeroelastic methods. Shakya et al. [29] observed that flap-torsional stiffness had elevated impact on critical flutter speed which is improved by 40% due to the unbalance in the complete segment of the blade with symmetric skin. Tamrakar et al. [30] found that the crack had a considerable effect on increasing the natural frequency of the rotor system in contrast to the uncracked rotor system. This is due to the buildup of the strain energy in the surrounding area of the crack. Yu Hua et al. [31] discussed the analysis of joint state and unknown input evaluation for linear systems with an unknown input and proposed two novel filters as advanced algorithmic control. Further Kai Wang et al. [32] proposed the Kalman filter algorithm for the estimation of state of charge (SOC) in supercapacitors and lithium batteries of electric vehicles. Chunli Liu et al. [33] suggested the new method of estimating the remaining useful life prediction of supercapacitors in energy storage devices. Further the occurrence of flutter instability in delaminated wind turbine blades has been studied [34]. Although these studies have analysed and revealed how prebending of the structure is altering the structural properties and stability, very few studies have been made to understand its influence on flutter limit. But, from these studies, it is clear that prebending seems to have a good impact on the blade's flutter performance. The change of dependency of modes on load conditions has not been studied. This study highlights the change in dependency of a mode on aerodynamic load due to prebending induced on the structure.

2. Mathematical Modeling

The equations of motion for a force applied on a body by airflow are dependent on the body's elastic deformation and it obeys both elasticity and aerodynamics theories. Figures 3 and 4 show the flow direction in a blade arrangement and representation of the blade aerofoil DU-97-W-300, respectively. The fluid flows demonstrate the relationship between elastic and aerodynamic parameters. The configuration is supposed to be such that the blade's centre axis is perpendicular to the flow direction and U represents the available free stream air velocity.

A blade can be considered a cantilever beam structure because of its high aspect ratio structure. The current study focuses on the effects of flutter instability, as well as the deformations that result in both torsion and flap directions. The deformation is measured by a deflection 'X' and rotation 'θ,' where X indicates downward displacement and θ indicates a twist with the leading edge up.

$$\begin{aligned} &\frac{\partial^2}{\partial x^2}\left(EI\frac{\partial^2 X}{\partial x^2}\right) + m\frac{\partial^2 X}{\partial t^2} + my_\theta\frac{\partial^2 \theta}{\partial t^2} + F_L = 0, \\ &-\frac{\partial}{\partial x}\left(GJ\frac{\partial \theta}{\partial x}\right) + I_\theta\frac{\partial^2 \theta}{\partial t^2} + my_\theta\frac{\partial^2 w}{\partial t^2} + F_M = 0. \end{aligned} \tag{1}$$

Bending and torsional rigidities are represented by EI and GJ, respectively, whereas lift force and twisting moment are represented by F_L and F_M, which are as follows:

$$\begin{aligned} F_L &= \frac{\rho U^2}{2} c\mathrm{C}_1, \\ F_M &= \frac{\rho U^2}{2} c^2\mathrm{C}_2. \end{aligned} \tag{2}$$

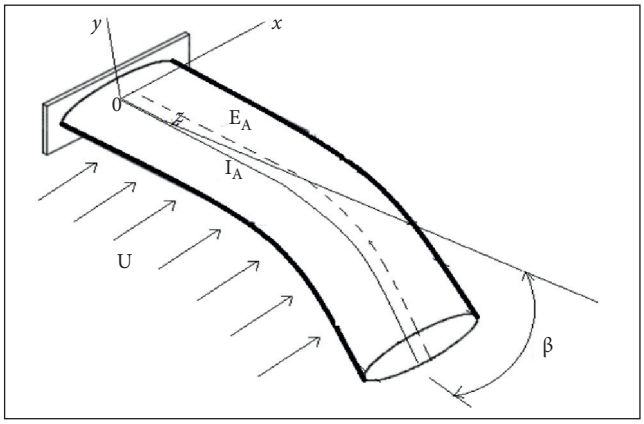

Figure 3: A view of blade arrangement and flow direction.

The lift coefficient C_1 and the moment coefficient C_2 are calculated using quasi-steady subsonic aerodynamic theory.

$$C_1 = \frac{dC_1}{dx}\left(\theta + \frac{1}{U}\frac{dx}{dt} + \frac{1}{U}\left(\frac{3}{4}C - x_0\right)\frac{d\theta}{dt}\right), \tag{3}$$

$$C_2 = -\frac{c\pi}{8U}\frac{d\theta}{dt} - \frac{1}{4}C_1. \tag{4}$$

The lift force is one-fourth (1/4) of the chord value, as shown in equation (4).

The moment and aerodynamic force of the prebend blade are given by quasi-steady double lattice approach in the aforementioned equations. By using (3) and (4), we get

$$\frac{\partial^2}{\partial x^2}\left(EI\frac{\partial^2 X}{\partial x^2}\right) + m\frac{\partial^2 X}{\partial t^2} + my_\theta\frac{\partial^2\theta}{\partial t^2} + \frac{\rho U^2}{2}c\frac{dC_1}{d\theta}\left[\theta + \frac{1}{U}\frac{dX}{dt} + \frac{1}{U}\left(\frac{3}{4}c - x_0\right)\frac{d\theta}{dt}\right] = 0, \tag{5}$$

$$-\frac{\partial}{\partial x}\left(GJ\frac{\partial\theta}{\partial x}\right) + I_\theta\frac{\partial^2\theta}{\partial t^2} + my_\theta\frac{\partial^2 w}{\partial t^2} + \frac{\rho U^2}{2}c^2 - \frac{c\pi}{8U}\frac{d\theta}{dt} - \frac{1}{4}\left\{\frac{dC_1}{d\theta}\left[\theta + \frac{1}{U}\frac{dX}{dt} + \frac{1}{U}\left(\frac{3}{4}c - x_0\right)\frac{d\theta}{dt}\right]\right\} = 0. \tag{6}$$

The boundary conditions to be used in the equation for the displacements 'θ', 'X' are given below:

$$X = \frac{\partial X}{\partial x} = 0; \text{ for } x \text{ values equal to } 0, \tag{7}$$

$$\frac{\partial^2 X}{\partial x^2} = \frac{\partial^3 X}{\partial x^3} = \frac{\partial\theta}{\partial x} = 0; \text{ for } x \text{ values equal to } L. \tag{8}$$

In the corresponding (5) and (6) the X, Y are considered as two independent equations for the values of U and $y_\theta = 0$, where U and y_θ represent the aerodynamic and inertial couplings and determined using the following equation:

$$X(x,t) = A(x)e^{\lambda t} an\ d\theta(x,t) = B(x)e^{\lambda t}. \tag{9}$$

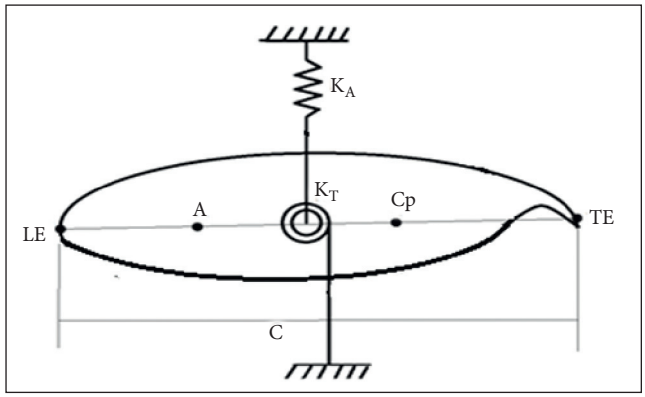

Figure 4: 2D diagram of aerofoil DU-97-W-300.

The ODE equation is obtained by dividing the equation by $e^{\lambda t}$. By applying equation (9) in (5) and (6), we get a complex DE.

$$(EIA'')'' + \frac{\rho U^2}{2}c\frac{dC_1}{d\theta}B + \lambda\frac{\rho U}{2}c\frac{dC_1}{d\theta}\left[A + c\left(\frac{3}{4} - \frac{y_\theta}{c}\right)B\right] + \lambda^2 m(A + y_\theta B) = 0, \tag{10}$$

$$-(GJB) - \frac{\rho U^2}{2}c^2\left(\frac{y_\theta}{c} - \frac{1}{4}\right)\frac{dC_1}{d\theta}B - \lambda\frac{\rho U}{2}c^2 \cdot \left\{\left(\frac{y_\theta}{c} - \frac{1}{4}\right)\frac{dC_1}{d\theta}A + c\left[\left(\frac{y_\theta}{c} - \frac{1}{4}\right)\left(\frac{3}{4} - \frac{y_\theta}{c}\right)\frac{dC_1}{d\theta} - \frac{\pi}{8}\right]B\right\} + \lambda^2(my_\theta A + I_\theta B) = 0, \tag{11}$$

where $(\ )' = d/dx$ and $(\ )'' = d^2/dx^2$

The boundary conditions are applied and remain the same as before, except the values X and θ, which are replaced by A and B. The partial derivatives of X are replaced by total derivatives. Since there is no way to solve (9) and (10) in closed form, an approximate answer is used in the study. The impact of airflow velocity U on wind blade is examined by eigenvalue which determines the structure's stability condition. The parameter (λ) depends upon the air velocity U in a continuous form. For the nonzero values of U, a small value takes an exponent value and becomes a complex value $\lambda = \alpha + i_\omega$. This value is examined using non-self-nearby (adjoint) values. For values which are not equal to zero but are very small, both the U and ($dC_1/d\theta$) with a condition of less than$< 2\pi$, the losses of blade are more with most of the energy being lost to the surrounding air. This causes the oscillatory motion to be damped and instability exhibiting asymptotically for which 'α' takes negative value.

As the value of U rises, "α" changes from negative to positive, and the "α" sign changes and becomes unstable at a point where α becomes positive. Also, when the critical velocity $\alpha = 0$ is the air velocity, that corresponds to 0 and is represented by Uc. There critical velocity values for U have numerous different values; however the lowest value for critical velocity value is used to determine the limit or operational range. The value of U can be used to distinguish between two critical circumstances. The critical divergent

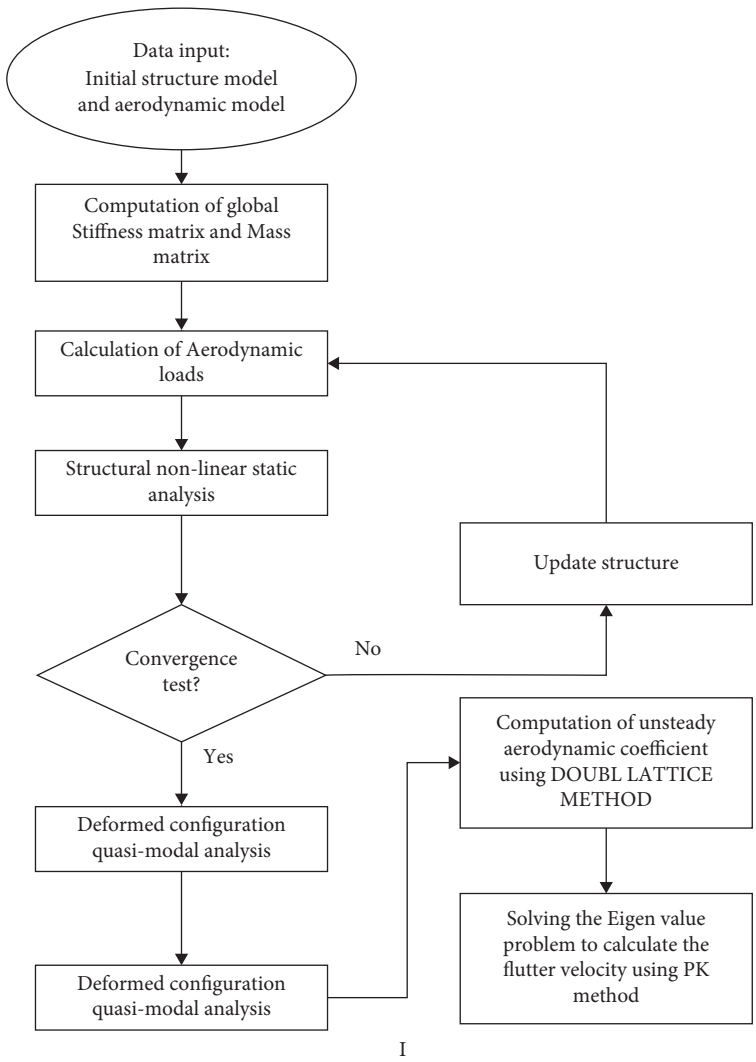

Figure 5: Flow process of the analysis.

Table 1: Ply stiffness properties.

Material	E_{xy} (GPa)	E_{yy} (GPa)	G_{xy} (GPa)	υxy	Density (kg/m^3)
Gel coat	3.44	3.44	1.38	0.3	1235
Resin	3.5	3.5	1.4	0.3	1100
Foam	0.256	0.256	0.022	0.3	200
TRIAX	27.7	13.65	7.2	0.39	1850
E-LT-5500	41.8	14.0	2.63	0.28	1920
Saertax	13.6	13.3	11.8	0.51	1780

Table 2: Flutter speed comparison.

References	Blade	Blade length (m)	Critical flutter speed (rpm)
Lobitz [25]	WindPACT 1.5 MW	33	42.3
Hansen [9]	NREL 5 MW	63	24.0
Owens and Griffith [27]	SNL 100	100	13.05
Current study	SNL 100	100	14.12

Table 3: Mode frequency comparison.

Frequency	Meng [26]	Jonkman et al. [28]	Paryaya et al. [5]	Hansen et al. [9]	Present study
1st flapwise	0.72	0.7	0.64	0.7	0.6
2nd flapwise	2.05	2.02	1.86	1.8	1.75
3rd flapwise	4.37	—	4.34	3.6	3.49
1st torsional	5.62	—	5.39	8	6.04

Table 4: Natural frequency of prebend and flat modes.

Mode	Prebend blade mode frequency (Hz)	Flat blade mode frequency (Hz)
1st bending mode	0.28	0.26
1st torsion mode	0.52	0.45
2nd bending mode	0.99	0.90
3rd bending mode	2.21	1.94
4th bending mode	2.24	2.03
2nd torsion mode	4.07	3.68
1st chordwise bending mode	4.91	4.66
3rd torsion mode	5.61	5.24
4th torsion mode	6.46	5.87
2nd chordwise bending mode	9.23	8.38

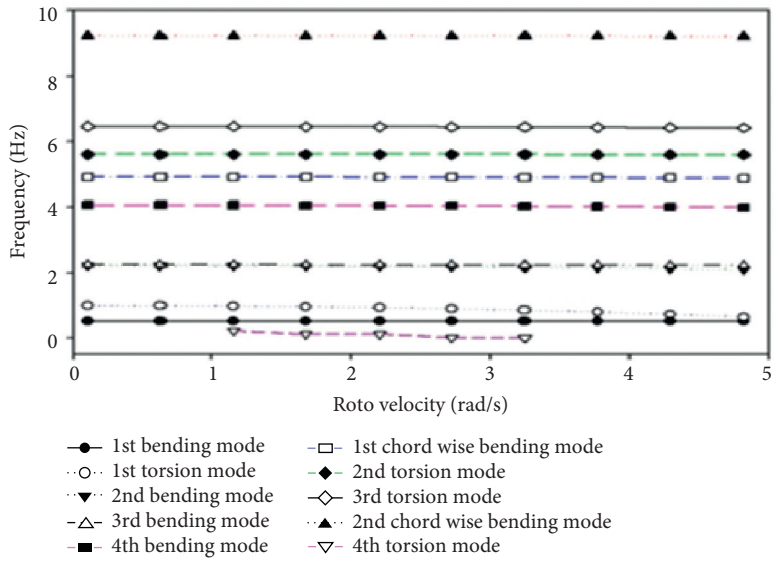

Figure 6: Eigen frequencies for the blade with respect to rotor velocity.

state is given by the values for $\alpha = 0$ and $\omega = 0$ for the wing and critical flutter condition for blade is given for the conditions of $\alpha = 0$ and $\omega \neq 0$.

3. Methodology

The Galerkin approach is used to solve the coupled partial differential equations of motion, which discretizes the equations spatially and provides an analysis of flexible structural instabilities owing to fluid flow.

The torsional and flapwise displacements using Galerkin approach are given by

$$A = \sum_{j=1}^{n} \varphi_1(x).q_1(t),$$
$$B = \sum_{j=n+1}^{n'} \varphi_2(x).q_2(t). \quad (12)$$

In this equation, φ_1 and φ_2 represent the torsion and flap wise mode whereas n and n^1 represent the mode numbers in both torsional and flapwise directions. Similarly, q_1, q_2 are synchronized with respect to the directions. The nondimensional lift and moment equations are substituted in the equation and multiplied by the values of Eigen values. The values are integrated with

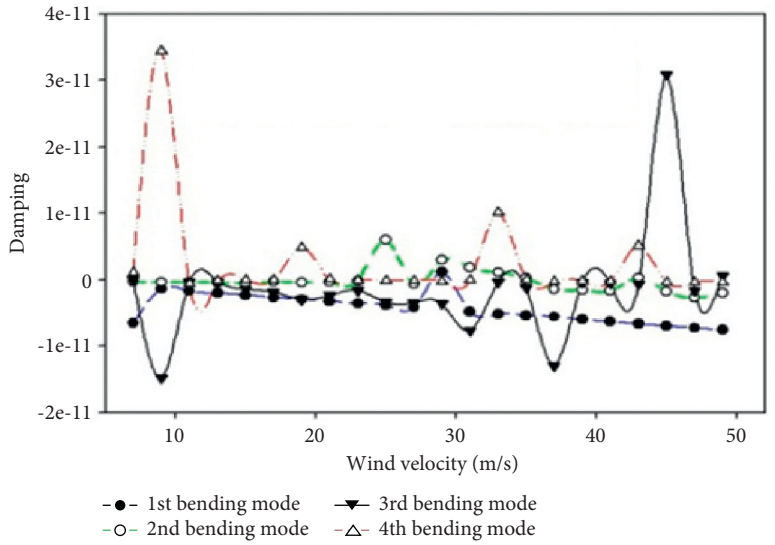

Figure 7: Damping curves of the blade bending modes with respect to the wind velocity.

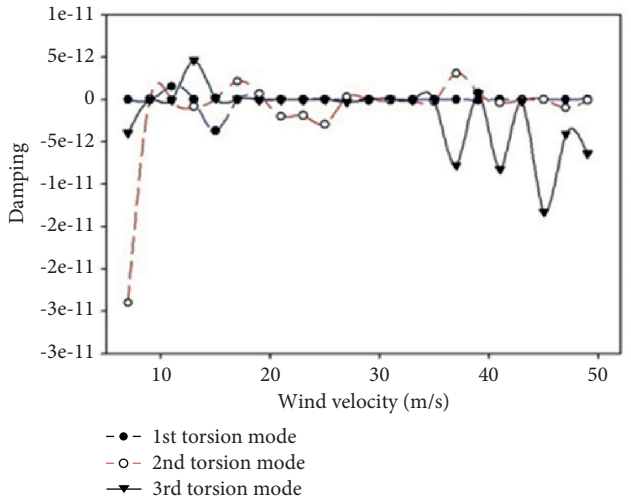

Figure 8: Damping curves in blade torsion modes with respect to the wind velocity.

respect to the length of the blade. The obtained equation corresponds to the eigenvalue problem, solving which gives the stability analysis of the blade structure. Figure 5 explains the computation of unsteady aerodynamic coefficient using double lattice method and solving the eigenvalue problem to calculate the flutter velocity using PK method.

The eigenvalue problem equation upon integration for the values of 0 to L, for the length of the blade,

$$\left[[K] + U^2[Q] + \lambda^2[M]\right]a = 0. \tag{13}$$

The equation is solved for the increased values of U to solve the value of U_c. The λ value will be negative for the small values of U and it is approximately equal to 0 for the first value of the critical air speed U_c. On approximating A and B, Uc values are obtained for the values of n and m equal to 1. For the values of $\lambda = i_\omega$, Uc will be equal to U, which gives an equation in the form of determinant.

$$\begin{bmatrix} i\omega & 0 & -1 & 0 \\ 0 & i\omega & 0 & -1 \\ k_{11} & U^2 h_{12} & i\omega m_{11} + U l_{11} & i\omega m_{12} + U l_{12} \\ 0 & k_{22} + U^2 h_{22} & i\omega m_{12} + U l_{21} & i\omega m_{22} + U l_{22} \end{bmatrix} = 0. \tag{14}$$

By substituting into the real part of (13), we can write the quadratic equation in U^2 as

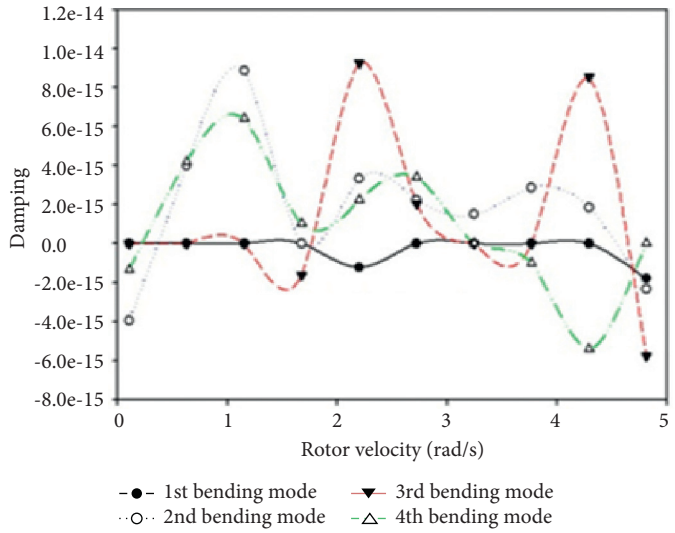

Figure 9: Damping curves of blade bending modes with respect to rotor velocity.

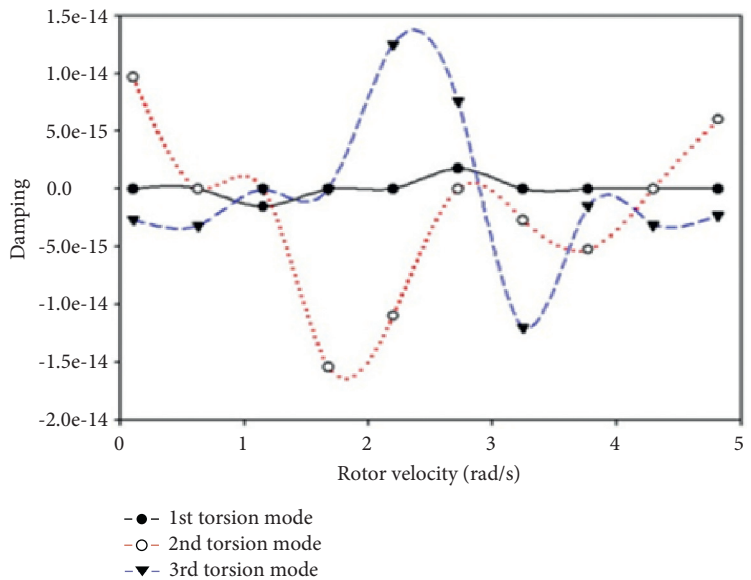

Figure 10: Damping curves of blade torsion modes with respect to rotor velocity.

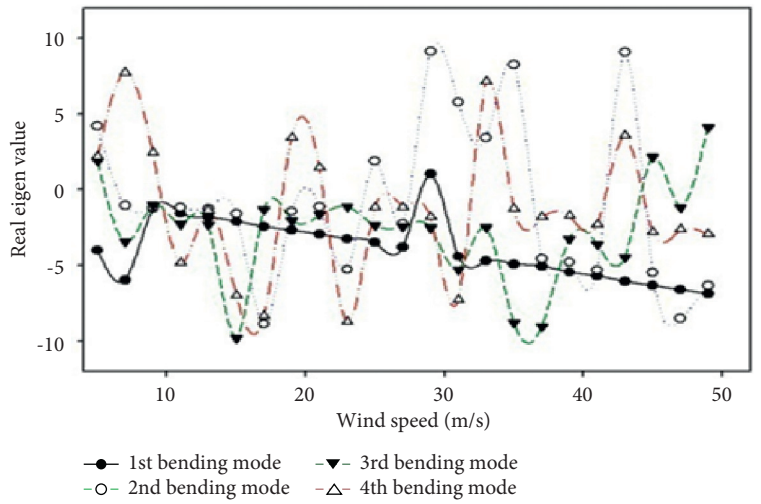

Figure 11: Impact of wind velocity for real eigenvalue in bending modes.

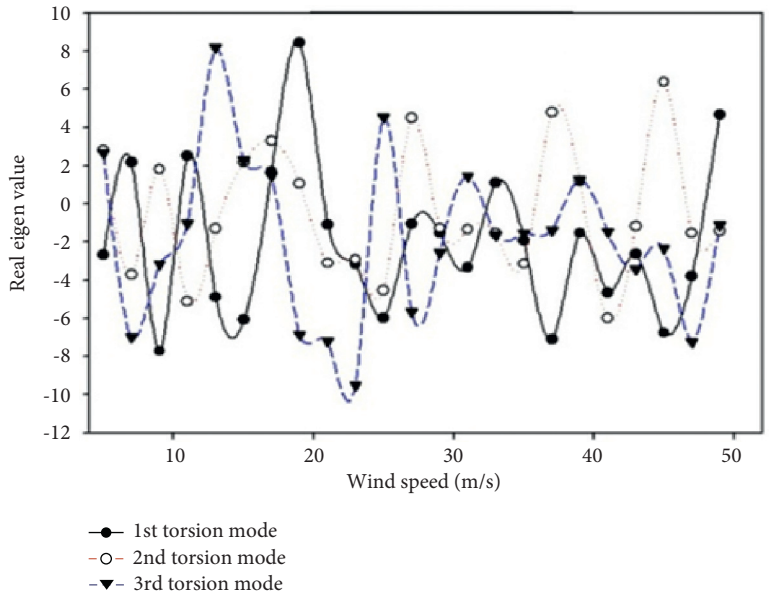

Figure 12: Impact of wind velocity in torsion modes.

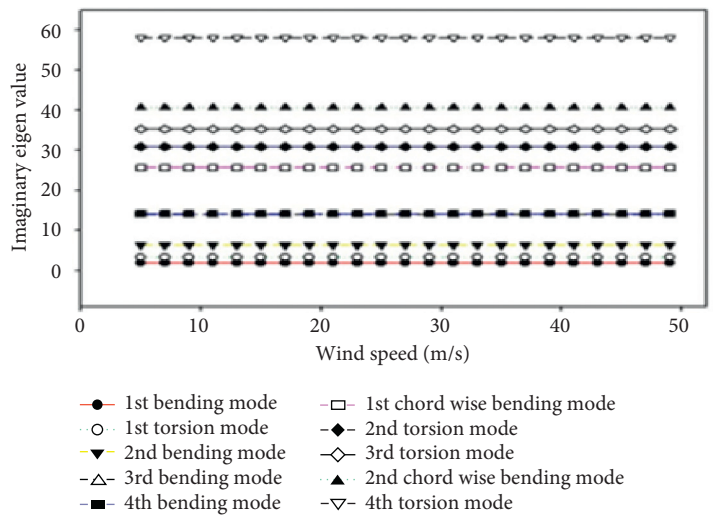

Figure 13: Imaginary part of the eigenvalue with respect to wind velocity.

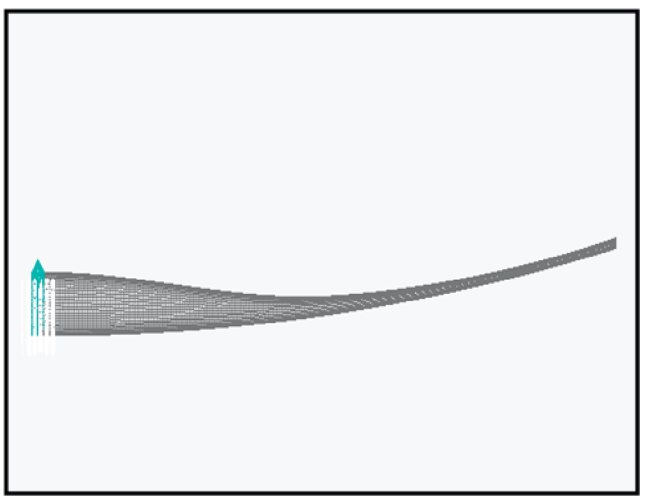

Figure 14: Prebend blade with initial tip deflection.

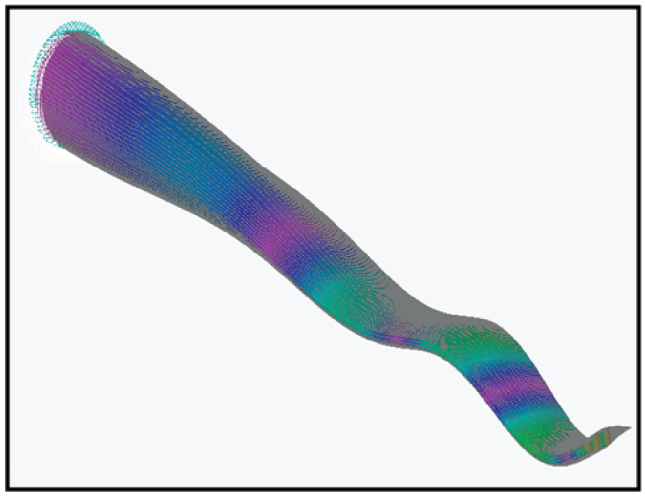

Figure 15: Bending mode of the prebend blade.

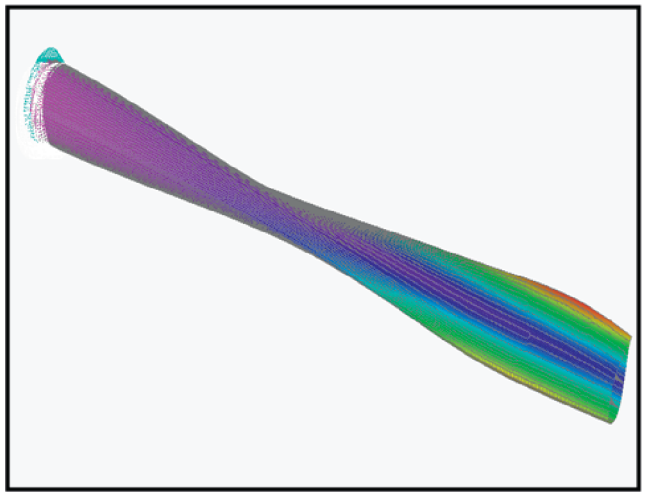

Figure 16: Torsion mode of the prebend blade.

$$CU^4 + DU^2 + F = 0. \tag{15}$$

On substituting the values in (13),

$$U^2 = -\frac{D}{2C} \pm \frac{1}{2C}\sqrt{D^2 - 4CF}. \tag{16}$$

The iterations are carried out for a number of U values, with the air speed with the least positive value taken as critical air speed for which the structural stability exists for the values below this critical air speed. The critical air speed is represented by U_C and is compared to that with prebend and flat blade to study the impact of flutter limit analysis in a wind turbine blade.

3.1. Estimation of Onset for the Flutter Instability. The predication of flutter limits in wind turbine blades is carried out by time dependent aeroelastic analysis or eigenvalue analysis. The eigenvalue analysis involves a model of steady state equilibrium, which is a linear model for blade. This eigenvalue problem is used to study the instability mechanisms. Standard FEA blade model code is used for different blade arrangements and its properties are given in Table 1. The 100-meter blade is used in this study with the boundary conditions applied as stated in (6) and (7), where the blade behaves similar to the cantilever beam. A 5 m tip deflection and an initial bend are also included in the structure. At an altitude of 121.92 meters, the airspeed is gradually increased from 0 m/s to 50 m/s, where the air density corresponds to replicating the blade's surrounding conditions. The blade DOF is depicted in 2D diagram (Figure 4). The mathematical model is solved by PK method for flutter analysis and validates equation by developing aerodynamic matrices for variables such as air speed and frequency. The blade model imported into the standard FEA code is assigned with the composite layup arrangement whose characteristics are listed in Table 1.

3.2. Parametric Study. Now, the parameters like aerodynamic load are varied by varying the wind speed and from its output, the damping curves for the prebend structure are presented with the help of Campbell diagram. Two graphs are obtained for damping ratio due to dynamic as well as inertial forces acting due to the speed of the rotor and change in wind velocity. Also, the comparison shows the influence of aerodynamic load and inertial forces on the modes can be understood. Similarly, the change in stability of the blade due to prebending can also be observed. And also, the flutter speed comparisons with previous research and present one have been shown in Table 2 and further mode frequency comparisons have been tabulated in Table 3.

4. Results and Discussion

The modes of the prebending are studied for natural frequencies and analysed with the same flat blade parameters. The frequency of all the modes in the study is in proximity to each other and thereby the prediction behaviour can be inferred due to the participation of all modes in flutter analysis of the blade structure. Table 4 compares the modal analysis output obtained for flat and prebend configuration of the blade structure.

The results are plot showing the Eigen frequencies with respect to the increasing rotor velocity of blade; in Figure 6, it is observed that the rotor velocity has a significant influence among 1st, 2nd, and 3rd bending mode and 1st torsional mode. Thus, this Campbell diagram can act as evidence to predict the modes that would contribute in the flutter analysis of the blade.

From Figure 7, the damping curve for bending modes is nonlinear and indicates the stability of the bending modes when the wind velocity is increased. The 3rd and 4th bending modes show a higher sensitivity to the wind velocity changes than the 1st and 2nd bending mode.

Figure 8 shows the damping curves with respect to wind velocity. It is also noted that 1st and 2nd torsion mode are capable of easily initiating instability as their curves lay close to zero throughout the graph. But the 1st torsion mode seems to be more stable while the 2nd mode is not as stable as the first one. The graph also indicates the dominance of the 2nd torsion mode when it comes to contributing to the flutter mode as change in dampening ratio shows the sign change in the flutter velocity.

The graph in Figure 9 with curves plotted for damping with respect to rotor velocity clearly depicts the drastic change in slope of all bending modes, where 1st bending mode shows exception for a critical rotor speed in the range between 20 and 30 rpm. The 3rd and 4th bending mode show a mild and sensitive variation with respect to the rotor velocity. The more stable conditions are obtained for low rotor velocities and it can be concluded that, with changing the design to improve the flutter limit, more ideal rotor speed is the velocity of less than 20 rpm for aerodynamic properties with an onset of flutter stability.

Figure 10 shows the damping curves variation along the rotor velocity. The graph shows that the 1st torsion mode is quite stable compared to the other torsion modes. Meanwhile, torsion modes 2 and 3 are found to be highly sensitive and nonlinear to rotor velocity.

Figures 11 and 12 reveal real part of eigenvalue for the bending and torsion modes and the plot is in acceptance with the inference gained from the damping ratio plots.

Figures 13 and 14 of flutter analysis show recorded behaviour of flap and torsional modes with the onset of flutter in the prebend blade.

In Figures 15 and 16, the initial tip deflection and simultaneous bending and torsion contribution of bending and torsion mode are clearly observed. It can be inferred that the deformation of blades is both flapwise and torsional revealing the excitation in both modes under the same frequency, and structure dampening capacity is exceeded due to the higher absorbed energy.

5. Conclusion

The investigation was carried out with a focus to detect the occurrence of flutter instability in a horizontal axis large wind turbine blade with prebend (HAWT). The literature presents and evaluates the mathematic model for a prebend blade for wind turbines at natural frequencies. The study was carried out by advanced beam model for ideal structure in a DU-97-W-300 cross sectional area. A Galerkin type of approach has been used to derive the equations and the analysis was performed involving a standard FEA code which involves PK method and double lattice method for calculating flutter solution and aerodynamic loads, respectively. The study is applied to structural stability, estimation of flutter region, nonlinear influence of blade length, and rotor velocity. The main conclusions from this paper are summarised as follows:

(1) The results reveal the significance of inducing prebending to improve the stability of the blade structures and hence, the flutter velocity has moved from 11 m/s to 23 m/s

(2) The results also ensure that prebending in blades can be used significantly to modify its performances and structural stability without changing its aerodynamic properties

(3) New technique of obtaining damping curves with and without aerodynamic loads helps the designer to decide whether to modify the aerodynamic properties or structural properties for improved flutter limits

For future work, the methods and theories used here can estimate the flutter region but cannot provide any details about interaction of fluid and the dynamic behaviour of the structure beyond the flutter point to study requires a more comprehensive model. The recommendation for further studies is that a wind turbine blade can be manufactured in sections (split blades) and it can be easy for transportation as well as for installation. Thus, integration of joints and structural nodes should be evaluated for performance parameters. It can be extended to determine the impact of prebending of the blade on AEP (annual energy production)

which can also be studied as the prebending will cause the turbine to have a higher AEP than rotors having straight blade due to the increase in the angle of attack along the length of the blade. And also, the impact of glue delamination of blade structure on flutter limits can be analysed [34].

Abbreviations

A and B: Constant coefficients
C, D, and F: Matrix variables
E: Young's modulus
G: Modulus of rigidity
J: Moment of inertia (polar)
I: Moment of inertia (Area) L blade length
P: Load (wind velocity)
X: Deflection due to pitch
U: Air speed/wind velocity
TE: Trailing edge
LE: Leading edge
w: Linear deflection
l: Element length
m: Mass
c: Chord length
q: Coordinates in directions
[K] and [M]: Positive definite stiffness and mass symmetric matrix
[Q]: Displacement matrix [P] load matrix
k: Stiffness
n and n^1: Number of modes
t: Time
j: Variable denoting the number of the mode shape
I_θ: Mass moment of inertia
C_1: Lift coefficient
C_2: Moment coefficient
U_c: Critical wind velocity
Z_G: Shear centre distance in Z direction
C_P: Centre of pressure
K_L: Bending stiffness
E_A: Elastic axis
Y_G:Shear centre distance in Y directionY_θ: Shear centre distance in Y directionY_θ Distance between mass centre and elastic axis at any section
F_L: Lift force
F_M: Moment
x_0: Distance between the aerodynamic centre and leading edge of the aerofoil
K_T: Torsional stiffness
A_C: Aerodynamic centre
I_A:Inertial axis DOF (degrees of freedom) angular deflectionλ: Inertial axis DOF (degrees of freedom) angular deflectionλ: Eigenvalue
α: Real eigenvalue.
ω: Complex eigenvalue
υ: Poison's ratio
ρ: Air density
φ: Mode shape.

Data Availability

The data used to support the findings of this study are included in the article.

Conflicts of Interest

The authors declare that they have no conflicts of interest.

References

[1] Y. Bazilevs, M.-C. Hsu, J. Kiendl, and D. J. Benson, "A computational procedure for prebending of wind turbine blades," *International Journal for Numerical Methods in Engineering*, vol. 89, no. 3, pp. 323–336, 2012.
[2] Y. C. Fung, *An Introduction to the Theory of Aero Elasticity*, John Wiley & Sons, Hoboken, NJ, USA, 2008.
[3] V. V. Bolotin, *Nonconservative Problems of the Theory of Elastic Stability*, Pergamon Press, Oxford, UK, 1963.
[4] R. L. Bisplinghoff, H. Ashley, and R. L. Halfman, *Aeroelasticity*, Dover publications, Inc, Mineola, NY, USA, 2013.
[5] P. Pariya, Y. M. Sadeghi, and M. Lackner, "A parametric study of coupled-mode flutter for MW-size wind turbine blades," *Wind Energy*, vol. 19, no. 3, pp. 497–514, 2016.
[6] P. Pariya, L. Caracoglia, and M. Lackner, "Stochastic analysis of flow-induced dynamic instabilities of wind turbine blades," *Journal of Wind Engineering and Industrial Aerodynamics*, vol. 137, pp. 37–45, 2015.
[7] P. Pariya, L. Caracoglia, M. Lackner, and Y. M. Sadeghi, "Perturbation methods for the reliability analysis of wind-turbine blade failure due to flutter," *Journal of Wind Engineering and Industrial Aerodynamics*, vol. 156, pp. 159–171, 2016.
[8] M. H. Hansen, J. N. Sorensen, S. Voutsinas, N. Sorensen, and H. A. Madsen, "State of the art in wind turbine aerodynamics and aeroelasticity," *Progress in Aerospace Sciences*, vol. 42, no. 4, Article ID 42285, 2006.
[9] M. H. Hansen, "Aeroelastic stability analysis of wind turbines using an eigenvalue approach," *Wind Energy*, vol. 7, no. 2, pp. 133–143, 2004.
[10] M. H. Hansen, "Vibrations of a three-bladed wind turbine rotor due to classical flutter," in *Proceedings of the Fortyth AIAA Aerospace Sciences Meeting and Exhibit, ASME Wind Energy Symposium*, Reno,NV, USA, January 2002.
[11] E. H. Dowell, "Nonlinear oscillation of a fluttering plate," *AIAA Journal*, vol. 4, no. 7, 1996.
[12] E. H. Dowell and H. M. Voss, "Theoretical and experimental panel flutter study," *AIAA Journal*, vol. 3, no. 12, 1995.
[13] F. Chen, J. Liu, and Y. Chen, "Flutter analysis of an airfoil with nonlinear damping using equivalent linearization," *Chinese Journal of Aeronautics*, vol. 27, no. 1, pp. 59–64, 2014.
[14] W. Hao, B. Ma, and J. J. Ding, "The analysis of the flutter region of wind turbine blade," *Applied Mechanics and Materials*, Trans Tech Publications, vol. 423, , 2013.
[15] S. M. Larwood, C. P. Van Dam, and D. Schow, "Design studies of swept wind turbine blades," *Renewable Energy*, vol. 71, pp. 563–571, 2014.

[16] S. M. Larwood, "Prediction and alleviation of flutter in swept wind turbine blades," in *Proceedings of the 33rd wind energy symposium, AIAA Journal*, vol. 1464, pp. 1–10, Kissimmee, FL, USA, January 2015.

[17] S. M. Larwood, "Flutter variations on a 5MW swept wind turbine blade," *Journal Of Solar Energy Engineering: Including Wind Energy and Building Energy Conservation*, vol. 138, no. 2, 2015.

[18] X. Guo, X. Fu, H. Shang, and J. Chen, "Integrated aero-structural optimization design of pre-bend wind turbine blades," *Journal of Mechanical Science and Technology*, vol. 30, no. 11, pp. 5103–5113, 2016.

[19] M. H. Hansen, "Aeroelastic properties of backward swept blades," in *Proceedings of the 49th AIAA Aerospace Sciences Meeting Including the New Horizons Forum and Aerospace Exposition*, Oriando, FL, USA, January 2011.

[20] C. pavese, T. Kim, and J. P. Murcia, "Design of a wind turbine swept blade through extensive load analysis," *Renewable Energy*, vol. 102, pp. 21–34, 2017.

[21] H. Salarieh, A. Alasty, and R. Vatankhah, "Vibration boundary control of micro-cantilever Timoshenko beam using piezoelectric actuators," *Scientia*, vol. 25, no. 2, pp. 711–720, 2018.

[22] S. S. Sahoo, C. K. Hirwani, and S. K. Panda, "Numerical analysis of vibration and transient behavior of laminated composite curved shallow shell structure: an experimental validation," *Scientia*, vol. 25, no. 4, pp. 2218–2232, 2018.

[23] M. H. Nahavandian and M. pourjafar, "Stability of thixotropic fluids in pipe flow," *Scientia Iranica B*, vol. 25, no. 2, pp. 790–798, 2018.

[24] J. Fakhraei, H. M. Khanlo, and M. Ghayour, "Chaotic behaviors of a ground vehicle oscillating system with passengers," *Scientia Iranica*, vol. 24, no. 3, pp. 1051–1068, 2017.

[25] D. W. Lobitz, "Parameter sensitivities affecting the flutter speed of a MW-sized blade," *Journal of Solar Energy Engineering*, vol. 127, no. 4, pp. 538–543, 2005.

[26] F. Meng, "Aero-elastic stability analysis for large-scale wind turbines," vol. 123, Aero-elastic stability analysis for large-scale wind turbines, Delft, Netherlands, 2011, Doctoral thesis.

[27] B. C. Owens, B. R. Resor, D. Griffith, and J. E. Hurtado, "Impact of Modelling Approach on Flutter Predictions for Very Large Wind Turbine Blade Designs," Sandia National Laboratories (SNL-NM), Albuquerque, NM, USA, No. SAND-3108C. 1-11, 2013.

[28] J. Jonkman, S. Butterfield, W. S. Musial, and G. Scott, *Definition of a 5-MW Reference Wind Turbine for Offshore System Development*, National Renewable Energy Laboratory, Calorado, CO, USA, 2009.

[29] P. Shakya, M. R. Sunny, and D. K. Maiti, "A parametric study of flutter behavior of a composite wind turbine blade with bend-twist coupling," *Composite Structures*, vol. 207, pp. 764–775, 2018.

[30] R. Tamrakar and N. D. Mittal, "Campbell diagram analysis of open cracked rotor," *Engineering Solid Mechanics*, vol. 4, pp. 159–166, 2016.

[31] Y. Hua, N. Wang, and K. Zhao, "Simultaneous unknown input and state estimation for the linear system with a rank-deficient distribution matrix," *Mathematical Problems In Engineering*, vol. 2021, Article ID 6693690, 11 pages, 2021.

[32] K. Wang, C. Liu, J. Sun et al., "State of charge estimation of composite energy storage systems with supercapacitors and lithium batteries," *Complexity*, vol. 2021, Article ID 8816250, 15 pages, 2021.

[33] C. Liu, Q. Li, and K. Wang, "State-of-charge estimation and remaining useful life prediction of supercapacitors," *Renewable And Sustainable Energy Reviews*, vol. 150, Article ID 111408, 2021.

[34] H. S. S. Kumar and R. B. Anand, "Parametric study on impact of delamination on flutter velocity of wind turbine blade structure," in *Proceedings of the AIP Conference Proceedings*, vol. 2039, no. 1, April 2018, Article ID 20040.

Hindawi
Mathematical Problems in Engineering
Volume 2023, Article ID 9895041, 1 page
https://doi.org/10.1155/2023/9895041

Retraction

Retracted: Accelerated Iterative Learning Control for Linear Discrete Time Invariant Switched Systems

Mathematical Problems in Engineering

Received 18 July 2023; Accepted 18 July 2023; Published 19 July 2023

This article has been retracted by Hindawi following an investigation undertaken by the publisher [1]. This investigation has uncovered evidence of one or more of the following indicators of systematic manipulation of the publication process:

(1) Discrepancies in scope
(2) Discrepancies in the description of the research reported
(3) Discrepancies between the availability of data and the research described
(4) Inappropriate citations
(5) Incoherent, meaningless and/or irrelevant content included in the article
(6) Peer-review manipulation

The presence of these indicators undermines our confidence in the integrity of the article's content and we cannot, therefore, vouch for its reliability. Please note that this notice is intended solely to alert readers that the content of this article is unreliable. We have not investigated whether authors were aware of or involved in the systematic manipulation of the publication process.

Wiley and Hindawi regrets that the usual quality checks did not identify these issues before publication and have since put additional measures in place to safeguard research integrity.

We wish to credit our own Research Integrity and Research Publishing teams and anonymous and named external researchers and research integrity experts for contributing to this investigation.

The corresponding author, as the representative of all authors, has been given the opportunity to register their agreement or disagreement to this retraction. We have kept a record of any response received.

References

[1] Y. Wang, S. Riaz, Z. Bao, and W. Zhang, "Accelerated Iterative Learning Control for Linear Discrete Time Invariant Switched Systems," *Mathematical Problems in Engineering*, vol. 2022, Article ID 5738826, 10 pages, 2022.

Hindawi
Mathematical Problems in Engineering
Volume 2022, Article ID 5738826, 10 pages
https://doi.org/10.1155/2022/5738826

Research Article

Accelerated Iterative Learning Control for Linear Discrete Time Invariant Switched Systems

Yongping Wang,[1] Saleem Riaz,[2] Ziyun Bao,[1] and Wenqian Zhang[3]

[1]*Ningxia Institute of Water Resources Research, Yinchuan 750021, China*
[2]*School of Automation, Northwestern Polytechnical University, 170072 Xi'an, Shaanxi, China*
[3]*School of Electrical and Control Engineering, Shaanxi University of Science and Technology, Xi'an 710021, China*

Correspondence should be addressed to Saleem Riaz; saleemriaznwpu@mail.nwpu.edu.cn

Received 24 December 2021; Accepted 10 January 2022; Published 30 January 2022

Academic Editor: Jinyan Song

For a class of linear discrete time invariant stochastic switched systems with repetitive operation characteristics, a novel P-type accelerated iterative learning control algorithm with association correction is proposed. Firstly, the concrete form of accelerated learning law is given, and the generation of correction in the algorithm is explained in detail; secondly, on the premise that the switching sequence does not change along the iteration axis but only along the time axis, the convergence of the algorithm is strictly mathematically proved by using the super vector method, and the sufficient conditions for the convergence of the algorithm are given; finally, the theoretical results show that the convergence speed mainly depends on the controlled object, the proportional gain of the control law, the switching sequence, the correction coefficient, the association factor, and the size of the learning interval. Simulation results show that the proposed algorithm has a faster convergence speed than the traditional open-loop P-type algorithm under the same conditions.

1. Introduction

In recent years, switching system has gradually become one of the research hotspots in the control field [1]. Switching system is a kind of important hybrid system, which is composed of a set of differential equations or difference equations and switching rules. According to the changes of actual environmental factors, the whole system can be switched between different subsystems through switching rules so as to meet the requirements of different working conditions and improve the system performance [2]. Therefore, switching systems are widely used in practical engineering systems, such as a traffic control system [3], power system, circuit system [4], and network control system [5]. At present, a large number of research results on switched systems are focused on the stability of switched systems [6], but the research results on the output tracking control of switched systems are very limited [7]. The reason is that it is much more difficult to realize the tracking control of switched systems than the stabilization and stability problems [8,9]. It is worth noting that the ILC algorithm and its optimal robust control [10]can be used in many industrial applications such as robotics control [11], industrial automation [12], power and energy sectors [13–15], chemical plant processing [16], servo control [17], and many other automation industries [18].

Iterative learning control [19], as a model-free control, has a simple structure and does not need specific model parameters. After enough repeated iterations in a limited interval, the behavior of the execution object can meet the expected requirements [18]. Due to the above characteristics, the learning algorithm has been favored by many scholars in recent years, which makes it widely used in the control of a robot rigid manipulator [12,20], batch processing in industries [21], aerodynamic system [22], traffic control system [23], electrical power system, etc. [24–26]. However, at present, most scholars have only performed a lot of research on the control of nonswitched systems, while there are few

research results on the iterative learning control of switched systems [27].

Xu-Hui et al. [28] proposed an open-loop P-type iterative learning control algorithm for a class of linear discrete stochastic switched systems on the premise that the switching sequence is randomly determined and analyzed the convergence of the algorithm by using the super vector method, realizing the complete tracking of the desired trajectory in the whole running finite time interval. For linear and nonlinear discrete switched systems, the convergence of an open-loop D-type ILC algorithm is analyzed in detail by using the compression mapping principle in references [29, 30]. In reference [31], an open-loop D-type ILC algorithm is proposed for a class of continuous random switched systems. Zhou et al. [32] proposed a discrete P-type iterative learning control algorithm for the trajectory tracking problem of a class of time-varying discrete switched systems with arbitrary switching sequences. The convergence of each subinterval was strictly proved by using compressed mapping, and the sufficient conditions of norm form for the convergence of the algorithm were given. Finally, it was compared with the state feedback robust control. Simulation results show the superiority of the iterative learning algorithm. Cao and Sun [33] proposed an iterative learning control algorithm with an attenuation factor, which reduces the influence of measurement noise during trajectory tracking. Bu et al. [34] analyzed the stability and convergence of a high-order PID iterative learning control algorithm in switched systems with state delay. In references [17, 35], aiming at the problem of model uncertainty and external noise of discrete switched systems, the PD type iterative learning algorithm is used to analyze the uncertainty and robustness.

It is important to note that the issue discussed in this article is analogous to the ILC for time-varying linear systems. There are, nevertheless, some critical distinctions. While the time-varying system accepts solutions that are parameterized merely by the initial condition, the switched system admits solutions that are parameterized by both the initial condition and the switching signal. The time-varying linear system in the super vector formulation has a constant lower-triangular Markov parameter matrix throughout the timespan, and the starting state is the same for the entire system. While in a linear switched system, the lifting matrix is defined by both the subsystems and the switching signal. Additionally, the initial condition is same for only the first subsystem, not for all subsystems, resulting in a different convergence approach than for time-varying systems.

Novel Points: The autoassociative ILC proposed in this paper is based on the traditional ILC, namely, using the current information to estimate the future input. Compared to traditional ILC, the new algorithm is characterized as follows: in each trial, the unlearned time is precorrected with the current time information. The algorithm can reduce the number of iterations and accelerate the learning convergence speed.

The algorithm proposed in this paper differs from the traditional discrete closed-loop algorithm and the higher-order algorithm as follows:

(1) Although the algorithm proposed in this paper is similar in form to the traditional closed-loop iterative learning algorithm, the principle is completely different from that of the traditional discrete closed-loop P-type algorithm (feedback algorithm). The traditional discrete closed-loop ILC algorithm is to correct the control input of the current time directly with the error of the previous time in the same trial. The algorithm proposed in this paper uses the error of the current time to pre-estimate the amount of control after which it does not occur at all times and plays the role of precorrection.

(2) Although the associative iterative learning algorithm proposed in this paper is similar in form to the traditional higher-order discrete learning algorithm, the learning process is completely different from the traditional higher-order iterative learning algorithm. The traditional high-order ILC is the algebraic overlay of the control information of the previous two or more trials at the corresponding time. The new iterative learning algorithm proposed in this paper is to precorrect the subsequent unoccurred time with the error value of the current time in the same trial.

The switched system is a piecewise controlled system. When the switching rules of the switched system are arbitrarily selected in the initial iteration and remain unchanged in the learning process, the dynamic structure of the switched system remains unchanged in the learning process, which meets the basic requirements of iterative learning control for the controlled system. On this premise, when the switched system runs repeatedly in a fixed finite time interval and meets certain conditions, iterative learning control can be used to realize the accurate control of the switched system. The proposed algorithms can obtain the consultations exactly in the piecewise means. Strict theoretical proof and corresponding experimental simulation are carried out, which will be published one after another.

Based on the above analysis, for a class of discrete time invariant arbitrary switching systems that perform repeated tracking tasks on the desired trajectory in a finite time interval, under the premise that the switching sequence is randomly determined and the iteration is unchanged, using the characteristics of iterative learning control, taking p-type as an example, a discrete iterative learning control algorithm with backward error association and correction of the control quantity of the next iterative learning is proposed. Combined with the theory of super vector and spectral radius, the convergence of the algorithm is discussed, and sufficient conditions for the convergence of the algorithm are given in theory.

2. Problem Formulation

A class of single input single output linear discrete time invariant switched systems with repetitive operation in a finite time period is considered as follows:

$$\begin{cases} x_k(t+1) = \mathbf{A}_{\sigma(t)}\mathbf{x}_k(t) + \mathbf{B}_{\sigma(t)}u_k(t), \\ y_k(t+1) = \mathbf{C}_{\sigma(t)}\mathbf{x}_k(t+1), \end{cases} \tag{1}$$

where discrete time $t \in \{0, 1, \ldots, N-1\}$, $\mathbf{x}_k(t) \in \mathbf{R}^m$, $u_k(t) \in \mathbf{R}$, $y_k(t) \in \mathbf{R}$ are the state vector, input vector, and output vector of the system; $\mathbf{A}_{\sigma(t)}$ and $\mathbf{B}_{\sigma(t)}$ and $\mathbf{C}_{\sigma(t)}$ are the constant matrices with appropriate dimension; $\sigma(t)$ is a random switching sequence, defined as $\sigma(t)$: $(0, 1, 2, \ldots) \longrightarrow M = \{1, 2, \ldots, m\}$, namely, $\sigma(t)$ takes value in a finite set $M = \{1, 2, \ldots, m\}$; $m > 1$ is the number of subsystems; when $\sigma(t) = i$, the i subsystem is activated; the subscript k indicates the number of iterations.

Hypothesis 1. In each iteration of the switched system, the initial state is equal to the ideal initial state, namely, $\mathbf{x}_k(0) = \mathbf{x}_d(0)$.

Hypothesis 2. Desired trajectory $y_d(t+1)$, $t \in \{0, 1, \ldots, N-1\}$ is predetermined, and it is not related to the number of iterations. Since $u_d(j)$ exists uniquely, the uniform convergence of the control profile $u(j)$ to $u_d(j)$ implies that the state and output tracking errors will be vanished. It is a reasonable assumption that the task for control should be feasible.

Hypothesis 3. For any given desired trajectory $y_d(t+1)$, there are desired states $x_d(t)$ and desired control signal $u_d(t)$ so that a desired output $y_{d(t)}$ is given, and there is only desired control input $u_{\mathrm{d(t)}}$ which generates $x_{d(t)}$ and $y_{d(t)}$, where $x_{d(t)}$ and $y_{d(t)}$ are desired state vector and desired output vector, respectively.

$$\begin{cases} \mathbf{x}_d(t+1) = \mathbf{A}_{\sigma(t)}\mathbf{x}_d(t) + \mathbf{B}_{\sigma(t)}u_d(t), \\ y_d(t+1) = \mathbf{C}_{\sigma(t)}\mathbf{x}_d(t+1), \quad t \in \{0, 1, \ldots, N-1\}. \end{cases} \tag{2}$$

Hypothesis 4. After the random switching sequence $\sigma(t)$ is randomly determined in the first iteration, the sequence is used in the subsequent iterations.

By system (1), the output signals at each time in array $[1, N]$ during the k-th iteration can be expressed as

$$\begin{aligned} y_k(1) &= \mathbf{C}_{\sigma(0)}\mathbf{x}_k(1) = \mathbf{C}_{\sigma(0)}\mathbf{A}_{\sigma(0)}\mathbf{x}_k(0) + \mathbf{C}_{\sigma(0)}\mathbf{B}_{\sigma(0)}u_k(0), \\ y_k(2) &= \mathbf{C}_{\sigma(1)}\mathbf{x}_k(2) = \mathbf{C}_{\sigma(1)}\mathbf{A}_{\sigma(1)}\mathbf{A}_{\sigma(0)}\mathbf{x}_k(0) + \mathbf{C}_{\sigma(1)}\mathbf{A}_{\sigma(1)}\mathbf{B}_{\sigma(0)}u_k(0) + \mathbf{C}_{\sigma(1)}\mathbf{B}_{\sigma(1)}u_k(1), \\ &\vdots, \\ y_k(N) &= \mathbf{C}_{\sigma(N-1)}\mathbf{x}_k(N) \\ &= \mathbf{C}_{\sigma(N-1)}\prod_{j=0}^{N-1}\mathbf{A}_{\sigma(j)}\mathbf{x}_k(0) + \mathbf{C}_{\sigma(N-1)}\prod_{j=1}^{N-1}\mathbf{A}_{\sigma(j)}\mathbf{B}_{\sigma(0)}u_k(0) + \mathbf{C}_{\sigma(N-1)}\prod_{j=2}^{N-1}\mathbf{A}_{\sigma(j)}\mathbf{B}_{\sigma(1)}u_k(1) \\ &\quad + \cdots + \mathbf{C}_{\sigma(N-1)}\mathbf{A}_{\sigma(N-1)}\mathbf{B}_{\sigma(N-2)}u_k(N-2) + \mathbf{C}_{\sigma(N-1)}\mathbf{B}_{\sigma(N-1)}u_k(N-1). \end{aligned} \tag{3}$$

For the convenience of description, the above formula is written in the form of super vector and introduced into super vector.

$$\begin{aligned} \mathbf{U}_k &= \left[u_k(0), u_k(1), \ldots, u_k(N-1)\right]^T, \\ \mathbf{Y}_k &= \left[y_k(1), y_k(2), \ldots, y_k(N)\right]^T. \end{aligned} \tag{4}$$

The above formula can be written as

$$\mathbf{Y}_k = \mathbf{G}U_k + \mathbf{V}, \tag{5}$$

where

$$G = \begin{bmatrix} \mathbf{C}_{\sigma(0)}\mathbf{B}_{\sigma(0)} & 0 & 0 & \cdots & 0 \\ \mathbf{C}_{\sigma(1)}\mathbf{A}_{\sigma(1)}\mathbf{B}_{\sigma(0)} & \mathbf{C}_{\sigma(1)}\mathbf{B}_{\sigma(1)} & 0 & \cdots & 0 \\ \mathbf{C}_{\sigma(2)}\mathbf{A}_{\sigma(2)}\mathbf{A}_{\sigma(1)}\mathbf{B}_{\sigma(0)} & \mathbf{C}_{\sigma(2)}A_{\sigma(2)}B_{\sigma(1)} & \mathbf{C}_{\sigma(2)}\mathbf{B}_{\sigma(2)} & \cdots & \vdots \\ \vdots & \vdots & \vdots & \ddots & 0 \\ \mathbf{C}_{\sigma(N-1)}\prod_{j=1}^{N-1}\mathbf{A}_{\sigma(j)}\mathbf{B}_{\sigma(0)} & \mathbf{C}_{\sigma(N-1)}\prod_{j=1}^{N-1}\mathbf{A}_{\sigma(j)}\mathbf{B}_{\sigma(1)} & \cdots & \mathbf{C}_{\sigma(N-1)}\mathbf{A}_{\sigma(N-1)}\mathbf{B}_{\sigma(N-2)} & \mathbf{C}_{\sigma(N-1)}\mathbf{B}_{\sigma(N-1)} \end{bmatrix}, \tag{6}$$

$$V = \left[\mathbf{C}_{\sigma(0)}\prod_{j=0}^{0}\mathbf{A}_{\sigma(j)}\mathbf{x}_k(0), C_{\sigma(1)}\prod_{j=0}^{1}\mathbf{A}_{\sigma(j)}\mathbf{x}_k(0), C_{\sigma(2)}\prod_{j=0}^{2}\mathbf{A}_{\sigma(j)}\mathbf{x}_k(0), \cdots\ldots, \mathbf{C}_{\sigma(N-1)}\prod_{j=0}^{N-1}\mathbf{A}_{\sigma(j)}\mathbf{x}_k(0)\right]^T.$$

A control law with backward error association and correction of subsequent control variables is considered as follows:

$$\widetilde{u}_k(t) = L\sum_{i=0}^{t} e_k(i+1)e^{K(i-t+1/N)^2}, \quad t \in \{0,1,\ldots,N-1\}, \tag{7a}$$

$$u_{k+1}(t) = u_k(t) + \widetilde{u}_k(t) + \Gamma e_k(t+1), \tag{7b}$$

where $u_{k+1}(t)$ is the control quantity at the time of the K+1th iteration process, $u_k(t)$ is the control quantity at time t of the k-th iteration process, $\widetilde{u}_k(t)$ is the correction of the control quantity by the error at the time and before the k-th iteration process, Γ is the iterative proportional gain, $e_k(t+1) = y_d(t+1) - y_k(t+1)$ is the tracking error. The goal of iterative learning control is to find a control signal sequence through a learning algorithm $\{u_k(t)\}$ and make the output trajectory $y_k(t+1)$ of the controlled system (1) under this sequence control, as the number of iterations increases, progressive tracking of desired trajectory $y_d(t+1)$, namely,

$$\lim_{k\longrightarrow\infty}\left|e_k(t+1)\right| = 0, \quad t \in \{0,1,\ldots,N-1\}. \tag{8}$$

As shown in Figure 1, in the k-th iterative learning process, the error $e_k(1)$ at point 1 will correct the control amount at N time in the (k+1)th iterative process, and the correction amount is shown in Table 1.

The error $e_k(2)$ at point 2 will correct the control amount at N-1 times in the (k + 1)th iteration, as shown in Figure 2, and the correction amount is shown in Table 2.

According to this method, up to point N, its error is $e_k(N)$, as shown in Figure 3, and it only corrects the control quantity of point N in the $K+1$th iteration, and the correction quantity is $Le_k(N)e^{K(1/N)^2}$.

For the discrete switched system (1) meeting the assumptions 1–4, combined with the characteristics of the switched system, the random switching sequence $\sigma(t)$ is added, and the P-type accelerated iterative learning control law for the random switched system is proposed on the basis of the control law (4):

$$\widetilde{u}_k(t) = L_{\sigma(t)}\sum_{i=0}^{t} e_k(i+1)e^{K_{\sigma(t)}(i-t+1/N)^2}, \quad t \in \{0,1,\ldots,N-1\}, \tag{9a}$$

$$u_{k+1}(t) = u_k(t) + \widetilde{u}_k(t) + \Gamma_{\sigma(t)}e_k(t+1), \tag{9b}$$

where $\sigma(t)$ is the random switching sequence.

3. Convergence Analysis

We have developed an accelerated algorithm of P-type ILC strategy with kernel-based auto-associative memory for a linear discrete system. During each iterative learning process, the control value of the current time is corrected. Meanwhile, the amount of control in the subsequent time is precorrected by association, which speeds up the learning process. The iterative learning algorithm based on the kernel function is revealed theoretically in depth. The convergence speed of the association algorithm is illustrated by simulation results, which is related with the proportional learning gain, the learning interval, and the exponential factor. This research method can be widely used to extend to study the influence of association depth and industrial control.

Theorem 1. *A linear discrete time invariant switched system with single input and single output (1) is considered, if assumptions 1–4 are satisfied, and a P-type accelerated iterative learning control algorithm with associative correction (5) is adopted, if the selected learning parameter matrix satisfies*

$$\rho = \max_t\left|1 - \left(L_{\sigma(t)}e^{K_{\sigma(t)}(1/N)^2} + \Gamma_{\sigma(t)}\right)\mathbf{C}_{\sigma(t)}\mathbf{B}_{\sigma(t)}\right| < 1. \tag{10}$$

The output trajectory uniformly converges to the desired trajectory, when $k \longrightarrow \infty$, $y_k(t+1) \longrightarrow y_d(t+1)$, $t \in \{0,1,\ldots,N-1\}$。

Proof. According to the iterative learning control algorithm (5), in the k+1th iterative learning process, the control variables at each time in the interval $[0, N-1]$ are respectively

$$\begin{aligned}
u_{k+1}(0) &= u_k(0) + L_{\sigma(0)}e_k(1)e^{K_{\sigma(0)}(1/N)^2} + \Gamma_{\sigma(0)}e_k(1),\\
u_{k+1}(1) &= u_k(1) + L_{\sigma(1)}\left[e_k(1)e^{K_{\sigma(1)}(0/N)^2} + e_k(2)e^{K_{\sigma(1)}(1/N)^2}\right] + \Gamma_{\sigma(1)}e_k(2),\\
u_{k+1}(2) &= u_k(2) + L_{\sigma(2)}\left[e_k(1)e^{K_{\sigma(2)}(-1/N)^2} + e_k(2)e^{K_{\sigma(2)}(0/N)^2} + e_k(3)e^{K_{\sigma(2)}(1/N)^2}\right] + \Gamma_{\sigma(2)}e_k(3),\\
&\vdots,\\
u_{k+1}(N-1) &= u_k(N-1) + L_{\sigma(N-1)}\Big[e_k(1)e^{K_{\sigma((N-1))}(N-2/N)^2} + e_k(2)e^{K_{\sigma((N-1))}(N-3/N)^2} + \cdots + e_k(N-1)e^{K_{\sigma((N-1))}(0/N)^2}\\
&\quad + e_k(N)e^{K_{\sigma((N-1))}(1/N)^2}\Big] + \Gamma_{\sigma(N-1)}e_k(N).
\end{aligned} \tag{11}$$

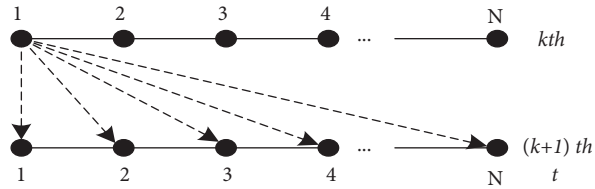

Figure 1: Error $e_k(1)$ correction of the control term at N times in the *(k+1)th* iteration.

Table 1: Associative correction of error $e_k(1)$ to the control quantity at N times of the next iteration.

1	2	3	⋯	$N-1$	N
$Le_k(1)e^{K(1/N)^2}$	$Le_k(1)e^{K(0/N)^2}$	$Le_k(1)e^{K(1/N)^2}$	⋯	$Le_k(1)e^{K(N-3/N)^2}$	$Le_k(1)e^{K(N-2/N)^2}$

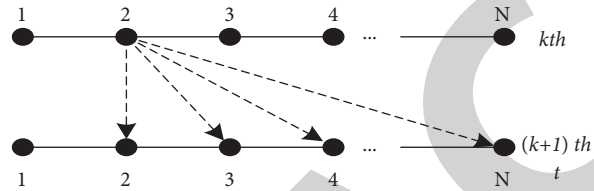

Figure 2: Error $e_k(2)$ correction of the control term at N-1 time in the (k+1)th iteration.

Table 2: Associative correction of error $e_k(2)$ to later time control quantity.

2	3	4	⋯	$N-1$	N
$Le_k(2)e^{K(1/N)^2}$	$Le_k(2)e^{K(0/N)^2}$	$Le_k(2)e^{K(1/N)^2}$	⋯	$Le_k(2)e^{K(N-4/N)^2}$	$Le_k(2)e^{K(N-3/N)^2}$

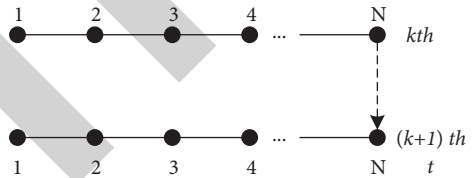

Figure 3: Error $e_k(N)$ up to point N in the K and $(K+1)$th iteration.

The super vector is introduced as follows:

$$\mathbf{E}_k = \left[e_k(1), e_k(2), \ldots, e_k(N)\right]^T. \tag{12}$$

Then,

$$\mathbf{U}_{k+1} = \mathbf{U}_k + (\mathbf{LH} + \Gamma)\mathbf{E}_k, \tag{13}$$

where

$$\mathbf{L} = \begin{bmatrix} L_{\sigma(0)} & & & & \\ L_{\sigma(1)} & L_{\sigma(1)} & & & \\ L_{\sigma(2)} & L_{\sigma(2)} & L_{\sigma(2)} & & \\ \vdots & \vdots & \ddots & \vdots & \\ L_{\sigma(N-2)} & L_{\sigma(N-2)} & \cdots & L_{\sigma(N-2)} & \\ L_{\sigma(N-1)} & L_{\sigma(N-1)} & L_{\sigma(N-1)} & L_{\sigma(N-1)} & L_{\sigma(N-1)} \end{bmatrix},$$

$$\mathbf{H} = \begin{bmatrix} e^{K_{\sigma(0)}(1/N)^2} & & & & & & \\ e^{K_{\sigma(1)}(0/N)^2} & e^{K_{\sigma(1)}(1/N)^2} & & & & & \\ e^{K_{\sigma(2)}(1/N)^2} & e^{K_{\sigma(2)}(0/N)^2} & e^{K_{\sigma(2)}(1/N)^2} & & & & \\ \vdots & \vdots & \ddots & \ddots & \vdots & & \\ e^{K_{\sigma(N-2)}\left(\frac{-(N-3)}{N}\right)^2} & e^{K_{\sigma(N-2)}\left(\frac{-(N-4)}{N}\right)^2} & \cdots & e^{K_{\sigma(N-2)}(0/N)^2} & e^{K_{\sigma(N-2)}(1/N)^2} & & \\ e^{K_{\sigma(N-1)}((-(N-2)/N))^2} & e^{K_{\sigma(N-1)}((-(N-3)/N))^2} & e^{K_{\sigma(N-1)}((-(N-4)/N))^2} & \cdots & e^{K_{\sigma(N-1)}(0/N)^2} & e^{K_{\sigma(N-1)}(1/N)^2} & \end{bmatrix}, \quad (14)$$

$$\Gamma = \begin{bmatrix} \Gamma_{\sigma(0)} & & & & & \\ & \Gamma_{\sigma(1)} & & & & \\ & & \Gamma_{\sigma(2)} & & & \\ & & \ddots & \vdots & & \\ & & & \Gamma_{\sigma(N-2)} & & \\ & & & & \Gamma_{\sigma(N-1)} & \end{bmatrix}.$$

According to the equivalent system (3),

$$\begin{aligned} \mathbf{E}_{k+1} &= \mathbf{Y}_d - \mathbf{Y}_{k+1} = \mathbf{Y}_d - (\mathbf{G}\mathbf{U}_{k+1} + \mathbf{V}) \\ &= \mathbf{Y}_d - \mathbf{G}[\mathbf{U}_k + (\mathbf{L}\mathbf{H} + \Gamma)\mathbf{E}_k] - \mathbf{V} \\ &= \mathbf{Y}_d - \mathbf{G}\mathbf{U}_k - \mathbf{V} - \mathbf{G}(\mathbf{L}\mathbf{H} + \Gamma)\mathbf{E}_k \\ &= \mathbf{E}_k - \mathbf{G}(\mathbf{L}\mathbf{H} + \Gamma)\mathbf{E}_k \\ &= [\mathbf{I}_{N\times N} - \mathbf{G}(\mathbf{L}\mathbf{H} + \Gamma)]\mathbf{E}_k \\ &= [\mathbf{I}_{N\times N} - \mathbf{G}(\mathbf{L}\mathbf{H} + \Gamma)]^2\mathbf{E}_{k-1} \\ &= \cdots = [\mathbf{I}_{N\times N} - \mathbf{G}(\mathbf{L}\mathbf{H} + \Gamma)]^k\mathbf{E}_0. \end{aligned} \quad (15)$$

According to the properties of spectral radius, the necessary and sufficient condition for $\lim_{k\longrightarrow\infty}(\mathbf{I}_{N\times N} - \mathbf{G}(\mathbf{L}\mathbf{H}+\Gamma))^k = 0$ is $\rho(\mathbf{I}_{N\times N} - \mathbf{G}(\mathbf{L}\mathbf{H} + \Gamma)) = \max|\lambda_i| < 1$. $\rho(\mathbf{M})$ represents the spectral radius of matrix M, and if λ_i is the eigenvalue of the matrix, then the necessary and sufficient condition for system convergence is

$$\rho = \max_t \left|1 - \left(L_{\sigma(t)}e^{K_{\sigma(t)}(1/N)^2} + \Gamma_{\sigma(t)}\right)\mathbf{C}_{\sigma(t)}\mathbf{B}_{\sigma(t)}\right| < 1. \quad (16)$$

Hence, the theorem is proved.

4. Numerical Simulation

In order to verify the effectiveness of the accelerated learning law in this paper, the following discrete switched systems with three subsystems are considered:

$$\begin{cases} \mathbf{x}_k(t+1) = \mathbf{A}_{\sigma(t)}\mathbf{x}_k(t) + \mathbf{B}_{\sigma(t)}u_k(t), \\ y_k(t+1) = \mathbf{C}_{\sigma(t)}\mathbf{x}_k(t), \end{cases} \quad (17)$$

where $t \in \{0, 1, \ldots, N-1\}$, $\sigma(t) \in \{1, 2, 3\}$ represents a random switching sequence. Any group is selected, as shown in Figure 4.

The parameters of the three subsystems are as follows:

$$\begin{aligned} \mathbf{A}_1 &= \begin{bmatrix} 0 & 1 \\ 0.125 & -0.2 \end{bmatrix}, \\ \mathbf{B}_1 &= \begin{bmatrix} 0 \\ 1 \end{bmatrix}, \\ \mathbf{C}_1 &= \begin{bmatrix} 0.1 & 1 \end{bmatrix}, \\ \mathbf{A}_2 &= \begin{bmatrix} -0.25 & 1 \\ 0 & -0.3 \end{bmatrix}, \\ \mathbf{B}_2 &= \begin{bmatrix} 0 \\ 1 \end{bmatrix}, \\ \mathbf{C}_2 &= \begin{bmatrix} -0.2 & 1 \end{bmatrix}, \\ \mathbf{A}_3 &= \begin{bmatrix} 1 & 0 \\ 0.2 & -0.1 \end{bmatrix}, \\ \mathbf{B}_3 &= \begin{bmatrix} 0 \\ 1 \end{bmatrix}, \\ \mathbf{C}_3 &= \begin{bmatrix} 0.5 & 1 \end{bmatrix}. \end{aligned} \quad (18)$$

Assuming that the learning parameters remain unchanged during the learning process and will not change with the switching sequence and the number of iterations. The iteration proportional gain is set to $\Gamma_{\sigma(i)} = 0.25$, the association factor is set to $K_{\sigma(1)} = 1$, the correction coefficient is set to $L_{\sigma(i)} = 0.2$, and the discrete time is set to $N = 60$, and the calculated $\rho_1 = \max_t|1 - (L_{\sigma(t)}e^{K_{\sigma(t)}(1/N)^2} + \Gamma_{\sigma(t)})\mathbf{C}_{\sigma(t)}\mathbf{B}_{\sigma(t)}| = 0.55 < 1$. The convergence condition is met. If $K_{\sigma(t)} = 1$ and $L_{\sigma(t)} = 0$, the above algorithm degenerates into a traditional P-type iterative learning control algorithm, and its convergence conditions are $\rho_2 = \max_t|1 - \Gamma_{\sigma(t)}\mathbf{C}_{\sigma(t)}\mathbf{B}_{\sigma(t)}| = 0.75 < 1$ and $\rho_1 < \rho_2$. According to the spectral radius theory, the smaller the convergence radius, the faster the iterative learning algorithm converges.

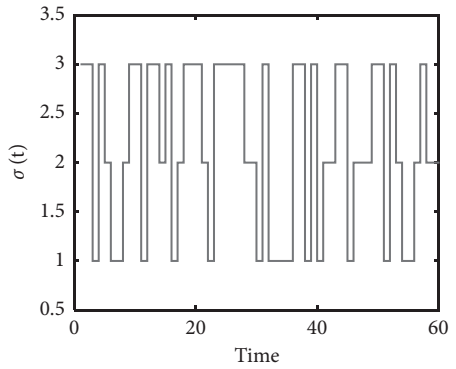

Figure 4: Random switching sequence $\sigma(t)$.

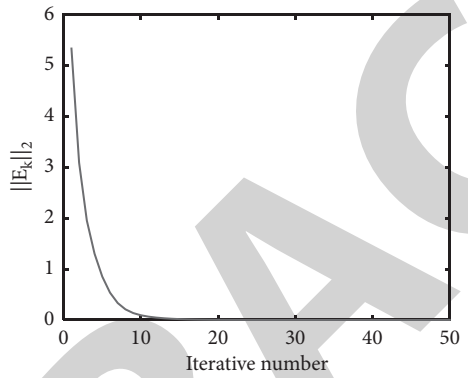

Figure 5: The variation trend of the error 2 norm of the accelerated ILC algorithm with the number of iterations.

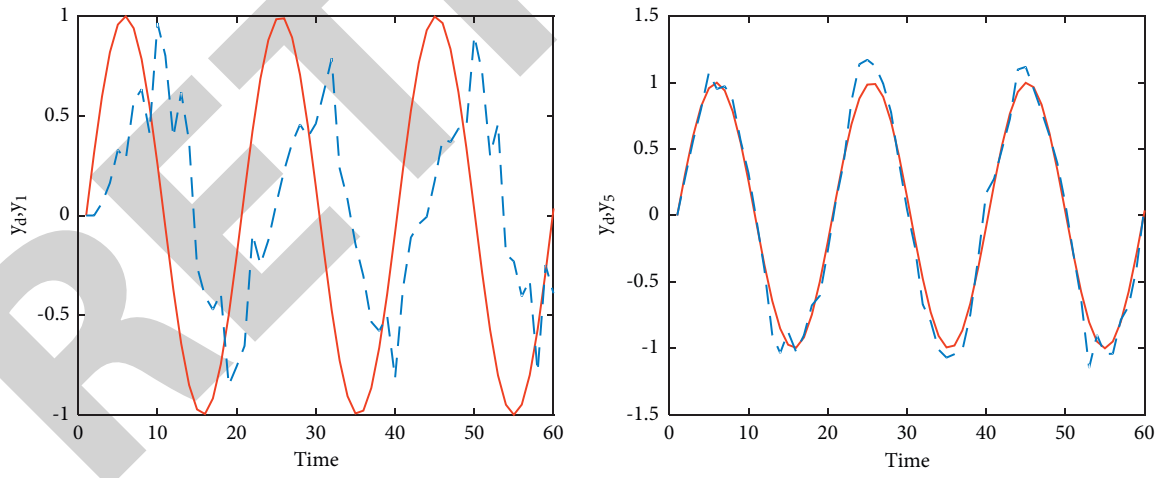

Figure 6: Continued.

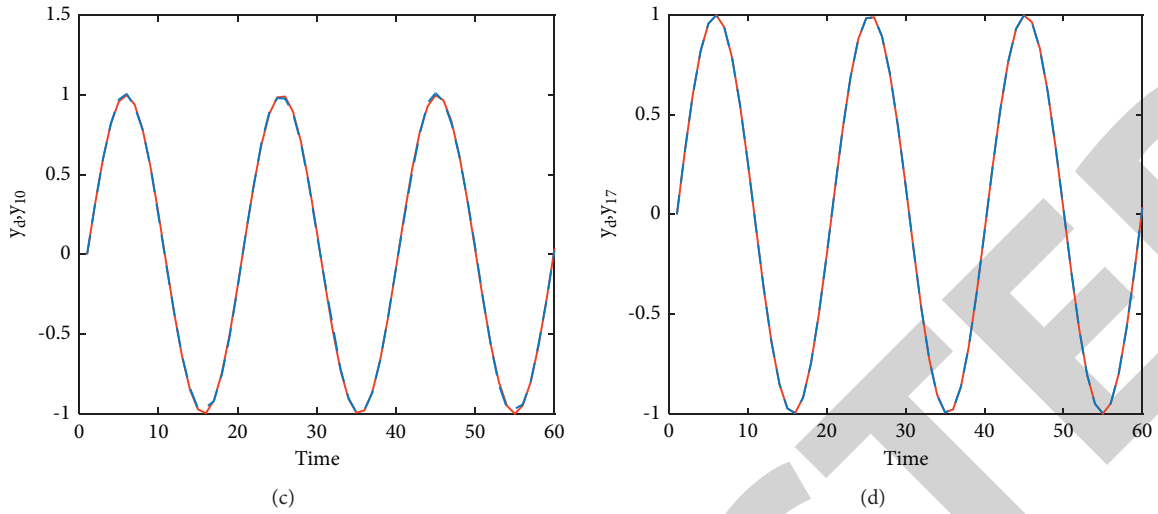

Figure 6: Output V/S desired trajectory. (a) After the first iteration. (b) After the 5th iteration. (c) After the 10th iteration. (d) After the 17th iteration.

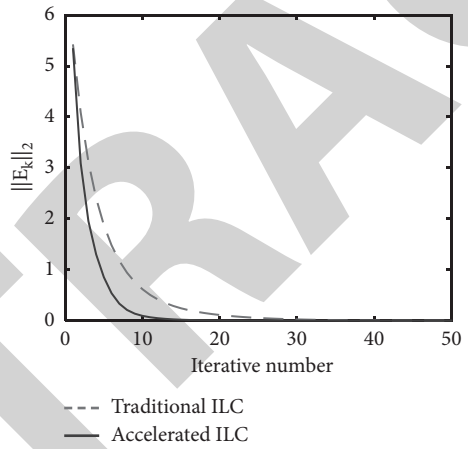

Figure 7: Traditional ILC VS. accelerated ILC.

Table 3: Comparison of ILC laws with proposed accelerated PD type ILC law.

Iteration number	D-type ILC law	Traditional P-type ILC law	Proposed accelerated P-type ILC law
1st	6.817316	5.617316	5.5217316
2nd	5.1217316	3.1217316	3.0127316
5th	4.549819	2.521928	1.232084
10th	2.603581	0.281079	0.029238
15th	1.07538	0.062823	0.003683

The desired trajectory is $y_d(t+1) = \sin(8t/25), \quad t \in \{0, 1, \ldots, 59\}$. The initial $\mathbf{x}_k(0) = 0, \forall k \in \mathbf{Z}^+$, the initial control vector is $u_1 = 0$. When using the accelerated P-type learning law proposed in this paper, from the first learning to the 50th time, the changing trend of $\|\mathbf{E}_{k2}\|$ is shown in Figure 5. It can be seen that the algorithm can ensure that $\|\mathbf{E}_{k2}\|$ converges to zero. Figure 6 shows the output of the system after the first, fifth, tenth, and seventeenth iterations, and the convergence process of the algorithm can be seen in more detail.

When the traditional P-type learning law is adopted, the proportional learning gain $\Gamma_{\sigma(t)} = 0.25$, which remains unchanged in the learning process. From the first learning to the 50th, the change trend of $\|\mathbf{E}_{k2}\|$ is shown in Figure 7. In addition, the figure also includes the change trend of $\|\mathbf{E}_{k2}\|$ using the acceleration algorithm proposed in this paper. In the figure, when the allowable error $\varepsilon = 0.01$, the traditional P-type algorithm needs 35 iterations and the accelerated P-type iterative learning algorithm needs 17 iterations; given that the allowable error $\varepsilon = 0.001$, the traditional p-type

algorithm needs 48 iterations and the accelerated P-type iterative learning algorithm needs 15 iterations. It can be seen intuitively that after using the P-type accelerated ILC algorithm proposed in this paper, the convergence speed of the system is obviously accelerated.

Table 3 shows that the highest tracking error of D, P, and accelerated proposed P-type ILC laws in the first iteration is 6.817316. After the 15th iteration, the error of the P-type law is 0.062823 and the D-type algorithm is 1.07538. Whereas the error of the proposed accelerated P law is 0.003683, from the column of Table 3 to the data, the tracking error of all ILC laws is reduced consecutively with the increase of the iteration number. However, from the horizontal data in Table 3, the tracking error of the proposed accelerated P-type ILC law is the smallest as compared to other ILC laws (D-type and Traditional P-type) under the same iteration number. Therefore, it can be easily observed from Table 3 that the convergence speed of the proposed accelerated P-type law in this paper is significantly higher than that of other traditional laws.

5. Conclusions

In this paper, a class of discrete time invariant switched systems with arbitrary switching sequences is studied. An open-loop P-type accelerated iterative learning algorithm with precorrection function is used, and the convergence conditions are given. The convergence radius of the algorithm is smaller than that of the traditional P-type ILC algorithm. The convergence and rapidity are strictly proved in theory by using the super vector. Numerical simulation examples verify the effectiveness of the proposed algorithm. The results show that for discrete switched systems with arbitrary switching in the time domain, the ILC method can ensure complete tracking control in a finite time period. At the same time, the accelerated ILC algorithm proposed in this paper can reduce the number of iterations when the error reaches the allowable error so as to accelerate the convergence. Since any switching sequence is randomly determined and does not change with the number of iterations, the system is still a determined system from the iteration axis, and ILC can be used to realize complete tracking. In future research, the author will consider the stability and convergence of iterative changing initial conditions, system model uncertainty, and measurement noise.

Data Availability

The data are included within the article. This is a mathematical-based simulation. The data can be provided on demand.

Conflicts of Interest

The authors declare that there are no conflicts of interest.

Authors' Contributions

Yongping Wang, Saleem Riaz, and Ziyun Bao conceptualized the study. Yongping Wang, Saleem Riaz, and Ziyun Bao developed the methodology. Yongping Wang, Saleem Riaz, Ziyun Bao, and Wenqian Zhang performed formal analysis. Ziyun Bao and Wenqian Zhang performed data curation. Yongping Wang wrote the original draft. Saleem Riaz and Ziyun Bao reviewed and edited the article. All authors have read and agreed to the published version of the manuscript.

Acknowledgments

This study has been supported by the Key Research and Development Plan of Ningxia Province (2018BBF02022), the youth top talent training project of Ningxia Province.

References

[1] H. Lin and P. J. Antsaklis, "Stability and stabilizability of switched linear systems: a survey of recent results," *IEEE Transactions on Automatic Control*, vol. 54, no. 2, pp. 308–322, 2009.

[2] D. Liberzon and A. S. Morse, "Basic problems in stability and design of switched systems," *IEEE Control Systems Magazine*, vol. 19, no. 5, pp. 59–70, 1999.

[3] A. Balluchi, M. D. Di Benedetto, C. Pinello, C. Rossi, and A. Sangiovanni-Vincentelli, "Hybrid control in automotive applications: the cut-off control," *Automatica*, vol. 35, no. 3, pp. 519–535, 1999.

[4] X. Wang and J. Zhao, "Partial stability and adaptive control of switched nonlinear systems," *Circuits, Systems, and Signal Processing*, vol. 32, no. 4, pp. 1963–1975, 2013.

[5] J. Yu, L. Wang, and M. Yu, "Switched system approach to stabilization of networked control systems," *International Journal of Robust and Nonlinear Control*, vol. 21, no. 17, pp. 1925–1946, 2011.

[6] D. Cheng, L. Guo, Y. Lin, and Y. Wang, "Stabilization of switched linear systems," *IEEE Transactions on Automatic Control*, vol. 50, no. 5, pp. 661–666, 2005.

[7] L. Li and C. Shao, "Observer-based H∞ output tracking control for a class of switched Lipschitz nonlinear systems," *Control and Decision*, vol. 27, no. 2, pp. 304–307, 2012.

[8] Y. Hua, N. Wang, and K. Y. Zhao, "Simultaneous unknown input and state estimation for the linear system with a rank-deficient distribution matrix," *Mathematical Problems in Engineering*, vol. 2021, Article ID 6693690, 11 pages, 2021.

[9] X. Feng, Y. Zhang, L. Kang et al., "Integrated energy storage system based on triboelectric nanogenerator in electronic devices," *Frontiers of Chemical Science and Engineering*, vol. 15, no. 2, pp. 238–250, 2021.

[10] S. Riaz, H. Lin, and M. P. Akhter, "Design and implementation of an accelerated error convergence criterion for norm optimal iterative learning controller," *Electronics*, vol. 9, no. 11, p. 1766, 2020.

[11] S. Riaz, H. Lin, M. Mahsud, D. Afzal, A. Alsinai, and M. Cancan, "An improved fast error convergence topology for PDα-type fractional-order ILC," *Journal of Interdisciplinary Mathematics*, vol. 24, no. 7, pp. 2005–2019, 2021.

[12] S. Riaz, H. Lin, F. Afzal, and A. Maqbool, "Design and implementation of novel LMI-based iterative learning robust nonlinear controller," *Complexity*, vol. 2021, Article ID 5577241, 13 pages, 2021.

[13] H. Xu, H. Du, L. Kang, Q. Cheng, D. Feng, and S. Xia, "Constructing straight pores and improving mechanical properties of GangueBased porous ceramics," *Journal of Renewable Materials*, vol. 9, no. 12, pp. 2129–2141, 2021.

Hindawi
Mathematical Problems in Engineering
Volume 2022, Article ID 5279919, 10 pages
https://doi.org/10.1155/2022/5279919

Research Article

Design of Intelligent Customer Service Questioning and Answering a System for Power Business Scenario Based on AI Technology

Shisong Wu

Digital Grid Research Institute, CSG, Guangzhou, China

Correspondence should be addressed to Shisong Wu; wushisong@yccxip.com

Received 29 October 2021; Accepted 27 December 2021; Published 27 January 2022

Academic Editor: Jinyan Song

In order to solve the problems of large demand for power business and small number of customer service, an intelligent customer service questioning and answering a system for power business scenario based on AI technology is designed. The approach first uses the particle swarm optimization algorithm to automatically classify the question attributes and then uses the fuzzy *c*-means clustering algorithm to match the answers with the highest similarity to the questions and return to the customers. The system collects the questions raised by customers through the acquisition module, uploads the question work order to the knowledge base through the information assistance module, and stores the preprocessed questions to the knowledge base. After completing the problem attribute classification through the particle swarm clustering algorithm classification model in the batch analysis and calculation module, the question answers are matched through fuzzy *c*-means clustering. At the same time, the similarity of different keywords is calculated to find a series of related questions. After the obtained data are analyzed in real time through the self-service customer service module, the answer is extracted and fed back to the customer, and the question answer is presented to the customer in the system interface. The experimental results show that the designed system has low worst-case time complexity, which is up to 0.35 only. The reason is that the system in this paper can use priority information to deal with the problems raised by customers, which is different from the past work where dealing with customers request via priority information is not used. The system can give the corresponding answers according to the customer's options. It has convenient operation, high integrated control ability, and good information management performance. Compared with the traditional approach which could waste a lot of resource and data, the proposed approach can reduce the differences between problem data, eliminate invalid data, and simplify the data classification process. The application of the system can effectively accelerate the information transmission efficiency of the power company and can be used for power exchange platform automation in the future.

1. Introduction

`The related businesses of power companies in different scenarios are gradually increasing, and some businesses have changed from offline services to various online remote services [1, 2]. However, both offline service and remote service will waste power business resources [3], such as the shortage of customer service personnel and the difference of business capacity [4], which will directly affect the service level. Therefore, the design of a high-quality power business intelligent customer service system has attracted the attention of relevant scholars [5].

Yt et al. [6] propose a method to construct the knowledge graph of power customer service domain and constructed a knowledge graph containing more than 15,000 entities and more than 20,000 relationships. Based on the knowledge map, an intelligent question answering application architecture is designed. The architecture is composed of several functional modules, such as dialogue process configuration, natural language processing, and business process processing. Provide more efficient and open knowledge retrieval services for power customer service business and improve the intelligent level of customer service questions and answers. However, this method has little experience in

customer service operation and maintenance and cannot use knowledge sharing to deal with problems raised by customers, resulting in massive historical operation and maintenance data being wasted. Li et al. [7] point out that customer service is changing from traditional manual service to automatic service. Automatic service uses different computational informatics to achieve more efficient and high-quality service. Automated customer service requires expertise in big data and data analysis as a prerequisite. However, many companies, especially small and medium-sized enterprises, do not have enough data and experience due to limited scale and resources. They need to rely on third parties, resulting in the lack of development of core customer service capabilities. In order to overcome these challenges, it proposes an open automatic customer service platform based on the Internet of things (IoT), blockchain, and automatic machine learning (AUTOML). Yu et al. [8] analyze the changes of the new generation power grid dispatching control system in system architecture, human-computer interaction mode, business organization mode, and so on. This paper combs the new requirements of the new generation power grid dispatching control system for access control and puts forward the service access control solution in the new generation power grid dispatching control system. The key technologies such as path-based resource identification definition, metadata-based resource management, rule-engine-based multifactor access control, and cross-system access control based on parent-child organization relationship are studied. The scheme has been verified in the prototype system and provides a multidimensional security access control means for the business in the new-generation power grid dispatching control system. However, during the time period when the system has no customer service, customers need to wait for the customer service to go to work.

Based on the aforementioned analysis, although most of the existing methods have realized the intelligent question answering of power business, there are still some problems such as poor keyword searching, inability in keywords decomposition of most customers, low data reusing rate, poor efficiency in question answering content management, and weak pertinence of answers [9, 10]. Therefore, we choose to apply the fuzzy c-means clustering algorithm [11], which can directly deal with the problems that a text belongs to multiple text classes, and class boundaries are fuzzy and overlapping regardless of the clustering category. Based on the aforementioned justification, this paper proposes to build an intelligent customer service questioning and answering a system for power business scenarios based on AI technology. AI technology has been widely used in the area of prediction [12], state estimation [13, 14], control [15–17], and optimization [18] and has made considerable contribution. Therefore, this research tries AI technology. The approach first uses the particle swarm optimization algorithm to automatically classify the question attributes and then uses the fuzzy c-means clustering algorithm to match the answers with the highest similarity to the questions and return to the customers. The approach can reduce the differences between problem data, eliminate invalid data, and simplify the data classification process. The system in this paper can use priority information to deal with the problems raised by customers, so it has a low worst-case time complexity.

2. Power Business Scenario Intelligent Customer Service Questioning and Answering a System Based on AI Technology

2.1. Overall System Structure. In order to improve the customer service quality of power business, an intelligent customer service questioning and answering a system for power business scenario based on AI technology is constructed. As shown in Figure 1, the problems raised by customers are solved by the designed system to improve the customer service quality.

As can be seen from Figure 1, the system collects various questions raised by customers through the acquisition module and then transmits the questions to the knowledge base in the form of work order through the auxiliary information module to realize the word, marking and identification of the preprocessed questions, and store them in the knowledge base. The answers matching with the answers with the highest similarity to the work order are retrieved in the batch analysis and calculation module. After the data are analyzed in real time by the self-service customer service module, the answers are extracted. The core module of the system is the batch analysis and calculation module, which uses the particle clustering algorithm to divide the attributes of the questions raised by customers and then uses the fuzzy c-means clustering algorithm to match the keywords related to the topic in the text, calculate the similarity of different keywords, find a series of related questions, and finally get the answers with the highest matching degree. The fuzzy c-means clustering algorithm is used to match the keywords related to the topic in the text, calculate the similarity of different keywords, find the answers related to relevant questions, and finally feed back to customers through the language processing of independent customer service to realize interactive questions and answers A with customers.

2.2. Problem Acquisition Module. The main function of this module is to collect relevant questions raised by users, count and divide them into a specific server directory, and convert them into intelligent customer service questions and answers A data of power business scenario. The main work of this module includes the following:

(1) Determine the time interval for the system to collect problem data, which is determined as 3 min.

(2) Apply TXT file type to store relevant files with problems in the system.

(3) Define the coding format of system acquisition problem file as UTF-8, build a data interface in series with Hadoop file system, obtain the problem, and save it in Hadoop.

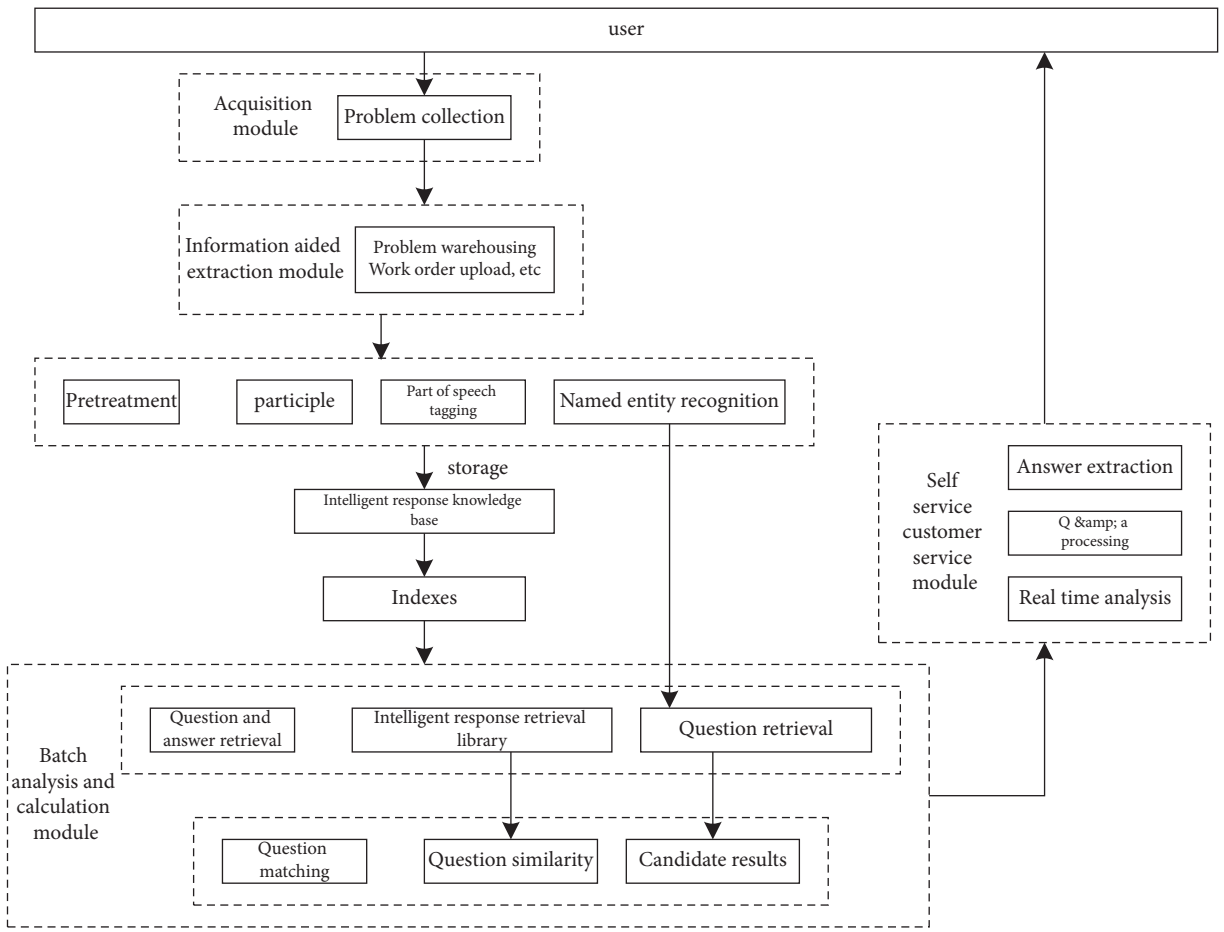

Figure 1: Power business scenario intelligent customer service questioning and answering a system.

2.3. Auxiliary Information Extraction Module. Figure 2 shows the details of the information-aided extraction module.

The four main functions of the information-aided extraction module are as follows: problem warehousing, transmitting work orders, changing problems to the knowledge base, and manually modifying the content of the knowledge base to the response base. As seen from Figure 2, if the customer raises a question, the module will automatically reply to the customer, submit the unsolvable problem to the service queue, provide various feedback methods to the response base, and then answer automatically through the knowledge base.

2.4. Batch Analysis and Calculation Module

2.4.1. Problem Attribute Classification. The core function of this module is to deeply analyze the collected operation problems and calculate the system. This method takes the existing problem data as the comparison basis to verify the similarity and clustering relationship between the problems. As the traditional word segmentation will produce a large number of resource waste and inefficient problems when putting forward the questions to be answered to the system, the module first uses the particle swarm optimization algorithm to automatically classify the question attributes [19, 20] and finally uses the fuzzy *c*-means clustering algorithm to match the answers with the highest similarity to the questions and return to the customers. Figure 3 shows the problem classification process.

In Figure 3, the general flow of problem attribute classification is described, which is, the preprocessed data set is pretrained. In the embedding layer, according to the word vector strategy, particle swarm clustering algorithm is used to complete the transformation of sentence vector, and a persistent classification model, which meets the standard accuracy and can be used for future classification is obtained through training.

2.4.2. Fuzzy c-Means Clustering Mathematical Model. Fuzzy *c*-means clustering algorithm is used for classification according to the similarity of the problem, and the ones with high similarity are judged as similar ones and classified into one group. Fuzzy *c*-means clustering is an unsupervised learning problem [21, 22]. For the problem data with unclear classification, the strategy can automatically match the best keywords in the text after training. Using fuzzy *c*-means clustering algorithm can improve the compactness of clustering data and change the dispersion between clusters.

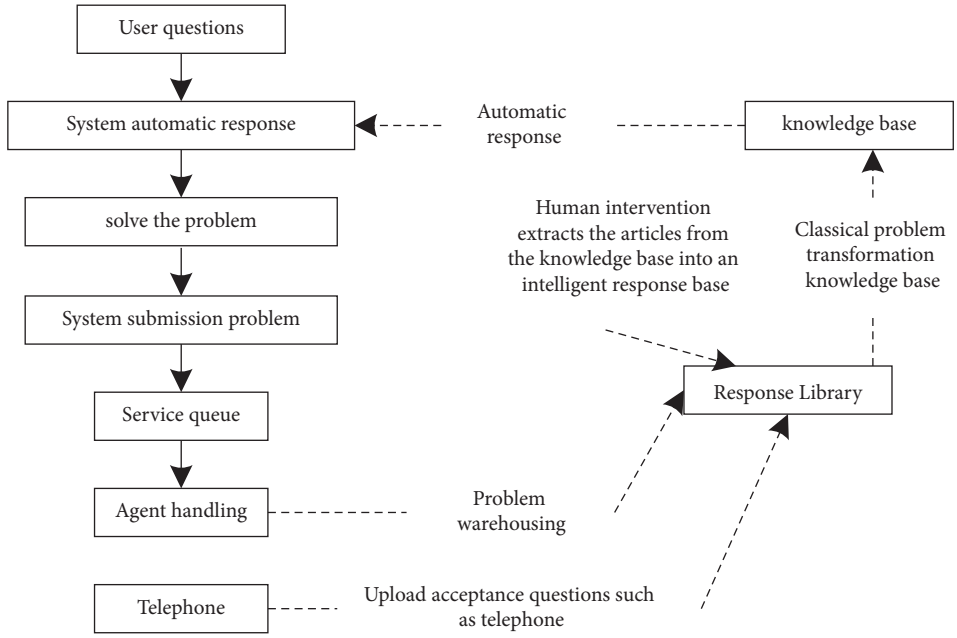

Figure 2: Auxiliary information-aided extraction module.

The fuzzy c-means clustering algorithm includes the following steps:

Step 1: Import the determined clustering parameter, e, and the sample set of the data object.

Step 2: Arbitrarily select sample points of e and record them as the original cluster center $T_1(a)$, T_2 (a), $\ldots, T_e(a)$, indicating the number of iterations. First, the iteration number $a = 1$.

Step 3: Based on the minimum distance specification, the samples are divided into class e $T_j(e)$ represented by the cluster center with the minimum distance, and the number of samples in each class is $a_j(e)$. The minimum distance specification is calculated as follows:

$$d = \sum_{i=1}^{a} \min_{j \in (1,2,\ldots e)} \left\| x_i - T_j \right\|^2. \quad (1)$$

Step 4: After calculating the center of gravity of each category, take it as a new cluster center to obtain the following equation:

$$T_j(e+1) = \frac{1}{a_j(k)} \sum_{X_i \in T_j(e)}^{a} x_i, \quad (2)$$

where, $j = 1, 2, \ldots, e$, $N_j(e)$ is the number of samples in $T_j(e)$, and the fuzzy c-means clustering algorithm needs to obtain the mean of e new clustering centers.

Step 5: Perform secondary division and iteration according to the new cluster center and terminate the iteration when the sample is consistent with the criterion function of distance.

The formula of the distance discriminant function is as follows:

$$D_j = \sum_{j=1}^{e} \sum_{i=1}^{a} \left\| x_i - T_j \right\|^2. \quad (3)$$

Formula (3) can effectively reduce the differences between problem data, eliminate invalid data, and simplify the data classification process. The fuzzy c-means clustering algorithm is used to normalize the order of magnitude of different problems so that it can uniformly expand the problem attribute classification on the order of magnitude and ensure the accuracy of the results.

2.5. Self-Service Customer Service Module. The self-service customer service module based on Web browser displays the intelligent analysis results of system operation. The self-service customer service module realizes the functions of real-time analysis, answer processing, and answer extraction. It can match the logic and similarity of questions in the batch analysis and calculation module, extract high-precision answers through the answer extraction function, and give feedback to customers on the online customer service page.

3. Experimental Analysis

This experiment takes iris data set and wine data set as the research object to test the fuzzy c-means clustering algorithm applied in the system. The clustering effect is shown in Figure 4.

As can be seen from Figure 4, the system in this paper can get good clustering effect after four cycles. The clustering points are clearer and clearer, and the clustering points are highly dense. There is no wrong clustering, indicating that the system in this paper has strong clustering ability.

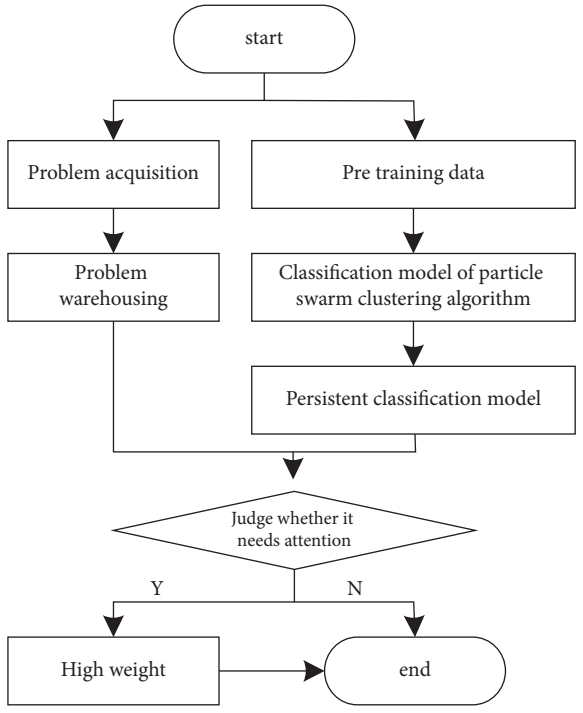

Figure 3: Problem attribute classification process.

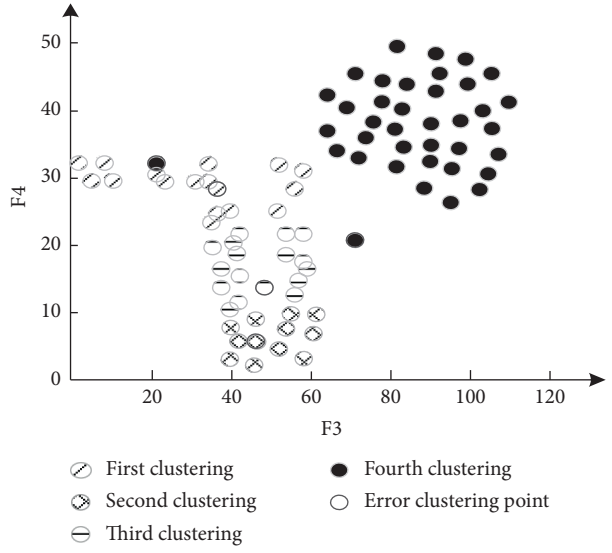

Figure 4: System clustering effect of this paper using fuzzy c-mean clustering method.

The designed system is compared with literature [6–8]. After 25 experiments on iris and wine data sets, the comparison results of the accuracy of the four systems are shown in Table 1.

It can be seen from Table 1 that the fuzzy c-means clustering algorithm adopted by the system in this paper can make the system obtain better clustering effect. Compared with the other three systems, the accuracy of the system application strategy in this paper is the highest in both data sets. In the process of experiment, this method can save storage space and reduce system running time.

3.1. Application Scenarios. In the experiment, taking intelligent speech technology as the core, the application scenarios such as voiceprint recognition, voice input method, automatic map adjustment, status query, question answering, page switching, and voice ticket issuing are designed. Voiceprint recognition and voice input method can be used as services to support other applications.

3.1.1. Voiceprint Recognition. The dual-recognition technology of voiceprint and voice is used for identity

Table 1: Cluster comparison results between the research and past work.

Algorithm	Iris dataset (%)	Wine dataset (%)
Design system	97.25	98.33
Yt et al. study [6]	88.38	93.31
Li et al. study [7]	83.57	95.27
Yu et al. study [8]	95.61	97.64

authentication to improve the recognition accuracy of login customers. Subsequent operations are bound with login customers to automatically record the working status, behavior, and habits of each regulator, so that the intelligent assistant can provide services more effectively. At the same time, voiceprint recognition service can be provided for other applications as an option for authentication.

Through voiceprint, the customer can log in quickly to avoid the cumbersome operation of entering password. The system automatically records the login status and associates the operations in the next period with the logged in customer.

Example: Voiceprint login.

Input voice: The controller inputs "XXX of a city dispatching" through mic.

Recognition confirmation: The background program recognizes the voiceprint information and returns the name of the controller.

Login: The controller checks the recognized name on the interface. If it is correct, click login directly. If it is incorrect, select it from the drop-down menu, and then click login.

Operation confirmation: Before the control personnel carry out important operations, for example, confirming the operation ticket, they can verify their identity by voiceprint and can only be carried out after confirmation.

3.1.2. Voice Input Method. Text input through voice can replace the function of the existing input method. The input text can act on any standard text input control such as word, web page input box, and OMS page to realize convenient text input. Note: this function is limited to Windows system. An example of documentation is shown as follows:

Step 1: Open word and start the voice input method function.

Step 2: Speak the text content to be entered normally through mic, and the recognized text will be displayed on the word page in real time.

Step 3: Further editing and improvement can be made by customers.

Repeat Steps 2 and 3 until documentation is complete.

3.1.3. Automatic Drawing Adjustment. In the D5000 graphic environment, the designated system diagram or plant station diagram is automatically opened by the voice of the controller to achieve the effect of rapid page switching. At the same time, it supports the positioning function of the designated equipment and improves the work efficiency of the controller. At this time, the control robot interface remains suspended.

Example: "please open the diagram of landing station" or "read the diagram of landing station."

Keywords "open," "plant and station map," "access."

Parameter: [Landing station].

Effect: open the specified station diagram.

3.1.4. Status Query. According to the voice requirements of the regulator, automatically collect relevant information from the regulation cloud or other systems, query the current or historical status of the power grid, broadcast in the form of voice and text, and visually display through customized templates.

Example: "please query the total power supply of an area on April 17."

Keywords "query" and "total power supply".

Parameters: [April 17], [a region].

Effect: Query the total power supply on the specified date from the control cloud and broadcast through voice.

3.1.5. Problem Solving. The city dispatching knowledge base based on offline modeling realizes the intelligent question and answer function between man and machine, supports the ability of multiround dialogue, and supports the online update of knowledge base. The content of knowledge base can include basic information of municipal dispatching, regulation regulations, power system knowledge, and so on. At the same time, it provides knowledge base management tools to supplement and update knowledge.

Example 1: "what are the local dispatching equipment?"

Voice broadcasting: Power plants, substations, lines, and other primary and secondary equipment for mode adjustment and switching operation ordered by the municipal dispatching. Text display: (1) machines and boilers of all power plants with 110 kV and above connected to a regional power grid, primary and secondary equipment of booster station and their parallel network cables; (2) 220 kV bus and switchgear of 500 kV substation; (3) 220 kV ring network equipment; (4) 110 kV and above load lines and corresponding side intervals; (5) substation equipment of 110 kV and above (excluding local dispatching equipment); (6) power grid equipment assigned by superior dispatching

to municipal dispatching; and (7) other equipment that the city dispatching deems necessary for direct dispatching.

3.1.6. Vice Ticket Issuing. The operation ticket can be processed by voice, including browsing the previous ticket and querying the current ticket status. For the new operation ticket, the text information can be entered by voice.

Example: "view the operation ticket being executed."

Keywords "view," "operation ticket."

Parameter: [executing].

Effect: Retrieve the operation tickets in circulation and display them in a list.

3.2. Power Business Problem Attribute Classification Effect. Through the analysis of the aforementioned application scenarios, it can be seen that the problem information of power companies is large and diverse. Effective classification can enhance the management effect of the system to a certain extent. For the test of system classification performance, five types of information such as power outage information, customer information, payment information, and meter reading time of power companies are classified and tested. These five types of information come from different communities and floors respectively. The classification performance of the system is measured by the attribute category of the problem, and the results are shown in Figure 5.

According to the test results in Figure 5, the system in this paper can effectively classify the attributes of five kinds of information. It can be seen that the payment information is close to the payment time attribute, indicating that the system in this paper can realize information classification according to the attributes of the problem and has a good classification effect.

3.3. Questions and Answers a Processing Effect. In order to deeply analyze the problem processing effect of the system, the posterior probability value of all data is used to measure the worst time complexity. The formula is as follows:

$$(\tau_1 + m\tau_2) \cdot n \cdot k = nk\tau_1 + mn\tau_2. \quad (4)$$

The number of information, attributes, and categories are described by n, m, and k, respectively; the posterior probability of certain information and the time of information increase are calculated by τ_1 and τ_2, respectively. For the case where n, m, and k are the same, the calculation formula of the worst time complexity is as follows:

$$O(n^3) = n^2\tau_1 + n^3\tau_2. \quad (5)$$

The worst time complexity is set as 0.5, the limit value to test the worst time complexity of the system intelligent questions and answers A in this paper. The worst time complexity of the system intelligent questions and answers A is negatively correlated with the system problem processing performance. The worst time complexity of the system intelligent questions and answers A is shown in Figure 6.

As can be seen from Figure 6, although the number of keywords is increasing, the worst-case time complexity of the system in this paper has increased. However, the increase is small, stable, and always lower than the limit value. This is because the system in this paper can use priority information to deal with the problems raised by customers, so it has a low worst-case time complexity. When the number of keywords is 25, the worst time complexity is 0.35, which shows that the system has good information management performance.

3.4. Effect of Power Business Resource Scheduling and Registration. The power business resource scheduling attenuation and registration degree of the design system are shown in Figures 7 and 8.

As can be seen from Figure 7, the information transmission performance and anti-inter symbol crosstalk performance of the system in this paper have been significantly improved. But they are lower than 4 dB, indicating that the information transmission performance of the system in this paper is good, has good anti-inter symbol crosstalk performance, and can optimize the information management performance of the system.

As shown in Figure 8, in the case of resource mobilization, the system achieves 88% regardless of resource size and registration degree. The increase of resource size has little impact on registration. When the resource size is 40 GB, the registration degree is the highest, reaching 97.8%, and when the resource size is 100 GB, the registration degree is 95.4%, indicating that the system has good information management effect. It can correctly realize resource matching and scheduling.

3.5. Work Efficiency. In order to verify the application effect of the system in the actual operation process, the work efficiency of the power company before and 1 month after the application of the system is compared. The results are shown in Figure 9.

As can be seen from Figure 9, after the application of this system, the processing time of customers' questions is significantly reduced, and customers can get corresponding answers in a short time. Before the application of this system, the processing time of customers' questions was longer because the number of customers is limited, customers need to wait in line, wasting more time, and the efficiency of power companies serving customers is low The problems raised by customers after the application of the system greatly improve the operation efficiency of the power company and the work efficiency of the operation and maintenance group of the power company.

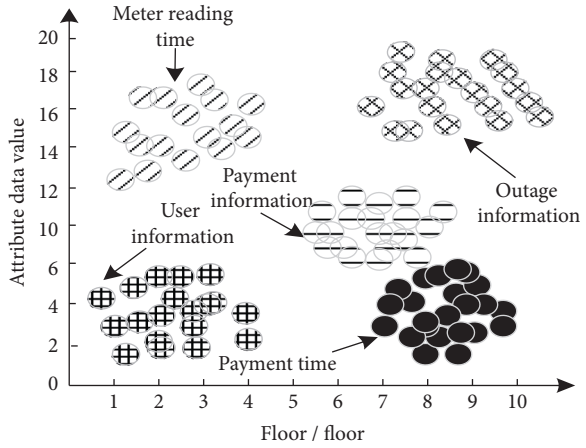

Figure 5: Test results of attribute classification.

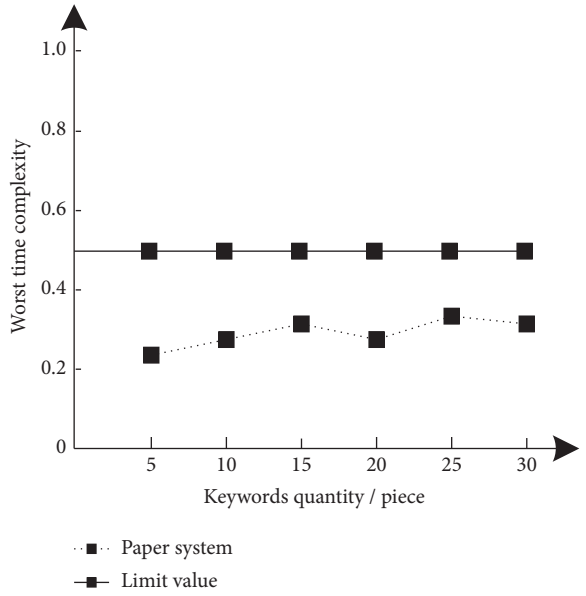

Figure 6: Worst time complexity of the system in this research.

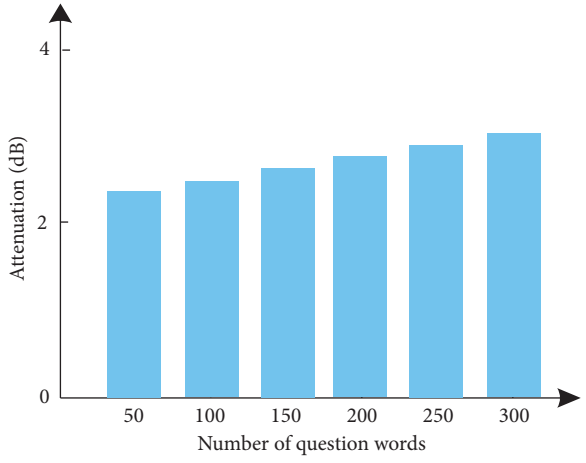

Figure 7: Resource scheduling attenuation of the proposed system in this paper.

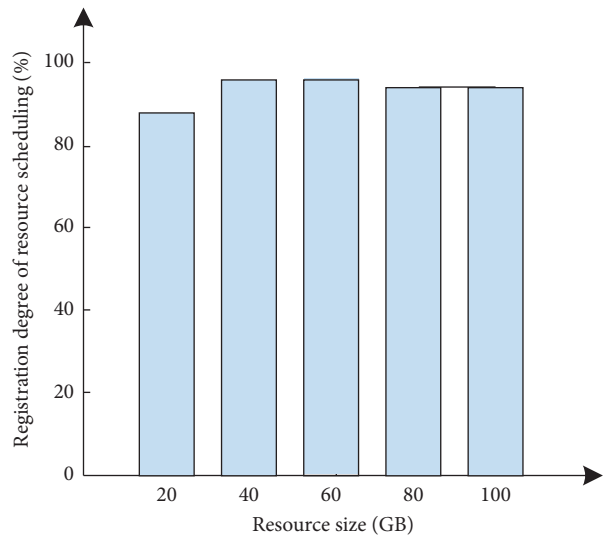

Figure 8: Resource scheduling registration degree of the proposed system.

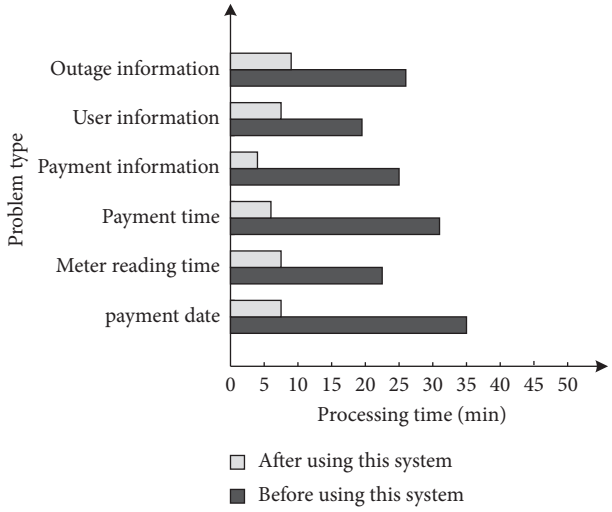

Figure 9: Comparison of effects before and after application of the proposed system.

4. Conclusion

According to the actual needs of power business customers, taking improving customer service quality as the starting point and improving the operation efficiency of the company as the goal, an intelligent customer service questioning and answering a system for power business scenario based on AI technology is designed through the combination of independent customer service and natural language. When customers ask questions, the solution strategy is obtained by designing the system self-service. The approach first uses the particle swarm optimization algorithm to automatically classify the question attributes and then uses the fuzzy *c*-means clustering algorithm to match the answers with the highest similarity to the questions and return to the customers. The experimental results show that the designed system has low worst-case time complexity, which is up to 0.35 only. The reason is that the system in this paper can use priority information to deal with the problems raised by customers, which is different from the past work where dealing with customers request via priority information is not used.

Compared with past work, the novelty of the proposed approach is shown as follows. The approach is AI-based, which combines the particle swarm optimization algorithm and the fuzzy *c*-means clustering algorithm to automatically classify the question attributes and match the answers with the highest similarity to the questions. It reduces the differences between problem data, eliminates invalid data, and simplifies the data classification process. It enables the proposed system to use priority information to deal with the problems raised by customers, leading to a low worst-case time complexity.

From the perspective of customers, the design system can meet the needs of customers and facilitate customers to obtain the solutions they need in time. From the perspective of the company, the existence of the design system can improve the processing speed of power business, strengthen

the information construction of the company, ensure its efficiency while saving operation cost, and make the operation and maintenance work of the company smoother. It is a powerful measure to promote the construction of power remote service and can be used for automation of power exchange platform in the future.

Data Availability

The data used to support the findings of this study are included within the article.

Conflicts of Interest

The authors declare that they have no conflicts of interest.

References

[1] O. Bassey, K. L. Butler-Purry, and B. Chen, "Dynamic modeling of sequential service restoration in islanded single master microgrids," *IEEE Transactions on Power Systems*, vol. 35, p. 1, 2019.

[2] P. S. Challagidad and M. N. Birje, "Local and remote recovery of cloud services using backward atomic backup recovery technique for high availability in strongly consistent cloud service: recovery of cloud service for high availability," *International Journal of Advanced Pervasive and Ubiquitous Computing*, vol. 11, 2019.

[3] J. Fan, D. F. Wu, and X. X. Liu, "Business data fragmentation and optimization in NB-IoT," *Computer Simulation*, vol. 37, no. 10, pp. 286–290+296, 2020.

[4] H. Larsen, "Normative power europe or capability–expectations gap? the performativity of concepts in the study of european foreign policy," *Journal of Communication and Media Studies: Journal of Common Market Studies*, vol. 58, no. 4, 2020.

[5] Y. Qiao, C. Zhang, R. Li, and Z. Liu, "A wireless intelligent business laundry service system," *Journal of Computer and Communications*, vol. 07, no. 7, pp. 105–113, 2019.

[6] A. Yt, A. Hx, B. Yw, A. Zz, B. Ya, and C. Yx, "Research on knowledge driven intelligent question answering system for electric power customer service," *Procedia Computer Science*, vol. 187, pp. 347–352, 2021.

[7] Z. Li, X. Liu, W. M. Wang, A. Vatankhah Barenji, G. Q. Huang, and G. Q. Huang, "CKshare: secured cloud-based knowledge-sharing blockchain for injection mold redesign," *Enterprise Information Systems*, vol. 13, no. 1, pp. 1–33, 2019.

[8] J. Yu, H. Ji, Q. Song, and L. Zhou, "Design and implementation of business access control in new generation power grid dispatching and control system," *Procedia Computer Science*, vol. 183, no. 22, pp. 761–767, 2021.

[9] Y. Chen, Z. Guo, H. Li, Y. Yang, and Z. Ding, "Selection of a critical time scale of real-time dispatching for power systems with high proportion renewable power sources," *IEEE Access*, vol. 8, pp. 52257–52267, 2020.

[10] Q. Yao, J. Liu, and Y. Hu, "Optimized active power dispatching strategy considering fatigue load of wind turbines during de-loading operation," *IEEE Access*, vol. 7, pp. 17439–17449, 2019.

[11] F. Hu, H. Chen, and X. Wang, "An intuitionistic kernel-based fuzzy c-means clustering algorithm with local information for power equipment image segmentation," *IEEE Access*, vol. 8, pp. 4500–4514, 2020.

[12] C. Liu, Q. Li, and K. Wang, "State-of-charge estimation and remaining useful life prediction of supercapacitors," *Renewable and Sustainable Energy Reviews*, vol. 150, Article ID 111408, 2021.

[13] Y. Hua, N. Wang, and K. Zhao, "Simultaneous unknown input and state estimation for the linear system with a rank-deficient distribution matrix," *Mathematical Problems in Engineering*, vol. 2021, Article ID 6693690, 11 pages, 2021.

[14] K. Wang, C. Liu, J. Sun et al., "State of charge estimation of composite energy storage systems with supercapacitors and lithium batteries," *Complexity*, vol. 2021, Article ID 8816250, 15 pages, 2021.

[15] K. Wang, W. Wang, L. Wang, and L. Li, "An improved SOC control strategy for electric vehicle hybrid energy storage systems," *Energies*, vol. 13, no. 20, p. 5297, 2020.

[16] X. Feng, Q. li, and K. Wang, "Waste plastic triboelectric nanogenerators using recycled plastic bags for power generation," *ACS Applied Materials & Interfaces*, vol. 13, no. 1, pp. 400–410, 2020.

[17] J. Zhao, F. Li, Z. Wang, P. Dong, G. Xia, and K. Wang, "Flexible PVDF nanogenerator-driven motion sensors for human body motion energy tracking and monitoring," *Journal of Materials Science: Materials in Electronics*, vol. 32, no. 11, pp. 14715–14727, 2021.

[18] S.-I. Gustafsson, "Optimal use of solar collectors for residential buildings," *International Journal of Energy Research*, vol. 25, no. 11, pp. 993–1004, 2001.

[19] K. Bhattacharjee and M. Pant, "Hybrid particle swarm optimization-genetic algorithm trained multi-layer perceptron for classification of human glioma from molecular brain neoplasia data," *Cognitive Systems Research*, vol. 58, pp. 173–194, 2019.

[20] J. Too, A. Abdullah, N. Mohd Saad, and W. Tee, "Emg feature selection and classification using a pbest-guide binary particle swarm optimization," *Computation*, vol. 7, no. 1, 2019.

[21] H. Verma, A. Gupta, and D. Kumar, "A modified intuitionistic fuzzy c-means algorithm incorporating hesitation degree," *Pattern Recognition Letters*, vol. 122, pp. 45–52, 2019.

[22] P. K. Mishro, S. Agrawal, R. Panda, and A. Abraham, "A novel type-2 fuzzy c-means clustering for brain mr image segmentation," *IEEE Transactions on Cybernetics*, no. 99, pp. 1–12, 2020.

Hindawi
Mathematical Problems in Engineering
Volume 2022, Article ID 6133969, 10 pages
https://doi.org/10.1155/2022/6133969

Research Article

Optimal Sizing of the Stand-Alone Photovoltaic System for a Solar-Powered Translational Sprinkler Irrigation Machine considering the Loss of Power Supply Probability

Kenan Liu, Bugong Sun, Xiaoyang Gao, Yang Zhang, Wei Sun, Quan Feng, and Wanxia Yang

School of Mechanical and Electrical Engineering, Gansu Agricultural University, Lanzhou 730070, China

Correspondence should be addressed to Bugong Sun; sunbg@gsau.edu.cn

Received 19 October 2021; Accepted 23 December 2021; Published 19 January 2022

Academic Editor: Licheng Wang

The translational sprinkler irrigation machine is widely used because of its high degree of automation, less manual investment, and convenient movement. However, when using the sprinkler irrigation machine, the power supply is difficult to be guaranteed in some remote power shortage areas. Solar energy has become one of the best choices for the power source of sprinkler irrigation machines. An important issue is the optimal sizing of the stand-alone photovoltaic system for a solar-powered translational sprinkler irrigation machine. This work conducts the optimal sizing of the stand-alone photovoltaic system for a solar-powered translational sprinkler irrigation machine considering the loss of power supply probability. Firstly, the self-developed translational sprinkler irrigation machine is introduced. The load power, which includes the driving power of the translational sprinkler irrigation machine, water intake pressure driving power, and the loss power of the controller and sensors, is considered in the calculation process. Subsequently, the photovoltaic generator model and the battery storage model are established. Then, the stand-alone photovoltaic system is optimized considering the loss of power supply probability (LPSP) and the life cycle cost (LCC). After the solar irradiance and ambient temperature of a typical sunny day in the test area are given, the optimal combination of the PV module and battery is obtained. The optimal sizing result is verified using the PV power, state of charge (SOC), and load power. The presented optimal sizing method is also compared with an existing method. Besides, the operation test of the sprinkler irrigation machine is also carried out to verify the optimal sizing result. The optimal sizing result is proved to be effective and applicable.

1. Introduction

The development of irrigation machinery is one of the guarantee factors to improve crop yield. How to save water and energy for irrigation has become an inevitable trend in modern agricultural development. The translational sprinkler irrigation machine is widely used because of its high degree of automation, less manual investment, and convenient movement. However, the power supply is difficult to guarantee when using the sprinkler irrigation machine in some remote power shortage areas. These power shortage areas cannot be irrigated in time. Solar energy is clean and environment-friendly energy. With the maturity of photovoltaic technology, solar energy has become one of the best choices for sprinkler irrigation machine power.

The solar-powered translational sprinkler irrigation machine transforms the traditional farmland irrigation mode into mobile sprinkler irrigation with high uniformity of irrigation. An important issue is the optimal sizing of the stand-alone photovoltaic system for a solar-powered translational sprinkler irrigation machine. At present, there are fewer studies on the matching of power demand and solar photovoltaic power during the operation of solar-powered sprinkler irrigation machines. The sprinkler irrigation machinery powered by solar is not mature, which limits its popularization and application in agriculture. At

present, the research on solar-powered machinery mostly focuses on the research of solar vehicles, such as [1–3].

Many efforts have been made regarding the optimal sizing of the stand-alone photovoltaic system. Benmouiza et al. [4] presented an optimization method for designing the stand-alone photovoltaic system. This work mainly compares the proposed method with the existing methods. However, the specific application of the method is not illustrated. Aziz et al. [5] optimized the stand-alone photovoltaic system by minimizing the loss of power supply probability. In this study, only the loss of power supply probability (LPSP) was considered without considering the stand-alone photovoltaic system's life cycle cost (LCC). Fezai et al. [6] proposed a methodology to study the load profile impact on the stand-alone photovoltaic system reliability and storage component. Senol et al. [7] studied the technical and economic feasibility of photovoltaic pumping of water in Turkey. This study only considered the life cycle cost (LCC), ignoring the loss of power supply probability (LPSP). Sallem et al. [8, 9] presented a new management approach that makes the decision on the optimum connection times of the elements of a photovoltaic water pumping installation. However, this paper does not optimize the configuration from the aspects of LCC and LPSP.

At present, most of the research on the optimal sizing of the stand-alone photovoltaic system focuses on the power supply-demand for residential households or rural areas. Abbes et al. [10] proposed a new methodology with the aim to design an autonomous hybrid PV-wind-battery system. The electric demand of a residential house is taken as an example to verify the proposed method. Bataineh et al. [11] designed a stand-alone photovoltaic (PV) system to provide the required electricity for a single residential household in a rural area in Jordan. Koutroulis et al. [12] presented a methodology for optimal sizing of stand-alone photovoltaic/wind generator systems. The proposed method has been applied to design a power generation system that supplies a residential household. Okoye et al. [13] studied the optimal sizing of stand-alone photovoltaic systems in residential buildings. As mentioned above, there are a few studies on the walking power demand and photovoltaic power matching design for the solar-powered sprinkler irrigation machine. Therefore, this work aims to optimize the stand-alone photovoltaic system for a solar-powered translational sprinkler irrigation machine considering the loss of power supply probability.

The rest of this paper is organized as follows. In Section 2, the stand-alone photovoltaic system configuration model is introduced. In Section 3, the stand-alone photovoltaic system is optimized considering the loss of power supply probability. In Section 4, the optimal combination of PV module and battery are obtained, and relevant discussions are carried out. Conclusions are drawn in Section 5.

2. Stand-Alone Photovoltaic System Configuration Model

2.1. The Self-Developed Translational Sprinkler Irrigation Machine. This study uses the self-developed translational sprinkler irrigation machine as the research objective, and its structural diagram is shown in Figure 1.

Figure 1 mainly introduces the main structure of the self-developed translational sprinkler irrigation machine. The self-developed translational sprinkler irrigation machine comprises the solar photovoltaic power supply, mechanical structure, and control system parts. As shown in Figure 1, the self-developed sprinkler irrigation machine mainly includes the solar photovoltaic module, battery, main water pipe, water pump, steering motor, high-clearance chassis, control cabinet, walking motor reducer, nozzle, and so on. The detailed information of the developed translational sprinkler irrigation machine is described in [14].

2.2. Driving Power of the Translational Sprinkler Irrigation Machine. The driving power of the translational sprinkler irrigation machine P_{d} can be given by

$$P_d = \frac{mgfv_{\max}}{\eta}\alpha, \tag{1}$$

where m is the maximum mass of the translational sprinkler irrigation machine after filling water into the water tank, g is the acceleration of gravity, f is the rolling resistance coefficient, $v_{\max}$ is the maximum travelling speed of the translational sprinkler irrigation machine, a is the safety factor, and η is the mechanical transmission efficiency. For this study, the parameters m, g, f, $v_{\max}$, α, and η are chosen as 3500 kg, 9.8 m/s^2, 0.3, 0.028 m/s, 1.2, and 0.8, respectively.

2.3. Water Intake Pressure Driving Power. The translational sprinkler irrigation machine is mainly used for crop irrigation, pesticide spraying, and fertilization. According to the inflow pressure and flow requirements of the unit design, the water intake pressure driving power required by sprinkler irrigation unit can be expressed as follows:

$$P_p = \frac{\rho gQH}{3600\eta_P}\alpha, \tag{2}$$

where ρ is the water density, Q is the flow of the pumping unit, H is the water-lift of the self-priming pump of the translational sprinkler irrigation machine, α is the safety factor, and η_{p} is the efficiency of the pump pressurization system, which includes water pump efficiency and DC brushless motor efficiency. For this study, the parameters ρ, Q, H, α, and η_{p} are chosen as 1000 kg/m^3, 12 m^3/h, 10 m, 1.2, and 0.54, respectively.

2.4. The Loss Power of the Controller and Sensors. The loss power of the controller and sensors of the unit P_{c} is also taken into consideration. In this study, P_{c} is chosen as 100 W.

The total load power P_{l} can be represented as follows:

$$P_l = P_d + P_p + P_c. \tag{3}$$

2.5. Photovoltaic Generator Model. The output electric power of the photovoltaic generator can be written as follows:

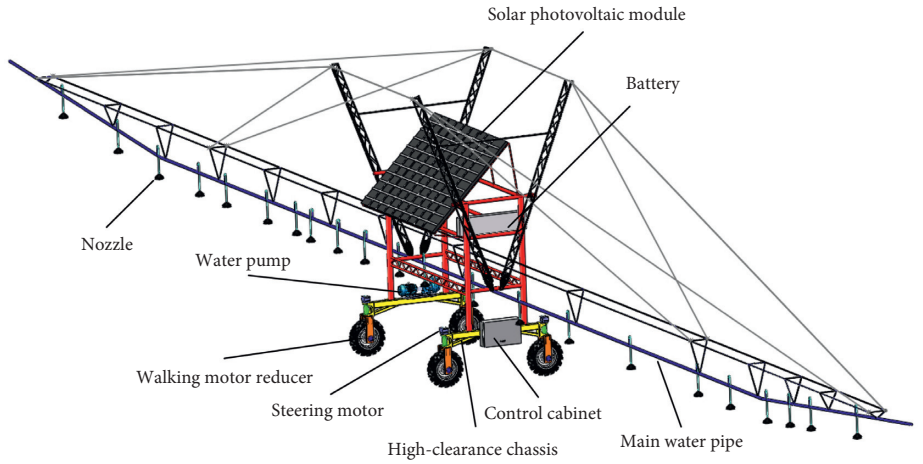

Figure 1: Structural diagrams of the developed translational sprinkler irrigation machine.

$$P_{\text{pv}} = N_{\text{pv}} \times \eta_{\text{pv}} \times A_{\text{pv}} \times I_r, \tag{4}$$

where N_{pv} is the number of PV modules, η_{pv} is the power conversion efficiency, A_{pv} is the surface area of PV panels of a single module, and I_r is the solar radiation. The power conversion efficiency η_{pv} can be expressed by the following equation:

$$\eta_{\text{pv}} = \eta_r \times \eta_{\text{pc}} \times \left[1 - \beta_{\text{getc}} \times (T_c - \text{NOCT})\right], \tag{5}$$

where η_r is the reference module efficiency, η_{pc} is the power condition efficiency, β_{getc} is the generator efficiency temperature coefficient, T_c is the cell temperature, and NOCT is the normal operating cell temperature when cells operate under standard operating conditions. T_c can be estimated as follows:

$$T_C = 30 + 0.0175 \times (I_r - 300) + 1.14 \times (T_a - 25), \tag{6}$$

where T_a is ambient temperature (°C).

2.6. Battery Storage Model. In this study, the lead-acid battery is used in the stand-alone photovoltaic system due to low cost, high reliability, convenient maintenance, and so on. The state of charge (SOC) is determined by using the difference between the generated PV power and the load power. When the generated PV power is greater than the load power, the energy produced by the PV system can satisfy the demand of the load. Meanwhile, the extra energy produced by the PV system will be stored in the battery, which corresponds to the charging process. On the contrary, when the generated PV power is less than the load power, the demand of load cannot be satisfied. The stored energy will be released to guarantee the demand of load, which corresponds to the discharging process.

The state of charge (SOC) is used to reflect the battery's remaining power in real-time. It can be defined by using the ratio of the battery's remaining capacity to the rated capacity at a certain time.

When charging, the SOC of the battery at the time t is expressed as follows:

$$\text{SOC}(t) = \text{SOC}(t - \Delta t) + \frac{\Delta E_{\text{store}} \eta_{\text{in}}}{N_b E_{\text{rate}}}. \tag{7}$$

When discharging, the SOC of the battery at the time t is expressed as follows:

$$\text{SOC}(t) = \text{SOC}(t - \Delta t) - \frac{\Delta E_{\text{store}}}{\eta_{\text{out}} N_b E_{\text{rate}}}, \tag{8}$$

where $\text{SOC}(t)$ and $\text{SOC}(t - \Delta t)$ are the states of charge of the battery at the time t and $t - \Delta t$, respectively, ΔE_{store} is the amount of energy charged or discharged by the battery during period Δt, η_{in} and η_{out} are the charging and discharging efficiency of the battery system, respectively, N_b is the number of batteries, and ΔE_{store} is the rated capacity of the battery.

When the PV power is greater than the load power, the extra PV power will be stored in the battery. The theoretical charging capacity of the battery within time t and $t + \Delta t$ is expressed as follows:

$$\Delta E_{\text{store}} = \left[P_{\text{pv}}(t) - \frac{P_l(t)}{\eta_{\text{inv}}}\right] \Delta t. \tag{9}$$

When the PV power is less than the load power, and the sum of the PV power and the battery discharge power is greater than the load power, the battery needs to release power to meet the load demand. The theoretical discharging capacity of the battery within time t and $t + \Delta t$ is expressed as follows:

$$\Delta E_{store} = \left[\frac{P_l(t)}{\eta_{inv}} - P_{pv}(t)\right] \Delta t. \tag{10}$$

The state of charge of the battery should not exceed the upper limit SOC_{max} and not be lower than the lower limit SOC_{min}, which is expressed as follows:

$$SOC_{\min} \le SOC(t) \le SOC_{\max}. \tag{11}$$

When $SOC(t + \Delta t) < SOC_{\min}$, the actual discharge capacity of the battery during time t and $t + \Delta t$ can be expressed as follows:

$$\Delta E_{discharge} = N_b E_{rate}\left(SOC(t) - SOC_{\min}\right). \quad (12)$$

When the sum of the PV power and the battery discharge power is less than the load power, the loss of power supply (LPS) will happen. The capacity of the LPS, i.e., $Q_{\mathrm{LPS}}(t)$, can be calculated as follows:

$$Q_{\mathrm{LPS}}(t) = \left[P_l(t) - \left(P_{\mathrm{pv}}(t) + P_{\mathrm{discharge}}\right) \times \eta_{\mathrm{inv}}\right]\Delta t, \quad (13)$$

where $P_{\mathrm{discharge}}$ is the discharge power of the battery.

When $\mathrm{SOC}(t + \Delta t) > \mathrm{SOC}_{\max}$, the actual charge capacity of the battery during time t and $t + \Delta t$ can be expressed as follows:

$$\Delta E_{\mathrm{charge}} = N_b E_{\mathrm{rate}}\left(\mathrm{SOC}_{\max} - \mathrm{SOC}(t)\right). \quad (14)$$

In this study, it is assumed that the battery is full charged. That is, the initial value of SOC is chosen as 100%.

3. Optimal Sizing of the Stand-Alone Photovoltaic System

3.1. Objective Function. Optimal sizing of the stand-alone photovoltaic system aims to minimize the life cycle cost (LCC) of the system on the premise of meeting the load power demand and power supply reliability. In this study, the LCC includes equipment cost C_{E}, the present worth of equipment replacement cost after n years C_{EnPW}, installation cost C_{Inst}, and the present worth of maintenance cost C_{MPW}. Therefore, the objective function of the LCC for the stand-alone photovoltaic system can be expressed as

$$\min \mathrm{LCC} = C_E + C_{\mathrm{EnPW}} + C_{\mathrm{Inst}} + C_{\mathrm{MPW}}, \quad (15)$$

where the equipment cost C_{E} mainly contains the cost of the PV modules, batteries, and controller, which are represented by C_{PV}, C_{B}, and C_{c}, respectively. Accordingly, the equipment cost C_{E} can be represented as

$$C_E = C_{\mathrm{PV}} + C_B + C_c. \quad (16)$$

In our study, the cost of each photovoltaic panel is 1000 RMB, the cost of each battery is 600 RMB, and the cost of the controller is 1600 RMB. Then, equation (16) can be rewritten as

$$C_E = 1000 \times N_{\mathrm{pv}} + 600 \times N_b + 1600. \quad (17)$$

In this work, the operating life of the photovoltaic system N is set as 20 years, namely, $N = 20$. The life of the battery is assumed to be five years, and the life of the PV modules and controller is assumed to be 20 years. Therefore, only the present worth of the battery replacement cost after n years i.e., C_{BnPW}, should be considered in the operating life of the photovoltaic system, i.e., $C_{\mathrm{EnPW}} = C_{\mathrm{BnPW}}$. The present worth of the battery replacement cost after n years can be calculated as follows:

$$C_{\mathrm{BnPW}} = C_B\left(\frac{1+i}{1+d}\right)^n, \quad (18)$$

where i and d represent the inflation rate and discount rate, respectively. During calculation, the inflation rate i and discount rate d are taken as 3% and 5%, respectively. Since the operating life of the photovoltaic system is 20 years and the life of the battery is assumed to be five years, n is chosen as 5, 10, and 15. Substituting the value of the parameters into equation (18), the following equation can be obtained:

$$C_{\mathrm{BnPW}} = 600 \times N_b \times \left[\left(\frac{1+3\%}{1+5\%}\right)^5 + \left(\frac{1+3\%}{1+5\%}\right)^{10} + \left(\frac{1+3\%}{1+5\%}\right)^{15}\right] = 1489.7 \times N_b, \quad (19)$$

The installation cost is assumed 10% of the PV modules cost, which can be expressed as follows:

$$C_{\mathrm{Inst}} = 10\% \times 1000 \times N_{\mathrm{pv}} = 100 \times N_{\mathrm{pv}}. \quad (20)$$

The present worth of maintenance cost $\mathrm{C_{MPW}}$ can be acquired as follows:

$$C_{\mathrm{MPW}} = C_{\mathrm{MPY}} \times \left(\frac{1+i}{1+d}\right) \times \frac{1 - ((1+i)/(1+d))^N}{1 - (1+i)/(1+d)}, \quad (21)$$

where C_{MPY} is the maintenance cost per year, which is assumed 2% of the PV modules cost. Substituting the parameter value into equation (21), we can get

$$C_{\mathrm{MPY}} = 2\% \times 1000 \times N_{\mathrm{pv}} \times \left(\frac{1+3\%}{1+5\%}\right) \times \frac{1 - ((1+3\%)/(1+5\%))^{20}}{1 - (1+3\%)/(1+5\%)} = 328.87 \times N_{\mathrm{pv}}. \quad (22)$$

Combining equations (17), (19), (20), and (22), the life cycle cost of the system LCC can be expressed as follows:

$$LCC = 1428.87 \times N_{\mathrm{pv}} + 2089.7 \times N_{\mathrm{b}} + 1600. \quad (23)$$

3.2. Optimization Constraints

3.2.1. Power Supply Reliability Constraint. The loss of power supply probability (LPSP) represents the probability that the photovoltaic system cannot meet the load power demand

within the evaluation period T. The LPSP can be expressed as the ratio of load power shortage to total load demand in the time period. In this study, LPSP is taken as the power supply reliability index, which can be calculated as follows:

$$\mathrm{LPSP}(t) = \frac{\sum_{t=t_0}^{t_0+k\Delta t}\left[P_l(t) - \left(P_{\mathrm{PV}}(t) + P_{\mathrm{discharge}}(t)\right) \times \eta_{\mathrm{inv}}\right]\Delta t}{\sum_{t=t_0}^{t_0+k\Delta t} P_l(t)\Delta t}, \tag{24}$$

where k is the time series for evaluation. When LPSP = 0, it indicates that the power supply of the system can be satisfied; when LPSP = 1, it indicates that the power supply of the system cannot be satisfied. Therefore, the constraint corresponding to the power supply reliability is expressed as

$$g1 = \max(\mathrm{LPSP}(t)) - \mathrm{LPSP}_{\max} \le 0. \tag{25}$$

3.2.2. Battery Power Constraint. To prevent the service life of the battery from being affected by over charge or over discharge, the state of charge of the battery should meet the following constraint:

$$\mathrm{SOC}_{\min} \le \mathrm{SOC}(t) \le \mathrm{SOC}_{\max}. \tag{26}$$

In this work, the $\mathrm{SOC}_{\min}$ and $\mathrm{SOC}_{\max}$ are chosen as the 20% and 80%, respectively.

To better demonstrate the optimization process and algorithm logic, the corresponding flow chart is presented, as shown in Figure 2.

4. Results and Discussion

4.1. Determination of the Optimal Combination of PV Module and Battery. Solar irradiance and ambient temperature are important input parameters of the optimization model. The AV6592 type portable tester (voltage accuracy 0.01 V, current accuracy 0.001 A, and power range 0.1~500 W) was used to monitor the solar irradiance and ambient temperature in the test area (east longitude 108.07°, northern latitude 34.28°, and height above sea level 521 m). The single-crystal photovoltaic panel type CS5M32-260 and the valve regulated fully sealed lead-acid battery typed 190H52 (capacity 200 A·h, rated voltage 12 V) are used in this work. The monitoring time is from April 29 to May 29, 2018, a total of 31 days. During the days of monitoring, the translational sprinkler irrigation machine works 8 hours a day, from 9 a.m. to 5 p.m. The solar irradiance and ambient temperature within 248 hours are shown in Figure 3.

As shown in Figure 3, the solar irradiance and ambient temperature within the total monitoring time show randomness and irregular variation due to the complex climatic conditions. In this study, the developed translational sprinkler irrigation machine has a lightweight and small- and medium-size structure powered by the stand-alone photovoltaic system. Suppose the sprinkler irrigation machine is guaranteed to operate continuously under non-sunny weather conditions. In that case, more photovoltaic modules and batteries will be required, which may exceed the bearing range of the design structure. Therefore, the developed translational sprinkler irrigation machine has the best applicability under sunny weather conditions. In addition, sprinkler irrigation is more necessary in sunny weather conditions. The solar irradiance and ambient temperature of a typical sunny day in the test area are shown in Figure 4.

In Figure 4(b), the red curve is the fitting of the ambient temperature for a typical sunny day. It can be seen from Figure 4 that under the typical sunny weather condition in the test area the solar irradiance and ambient temperature reach the maximum between 13:00 and 14:00. The other main input parameters are listed in Table 1.

As mentioned above, when the photovoltaic (PV) system cannot meet the load power demand, the loss of power supply will happen. The loss of power supply probability (LPSP) varies with the combinations of PV module and battery. Considering the small- and medium-size structure of the developed translational sprinkler irrigation machine, the number of photovoltaic modules and batteries should not be too large. In this study, the number of photovoltaic modules ranges from 1 to 25, and the number of batteries also ranges from 1 to 25. That is, $1 \le N_{\mathrm{pv}} \le 25$, and $1 \le N_{\mathrm{b}} \le 25$. The relationship among the number of photovoltaic modules, the number of batteries, and the LPSPs is shown in Figure 5.

In Figure 5, the curves are the boundaries between the desirable and undesirable LPSPs. It can be seen from Figure 5 that the larger the LPSP, the more combinations of PV module and battery can be selected. The purpose of optimal sizing is to minimize the life cycle cost (LCC) on the premise that LPSP meets the requirements. The life cycle cost (LCC) comparison for different combinations of photovoltaic module and battery is shown in Table 2.

As shown in Table 2, with the increase of the number of PV modules and batteries, the LPSPs decrease, but the corresponding LCC increases. In addition, when $N_{\mathrm{pv}} = 16$ and $N_{\mathrm{b}} = 2$, it can also make LPSP = 0. The relationship between LPSP and LCC is shown in Figure 6.

As can be seen from Figure 6, we mainly divide the parameter plane into three regions, i.e., regions A, B, and C. The LPSP corresponding to region A is small, but the smaller LPSP is based on the sacrifice of LCC. As for region B, the corresponding LPSP is greater than that in region A, while the corresponding LCC is not reduced much. The LPSP corresponding to region C is larger than that in regions A and B, but the corresponding LCC is smaller than that in regions A and B. In this study, to ensure the continuous operation of the sprinkler irrigation machine, the maximum LPSP is set to 0; that is, there is no power loss during the operation of the sprinkler irrigation machine under typical sunny weather conditions.

After comparative analysis, the combination of PV module and battery with $N_{\mathrm{pv}} = 16$ and $N_{\mathrm{b}} = 2$ is proved the optimal one, the LCC of which is minimum and whose LPSP also meets the requirements (LPSP = 0).

4.2. Comparison with the Existing Method. In this section, by combining the data listed in Table 2, the optimization sizing method presented in this manuscript is compared with the

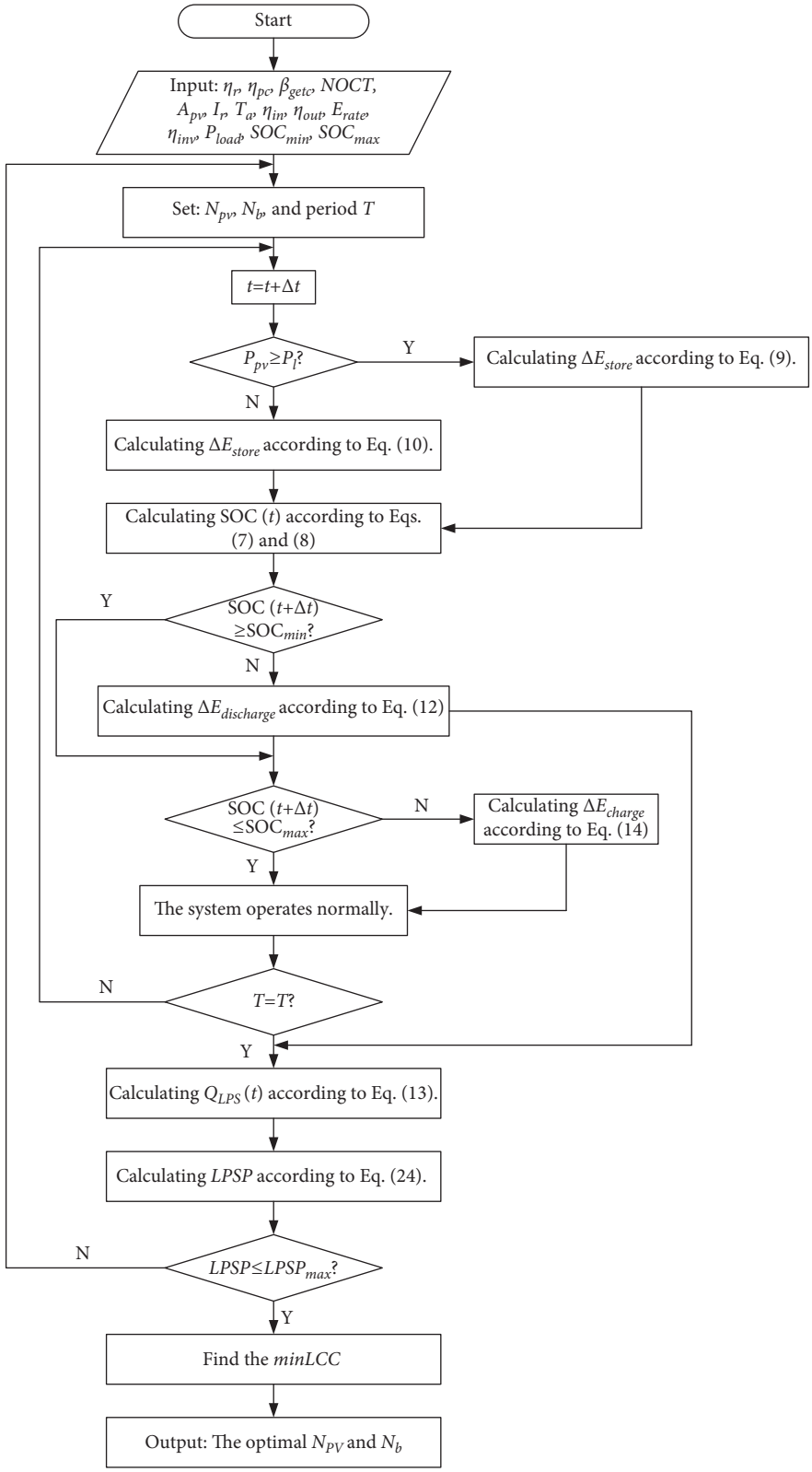

Figure 2: Flow chart of the optimization process and algorithm logic.

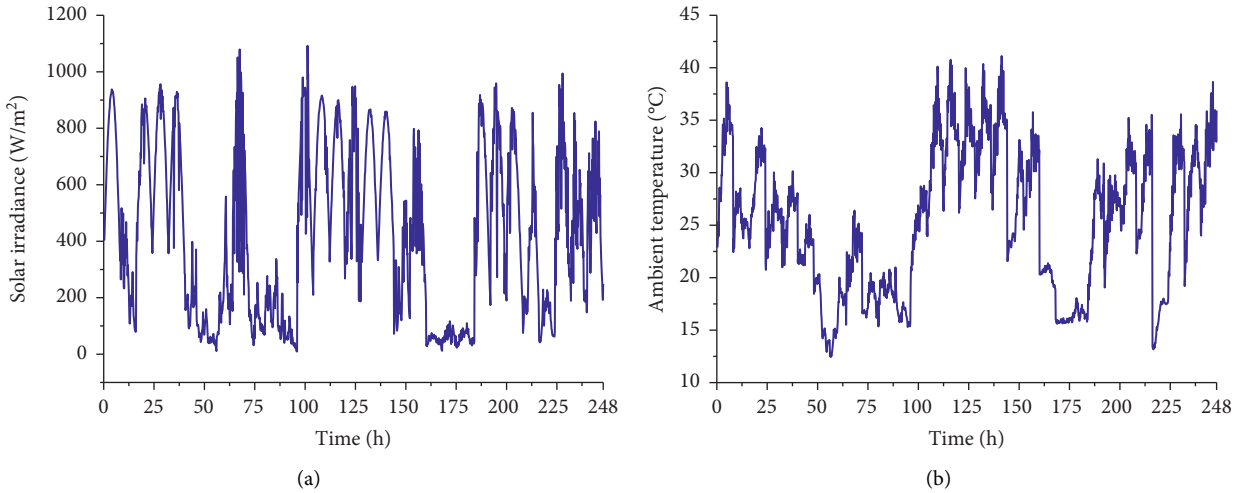

Figure 3: Solar irradiance and ambient temperature during the total monitoring time. (a) Solar irradiance. (b) Ambient temperature.

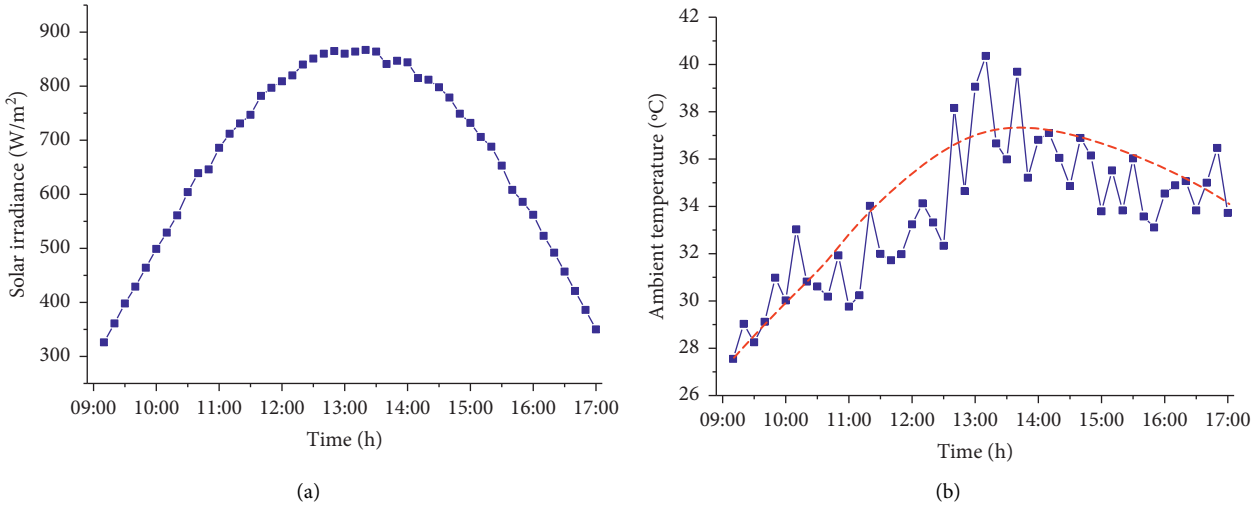

Figure 4: Solar irradiance and ambient temperature of a typical sunny day in the test area. (a) Solar irradiance. (b) Ambient temperature.

Table 1: The other main input parameters.

Parameters	Value
η_r	0.12
η_{pc}	0.9
β_{getc}	0.0045
NOCT	45
A_{pv} (m^2)	1.5
η_{in}	0.9
η_{out}	0.85
E_{rate} (A·h)	200
η_{inv}	0.95

existing method reported in [7]. In [7], the technical and economic feasibility of photovoltaic pumping of water is studied. However, the loss of power supply probability (LPSP) is not considered in [7].

According to Table 2, the optimal combination of PV module and battery determined by the proposed method corresponds to No. 15 with $N_{pv} = 16$ and $N_b = 2$, and the minimum LCC is 28641.32 RMB. Besides, the sprinkler irrigation machine can operate continuously without loss of power supply. If the loss of power supply probability (LPSP) is not considered, the optimal combination of PV module and battery obtained using the method presented in [7] may correspond to No. 1 with $N_{pv} = 3$ and $N_b = 4$, and the minimum LCC is 14245.41 RMB. Although the LCC obtained using the method presented in [7] is relatively smaller, the corresponding LPSP is as high as 76.47%. Consequently, the machine cannot work continuously, and the effective working time is very short.

4.3. Operation Test of Sprinkler Irrigation Machine. To verify the optimal sizing results, the solar irradiance and ambient temperature on June 5, 2018 (typical sunny day) are observed, as shown in Figure 7. Meanwhile, the sprinkler irrigation operation is also carried out using the developed sprinkler irrigation machine in the test area.

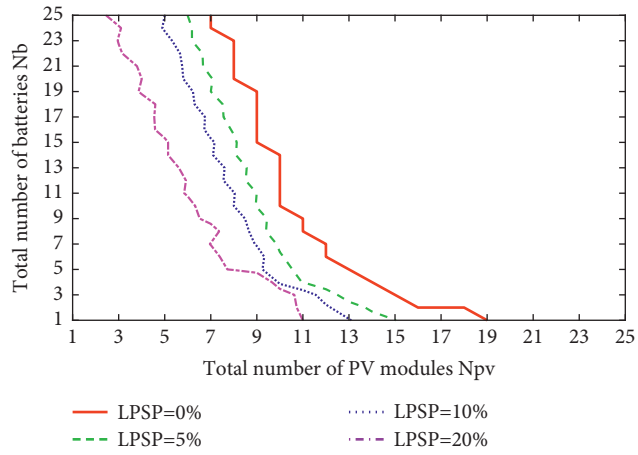

Figure 5: Relationship among the number of photovoltaic modules, the number of batteries, and the LPSPs.

Table 2: LCC comparison for different combinations of photovoltaic module and battery.

No.	Life cycle cost (LCC)	Loss of power supply probability (LPSP)	Number of PV modules (N_{pv}) (%)	Number of batteries (N_b)
1	14245.41	76.47	3	4
2	17763.98	70.68	4	5
3	21282.55	31.84	5	6
4	24801.12	24.43	6	7
5	28319.69	22.46	7	8
6	31838.26	12.65	8	9
7	35356.83	4.74	9	10
8	38875.40	0	10	11
9	42393.97	0	11	12
10	45912.54	0	12	13
11	49431.11	0	13	14
12	52949.68	0	14	15
13	56468.25	0	15	16
14	59986.82	0	16	17
15	28641.32	0	16	2

It can be seen from Figure 7 that the overall change trend of solar irradiance and ambient temperature on the test day is consistent with that on the typical sunny day described in Figure 4. The solar irradiance increases first and then decreases and reaches the maximum between 13:00 and 14:00. The ambient temperature rises first and then decreases slightly.

After substituting the optimal combination of PV module and battery ($N_{pv} = 16$ and $N_b = 2$) into the PV system model and battery storage model, the PV power, state of charge (SOC), and load power at each time can be obtained, as shown in Figure 8. Note that the factors affecting the operation of sprinkler irrigation machines are complicated. The load power at each time is assumed to be equal to the full load power in the calculation process to ensure the normal operation of the sprinkler irrigation machine.

As shown in Figure 8, the PV power is greater than the load power at most time points. In Figure 8, between 9:00 and 10:00, the PV power is less than the load power due to the low irradiance and ambient temperature. Consequently, the battery needs to be discharged to meet the load demand. Accordingly, the state of charge (SOC) of the battery also shows a downward trend. From 10:00 to 16:30, the PV power is greater than the load power, which can meet the demand of the load. During this time period, the SOC curve fluctuates with time. The SOC value rises because the PV power is greater than the load power, and the SOC is calculated according to equation (7). The decrease of SOC value is because SOC is greater than SOC_{max}, and SOC is calculated according to equation (14). From 16:30 to 17:00, the solar irradiance and ambient temperature decrease, which makes the PV power lower than the load power, and then the SOC also shows a downward trend.

In order to further verify the practicability of the self-developed translational sprinkler irrigation machine and the feasibility of the optimal sizing result, the sprinkler irrigation experiment using the developed sprinkler irrigation machine was carried out in the experimental site, as shown in Figure 9.

The developed sprinkler irrigation machine, which installed 16 photovoltaic modules and two batteries, runs from 9:00 to 17:00 for a total of 8 hours, and the maximum running speed is 0.028 m/s. During operation, the flow of the pumping unit is 12 m^3/h, and the water-lift of the self-priming pump of the translational sprinkler irrigation machine is 10 m. Within 8 hours of operation, the sprinkler

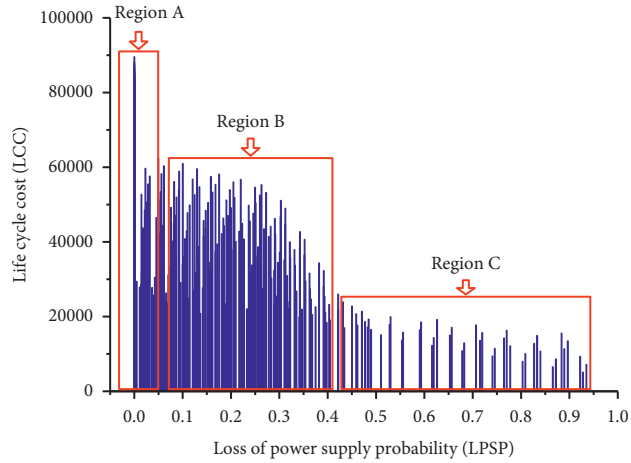

Figure 6: Relationship between LPSP and LCC.

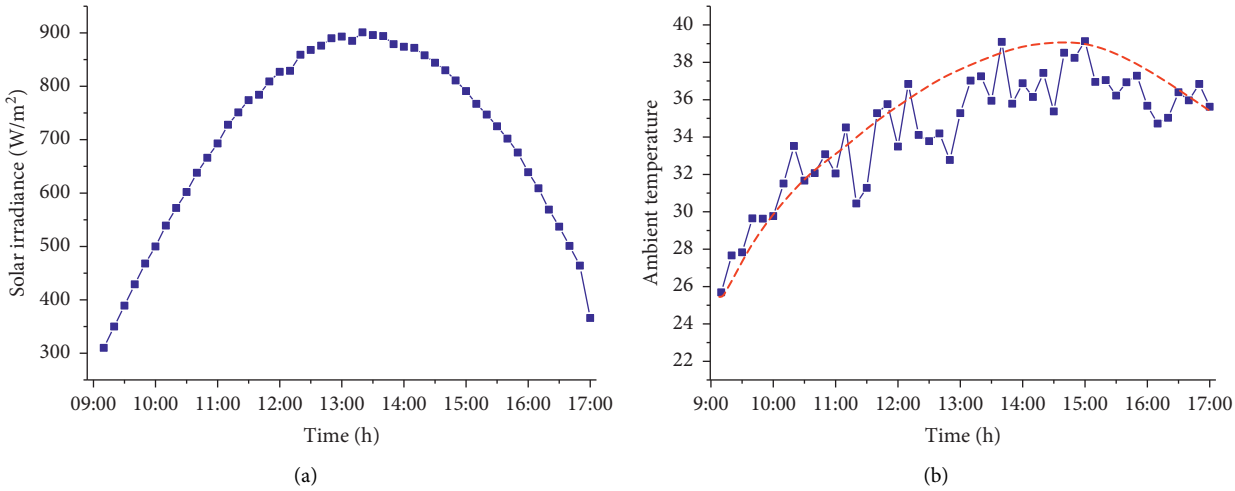

Figure 7: Solar irradiance and ambient temperature of the test day. (a) Solar irradiance. (b) Ambient temperature.

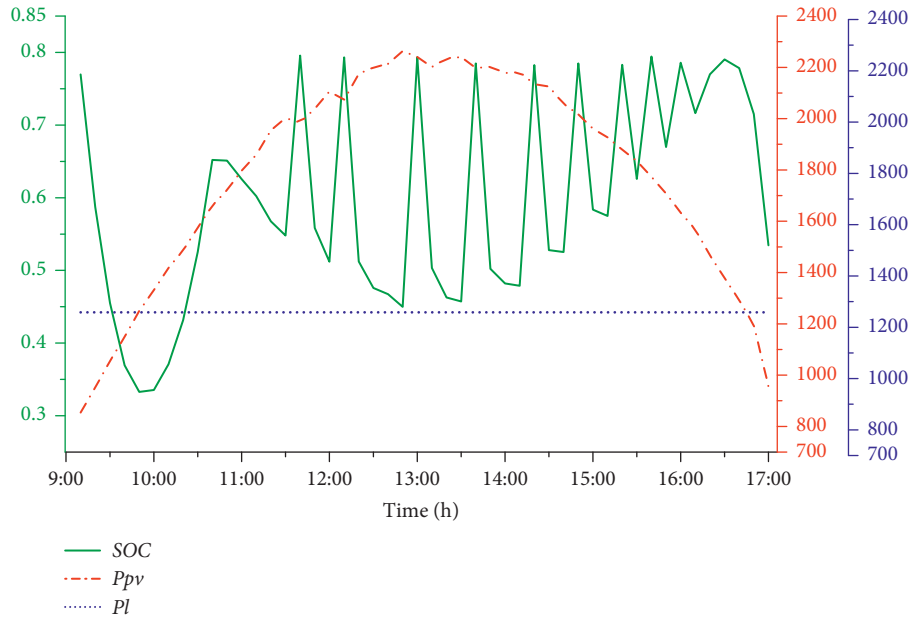

Figure 8: The PV power, state of charge (SOC), and load power at different time points.

Figure 9: Sprinkler irrigation experiment site using the developed sprinkler irrigation machine.

irrigation machine operated continuously without loss of power supply, which further verified the effectiveness of the optimal sizing results.

5. Conclusions

This paper aims to optimize the stand-alone photovoltaic system for a solar-powered translational sprinkler irrigation machine. The following conclusions can be drawn:

(1) The load power, which includes the driving power of the translational sprinkler irrigation machine, water intake pressure driving power, and the loss power of the controller and sensors, is considered in the calculation process. Meanwhile, the photovoltaic generator model and the battery storage model are established.

(2) The stand-alone photovoltaic system is optimized considering the loss of power supply probability (LPSP) and the life cycle cost (LCC). The combination of PV module and battery with $N_{pv} = 16$ and $N_b = 2$ is proved the optimal one.

(3) By analyzing the PV power, state of charge (SOC), and load power of a typical sunny day, the optimal sizing result is proven effective and applicable. Besides, the optimal sizing result is also verified by the operation test of the sprinkler irrigation machine.

Data Availability

The data used to support the findings of this study are included within the article.

Conflicts of Interest

The authors declare no conflicts of interest.

Acknowledgments

This research was funded by the Youth Science and Technology Fund Project of Gansu Province (20JR10RA555, 20JR10RA557), the FuXi Talent Program of Gansu Agricultural University (GAUfx-04Y02), the National Natural Science Foundation of China (61661003, 61862002, 51765004, 52165028, and 52065005), the Teaching Team Project of Electrical Specialty of Gansu Agricultural University (GAU-JXTD-201904), the New Engineering Research and Practice Project of Gansu Agricultural University (GAU-XGKYJSJ-202007), and the Discipline Construction Fund of Gansu Agricultural University (GAU-XKJS-2018-190).

References

[1] A. Hilliard and G. A. Jamieson, "Ecological interface design for solar car strategy: from state equations to visual relations," in *Proceedings of the IEEE International Conference on Systems, Man and Cybernetics*, pp. 139–144, IEEE, Montreal, QC, Canada, Oct. 2007.

[2] M. E. Gamez, E. N. Sanchez, and L. J. Ricalde, "Optimal operation via a recurrent neural network of a wind-solar energy system," in *Proceedings of the 2012 IEEE World Automation Congress (WAC)*, pp. 1–6, IEEE, San Jose, CA, USA, Aug. 2011.

[3] J. Wang, X. Zhang, and D. Kang, "Parameters design and speed control of a solar race car with in-wheel motor," in *Proceedings of the 2014 IEEE Transportation Electrification Conference and Expo (ITEC)*, pp. 1–6, IEEE, Dearborn, MI, USA, June 2014.

[4] N. D. Nordin and H. Abdul Rahman, "A novel optimization method for designing stand alone photovoltaic system," *Renewable Energy*, vol. 89, pp. 706–715, 2016.

[5] N. I. Abdul Aziz, S. I. Sulaiman, S. Shaari, I. Musirin, and K. Sopian, "Optimal sizing of stand-alone photovoltaic system by minimizing the loss of power supply probability," *Solar Energy*, vol. 150, pp. 220–228, 2017.

[6] S. Fezai and J. Belhadj, "Sizing optimization of a stand-alone photovoltaic system using genetic algorithm," in *Proceedings of the 18th international conference on Sciences and Techniques of Automatic control & computer engineering (STA 2017)*, pp. 499–504, IEEE, Monastir, Tunisia, December 2017.

[7] R. Senol, "An analysis of solar energy and irrigation systems in Turkey," *Energy Policy*, vol. 47, pp. 478–486, 2012.

[8] S. Sallem, M. Chaabene, and M. B. A. Kamoun, *Optimum Energy Management of a Photovoltaic Water Pumping SystemSustainability in Energy and Buildings*, R. J. Howlett, L. C. Jain, and S. H. Lee, Eds., Springer, Berlin, Heidelberg, pp. 187–197, 2009.

[9] S. Sallem, M. Chaabene, and M. B. A. Kamoun, "Energy management algorithm for an optimum control of a photovoltaic water pumping system," *Applied Energy*, vol. 86, no. 12, pp. 2671–2680, 2009.

[10] D. Abbes, A. Martinez, and G. Champenois, "Life cycle cost, embodied energy and loss of power supply probability for the optimal design of hybrid power systems," *Mathematics and Computers in Simulation*, vol. 98, pp. 46–62, 2013.

[11] K. Bataineh and D. Dalalah, "Optimal configuration for design of stand-alone PV system," *Smart Grid and Renewable Energy*, vol. 03, no. 02, pp. 139–147, 2012.

[12] E. Koutroulis, D. Kolokotsa, A. Potirakis, and K. Kalaitzakis, "Methodology for optimal sizing of stand-alone photovoltaic/wind-generator systems using genetic algorithms," *Solar Energy*, vol. 80, no. 9, pp. 1072–1088, 2006.

[13] C. O. Okoye and O. Solyalı, "Optimal sizing of stand-alone photovoltaic systems in residential buildings," *Energy*, vol. 126, pp. 573–584, 2017.

[14] K. Liu, W. Zhao, B. Sun, P. Wu, and D. Zhu, "Application of ushak filter in the navigation of a translational sprinkler irrigation machine," *Water*, vol. 11, no. 6, p. 1269, 2019.

Hindawi
Mathematical Problems in Engineering
Volume 2021, Article ID 2442071, 12 pages
https://doi.org/10.1155/2021/2442071

Research Article

The Impact of Innovation Investment Volatility on Technological Innovation of Enterprises in Different Life Cycles

Miaomiao Li,[1] **Zhaoxing Hao**,[1] **Meng Luan**,[2] **Haibo Li**,[3] **and Guikun Cao**[1]

[1]*School of Business, Qingdao University, Qingdao 266071, China*
[2]*COSCO Shipping,(Qingdao) Co., Ltd, Qingdao 266001, China*
[3]*Institute of Science and Technology for Development of Shandong, Jinan 250000, China*

Correspondence should be addressed to Miaomiao Li; qdl2014@126.com and Zhaoxing Hao; hzxing1996@163.com

Received 22 October 2021; Accepted 15 December 2021; Published 31 December 2021

Academic Editor: Yong Aaron Tan

Empirical findings from the impact of innovation investment volatility on enterprise technological innovation are mixed. Based on the punctuated equilibrium theory, this study explores the impact of innovation investment volatility on enterprise technological innovation in different life cycles and whether innovation subsidy has expected effects on enterprises' technological innovation. By using the 205 Chinese listed enterprises in strategic emerging industries from 2010 to 2019 as the research sample, the results show that the innovation investment volatility has a positive impact on technological innovation of enterprise in the growing stage, while it has no significant effect on enterprise technological innovation in the mature and declining stages. In addition, the negative moderating effect of innovation subsidy on the relationship between innovation investment volatility and technological innovation is the most significant for enterprises in the growing stage, weakly significant for enterprises in the mature stage, and insignificant for enterprises in the declining stage.

1. Introduction

In recent years, in order to realize the optimization of economic structure and the transformation of growth momentum, the Chinese government has proposed to build an innovative country [1]. The construction of an innovative country requires the support of enterprise technological innovation [2]. Under such a background, China's enterprises have been very active in innovation activities. The innovation investment in China's enterprises is increasing every year (see Figure 1), and the total amount of innovation investment has consistently been the second-highest in the world. However, the continuous increase in innovation investment has not led to improvement in innovation level, and China's enterprises as a whole continue to show a relatively low level of innovation. The reality of the innovation paradox has made innovation investment questioned. Recent studies have pointed out that the volatility of enterprises' innovation investment is more likely to promote the level of innovation. First, the innovation investment volatility has an effect on resource allocation. It eases the resource constraints of dual innovation through time separation [3]. When the technological environment is relatively stable, enterprises focus innovation resources on product improvement and technology refinement, which is conducive to forming incremental innovation [4, 5]. When the technological environment is turbulent and profoundly changing, enterprises focus innovation resources on exploratory innovation into new knowledge areas, which is conducive to fostering disruptive innovation [6]. Second, the innovation investment volatility has the effect of signal transmission. The high level of innovation investment volatility indicates that the enterprise is conducting both exploratory and exploitative innovation activities at the same time [7]. The innovation signal indicates the enterprise's competitive market advantage, low default risk, and strong governance capabilities. Enterprises with higher levels of innovation investment volatility are more likely to be favored by investors, which can alleviate the financial constraints required for enterprise technological innovation.

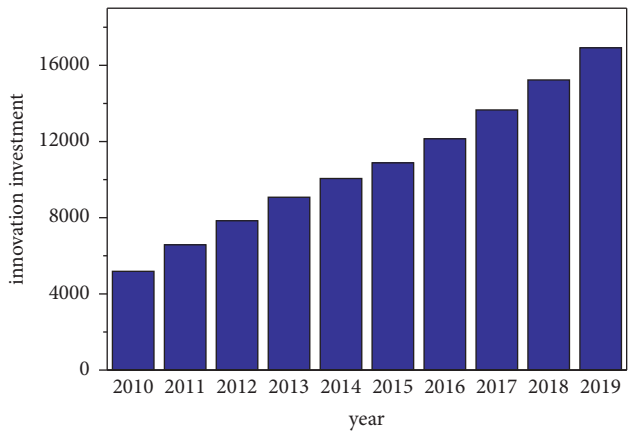

Figure 1: Innovation investment in China's enterprises (unit: 100 million yuan; source: Statistical Bulletin on China's Scientific and Technological Expenditure).

Therefore, they also tend to be more active in improving the level of innovation. However, whether China's enterprises are applicable to this mechanism needs to be further tested. Most of the existing literature regards enterprises as a homogeneous sample, ignoring the heterogeneity effect in different life cycle stages. Therefore, it is necessary to further explore the impact of innovation investment volatility on enterprise technological innovation in different life cycles.

Based on these insights, this study selects 205 Chinese listed enterprises in strategic emerging industries from 2010 to 2019 as a research sample to explore the impact of innovation investment volatility on technological innovation in different life cycles. Further, the public product nature of innovation activities often leads to market failure [8]. Innovation subsidy, as a significant means for the Chinese government to intervene in innovation activities, has an impact on innovation activities. Therefore, the study further introduces innovation subsidy policy as a moderating variable to test its influence on the relationship between innovation investment volatility and technological innovation of enterprises in different life cycles. Through the regression test of panel data, the research conclusions are as follows First, the innovation investment volatility has a positive impact on enterprise technological innovation in the growing stage, while it has an insignificant effect on enterprise technological innovation in the mature and declining stages. Second, the negative moderating effect of innovation subsidy on the relationship between innovation investment volatility and technological innovation of enterprises in the growing stage is the most significant, followed by the mature stage and the least in the declining stage. This study has several contributions. First, the study is conducive to deepening the theoretical study of innovation investment volatility and providing brand-new ideas for enterprise innovation investment activities by separately testing the impacts of innovation investment volatility on technological innovation of enterprises in different life cycles. Second, by distinguishing whether the innovation subsidy is effective in the life cycle stage of enterprises, the study provides a theoretical basis for formulating a more accurate innovation subsidy policy. It is also conducive to avoiding the waste of policy resources and creating a win-win situation between the government and enterprises. Finally, enterprises in strategic emerging industries of China are selected as the research sample. The impact of industry differences has been eliminated, which will provide reliable China microevidence for the research on innovation investment volatility.

The rest of the study is structured as follows. Section 2 reviews the previous research and analyzes the theoretical basis of the research. Section 3 explains the constructed research framework and hypotheses. Section 4 introduces the data and methodology. Section 5 contains the main results and robustness tests. In the last section, the study ends up with a discussion and conclusion.

2. Conceptual Framework

Depending on the different reasons for the volatility, innovation investment volatility includes three types: proactive innovation management, internal financing, and innovation manipulation. First, one of the reasons for the innovation investment volatility is proactive innovation management, which regards innovation investment volatility as a result of proactive management by managers [8]. The manager is not passively waiting for the results of innovation but allocates innovation resources in a timely manner based on the innovation stage and invests more resources into high-value innovation projects [8]. Therefore, it can lead to the volatility of innovation investment by the management of the innovation stage or resource allocation of innovation projects. Second, one of the reasons for the innovation investment volatility is internal financing, which regards the change of internal financing as the cause of innovation investment volatility [9]. Due to the high risk of innovation activities, the uncertainty of returns, and the asymmetry of information, there are constraints on external financing channels [9]. Internal financing channels have become the main source of innovation investment. When the amount of internal financing decreases, there will be a shortage of funds for the investment activities that have already been carried out. Enterprises tend to use tight internal funds to pay for investment activities with fast returns, low risk, and low uncertainty. Thus, when enterprises face financial problems, innovation investments of enterprises that rely on internal financing are characterized by volatility. Finally, one of the reasons for the innovation investment volatility is innovation manipulation, which regards innovation investment volatility as a result of innovation investment manipulation [8]. Managers may manipulate innovation expenditures to satisfy the expected returns or opportunistically manipulate innovation investment to obtain more government subsidies [10, 11]. Both performance catering and policy rent-seeking can lead to a sudden increase in innovation intensity, which will lead to a volatile character of innovation investment.

Enterprises in each life cycle stage have different financing constraints, innovation decisions, innovation capabilities, etc. Therefore, the causes for their innovation

investment volatility are also different in different life cycles. The innovation investment volatility in the growing stage is caused by proactive innovation management. First, enterprises in the growing stage face great pressure on innovation funds. They have internal and external financing constraints, resulting in limited innovation resources, which require managers to proactively identify the value of innovation projects and invest innovation resources in higher-value projects. The phenomenon of actively allocating innovation resources leads to innovation investment volatility. Second, enterprises in this stage have less internal financing. They still do not have the ability to make stable profits and lack sufficient internal funding to support innovation activities [12]. Therefore, the innovation investment volatility of enterprises in the growing stage is not caused by internal financing. Finally, innovation manipulation by enterprises in the growing stage may endanger their survival. In this stage, enterprises have not established a stable foothold and good reputation in the industry. Once they are found to have carried out innovation manipulation, it will bring negative consequences to the economy and reputation [13]. Therefore, the innovation investment volatility of enterprises in the growing stage is not caused by innovation manipulation.

Innovation investment volatility of enterprises in the mature stage is caused by internal financing. First, the internal financing of enterprises in this stage is sufficient. Enterprises with gradually mature production and operation model can obtain stable profits [14]. They have adequate internal financing. However, the cost of external financing tends to be higher compared to internal financing. Enterprises in the mature stage tend to use internal financing as the source of innovation investment. When internal financing is reduced, they naturally choose to prioritize internal funds to pay for investment activities with fast returns, low risk, and low uncertainty. Therefore, the innovation investment of enterprises in the mature stage presents the characteristics of volatility. Second, it is difficult for them to proactively manage innovation projects. Compared to enterprises in other stages, enterprises in the mature stage have a higher degree of diversity [7]. Manager's innovation decisions are mainly based on standardized experience rather than proactive management [15]. Therefore, the innovation investment volatility of enterprises in the mature stage is not caused by proactive innovation management. Finally, enterprises in the mature stage are less likely to engage in innovation manipulation. They have richer innovation experience and higher output levels. When allocating subsidy funds, government officials need to be under pressure to avoid waste. Enterprises with higher levels of innovation output are likely to be granted subsidies [16]. Therefore, they do not need to use innovation manipulation to obtain government subsidies. The innovation investment volatility in the mature stage is not caused by innovation manipulation.

The innovation investment volatility of enterprises in the declining stage is caused by innovation manipulation. First, the innovation manipulation motivation of enterprises in the declining stage is more likely to occur. In this stage, enterprises often face the risk of delisting or being merged. To prevent the continuous decline of stock prices, they may make an adverse selection. Innovation subsidy, as a low-cost source of funding for innovation activities, is naturally favored by enterprises in the declining stage. Therefore, to satisfy the criteria of innovation subsidy, enterprises may choose to increase innovation investment, which in turn leads to the volatility of innovation investment. Second, enterprises in the declining stage are less likely to undertake proactive management of innovation projects. They often suffer from institutional rigidity, section redundancy, and increased internal shifting of responsibilities [17]. Their judgment of innovation projects often follows the principle of path dependence rather than relying on proactive management. Therefore, the innovation investment volatility of enterprises in the declining stage is not caused by proactive innovation management. Finally, the sales of enterprises begin to decrease, and the market share shows a downward trend in the declining stage, resulting in limited internal financing. Therefore, the innovation investment volatility of enterprises in the declining stage is not caused by internal financing.

3. Hypotheses

3.1. The Different Impact of Innovation Investment Volatility. First, the innovation investment volatility caused by proactive innovation management can alleviate the limitations of innovation resources for enterprises in the growing stage, which can promote their technological innovation level. Although enterprises in the growing stage have an intense will for innovation, they have internal and external financing constraints due to the instability of profitability and information asymmetry, which restricts the development of innovation activities. However, the innovation investment volatility caused by proactive innovation management signals to outside investors that the enterprise is focusing on innovation. It conveys a low default risk and strong governance ability which is beneficial for the enterprise to access external financing. This enriches enterprise innovation funds. It can also alleviate the resource constraints of dual innovation through time compartmentalization and maximize the utilization of available resources [3]. Therefore, the volatility of innovation investment has a positive impact on the technological innovation of enterprises in the growing stage.

Second, the innovation investment volatility of enterprises in the mature stage is a result of the change in internal financing. The production and operation models of enterprises in the mature stage are becoming more mature and their profitability is strong. Internal financing channels are the main source of innovation investment for them. However, due to environmental uncertainties, policy uncertainties, and other factors, the internal financing of enterprises in the mature stage often exhibits volatility characteristics. When the amount of internal financing decreases, enterprises in the stage tend to prioritize internal funds to pay for investment activities with fast returns, low risk, and low uncertainty. The innovation investment becomes the main target of reduction. When the amount of

internal financing increases, enterprises in this stage tend to use internal funds to pay for innovation projects with long return cycles and large future returns. However, the increase or decrease of innovation investments is not an innovation decision based on changes in the market environment, but an adjustment behavior influenced by changes in internal financing. It may affect the normal innovation process of enterprises and may not improve the level of technological innovation. Therefore, the innovation investment volatility of enterprises in the mature stage has an insignificant incentive effect on technological innovation.

Finally, the innovation investment volatility caused by innovation manipulation is a strategic innovation behavior because enterprises in the declining stage lack new profit growth points or even face the threat of delisting [14]. To reach the criteria of government subsidy, enterprises in the stage often use accounting account adjustments to inflate innovation investment or purchase some advanced innovation equipment that is not put into actual operation [11]. The innovation manipulation does not substantially invest innovation funds into innovation activities. Therefore, the innovation investment volatility does not contribute to the level of technological innovation of enterprises in the declining stage but is merely a manifestation of policy rent-seeking. Based on the above analysis, the following hypotheses are proposed in this study.

H1: The volatility of innovation investment has a positive impact on enterprise technological innovation in the growing stage, while it has no significant effect on enterprise technological innovation in the mature and declining stages.

3.2. The Moderating Effect of Innovation Subsidy. The general impact of innovation investment volatility on technological innovation of enterprises in different life cycles is analyzed above. It has been found that the impact of innovation subsidy varies depending on the life cycle stage of the enterprise [18]. First, innovation subsidy weakens the effect of the innovation investment volatility by enterprises in the growing stage. The innovation investment volatility promotes the technological innovation level of enterprises in the growing stage by alleviating the limitations of their innovation resources. Although innovation subsidy directly complements the lack of innovation resources for enterprises in the growing stage and reduces their pressure to proactively manage innovation investments, it also transmits to outside investors that enterprises in the growing stage are too dependent on the government [19], weakening the signal that enterprises are innovation-oriented and hindering external financing channels. Thus, innovation subsidy weakens the positive impact of innovation investment volatility on enterprise technological innovation in the growing stage.

Second, innovation subsidy has led to changes in the reasons for innovation investment volatility of enterprises in the mature stage. When the amount of internal financing decreases, enterprises in the mature stage can also use innovation subsidies to support the research and development activities. In fact, the availability of innovation subsidies brings more media attention to enterprises. Managers are forced by media pressure to terminate little-value innovation projects in time. Therefore, the volatility of innovation investment in the mature stage becomes proactively managed. The innovation investment volatility caused by proactive innovation management invests innovation funds into more valuable projects through resource allocation, which promotes technological innovation of enterprises in the mature stage. However, while innovation subsidy brings media attention, it may also interfere with managers' judgments on the innovation stage [20]. Managers are more confident in devoting significant resources to exploratory innovation activities. Due to the originality and high risk of exploratory innovation, the exploratory innovation will consume a lot of resources and affect other innovation projects [21]. Thus, innovation subsidy has a negative effect on the relationship between the volatility of innovation investment and technological innovation of enterprises in the mature stage.

Finally, while innovation subsidy enhances the innovation investment volatility of enterprises in the declining stage, it does not substantially promote the level of technological innovation. In order to recover losses, enterprises in the declining stage often carry out innovation manipulation to acquire police resources. The acquisition of innovation subsidy, in turn, stimulates the motivation of innovation manipulation by enterprises in the declining stage and enhances the volatility of innovation investment. However, after receiving an innovation subsidy, enterprises in the stage often use it to recover losses or prevent stock price declines instead of using it for innovation activities. Thus, although innovation subsidy enhances the innovation investment volatility of enterprises in the declining stage, the level of technological innovation has not been substantially improved. Based on the above analysis, the following hypotheses are proposed in this study.

H2: The negative moderating effect of innovation subsidy on the relationship between innovation investment volatility and technological innovation is the most significant for enterprises in the growing stage, weakly significant for enterprises in the mature stage, and insignificant for enterprises in the declining stage.

4. Data and Methodology

4.1. Sample. Our data covers the listed enterprises of Chinese strategic emerging industries from 2010 to 2019. First, compared with other industries, listed enterprises in strategic emerging industries have the characteristics of active innovation investment activities, which creates realistic conditions for the observation of the volatility of innovation investment in this study. Second, data selection started in 2010. After the international financial crisis in 2008, the business activities and innovation investment activities of strategic emerging industries have gradually stabilized after two years of adjustment, which provides a realistic basis for our research. According to relevant studies, in the digital economy era, most enterprises, especially those in strategic emerging industries, can complete profound changes in two years [22]. Therefore, for the robustness of the study findings, only samples with innovation investment observations

for more than 3 consecutive years are retained in this study. Finally, data of doubtful reliability were excluded, including missing, incorrect, or unreasonable data, and enterprises' registration period of less than 2 years. The final sample of 205 enterprises was obtained, and the total number of observations was 1681. The patent data used in the study are drawn from the Chinese Research Data Services (CNRDS) database, while other data are drawn from the China stock market and accounting research (CSMAR) database.

At present, there is no consensus on the division of the enterprise life cycles. Compared with the traditional financial comprehensive index method and single variable method, the cash flow model method can reflect the characteristics of the operating conditions, profitability, and growth rate of enterprises in different life cycle stages, which has strong objectivity. Based on the above analysis, the study selects the cash flow model method to divide the enterprise life cycle into three stages: the growing, mature, and declining stages [14]. A total of 194 samples and 877 observations are finally obtained for enterprises in the growing stage, 176 samples and 543 observations for enterprises in the mature stage, and 123 samples and 261 observations for enterprises in the declining stage.

4.2. Measures

4.2.1. Dependent Variables. The number of patents is one of the most direct measures of enterprise technological innovation. The study adds 1 to the number of patents granted variable and then takes a natural logarithm to measure enterprise technological innovation (ETI) [8, 23]. In addition, in the robustness test section, the study adds 1 to the number of invention patents granted variable and then takes a natural logarithm to remeasure the enterprise technological innovation.

4.2.2. Independent Variables. In order to eliminate the effect of price, based on the algorithm of Mudambi and Swift [7] and Patel et al. [24], the actual innovation investment is used to measure the variable of innovation investment volatility (IIV), as shown in Table 1. The actual innovation investment is equal to the nominal research and development expenditure divided by the enterprise research and development expenditure price index (with 2010 as the base period). Among them, the enterprise research and development expenditure price index is obtained by the weighted summation of the consumer price index and fixed asset investment price index of the base period in 2010 [25].

4.2.3. Moderating Variables. Learning from the research of Chen et al. [26], the method of text analysis is used to search for the keywords of the innovation subsidy details. This is coded as 1 if the enterprise was supported by the innovation subsidy policy in the current year and 0 otherwise (IS). In addition, the number of the innovation subsidy plus 1 in the natural logarithm scale is used to measure the robustness test section.

4.2.4. Control Variables. Enlightened by the extant researches, the study also takes these variables as crucial control variables: enterprise growth, enterprise age, enterprise innovation effort, enterprise profitability level (pro), debt assets ratio, enterprise size, and enterprise human capital. The definitions of all the control variables are shown in Table 1.

5. Results

5.1. Main Results. Table 2 presents the means, standard deviations, minimum and maximum values, and correlations for the variables of the full sample and each life cycles samples. As can be seen from the results, the observations in the growing and mature stages account for 84.5% of the total sample, indicating that the vast majority of listed enterprises in Chinese strategic emerging industries are in the growing or mature stages. There is a large difference between the maximum and minimum values of the number of patent grants and innovation investment volatility, which indicates that the degree of innovation investment volatility and innovation capability of each enterprise differs greatly. From the perspective of different life cycle stages, the average value of the number of patents granted is the largest in the mature stage of the enterprise, followed by the growing stage, and the least in the declining stage. In addition, the size of the enterprise will gradually decrease with the evolution of the life cycle. From the results of the correlation coefficient test between variables, there is a correlation between the number of patent grants and the volatility of innovation investment in different life cycle stages. In addition, the variance inflation factor (VIF) is used to test multicollinearity. VIF values are all less than 1.5, indicating that there is no serious multicollinearity problem among the variables.

After using the Hausman test, the two-way random-effects model was finally chosen in this study. The estimation results are shown in Table 3.

Model 1 shows that the coefficient of IIV is significantly positive with ETI in Chinese strategic emerging industries because innovation investment volatility can alleviate the internal and external financing constraints of strategic emerging industry enterprises through time division and signal transmission and then promote their technological innovation. In model 2, the study included the moderator variables finding that IS has a significant negative moderating effect on the relationship between IIV and ETI (see Figure 2). Because the innovation resources are supplemented, the pressure for enterprises to take advantage of innovation investment volatility is reduced. Innovation subsidy intervenes in the allocation of internal resources, which is not conducive to promoting the level of technological innovation.

Models 3, 5, and 7, respectively, examine the impact of innovation investment volatility on the technological innovation of enterprises in different life cycles. In model 3, the regression results show that the coefficient of IIV is significantly positive with ETI. In the growing stage, the innovation investment volatility of enterprises is caused by proactive innovation management. That is conducive to

Table 1: Variable description and definition.

Dependent variables	Definition
ETI	The number of patents granted plus 1 in the natural logarithm scale
Independent variables	
IIV	Based on the regression of time trends in innovation investment, innovation investment volatility is equal to the standard residual term of the time trend regression divided by the mean value of innovation investment of the enterprise
Moderating variables	
IS	This is coded as 1 if the enterprise was supported by the innovation subsidy policy in the current year and 0 otherwise
Control variables	
Grow	(Operating income of the current year - operating income of the previous year)/Operating income of the previous year
Age	Total number of years between business registration year and research year
Effort	Natural logarithm of innovation expenditure costs
Pro	Earnings per share
Size	Natural logarithm of total corporate assets
Debt	Total liabilities/total assets
Human	Natural logarithm of the number of employees in the enterprise

Table 2: Sample distribution and statistics.

	Variables	Mean	SD	Min	Max	1	2	3	4	5
Full sample ($N = 1681$)	1.ETI	0.800	1.347	0	6.466	1				
	2. IIV	−0.445	0.992	−14.076	0.195	0.163***	1			
	3. grow	0.241	1.459	−0.790	55.759	−0.031	0.011	1		
	4. size	22.545	1.317	18.793	27.468	0.285***	0.180***	0.029	1	
	5.effort	−3.256	1.174	−14.539	6.783	0.046*	0.221***	−0.062**	−0.224***	1
The growing stage ($N = 877$)	1.ETI	0.796	1.393	0	6.466	1				
	2. IIV	−0.446	1.179	−14.076	0.146	0.145***	1			
	3. grow	0.321	1.992	−0.680	55.759	−0.037	0.014	1		
	4. size	22.664	1.236	19.270	26.651	0.294***	0.098***	0.041	1	
	5.effort	−3.323	1.263	−14.539	6.783	0.046	0.261***	−0.063*	−0.181***	1
The mature stage ($N = 543$)	1.ETI	0.863	1.359	0	6.120	1				
	2. IIV	−0.412	0.714	−6.00	0.195	0.212***	1			
	3. grow	0.154	0.292	−0.489	2.894	−0.030	0.054	1		
	4. size	22.429	1.420	18.893	27.468	0.306***	0.300***	−0.033	1	
	5.effort	−3.194	1.021	−12.303	0.063	0.013	0.163***	−0.058	−0.260***	1
The declining stage ($N = 261$)	1.ETI	0.678	1.150	0	5.209	1				
	2. IIV	−0.511	0.779	−5.368	0.172	0.181***	1			
	3. grow	0.154	0.402	−0.790	3.596	−0.064	−0.104*	1		
	4. size	22.388	1.327	18.793	27.386	0.215***	0.396***	−0.044	1	
	5.effort	−3.171	1.161	−11.848	−0.847	0.122**	0.122**	−0.161***	−0.285***	1

*, **, and ***represent 10%, 5%, and 1% significance levels, respectively.

promoting the level of technological innovation because it can alleviate the internal and external financing constraints of enterprises through time separation and signal transmission. Therefore, innovation investment volatility is conducive to promoting the level of technological innovation. Model 5 shows that the coefficient of IIV is positive but insignificant. The result suggests that the incentive effect of innovation investment volatility on technological innovation of enterprises in the mature stage is insignificant. A tentative explanation for this finding is that the innovation investment volatility of enterprises in the mature stage is caused by internal financing. In this stage, innovation investment volatility is an adjustment behavior affected by the change of internal financing, rather than an innovation decision made according to the change of market environment. This may affect the normal innovation process of enterprises in the mature stage. Thus, innovation investment volatility is not conducive to improving their technological innovation level. Model 7 indicates that the coefficient of IIV is positive but insignificant. The result suggests that the innovation investment volatility has no significant incentive effect on enterprise technological innovation in the declining stage because the innovation investment volatility of enterprises in the declining stage caused by innovation manipulation has not actually invested innovation funds in innovation activities. Therefore, their technological innovation level has not been substantially improved. In conclusion, H1 is supported.

Table 3: Regression results.

	Full sample		The growing stage		The mature stage		The declining stage	
	(1)	(2)	(3)	(4)	(5)	(6)	(7)	(8)
IIV	0.094** (0.045)	0.159*** (0.058)	0.108** (0.052)	0.187*** (0.069)	0.071 (0.091)	0.229** (0.116)	0.132 (0.090)	0.041 (0.112)
IIV × IS		−0.068** (0.030)		−0.078** (0.035)		−0.026* (0.143)		0.122 (0.100)
IS	−0.048 (0.059)	−0.085 (0.068)	−0.082 (0.084)	−0.132 (0.097)	−0.126 (0.101)	−0.217* (0.122)	0.117 (0.116)	0.189 (0.140)
Human	0.107* (0.058)	0.104* (0.058)	0.107 (0.071)	0.101 (0.071)	0.180* (0.097)	0.176* (0.096)	0.016 (0.070)	0.020 (0.070)
Grow	−0.013** (0.005)	−0.013** (0.005)	−0.018*** (0.006)	−0.017*** (0.006)	−0.053 (0.221)	−0.064 (0.224)	−0.017 (0.112)	−0.019 (0.070)
Age	−0.007 (0.017)	−0.007 (0.017)	−0.005 (0.018)	−0.005 (0.018)	−0.017 (0.019)	−0.016 (0.019)	−0.015 (0.018)	−0.019 (0.111)
Effort	0.034 (0.025)	0.030 (0.025)	0.017 (0.029)	0.009 (0.030)	0.058 (0.044)	0.059 (0.044)	0.120** (0.048)	0.124*** (0.047)
Pro	0.024 (0.055)	0.022 (0.055)	0.057 (0.071)	0.055 (0.071)	−0.008 (0.116)	−0.005 (0.117)	0.021 (0.068)	0.021 (0.068)
Debt	0.038 (0.038)	0.035 (0.037)	0.039 (0.200)	0.020 (0.202)	0.002 (0.033)	0.006 (0.033)	0.127* (0.075)	0.130* (0.075)
Size	0.104* (0.057)	0.103* (0.057)	0.155* (0.079)	0.154* (0.079)	0.118* (0.066)	0.132** (0.066)	0.234** (0.115)	0.237** (0.116)
Constant	−2.352** (1.119)	−2.290** (1.113)	−3.587** (1.497)	−3.499** (1.493)	−2.736** (1.287)	−2.948** (1.293)	−4.241** (2.108)	−4.397** (2.118)
Enterprise	Yes	Yes	Yes	Yes	Yes	Yes	Yes	Yes
Year	Yes	Yes	Yes	Yes	Yes	Yes	Yes	Yes
N	1681	1681	877	877	543	543	261	261
R^2	0.113	0.115	0.123	0.124	0.136	0.142	0.098	0.100

Note that standard errors are in parentheses. *, **, and ***represent 10%, 5%, and 1% significance levels, respectively.

Subsequently, this study adds the interaction of the innovation investment volatility with innovation subsidy to test the regulatory effect of innovation subsidy in different life cycles. As shown in model 4, the coefficient of IIV×IS is negative and significant, indicating that innovation subsidy has a significant negative effect on the relationship between innovation investment volatility and technological innovation of enterprises in the growing stage (see Figure 3). Perhaps, it can be explained that innovation subsidy transmits to external investors that enterprises in the growing stage rely too much on the government [24], which will hinder external financing channels and is not conducive to their technological innovation. In model 6, the coefficient of innovation IIV × IS is negative and significant, which means that innovation subsidy has a significantly weak negative regulatory effect on the relationship between innovation investment volatility and technological innovation of enterprises in the mature stage (see Figure 4). Because innovation subsidy may interfere with managers' judgment on the innovation stage, managers are more confident to use a large number of resources for exploratory innovation activities. Exploratory activities are innovative and high risk, which will consume a lot of resources of the enterprise. The development of other innovation projects may be affected [21]. In model 8, the coefficient of IIV×IS is positive but insignificant, which means that innovation subsidy has an insignificant effect on the relationship between innovation investment volatility and enterprise technological innovation in the declining stage because enterprises in the declining stage often use innovation subsidies to recover losses or prevent the decline of stock prices instead of actually using them in innovation activities. In conclusion, H2 is supported.

5.2. Robustness Checks

5.2.1. Substitution of Dependent Variables. To verify whether the model constructed is influenced by the choice of variables, the study adds 1 to the number of invention patents granted and then takes a natural logarithm as the substitute variable for the number of granted patents [23]. Table 4 shows that the results have not changed greatly.

5.2.2. Substitution of Moderating Variables. The number of the innovation subsidy plus 1 in the natural logarithm scale is used as the substitute variable [26]. Table 5 shows that the results are consistent with the findings of the above study.

5.2.3. Delete Sensitive Years. Considering the impact of the 2012 National Strategic Emerging Industry Development Plan on innovation investment volatility of the sample enterprises, the 2012 sample is removed and reregressed [27]. Table 6 shows that the results are consistent with the findings of the above study.

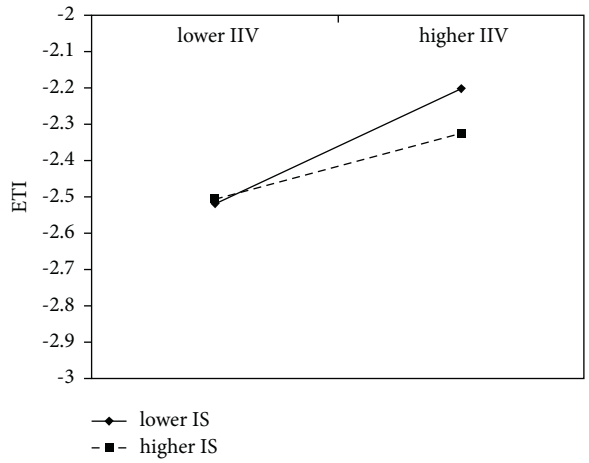

Figure 2: The relationship between IIV and ETI—moderated by IS.

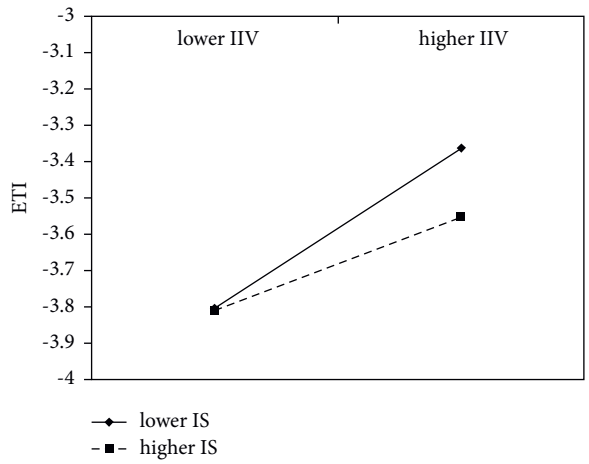

Figure 3: The relationship between IIV and ETI in the growing stage—moderated by IS.

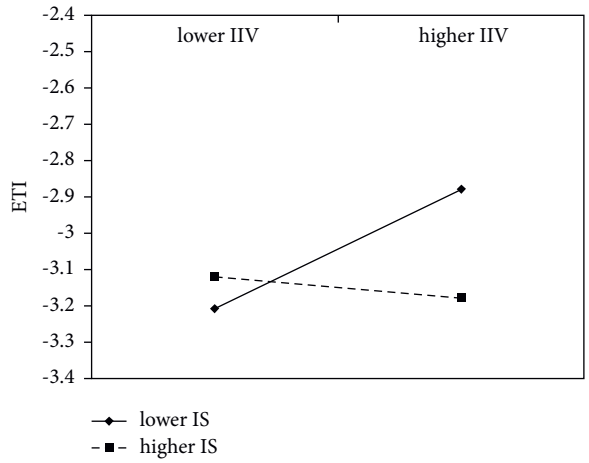

Figure 4: The relationship between IIV and ETI in the mature stage—moderated by IS.

Table 4: Substitution of dependent variables.

	Full sample		The growing stage		The mature stage		The declining stage	
	(9)	(10)	(11)	(12)	(13)	(14)	(15)	(16)
IIV	0.099** (0.040)	0.155*** (0.05)	0.099** (0.043)	0.167*** (0.057)	0.097 (0.069)	0.230** (0.104)	0.110 (0.067)	0.029 (0.097)
IIV × IS		−0.059** (0.026)		−0.069** (0.030)		−0.230* (0.121)		0.109 (0.110)
IS	−0.044 (0.052)	−0.075 (0.061)	−0.082 (0.077)	−0.125 (0.090)	−0.080 (0.089)	−0.159 (0.108)	0.034 (0.095)	0.099 (0.106)
Human	0.076 (0.049)	0.073 (0.049)	0.075 (0.063)	0.070 (0.063)	0.123 (0.075)	0.119 (0.074)	−0.007 (0.049)	−0.003 (0.050)
Grow	−0.012** (0.005)	−0.012** (0.005)	−0.017*** (0.006)	−0.016*** (0.006)	−0.026 (0.205)	−0.035 (0.208)	−0.033 (0.111)	−0.035 (0.111)
Age	−0.002 (0.012)	−0.0015 (0.012)	0.001 (0.013)	0.001 (0.013)	−0.005 (0.014)	−0.0037 (0.014)	−0.0165 (0.014)	−0.016 (0.014)
Effort	0.023 (0.022)	0.019 (0.022)	0.010 (0.026)	0.003 (0.027)	0.046 (0.035)	0.0469 (0.036)	0.082** (0.040)	0.086** (0.040)
Pro	0.022 (0.049)	0.020 (0.049)	0.051 (0.061)	0.049 (0.061)	−0.003 (0.088)	−0.002 (0.089)	0.046 (0.062)	0.046 (0.062)
Debt	0.041 (0.033)	0.038 (0.032)	−0.015 (0.178)	−0.032 (0.180)	0.0084 (0.026)	0.012 (0.026)	0.091 (0.067)	0.094 (0.067)
Size	0.105** (0.050)	0.105** (0.050)	0.145** (0.070)	0.144** (0.070)	0.109** (0.056)	0.121** (0.056)	0.201** (0.086)	0.204** (0.087)
Constant	−2.403** (0.955)	−2.352** (0.948)	−3.326*** (1.291)	−3.253** (1.288)	−2.476** (1.058)	−2.671** (1.072)	−3.556** (1.599)	−3.695** (1.599)
Enterprise	Yes	Yes	Yes	Yes	Yes	Yes	Yes	Yes
Year	Yes	Yes	Yes	Yes	Yes	Yes	Yes	Yes
N	1681	1681	877	877	543	543	261	261
R^2	0.118	0.120	0.129	0.130	0.135	0.139	0.112	0.114

Note that standard errors are in parentheses. *, **, and ***represent 10%, 5%, and 1% significance levels, respectively.

Table 5: Substitution of moderating variables.

	Full sample		The growing stage		The mature stage		The declining stage	
	(17)	(18)	(19)	(20)	(21)	(22)	(23)	(24)
IIV	0.094** (0.045)	0.148*** (0.057)	0.109** (0.052)	0.168** (0.068)	0.071 (0.091)	0.218* (0.113)	0.132 (0.090)	0.059 (0.113)
IIV × IS		−0.005* (0.003)		−0.005* (0.003)		−0.019* (0.011)		0.0068 (0.007)
IS	−0.004 (0.004)	−0.007 (0.005)	−0.009 (0.006)	−0.012* (0.007)	−0.008 (0.007)	−0.014 (0.009)	0.034 (0.095)	0.012 (0.010)
Human	0.107* (0.058)	0.105* (0.058)	0.075 (0.063)	0.105 (0.071)	0.182* (0.096)	0.182* (0.095)	0.014 (0.069)	0.017 (0.070)
Grow	−0.013** (0.005)	−0.013** (0.005)	0.107 (0.071)	−0.017*** (0.006)	−0.055 (0.221)	−0.064 (0.224)	−0.016 (0.112)	−0.018 (0.111)
Age	−0.007 (0.017)	−0.007 (0.017)	−0.018*** (0.006)	−0.005 (0.018)	−0.017 (0.019)	−0.016 (0.019)	−0.015 (0.018)	−0.014 (0.018)
Effort	0.034 (0.025)	0.031 (0.025)	−0.005 (0.018)	0.011 (0.030)	0.059 (0.044)	0.061 (0.044)	0.120** (0.048)	0.123*** (0.047)
Pro	0.024 (0.055)	0.022 (0.055)	0.015 (0.030)	0.058 (0.070)	−0.006 (0.116)	−0.006 (0.117)	0.020 (0.070)	0.020 (0.070)
Debt	0.038 (0.038)	0.037 (0.037)	0.058 (0.070)	0.026 (0.201)	0.002 (0.033)	0.007 (0.033)	0.127* (0.075)	0.126* (0.076)
Size	0.105* (0.057)	0.105* (0.057)	0.041 (0.200)	0.156** (0.079)	0.121* (0.066)	0.135** (0.066)	0.232** (0.115)	0.235** (0.116)
Constant	−2.368** (1.116)	−2.354** (1.113)	−3.582** (1.487)	−3.557** (1.487)	−2.806** (1.288)	−3.083** (1.304)	−4.194** (2.098)	−4.314** (2.106)
Enterprise	Yes	Yes	Yes	Yes	Yes	Yes	Yes	Yes
Year	Yes	Yes	Yes	Yes	Yes	Yes	Yes	Yes
N	1681	1681	877	877	543	543	261	261
R^2	0.114	0.115	0.125	0.126	0.137	0.143	0.099	0.102

Note that standard errors are in parentheses. *, **, and ***represent 10%, 5%, and 1% significance levels, respectively.

Table 6: Delete the 2012 sample.

	Full sample		The growing stage		The mature stage		The declining stage	
	(25)	(26)	(27)	(28)	(29)	(30)	(31)	(32)
IIV	0.098** (0.045)	0.174*** (0.057)	0.107** (0.051)	0.202*** (0.068)	0.113 (0.088)	0.257** (0.126)	0.115 (0.097)	0.007 (0.135)
IIV × IS		−0.075** (0.0293)		−0.089*** (0.034)		−0.246 (0.150)		0.137 (0.114)
IS	−0.070 (0.060)	−0.112 (0.070)	−0.110 (0.082)	−0.168* (0.095)	−0.155 (0.109)	−0.240* (0.134)	0.133 (0.127)	0.217 (0.159)
Human	0.106* (0.058)	0.101* (0.058)	0.093 (0.074)	0.086 (0.074)	0.168* (0.097)	0.165* (0.096)	0.028 (0.072)	0.030 (0.073)
Grow	−0.013** (0.005)	−0.012** (0.005)	−0.018*** (0.006)	−0.017*** (0.006)	−0.065 (0.238)	−0.071 (0.240)	−0.010 (0.117)	−0.011 (0.116)
Age	−0.007 (0.017)	−0.007 (0.017)	−0.001 (0.018)	−0.001 (0.018)	−0.021 (0.019)	−0.020 (0.020)	−0.014 (0.019)	−0.012 (0.019)
Effort	0.029 (0.025)	0.024 (0.025)	0.017 (0.029)	0.006 (0.030)	0.051 (0.040)	0.052 (0.041)	0.130** (0.053)	0.136*** (0.052)
Pro	0.019 (0.058)	0.017 (0.058)	0.071 (0.075)	0.071 (0.075)	0.027 (0.119)	0.028 (0.120)	0.019 (0.070)	0.018 (0.069)
Debt	0.047 (0.035)	0.044 (0.034)	0.038 (0.190)	0.018 (0.192)	−0.001 (0.033)	0.004 (0.033)	0.129* (0.078)	0.135* (0.078)
Size	0.102* (0.057)	0.101* (0.057)	0.166** (0.081)	0.164** (0.081)	0.105 (0.066)	0.118* (0.066)	0.241** (0.122)	0.251** (0.123)
Constant	−2.313** (1.119)	−2.231** (1.111)	−3.729** (1.509)	−3.613** (1.503)	−2.327* (1.254)	−2.541** (1.264)	−4.449** (2.265)	−4.740** (2.295)
Enterprise	Yes	Yes	Yes	Yes	Yes	Yes	Yes	Yes
Year	Yes	Yes	Yes	Yes	Yes	Yes	Yes	Yes
N	1503	1503	794	794	471	471	238	238
R^2	0.111	0.112	0.124	0.125	0.136	0.137	0.100	0.101

Note that standard errors are in parentheses. *, **, and ***represent 10%, 5%, and 1% significance levels, respectively.

6. Discussion and Conclusion

6.1. Theoretical Contributions. This study provides several theoretical contributions to the research of firm innovation investment. First, the study proposes that the reasons for enterprises' innovation investment volatility in different life cycle stages are different and their impact on technological innovation is also different. Most prior studies have discussed the effect of innovation investment volatility in a homogeneous sample of enterprises. The differences in the effect of innovation investment volatility for enterprises in different life cycle stages may be ignored. The study finds that the innovation investment volatility of enterprises in the growing stage is caused by proactive innovation management and it has a positive impact on technological innovation. In contrast, innovation investment volatility of enterprises in the mature and declining stages, respectively, is caused by internal financing and innovation manipulation, which has no significant effect on technological innovation.

Second, our framework provides a heterogeneous perspective extending the research related to the volatility of innovation investment by treating innovation subsidy as a shock to the enterprise's external environment. Most existing studies emphasized the impact of internal enterprise factors such as resource redundancy and technological capability on the volatility of innovation investment [9, 28]. Few studies have considered the impact of the enterprise's external environment. This study finds that innovation subsidy does not have the desired effect, which is consistent with the research of Zhou et al. [23]. They found that, with the development of market mechanisms, the government's role in promoting enterprise technological innovation will decline.

Finally, this study adopts the data of Chinese strategic emerging industry enterprises as a sample to further explore, enriching the relevant research on the innovation investment volatility. Most previous studies focusing on the volatility of innovation investment mostly used samples from enterprises in developed countries such as the United States and South Korea [9, 28]. However, the technology path constraint and the nonsustainability of innovation investment fees are more prominent in developing countries. Meanwhile, most innovation investment in developed countries exhibits countercyclical characteristics, while innovation investment in developing countries tends to show procyclical characteristics [29]. Therefore, it remains to be tested whether the relevant studies on the volatility of innovation investment in developed countries are applicable to China, an emerging economy.

6.2. Implications for Managers and Policy Makers. Based on the perspective of punctuated equilibrium and life cycle theory, we examine the impact of innovation investment volatility on enterprise technological innovation and the moderating role of innovation subsidy in a sample of listed enterprises in China's strategic emerging industries from 2010 to 2019. The study finds that the volatility of innovation investment eases the financing constraints of enterprises,

which is conducive to improving the level of technological innovation of enterprises in the growing stage. However, the innovation investment volatility of enterprises in the mature stage is caused by internal financing, which may affect the normal process of innovation activities. It is difficult to improve the level of enterprise technological innovation. The innovation investment of enterprises in the declining stage is caused by using innovation manipulation to obtain government subsidies, and it is also difficult to improve the level of enterprise technological innovation. This study further finds that innovation subsidy cannot interfere with the relationship between the volatility of innovation investment and the technological innovation of enterprises in the declining stage. The innovation subsidy policy has counterproductive effects on the volatility of innovation investment and technological innovation in the growing and mature stage. For enterprises in the growing stage, innovation subsidy not only reduces the pressure on innovation investment but also weakens the enterprises' signal of reinnovation, which is not conducive to improving the level of technological innovation. For enterprises in the mature stage, the acquisition of innovation subsidy makes the managers more confident to use their main resources for exploratory innovation activities, which consumes a lot of resources and affects the development of other innovative projects.

The research conclusions provide several practical insights for business managers and the government. First, enterprise technological innovation is affected not only by the absolute amount of innovation investment but also by the volatility of innovation investment. However, not all types of innovation investment volatility can promote enterprise technological innovation level. The study finds that the innovation investment volatility caused by proactive management is conducive to improving the level of enterprise technological innovation. Therefore, managers should implement proactive management of innovation projects. When new opportunities appear in the external environment, managers should increase innovation investment in time. They should also promptly terminate investment in projects that do not have prospects rather than increase or decrease investment in the process of innovation.

Second, the life cycle stage of enterprises should be fully taken into consideration when the manager formulates the innovation strategy. For enterprises in the growing stage, the innovation investment volatility is conducive to improving the level of enterprises' technology innovation. However, for enterprises in the mature or declining stage, innovation investment volatility is not conducive to promoting technological innovation levels. Therefore, managers of enterprises in the growing stage should take advantage of organizational flexibility to adjust the focus and direction of innovation projects in a timely manner. Managers of enterprises in the mature stage should ensure adequate internal financing and avoid innovation investment volatility. For enterprises in the declining stage, managers should devote resources to imitative innovation activities and avoid the waste of limited resources caused by strategic innovation.

Finally, although the Chinese government has been committed to helping enterprises promote their technological innovation, with the development of market mechanisms, the role of innovation subsidy in promoting technological innovation of enterprises is declining. In some cases, innovation subsidies can even have counterproductive effects. For example, enterprises in the growing stage that receive innovation subsidies may weaken their pressure to proactively manage innovation resources and reduce the effect of innovation investment volatility. The acquisition of innovation subsidy by enterprises in the mature stage may increase the confidence of managers in exploratory innovation activities, which makes the enterprise at a high level of risk in the long term. Therefore, the life cycle stage of the enterprise should be considered when the government formulates an innovation subsidy policy.

6.3. Limitations and Future Research. First, the study only involves a specific industry (strategic emerging industry) in a specific emerging economy (China). Although China is the largest emerging economy, it may be different from other economies in terms of institutions, culture, etc. Compared with other industries, innovation investment in strategic emerging industries is more active in China. Therefore, the choice of other economies or industries may affect the results of the research. The research objects can be reselected for testing in future studies. Second, the study only considers the effects of different life cycle stage characteristics of enterprises. In future research, we can further examine the influence of other internal factors of the enterprise, such as the nature of enterprise ownership and the degree of enterprise financialization to supplement related research. Finally, regarding the impact of the external environment of the enterprise, our analysis only considers the institutional environment of innovation subsidy. Further research is needed to examine the impact of other policies (such as talent subsidy, high-tech enterprise qualification recognition, etc.) or other external environments (such as the market environment).

Data Availability

The data used to support the findings of this study are available from the corresponding author upon request.

Conflicts of Interest

The authors declare that there are no conflicts of interest regarding the publication of this study.

Authors' Contributions

Miaomiao Li and Zhaoxing Hao explored the whole research ideas and wrote the paper. Zhaoxing Hao and Meng Luan carried out the empirical analysis. Miaomiao Li and Haibo Li provided guidance for the research process and supervised the entire project. Meng Luan and Guikun Cao revised the manuscript. All the authors participated in this research project.

Acknowledgments

This work was supported by the Shandong Social Science Planning Project named Research on the Dynamic Mechanism of the Triple Helix of Regional Innovation (No. 18CQXJ01).

References

[1] F. Xiao, Q. Li, and K. Wang, "Waste plastic triboelectric nanogenerators using recycled plastic bags for power generation," *ACS Applied Materials & Interfaces*, vol. 13, no. 1, pp. 400–410, 2020.

[2] C. L. Liu, Q. Li, and K. Wang, "State-of-charge estimation and remaining useful life prediction of supercapacitors," *Renewable and Sustainable Energy Reviews*, vol. 150, no. 2, Article ID 111408, 2021.

[3] A. K. Gupta, K. G. Smith, and C. E. Shalley, "The interplay between exploration and exploitation," *Academy of Management Journal*, vol. 49, no. 4, pp. 693–706, 2006.

[4] J. C. Zhao, F. Li, Z. Wang, and P. Dong, "Flexible PVDF nanogenerator-driven motion sensors for human body motion energy tracking and monitoring," *Journal of Materials Science: Materials in Electronics*, vol. 32, no. 11, pp. 14715–14727, 2021.

[5] H. Yu, N. Wang, and K. Y. Zhao, "Simultaneous unknown input and state estimation for the linear system with a rank-deficient distribution matrix," *Mathematical Problems in Engineering*, vol. 2021, no. 12, 11 pages, Article ID 6693690, 2021.

[6] M. J. Benner and M. L. Tushman, "Exploitation, exploration, and process management: the productivity dilemma revisited," *Academy of Management Review*, vol. 28, no. 2, pp. 238–256, 2003.

[7] R. Mudambi and T. Swift, "Proactive R&D management and firm growth: a punctuated equilibrium model," *Research Policy*, vol. 40, no. 3, pp. 429–440, 2011.

[8] M. Meuleman and W. D. Maeseneire, "Do R&D subsidies affect SMEs' access to external financing?" *Research Policy*, vol. 41, no. 3, pp. 580–591, 2012.

[9] T. Kang, B. Chulwoo, and J. D. Lee, "The persistency and volatility of the firm R&D investment: revisited from the perspective of technological capability," *Research Policy*, vol. 46, no. 9, pp. 1570–1579, 2017.

[10] B. J. Bushee, "The influence of institutional investors on myopic R&D investment behavior," *The Accounting Review*, vol. 73, no. 3, pp. 305–333, 1998.

[11] G. Dosi, L. Marengo, and C. Pasquali, "How much should society fuel the greed of innovators?: on the relations between appropriability, opportunities and rates of innovation," *Research Policy*, vol. 35, no. 8, pp. 1110–1121, 2006.

[12] I. M. Jawahar and G. L. McLaughlin, "Toward a descriptive stakeholder theory: an organizational life cycle approach," *Academy of Management Review*, vol. 26, no. 3, pp. 397–414, 2001.

[13] X. C. Zhou and C. Chen, "Investigate relationships between accrual earnings management and real earnings management from the perspective of corporate life cycle," *Journal of Management Science*, vol. 29, no. 1, pp. 108–122, 2016.

[14] S. Y. Liu, Z. F. Lin, and Z. P. Leng, "Whether tax incentives stimulate corporate innovation: empirical evidence based on corporate life cycle theory," *Economic Research Journal*, vol. 55, no. 6, pp. 105–121, 2020.

[15] R. E. Hoskisson, M. A. Hitt, and C. W. Hill, "Managerial incentives and investment in R&D in large multiproduct firms," *Organization Science*, vol. 4, no. 2, pp. 325–341, 1993.

[16] S. Lach, "Do R&D subsidies stimulate or displace private R&D? Evidence from Israel," *The Journal of Industrial Economics*, vol. 50, no. 4, pp. 369–390, 2002.

[17] M. Bertrand and S. Mullainathan, "Enjoying the quiet life? Corporate governance and managerial preferences," *Journal of Political Economy*, vol. 111, no. 5, pp. 1043–1075, 2003.

[18] M. P. Feldman and M. R. Kelley, "The ex-ante assessment of knowledge spillovers: government R&D policy, economic incentives and private firm behavior," *Research Policy*, vol. 35, no. 10, pp. 1509–1521, 2006.

[19] Z.-J. Zhou, P.-Y. Zhang, M.-M. Lu, and Z. Gao, "The influence of government intervention on the performance of independent innovation under financial support based on data of listed companies in strategic emerging industries," *Mathematical Problems in Engineering*, vol. 2020, Article ID 5063986, 9 pages, 2020.

[20] C. Wang, Y. Hu, J. Zhang, and C. Miao, "CEO media exposure and green technological innovation decision: evidence from Chinese polluting firms," *Mathematical Problems in Engineering*, vol. 2020, Article ID 8271621, 14 pages, 2020.

[21] A. K. Gupta and V. Govindarajan, "Resource sharing among SBUs: strategic antecedents and administrative implications," *Academy of Management Journal*, vol. 29, no. 4, pp. 695–714, 1986.

[22] E. Romanelli and M. L. Tushman, "Organizational transformation as punctuated equilibrium: an empirical test," *Academy of Management Journal*, vol. 37, no. 5, pp. 1141–1166, 1994.

[23] K. Z. Zhou, G. Y. Gao, and H. Zhao, "State ownership and firm innovation in China: an integrated view of institutional and efficiency logics," *Administrative Science Quarterly*, vol. 62, no. 2, pp. 375–404, 2017.

[24] P. C. Patel, M. J. Guedes, N. Soares, and V. da Conceição Gonçalves, "Strength of the association between R&D volatility and firm growth: the roles of corporate governance and tangible asset volatility," *Journal of Business Research*, vol. 88, pp. 282–288, 2018.

[25] P. F. Zhu and W. M. Xu, "On the impact of government' s S&T incentive policy on the R&D input and its patent output of large and medium -sized industrial enterprises in Shanghai," *Economic Research Journal*, vol. 26, pp. 45–53, 2003.

[26] J. Chen, C. S. Heng, B. C. Y. Tan, and Z. Lin, "The distinct signaling effects of R&D subsidy and non-R&D subsidy on IPO performance of IT entrepreneurial firms in China," *Research Policy*, vol. 47, no. 1, pp. 108–120, 2018.

[27] J. Cen, Y. Yang, C. Y. Zhang, and L. L. Zhou, "Technological knowledge system and innovation leap: the ambidextrous transition perspective," *Studies in Science of Science*, vol. 37, no. 11, pp. 2073–2081, 2019.

[28] R. Mudambi and T. Swift, "Knowing when to leap: transitioning between exploitative and explorative R&D," *Strategic Management Journal*, vol. 35, no. 1, pp. 126–145, 2014.

[29] P. Aghion, G.-M. Angeletos, A. Banerjee, and K. Manova, "Volatility and growth: credit constraints and the composition of investment," *Journal of Monetary Economics*, vol. 57, no. 3, pp. 246–265, 2010.

Hindawi
Mathematical Problems in Engineering
Volume 2021, Article ID 9590969, 10 pages
https://doi.org/10.1155/2021/9590969

Research Article

High-Temperature Superconducting Cable Fault Location Method Based on Improved Time-Frequency Domain Reflection Method and EEMD Noise Reduction

Bo Yang,[1] Jun Tang,[1] Chen Yang,[1] Xiaofeng Dong,[1] Kun Huang,[2,3] and Changsen Feng[4]

[1]*State Grid Suzhou Power Supply Company, Suzhou 215004, China*
[2]*Nari Technology Co., Ltd., Nanjing 211100, China*
[3]*Nanjing University of Posts and Telecommunications, Nanjing 210023, China*
[4]*College of Information Engineering, Zhejiang University of Technology, Hangzhou, 310023, China*

Correspondence should be addressed to Changsen Feng; fcs@zjut.edu.cn

Received 20 October 2021; Accepted 7 November 2021; Published 2 December 2021

Academic Editor: Jinyan Song

Aiming at the operation and maintenance requirements of the fault location of high-temperature superconducting cables, a fault location method of high-temperature superconducting cables based on the improved time-frequency domain reflection method and EEMD noise reduction is proposed. Considering the cross-term interference problem in the traditional time-frequency domain reflection method, this paper introduces the affine transformation to project the time-frequency distribution of the self-term and the cross term and further highlights the characteristic differences between the two through coordinate transformation, and the particle swarm algorithm is employed to solve the optimal stagger angle of the affine transformation. The unscented particle filter is adopted to separate the cross term, and EEMD noise reduction is introduced to solve the signal noise problem. Finally, two software programs, PSCAD and MATLAB, are employed for joint simulation to build a model of high-temperature superconducting cable. The simulation example shows that the proposed method in this paper can eliminate the cross-term interference of the traditional time-frequency domain reflection method, effectively locate the fault of the high-temperature superconducting cable, and improve the positioning accuracy.

1. Introduction

In recent years, with the continuous development of social economy, conventional urban cable transmission capacity is small, covers a large area, and has high line loss, so the shortcomings such as the difficulty of grid expansion are increasingly prominent, which restricts the development of smart grid [1–3]. Compared with conventional cables, high-temperature superconducting cables take advantage of the non-resistance and high current density properties of superconducting materials in the superconducting state and have significant advantages such as high capacity, low line loss, light weight, and environmental friendliness, providing an efficient and environmentally friendly way to transmit over long distances for smart grids [4–7]. Currently, several countries around the world are planning to advance the large-scale commercial application of high-temperature superconducting cables in an orderly manner [8, 9]. Accurately locating high-temperature superconducting cable faults and exploring practical, effective, and convenient fault detection methods can help to quickly remove faults and repair them to ensure the safe and stable operation of the power systems.

At present, there have been many studies on cable fault location, mainly focusing on the low-voltage pulse reflection method based on traveling wave theory [10], pulse current method [11], pulse voltage method [12], wavelet analysis method [13], and so on, while there are very few results dedicated to the study of high-temperature superconducting cable fault location. Based on distributed optical fiber temperature measurement technology, Huang et al. [14] proposed a local loss of superconducting cable detection and

protection method, which can effectively respond to local loss of superfault, alarming, and tripping according to the size and temperature of the heat generating area. Wang et al. [15] conducted a high-temperature superconducting cable fault location study based on time-frequency domain reflectometry (TFDR) and introduced the pseudo-Wigner–Ville distribution (PWVD) to analyze the time-frequency of the signal. A real 35 kV high-temperature superconducting cable is analyzed for the variation pattern of waveforms at different temperatures, different fault types, and different signal parameters. Although the time-frequency domain analysis method is more advantageous than the single-domain analysis method when the reflected signal is weak and the signal attenuation is large, the introduction of the PWVD will generate cross-term interference when multiple signals are superimposed, which will seriously affect the analysis results. In [16–20], generalized regression neural network, heterogeneous cuckoo algorithm, analysis of the time domain energy of the reflected signal, analysis of the Euclidean distance and tangent distance of the incoming reflection time-frequency distribution, and affine transformation were proposed for this problem, which effectively improved the traditional time-frequency domain analysis method to some extent.

Signals are often noisy during transmission, and the accuracy of fault location can be improved by using suitable noise reduction methods. In literature [21], empirical mode decomposition (EMD) was used to reduce noise in the echo signal of full-waveform laser altimetry system for complex scenes with multiple height layers, and a good noise reduction effect was achieved. However, the EMD suffers from mode aliasing, which limits the noise reduction effect. To overcome this shortage, this paper introduces the ensemble empirical mode decomposition (EEMD) [22, 23] method, which introduces Gaussian white noise to maximize the retention of the real signal.

This paper proposes a fault location method for high-temperature superconducting cables based on the improved time-frequency domain reflection method and EEMD noise reduction. Firstly, the affine transformation is introduced to solve the cross-term interference problem of time-frequency domain reflection method, and the particle swarm algorithm is applied to solve the problem of optimal stagger angle accuracy, and the cross-term separation is achieved by the unscented particle filter algorithm. Secondly, the signal is denoised by EEMD to make the positioning results more accurate. Finally, the simulation environment is built to verify the validity and accuracy of the model in this paper.

2. Improved Time-Frequency Domain Reflection Method

2.1. Traditional TFDR. As a cable fault non-destructive detection method, TFDR sends an incident signal to the cable and uses a digital oscilloscope to pick up the folded reflection signal generated by the incident signal at the point of impedance discontinuity, so as to locate the high-temperature superconducting cable fault location, and the schematic diagram is described in Figure 1.

The incident signal is usually a linearly modulated signal with Gaussian envelope that provides localized information in the time and frequency domains, and its mathematical expression is

$$s(t) = \left(\frac{\alpha}{\pi}\right)^{1/4} e^{-\alpha\left(t-t_0\right)^2/2+\mu\beta\left(t-t_0\right)^2/2+\mu\omega_0\left(t-t_0\right)}, \tag{1}$$

where α is the duration of the signal, t_0 is the time center of the signal, μ is the bandwidth of the signal, and ω_0 is the center frequency of the signal. The signal pulse width becomes narrower when α increases, and the signal bandwidth becomes wider when β increases.

The incident signal produces folded reflection at the point of impedance discontinuity, and the reflected signal is correlated with the incident signal in the time-frequency domain. TFDR uses the Wigner–Ville distribution (WVD) to analyze the signal in the time-frequency domain, that is,

$$W(t,\omega) = \int_{-\infty}^{+\infty} s\left(t+\frac{\tau}{2}\right)s^*\left(t-\frac{\tau}{2}\right)e^{-b\omega\tau}\mathrm{d}\tau, \tag{2}$$

where $s(t)$ is the incident signal, ω denotes the frequency, and τ and b are the signal parameters.

TFDR calculates the time-frequency correlation function of the incident and reflected signals.

$$C_{sr}(t) = \frac{2\pi}{E_s E_r(t)} \int_{t'=t-T_s}^{t'=t+T_s} \int W_r(t',\omega) W_s(t'-t,\omega)\mathrm{d}\omega\mathrm{d}t, \tag{3}$$

where Es is the time-frequency domain energy of the incident signal, Er (t) is the time-frequency domain energy of the reflected signal, and Wr (t, ω) and Ws (t, ω) are the WVDs of the reflected signal and the incident signal. The time-frequency correlation function $C_{sr}(t)$ will present a local peak when W_r and W_s match, and the peak position can be used to detect the fault location. Suppose that the time difference between the incident signal reflected at the head point of the HTS cable and the local peak reflected at the fault point is Δt; then, the distance between the fault point and the head point of the cable can be calculated as

$$l = \frac{(v \times \Delta t)}{2}, \tag{4}$$

where v is the propagation speed of the signal.

Due to the attenuation of the incident signal as it propagates in the high-temperature superconducting cable, both the time center and frequency center of the signal are shifted, requiring a time compensation for the time difference Δt.

$$\Delta t' = \Delta t + \frac{\delta_\omega}{\theta}, \tag{5}$$

where δ_ω is the frequency offset and θ is the waveform parameter.

2.2. Affine Transformation. Conventional TFDR faces the cross-term interference problem, thus causing misclassification. References [15, 17] use the windowing strategy to

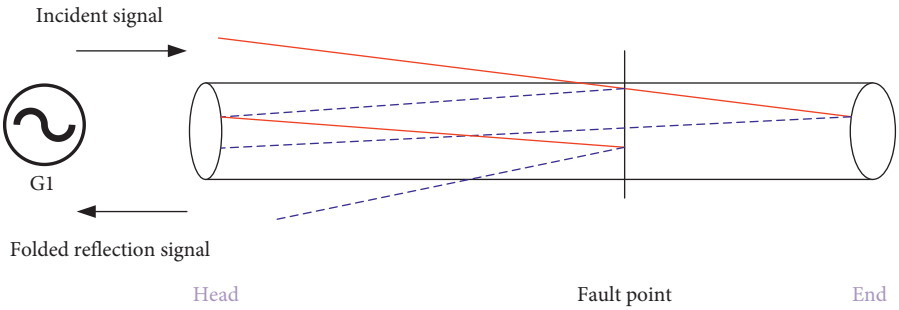

Figure 1: TFDR schematic.

suppress the cross terms, but it is easy to interfere with the self-term and reduce the localization resolution. Studies have shown that the lateral characteristics of the self-term and cross term differ significantly, and the self-term energy distribution is concentrated and smooth, while the cross-term distribution exhibits positive and negative oscillations [20]. Therefore, the time-frequency distributions of the self-term and cross term can be considered for projection, and the differences in the characteristics of the two can be further highlighted by means of coordinate transformation, and the cross term can be separated by means of filtering.

The affine transformation is a two-dimensional planar transformation method widely used in the field of image processing with homogeneity and union, and the features of the transformed figure still retain their original characteristics [24, 25]. The affine transformation includes rotation, stretching, stagger, translation, and other change means, and a straight line is still a straight line after affine transformation, and a parallel line is still a parallel line after affine transformation. The affine transformation is employed to project the time-frequency distribution of TFDR to be parallel to the coordinate axis, which can be analyzed in single time domain or single frequency domain.

The key of affine transformation is to obtain the affine transformation matrix, and the result matrix after affine transformation can be obtained by the product of this matrix and the time-frequency distribution matrix. The solution process is usually based on the Fourier transform to find the matching expression of the spectral integral curve in logarithmic polar coordinates and then to find the extreme value point of the curve or to directly fit the curve after the transformation non-linearly. In the literature [20], the solution process is simplified by using the affine transformation with a cross-axis tangent based on the characteristics of the self-term and cross term obtained by TFDR for high-temperature superconducting cables. The affine transformation matrix M of the cross-axis stagger can be expressed as

$$M = \begin{bmatrix} 1 & 0 & 0 \\ -\frac{1}{k} & 0 & 0 \\ 0 & 0 & 1 \end{bmatrix}. \tag{6}$$

The optimal stagger angle q can be formulated as

$$q = \arg\max\left(\max\left(\mathrm{sum}\left(\mathrm{col}\left(\mathbf{M}_v\right)\right)\right)\right), \tag{7}$$

where argmax () denotes the value corresponding to the maximum value when taken, col () represents each column of the matrix, and $\mathbf{M}v$ denotes the transformed time-frequency matrix. The selection of q value directly affects the accuracy of affine transformation and fault location.

2.3. Particle Swarm Algorithm. Particle swarm algorithm is a common artificial intelligence optimization algorithm, which has the advantages of simplicity, easy implementation, and fast convergence compared to the genetic algorithms and simulated annealing methods [26, 27]. Its iterative process can be described as follows:

$$\begin{cases} \mathrm{pv}^{m+1}(i) = u \cdot \mathrm{pv}^{m}(i) + d_1 r_1 \left(p\mathrm{Best}^{m} - \mathrm{px}^{m}(i)\right) + d_2 r_2 \left(g\mathrm{Best}^{m} - \mathrm{px}^{m}(i)\right), \\ \mathrm{px}^{m+1}(i) = \mathrm{px}^{m}(i) + \mathrm{pv}^{m+1}(i), \end{cases} \tag{8}$$

where $\mathrm{pv}^{m}(i)$ and $\mathrm{px}^{m}(i)$ are the velocity and the position of particle i at the m_{th} generation, respectively, u is the inertia weight factor, d_1 and d_2 are the local and global learning factors, respectively, r_1 and r_2 are random numbers between 0 and 1, $p\mathrm{Best}^{m}$ denotes the historical optimal position of particle i at each iteration, and $g\mathrm{Best}^{m}$ represents the global optimal position of the whole particle swarm at each iteration.

In this paper, the particle swarm algorithm is used to solve the optimal stagger angle, and the affine transformation matrix can be obtained. In order to maintain the diversity of the population, this paper draws on the idea of genetic algorithm and introduces the variation operator into the particle swarm algorithm, where the particle positions may be mutated at each iteration, and its expression is as follows:

$$\begin{cases} a^m = 1 - \lambda^{(1-m/N)^2}, R_1 > 0.7, \\ \mathrm{px}^{m+1}(i)' = \mathrm{px}^{m+1}(i) + a^m \cdot \mathrm{px}^{m+1}(i) \cdot R_1, R_2 > 0.5, \\ \mathrm{px}^{m+1}(i)' = \mathrm{px}^{m+1}(i) - a^m \cdot \mathrm{px}^{m+1}(i) \cdot R_1, R_2 \le 0.5, \end{cases} \tag{9}$$

where a^m is the mutation operator after the m_{th} iteration, λ is the mutation parameter in the range of [0, 1], N is the preset maximum number of iterations, R_1 and R_2 are both random numbers in the range of [0, 1], and $\mathrm{px}^{m+1}(i)'$ denotes the new particle position after the m_{th} iteration after mutation. At the beginning of the iteration, a^m takes a larger value to strengthen the global search ability of the particle, while at the end of the iteration, a^m takes a smaller value to strengthen the local search ability of the particle.

2.4. Unscented Particle Filter. After affine transformation, the self-term is distributed in the low-frequency part and the cross term is distributed in the high-frequency part, so the cross term can be eliminated by low-pass filtering. This method does not affect the self-term resolution, which is theoretically more advantageous than the window addition method.

The unscented particle filter method is based on Bayesian estimation theory and is very suitable for non-Gaussian nonlinear systems with high estimation accuracy and fast computational efficiency and is widely used in modern signal processing [28, 29]. Its filtering steps are as follows:

(1) Initialization is performed using the following expression:

$$\begin{cases} \mathbf{x}_0^i = E\left[\mathbf{x}_0^i\right], k = 0, \\ \mathbf{P}_0^i = E\left[\left(\mathbf{x}_0^i - \overline{x}_0^i\right)\left(\mathbf{x}_0^i - \overline{x}_0^i\right)^T\right], k = 0, \\ \overline{x}_0^{ia} = E\left[\overline{x}_0^{ia}\right], k = 0, \end{cases} \tag{10}$$

where $\boldsymbol{x}_0{}^i$ denotes the initial state variable at the number of iterations $k = 0$, $\boldsymbol{P}_0{}^i$ is the covariance matrix, and $\overline{x}_0^{ia}$ represents the original particle set. When k is greater than 0, let $k = k + 1$ iterations to get a new round of particle set.

(2) Calculate the sigma point set, conduct one-step prediction, and calculate the covariance matrix:

$$\begin{aligned} \mathbf{x}_{k|k-1}^{ia} &= f\left(\mathbf{x}_{k-1}^{ix}, \boldsymbol{i}_{k-1}\right), \\ \overline{x}_{k|k-1}^i &= \sum_{j=0}^{2n_a} W_j^m \mathbf{x}_{j,k|k-1}^{ix}, \\ \mathbf{P}_{k|k-1}^i &= \sum_{j=0}^{2n_a} W_j^c \left[\mathbf{x}_{j,k|k-1}^{ix} - \overline{x}_{k|k-1}^i\right]\left[\mathbf{x}_{j,k|k-1}^{ix} - \overline{x}_{k|k-1}^i\right]^T. \end{aligned} \tag{11}$$

(3) Calculate the observed predictions:

$$\begin{aligned} \mathbf{z}_{k|k-1}^i &= F\left(\mathbf{x}_{k|k-1}^{ix}, i_{k-1}\right), \\ \overline{z}_{k|k-1}^i &= \sum_{j=0}^{2n_a} W_j^c \mathbf{z}_{j,k|k+1}^j. \end{aligned} \tag{12}$$

(4) Calculate the system covariance matrix according to the weighted values:

$$\begin{aligned} \mathbf{P}_{z_k z_k} &= \sum_{j=0}^{2n_a} W_j^c \left[\mathbf{z}_{j,k|k-1}^i - \overline{z}_{k|k-1}^i\right]\left[\mathbf{z}_{j,k|k-1}^i - \overline{z}_{k|k-1}^i\right]^T, \\ \mathbf{P}_{x_k z_k} &= \sum_{j=0}^{2n_a} W_j^c \left[\mathbf{x}_{j,k|k-1}^i - \overline{x}_{k|k-1}^i\right]\left[\mathbf{x}_{j,k|k-1}^i - \overline{x}_{k|k-1}^i\right]^T. \end{aligned} \tag{13}$$

(5) Calculate the Kalman gain and update the system state and covariance matrices:

$$\begin{aligned} \mathbf{K}_k &= \mathbf{P}_{x_k z_k} \mathbf{P}_{z_k z_k}^{-1}, \\ \overline{x}_k^i &= \overline{x}_{k|k-1}^i + \mathbf{K}_k\left(\mathbf{z}_k - \overline{z}_{k|k-1}^i\right), \\ \widehat{P}_k^i &= \mathbf{P}_{k|k-1}^i - \mathbf{K}_k \mathbf{P}_{z_k z_k} \mathbf{K}_k^T. \end{aligned} \tag{14}$$

(6) Determine whether resampling is required, continuously update the particle state until the iteration termination condition is satisfied, calculate the normalized weights for the particles, and update the particles:

$$\widehat{x}_k^i = q\left(\mathbf{x}_k^i | \mathbf{x}_{0:\,k|k-1}^i, z_{1:\,k}\right) = N\left(\overline{x}_k^i, \widehat{P}_k^i\right), \tag{15}$$

where $N(.)$ represents the Gaussian distribution.

3. EEMD Noise Reduction Method

3.1. Conventional EMD. Incident signals may be noisy when transmitted in high-temperature superconducting cables, and the accuracy of fault location can be improved by using suitable noise reduction methods. Empirical mode decomposition is a widely used adaptive time-frequency signal processing method, which can decompose the trends in the original signal at different scales one by one to obtain a finite number of intrinsic mode functions (IMFs), which contain local features at different time scales. The decomposition process is as follows:

(1) Use the method of cubic spline interpolation to find out all the maximal and minimal values of the signal sequence $y(t)$ and form the upper and lower envelopes $y_{\max}(t)$ and $y_{\min}(t)$. Calculate the mean value of the envelope avg (t) and the deviation de (t) of the mean and signal sequence.

$$\begin{aligned} \mathrm{avg}(t) &= \left[\frac{y_{\max}(t) + y_{\min}(t)}{2}\right], \\ \mathrm{de}(t) &= y(t) - \mathrm{avg}(t). \end{aligned} \tag{16}$$

(2) Determine whether the deviation de (t) meets the conditions of IMF: (1) the mean value of the envelope is always 0; (2) the difference between the number of poles and the number of zeros is not greater than 1. If satisfied, the first IMF is recorded as $\zeta_1(t) = \mathrm{de}(t)$, and the difference between the IMF and the original signal can be obtained by $su_1(t) = y(t) - \zeta_1(t)$; if not, repeat several times until the conditions are met.

(3) $su_1(t)$ is taken as the new signal to be decomposed and keep repeating the above process until the remaining signal is a monotonic function.

$$y(t) = \mathrm{su}_n(t) + \sum_{i=1}^{n} \zeta_i(t). \tag{17}$$

3.2. EEMD. The EMD has the shortage of mode mixing, which limits the noise reduction effect. To overcome this problem, EEMD introduces Gaussian white noise and achieves a better improvement effect. The decomposition steps are as follows:

(1) Add a zero-mean Gaussian white noise sequence to the original signal $y(t)$ to form a new sequence $y'(t)$.

(2) Perform EMD on the new sequence $y'(t)$ to obtain several IMFs.

(3) Repeat steps (1) and (2) several times, with different white noise added each time.

(4) Derive the mean value of the IMF obtained several times as the IMF of the EEMD.

4. High-Temperature Superconducting Cable Fault Location Method Based on Improved Time-Frequency Domain Reflection Method and EEMD Noise Reduction

In this paper, we propose a fault location method for high-temperature superconducting cables. Firstly, incident signals are sent to the cables, and the folded reflection signals generated by the incident signals at the impedance discontinuities can be obtained by the digital oscilloscope. Secondly, the time-frequency domain reflection method is applied to locate cable faults. The affine transformation is introduced to solve the cross-term interference problem of the time-frequency domain reflection method. The particle swarm algorithm is used to improve the accuracy of the stagger angle. Additionally, the unscented particle filter algorithm is employed to achieve cross-term separation and EEMD is introduced to denoise the signal to make the localization results more accurate. The steps of the method in this paper are as follows, and the flowchart is shown in Figure 2.

(1) Set up the simulation environment and model of high-temperature superconducting cable and set the appropriate parameters.

(2) Apply the TFDR method to send incident signal to the cable and use the digital oscilloscope to pick up the fold reflection signal generated by the incident signal at the impedance discontinuity point.

(3) The affine transformation is conducted to solve the cross-term interference problem.

(4) Particle swarm algorithm is used to improve the accuracy of the stagger angle.

(5) The unscented particle filter algorithm is employed to filter out the high-frequency cross term.

(6) The filtered transformed signal is inverse affine transformed back to the original coordinate system.

(7) Denoise the signal by EEMD.

(8) Locate the fault point based on the denoised folded reflection signal.

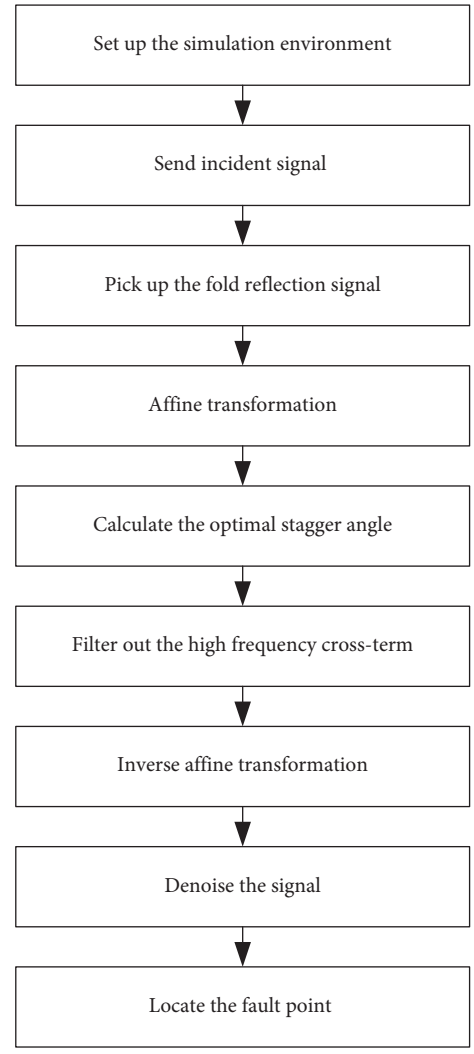

Figure 2: Algorithm flowchart.

5. Case Study

5.1. High-Temperature Superconducting Cable Simulation Construction. In this paper, two software programs, PSCAD and MATLAB, are used for joint simulation. Since PSCAD does not have a model of high-temperature superconducting

cable at the moment, it needs to be built manually. This study borrows the simulation construction method from the literature [30, 31] and uses the non-linear resistance instead of HTS in PSCAD, and the resistance value is calculated by writing the cable model in MATLAB, and the calculation block diagram is displayed in Figure 3.

As can be seen from Figure 3, during the PSCAD simulation, the HTS node currents obtained within each step are passed to the MATLAB program through the interface, and the cable resistance R and cable temperature T are calculated based on the cable model and then returned to PSCAD through the interface for display and completion of one step of simulation, and so on and so forth.

During actual operation, insulation faults and short-circuit faults may occur in high-temperature superconducting cables. In this paper, the HTS model is established by PSCAD and MATLAB to simulate a 50 m long high-temperature superconducting cable with a three-phase short-circuit fault at 20 m from the head end. Since the high-temperature superconducting cable normally operates in a liquid nitrogen cryogenic environment, this paper assumes that the cable temperature during steady-state operation of the high-temperature superconducting cable is 80 K.

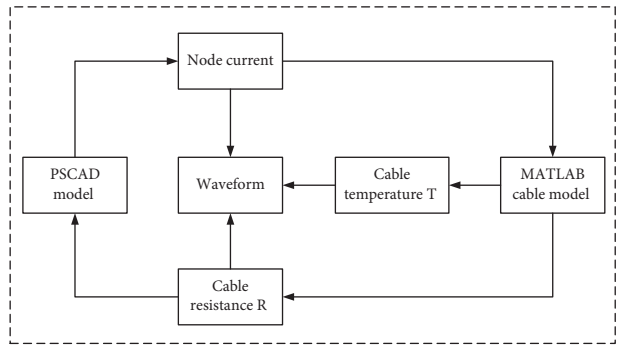

Figure 3: Calculation diagram of high-temperature superconducting cable model.

5.2. Simulation Results. In order to verify the accuracy and validity of the method in this paper, the following six models are selected for comparison with the proposed method in this paper.

Case 1: the PWVD-TFDR model of Zheng [12].

Case 2: the GRNN-TFDR model of Rafinia and Moshtagh [13].

Case 3: the affine transformation-TFDR model of Liu et al. [17].

Case 4: the method proposed in this paper and that without EEMD noise reduction.

Case 5: the affine transformation-TFDR-particle swarm-Fourier filtering-EEMD noise reduction model is considered in this case.

Case 6: the affine transformation-TFDR-unscented particle filter-EEMD noise reduction is considered.

The localization polar spectrum of the above six control group models is shown in Figures 4–9, respectively, and the localization polar spectrum of the proposed method in this paper is depicted in Figure 10. For the convenience of observation, only each wave peak is labelled in the figure, and the remaining values are taken as 0. The following conclusions can be drawn from the comparison analysis of the figures.

(1) The PWVD-TFDR cannot completely eliminate the cross-term interference, and there are more interference peaks.

(2) GRNN-TFDR has slightly less interference peaks than pseudo-Wigner distribution-TFDR, but the localization accuracy is not as good as the latter.

(3) The affine transformation-TFDR eliminates the interference peaks to a great extent, and there is only one small interference peak in the figure, and the localization accuracy is better than that of the pseudo-Wigner distribution-TFDR and GRNN-TFDR, which verifies the advantage of the affine transformation idea in removing the cross-term interference.

(4) Compared with affine transformation-TFDR, affine transformation-TFDR-particle swarm-unscented particle filter further reduces the interference peaks and improves the localization accuracy, which verifies that particle swarm and unscented particle filter are beneficial to the accuracy improvement of the algorithm.

(5) Compared with the affine transformation-TFDR, the affine transformation-TFDR-particle swarm-Fourier filter-EEMD noise reduction further reduces the interference peaks and improves the localization accuracy, which verifies that the processing of particle swarm search for the stagger angle and EEMD noise reduction can improve the algorithm accuracy.

(6) Compared with the affine transformation-TFDR, the affine transformation-TFDR-unscented particle filter-EEMD noise reduction further reduces the interference peaks and improves the localization accuracy, and it is verified that the unscented particle filter and EEMD noise reduction are beneficial to the algorithm accuracy improvement.

The proposed method of this paper basically eliminates all the interference peaks and performs better compared with the 4th, 5^{th}, and 6th control groups, which verifies that the three measures introduced in this paper, namely, particle swarm search for stagger angle, unscented particle filter for high-frequency cross terms, and EEMD noise reduction, are effective in improving the fault location accuracy.

The comparison of the positioning accuracy of each algorithm is shown in Table 1. As can be seen from Table 1, the algorithm of this paper outperforms the six control group algorithms, and the relative error is only 0.05%, which is the smallest relative error of all algorithms, verifying the accuracy and effectiveness of the algorithm of this paper.

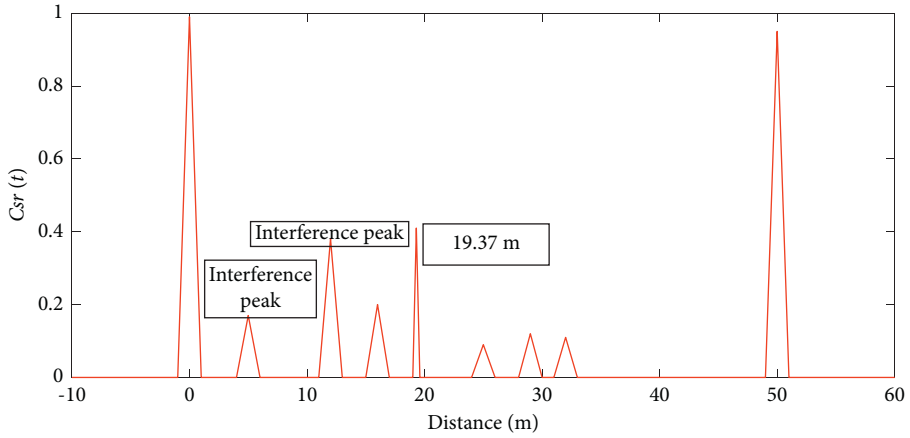

Figure 4: Positioning result of the PWVD-TFDR model.

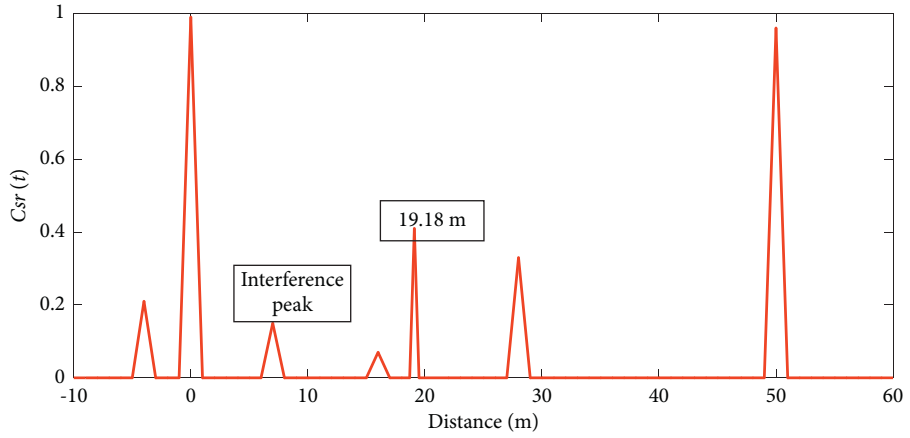

Figure 5: Positioning result of the GRNN-TFDR model.

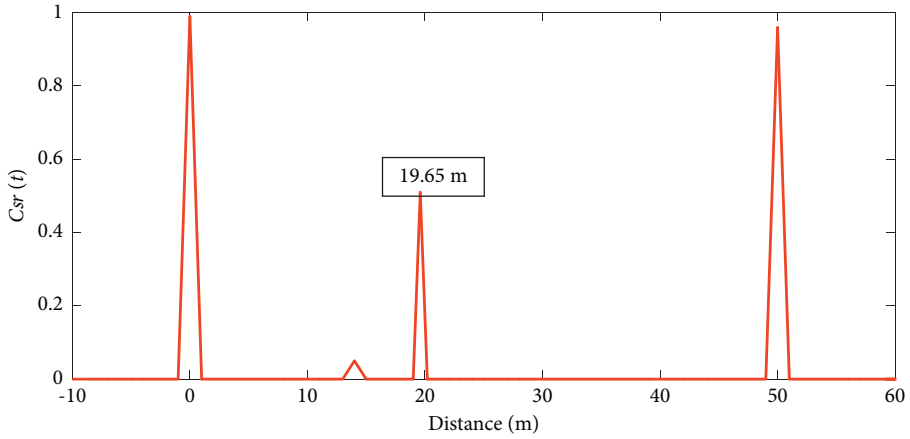

Figure 6: Positioning result of the affine transformation-TFDR model.

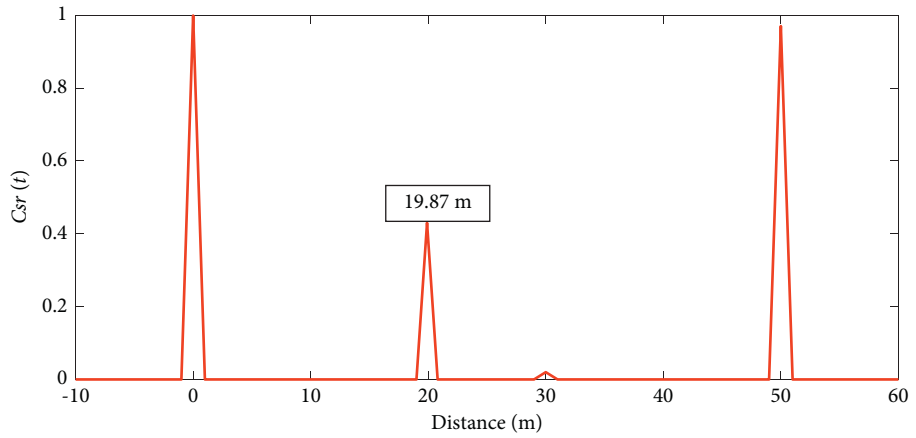

Figure 7: Positioning result of the affine transformation-TFDR-particle swarm-unscented particle filter model.

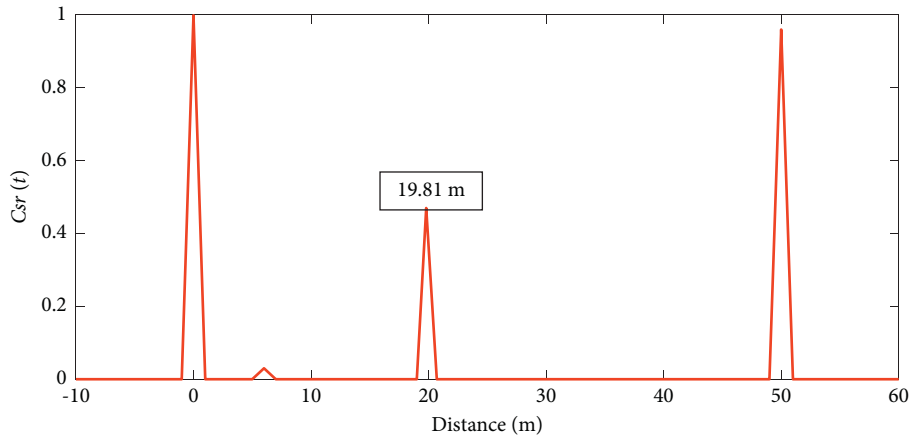

Figure 8: Positioning result of the affine transform-TFDR-particle swarm-Fourier filter-EEMD noise reduction model.

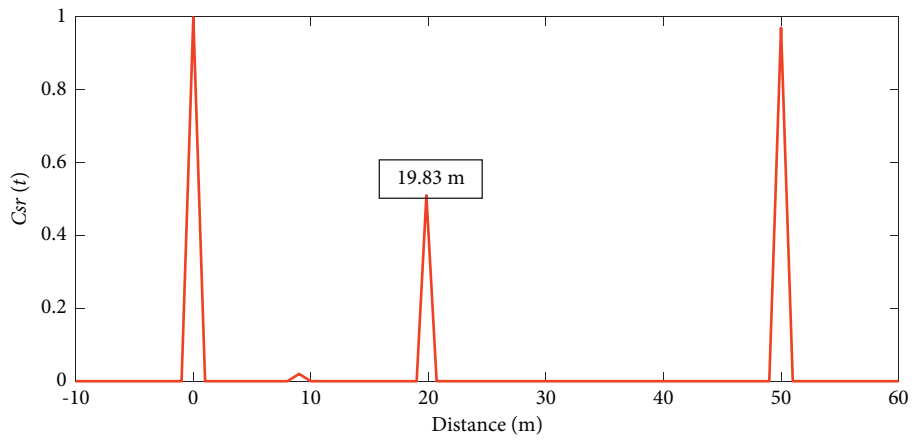

Figure 9: Positioning result of the affine transformation-TFDR-unscented particle filter-EEMD noise reduction model.

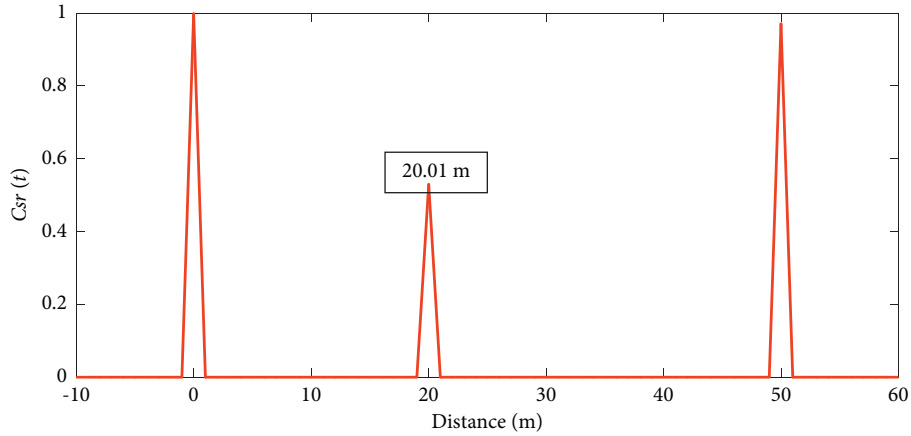

Figure 10: Positioning result of the proposed method.

Table 1: Comparison of positioning accuracy of various algorithms.

Cases	Fault point (m)	Absolute error (m)	Relative error (%)
Case 1	19.37	0.63	3.15
Case 2	19.18	0.82	4.10
Case 3	19.65	0.35	1.75
Case 4	19.87	0.13	0.65
Case 5	19.81	0.19	0.95
Case 6	19.83	0.17	0.85
The proposed method in this paper	20.01	0.01	0.05

6. Conclusions

In this paper, a fault location method for high-temperature superconducting cables is proposed, which can improve the fault location accuracy by effectively solving the problems of self-term resolution reduction and incomplete cross-term removal that may be caused when removing cross-term interference.

This paper combines PSCAD and MATLAB software programs to build a high-temperature superconducting cable model, adopts the time-frequency domain reflection method to locate cable faults, introduces the affine transformation, applies particle swarm algorithm to improve the accuracy of the affine transformation stagger angle, realizes the cross-term separation according to the unscented particle filter algorithm, and finally performs EEMD denoising on the signal. The simulation results show that this method has good fault location accuracy for high-temperature superconducting cables, which has certain reference significance for engineering practice.

Data Availability

The data used to support the findings of this study are included within the article.

Conflicts of Interest

The authors declare that they have no conflicts of interest.

Acknowledgments

This study was supported by the Tongli High-Temperature Superconducting DC Cable Demonstration Project of Jiangsu Suzhou.

References

[1] M. Buhari, V. Levi, and S. K. E. Awadallah, "Modelling of ageing distribution cable for replacement planning," *IEEE Transactions on Power Systems*, vol. 31, no. 5, pp. 3996–4004, 2015.

[2] R. Bayindir, I. Colak, G. Fulli, and K. Demirtas, "Smart grid technologies and applications," *Renewable and Sustainable Energy Reviews*, vol. 66, pp. 499–516, 2016.

[3] C. Liu, Y. Zhang, and J. Sun, "Stacked bidirectional LSTM RNN to evaluate the remaining useful life of supercapacitor," *International Journal of Energy Research*, pp. 1–10, 2021.

[4] C. Lee, H. Son, and Y. Won, "Progress of the first commercial project of high-temperature superconducting cables by KEPCO in Korea," *Superconductor Science and Technology*, vol. 33, no. 4, 2020.

[5] G. Xia, Y. Huang, F. Li et al., "A thermally flexible and multi-site tactile sensor for remote 3D dynamic sensing imaging," *Frontiers of Chemical Science and Engineering*, vol. 14, no. 6, pp. 1039–1051, 2020.

[6] J. H. Choi, H. Park, and R. Baldick, "Transmission investment and expansion planning for systems with high-temperature superconducting cables," *IEEE Transactions on Applied Superconductivity*, vol. 29, no. 8, pp. 1–9, 2019.

[7] O. Rahman, K. M. Muttaqi, and D. Sutanto, "High temperature superconducting devices and renewable energy

resources in future power grids: a case study," *IEEE Transactions on Applied Superconductivity*, vol. 29, no. 2, pp. 1–4, 2019.

[8] J. X. Jin, Y. Ying Xin, Q. L. Wang et al., "Enabling high-temperature superconducting technologies toward practical applications," *IEEE Transactions on Applied Superconductivity*, vol. 24, no. 5, pp. 1–12, 2014.

[9] W. Yuan, S. Venuturumilli, Z. Zhang, Y. Mavrocostanti, and M. Zhang, "Economic feasibility study of using high-temperature superconducting cables in U.K.'s electrical distribution networks," *IEEE Transactions on Applied Superconductivity*, vol. 28, no. 4, pp. 1–5, 2018.

[10] Z. Feng, C. H. I. Zhen, and F. U. Sheng-Qun, "Design of the pulse source of cable fault location based on pulse reflection method," *Journal of Harbin University of Science & Technology*, vol. 19, no. 3, 2014.

[11] S. Y. Tao, Y. Feng, and T. C. Zhang, "High-voltage switch cabinet partial discharge on-line monitoring device based on pulse current method," *Power System Protection and Control*, vol. 47, no. 9, pp. 145–149, 2019.

[12] G. M. Zheng, "A reflectometer for cable fault location with multiple pulse reflection method," *Sensors & Transducers*, vol. 183, no. 12, 2014.

[13] A. Rafinia and J. Moshtagh, "A new approach to fault location in three-phase underground distribution system using combination of wavelet analysis with ANN and FLS," *International Journal of Electrical Power & Energy Systems*, vol. 55, pp. 261–274, 2014.

[14] J. P. Huang, Z. Zhang, and W. Wang, "A local quench detection and protection method for a superconducting cable based on distributed optical fiber temperature measurement technology," *Power System Protection and Control*, vol. 48, no. 14, pp. 76–84, 2020.

[15] Y. Y. Wang, Z. F. Yao, and W. Xie, "Research on fault location of high temperature superconducting cable based on time-frequency domain reflectometry," *Proceedings of the CSEE*, vol. 41, no. 5, pp. 1540–1546, 2021.

[16] G.-Y. Kwon, C.-K. Lee, and Y.-J. Shin, "Diagnosis of shielded cable faults via regression-based reflectometry," *IEEE Transactions on Industrial Electronics*, vol. 66, no. 3, pp. 2122–2131, 2019.

[17] C. Liu, Q. Li, and K. Wang, "State-of-charge estimation and remaining useful life prediction of supercapacitors," *Renewable and Sustainable Energy Reviews*, vol. 150, no. 2, p. 111408, 2021.

[18] Y. H. Lee, S. S. Bang, and G. Y. Kwon, "Analysis of wave propagation of HTS cables for compensation of thermal loss on connectors," *IEEE Transactions on Applied Superconductivity*, vol. 27, no. 4, p. 4801105, 2017.

[19] G.-Y. Kwon, C.-K. Lee, G. S. Lee et al., "Offline fault localization technique on HVDC submarine cable via time-frequency domain reflectometry," *IEEE Transactions on Power Delivery*, vol. 32, no. 3, pp. 1626–1635, 2017.

[20] K. Wang, C. L. Liu, and J. R. Sun, "State of charge estimation of composite energy storage systems with supercapacitors and lithium batteries," *Complexity*, vol. 2021, Article ID 8816250, 15 pages, 2021.

[21] J. Chang, L. Zhu, H. Li, F. Xu, B. Liu, and Z. Yang, "Noise reduction in Lidar signal using correlation-based EMD combined with soft thresholding and roughness penalty," *Optics Communications*, vol. 407, pp. 290–295, 2018.

[22] W.-C. Wang, K.-W. Chau, D.-M. Xu, and X.-Y. Chen, "Improving forecasting accuracy of annual runoff time series using ARIMA based on EEMD decomposition," *Water Resources Management*, vol. 29, no. 8, pp. 2655–2675, 2015.

[23] X. Feng, Q. Li, and K. Wang, "Waste plastic triboelectric nanogenerators using recycled plastic bags for power generation," *ACS Applied Materials & Interfaces*, vol. 13, no. 1, pp. 400–410, 2020.

[24] B. Zhang, Z. Zou, and S. J. Chen, "Fabric image registration based on affine transform and Levenberg-Marquardrt algorithm," *Acta Optica Sinica*, vol. 37, no. 1, 2017.

[25] K. Wang, W. Wang, L. Wang, and L. Li, "An improved SOC control strategy for electric vehicle hybrid energy storage systems," *Energies*, vol. 13, no. 20, p. 5297, 2020.

[26] R. A. Ibrahim, A. A. Ewees, D. Oliva, M. Abd Elaziz, and S. Lu, "Improved salp swarm algorithm based on particle swarm optimization for feature selection," *Journal of Ambient Intelligence and Humanized Computing*, vol. 10, no. 8, pp. 3155–3169, 2019.

[27] S. Almahdi and S. Y. Yang, "A constrained portfolio trading system using particle swarm algorithm and recurrent reinforcement learning," *Expert Systems with Applications*, vol. 130, pp. 145–156, 2019.

[28] H. Zhang, Q. Miao, X. Zhang, and Z. Liu, "An improved unscented particle filter approach for lithium-ion battery remaining useful life prediction," *Microelectronics Reliability*, vol. 81, pp. 288–298, 2018.

[29] G. Vezzani, U. Pattacini, G. Battistelli, L. Chisci, and L. Natale, "Memory unscented particle filter for 6-DOF tactile localization," *IEEE Transactions on Robotics*, vol. 33, no. 5, pp. 1139–1155, 2017.

[30] X. Y. Chen, *Experimental and Simulation on 110kV Cold Dielectric High Temperature Superconducting Cable*, Beijing Jiaotong University, Beijing, China, 2015.

[31] Y. X. Li, *The Study of HTS Model Cable Simulation Model Based on PSCAD*, School of Electrical and Electronic Engineering, Beijing, China, 2014.

Hindawi
Mathematical Problems in Engineering
Volume 2021, Article ID 2506286, 10 pages
https://doi.org/10.1155/2021/2506286

Research Article

Fault Diagnosis of Data-Driven Photovoltaic Power Generation System Based on Deep Reinforcement Learning

Shuang Dai,[1] Dingmei Wang,[2] Weijun Li,[3] Qiang Zhou,[2] Guangke Tian,[1] and Haiying Dong[3]

[1]*Key Laboratory of Optoelectronic Technology and Intelligent Control, Ministry of Education, Lanzhou Jiaotong University, Lanzhou 730030, China*
[2]*State Grid Gansu Electric Power Company Electric Power Science Research Institute, Lanzhou 730030, China*
[3]*School of New Energy and Power Engineering, Lanzhou Jiaotong University, Lanzhou 730030, China*

Correspondence should be addressed to Haiying Dong; hydong@mail.lzjtu.cn

Received 21 September 2021; Accepted 6 November 2021; Published 29 November 2021

Academic Editor: Licheng Wang

Aiming at the problem of fault diagnosis of the photovoltaic power generation system, this paper proposes a photovoltaic power generation system fault diagnosis method based on deep reinforcement learning. This method takes data-driven as the starting point. Firstly, the compressed sensing algorithm is used to fill the missing photovoltaic data and then state, action, strategy, and return functions from the environment. Based on the interaction rules and other factors, the fault diagnosis model of the photovoltaic power generation system is established, and the deep neural network is used to approximate the decision network to find the optimal strategy, so as to realize the fault diagnosis of the photovoltaic power generation system. Finally, the effectiveness and accuracy of the method are verified by simulation. The simulation results show that this method can accurately diagnose the fault types of the photovoltaic power generation system, which is of great significance to enhance the security of the photovoltaic power generation system and improve the intelligent operation and maintenance level of the photovoltaic power generation system.

1. Introduction

With the continuous advancement of energy transformation, the proportion of clean energy in the energy supply is increasing year by year. At present, the development of photovoltaic power generation technology has been relatively mature and has been more and more widely used at home and abroad. Statistics show that, by the end of 2020, the cumulative installed capacity of photovoltaic power generation in China has reached 204.3 million kW, and the total annual photovoltaic power generation has reached 224.3 billion kWh [1]. Because solar energy is intermittent energy, in order to ensure the normal operation of the photovoltaic system and reduce the life reduction and power loss caused by faults, the research on accurate and fast photovoltaic fault diagnosis method is of great significance.

With the development of artificial intelligence technology, there are various fault diagnosis methods based on intelligent algorithms. The neural network method proposed in [2] can judge the existence of short-circuit fault after learning by establishing several neural network structures. The fuzzy algorithm proposed in [3] estimates the output power value under normal conditions and then compares the value with the real-time measured value. If the difference between the two is greater than the set threshold, it is proved that there is a fault. References [4, 5] proposed a photovoltaic array fault detection method based on pattern recognition. This method obtains appropriate fault characteristic parameters through signal decomposition technology and then uses a fuzzy inference system to judge whether the photovoltaic array has a fault. This method needs to formulate fuzzy rules in advance, and the formulation of fuzzy rules often depends on experience or experts in this field, so it is

difficult to obtain fuzzy rules. Reference [6] proposed a fault diagnosis method of photovoltaic power generation system based on BP neural network, which has strong adaptive nonlinear pattern recognition ability and is suitable for multifault complex systems. Reference [7] proposes a multiclassification supported axis to diagnose the faults between neutral lines and equipment faults of photovoltaic cells. Reference [8] proposed a graph-based semisupervised detection method for fault diagnosis of short circuits, open circuits, and line to line faults. Reference [9] proposes a method of applying investigation to solve photovoltaic fault, but this method needs to obtain the data of fault data set in advance. Reference [10] proposes a photovoltaic array fault diagnosis method based on long-term and short-term memory neural network (LSTM). This method establishes the LSTM neural network fault diagnosis model and trains the model by collecting the characteristic parameters of the photovoltaic array under different fault conditions as training samples.

The above literature provides a good reference for the fault diagnosis research of the photovoltaic power generation system, but most of the above research depends on specific algorithm models, with low monitoring accuracy and lack of self-learning of diagnosis methods [11].

In order to accurately diagnose the fault types of the photovoltaic power generation system, a photovoltaic power generation system fault diagnosis method based on deep reinforcement learning is proposed in this paper. Firstly, for the photovoltaic power generation system data summarized by the operation and maintenance platform, the compressed sensing algorithm is used to fill in the missing data, then the enhanced learning algorithm is used to establish the fault diagnosis model of the photovoltaic power generation system, and the deep neural network is used to approximate the decision network to find the optimal strategy, so as to realize the fault diagnosis of the photovoltaic power generation system. Finally, the feasibility and accuracy of the proposed method are verified by simulation experiments.

2. Deep Reinforcement Learning Algorithm

2.1. Reinforcement Learning. Reinforcement learning is a branch of machine learning, which is mainly used to learn control strategies. Its learning process is similar to the process of living organisms getting along with the external environment, which is in line with human behavioral psychology. The model of reinforcement learning is shown in Figure 1. The brain represents the agent, and the Earth represents the environment. The agent continuously interacts with the environment for learning, that is, the process of reinforcement learning [12].

As can be seen from Figure 1, the interaction between the agent and the environment will produce a time series $\{s_1, a_1, r_1, s_2, a_2, r_2, \ldots, s_t, a_t, r_t\}$ composed of state, action, and return. Based on the premise of time series and certainty, reinforcement learning can be regarded as a Markov decision-making process.

Markov decision process is usually defined by five tuples: $\langle S, A, P_a(s_t, s_{t+1}), r(s_t, a_t), \gamma \rangle$.

(1) S represents the state space, which is the external environment that the agent can perceive.

(2) A represents the action space that the agent can choose. In each state, the agent selects a behavior action to feedback to the environment according to the strategy.

(3) $P_a(s_t, s_{t+1})$ represents the state transition probability of the environment. See formula (1). $P(s_{t+1}|s_t, a)$ represents the probability that the environment reaches state st + 1 after deciding to take action a in state st. At this time, state st + 1 is only related to st and action a and has nothing to do with all states before time t.

$$P_a(s_t, s_{t+1}) = P(s_{t+1}|s_t, s) = P(s_{t+1}|s_t, s_t \cdot s_{t-1}, \ldots, s_0, a). \tag{1}$$

(4) r(st, at) refers to the return of the agent to implement the action at through decision-making when the agent is in the state st.

(5) γ represents the discount factor. $\gamma \in [0, 1]$; the discount factor is the important parameter that determines each return.

In reinforcement learning, two important state value functions are defined to describe the importance of state and value, respectively, as shown in the following equations:

$$V_\pi(s) = \sum_{a \in A} \pi(a|s) \left(R_s^a + \gamma \sum_{s' \in S} P_{ss'}^a V_\pi(s') \right), \tag{2}$$

$$q_\pi(s, a) = R_s^a + \gamma \sum_{s' \in S} P_{ss'}^a \sum_{a \in A} \pi(a'|s') q_\pi(s', a'). \tag{3}$$

Through the interactive process of enhanced learning, it is finally required to find the optimal strategy $\pi^*(s)$ that can maximize the benefits of the agent:

$$q_\pi(s, a) = R_s^a + \gamma \sum_{s' \in S} P_{ss'}^a \sum_{a \in A} \pi(a'|s') q_\pi(s', a'). \tag{4}$$

The state value function is an iterative expression, which meets the requirements of the Behrman equation, so it can be solved by the iterative method. When the transition probability between states is known, the value iteration method is adopted, that is, the state value function is updated through the iterative method, and the adopted strategy is changed according to its value, and the final convergence result is the optimal state value function.

The main content of the Q (Q-learning) learning algorithm is to calculate the maximum value function of state and behavior, update it by using the past and recent weight average, and then solve it by using the optimal action state value function to obtain the optimal state value function, to obtain the optimal learning strategy [13, 14]. As shown in the following equation,

$$Q(s, a) = r(s, a) + \gamma \max_{a'} Q(s', a'). \tag{5}$$

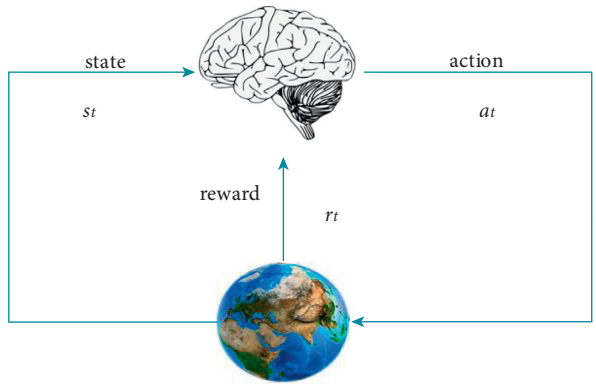

Figure 1: Interaction model between agent and environment.

2.2. DQN Algorithm. The deep neural network is introduced into the Q-learning algorithm, which is called DQN (Deep Q-learning Net) algorithm [15]. Neural network training samples need to have labels, and reinforcement learning is a type of learning without direct labels. Therefore, the target Q value is used as the training label, and the purpose of training is to make the Q value close to the target Q value. The calculation of the target Q value is as the formula in step 11 of Algorithm 1 and then makes a difference with the output $Q(\phi_j, \alpha_j; \theta)$ of the current network. The parameters of the neural network are updated by the method of back-propagation gradient descent until the Q network converges [16].

The implementation of the DQN algorithm involves the experience playback mechanism; that is, the information of each interaction is stored. During training, a sample is randomly selected from the experience pool for training, which can maintain independent and identically distributed among samples and eliminate the correlation between samples [17].

In the DQN algorithm, the Q-learning algorithm and deep learning network are trained at the same time. A large number of training samples are obtained through Q-learning, and then the neural network is trained. The key lies in the label (i.e., target Q value).

3. Photovoltaic Data Filling Based on Compressed Sensing Algorithm

3.1. Compressed Sensing Algorithm. A compressed sensing algorithm is an algorithm that compresses the signal at a very high compression rate and reconstructs and recovers the compressed signal after transmission [18]. This algorithm can change the asymmetry of the signal in the process of acquisition, transmission, and processing. The signal acquisition is generally carried out by using sensor devices. Generally, these devices have poor storage endurance and do not support complex processing such as collecting a large amount of data and compressing the data. After transmission to computers and other devices with strong computing power, the computer only needs to do some simple decompression; this asymmetry brings great pressure to the sensor acquisition equipment [19]. The compressed sensing technology completes the compression in the sampling process, so it only needs to collect a small amount of data and use the computer to process a large amount of reconstruction calculation. Therefore, the compressed sensing algorithm is widely used in signal processing and so on.

Compressed sensing algorithm: one is the sparse representation of the signal. For a signal $X \in R^{N\times 1}$, we select a group of orthogonal transformation basis Ψ to sparse decompose the signal to obtain a group of sparse signals. Second, the observation matrix is designed to observe the signal. The observation matrix is required to be uncorrelated with the sparse orthogonal transformation basis [20, 21], and an observation matrix with the size $M \times N$ is selected Φ. The sparse representation of the original signal S is projected into M dimensionality reduction vectors $Y = \Phi S$, where $\Phi \in R^{M\times N}$. The third is signal reconstruction. The process of signal reconstruction is the process of finding the optimal solution under constraints. The reconstruction algorithm is equivalent to the following mathematical programming problem.

Objective function: $\min\|S\|$. Constraints: $\phi\psi^T X = Y$.

The flow chart of the compressed sensing algorithm is shown in Figure 2.

Compressed sensing is that the data is incompletely sampled when it is less than Nyquist sampling law, and then the original signal is reconstructed, which is very similar to the partial loss of photovoltaic monitoring data. Therefore, the compressed sensing algorithm is used for photovoltaic missing data reconstruction. In the photovoltaic monitoring signal, the same physical quantity is sampled in adjacent periods. The change between the two sampling values is very small and smooth. After sparse transformation, it has the characteristics of a sparse signal. The compressed sensing algorithm is used for data filling, and finally, the reconstructed signal is used for filling. Secondly, in the design of the observation matrix, the observation matrix is designed according to the location of the missing data, so that the sparse representation basis of the observation matrix has little correlation. The signal reconstruction process uses the orthogonal matching pursuit algorithm, which can reconstruct the signal with high quality.

3.2. Photovoltaic Data Filling. The photovoltaic monitoring system is an important part of the photovoltaic power generation system, which can collect a large amount of data. Through the extraction and analysis of the collected massive data, much valuable information is obtained, which plays a positive role in improving the power generation efficiency of the photovoltaic power generation system and power station operation and maintenance. However, in practice, the collected data are missing due to various reasons (such as transmission fault, sensor fault, etc.), and these missing data may have a great impact on the analysis and mining of later photovoltaic data and the fault diagnosis of the photovoltaic power generation system. In serious cases, it may lead to the direct failure of the fault diagnosis model of the photovoltaic power generation system. Compared with statistical and intelligent algorithms, this paper uses a compressed sensing

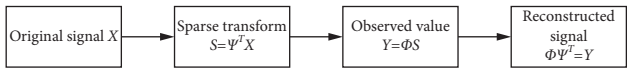

Figure 2: Flow chart of the compressed sensing algorithm.

algorithm to fill in the missing photovoltaic data. Compared with statistical and intelligent algorithms, this paper uses a compressed sensing algorithm to fill in the missing photovoltaic data. The process is as follows:

(1) Suppose a monitoring signal sampled at a certain time is $X \in R^{M\times 1}$, in which there is some missing data. After the missing data is supplemented with zero, the signal $X' \in R^{N\times 1}$ is obtained again; that is,$N - M$ data is missing.

(2) The photovoltaic monitoring data $X' \in R^{N\times 1}$ is calculated by using a matrix Ω_1 to obtain $\Omega_1 X'$. The obtained signal $X'' \in R^{N\times 1}$ is sparsely represented by discrete cosine transform; that is $S = \Psi^T X''$.

$$\Omega_1 = \begin{bmatrix} 1 & -1 & 0 & \cdots \\ 0 & 1 & -1 & \cdots \\ 0 & 0 & 1 & \cdots \\ \cdots & \cdots & \cdots & \cdots \end{bmatrix}. \quad (6)$$

(3) Design the observation matrix. By deleting the missing data in the unit matrix I of $N \times N$ relative to the signal X', an observation matrix Ω_2 of $M \times N$ can be obtained. Observe the signal S after the observation matrix Ω_2 is sparsely represented to obtain $Y = \Omega_2 S$.

(4) Reconstruct the signal. The reconstruction algorithm is equivalent to the following mathematical programming problem.

Objective function: $\min\|S\|$, constraint condition: $\phi\psi^T X = Y$. The problem is solved by an orthogonal matching pursuit algorithm.

(5) The filling value of missing data can be obtained by inverse discrete cosine transform of the obtained signal X''.

(6) Calculate the mean square error.

4. Fault Diagnosis of Photovoltaic Power Generation System Based on DQN Algorithm

4.1. Diagnostic Model. The fault diagnosis model of the photovoltaic power generation system is established based on the DQN algorithm. Figure 3 is the schematic diagram of fault diagnosis of photovoltaic power generation system based on DQN algorithm. The modeling process is as follows.

4.1.1. Diagnostic Tasks and Interaction Rules. The diagnosis task is constructed as a continuous decision-making process of the agent: the agent successively diagnoses the fault of each training sample in the environment, uses the reward to guide the agent to carry out training and learning, and gives the corresponding reward according to a certain reward principle. The training goal is to maximize the cumulative return of agents in diagnostic tasks.

In the fault diagnosis task of the photovoltaic power generation system, to guide the agent to learn the fault diagnosis strategy, the interaction rules between the agent and the environment are formulated: determine a corresponding return according to the distribution of each category. The principle is that if the agent correctly diagnoses the fault type in the sample, it will give the agent a positive return, and if the agent diagnoses the fault, it will give a negative return; that is, it needs to be deducted from the reward.

In reinforcement learning, the agent is allowed to interact with the environment continuously, record each interaction completely, and then store it in the experience pool. The subsequent learning is to continuously sample and train from the experience pool. Each training process starts from the first sample and ends when the most common fault type in the sample is diagnosed incorrectly. This process is called a plot.

4.1.2. Simulation Environment. The environmental state is an important element in the reinforcement learning model. In the fault diagnosis of the photovoltaic power generation system, because the fault diagnosis of photovoltaic power generation system mainly depends on the data at a certain time, the collection of photovoltaic monitoring data collected at a certain time is regarded as a state, and the data at each time represents a state.

4.1.3. Action Space. The action space of the agent corresponds to the label of the sample (i.e., fault type). There are as many actions as there are fault types for the agent to select during fault diagnosis. Here, the fault types are numbered with Arabic numerals.

4.1.4. Return Function. In the training process, the value of agent action is evaluated by the return function. If the fault distribution is balanced, all samples shall be treated equally. However, due to the unbalanced distribution of photovoltaic power generation system faults, the fault distribution of photovoltaic power generation system equipment of different regions and manufacturers is also different. To better guide learning and training, the return after each fault diagnosis shall be given according to the actual distribution of various faults in the power plant. If the agent correctly diagnoses many faults in the sample, it will give a relatively small positive return. If the agent correctly diagnoses a few faults in the sample, it will give a relatively large positive return. On the contrary, if the agent makes a relatively negative return for this kind of fault diagnosis error with few samples, if the agent makes a diagnosis error for many common faults in the sample, it indicates that the agent has not learned experience and knowledge at all, so it is not

necessary to continue, and the current round of diagnosis process should be terminated immediately.

In the fault diagnosis of the photovoltaic power generation system, it is assumed that there are n fault types, the label is defined as k, the training sample set of photovoltaic power generation system fault type is D_k, $|D_k|$ is the number of training samples of label k, and the imbalance proportion of category k is defined as $\rho(k)$, as shown in formula (7). Take all the training samples of the most unbalanced n categories as D_S, and the return function is formula (8). When the agent classifies the samples in D_S incorrectly, the current classification task will be terminated.

$$\rho(k) = \frac{|D_k|}{\max_i\{|D_i|\}}, \tag{7}$$

$$r_t = \begin{cases} \rho(k), & a_t = y_t, \\ \rho(k), & a_t \neq y_t. \end{cases} \tag{8}$$

4.1.5. Classification Task Termination Condition. For the problem of fault diagnosis of the photovoltaic power generation system, when the agent diagnoses the fault of the sample with the largest number of samples, this scenario ends, and the score of the agent in this scenario is cleared. If the previous situation does not occur, but the agent completes the fault diagnosis of all samples, it will reset the agent's cumulative return and start a new round of tasks.

4.1.6. Tactics. In the training stage, to enable agents to fully learn knowledge and experience, they began to focus on exploration, followed by utilization, so linear annealing greedy strategy is used [22]. The purpose of the test phase is mainly to detect the learning situation of the agent, mainly for utilization. Therefore, the greedy strategy is used; that is, we select an action with the largest Q value every time:

$$\pi(s) = \arg\max_a Q(s, a). \tag{9}$$

4.1.7. Training Objectives. Deep reinforcement learning is applied to the fault diagnosis of photovoltaic power generation systems. A large number of training samples are learned through a data-driven method, and the ultimate goal is to correctly diagnose the fault types.

Because the DQN algorithm uses an empirical playback mechanism, it is necessary to use a submechanism to train samples when designing a photovoltaic power generation system fault diagnosis model based on deep reinforcement learning. Store the information $\langle s, a, r, s', \text{terminal}\rangle$ of each interaction in the experience pool, and then, randomly sample it to train the Q network. The specific process is shown in Figure 3. When the depth neural network is used to fit the Q function, the actual Q value of the target state s is the output value of the current Q network, and the target Q value is recorded as y, which is determined by the progress of the classification task, as shown in equation (8).

$$y = \begin{cases} r, & \text{terminal} = \text{Ture}, \\ r + \gamma \max_{a'} Q(s', a', \theta_{k-1}), & \text{terminal} = \text{Fals}, \end{cases} \tag{10}$$

Taking the target Q value as the label of deep neural network training, the loss function of Q network training is $L(\theta_k)$, as shown in equation (11). According to equation (11), the parameters of the neural network are updated by the gradient descent method through backpropagation until convergence, and the Q function is obtained.

$$L(\theta_k) = (y - Q(s, a; \theta_k))^2, \tag{11}$$

$$\begin{aligned} \theta_k &= \theta_{k-1} + \alpha \frac{\nabla L(\theta_k)}{\nabla \theta_k} = \theta_{k-1} \\ &\quad + \alpha \times \left[-2(y - Q(s, a; \theta_k)) \frac{\nabla Q(s, a; \theta_k)}{\nabla \theta_k} \right]. \end{aligned} \tag{12}$$

4.2. Evaluation Index. In this experiment, firstly, the fault distribution of the photovoltaic power generation system is counted according to the obtained photovoltaic monitoring historical data, and then, the obtained photovoltaic monitoring data are sampled according to a certain proportion to simulate the fault distribution of other photovoltaic power generation systems to verify the effectiveness of the model, to explore the influence of fault distribution on the effect of photovoltaic power generation system fault diagnosis model based on deep reinforcement learning.

In this paper, $G - \text{mean}_{\text{total}}$ is taken as the evaluation index of fault diagnosis [23]. Two categories c_i and c_j are selected from the fault types of photovoltaic power generation system to calculate the $G - \text{mean}(c_i, c_j)$ index of the two fault diagnosis results, and then, all G – mean values are weighted and summed [24, 25]. The calculation formulas are shown in equations (13) and (14), respectively.

$$G - \text{mean}(c_i, c_j) = \sqrt{\frac{\text{TP}}{\text{TP} + \text{FN}} \times \frac{\text{TN}}{\text{TN} + \text{FP}}}, \tag{13}$$

$$G - \text{mean}_{\text{total}} = \frac{2}{K(K-1)} \sum_{1 \le i < j \le K} G - \text{mean}(c_i, c_j). \tag{14}$$

In equation (13), TP refers to the number of correct diagnoses of most samples, TN refers to the number of correct diagnoses of a few samples, FP refers to the number of diagnostic errors of most samples, and FN refers to the number of diagnostic errors of a few samples.

At the same time, accuracy and $G - \text{mean}_{\text{total}}$ index are used as evaluation indexes.

5. Example Analysis

5.1. Data and Parameter Design. Based on the historical data of a photovoltaic power station, fifty thousand groups of daytime photovoltaic power station operation monitoring data are selected and recorded as PV monitoring data set. The data set is shown in Table 1. The collected monitoring information mainly includes meteorological environment

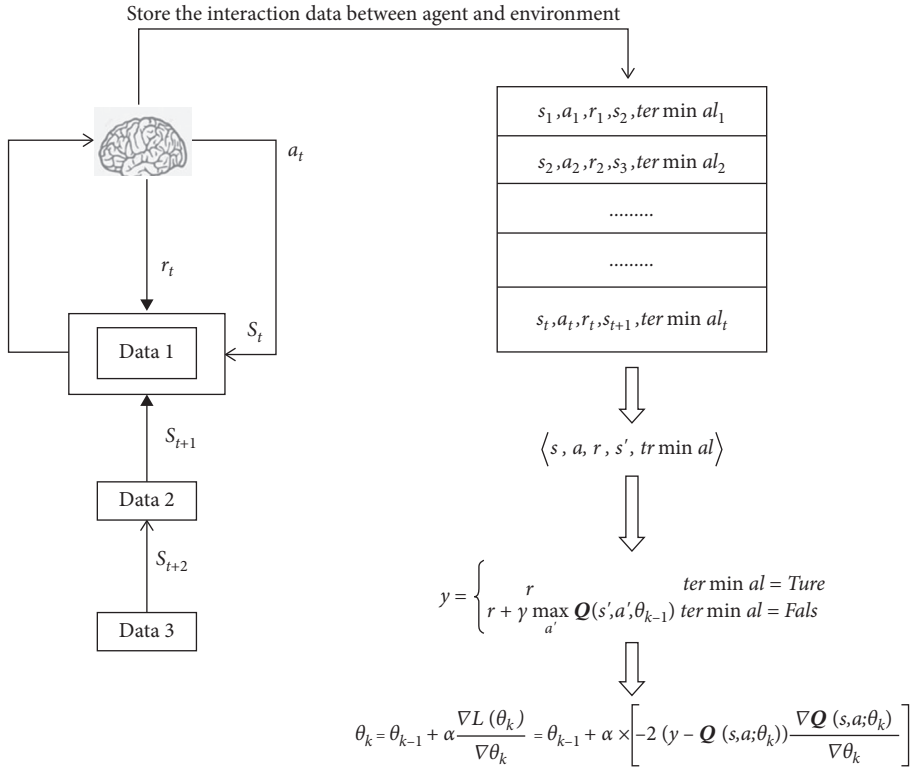

Figure 3: Schematic diagram of photovoltaic fault diagnosis based on DQN algorithm.

(1) All parameters w of the Q network are initialized randomly with the corresponding value Q
(2) Clear set D of experience playback
(3) for episode = 1, M do
(4) Initialization status $S_1 = \{x_1\}$, then get the eigenvector $\phi_1 = \phi(s_1)$
(5) for $t = 1$, T do
(6) Use ε–greedy selection action$a_t = \pi^{\varepsilon}(\phi(s_t))$
(7) Execute action a_t to get return value r_t and next state $s_{t+1} = \{x_{t+1}\}$
(8) Sets $s_{t+1} = \{x_{t+1}\}$ and gets $\phi_{t+1} = \phi\{s_{t+1}\}$
(9) Stores $(\phi_t, a_t, r_t, \phi_{t+1})$ back to experience pool
(10) Randomly collect a sample $(\phi_t, a_t, r_t, \phi_{t+1})$ from the experience pool
(11) Update:
(12) Perform gradient descent steps: $(y_j - Q(\phi_j, a_j; \theta))^2$
(13) End

Algorithm 1: DQN algorithm.

information, photovoltaic array information, combiner box information, photovoltaic inverter DC and AC side information, and grid connection information. The amount of information related to photovoltaic power generation system fault diagnosis is selected for photovoltaic power generation system fault diagnosis.

This paper mainly focuses on the five common fault types in Table 2. There are 6 operating states, including 5 fault states and one normal operating state. Each group of monitoring data has only one operation state. There are thirty thousand groups of normal operation state data, four thousand groups of data for fault 1, four thousand groups of data for fault 2, four thousand groups of data for fault 3, four thousand groups of data for fault 4, and four thousand groups of data for fault 5.

Label the six operating states, respectively, normal operation (label 0), fault 1 (label 1), fault 2 (label 2), fault 3 (label 3), fault 4 (label 4), and fault 5 (label 5).

The simulation experiment in this paper is based on the photovoltaic power station data set. To simulate the distribution of faults of different photovoltaic power generation systems and study the impact of the distribution of fault samples on the experimental results, the obtained photovoltaic monitoring data set is selected from the samples labeled 0–5 according to different methods, as follows:

Table 1: Monitoring data of photovoltaic power station (part).

Serial number	Temperature	Illumination	Humidity	...	Current	Power3	Fault type
1	24.4	1500	27%	...	8.9	1980	0
2	23.4	1500	26.9%	...	8.9	1980	0
3	23.5	1570	26.9%	...	7.6	1690	3
4	23.7	900	26.8%	...	4.3	1980	2
5	23.7	1500	26.8%	...	8.9	1980	5
6	23.6	1600	26.7%	...	8.7	1750	4
...	...	...	...	...	...	...	...

Table 2: Common fault types of the photovoltaic power generation system.

Fault ID	Fault type
1	Photovoltaic panel aging
2	Photovoltaic panel shielding and dust coverage
3	Inverter open circuit
4	Inverter short circuit
5	Inverter DC protection

(1) The distribution of various faults in the original sample is shown in Figure 4, and this data set is recorded as DS0.

(2) 4000 samples are taken from label 0, and all other labels are taken. The fault distribution data of the photovoltaic power generation system obtained after sampling is shown in Figure 5. At this time, the number of samples of various tag types is equal and the distribution is balanced. This data set is recorded as DS1.

(3) The fault types of No. 1, No. 3, and No. 5 labels are selected according to 50%. The fault distribution data of the photovoltaic power generation system obtained after sampling is shown in Figure 6. This data set is recorded as DS2.

(4) Label 0, label 2, and label 4 are sampled by 50%. The fault distribution data of the photovoltaic power generation system obtained after sampling is shown in Figure 7. This data set is recorded as DS3.

Due to the complexity of the photovoltaic power generation system, there are many related physical quantities to be monitored, and the units of each physical quantity are also different. During data analysis, the number size problem caused by the problem of each physical quantity unit may occur, which may have an impact on the analysis. Therefore, these data need to be dedimensioned before data analysis.

For the PV monitoring data set, firstly, convolution neural network CNN is used to extract the features of normalized signals. Four convolution layers with a convolution kernel size of three are used, and then, the fault of the photovoltaic power generation system is diagnosed through a fully connected neural network. Because deep reinforcement learning is a fitting regression model, the output layer cannot use the activation function when using the neural network, so the fully connected result is directly used as the output result of the neural network.

In training, the input of the neural network is the number of system states. The number of output neurons is the number of fault types. The activation functions used by all neurons are ReLU, and the loss function is the mean square error. The Adam optimizer is used for model training. The network learning rate is 0.00025 and the discount rate of immediate return is 0.99. When using the DQN algorithm and linear annealing strategy, we set ε start with one.

The imbalance rate and return function of the three extracted data sets are calculated for use in the experiment. The details are as follows:

(1) The unbalance rate and return function of the original sample DS0 data set are shown in Table 3.

(2) For the DS1 data set with four thousand samples taken from tag 0 and all other tags, the imbalance rate and return function are shown in Table 4.

(3) For the DS2 data set extracted according to 50% for labels 1, 3, and 5, the imbalance rate and return function are shown in Table 5.

(4) For the DS3 data set extracted according to 50% for labels 0, 2, and 4, the imbalance rate and return function are shown in Table 6.

5.2. Result Analysis. The imbalance rates of the four experimental data set DS0, DS1, DS2, and DS3 after processing are different, and the return function in training is also different. Among them, data set DS1 is a balanced data set, the number of other samples is equal, and other data sets can be compared with data set DS1.

Table 7 shows the fault diagnosis accuracy of various data sets under the DQN algorithm. Table 8 shows the $G - \text{mean}_{\text{total}}$ evaluation indexes of fault diagnosis under the DQN algorithm for different data sets.

It can be seen from Tables 7 and 8 that the fault diagnosis of a photovoltaic power generation system based on a deeply enhanced learning algorithm performs well under four

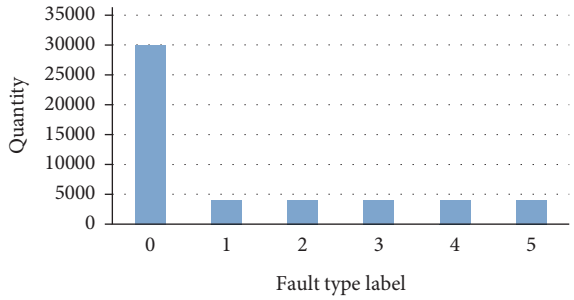

Figure 4: Original sample fault distribution.

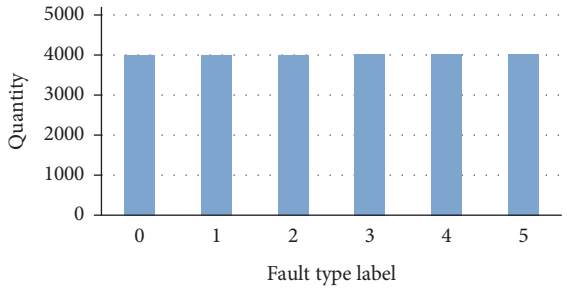

Figure 5: Take four thousand samples for label 0, and other samples remain unchanged.

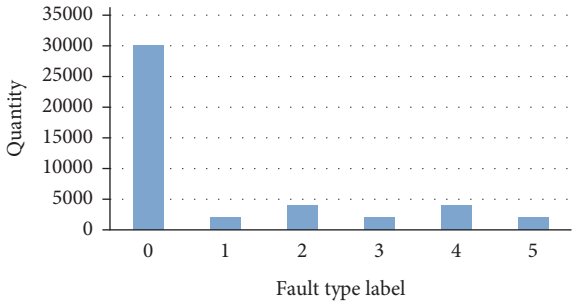

Figure 6: The 1, 3, and 5 labels are extracted by 50%.

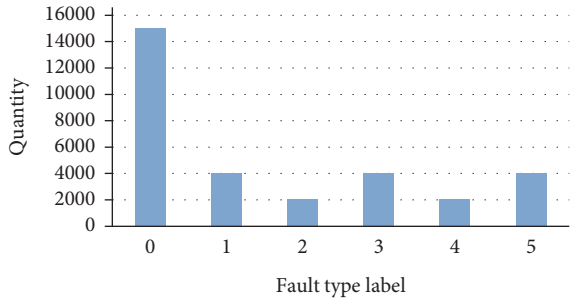

Figure 7: The 0, 2, and 4 labels are extracted by 50%.

different distributed data sets, which shows that it is feasible to introduce a deeply enhanced learning algorithm into the fault diagnosis of the photovoltaic power generation system, and reflects that this method can be applied to different photovoltaic power generation systems in different regions.

In addition, it can be seen from Tables 7 and 8 that the number of samples of each fault type of data set DS1 is the same, the distribution between samples is balanced, and the return function of each fault type is the same during training. Therefore, the fault diagnosis accuracy of the data set reaches 96.6% in the DQN algorithm. Through the comparative experiment of different distributed data sets under the same algorithm, it can be seen that the actual effect of photovoltaic power generation system fault diagnosis is related to the distribution of various faults and the balance rate between faults. For the fault diagnosis of different photovoltaic power

Table 3: Imbalance rate and return function of DS0 data set.

Fault label	0	1	2	3	4	5
Unbalance ratio	1	0.133	0.133	0.133	0.133	0.133
Correct diagnosis returns	1	0.133	0.133	0.133	0.133	0.133
Return of diagnostic errors	End	−0.133	−0.133	−0.133	−0.133	−0.133

Table 4: Imbalance rate and return function of DS1 data set.

Fault label	0	1	2	3	4	5
Unbalance ratio	1	1	1	1	1	1
Correct diagnosis returns	1	1	1	1	1	1
Return of diagnostic errors	−1	−1	−1	−1	−1	−1

Table 5: Imbalance rate and return function of DS2 data set.

Fault label	0	1	2	3	4	5
Unbalance ratio	1	0.067	0.133	0.067	0.133	0.067
Correct diagnosis returns	1	0.067	0.133	0.067	0.133	0.067
Return of diagnostic errors	End	−0.067	−0.067	−0.067	−0.067	−0.067

Table 6: Imbalance rate and return function of DS3 data set.

Fault label	0	1	2	3	4	5
Unbalance ratio	1	0.267	0.133	0.267	0.133	0.267
Correct diagnosis returns	1	0.267	0.133	0.267	0.133	0.267
Return of diagnostic errors	End	−0.267	−0.133	−0.267	−0.133	−0.267

Table 7: Fault diagnosis accuracy.

Data set	DQN (%)
DS0	86.2.
DS1	96.6
DS2	84.0
DS3	89.4

Table 8: Fault diagnosis $G - \text{mean}_{\text{total}}$.

Data set	DQN
DS0	0.862
DS1	0.965
DS2	0.840
DS3	0.893

Table 9: Fault diagnosis accuracy of three models.

Model Name	Accuracy (%)
DQN	96.60
Cascade random forest	89.63
BP neural network	88.00

generation systems, the return function should be designed according to the distribution of various faults of photovoltaic power generation systems.

In order to verify that the fault diagnosis method proposed in this paper has high accuracy, the model in this paper is simulated and compared with cascade random forest [26] and BP neural network [27]. One thousand groups of labeled data are used as training samples, and seven hundred and fifty groups of data are randomly selected as test samples. Fault samples account for 20% and 4% from fault 1 to fault 5; that is, 30 data are randomly selected for each fault type as markers for simulation experiments.

It can be seen from Table 9 that the accuracy of the DQN algorithm is 96.6%, that of the cascade random forest model is 89.63%, and that of the BP neural network model is 88.00%. Therefore, under the same sample size, the DQN algorithm has higher accuracy than cascade random forest and BP neural network.

6. Conclusion

Based on the operation and maintenance data of a photovoltaic power station, in order to realize the accurate fault diagnosis of a photovoltaic power generation system, a data-driven photovoltaic power generation system fault diagnosis method based on deep reinforcement learning is proposed. It is verified and analyzed by simulation, and the following conclusions are drawn:

(1) Through the simulation of different distributed data sets under the DQN algorithm, it is concluded that the actual effect of fault diagnosis of photovoltaic power generation system is related to the distribution of various faults and the balance rate between faults.

(2) The accuracy of the photovoltaic power generation system fault diagnosis model based on deep reinforcement learning is 96.60%. Under the same sample size, the proposed method can effectively judge the fault type of the photovoltaic power generation system and has higher accuracy than other diagnostic methods.

Data Availability

The data used to support the findings of this study are available from the corresponding author upon request.

Conflicts of Interest

The authors declare that they have no conflicts of interest.

Acknowledgments

This paper is one of the phased achievements of State Grid Gansu Electric Power Company's science and technology project "Research on distributed photovoltaic power station monitoring and forecasting technology based on ubiquitous power Internet of things holographic sensing" (522722190002) and Tianyou innovation team of Lanzhou Jiaotong University (TY202009).

References

[1] D. Zhang, M. Xin, and L. Liu, "Research on big data technology development of smart grid," *China Journal of Electrical Engineering*, vol. 35, no. 01, pp. 2–12, 2015.

[2] E. Syafaruddin and T. H. Karatepe, "Controlling of artificial neural network for fault diagnosis of photovoltaic array," in *Proceedings of the 16th International Conference on Intelligent System Application to Power Systems*, pp. 1–6, Hersonisos, Greece, September 2011.

[3] D. Pietro, F. Michela, and L. Beatrice, "An intelligent system for detecting faults in photovoltaic fields," in *Proceedings of the IEEE 11th International Conference on Intelligent Systems Design and Applications*, pp. 1341–1346, IEEE, Cordoba, Spain, December 2011.

[4] A. Massi Pavan, A. Mellit, D. De Pieri, and S. A. Kalogirou, "A comparison between BNN and regression polynomial methods for the evaluation of the effect of soiling in large scale photovoltaic plants," *Applied Energy*, vol. 108, pp. 392–401, 2013.

[5] Z. Yi and A. Etemadi, "Fault detection for photovoltaic systems based on multi-resolution signal decomposition and fuzzy inference systems," *IEEE Transactions on Smart Grid*, vol. 99, pp. 1–11, 2017.

[6] W. Yu and G. Liu, "Fault diagnosis method of photovoltaic system based on BP neural network," *Journal of Hangzhou University of Electronic Science and Technology*, vol. 38, no. 04, pp. 52–57, 2018.

[7] K.-H. Chao, C.-T. Chen, M.-H. Wang, and C.-F. Wu, "A novel fault diagnosis method based-on modified neural networks for photovoltaic systems," *Lecture Notes in Computer Science*, vol. 10, pp. 531–539, 2010.

[8] V. Navarro, A. L. D. Silva, and L. A. V. D. Carvalho, "Artificial neural networks for power systems diagnosis," in *Proceedings of the IEEE International Conference on Neural Networks*, pp. 3738–3743, Shenzhen, China, June 1994.

[9] M. Dhimish, V. Holmes, B. Mehrdadi, and M. Dales, "Diagnostic method for photovoltaic systems based on six layer detection algorithm," *Electric Power Systems Research*, vol. 151, pp. 26–39, 2017.

[10] W. Zhang, Y. Lin, and L. Jing, "Photovoltaic array fault diagnosis based on long-term and short-term memory neural network," *Thermal Power Generation*, vol. 50, no. 06, pp. 60–68, 2021.

[11] W. Han, H. Wang, and C. Wang, "Photovoltaic module fault diagnosis model based on parameter identification," *Power grid technology*, vol. 39, no. 05, pp. 1198–1204, 2015.

[12] C. Xiong, "Recent progress in deep reinforcement learning for computer vision and NLP," *Recognizing Families In the Wild*, vol. 1, 2017.

[13] M. F. Al-Roby and A. M. El-Halees, "Classifying multi-class imbalance data," *Egyptian Computer Science Journal*, vol. 37, no. 5, pp. 74–81, 2013.

[14] K. Wang, W. Wang, L. Wang, and L. Li, "An improved SOC control strategy for electric vehicle hybrid energy storage systems," *Energies*, vol. 13, no. 20, 2020.

[15] A. G. Barto, R. S. Sutton, and C. W. Anderson, "Neuronlike adaptive elements that can solve difficult learning control problems," *IEEE Transactions on Systems Man & Cybernetics*, vol. 13, no. 5, pp. 834–846, 2012.

[16] V. Mnih, K. Kavukcuoglu, D. Silver et al., "Human-level control through deep reinforcement learning," *Nature*, vol. 518, no. 7540, pp. 529–533, 2015.

[17] X. Qi, *Research on Deep Reinforcement Learning in Unbalanced Classification*, South China University of Technology, Guangzhou, China, 2015.

[18] K.. Tang, *Research on Adaptive Compressed Sensing Reconstruction Algorithm*, Nanjing University of Posts and Telecommunications, Nanjing, China, 2018.

[19] Z. Yin and J. Wang, "Fast algorithm for image reconstruction from sparse decomposition of image," *Journal of University of Electronic Science and technology*, vol. 35, no. 4, pp. 447–449, 2006.

[20] G. Hu, *Modern Signal Processing Course*, Tsinghua University, Beijing, China, 2015.

[21] jinku Guo, G. Liu, and Z. Yu, *Signal Sparse Representation Theory and its Application*, Science Press, Beijing, China, 2013.

[22] R. P. Espíndola and N. F. F. Ebecken, "On extending f-measure and g-mean metrics to multi-class problems," *WIT Transactions on Information and Communication Technologies*, vol. 35, pp. 25–34, 2005.

[23] M. F. Duarte, M. A. Davenport, D. Takhar et al., "Single-pixel imaging via compressive sampling," *IEEE Signal Processing Magazine*, vol. 25, no. 2, pp. 83–91, 2008.

[24] P. Tiago, A. Maryam, and R. Bernardete, "Diversity oriented Deep Reinforcement Learning for targeted molecule generation," *Journal of Cheminformatics*, vol. 13, no. 1, p. 21, 2021.

[25] C. Liu, Li Qiang, and K. Wang, "State-of-charge estimation and remaining useful life prediction of supercapacitors," *Renewable and Sustainable Energy Reviews*, vol. 150, 2021.

[26] Ye Jin, Q. Lu, Y. Wang, S. Chang, H. Chen, and L. Hu, "Research on photovoltaic fault diagnosis model based on cascaded random forest," *Journal of solar energy*, vol. 42, no. 03, pp. 358–362, 2021.

[27] Ke. Tang, "Application of neural network in fault diagnosis of photovoltaic power generation system," *China Equipment Engineering*, vol. 15, pp. 93-94, 2018.

Hindawi
Mathematical Problems in Engineering
Volume 2021, Article ID 5975158, 12 pages
https://doi.org/10.1155/2021/5975158

Research Article

An Accelerated Error Convergence Design Criterion and Implementation of Lebesgue-p Norm ILC Control Topology for Linear Position Control Systems

Saleem Riaz,[1] **Hui Lin**,[1] **Muhammad Waqas**,[2] **Farkhanda Afzal**,[3] **Kai Wang**,[4] **and Nasir Saeed**[5]

[1]*School of Automation, Northwestern Polytechnical University, Shaanxi, Xi'an 170072, China*
[2]*Department of Material Science and Mechanical Engineering, Beijing University of Technology, Beijing, China*
[3]*MCS, National University of Sciences and Technology, Islamabad, Pakistan*
[4]*School of Electrical Engineering, Qingdao University, Qingdao 266000, China*
[5]*Department of Electrical Engineering, National University of Technology, Islamabad, Pakistan*

Correspondence should be addressed to Farkhanda Afzal; farkhanda@mcs.edu.pk

Received 3 October 2021; Accepted 5 November 2021; Published 24 November 2021

Academic Editor: Alessandro Della Corte

Traditional and typical iterative learning control algorithm shows that the convergence rate of error is very low for a class of regular linear systems. A fast iterative learning control algorithm is designed to deal with this problem in this paper. The algorithm is based on the traditional P-type iterative learning control law, which increases the composition of adjacent two overlapping quantities, the tracking error of previous cycle difference signals, and the current error difference. Using convolution to promote Young inequalities proved strictly that, in terms of Lebesgue-p norm, when the number of iterations tends to infinity, the tracking error converges to zero in the system and presents the convergence condition of the algorithm. Compared with the traditional P-type iterative learning control algorithm, the proposed algorithm improves convergence speed and evades the defect using the norm metric's tracking error. Finally, the validation of the effectiveness of the proposed algorithm is further proved by simulation results.

1. Introduction

Iterative learning control is suitable for controlled objects with repetitive motion (running) properties in a limited time interval. It uses the data generated during the previous iteration of the system to correct undesirable control signals and generate the control signals used in the current iteration to make the system control. The performance is gradually improved, and finally the complete tracking in a limited time interval is achieved. In a comparison with other control methods, the iterative learning control method has a simple controller structure, a small amount of calculation, and only less knowledge of dynamic characteristics and can get precise control. The characteristics of precise tracking control are applied in many industrial applications such as assembly line industrial robots and chemical intermittent processes. The iterative learning control algorithm is different from other learning algorithms such as neural networks and adaptive control. The iterative learning control algorithm aims at the controlled system with repeated operation characteristics in the finite time interval. It uses the tracking error stored in the system to modify the control input one by one to realize the goal of completely tracking the expected trajectory [1–3]. The iterative learning controller can be designed without precise model information, which has the advantages of simple structure, batch processes, etc. [4, 5]. The iterative learning control [6] has achieved many research results in theoretical research and practical application since it was proposed [7, 8]. The ILC optimal approach is also used in recent days for the error convergence [9]. The soft, inflatable robotic manipulator has many useful features. High compliance and low inertia

combined with pneumatic execution assist fast but still secure operations and applications [10–12]. However, precise position control is challenging for soft manipulators since they usually take many potential coupling and uncontrollable degrees of freedom [13, 14]. Besides, soft materials' dynamical behavioral properties act as viscoelastic materials, which are problematic to model from first principles [15]. The body of a soft robot is made of soft and compliant materials in nature. This inherent softness allows them to interact with faint objects and passively adjust their shape to adapt to amorphous atmospheres [16]. These features are desired for robotic applications that require safe human-computer interaction, such as wearable robots, home assistant robots, and medical robots. These robots' soft bodies also present modeling and control challenges that have limited their functions so far. The challenge in constructing such precise control technology is the difficulty in designing a soft robot model suitable for model-based control design technology. Consider, for example, a rigid mechanical system, which is connected by rigid links through discrete joints. Since the joint displacement can completely describe the configuration of the rigid body system, the joint displacement and its derivative are the natural choice of the state variables of the rigid body robot.

Furthermore, many typical paths tracking control strategies have been adopted for soft manipulators [17]. A pneumatic control system-based open-loop and mechanical feedback control topology are discussed in [18]. Model predictive control (MPC) and neural network-based nonlinear MPC methodology are adopted to achieve error convergence for soft actuators [19]. Further advancement made in the control method is the reinforcement learning method, which is introduced for precise position tracking in these manipulators [4, 20].

In [21], the authors used a learned inverse kinematics model to enhance the tracking accuracy of position with soft processing aid. Iterative learning control (ILC) is applied in [22] to find a control strategy for the soft mesh worm robot. The authors of [23] used ILC to generate flexible impact behavior, and the authors of [24] reported an ILC-based method to learn the grasping task of a soft, fluid, and elastomeric manipulator. A graph-based, model-free flexible robot motion control framework was proposed in [25–27]. In literature [28, 29], the authors have suggested a control strategy influenced by marine life. Both of these solutions are only concerned with the coarse-grained motion of the soft robot. It has fine-grained control and dynamic response adjustment. Reference [30] uses a numerical model to control the system response, but this technique is applied to a linear predictable model. Such assumptions and the lack of feedback loops can make the system unbalanced and yield unwanted responses. References [31–33] proposed a control strategy based on the Finite Element Method (FEM), which can attain high accuracy but needs a detailed understanding of soft structural materials' mechanical properties. The controller strategy based on FEM will produce a high computational cost, making it impossible to execute in real-time on the embedded processor. The solution is to run the FEM-based mechanism in a feedforward open-loop mode, which leads to control error dominance and reduces the system's overall robustness. A model-based soft robot dynamic response optimization control strategy is proposed in [24, 34, 35].

So far, most of the literature on iterative learning control has been focused on the convergence of the algorithm in the sense of norm metric, pointing out that the algorithm's convergence can only be guaranteed if λ is large enough [36–38]. Since λ norm is an upper-bounded negative exponential function norm, the error's essential characteristics cannot be objectively quantified. The paper [39] found that even though the learning algorithm is theoretically convergent when it gets an enormous parameter value, the upper bound of the error during the initial stage of system operation often exceeds the allowable error range of practical engineering. To avoid the above defects of the λ norm, the papers [40, 41] presented the convergence of PD iterative learning control algorithm in the sense of PD measurement in the definite upper norm [42, 43]. It is found that the learning algorithm is convergent only in a subinterval of the system running time interval. In [44], to make the iterative learning control algorithm convergent in the sense of upper-bounded norm measurement, the algorithm is adjustable and learning law subinterval modified accordingly. However, the algorithm structure is quite complex, and it is not easy to apply in practical nonlinear engineering systems [45].

Furthermore, the Lebesgue-p norm is more reasonable in terms of the properties of quantization and reaction function f. It considers both the upper bound value of the function f in the whole time interval and the p integral function value at each running time [46]. Based on literature [47, 48], the tracking performance of iterative learning control is discussed using the Lebesgue-p norm, but the algorithm's convergence is not involved. In references [49, 50], the stability of iterative learning control for multistate delay linear systems is studied, and Lebesgue-2 norm is used to evaluate the learning algorithm's tracking performance. In [51], convergence analysis is carried out for PD iterative learning control with feedback information regarding Lebesgue-p norm measurement of linear time-invariant systems. Literature [52, 53] analyzes the convergence of fractional-order iterative learning control laws in the sense of the Lebesgue-p norm. Based on the Lebesgue-p norm, an accelerated initial state error convergence topology is discussed in the literature [48, 54].

Further, the convergence of variable gain iterative learning control algorithm is discussed in [55] in the sense of Lebesgue-p norm. It can be found from the analysis literature [49, 51–55] that although these research results avoid the defect of using the tracking error of the λ norm metric, they are all convergent analysis for the complete, on-regular system with $D = 0$, and their conclusions do not apply to the regular system $D \neq 0$. The reason is that, for a completely nonregular system, there must be derivative of tracking error in the iterative learning control law, namely, derivative (D) or PID iterative learning law. As for the regular system, only following error, namely, the proportional (P) iterative learning law, would be used to correct the control law. Because the traditional P-type iterative learning algorithm

only uses the previous tracking error to correct the control law, the tracking speed is low. To improve the conventional P-type iterative learning algorithm's convergence speed, an iterative learning control algorithm is proposed in the literature [56], but its convergence analysis still adopts the norm. In the theoretical analysis, λ norm was mainly used in the measurement of tracking error. However, the convergence condition of the control algorithm could be satisfied when the parameter λ was relatively large, but the maximum value of transient tracking error fell beyond the allowable range of practical engineering application in the repeated operation of the system, leading to system collapse [57–59]. In literature [60, 61], Ruan et al. studied the convergence of P-type and PD-type iterative learning control algorithms for linear time-invariant systems using Lebesgue-p (Lp) norm and found that the convergence condition of the system is independent of the value of the parameter λ and mainly depends on the system's own properties and the learning gain matrix. Furthermore, in the sense of Lebesgue-p norm, the convergence of fractional-order iterative learning control algorithm for fractional-order linear systems is discussed in literature [62]. In order to cope the above defects, this paper proposes a class of regular system to improve the convergence speed of traditional P-type iterative learning algorithm. Furthermore, it also overcomes the λ-norm to measure the tracking error using the tracking error of system before storage and the current tracking error information as well as adjust iterative axis on the difference between two-time error signal. The control input of successive modified fast iterative learning control algorithm gives accelerated and better convergence of the Lebesgue-p norm for particular satisfied conditions. This paper is organized into the following sections. Section 2 presents the problem description and its importance as well as basic mathematical background of relevant problems. Section 3 refers to the convergence and proof of the error convergence and analysis. It also gives the sufficient conditions for the validation of the proposed algorithm. Section 4 elaborates the validation of the proposed algorithm and its result discussion. Finally concluding remarks are given in Section 5.

2. Problem Description

Consider a class of regular systems with repetitive running characteristics:

$$\begin{cases} \dot{x}_k(t) = Ax_k(t) + Bu_k(t), \\ y_k(t) = Cx_k(t) + Du_k(t), \end{cases} \tag{1}$$

where k denotes the number of iterations, t is the time interval of the system, $x_k(t) \in R^n$ is the state vector of the system running in the kth time, and $u_k(t) \in R^r$ and $y_k(t) \in R^m$ are the control input vector and output vector, respectively, in the system running in the kth time. The proper dimensions are taken for all A, B, C, and D matrices.

It is considered that the initial state of the system for every iteration is consistent with the expected initial state; that is, $x_k(0) = x_d(0), k = 0, 1, 2, \ldots$.

Hypothesis 1. There is a unique ideal input $u_d(t)$ to make (2) true:

$$\begin{cases} \dot{x}_j(t) = Ax_j(t) + Bu_j(t), \\ y_j(t) = Cx_j(t) + Du_j(t), \end{cases} \tag{2}$$

where $y_d(t)$ denotes the expected trajectory and $x_d(t)$ is the expected state.

2.1. Control Target. This research's primary and vital control objective is to design a fast iterative learning control algorithm for a regular linear system described in (1) and to overcome the shortcoming of the low convergence speed of the traditional P-type iterative learning control algorithm. Simultaneously, the convergence of the algorithm is analyzed by using the Lebesgue-p norm to overcome the defect of using the tracking error measured norm.

For this control goal, the fast iterative learning control algorithm is designed as follows:

$$\mathbf{u}_{k+1}(t) = \mathbf{u}_k(t) + \mathbf{L}_{p1}\mathbf{e}_k(t) + \mathbf{L}_{d1}\Delta\mathbf{e}_k(t) + \mathbf{L}_{p2}\mathbf{e}_{k+1}(t) + \mathbf{L}_{d2}\Delta\mathbf{e}_{k+1}(t), \tag{3}$$

where $e_k(t) = y_d(t) - y_k(t)$ is the tracking error of the k thtrial and $e_{k+1}(t) = y_d(t) - y_{k+1}(t)$ is the tracking error of the $(k+1)$thtrial. $\Delta e_k(t) = e_{k-1}(t) - e_k(t)$ and $\Delta e_{k+1}(t) = e_k(t) - e_{k+1}(t)$ like the iteration axis on the difference between two-time error signal, where $\Delta e_k(t)$ is called the last difference signal and $\Delta e_{k+1}(t)$ is called the differential signal of the current time. L_{p1} is the learning gain of the kth tracking error, L_{p2} is the feedback gain of the $(k+1)$th tracking error, and L_{d1} and $L_{d2}$are the learning gain and feedback gain of the differential signal, respectively.

According to algorithm (3), when L_{p2} and L_{d2} are set at zero, algorithm (3) is the open-loop iterative learning control algorithm:

$$u_{k+1}(t) = u_k(t) + L_{p1}e_k(t) + L_{d1}\Delta e_k(t). \tag{4}$$

When $L_{p2}$and L_{d2} are all set at zero, algorithm (3) becomes the traditional P-type iterative learning control algorithm.

$$u_{k+1}(t) = u_k(t) + L_{p1}e_k(t). \tag{5}$$

The question is now raised that what would be the control law designed for linear regular system (1) to make it convergent using algorithm (3) and also what conditions should be chosen for L_{d1}, L_{p2}, and L_{d2}?

2.2. Preliminaries Knowledge. Convergence is obtained through the following definitions and lemmas: define one vector-valued function f: $[0, T] \longrightarrow R^n$ and λ norm [63] as

$$\|f(\cdot)\|_A = \sup_{1:\,0} e^{-\lambda t}\left(\max_{1\le i\le n}\left|f^i(t)\right|\right); \quad \lambda > 0. \tag{6}$$

The upper vertical-bound norm [10] and Lebesgue-p norm [64] of vector-valued function f are defined as follows:

$$\|f(\cdot)\|_{\sup} = \sup_{t\in\mathbb{D},\eta}\left(\max_{1\le i\le n}\left|f^i(t)\right|\right),$$
$$\|f(\cdot)\|_p = \left[\int_0^T \left(\max_{1\le i\le n}|f(t)|\right)^p dt\right]^{1/p}, \quad 1\leqslant p\leqslant\infty. \tag{7}$$

An important conclusion is given in the literature [65]: the upper-bounded norm is a particular case of Lebesgue-p norm, namely,

$$\lim_{p\longrightarrow\infty}\|f(\cdot)\|_p = \|f(\cdot)\|_\infty = \|f(\cdot)\|_{\sup}. \tag{8}$$

Lemma 1 [66]. *If the vectometric function g, h: $[0,T] \longrightarrow R$ is integrable for Lebesgue, then the generalized convolution Young inequality is*

$$\left\|(g^* h)(\cdot)\right\|_r \le \|g(\cdot)\|_q \|h(\cdot)\|_p, \tag{9}$$

where $(g * h)(t) = \int_0^t g(t-\tau)\mathbf{h}(\tau)d\tau$ is the convolution of g and h, and the parameters p, q, $r$satisfy $1 \le p, q, r \le +\infty$ and $1/r = 1/p + 1/q - 1$. In particular, when $r = p, q = 1$, Young's inequality applies $\|(g * h)(\cdot)\|_p \le \|g(\cdot)\|_1 \|h(\cdot)\|_p$.

3. Convergence Analysis

Theorem 1. *uses the designed algorithm (3) to control system (1) that meets Hypothesis 1. Suppose that the following conditions are satisfied:*

(1) $\rho^{-1} > 0$.

(2) $\rho^- = \rho^{-1}(\rho 1 + \rho 2) < 1$.

Among them, $\rho = \|I + DK_2\| - -\|C\exp(A\cdot(\cdot))BK_2\|_1$, $\rho 1 = \|DL_{d1}\| + \|C\exp(A\cdot(\cdot))BL_{d1}\|_1$, $\rho 2 = \|(A\cdot(\cdot)C\exp(A\cdot(\cdot))BK_1\|_1$, $K_1 = L_{p1} + L_{d1} + L_{d2}$, $K_2 = L_{p2} - L_{d2}$. As the number of iterations $k \longrightarrow \infty$, the tracking error of the system in the Lebesgue-p norm tends to zero, so the limit k goes to infinity$\|ek+1(\cdot)\|_p = 0$. The proof can be seen from system (1).

For Hypothesis 2 we need to do some assumption as follows:

Assumption 1. Assume that the initial state and expected initialization of system (1) satisfy the states$\mathbf{x}_k^1(0) = \mathbf{x}_d^1(0)(k = 1, 2, 3, \ldots,)$, where

$$\mathbf{x}_k(t) = \begin{bmatrix}\mathbf{x}_k^1(t)\\ \mathbf{x}_k^2(t)\end{bmatrix}, \quad \mathbf{x}_k^1(t) \in \mathbf{R}^r, \mathbf{x}_k^2(t) \in \mathbf{R}^{n-r}. \tag{10}$$

We consider a class of single input single output linear time-invariant systems as follows:

$$\begin{cases}\dot{x}(t) = A\mathbf{x}(t) + Bu(t),\\ y(t) = C\mathbf{x}(t),\\ \mathbf{x}(0) = 0, \quad t \in [0,T].\end{cases} \tag{11}$$

The system operation interval $x(t) \in R^n$ is an n-dimensional state variable. $u(t)$ and $y(t)$ are the control input and output, respectively. A, B, and C, are matrices with corresponding dimensions, and it is assumed that $CB \neq 0$. Without loss of generality, it is taken that the dynamics of system (1) is not entirely known, but the initial state of system (1) when repeatedly running on the interval $[0,T]$ is resettable, and the desired ideal trajectory is given. To realize the system's ultimate complete tracking of the ideal trajectory, we construct a P-type iterative learning control law with feedback information.

Obviously, in control law (3) above, when L_{p2} and L_{d2} are set at zero, the control law of degradation of specific iterative learning control law (4) is as follows:

$$u_{k+1}(t) = u_k(t) + L_{p1}e_k(t) + L_{d1}\Delta e_k(t). \tag{12}$$

Furthermore, set all the L_{d1}, L_{p2}, and L_{d2} to zero results in typical P-Type ILC law as follows:

$$u_{k+1}(t) = u_k(t) + L_{p1}e_k(t). \tag{13}$$

(1) $u_1(t)$, $t \in [0,T]$, for any initial control input when $k = 1, 2, \ldots$.

When the control input $u(t)$ in system (1) is replaced by$u_{K+1}(t)$ in control law (3), (4), or (5), the corresponding system dynamics is

$$\begin{cases}\dot{x}_{k+1}(t) = A\mathbf{x}_{k+1}(t) + Bu_{k+1}(t),\\ y_{k+1}(t) = C\mathbf{x}_{k+1}(t),\\ \mathbf{x}_{k+1}(0) = 0, \quad t \in [0,T],\end{cases} \tag{14}$$

where $x_{k+1}(t)$, $u_{k+1}(t)$, and $y_{k+1}(t)$ are the corresponding state variables, controlling input and controlling output of the system for the $(k+1)$ th iteration. In this paper, Lebesgue-p norm is used to demonstrate the convergence of the algorithm. For easy comparison, the λ upper bound norm and Lebesgue-p norm are defined as follows:

$\mathbf{f}$: $[0,T] \longrightarrow \mathbf{R}^m, \mathbf{f}(t) = [f^1(t), \ldots, f^m(t)]^{\mathrm{T}}$ is a vector-valued function, and λ is a positive real number; then, the λ norm of the vector-valued function $\mathbf{f}$ can be expressed as

$$\|\mathbf{f}(\cdot)\|_\lambda = \sup_{0\le t\le T} e^{-\lambda t}\left(\max_{1\le i\le m}\left|f^i(t)\right|\right). \tag{15}$$

The upper verticality [59] and Lebesgue-p norm [65] of vector-valued function $\mathbf{f}$ are

$$\|\mathbf{f}(\cdot)\|_{\sup} = \sup_{0\le t\le T}\left(\max_{1\le i\le m}\left|f^i(t)\right|\right)$$
$$\|\mathbf{f}(\cdot)\|_p = \left[\int_0^T \left(\max_{1\le i\le m}|f^i(t)|\right)^p dt\right]^{1/p}, \quad 1 \le p \le \infty. \tag{16}$$

In the literature [65], an important conclusion is that $\lim_{p\longrightarrow\infty}\|\mathbf{f}(\cdot)\|_p = \|f(\cdot)\|_\infty = \|\mathbf{f}(\cdot)\|_{\sup}$. That is, the upper-bounded norm is a particular case of the Lebesgue-p norm.

Proof. of Error Convergence.

There is unique ideal input according to Hypothesis 1, such as

$$\begin{cases} L_{\mathrm{PD}}(1): \\ \Delta \\ u_{k+1}(t) = u_k(t) + L_{\mathrm{p}} e_k(t) + L_{\mathrm{d}} \dot{e}_k(t) + \\ \exp(At).\phi_k(t)x(0) \\ t \in [0,T], \quad k = 1,2,\ldots, \end{cases} \tag{17}$$

where

$$\phi_k(t) = \begin{cases} \dfrac{2a^k}{h}\left(1 - \dfrac{a^k}{h}t\right), t \in \left[0, \dfrac{h}{a^k}\right), \\ \qquad\qquad\qquad\qquad a > 1, 0 < h < T, \\ 0, t \in \left[\dfrac{h}{a^k}, T\right] \end{cases} \tag{18}$$

$$x_k(0) = L_{\mathrm{d}} e_k(0) + \frac{1}{B}\left(x_k(0) - x_{k+1}(0)\right).$$

The above-mentioned Δ is an arbitrary value, subscript $k$represents the number of iterations, and L_p and L_{d} are denoted separately, describing proportional and differential learning gain matrix. □

Hypothesis 2. PD-type iterative learning controller (3) is used for system (1), if the condition $\rho < 1$ is met, where

$$\rho = \left\| I - CL_{\mathrm{d}} \right\| + \left\| C \exp(A(\cdot))\left(L_{\mathrm{p}} + AL_{\mathrm{d}}\right) \right\|_1. \tag{19}$$

Then, the number of iterations approaches infinity, and the norm of Lebesgue-P becomes significant.

(1) When $t \in [0, h/a^k)$ is caused by the deviation of initial state value, the system output cannot follow the desired trajectory.

(2) In the period$t \in [h/a^k, T]$, the tracking error monotonously tends to zero, and the system outputs the expected trajectory at the output of tracking; i.e.,$\|e_{k+1}(\cdot)\|_p \leqslant \rho \|e_k(\cdot)\|_p, \quad k = 1,2,\ldots,$

$$\lim_{k \longrightarrow \infty} \sup_{t \in [h/a^k, T]} \left\| e_{k+1}(\cdot) \right\|_p = 0,$$

$$\begin{aligned} & e_{k+1}(t) = y_d(t) - y_{k+1}(t) = e_k(t) - [\exp(At)x_{k+1}(0) - \\ & C\exp(At)x_k(0) + C\int_b {}'\exp(A(t-\tau))Bu_{k+1}(\tau)\mathrm{d}\tau + \\ & Du_{k+1}(t) - C\int_0^t \exp(A(t-\tau))Bu_k(\tau)\mathrm{d}\tau - Du_k(t)\Big] = \\ & e_k(t) - \Big[C\exp(At)\left(x_{k+1}(0) - x_k(0)\right) + C\int_0^1 \exp(A(t-\tau)) \\ & B\left(u_{k+1}(\tau) - u_k(\tau)\right)\mathrm{d}\tau + D\left(u_{k+1}(t) - u_k(t)\right)\Big]. \end{aligned} \tag{20}$$

According to Hypothesis 1 and by substituting (3) into (20), we can get

$$\begin{aligned} & e_{k+1}(t) = e_k(t) - C\int_0^t \Big[\exp(A(t-\tau))B\Big(L_{pl}e_k(\tau) + \\ & L_{d1}\Delta e_k(\tau) + L_{p2}e_{k+1}(\tau) + L_d\Delta e_{k+1}(\tau)\Big)\Big]\mathrm{d}\tau - \\ & D\Big(L_{dl}\Delta e_k(t) + L_{p2}e_{k+1}(t) + L_d\Delta e_{k+1}(t)\Big) = \\ & e_k(t) - C\int_0 \Big\{\exp(A(t-\tau))B\Big[L_{d1}e_{k-1}(\tau) + \Big(L_{p1} + \\ & L_{d2} + L_{d1}\Big)e_k(\tau) + \Big(L_{p2} - L_{d2}\Big)e_{k+1}(\tau)\Big]\Big\}\mathrm{d}\tau - D\big[L_{d1} \\ & e_{k-1}(t) + \Big(L_{p2} + L_{d2} + L_{d1}\Big)e_k(t) + \Big(L_{p2} - L_{d2}\Big) \\ & e_{k+1}(t)\big] = e_k(t) - C\int_0^1 \exp(A(t-\tau))BL_{d1} \\ & e_{k-1}(\tau)\mathrm{d}\tau - C\int_0^t \exp(A(t-\tau))BK_1e_k(\tau)\mathrm{d}\tau - \\ & C\int_0^d \exp(A(t-\tau))BK_2e_{k+1}(\tau)\mathrm{d}\tau - DL_{dl}e_{k-1}(t) - \\ & DK_1e_k(t) - DK_2e_{k+1}(t). \end{aligned} \tag{21}$$

Arrangement formula (21) can be obtained as follows:

$$\begin{aligned} & \left(I + DK_2\right)e_{k+1}(t) = \left(I - DK_1\right)e_k(t) - C\int_0^t \exp(A(t-\tau)) \\ & BL_{d1}e_{k-1}(\tau)\mathrm{d}\tau - C\int_0^t \exp(A(t-\tau))BK_1 \\ & \mathbf{e}_k(\tau)\mathrm{d}\tau - \mathbf{C}\int_0^t \exp(A(t-\tau))\mathbf{BK}_2\mathbf{e}_{k+1}(\tau)\mathrm{d}\tau - \mathbf{DL}_{d1}\mathrm{e}_{k-1}(t). \end{aligned} \tag{22}$$

Lebesgue-p norm is taken from both sides of (22), and Young inequality is applied to obtain

$$\begin{aligned} & \left\|I + DK_2\right\|\left\|e_{k+1}(\cdot)\right\|_p \leqslant \left\|I - DK_1\right\|\left\|e_k(\cdot)\right\|_p + \\ & \left\|C\exp(A\cdot(\cdot))BL_{d1}\right\|_1\left\|e_{k-1}(\cdot)\right\|_p + \\ & \left\|C\exp(A\cdot(\cdot))BK_1\right\|_1\left\|e_k(\cdot)\right\|_p + \\ & \left\|C\exp(A\cdot(\cdot))BK_2\right\|_1\left\|e_{k+1}(\cdot)\right\|_p + \\ & \left\|DL_{d1}\right\|\left\|e_{k-1}(\cdot)\right\|_p. \end{aligned} \tag{23}$$

Preparation equation (23) can be obtained as follows:

$$\begin{aligned} & \left(\left\|I + DK_2\right\| - \left\|C\exp(A\cdot(\cdot))BK_2\right\|_1\right) \\ & \left\|e_{k+1}(\cdot)\right\|_p \leqslant \left(\left\|DL_{d1}\right\| + \left\|C\exp(A\cdot(\cdot))BL_{d1}\right\|_1\right) \\ & \left\|e_{k-1}(\cdot)\right\|_p + \left(\left\|I - DK_1\right\| + \right. \\ & \left.\left\|C\exp(A\cdot(\cdot))BK_1\right\|_1\right)\left\|e_k(\cdot)\right\|_p. \end{aligned} \tag{24}$$

That is,

$$\begin{aligned} & \rho\left\|e_{k+1}(\cdot)\right\|_p \leqslant \rho_1\left\|e_{k-1}(\cdot)\right\|_p + \rho_2\left\|e_k(\cdot)\right\|_p \leqslant \\ & (\rho_1 + \rho_2)\max\left\{\left\|e_{k-1}(\cdot)\right\|_p, \left\|e_k(\cdot)\right\|_p\right\}. \end{aligned} \tag{25}$$

Procedure formula (25) can be obtained as follows:

$$\begin{aligned}\left\|e_{k+1}(\cdot)\right\|_p &\le \rho^{-1}(\rho_1+\rho_2)\max\left\{\left\|e_{k-1}(\cdot)\right\|_p,\right.\\ \left.\left\|e_k(\cdot)\right\|_p\right\} &= \overline{\rho}\max\left\{\left\|e_{k-1}(\cdot)\right\|_p,\left\|e_k(\cdot)\right\|_p\right\}.\end{aligned} \tag{26}$$

The conditions of the theorem (26) show that it satisfies $\overline{\rho} < 1$ and $k \longrightarrow^{\lim} \infty \|e_{k+1}(\cdot)\|_P = 0$ is true; that is, when the number of iterations approaches infinity, the tracking error of the system approaches zero.

Note 1. In general, the Young inequality based on generalized convolution is also true for vector-valued functions. The conclusion obtained in this paper is also true for multi-input and multioutput systems in the case of the Lebesgue-p norm defined for vector-valued functions as described in this paper. The demonstration process only needs to replace the single input single output scalar with the corresponding multidimensional vector in this paper's demonstration process and follow the vector algorithm for the deduction, so it will not be described further.

Note 2. When $L_{p1} = L_{d1} = 0$, the control law of degradation (2) for specific iterative learning control law (3), the PD-type control law (3), and the convergence conditions for $\rho = |1 - CBL_{d1}| + \|C\exp(A\cdot(\cdot))(ABL_{d1} + BL_{p1})\|_1 < 1$ show that, in the sense of Lebesgue-p norm, the convergence of PD-type iterative learning control law (3) not only depends on the system input and output matrix of CB and the differential learning gain L_{d1} values, but also depends on the proportion of the system state matrix A and learning gain L values of p. Although the convergence conditions relative to the λ norm in the sense of $\rho^* = |1 - CBL_{d1}| < 1$ are conventional, in this paper, the error in measurement and the analysis of convergence are not dependent on the parameter selection of λ, and convergence conditions $\rho < 1$ essentially describe the system dynamics and control law of learning gain decided to the convergence of the leading role.

Note 3. Compared with the convergence conditions under the λ norm, the convergence conditions given in this paper are conservative, but their convergence is no longer dependent on selecting the λ value. Simultaneously, the article gets the convergence condition as $\overline{\rho} = \rho^{-1}(\rho_1 + \rho_2) < 1$, and must satisfy $\rho^{-1} < 1$ or $(\rho_1 + \rho_2) < 1$, and so make when selecting feedback gain and the learning gain more immense freedom.

4. Simulation Examples and Discussion

4.1. Algorithm Application to Soft Robotic Position Control. The soft structure has unlimited degrees of freedom; therefore, building a model as accurate as a rigid structure is challenging. It makes the quite fine-grained control structure challenging, especially when tuning the dynamic response. Therefore, people have raised serious concerns, especially in rehabilitation applications where fine-grained control of muscles under the support of soft structures is compulsory. A further illustration is high-speed applications, such as industrial robots with soft tentacles, where fine-tuned dynamic response is necessary. As an emerging field, soft robots have very limited research on precise modeling and vibrant response tuning [67]. The method to improve the tracking accuracy and performance of flexible and inflatable manipulators is to syndicate flexible structures with stiff parts. Compared with a completely soft design, this hybrid design usually has worse inclusive compliance and higher inertia, but the degree of freedom is also reduced. As a result, the control action of the remaining degrees of freedom can be amplified, accordingly improving the tracking control performance. The literature [68–71] describes such kind of examples.

The rigid body dynamics of the soft robotic arm are calculated by defining the difference in pressure between the two actuators, $\Delta p = p_A - p_B$, as shown in Figure 1. In the positive alpha direction, the positive pressure difference p accelerates the arm (compare Figure 2). To describe the dynamics of the robotic arm with p as input and arm angle α as an output, use device recognition. Apply the same mechanism of an acknowledgement as in [72]. The following continuous-time transfer function is obtained:

$$G(s) = \frac{\alpha(s)}{\Delta p(s)} = \kappa\frac{\omega_0^2}{\omega_0^2 + 2\delta\omega_0 s + s^2}, \tag{27}$$

where the parametric values are taken as $\kappa = 7.91$ rad/bar, $\omega_0 = 14.141$/s, $\delta = 0.31$. Now discretizing this transfer function can be obtained by taking sampling time of 0.02 s.

$$\begin{aligned}\begin{bmatrix}x_1(k)\\ x_2(k)\end{bmatrix} &= \begin{bmatrix}0.96 & 0.18\\ -0.36 & 0.80\end{bmatrix}\begin{bmatrix}x_1(k-1)\\ x_2(k-1)\end{bmatrix} + \begin{bmatrix}0.09\\ 0.91\end{bmatrix}u(k-1),\\ y(k) &= [10]\begin{bmatrix}x_1(k)\\ x_2(k)\end{bmatrix},\end{aligned} \tag{28}$$

where k denotes the time index and the states are being described as $k(x_1, x_2)^T = (\alpha, \dot{\alpha})\cdot\alpha$ is the arm deflection angle that is directly measurable and that is normalized $(\pi, 10\pi)$. u is the control input and initial condition for this $u_0 = 0$. For this proposed controller, parameters are $L_{p1} = 0.5$, $L_{d1} = 0.01$, $L_{p2} = 0.2$, $L_{d2} = 0.002$, and the desired trajectory is taken as $y_d = 30^\circ \sin(2\pi t)$.

When algorithm (3) is applied to the soft robotic system (28), the system's output tries to reach its desired trajectory. It can be seen from Figure 1 that after the second iteration, the controller effort of the learning algorithm (3) is remarkable, but the error is still significant. After a few iterations, it can be noted, as in Figure 3, that the error reaches its convergent limit compared to the super norm. The error of the super norm is more prominent as well as not converging to zero. The reason is that, when iterative learning control algorithm (3) is used for system (1), if the condition $\rho < 1$ is met, where$\rho = \|I - CL_d\| + \|C\exp(A(\cdot))(L_p + AL_d)\|_1$, then as the number of iterations approaches infinity, the sup-norm is significant. When $t \in [0, h/a^k)$ is caused by the deviation of the initial state value, system output cannot follow the desired trajectory, so the error does not converge

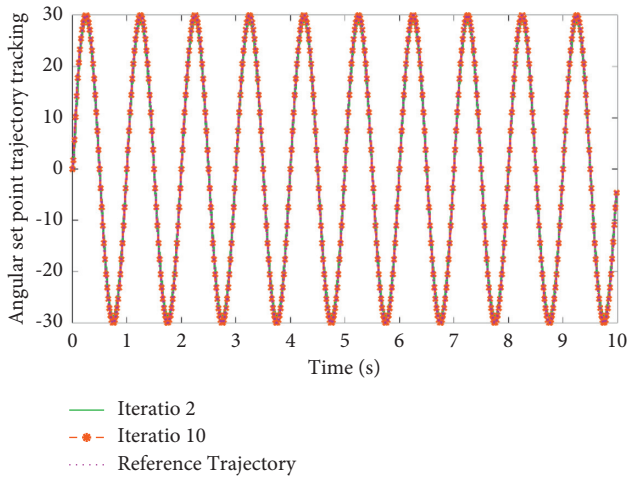

Figure 1: Position set point trajectory tracking.

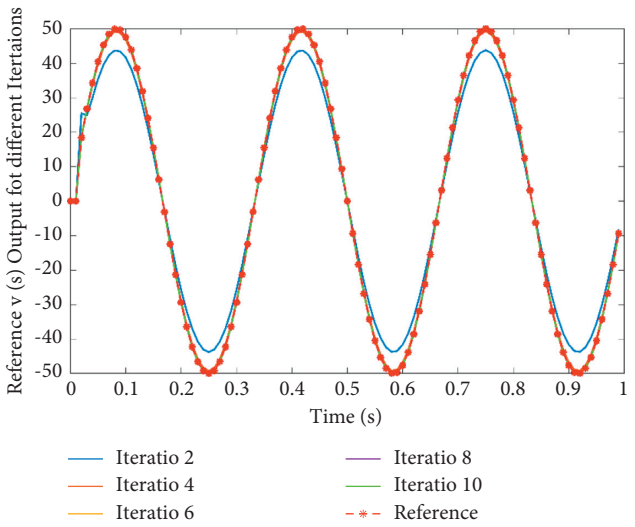

Figure 2: Position control of PMSM servo system.

to zero as expected. In contrast with the period $t \in [h/a^k, T]$, the tracking error monotonously tends to zero, and the system outputs tracks ultimately as the expected output, i.e., $\|e_{k+1}(\cdot)\|_p \leq \rho \|e_k(\cdot)\|_p, k = 1, 2, \ldots,$.

Algorithm (3) uses previous and current error information, and its convergence is proved through sufficient conditions. Under the above conditions, when the algorithms proposed in (3) and (4) are applied to the soft robotic systems (21) having an arbitrary initial state, the system tracking errors are shown in Figure 3. According to the Lebesgue-p norm, errors in the proposed algorithms' follow-up (2) and (3) tend monotonously to zero with the increase in iteration number. At this point, the tracking error reaches the error convergence limits when algorithm (3) executes four iterations. In contrast, algorithm (4) requires more iterations to achieve the convergence limit but cannot reach zero. Therefore, under the given appropriate learning gain, algorithm (3) has a faster convergence speed and higher control accuracy than algorithms (4) and (5). Algorithm (3) updating law includes feedback gains with current and

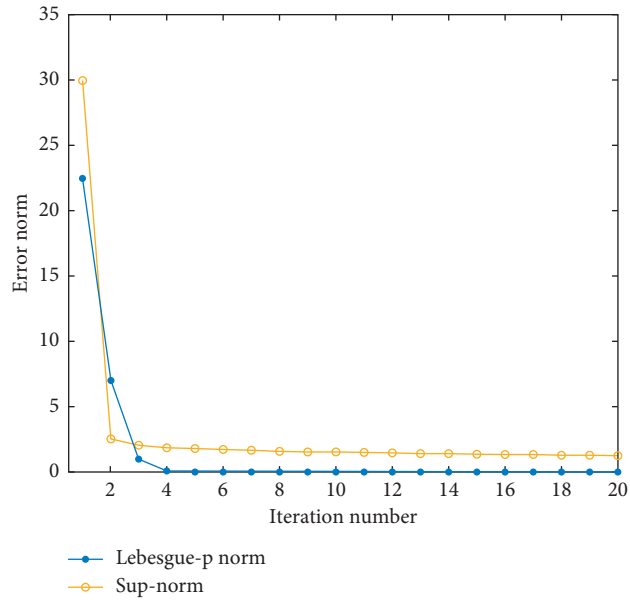

Figure 3: Comparison of error convergence.

previous information of the errors such as $e_k(t)$, $\Delta e_k(t)$ and $\Delta e_{k+1}(t)$. As the number of iterations $k \longrightarrow \infty$, the tracking error of the system in the Lebesgue-p norm tends to zero, the output of the system tries to follow within the finite time interval $t \in [0, T]$, and ultimately a perfect desired trajectory is achieved. Algorithm (3) is more robust and guarantees monotonic error convergence for position tracking, especially in soft robotic applications. This robust topology is also applied to higher-order high dynamical systems with little modifications in the learning proportional and derivative gains according to the system requirements.

4.2. Validation for Typical PMSM Servo Position Control System. A typical PMSM (permanent magnet synchronous motor)-based servo position control system is taken as an example for validating the proposed algorithm. The standard state-space linear servo position control model of the PMSM can be described as follows:

$$\begin{cases} \dfrac{d\theta(t)}{dt} = \omega(t), \\ \dfrac{d\omega(t)}{dt} = \dfrac{1}{J} T_e(t) - \dfrac{1}{J} T_L(t) - \dfrac{B_f}{J} \omega(t), \end{cases} \tag{29}$$

which the value of each parameter is described in Table 1.

The state-space equation for the given system in a standard form can be expressed as follows:

$$\begin{cases} \dot{x}(t) = Ax(t) + Bu(t), \\ y(t) = Cx(t). \end{cases} \tag{30}$$

The states of the system are described as $x = [\theta(t), \omega(t)]^T$, and the control input is $u = T_e(t) = k_t i_q(t)$, for which each matrix of the system can be calculated as follows:

Table 1: PMSM servo control parameters.

Parameter	Symbol
Electromagnetic torque	T_e
Load torque	T_L
Mechanical angle of the motor	$\theta(t)$
Coefficient of viscous friction	B_f
Mechanical angular velocity	$\omega(t)$
System moment of inertia	J

$$A = \begin{bmatrix} 0 & 1 \\ 0 & \dfrac{-B_f}{J} \end{bmatrix},$$
$$B = \begin{bmatrix} 0 & \dfrac{1}{J} \end{bmatrix}^{\mathrm{T}}, \tag{31}$$
$$C = \begin{bmatrix} 1 & 0 \end{bmatrix}.$$

To validate the Lebesgue-p norm proposed in this paper, we assume the parameters to be as follows: the rotational inertia $J = 0.004\,\mathrm{kg.m}^2$ and viscous friction coefficient $B_f = 0.0001\,\mathrm{Nm/rad/s}$. For ILC, the parameters are taken as $L_{p1} = 0.8$, $L_{d1} = 0.01$, $L_{p2} = 0.3$, $L_{d2} = 0.006$, and the desired trajectory for the system is $y_d = 50^{\circ}\sin(2\pi t)$.

The controller's effort is shown in Figure 2, which describes the output of system (31), attempting to follow the desired position. The figure displays the simulation results and interpretation and also shows the control consequence of a particular iteration of the method. As we have seen, the performance of the second iteration is not better and initially has significant errors, the delay is relatively apparent, and the error is critical. The operation of the ILC control additionally reduces the error and attempts to exceed its goal. The error converges rapidly to its limit after a limited amount of time and several iterations, and the performance of the method precisely tracks the target location.

In comparison, these conditions still occur despite modifying the controller parameters several times. As shown in Figure 2, the system's desired and output position can be seen and automatically updated by the output accurately following the optimal level. The controller's action is stable and sufficient for the error to converge to its monotone convergence limit under satisfactory conditions.

The system's tracking curve is seen in Figure 2 in the second iteration of the learning system, and the error curve indicates that the error is too high. In Figure 4, the results of the different iterations errors are shown. The error trajectory of the device is already greatly decreased, and the most significant error in the tenth iteration relative to the second trial (the results are shown in Figure 4) has very good tracking accuracy for algorithm (3) as compared to the other two algorithms. The error is too small to meet the demands of the system. Therefore, we can say that the proposed Lebesgue-p norm scheme for accurate position tracking is significantly fast compared to algorithms (4) and (5). The sufficient conditions and the Lebesgue-P error criterion suggest that the findings are acceptable and that the

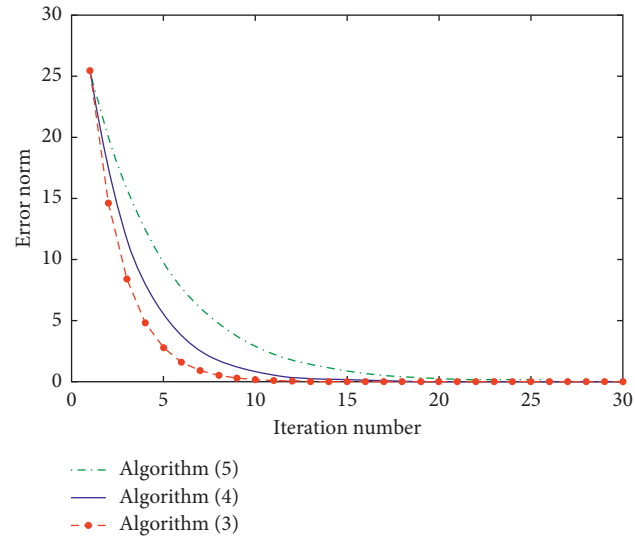

Figure 4: Error convergence comparison of algorithms (3)–(5).

mechanism is stable enough to monitor the PMSM servo control position. This approach can also be implemented with a specific additional extension to other complicated speed and position servo systems for the broad range of traditional automation applications.

4.3. Application and Validity for Other Linear Systems. The following linear system is taken to validate the proposed algorithm's effectiveness further, and it is obtained from [73].

$$\begin{cases} \dot{x}(t) = \begin{bmatrix} -2 & 3 \\ 0 & 1 \end{bmatrix} x(t) + \begin{bmatrix} 1 \\ 0 \end{bmatrix} u(t), \\ y(t) = \begin{bmatrix} 2 & 0 \end{bmatrix} x(t) + u(t), \end{cases} \tag{32}$$

where $t \in [0, 2]$. Algorithm (3) was used to control system (32). It was assumed that $y_d(t) = \sin(5t)$ of the desired trajectory, and the initial state of the system was$x_1(0) = 0$ $x_2(0) = 0$. The initial control was set as $u(t) = 0$, and $L_{p1} = 0$. If the convergence condition is satisfied, then the control parameters are chosen as $L_{p1} = 0.3$, $L_{d1} = 0.1$, $L_{p2} = 0.2$, and $L_{d2} = 0.1$. To validate the effectiveness of algorithm (3) proposed in this paper, simulation comparisons are made with open-loop algorithm (4) and traditional P-type algorithm (5). The simulation results are shown in Figure 5–7. Figure 5 shows the output tracking curve of different iteration times during algorithm (3) control. Figure 6 shows the tracking error curve in the sense of the norm of upper certainties and Lebesgue-2 norm; Figure 7 shows the tracking error curves of algorithms (3)–(5) in the Lebesgue-2 norm sense.

As shown in Figure 5, after the 20^{th} iteration, the system output has been fully tracked on the expected trajectory in a finite time. It can be seen from Figure 6 that the Lebesgue-2 norm and the upper-bounded norm of algorithm (3) converge to 0. As can be seen from Figure 7, algorithm (3) has the highest convergence rate, algorithm (4) comes second, and algorithm (5) has the lowest convergence rate. The

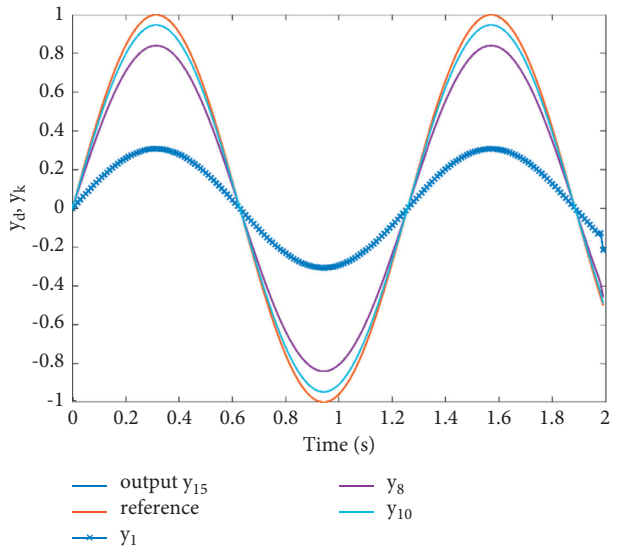

Figure 5: Desired tracking trajectory vs. output curve for different iterations.

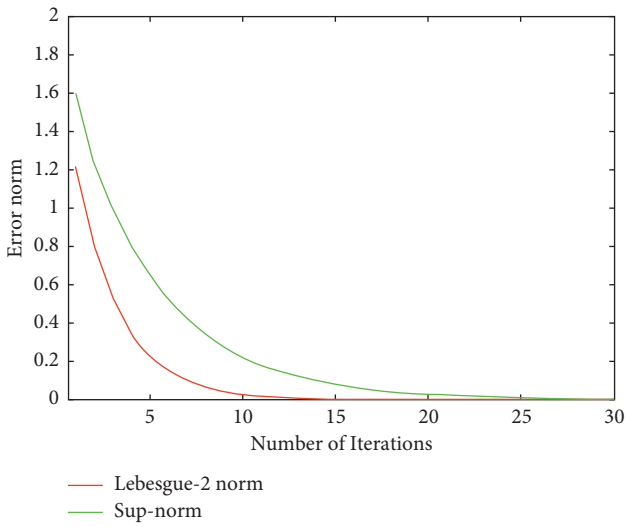

Figure 6: Error convergence rate.

reason lies in the fact that algorithm (4) increases the difference signal of error in two adjacent iterations based on algorithm (5). Algorithm (3) uses the current error and the previous error to form the difference signal, while algorithm (4) only uses the previous error to create the difference signal. Compared with algorithm (4), algorithm (3) makes full use of the current error information. To better illustrate the effectiveness of algorithm (3) designed in this paper, the numerical values of tracking errors of algorithms (3)–(5) under different iteration times are given below, as shown in Table 2.

Table 2 shows that the tracking error of algorithms (3)–(5) in the first iteration is 1.217316. After the 15th iteration, the error of algorithm (5) is 0.07538, and the error of algorithm (4) is 0.024335. The error of algorithm (3) is 0.003683. From the vertical data in Table 2, the three algorithms' tracking error can be reduced successively with the

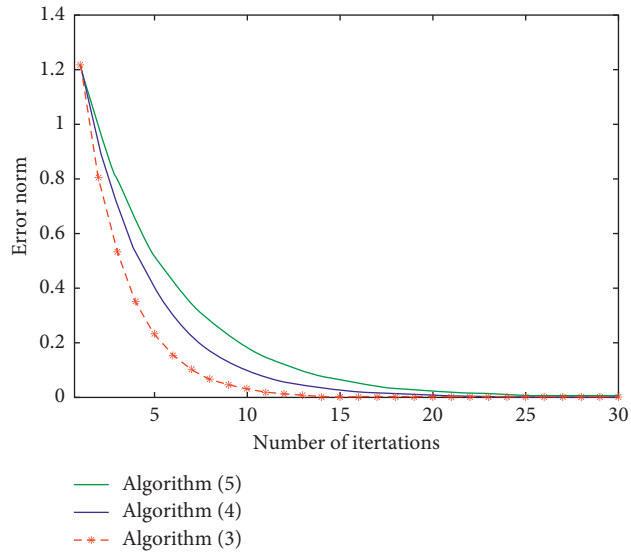

Figure 7: Comparison of error convergence curves.

Table 2: Comparison of error convergence rate at the same iteration number.

Iteration number k	Algorithm (3) e	Algorithm (4) e	Algorithm (5) e
1	1.217316	1.217316	1.217316
6	0.153358	0.300994	0.450737
8	0.066961	0.172115	0.302922
10	0.029238	0.098419	0.203581
15	0.003683	0.024335	0.07538

increase of iteration number. However, from the horizontal data in Table 2, the tracking error of algorithm (3) is the smallest, followed by algorithm (4), and that of algorithm (5) under the same iteration number is the largest. Therefore, it is easily observed from Table 1 that the convergence speed of the fast iterative learning control algorithm (3) designed in this paper is significantly higher than that of algorithms (4) and (5).

4.4. Validation for Other Linear System. To illustrate the tracking capability of algorithm (3) in this paper for different expected signals, let us assume the expected trajectory, y_d, to be as follows:

$$y_d(t) = \begin{cases} 0, & 0 \le t < 0.4, \\ 1, & 0.4 \le t < 0.8, \\ 0, & 0.8 \le t < 1.2, \\ 1, & 1.2 \le t < 1.6, \\ 0, & 1.6 \le t \le 2. \end{cases} \quad \text{other linear system,} \tag{33}$$

The value is the same as that of the above expected sinusoidal trajectory. The tracking effect of the output curve on the predicted trajectory under different iteration times is shown in Figure 8, which shows the tracking effect of iteration 2, iteration 10, and iteration 15.

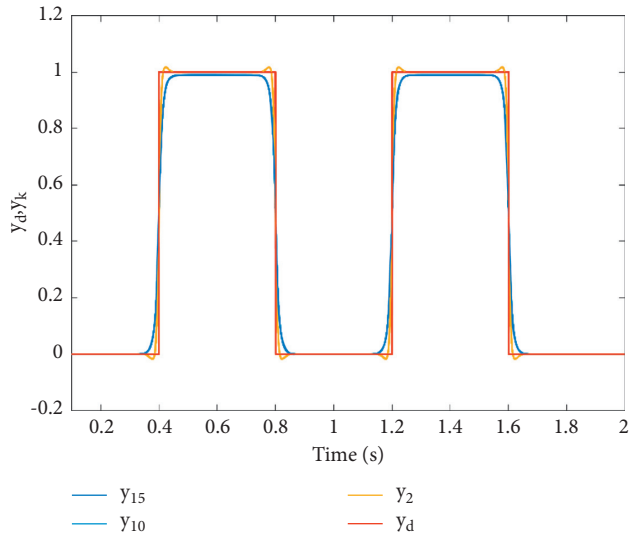

Figure 8: Desired tracking trajectory vs. output of the system.

It can be seen from Figures 5 and 8 that the control algorithm (3) designed in this paper can achieve complete tracking of different expected tracks in the finite time interval with the increase of iteration numbers for the predicted trajectory of slow and abrupt changes. The new proposed updating input iterative learning law includes feedback gains with current and previous information of the errors such as $e_k(t)$, $\Delta e_k(t)$, and $\Delta e_{k+1}(t)$. As the number of iterations $k \longrightarrow \infty$, the system's tracking error in the Lebesgue-p norm tends to zero. The system's output tries to follow within the finite time interval as specified for this system, $t \in [0, 2]$. Ultimately, a perfect desired trajectory y_d is achieved. The result of the system is shown for the different iterations in Figure 8. When the tracking error converges after 15 or more iterations and tends to zero, the system's output precisely follows the desired trajectory y_d. Accordingly, algorithm (3) in the sense of the Lebesgue-p norm is robust and satisfies $\overline{\rho} < 1$, and $k \longrightarrow^{\lim} \infty \|e_{k+1}(\cdot)\|_P = 0$ is accurate. When the number of iterations approaches infinity, the tracking error of the system approaches zero. This robust control topology is also applied to higher-order dynamic systems with little change in proportional and derivative learning gains as required by the system. Furthermore, it can also correctly work for the motor position control, aircraft altitude and latitude control, angle of attack, soft articulated robot position control, satellite positioning systems, and piezoelectric nanopositioning control systems.

5. Conclusion

This research paper has discussed a fast iterative learning control algorithm for a class of regular linear systems with direct input-output transmission terms of Lebesgue-p norm. The convergence of the algorithm is proved under the Lebesgue-p norm, and sufficient conditions are given for the convergence of the norm form of the algorithm. This algorithm not only has a higher convergence rate than the traditional P-type algorithm, but also avoids the defect of using the tracking error of the norm metric and increases the degree of freedom of learning gain selection. Due to the convolution limitation of Lemma 1, the algorithm in this paper is only applicable to regular linear systems. Therefore, in future studies, the convergence of typical nonlinear systems in the Lebesgue-p norm can be further analyzed.

Data Availability

The data used to support the findings of this study are included within the article.

Conflicts of Interest

The authors declare that they have no conflicts of interest.

References

[1] L. Zhou, L. Jia, Y.-L. Wang, D. Peng, and W. Tan, "An integrated robust iterative learning control strategy for batch processes based on 2D system," *Journal of Process Control*, vol. 85, pp. 136–148, 2020.

[2] R. Mengacci, F. Angelini, M. G. Catalano, G. Grioli, A. Bicchi, and M. Garabini, "On the motion/stiffness decoupling property of articulated soft robots with application to model-free torque iterative learning control," *The International Journal of Robotics Research*, vol. 40, no. 1, pp. 348–374, 2020.

[3] W. Qiu, Z. Xiong, J. Zhang, Y. Hong, and W. Li, "Integrated predictive iterative learning control based on updating reference trajectory for point-to-point tracking," *Journal of Process Control*, vol. 85, pp. 41–51, 2020.

[4] X. Wu and C. Wang, "Model-free optimal tracking control for an aircraft skin inspection robot with constrained-input and input time-delay via integral reinforcement learning," *International Journal of Control, Automation and Systems*, vol. 18, no. 1, pp. 245–257, 2020.

[5] W. Yu, J. Song, and J. Yu, "Robust hybrid controller design for batch processes with time delay and its application in industrial processes," *International Journal of Control, Automation and Systems*, vol. 17, no. 11, pp. 2881–2894, 2019.

[6] Y. Tian, Z. Sun, H. Li, and J. Wang, "A review of optimal and control strategies for dynamic walking bipedal robots," *Acta Automatica Sinica*, vol. 42, no. 8, pp. 1142–1157, 2016.

[7] D. Van Chien, K. J. Sung, and J.-W. Kim, "Sensory reflex control of a humanoid robot using FSR sensor," in *Proceedings of the 2015 IEEE International Conference on Advanced Intelligent Mechatronics (AIM)*, pp. 1406–1409, IEEE, Busan, South Korea, July 2015.

[8] J.-W. Kim, T. T. Tran, C. Van Dang, and B. Kang, "Motion and walking stabilization of humanoids using sensory reflex control," *International Journal of Advanced Robotic Systems*, vol. 13, no. 2, p. 77, 2016.

[9] F. Memon and C. Shao, "An optimal approach to online tuning method for PID type iterative learning control," *International Journal of Control, Automation and Systems*, vol. 18, no. 8, pp. 1926–1935, 2020.

[10] B. Gorissen, D. Reynaerts, S. Konishi, K. Yoshida, J.-W. Kim, and M. De Volder, "Elastic inflatable actuators for soft robotic applications," *Advanced Materials*, vol. 29, no. 43, Article ID 1604977, 2017.

[11] C. M. Best, J. P. Wilson, and M. D. Killpack, "Control of a pneumatically actuated, fully inflatable, fabric-based, humanoid robot," in *Proceedings of the 2015 IEEE-RAS 15th*

International Conference on Humanoid Robots (Humanoids), pp. 1133–1140, IEEE, Seoul, South Korea, November 2015.

[12] S. Sanan, M. H. Ornstein, and C. G. Atkeson, "Physical human interaction for an inflatable manipulator," in *Proceedings of the 2011 Annual International Conference of the IEEE Engineering in Medicine and Biology Society*, pp. 7401–7404, IEEE, Boston, MA, USA, August 2011.

[13] C. C. Beltran-Hernandez, D. Petit, I. G. Ramirez-Alpizar et al., "Learning force control for contact-rich manipulation tasks with rigid position-controlled robots," *IEEE Robotics and Automation Letters*, vol. 5, no. 4, pp. 5709–5716, 2020.

[14] L. Pan, T. Gao, F. Xu, and L. Zhang, "Enhanced robust motion tracking control for 6 degree-of-freedom industrial assembly robot with disturbance adaption," *International Journal of Control, Automation and Systems*, vol. 16, no. 2, pp. 921–928, 2018.

[15] R. Garcia, "Nanomechanical mapping of soft materials with the atomic force microscope: methods, theory and applications," *Chemical Society Reviews*, vol. 49, no. 16, pp. 5850–5884, 2020.

[16] B. Mosadegh, P. Polygerinos, C. Keplinger et al., "Pneumatic networks for soft robotics that actuate rapidly," *Advanced Functional Materials*, vol. 24, no. 15, pp. 2163–2170, 2014.

[17] Z. Lu, "Iterative learning control algorithm for optimal path of robot," *Journal of Intelligent and Fuzzy Systems*, pp. 1–8.

[18] T. G. Thuruthel, E. Falotico, M. Manti, and C. Laschi, "Stable open loop control of soft robotic manipulators," *IEEE Robotics and Automation Letters*, vol. 3, no. 2, pp. 1292–1298, 2018.

[19] M. T. Gillespie, C. M. Best, and M. D. Killpack, "Simultaneous position and stiffness control for an inflatable soft robot," in *Proceedings of the 2016 IEEE international conference on robotics and Automation (ICRA)*, pp. 1095–1101, IEEE, Stockholm, Sweden, May 2016.

[20] Y. Ansari, M. Manti, E. Falotico, M. Cianchetti, and C. Laschi, "Multiobjective optimization for stiffness and position control in a soft robot arm module," *IEEE Robotics and Automation Letters*, vol. 3, no. 1, pp. 108–115, 2017.

[21] F. Reinhart and J. J. Steil, "Hybrid mechanical and data-driven modeling improves inverse kinematic control of a soft robot," *Procedia Technology*, vol. 26, 2016.

[22] S. Seok, C. D. Onal, K.-J. Cho, R. J. Wood, D. Rus, and S. Kim, "Meshworm: a peristaltic soft robot with antagonistic nickel titanium coil actuators," *IEEE/ASME Transactions on mechatronics*, vol. 18, no. 5, pp. 1485–1497, 2012.

[23] C. Della Santina, M. Bianchi, G. Grioli et al., "Controlling soft robots: balancing feedback and feedforward elements," *IEEE Robotics and Automation Magazine*, vol. 24, no. 3, pp. 75–83, 2017.

[24] A. D. Marchese, R. Tedrake, and D. Rus, "Dynamics and trajectory optimization for a soft spatial fluidic elastomer manipulator," *The International Journal of Robotics Research*, vol. 35, no. 8, pp. 1000–1019, 2016.

[25] V. Vikas, P. Grover, and B. Trimmer, "Model-free control framework for multi-limb soft robots," in *Proceedings of the 2015 IEEE/RSJ International Conference on Intelligent Robots and Systems (IROS)*, pp. 1111–1116, IEEE, Hamburg, Germany, 2015.

[26] H.-T. Lin, G. G. Leisk, and B. Trimmer, "GoQBot: a caterpillar-inspired soft-bodied rolling robot," *Bioinspiration & Biomimetics*, vol. 6, no. 2, Article ID 026007, 2011.

[27] X. Zhu and J. Wang, "Double iterative compensation learning control for active training of upper limb rehabilitation robot," *International Journal of Control, Automation and Systems*, vol. 16, no. 3, pp. 1312–1322, 2018.

[28] M. Calisti, M. Giorelli, G. Levy et al., "An octopus-bioinspired solution to movement and manipulation for soft robots," *Bioinspiration & Biomimetics*, vol. 6, no. 3, Article ID 036002, 2011.

[29] A. D. Marchese, C. D. Onal, and D. Rus, "Autonomous soft robotic fish capable of escape maneuvers using fluidic elastomer actuators," *Soft Robotics*, vol. 1, no. 1, pp. 75–87, 2014.

[30] P. Polygerinos, S. Lyne, Z. Wang et al., "Towards a soft pneumatic glove for hand rehabilitation," in *Proceedings of the 2013 IEEE/RSJ International Conference on Intelligent Robots and Systems*, pp. 1512–1517, IEEE, Tokyo, Japan, November 2013.

[31] F. Largilliere, V. Verona, E. Coevoet, M. Sanz-Lopez, J. Dequidt, and C. Duriez, "Real-time control of soft-robots using asynchronous finite element modeling," in *Proceedings of the 2015 IEEE International Conference on Robotics and Automation (ICRA)*, pp. 2550–2555, IEEE, Seattle, WA, USA, May 2015.

[32] F. Faure, C. Duriez, H. Delingette et al., "Sofa: a multi-model framework for interactive physical simulation," in *Soft Tissue Biomechanical Modeling for Computer Assisted Surgery*, pp. 283–321, Springer, Berlin, Germany, 2012.

[33] C. Duriez, "Control of elastic soft robots based on real-time finite element method," in *Proceedings of the 2013 IEEE international conference on robotics and automation*, pp. 3982–3987, IEEE, Karlsruhe, Germany, May 2013.

[34] F. Renda, M. Giorelli, M. Calisti, M. Cianchetti, and C. Laschi, "Dynamic model of a multibending soft robot arm driven by cables," *IEEE Transactions on Robotics*, vol. 30, no. 5, pp. 1109–1122, 2014.

[35] I. A. Gravagne, C. D. Rahn, and I. D. Walker, "Large deflection dynamics and control for planar continuum robots," *IEEE/ASME Transactions on Mechatronics*, vol. 8, no. 2, pp. 299–307, 2003.

[36] G. Chen, J. Wang, and L. Wang, "Gait planning and compliance control of a biped robot on stairs with desired ZMP," *IFAC Proceedings Volumes*, vol. 47, no. 3, pp. 2165–2170, 2014.

[37] J. Li, W.-D. Chen, L.-J. Wang, X.-G. Gao, J. Yang, and M.-J. Li, "Stability control for biped walking on unknown rough surface," *Dianzi Xuebao (Acta Electronica Sinica)*, vol. 38, no. 11, pp. 2669–2674, 2010.

[38] S. Riaz, H. Lin, and M. P. Akhter, "Design and implementation of an accelerated error convergence criterion for norm optimal iterative learning controller," *Electronics*, vol. 9, no. 11, p. 1766, 2020.

[39] H. Sasaki, T. Horiuchi, and S. Kato, "A study on behavior acquisition of mobile robot by deep Q-network," *ICIC Express Letters. Part B, Applications: An International Journal of Research and Surveys*, vol. 8, no. 4, pp. 727–733, 2017.

[40] L. Tai, S. Li, and M. Liu, "A deep-network solution towards model-less obstacle avoidance," in *Proceedings of the 2016 IEEE/RSJ international conference on intelligent robots and systems (IROS)*, pp. 2759–2764, IEEE, Daejeon, South Korea, October 2016.

[41] M. Hamidaoui, C. Shao, and S. Haouassi, "A PD-type iterative learning control algorithm for one-dimension linear wave equation," *International Journal of Control, Automation and Systems*, vol. 18, no. 4, pp. 1045–1052, 2020.

[42] X. Li and X. Ruan, "Monotonic convergence and robustness of higher-order gain-adaptive iterative learning control," *International Journal of Robust and Nonlinear Control*, vol. 30, no. 10, pp. 3960–3981, 2020.

[43] S. Riaz, H. Lin, M. Bilal Anwar, and H. Ali, "Design of PD-type second-order ILC law for PMSM servo position control," *Journal of Physics: Conference Series*, vol. 1707, Article ID 012002, 2020.

[44] S. Gu, E. Holly, T. Lillicrap, and S. Levine, "Deep reinforcement learning for robotic manipulation with asynchronous off-policy updates," in *Proceedings of the 2017 IEEE international conference on robotics and Automation (ICRA)*, pp. 3389–3396, IEEE, Singapore, May 2017.

[45] K. Wan and Y.-S. Wei, "Adaptive ILC of tracking non-repetitive trajectory for two-dimensional nonlinear discrete time-varying fornasini-marchesini systems with iteration-varying boundary states," *International Journal of Control, Automation and Systems*, vol. 19, no. 1, pp. 417–425, 2020.

[46] C. Tan, S. Wang, and J. Wang, "Robust iterative learning control for iteration-and time-varying disturbance rejection," *International Journal of Systems Science*, vol. 51, no. 3, pp. 461–472, 2020.

[47] V. Mnih, "Playing atari with deep reinforcement learning," 2013, https://arxiv.org/abs/1312.5602.

[48] P. Gu and S. Tian, "P-type iterative learning control with initial state learning for one-sided Lipschitz nonlinear systems," *International Journal of Control, Automation and Systems*, vol. 17, no. 9, pp. 2203–2210, 2019.

[49] M. H. Raibert, "Hopping in legged systems - modeling and simulation for the two-dimensional one-legged case," *IEEE Transactions on Systems, Man, and Cybernetics*, vol. SMC-14, no. 3, pp. 451–463, 1984.

[50] Z. Qunli, "The application of zhang-gradient method for iterative learning control," *Journal of Advances in Applied Mathematics*, vol. 5, no. 1, p. 21, 2020.

[51] H. Jun and H. Li, "Trajectory planning and simulation of robot in joint coordinate system," *Journal of Nanjing University of Science and Technology*, vol. 24, no. 6, pp. 540–543, 2000, ISSU 115.

[52] J. Yang, Q. Huang, J. Li, C. Li, and K. Li, "Walking pattern generation for humanoid robot considering upper body motion," in *Proceedings of the 2006 IEEE/RSJ International Conference on Intelligent Robots and Systems*, pp. 4441–4446, IEEE, Beijing, China, October 2006.

[53] L. Baird, "Residual algorithms: reinforcement learning with function approximation," in *Machine Learning Proceedings*, pp. 30–37, Elsevier, Amsterdam, Netherlands, 1995.

[54] V. Mnih, K. Kavukcuoglu, D. Silver et al., "Human-level control through deep reinforcement learning," *Nature*, vol. 518, no. 7540, pp. 529–533, 2015.

[55] T. Lan and H. Lin, "Accelerated iterative learning control algorithm with variable gain and adjustment of learning interval," *Systems Engineering and Electronics*, vol. 39, no. 4, pp. 883–887, 2017.

[56] W. Hong-Bin and W. Yan, "Open-closed loop ILC corrected with angle relationship of output vectors for tracking control of manipulator," *Acta Automatica Sinica*, vol. 36, no. 12, pp. 1758–1765, 2010.

[57] P. Cheng, S. He, X. Luan, and F. Liu, "Finite-region asynchronous H∞ control for 2D Markov jump systems," *Automatica*, vol. 129, Article ID 109590, 2021.

[58] P. Cheng, S. He, J. Cheng, X. Luan, and F. Liu, "Asynchronous output feedback control for a class of conic-type nonlinear hidden Markov jump systems within a finite-time interval," *IEEE Transactions on Systems, Man, and Cybernetics: Systems*, 2020.

[59] H.-S. Lee and Z. Bien, "A note on convergence property of iterative learning controller with respect to sup norm," *Automatica*, vol. 33, no. 8, pp. 1591–1593, 1997.

[60] X. Ruan, Z. Z. Bien, and Q. Wang, "Convergence characteristics of proportional-type iterative learning control in the sense of Lebesgue-p norm," *IET Control Theory & Applications*, vol. 6, no. 5, pp. 707–714, 2012.

[61] X. Ruan, Z. Z. Bien, and Q. Wang, "Convergence properties of iterative learning control processes in the sense of the Lebesgue-P norm," *Asian Journal of Control*, vol. 14, no. 4, pp. 1095–1107, 2012.

[62] L. Li, "Lebesgue-p norm convergence analysis of PDα-type iterative learning control for fractional-order nonlinear systems," *Discrete Dynamics in Nature and Society*, vol. 2018, Article ID 5157267, 10 pages, 2018.

[63] M. Hieber and J. Prüss, "Functional calculi for linear operators in vector-valued $ L^p $-spaces via the transference principle," *Advances in Differential Equations*, vol. 3, no. 6, pp. 847–876, 1998.

[64] E. S. Pérez, "Compactness arguments for spaces of $ p $-integrable functions with respect to a vector measure and factorization of operators through Lebesgue-Bochner spaces," *Illinois Journal of Mathematics*, vol. 45, no. 3, pp. 907–923, 2001.

[65] M. A. Pinsky, *Introduction to Fourier Analysis and Wavelets*, American Mathematical Society, Providence, RI, USA, 2008.

[66] X.-E. Ruan, J.-B. Lian, and H.-Z. Wu, "Convergence of iterative learning control with feedback information in the sense of Lebesgue-p norm," *Acta Automatica Sinica*, vol. 37, no. 4, pp. 513–516, 2011.

[67] M. Hofer and R. D'Andrea, "Design, modeling and control of a soft robotic arm," in *Proceedings of the 2018 IEEE/RSJ International Conference on Intelligent Robots and Systems (IROS)*, pp. 1456–1463, IEEE, Madrid, Spain, October 2018.

[68] H.-J. Kim, A. Kawamura, Y. Nishioka, and S. Kawamura, "Mechanical design and control of inflatable robotic arms for high positioning accuracy," *Advanced Robotics*, vol. 32, no. 2, pp. 89–104, 2018.

[69] M. Jordan, D. Pietrusky, M. Mihajlov, and O. Ivlev, "Precise position and trajectory control of pneumatic soft-actuators for assistance robots and motion therapy devices," in *Proceedings of the 2009 IEEE International Conference on Rehabilitation Robotics*, pp. 663–668, IEEE, Kyoto, Japan, June 2009.

[70] R. F. Natividad, M. R. Del Rosario, P. C. Chen, and C.-H. Yeow, "A hybrid plastic-fabric soft bending actuator with reconfigurable bending profiles," in *Proceedings of the 2017 IEEE International Conference on Robotics and Automation (ICRA)*, pp. 6700–6705, IEEE, Singapore, May 2017.

[71] S. Riaz, H. Elahi, K. Javaid, and T. Shahzad, "Vibration feature extraction and analysis for fault diagnosis of rotating machinery-a literature survey," *Asia Pacific Journal of Multidisciplinary Research*, vol. 5, no. 1, pp. 103–110, 2017.

[72] M. Hofer, L. Spannagl, and R. D'Andrea, "Iterative learning control for fast and accurate position tracking with a soft robotic arm," in *Proceedings of the 2019 IEEE/RSJ International Conference on Intelligent Robots and Systems (IROS)*, Macau, China, November 2019.

[73] B. Xuhui, C. Zihao, and H. Zhongsheng, "Iterative learning control for discrete-time systems with quantized measurements," in *Proceedings of the 27th Chinese Control and Decision Conference (2015 CCDC)*, pp. 1080–1084, IEEE, Qingdao, China, May 2015.

Hindawi
Mathematical Problems in Engineering
Volume 2021, Article ID 1196369, 18 pages
https://doi.org/10.1155/2021/1196369

Review Article

Review on Reactive Power and Voltage Optimization of Active Distribution Network with Renewable Distributed Generation and Time-Varying Loads

Xingmin Li[1], **Hongwei Li**[1], **Shuaibing Li**[2], **Ziwei Jiang**[2] and **Xiping Ma**[3]

[1]*School of Automation & Electrical Engineering, Lanzhou Jiaotong University, Lanzhou, China*
[2]*School of New Energy & Power Engineering, Lanzhou Jiaotong University, Lanzhou, China*
[3]*Electric Power Research Institute of State Grid Corporation Gansu Electric Power Company, Lanzhou, China*

Correspondence should be addressed to Shuaibing Li; lishuaibing1105@163.com

Received 12 October 2021; Accepted 5 November 2021; Published 23 November 2021

Academic Editor: Licheng Wang

With a high proportion of renewable distributed generation and time-varying load connected to the distribution network, great challenges have appeared in the reactive power optimization control of the active distribution networks. This paper first introduces the characteristics of active distribution networks, the mechanism and research status of wind power, photovoltaic, and other renewable distributed generators, and time-varying loads participating in reactive power and voltage optimization. Then, the paper summarizes the methods of reactive power optimization and voltage regulation of active distribution network, including multi-timescale voltage optimization, coordinated optimization of network reconfiguration and reactive power optimization, coordinated optimization of active and reactive power optimization based on model predictive control, hierarchical and zoning control of reactive power, and voltage and power electronic switch voltage regulation. The pros and cons of the reactive power optimization algorithms mentioned above are summarized. Finally, combined with the development trend of the energy Internet, the future directions of reactive power and voltage control technology in the active distribution network are discussed.

1. Introduction

As one of the most abundant renewable energy areas in China, the total exploitable amount of wind and photovoltaic energy resources in Northwest China ranks at the forefront. Due to the high altitude, less water vapor, and thin clouds, the photovoltaic energy resource reserves in this area are extremely rich with annual sunshine above 3200 hours and the total annual radiation over 6690–8360 MJ/m^2 per year [1]. The statistics showed that the exploitable wind energy resources in this region can be up to 300 million kW, and the available wind resources in Gansu, Xinjiang, and Ningxia provinces accounted for about 1/3 of the total land wind energy in China [2]. With the in-depth promotion of a new round of the development of the western region strategy in China, green economy development based on renewable energy is an effective way to promote the economic development of Western China.

By 2021, the new energy power generation dominated by renewable distributed generation (RDG) such as wind power and photovoltaic accounted for about 11% of the power consumption of the whole society, of which Qinghai and Gansu provinces account for more than 50% and 40%, respectively. To achieve the goal of "Carbon Peaking and Carbon Neutralization," the National Energy Administration issued the notice on matters related to the development and construction of wind power and photovoltaic power generation in 2021. It was expected that by 2030, the proportion of non-fossil energy in primary energy consumption will decline to 25%, and the total installed capacity of wind power and photovoltaic power generation will increase to more than 1.2 billion kW. To promote energy conservation and emission reduction, develop a green economy, and help

achieve the goal of "Carbon Peaking and Carbon Neutralization" in advance, developing new energy sources dominated by renewable distributed power and vigorously developing distribution networks containing RDG can effectively improve the energy efficiency of power system generation, transmission, distribution, and utilization. Building a new power system dominated by a high proportion of new energy becomes an effective measure to improve the consumption of new energy [3, 4].

With the continuous development of social economy and power grid structure, in addition to renewable distributed generation such as wind power and photovoltaic power, there are also various loads with time-varying characteristics such as electric vehicles (EVs) and industrial loads [5], which brings challenges to the operation and control of active distribution network, especially the control of reactive power and voltage. This has become the primary technical problem of active distribution network [6, 7]. To solve the aforementioned problems, it is necessary to consider the collaborative optimization of various schemes, to realize the optimal control of ADN parameters, especially reactive power and voltage.

Therefore, by expounding the characteristics of active distribution network with RDGs and time-varying loads, this paper discusses the voltage regulation mechanism of wind power, photovoltaic, and other renewable distributed generation participating in active distribution network and the research status of time-varying load participating in voltage regulation. And it also analyzes the reactive power optimization methods of active distribution network in detail, including multi-timescale voltage optimization, coordination of network reconfiguration and reactive power optimization, coordination and optimization of active and reactive power, model predictive control (MPC), hierarchical and zoning control, and power electronic switch voltage regulation.

The possible measures of dealing with uncertain problems are introduced, and the advantages and disadvantages of the reactive power optimization algorithm are summarized. According to the development needs of the energy Internet, the future research directions of multienergy collaborative reactive power optimization control, interactive voltage optimization between users and power suppliers, and power electronic equipment participating in reactive power and voltage optimization regulation are discussed.

The rest of this paper is organized as follows: the second part introduces the characteristics of active distribution network, the third part introduces the source load reactive power regulation mechanism in active distribution network, the fourth part summarizes the reactive power optimization methods, uncertain problem processing methods, and solution algorithms, the fifth part prospects the future research, and the sixth part gives the conclusion.

2. Characteristics of Active Distribution Network with RDG and Time-Varying Load

Active distribution network is the distribution network with internal distributed power generation and control and operational capability. Figure 1 is a schematic diagram of a typical active distribution network. Compared with the traditional distribution network, the characteristics of active distribution network with RDG and time-varying load mainly include the following.

2.1. The Uncertainty of Power Output and Load Demand. The grid connection of a high proportion of renewable distributed generators and the access of a variety of time-varying loads on the load side to the distribution network make the source load and both ends of the distribution network uncertain [8].

The active power output of wind power generation and photovoltaic power generation is strongly correlated with season and climate conditions, with strong randomness and volatility. Figure 2 shows the wind power and photovoltaic output curve of a new energy station in Northwest China. As the wind power output is affected by wind speed, the wind power output is more at 00 : 00-08 : 00 and 19 : 00-24 : 00, less at 08 : 00-10 : 00 and 15 : 00-19 : 00, and the output is the least at 10 : 00-15 : 00. The photovoltaic output is greatly affected by the light intensity, and almost no electric energy is generated in 00 : 00-08 : 00 and 18 : 00-24 : 00. The photovoltaic power generation increases with the increase of light intensity in 08 : 00-13 : 00 and gradually decreases in 13 : 00-18 : 00.

Electric vehicles are charged disorderly in the charging station [9]. Figure 3 shows the daily charging demand forecast curve of electric vehicles in a certain area of Northwest China. From 08 : 00 to 11 : 00, a small number of users charge electric vehicles, and most users charge electric vehicles from 18 : 00 to 23 : 00. The load demand is closely related to users' charging behaviour, with strong uncertainty. The electric arc furnace and rolling mill are nonlinear and time-varying loads in the steel plant. The electric energy required under different production conditions is very different in the process of steelmaking and rolling.

2.2. High Proportion Power Electronics. On the power supply side, the grid connection of wind power and photovoltaic power is inseparable from power electronic devices, which means that the distribution network has more power electronic interfaces [10]. On the grid side, power electronic transformers and power electronic switches have fast real-time response speed and strong regulation ability, so a large number of power electronic devices replace traditional equipment and further power electronation of active distribution network [11]. On the load side, the working mechanism of the electric vehicle charging pile is three-phase AC input. After filtering and rectification (AC/DC), pulsating DC is obtained, then the high-frequency inverter is carried out through a power conversion circuit (DC/DC), and finally, secondary high-frequency current integration filtering is carried out through a high-frequency isolation transformer to achieve stable DC output [12, 13]. Impact loads such as electric arc furnaces and rolling mills will cause extremely serious voltage fluctuation, flicker, negative sequence, and harmonic disturbance during production. Therefore, local reactive power compensation measures will generally be taken

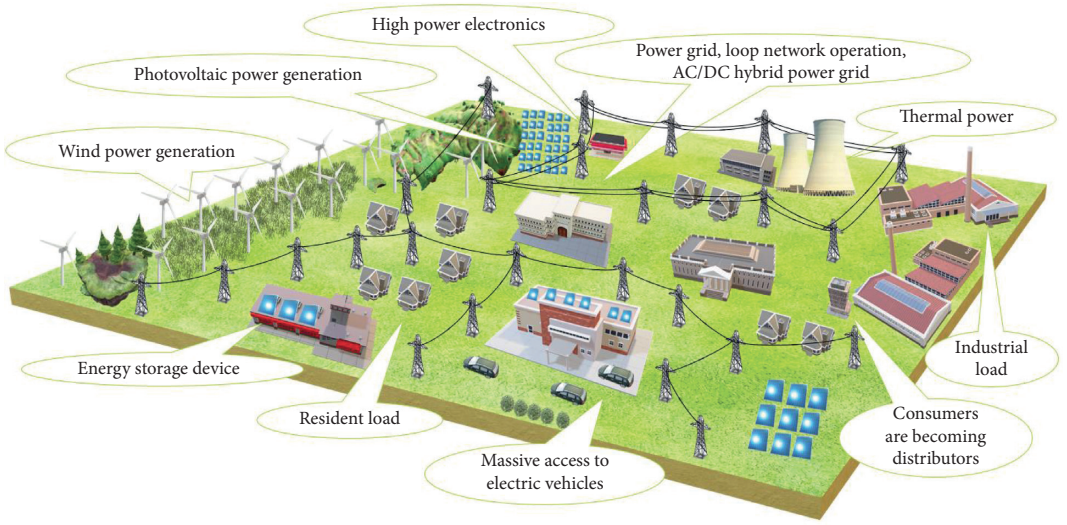

Figure 1: Schematic diagram of active distribution network architecture.

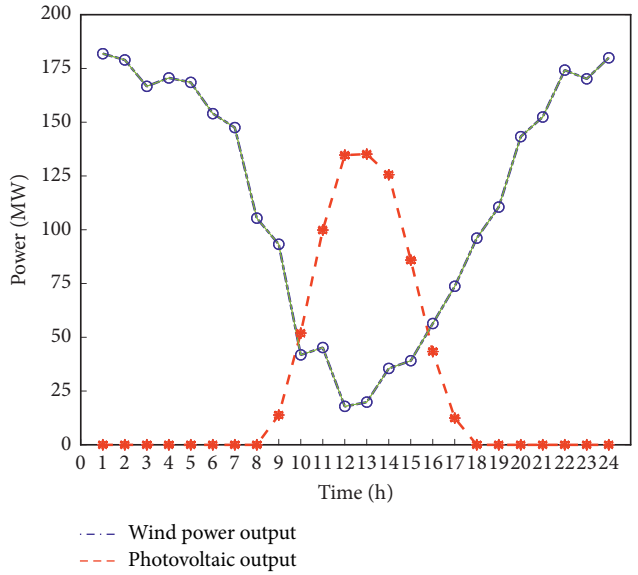

Figure 2: Photovoltaic daily output curve of wind power in a certain area of Northwest China.

to suppress load fluctuation and improve power quality. Common reactive power compensation devices include switching virtual circuit(SVC), static var generator (SVG), and static synchronous compensator (STATCOM) [14], which are typical power electronic devices.

2.3. Diversified Operation Scenarios. Considering a large number of renewable distributed generation and time-varying loads connected to the distribution network, there is serious uncertainty at both ends of the source load, and the output at both ends of the source load has a time-series correlation with the power demand, and the operation scenarios are diversified [15]. For example, in the reactive power optimization of the distribution network, the modelling and solution of uncertain problems need to divide the distribution network into scenes. The purpose is to convert the uncertain factors into multiple deterministic factors, thus simplifying the difficulty of the solution.

2.4. The Fuzzification of Source Charge Boundary. Since the existence of renewable energy in the power grid is the co-existence of centralized and distributed energy, the large-scale access of electric vehicles and distributed energy storage to the power grid makes it possible for the load in the traditional distribution network to become a power source to provide power to the power system. The interaction technology between multiuser and power grid supply and demand and the intelligent interaction technology between the electric vehicle and power grid are the technical bottlenecks in the process of "new electrification" of the new

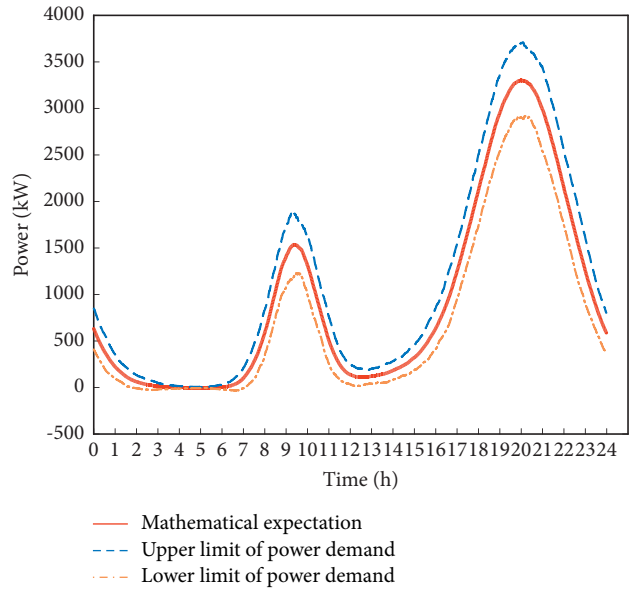

Figure 3: Prediction curve of daily charging demand of electric vehicles in a certain area of Northwest China.

power system [16]. In the future, the boundary between source loads will be gradually confused with the development of the power system.

3. Regulation Mechanism of Source Load Reactive Power in Active Distribution Network

The technical requirements for grid connection of distributed generation (GB/T 33593-2017) pointed out that the ways for renewable distributed generation to participate in the voltage regulation of distribution network can include adjusting the reactive power of power supply, adjusting the input of reactive power compensation equipment, and adjusting the transformation ratio of power supply transformer. This section introduces the mechanism of photovoltaic, wind power, and electric vehicles participating in reactive power and voltage regulation from two aspects, both the source and the load.

3.1. Mechanism of Photovoltaic Power Generation Participating in Reactive Power Optimization. Photovoltaic power generation can participate in the voltage regulation of active distribution network for reactive power and voltage control [17]. Photovoltaic power generation has reactive power control capability and can output reactive power to the distribution network [18–20]. The main reason is that the photovoltaic inverter has the ability of reactive power control. The topology of the photovoltaic grid-connected inverter is shown in Figure 4.

Since the topology of the grid-connected inverter is the same as that of an active reactive power compensation device, a photovoltaic array will transmit certain reactive power while transmitting active power to the power grid [21, 22]. To output standard sine wave current, PV grid-connected inverter generally adopts PQ control. The output active power and reactive power are shown in the following equations, respectively:

$$P = \frac{U_{oc}U}{2\pi fL}\sin\alpha, \tag{1}$$

$$Q = \frac{U_{oc}^2}{2\pi fL} - \frac{U_{oc}}{2\pi fL}\cos\alpha, \tag{2}$$

where U_{oc} is the output voltage of the inverter; U is the grid voltage; α is the phase angle difference between U_{oc} and U; L is the value of coupling inductance; and f is the system frequency.

The reactive power regulation capacity of the grid-connected inverter is limited, and its output range is shown in as follows:

$$-\sqrt{S_{max}^2 - P_{PV}^2} \le Q_{PV} \le \sqrt{S_{max}^2 - P_{PV}^2}, \tag{3}$$

where P_{PV} is the active output of the inverter; Q_{PV} is the reactive output of the inverter; and S_{max} is the inverter capacity.

Figure 5 shows the $P-Q$ capacity curve of the photovoltaic inverter. At point A: PV's active power rating is $P_{PV,max}$, and reactive power regulation range is $[-Q_{PV,1}, Q_{PV,1}]$. At point B: inverter cut-in and cut-out power $P_{PV,cut}$, reactive power regulation range $[-Q_{PV,2}, Q_{PV,2}]$. During the day, the reactive power regulation range of the inverter is $[-Q_{PV,2}, -Q_{PV,1}] \cup [Q_{PV,1}, Q_{PV,2}]$. At night, the active output of the inverter is 0, and the reactive power regulation range is the rated capacity of the inverter, and the regulation capacity is strong.

3.2. Reactive Power Regulation Characteristics of Doubly Fed Induction Generator Wind Turbine. The basic structure of doubly fed induction generator (DFIG) is shown in Figure 6 [23, 24], which is composed of a wind turbine, doubly fed

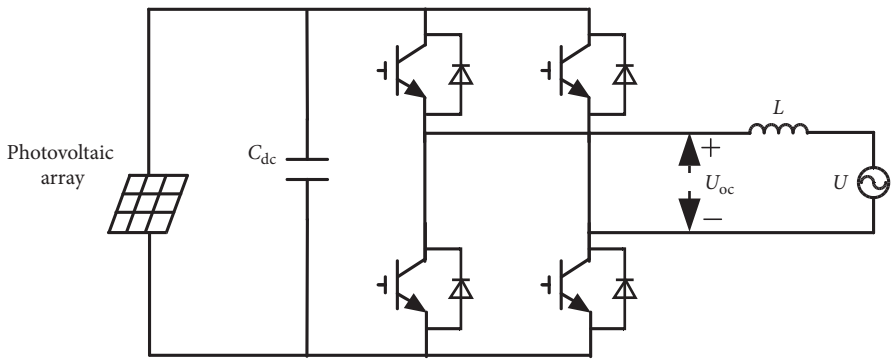

Figure 4: Topology of photovoltaic grid-connected inverter.

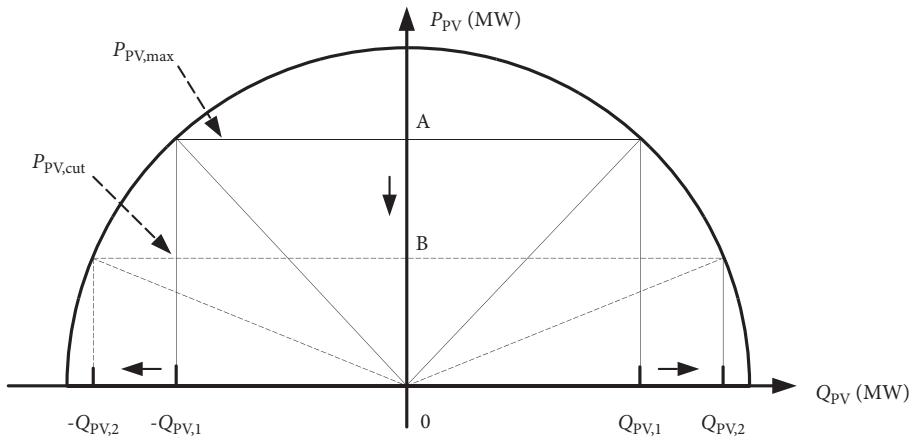

Figure 5: $P - Q$ capacity curve of photovoltaic inverter.

generator, and two AC/DC rotor pulse width modulation (PWM) converters based on insulated gate bipolar transistor (IGBT) [25]. The stator side and grid-side converters emit or absorb reactive power. The grid-side converter of a doubly fed induction wind motor generally operates in the unit power factor mode. Because the reactive power transmitted by the PWM converter is small, it could be ignored [26].

The reactive power Q_T of DFIG is the same as the reactive power Q_S transmitted at the stator side. The DFIG active and reactive power calculation formula is shown in the following equations:

$$\left(\frac{P_T}{1-s}\right)^2 + Q_T^2 = (3U_S I_S)^2, \tag{4}$$

$$\left(\frac{P_T}{1-s}\right)^2 + \left(Q_T + 3\frac{U_S^2}{X_S}\right)^2 = \left(3\frac{X_M}{X_S}U_S I_R\right)^2, \tag{5}$$

$$P_T = (1-s)P_S, \tag{6}$$

where P_T and Q_T are active output and reactive output of doubly fed induction wind turbine; U_S, P_S, and X_S are stator side voltage, active power, and stator leakage reactance, respectively; I_R and I_S are rotor transformer current and stator winding current, respectively; and s is the slip rate of the motor and X_M is the excitation reactance.

The $P - Q$ capacity curve of a doubly fed induction wind turbine is displayed in Figure 7. It can be seen that when the active power increases, the regulation range of reactive power will decrease. When the active output P_H of DFIG is constant, DFIG adjusts the reactive power within $[Q_{H,min}, Q_{H,max}]$ by adjusting the PWM converter current I_R and stator winding current I_S. $Q_{H,min}$ is the static stability limit of the doubly fed induction wind turbine. When the absorbed reactive power of DFIG exceeds $Q_{H,min}$, DFIG works in an unstable state.

3.3. Electric Vehicles Participate in Voltage Regulation of Active Distribution Network. Large-scale access of electric vehicles to the modern smart grid is an inevitable development trend. EVs can be used as distributed power supply or battery energy storage equipment and can be flexibly connected to or separated from the power grid, so they have the ability of reactive power and voltage regulation [27]. It mainly includes (i) load shedding or reverses power supply, (ii) reactive power response of electric vehicle charging pile, and (iii) build a real-time electric vehicle charging price scheme to stimulate users' charging behavior.

For the reactive power regulation of electric vehicles, a series of measures were conducted. Qi et al. [28] established the topology of grid-connected voltage regulation of EVs. It

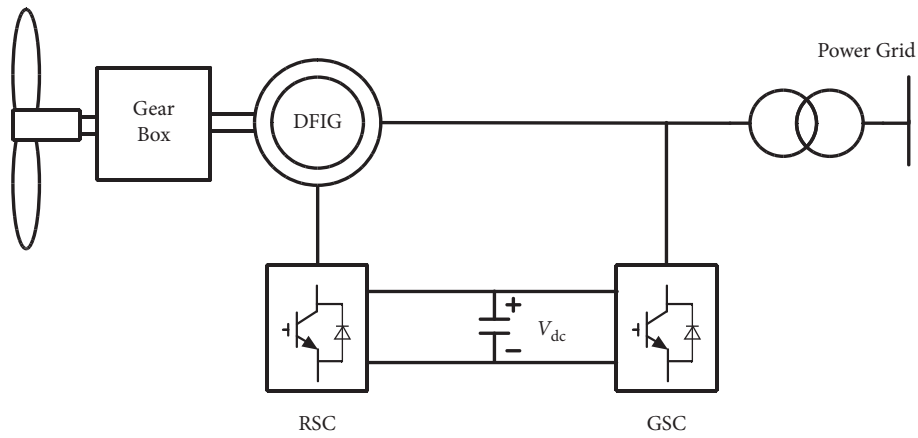

Figure 6: The basic structure of the DFIG wind turbine.

was reported that adjusting the power factor of the charger to compensate for the reactive power of the node and changing the charging active power was an effective control strategy, which had a significant effect on the voltage security, stability, and economy of the distribution network [29]. To change the charging behaviour of users through real-time electricity price, some methods were used to conduct this, including quantifying the response of vehicle owners to electricity price stimulation combining with the principle of consumer psychology, formulating dynamic time-of-time electricity price according to the predicted reactive load value, and making the vehicles in the occupation period cooperate with the reactive power compensation device to participate in reactive power optimization by changing the operation model of charging device [30]. A distributed load shedding control method was proposed to prevent voltage instability considering the interruptible characteristics of electric vehicles [31].

4. Reactive Power and Voltage Optimization of Active Distribution Network

4.1. Reactive Power and Voltage Optimization Method. For the voltage problems existing in the distribution network, voltage regulation is usually carried out by adjusting the tap of the on-load tap changer (OLTC) or switching slow-moving reactive power regulation resources such as shunt capacity bank (SCB) [32]. This kind of regulation mode is discrete and cannot be adjusted flexibly. As RDG is connected to the distribution network extensively, adjustable resources in the distribution network are gradually diversified, and the ways of reactive power optimization are becoming more and more abundant [33, 34].

This section summarizes the latest research progress of reactive power optimization of active distribution network at home and abroad, mainly including the following six aspects: multi-timescale voltage optimization of active distribution network, collaborative optimization of active distribution network reconfiguration and reactive power optimization, active and reactive power coordination optimization of active distribution network, reactive power optimization of active distribution network based on model predictive control, and voltage optimization of active distribution network with power electronic switches.

4.1.1. Multi-Timescale Voltage Optimization of Active Distribution Network. Multi-timescale voltage optimization divides voltage optimization into different stages. Different states have different timescales. Generally, it is divided into two stages [35]. The timescale of the first stage is usually 24 hours or 1 hour, which is called the day-ahead optimization. The timescale of the second stage is usually 15 min and 5 min, which is called intraday optimization. The principle of multitimescale voltage optimization is shown in Figure 8.

In Figure 8, in the first stage, based on the power supply and load prediction data, the reactive power access of discrete reactive power compensation devices, on-load tap changer, and other slow-moving equipment in the active distribution network is adjusted in advance so that the active power and reactive power of each node of the distribution network will be in a reasonable range in the next 24 hours or 1 hour. The second stage is to adjust renewable distributed generation output, switching virtual circuit, static var generator, and other reactive power compensation device access and energy storage port output in real-time based on the current power output, load demand, and grid operation status information on the premise of configuring slow motion equipment in the first stage, thus stabilizing the insufficient or out-of-limit reactive voltage caused by RDG output and load demand fluctuation in the next 15 min or 5 min.

For the day-ahead optimization and intraday optimization, Peng et al. [36] used the idea of MPC to configure discrete reactive power compensation devices in the day ahead and used continuously intraday power compensation devices to control voltage. Guowei et al. [37] used energy storage for day ahead and intraday voltage optimization of distribution network and realized voltage optimization by limiting the energy storage power range in the day ahead and adjusting the port output in real-time in intraday. Considering the influence of photovoltaic, Wei et al. [38] proposed a multi-time scale optimization control method for

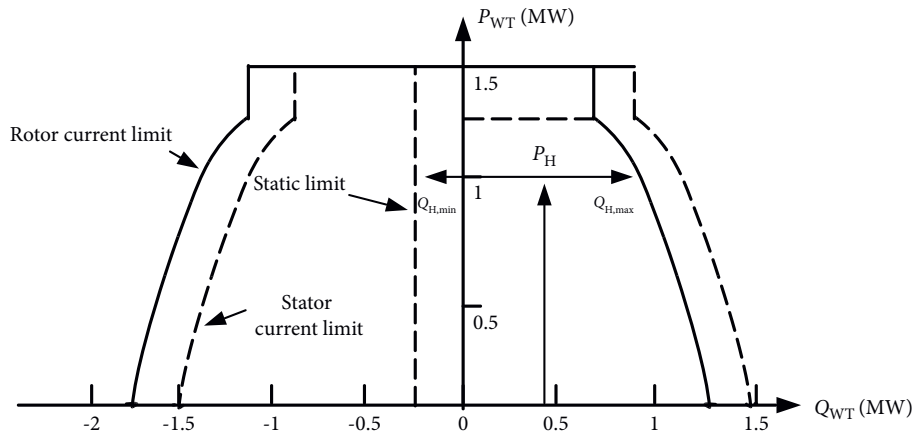

Figure 7: $P-Q$ capacity curve of doubly fed induction wind turbine.

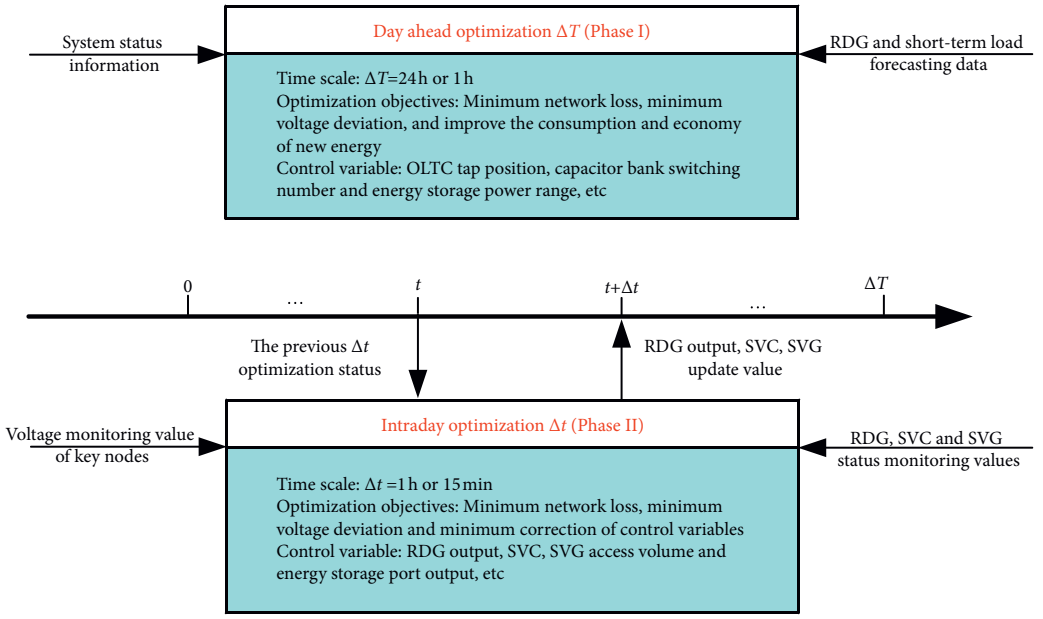

Figure 8: Principle of multi-time scale voltage optimization.

photovoltaic grid-connected distributed generation system, which aimed at minimizing the expected value of operation cost and carries out reactive power optimization of the distribution network in long timescale and short timescale. Further considering the influence of load characteristics on voltage, Zhiqiang et al. [39] carried out reactive power optimization in two stages: day-ahead optimization and real-time optimization and added the correction of the day-ahead optimization in the day. At the same time, considering the uncertainty of new energy and flexible load, double time-scales (1-hour level and 15-minute level) [40] were proposed, which used the traditional on-load voltage regulating transformer on-load tap changer and shunt capacitor for hour level voltage optimization and used the reactive power output of new energy units for 15-minute level to control the voltage deviation of nodes.

4.1.2. Collaborative Optimization of Active Distribution Network Reconfiguration and Reactive Power Optimization. The active distribution network has black start RDG as backup power supply and a large number of flexible loads, including source load that can interact with the distribution network in two directions and adjustable load regulated in one direction by the distribution network [41, 42].

Figure 9 shows the characteristic analysis of network reconfiguration. The topology of active distribution network is flexible and changeable. A reasonable network reconfiguration scheme can reduce network loss, promote RDG consumption, and improve the economy of the distribution network [43, 44]. Network reconfiguration also provides more possibilities for reactive power and voltage optimization of active distribution network.

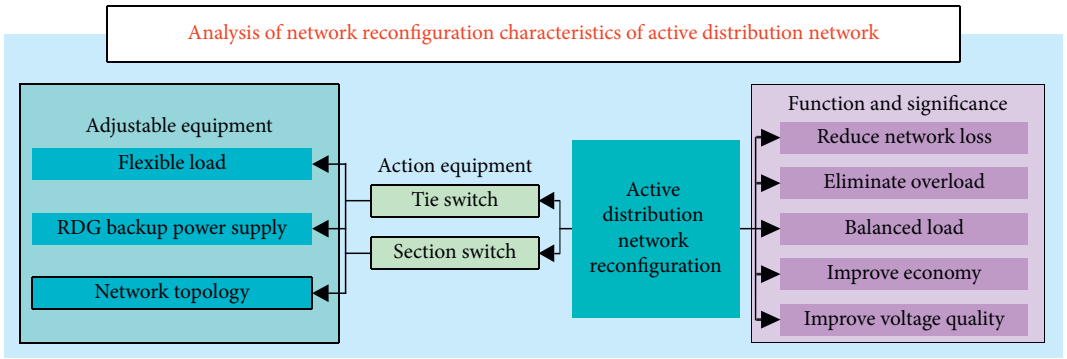

Figure 9: Network reconfiguration characteristics of active distribution network.

Considering the influence of the uncertainty of renewable distributed generation and time-varying load on active distribution network, Haishu et al. [33] proposed a comprehensive optimization model of ADN combining dynamic reconfiguration and reactive power optimization. Ping et al. [45] proposed a two-stage reactive power and voltage optimization method. In the first stage, the reconstruction scheme and the operation state of slow action equipment were determined, and in the second stage, the influence of fast action equipment on RDG random output was adjusted. Dihong [46] introduced renewable distributed generation into the process of distribution network reconfiguration and coordinated the two schemes of network reconfiguration and adjusting RDG injection power to obtain lower network loss and higher voltage quality.

With the increase of DC load in the distribution network, the distribution network gradually develops to AC/DC hybrid distribution network. Xu et al. [47] applied network reconfiguration to the AC/DC power grid, which can optimize the power flow distribution of the distribution system and improve the economy. Further considering the temporal and spatial imbalance of the net load of the distribution network, Wang et al. [48] took the light abandonment, load loss, and minimum switching cost as the goal and divided the period according to the load timing characteristics; the multiperiod and multilevel reconfiguration scheme of active distribution network was obtained.

4.1.3. Active and Reactive Power Coordination Optimization of Active Distribution Network. Large-timescale renewable distributed generation grid connection makes active power and reactive power coupling of active distribution network strong [49]. In terms of distribution network distributed optimization, relevant research at home and abroad mainly focused on reactive power optimization, and there was less research on active and reactive power coordination optimization. Active power optimization can reduce distribution network loss and improve economic efficiency. Figure 10 analyzes the regulation significance of active power optimization and reactive power optimization to active distribution network from the perspectives of economy and safety and defines the necessity of active and reactive power coordination optimization to active distribution network regulation.

To centralize the management and control of multiple types of distributed generators and multiple types of loads in active distribution network, Lingfeng et al. [50] modelled the active and reactive power output characteristics of various schedulable resources in ADN, planned and scheduled the adjustable active and reactive power in the system in real time, improved the consumption level of new energy and reduces voltage deviation. The new power electronic switch was applied to the active and reactive power coordination optimization. In [51], the flexible distribution switch (FDS) was applied to the active and reactive power coordination optimization to realize the distributed adaptive control of feeder load rate and voltage. To consider the participation of energy storage in active and reactive power coordination optimization, Hong et al. [52] considered power flow constraints, line operation constraints, distributed generation and shunt capacitor constraints, and energy storage charge and discharge constraints to achieve overall optimization.

4.1.4. Reactive Power Optimization of Active Distribution Network Based on Model Predictive Control. Model predictive control is a closed-loop control method based on finite time domain rolling optimization of the predictive model, which can deal with the influence of uncertain factors in the distribution system [53]. The MPC and multi-time scale combined reactive power and voltage optimization have a daily dispatching stage, intraday rolling scheduling stage, and real-time feedback correction stage, and the coordination relationship of each stage is shown in Figure 11.

Applying model predictive control to multi-timescale voltage optimization can greatly improve the control accuracy. Peng et al. [36] applied MPC to multi-timescale voltage optimization of high-proportion wind power connected to the distribution network, which made full use of switching virtual circuit, static var generator, and other reactive power compensation equipment, and suppressed frequent and rapid voltage fluctuation of the distribution network through reactive power and voltage rolling optimization and correction of MPC.

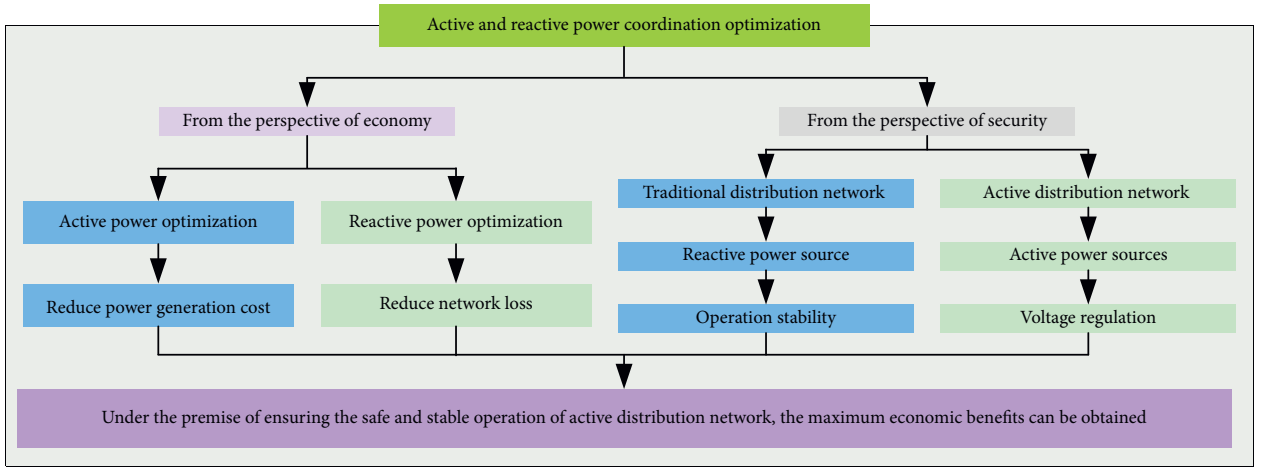

Figure 10: Active and reactive power optimization characteristics of active distribution network.

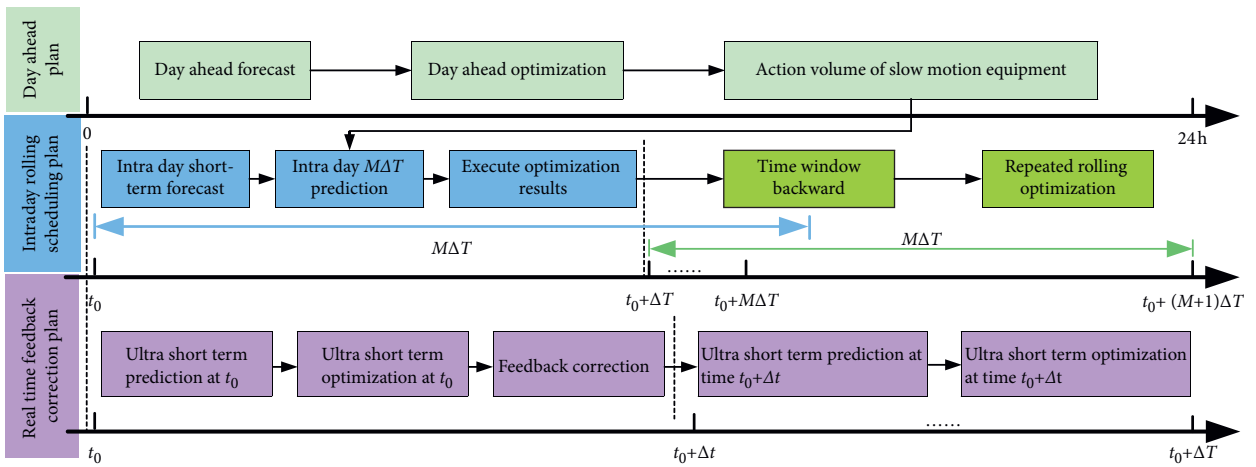

Figure 11: Voltage optimization principle of model predictive control.

To study the influence of renewable distributed generation on distribution network voltage, Hao et al. [54] established the voltage prediction model of each node. Aiming at minimizing the deviation between the predicted voltage and rated voltage of each node, the influence of random fluctuation of renewable distributed generation on voltage is eliminated through model predictive control rolling optimization and feedback correction. Further study on RDG's participation in power grid voltage regulation was discussed. Xiangwu et al. [53] carried out MPC on distribution network at multiple timescales and fine regulated power grid reactive voltage by coordinating reactive power equipment, rolling regulation of RDG, and load short-term prediction and feedback correction.

To consider the influence of time-varying load on power grid voltage regulation, Hongtao et al. [55] established an ADN optimal dispatching model, which used a model predictive control to meet the need of charging users and voltage regulation performance at the same time, reduce power fluctuation, and improve the economy.

4.1.5. Hierarchical and Zonal Control of Reactive Power and Voltage in Active Distribution Network. The centralized optimization of active distribution network has the problems of long optimization time, weak privacy protection in the region, and uncertain source load output. The ADN can be controlled by layers or zones. Figure 12 briefly analyzes the principle of reactive power and voltage stratification and the basic principle of reactive power and voltage zoning.

For the demand of multilayer information distributed storage and rapid optimization of active distribution network, a hierarchical time-varying optimization tracking algorithm was proposed in the literature [56]. Fei et al. [57] divided the control area into self-made control area and coordinated control area and made full use of the adjustable equipment in the distribution network to adjust the voltage from top to bottom. For hybrid AC/DC distribution networks, Haiping et al. [58] considered the source load uncertainty and aimed to minimize the sum of expected operating costs of prediction scenarios and sampling scenarios, which were decomposed into main and subproblems

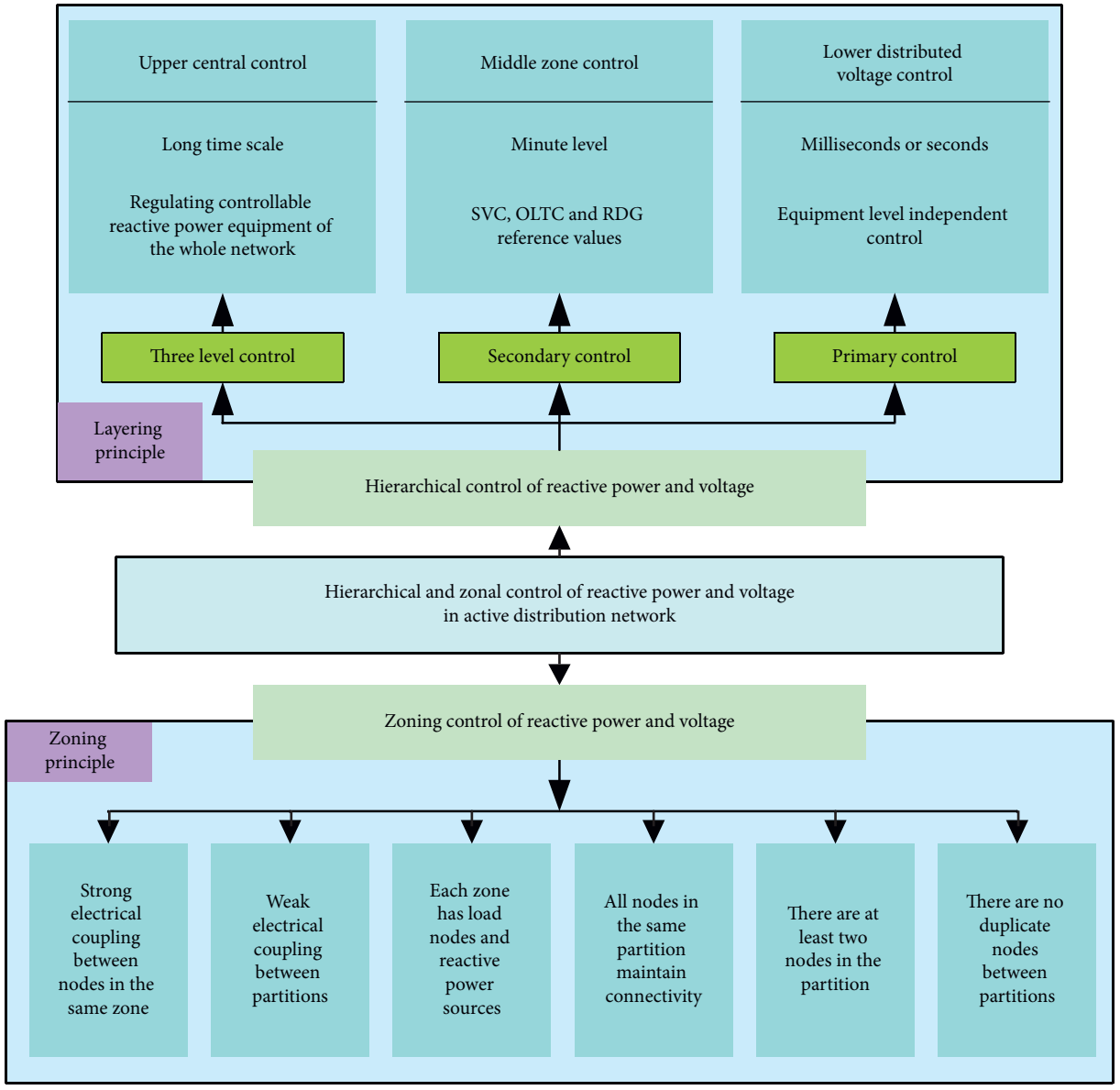

Figure 12: Hierarchical and zonal control of reactive power and voltage in active distribution network.

by the benders decomposition algorithm. The overall optimization is formed between and within regions to achieve global optimization. In [50], for the rational zoning of active distribution network, the distributed accelerated alternating multiplier method was used to solve the subproblems in this region, and the global optimal solution was obtained by iterative optimization.

4.1.6. Participation of Power Electronic Switches in Reactive Power Optimization of Active Distribution Network. A soft open point (SOP) is a fully controlled power electronic device [59], which can accurately control the active power transmitted between the feeders connected on both sides and provide certain reactive power and voltage support. Compared with traditional voltage regulating equipment such as an on-load transformer and capacitor bank, SOP has no limit on the number of actions and has a fast real-time response speed. It is more suitable for scenes with frequent voltage fluctuations. Figure 13 summarizes the advantages of SOP, which not only has efficient voltage regulation capacity but also has a very wide application prospect. However, credited to the high investment and operation cost of SOP, it can not completely replace the traditional voltage regulating equipment. Therefore, the coordination of SOP, tie switch, and traditional voltage regulating equipment should be considered in the reactive power and voltage optimization of active distribution network.

To study the ability of soft open point to coordinate with traditional voltage regulating equipment to control the voltage of active distribution network, Ruonan et al. [60] optimized the voltage of active distribution network in three stages. In the first stage, the tap position of the on-load voltage regulating transformer and the switching number of

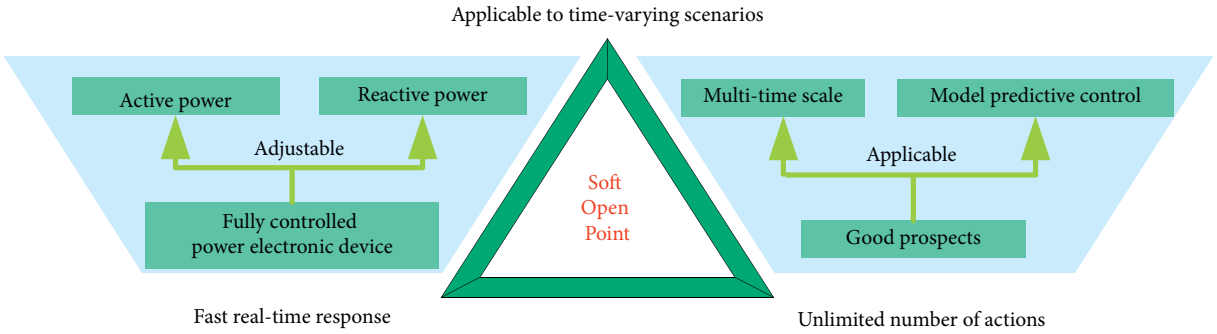

Figure 13: Advantages and application of the intelligent soft switch.

Table 1: Summary of treatment methods for uncertain problems.

Method	Existing advantages	Potential deficiency
Stochastic optimization [62]	Good economy and poor robustness	Discrete scenes are often of large scale and take a long time to solve
Robust optimization [63]	Strong robustness and low sensitivity of the optimal solution to parameter changes	Difficult to solve directly
Distributionally robust optimization [64]	The economy and robustness are good, and the solution time is short	For the problem of uncertainty in a single time, the research on data correlation between multiple time periods is insufficient
Scene analysis [65]	Avoid complex modelling processes and reduce the amount of calculation	There are errors
Monte Carlo simulation [66]	Accurate conclusion	Low efficiency
Probabilistic clustering [67]	Reduce the amount of calculation	Complex modelling
Chance constrained programming [68]	Good applicability and strong robustness	Optimization results are affected by random factors
Time-division optimization [69]	Highlight the overall change characteristics of uncertain factors	The method of time-division may be subjective
Interval optimization [70]	According to the subjective preference of decision-makers, give flexible consideration to optimality and robustness	Slow operation speed
Fuzzy set theory [71]	Strong processing capacity	Lack of systematicness
Rough set theory [72]	Without any prior information, the description is objective	Limitations: it may not be able to fully and effectively describe uncertain problems

the capacitor bank was adjusted. In the second stage, the active power and voltage reactive droop curves of SOP are optimized. In the third stage, the SOP reactive power output is dynamically adjusted in real time. Further considering that SOP and network reconfiguration participate in voltage optimization together, Pengwei et al. [61] established SOP feedback rolling optimization control model based on model predictive control and used mixed-integer second-order cone programming method to solve the coordinated optimization of SOP and network reconfiguration. Yuanquan et al. [51] established a multiperiod active reactive power coordinated optimal operation model considering flexible multistate switches and ADN and fully coordinated the configuration of flexible switches and adjustable factors in active distribution network. From the published research results, it can be seen that there is still much room for improvement in reactive power optimization of ADN through joint coordination between SOP and traditional voltage control equipment.

4.2. Methods for Dealing with Uncertainties in Active Distribution Network. Renewable distributed generation and time-varying loads of different properties are connected to the distribution network, and their uncertainty significantly affects the power supply reliability of the distribution network [54]. Common methods to deal with multiple uncertain factors in the distribution system include the scene analysis method, Monte Carlo simulation method, probability clustering method, opportunity constrained programming method, robust optimization method, and time-division optimization method. Table 1 briefly analyzes the advantages and disadvantages of the above treatment methods.

4.3. Reactive Power Optimization Algorithm. The reactive power and voltage optimization problem of active distribution network is a multidimensional nonlinear problem with multivariable and multiconstraints [73, 74]. How to

Table 2: Comparison of advantages and disadvantages of different reactive power optimization algorithms.

Classification	Condition		Existing advantages	Potential deficiency
Traditional optimization algorithm	Linear programming method	Sensitivity analysis [75]	It is convenient to introduce various constraints, and the result is ideal	The amount of calculation is large, and there are many requirements for memory and time
		Interior point method [76]	It has good robustness and convergence, and the calculation time is not affected by the scale of the system	The results obtained have errors compared with the actual results
		Simplified gradient method [77]	The principle is simple, the storage requirement is small, and it is easy to implement	Weak convergence performance
	Nonlinear programming method	Newton method [78]	The search direction is reasonable, with second-order convergence speed and a small amount of calculation	It takes time to solve the comparison
		Quadratic programming method [79]	Good convergence characteristics	It can only solve the problem whose objective function is quadratic and the constraint condition is linear
	Mixed-integer programming [80]		Integer variables and continuous variables can be treated separately	Poor integrity, complex calculation process, a large amount of calculation, slow convergence, and easy oscillation in the calculation process

Table 2: Continued.

Classification	Condition	Existing advantages	Potential deficiency
Artificial intelligence algorithm	Dynamic programming method [80]	The global optimal solution can be obtained without strictly observing the linearity and convexity of the objective function and constraints, and the convergence is good.	When there are many variables, the modelling is complex and the calculation speed is slow.
	Tabu search method [81]	The number of iterations is small and the convergence rate is high.	The convergence speed and the quality of the final solution are closely related to the appropriate selection of the initial value, and the global search ability is not good.
	Particle swarm optimization [82]	Strong search accuracy and global searchability	Slow convergence
	Ant colony algorithm [73]	Strong robustness and optimization ability	The solution result is related to the parameter setting.
	Immune genetic algorithm [83]	Strong global search ability, strong robustness, and computing power	Poor local optimization ability, slow convergence, and low resolution.
	Tabu search [84]	Strong local development ability, fast convergence speed, and strong universality	The global development ability is weak, and only the locally optimal solution is obtained.
	Gray wolf algorithm [85]	Strong convergence performance, few parameters, and strong global searchability	The accuracy is slightly poor.
	Whale algorithm [86]	Simple structure, few parameters, and strong searchability	Easy to fall into local extremum and slow convergence
	Cuckoo algorithm [87]	Few parameters, simple operation, easy implementation, random search path optimization, and strong optimization ability	The step size is generated randomly, which is not conducive to the calculation
	Bee colony algorithm [88]	Few control parameters and fast convergence speed	The amount of iterative calculation is large and the scope of application is limited.
	Ant lion algorithm [89]	Few adjustment parameters, high convergence accuracy, and good robustness	The global search ability is insufficient, and it is easy to fall into local optimization.
	Bat algorithm [90]	High calculation accuracy and efficiency, fast convergence speed	There is local repeated search; the larger the system scale, the more complex the algorithm and the slower the calculation speed.
	Simulated annealing algorithm [91]	The principle is simple and easy to implement.	There is local repeated search; the larger the system scale, the more complex the algorithm and the slower the calculation speed.
	Fish swarm algorithm [92]	Good convergence and robustness	The search efficiency is ordinary.
	Neural network [93]	Good nonlinear characteristics, predictability, guidance, convergence, and flexibility	It is easy to fall into local optimal solution, which is not conducive to the online and rapid control of the system.
Hybrid optimization algorithm	Tabu search particle swarm optimization [84]	Strong optimization ability, high calculation efficiency, and accuracy	The algorithm is complex.
	Genetic simulated annealing algorithm [91]	High calculation accuracy and fast calculation speed	When the population size is small, it will fall into local optimization.
	Improved quantum particle swarm optimization [94]	Fast convergence speed and strong optimization ability	It is easy to fall into the problem of premature convergence.
	Genetic quasi-Newton hybrid algorithm [95]	High search efficiency and high precision	Convergence to the extreme value cannot be guaranteed.
	Particle swarm optimization interior-point hybrid algorithm [96]	The global optimization ability and convergence are strong, and the accuracy of the optimal solution is high.	Not suitable for large-scale power grid
	Chaotic bat algorithm [97]	The model is simple, the control parameters are few, and the convergence speed is fast.	It is easy to fall into local optimization and poor population diversity.

deal with the nonlinear objective function, improve the convergence of optimization algorithm, and realize accurate control has always been the focus of research.

Credited to the high investment and operation cost of SOP, it can not completely replace the traditional voltage regulating equipment. To the rapid development of computer technology and mathematical theory, there are more and more new reactive power optimization algorithms, which can be divided into three categories: traditional optimization algorithms, intelligent optimization algorithms, and hybrid optimization algorithms.

Table 2 summarizes the advantages and disadvantages of various basic optimization algorithms in detail. With the high proportion of power electronic devices, new energy generation, and flexible loads connected to the distribution network, a single optimization algorithm can no longer meet our expectations for solution speed, accuracy, convergence, and robustness. In the optimization process, the improved intelligent optimization algorithm or hybrid optimization algorithm is usually used to obtain the optimal solution.

5. Prospect of Further Research

To promote the efficient utilization of renewable distributed generation, active distribution network extends the controllable objects to distributed energy including RDG, energy storage, and controllable load. In recent years, the reform of the electricity market and the popularization and application of new technologies such as the Internet, communication technology, and intelligent electricity will bring about a series of new problems as well as advanced problems in the active distribution network.

5.1. Multi-Energy Cooperative Reactive Power Optimization Control. The energy Internet is a multi-energy coupling, represented by the integrated energy system, which expands the power network in space, connects different regional power grids, and realizes the cross-regional consumption of different types of new energy in different regions. Dynamic reactive power optimization is the fundamental means to improve the voltage stability of ADN. At present, the contents to be studied include a variety of heterogeneous energy coupling mechanisms and methods, the interaction of multiple heterogeneous energy sources at different time scales, capability evaluation, and practical application of various heterogeneous energy sources in reactive power optimization.

5.2. Source Load Supply Demand Interaction to Participate in Reactive Power Optimization. Under the condition of energy Internet, to realize the integration of electric vehicles, intelligent transportation, and smart grid, it is necessary to control its charge and discharge behaviour on two-timescales: vehicle guidance before connecting to the grid and charge and discharge control after connecting to the grid.

At present, the research and application of the business model and the market mechanism of the interaction between electric vehicles and the power grid are still in their infancy. How to establish the market mechanism in terms of electricity price, auxiliary service price, renewable energy carbon tax, and so on should be considered. This is of great significance for the interactive voltage optimization between users and power grid supply and demand.

5.3. Application of New Power Electronic Equipment in Reactive Power and Voltage Optimal Control of Active Distribution Network. At present, power electronics have shown a diversified development period: the development of devices is mainly full control hybrid module devices and wide bandgap devices. Power electronic devices have been able to meet more application requirements of active distribution network, with more multifunctional converters composed of multiple conversion units and more forms of multiport, multilevel connection, multiflow direction, and multiform power conversion. The application of new power electronic equipment in reactive power optimization is the key point of future research.

5.4. Intelligent Reactive Power and Voltage Control of Active Distribution Network. Under the guidance of the concept of the smart grid, the informatization level of the entire power system has been significantly improved. By integrating network, computing, and physical resources, the information physics system makes each module and subsystem in the system work and cooperate so that the resources of the system can be allocated organically and the operation efficiency can be improved.

In the future, the energy network structure in China will continue to be optimized. Low carbon and energy conservation are important prerequisites for the development of ADN. Active distribution network will gradually become intelligent with the development of information physical systems. Two aspects need to be studied: one is to use the information physical system technology to realize the data and transparency of energy resources, and the other is to use the data information provided by the information physical system to improve the reactive power and voltage operation level of active distribution network.

6. Conclusion

This paper introduces the characteristics of active distribution network with renewable distributed generation and time-varying load and introduces the principle and application of source load participation in voltage regulation in active distribution network, and it reviews the modelling methods of reactive power and voltage optimization in active distribution network. Summary and analysis of the modelling methods of reactive power optimization are carried out in six aspects: multi-timescale, network reconstruction, active and reactive power coordination optimization, model predictive control, hierarchical zoning of distribution network, and participation of power electronic switches in reactive power regulation. The methods of dealing with uncertain factors in the process of reactive power optimization are briefly described, and the pros and cons of reactive

power optimization algorithms are compared and analysed. The development direction of reactive power and voltage control technology in active distribution network in the future is prospected at last.

Nomenclature

RDG: Renewable distributed generation
ADN: Active distribution network
EVs: Electric vehicles
MPC: Model predictive control
SOP: Soft open point.

Conflicts of Interest

The authors declare that they have no conflicts of interest regarding the publication of this paper.

Acknowledgments

This research was funded in part by Gansu University Innovation Fund Project under contracts nos. 2020A-036 and 2021B-111, in part by the Natural Science Foundation of Gansu Province under contract no. 21JR1RA255, and in part by the Young Doctor Foundation of JYT.GANSU.GOV.CN under contract no. 2021QB-060 and also supported by the Tianyou Youth Talent Lift Program of Lanzhou Jiaotong University.

References

[1] L. Hong, W. Ke, and M. Jiao, "Climate effect assessment of ideal large -scale solar and wind power farms in northwest China," *Climatic and Environmental Research*, vol. 26, no. 02, pp. 123–141, 2021.

[2] C. Yang, Z. Jiarui, Z. Wuzhi, W. Zheng, and Z. Yuting, "Scheduling strategy of wind penetration multi-source system considering multi-time scale source-load coordination," *Power System Technology*, vol. 45, no. 05, pp. 1828–1837, 2021.

[3] X. Feng, Q. Li, and K. Wang, "Waste plastic triboelectric nanogenerators using recycled plastic bags for power generation," *ACS Applied Materials & Interfaces*, vol. 13, no. 1, pp. 400–410, 2020.

[4] X. Chen, M. B. Mcelroy, Q. Wu, Y. Shu, and Y. Xue, "Transition towards higher penetration of renewables: An overview of interlinked technical, environmental and socio-economic challenges," *Journal of Modern Power Systems and Clean Energy*, vol. 7, no. 01, pp. 1–8, 2019.

[5] Y. Yu, P. Ju, Y. Peng, B. Lou, and H. Huang, "Analysis of dynamic voltage fluctuation mechanism in interconnected power grid with stochastic power disturbances," *Journal of Modern Power Systems and Clean Energy*, vol. 8, no. 01, pp. 38–45, 2020.

[6] J. S. Chen, T. Xu, and J. H. Zhou, "Voltage profile optimization of active distribution network through a distributed approach," in *Proceedings of the International Conference on Renewable Power Generation (RPG 2015)*, pp. 1–5, Beijing, China, October 2015.

[7] X. Peng, W. Beibeil, and B. Yuqing, "Online voltage control method based on topology resource of network and the solving method via transfer reinforcement learning," *Proceedings of the CSEE*, vol. 40, no. 22, pp. 7317–7328, 2020.

[8] A. Casavola, F. Tedesco, and M. Vizza, "Command governor strategies for the online management of reactive power in smart grids with distributed generation," *IEEE Transactions on Automation Science and Engineering*, vol. 14, no. 2, pp. 449–460, 2017.

[9] Z. Bie, H. Xie, G. Hu, and G. Li, "Optimal scheduling of power systems considering demand response," *Journal of Modern Power Systems and Clean Energy*, vol. 4, no. 02, pp. 180–187, 2016.

[10] J. M. Maza-Ortega, E. Acha, S. García, and A. Gómez-Expósito, "Overview of power electronics technology and applications in power generation, transmission and distribution," *Journal of Modern Power Systems and Clean Energy*, vol. 5, no. 04, pp. 499–514, 2017.

[11] D. Lei, Z. Tao, P. Tianjiao, C. Naishi, and S. Yingyun, "Optimization method for voltage imbalance suppression of ac/dc distribution network with pet," *Power System Technology*, vol. 42, no. 11, pp. 3609–3616, 2018.

[12] K. Wang, C. Liu, and J. Sun, "State of charge estimation of composite energy storage systems with supercapacitors and lithium batteries," vol. 2021, Article ID 8816250, 2021.

[13] H. Yu, W. Na, and Z. Keyou, "Simultaneous unknown input and state estimation for the linear system with a rank-deficient distribution matrix," *Mathematical Problems in Engineering*, vol. 2021, Article ID 6693690, 2021.

[14] A. Luo, Q. Xu, F. Ma, and Y. Chen, "Overview of power quality analysis and control technology for smart grid," *Journal of Modern Power Systems and Clean Energy*, vol. 4, no. 01, pp. 1–9, 2016.

[15] X. Fang, B.-M. Hodge, F. Li, E. Du, and C. Kang, "Adjustable and distributionally robust chance-constrained economic dispatch considering wind power uncertainty," *Journal of Modern Power Systems and Clean Energy*, vol. 7, no. 03, pp. 658–664, 2019.

[16] K. Wang, W. Wang, L. Wang, and L. Li, "An improved soc control strategy for electric vehicle hybrid energy storage systems," *Energies*, vol. 13, no. 20, p. 5297, 2020.

[17] L. Wang, R. Yan, F. Bai, T. Saha, and K. Wang, "A distributed inter-phase coordination algorithm for voltage control with unbalanced pv integration in lv systems," *IEEE Transactions on Sustainable Energy*, vol. 11, no. 4, pp. 2687–2697, 2020.

[18] Y. Liu, L. Guo, C. Lu, Y. Chai, S. Gao, and B. Xu, "A fully distributed voltage optimization method for distribution networks considering integer constraints of step voltage regulators," *IEEE Access*, vol. 7, pp. 60055–60066, 2019.

[19] W. Xian, L. Wenying, X. Peng, N. Yanan, and W. Weizhou, "Reactive power optimization control method for pv station participating in active voltage regulation of power grid," *Electric Power Automation Equipment*, vol. 40, no. 07, pp. 76–83, 2020.

[20] S. S. AlKaabi, V. Khadkikar, and H. H. Zeineldin, "Incorporating pv inverter control schemes for planning active distribution networks," *IEEE Transactions on Sustainable Energy*, vol. 6, no. 4, pp. 1224–1233, 2015.

[21] L. Wang, R. Yan, and T. K. Saha, "Voltage regulation challenges with unbalanced pv integration in low voltage distribution systems and the corresponding solution," *Applied Energy*, vol. 256, p. 113927, 2019.

[22] L. Zhaoyuan, W. Ping, and Z. Neng, "Coordinated active-reactive power optimization of distribution network considering controllable photovoltaic system," *Power System Technology*, vol. 43, no. 01, pp. 294–301, 2019.

[23] H. Huang, P. Ju, and X. Pan, "Phase–amplitude model for doubly fed induction generators," *Journal of Modern Power Systems and Clean Energy*, vol. 7, no. 02, pp. 369–379, 2019.

[24] H. Zhou, P. Ju, Y. Xue, and J. Zhu, "Probabilistic equivalent model of dfig-based wind farms and its application in stability analysis," *Journal of Modern Power Systems and Clean Energy*, vol. 4, no. 02, pp. 248–255, 2016.

[25] M. Q. Duong and G. N. Sava, "Coordinated reactive power control of dfig to improve lvrt characteristics of fsig in wind turbine generation," in *Proceedings of the 2017 International Conference on Electromechanical and Power Systems (SIELMEN)*, pp. 256–260, Iasi, Romania, October 2017.

[26] L. Junlei, C. Na, and Q. Feng, "Analysis of unit oscillation in wind farm considering control parameters of converter for dfig-based wind turbine," *Automation of Electric Power Systems*, vol. 45, no. 10, pp. 42–49, 2021.

[27] K. Knezović, M. Marinelli, P. B. Andersen, and C. Træholt, "Concurrent provision of frequency regulation and overvoltage support by electric vehicles in a real Danish low voltage network," in *Proceedings of the 2014 IEEE International Electric Vehicle Conference (IEVC)*, pp. 1–7, Florence, Italy, December 2014.

[28] Z. Qi, A. Haiyun, and D. Meimei, "Energy-saving and loss-reduction control method for power grid considering the reactive power response capability of electric vehicle chargers," *Proceedings of the CSU-EPSA*, vol. 29, no. 05, pp. 129–134, 2017.

[29] S. Su, H. Yong, W. Wei, and W. Shidan, "Voltage regulation strategy for distribution network based on reactive power compensation of electric vehicles," *Automation of Electric Power Systems*, vol. 41, no. 10, pp. 72–81, 2017.

[30] Z. Dongmei and M. Taiyi, "Reactive power optimization strategy of power grid with electric vehicles based on dynamic time-of-use tariffs," *Journal of North China Electric Power University*, pp. 1–10, 2021, https://kns.cnki.net/kcms/detail/13.1212.TM.20210623.1703.002.html.

[31] C. Wei, Z. Xianzheng, L. Yanjun, and G. Chuangxin, "A robust islanding restoration policy for active distribution network considering optimal allocation of emergency electric vehicles," *Proceedings of the CSEE*, vol. 38, no. S1, pp. 58–67, 2018.

[32] C. Liu, Q. Li, and K. Wang, "State-of-charge estimation and remaining useful life prediction of supercapacitors," *Renewable and Sustainable Energy Reviews*, vol. 150, no. 2, Article ID 111408, 2021.

[33] G. Haishu, Z. Yumin, J. Xingquan, Z. Xiao, and Y. Yongjin, "Scenario clustering based distributionally robust comprehensive optimization of active distribution network," *Automation of Electric Power Systems*, vol. 44, no. 21, pp. 32–41, 2020.

[34] N. Shuang, C. Chenggang, and Y. Ning, "Multi-time- scale online optimization for reactive power of distribution network based on deep reinforcement learning," *Automation of Electric Power Systems*, vol. 45, no. 10, pp. 77–85, 2021.

[35] X. Ye, K. He, T. Kang, and M. Bai, "Two stage operation optimization of active distribution network based on imohs algorithm," in *Proceedings of the 2021 IEEE 13th International Conference on Computer Research and Development (ICCRD)*, pp. 78–82, Beijing, China, January 2021.

[36] X. Peng, L. Wenying, Z. Dan, W. Ningbo, and H. Xia, "Multi-time scale optimal control method of reactive power and voltage based on model predictive control," *Electric Power Automation Equipment*, vol. 39, no. 03, pp. 64–70, 2019.

[37] C. Guowei, Z. Youwang, G. Le, and W. Lixin, "Multi-time-scale voltage optimization of flexible interconnected distribution network with self-energy storage," *Automation of Electric Power Systems*, vol. 45, no. 09, pp. 71–79, 2021.

[38] H. Wei, L. Siliang, Y. Yingqi, W. Zhaolong, and Z. Yongjun, "Multi-time scale slack optimal control in distribution network based on v oltage optimization for point of common coupling of pv," *Automation of Electric Power Systems*, vol. 43, no. 03, pp. 92–100, 2019.

[39] W. Zhiqiang, G. Chenyang, L. Wenxia, L. Chunhui, and W. Jiawei, "Multi-time scale voltage control and coordinated correction for distribution networks considering load characteristics," *Automation of Electric Power Systems*, vol. 41, no. 15, pp. 51–57, 2017.

[40] J. Dan, "Two-time-scale multi-objective coordinated volt/var optimization for active distribution networks," Tianjin University, Tianjin, China, 2018.

[41] N. Karthikeyan, J. R. Pillai, B. Bak-Jensen, and J. W. Simpson-Porco, "Predictive control of flexible resources for demand response in active distribution networks," *IEEE Transactions on Power Systems*, vol. 34, no. 4, pp. 2957–2969, 2019.

[42] Y. Hongtao, W. Gang, and Z. He, "Robust optimal scheduling of active distribution network considering with the charging-swapping storage integrated station," *Proceedings of the CSEE*, vol. 40, no. 08, pp. 2453–2468, 2020.

[43] S. Chen, W. Hu, and Z. Chen, "Comprehensive cost minimization in distribution networks using segmented-time feeder reconfiguration and reactive power control of distributed generators," *IEEE Transactions on Power Systems*, vol. 31, no. 2, pp. 983–993, 2016.

[44] M. R. Dorostkar-Ghamsari, M. Fotuhi-Firuzabad, M. Lehtonen, and A. Safdarian, "Value of distribution network reconfiguration in presence of renewable energy resources," *IEEE Transactions on Power Systems*, vol. 31, no. 3, pp. 1879–1888, 2016.

[45] Z. Ping, Z. Qiqi, and A. Xiaomeng, "Network reconfiguration and reactive power voltage regulation coordinated robust optimization for active distribution network considering extreme scenarios," *Transactions of China Electrotechnical Society*, pp. 1–11, 2021, https://kns.cnki.net/kcms/detail/11.2188.TM.20210512.1821.001.html.

[46] O. Dihong, "Research on distribution network reconfiguration based on several optimization methods," South China University of Technology, Guangzhou, China, 2012.

[47] Z. Xu, Y. Li, C. Chen, F. Risheng, and L. Jikeng, "A new two-stage robust model for the co-optimization of reconfiguration and reactive power in ac/dc hybrid distribution network," pp. 1–20, Power System Technology, 2021.

[48] M. Wang, G. Hongjun, and Y. Yanhong, "Two-stage optimal operation for distribution network based on fast ldentification of reconfiguration level," *Proceedings of the CSEE*, pp. 1–16, 2021, https://kns.cnki.net/kcms/detail/11.2107.TM.20210630.1400.005.html.

[49] B. Ping, X. Zhang, and Q. Song, "Voltage control strategy for integrated medium and low voltage distribution network based on active-reactive power coordination optimization," in *Proceedings of the 2020 Chinese Automation Congress (CAC)*, pp. 1187–1192, Qingdao, China, September 2020.

[50] K. Lingfeng, W. Ming, and L. Yang, "Optimization and control method of distributed active and reactive power in active distribution network," *Proceedings of the CSEE*, vol. 40, no. 06, pp. 1856–1865, 2020.

[51] P. Yuanquan, M. Zhiyuan, and A. Wei, "Active and reactive power coordinated dynamic optimization for active

distribution network with flexible distribution switch," *Automation of Electric Power Systems*, vol. 44, no. 14, pp. 54–61, 2020.

[52] L. Hong, X. Zhengyang, and G. Shaoyun, "Coordinated operation of active- reactive power and voltage control for active distribution network considering regulation of energy storage," *Automation of Electric Power Systems*, vol. 43, no. 11, pp. 51–58, 2019.

[53] Y. Xiangwu, X. Yun, L. Ruojin, J. Yongsheng, and L. Tie, "Multi-time scale reactive power optimization of distribution grid based on m odel predictive control and including rdg regulation," *Transactions of China Electrotechnical Society*, vol. 34, no. 10, pp. 2022–2037, 2019.

[54] X. Hao, P. Wei, D. Wei, and K. Li, "Analysis of the impact of distributed generation on distribution network voltage and its optimal control strategy," *Transactions of China Electrotechnical Society*, vol. 31, no. S1, pp. 203–213, 2016.

[55] Y. Hongtao, W. Gang, Z. He, L. Zhigang, and H. Jue, "Model predictive control b ased optimal operation of distribution network with charging-swapping-storage integrated station," *Automation of Electric Power Systems*, vol. 44, no. 05, pp. 187–197, 2020.

[56] Z. Xingxu, H. Xueshan, and Y. Ming, "A layered time -varying optimization tracking algorithm for active distribution networks," *Proceedings of the CSEE*, vol. 39, no. 24, pp. 7093–7106, 2019.

[57] C. Fei, L. Dong, and C. Yunhui, "Hierarchically distributed voltage control strategy for active distribution network," *Automation of Electric Power Systems*, vol. 39, no. 09, pp. 61–67, 2015.

[58] L. Haiping, W. Yan, L. Yingpei, and W. Xinming, "Hierarchical- distributed optimal scheduling of hybrid ac/dc active distribution network considering source and load uncertainties," *Electric Power Automation Equipment*, pp. 1–9, 2021.

[59] Z. Li, J. He, X. Wang, T. Yip, and G. Luo, "Active control of power flow in distribution network using flexible tie switches," in *Proceedings of the 2014 International Conference on Power System Technology*, pp. 1224–1229, London, UK, July 2014.

[60] H. Ruonan, W. Wei, W. Xuezhi, J. Long, and M. We, "Three-stage robust voltage control method for active distribution network with soft open points," *High Voltage Engineering*, vol. 46, no. 11, pp. 3752–3763, 2020.

[61] C. Pengwei, T. Wei, L. Chengwei, Z. Bo, and Z. Lu, "Two-stage coordination optimization control of soft open point and tie switch in active distribution network with high penetration renewable energy generation," *Transactions of China Electrotechnical Society*, vol. 34, no. 06, pp. 1263–1272, 2019.

[62] S. Lu, C. Wang, Y. Fan, and B. Lin, "Robustness of building energy optimization with uncertainties using deterministic and stochastic methods: Analysis of two forms," *Building and Environment*, vol. 205, Article ID 108185, 2021.

[63] F. Yang, Z. Zhiquan, and L. Zhenkun, "Research on reactive power voltage control strategy for hybrid ac/dc distribution network based on two-stage robust optimization model," *Proceedings of the CSEE*, vol. 39, no. 16, pp. 4764–4774, 2019.

[64] H. Shuaijia, R. Hebin, G. Hongjun, and L. Junyong, "Overview on theory analysis and application of distributionally robust optimization method in power system," *Automation of Electric Power Systems*, vol. 44, no. 14, pp. 179–191, 2020.

[65] W. Lingling, W. Xin, and Z. Yihui, "Reactive power optimization of distribution network considering output correlation of multiple wind turbines," *Power System Technology*, vol. 41, no. 11, pp. 3463–3469, 2017.

[66] W. L. ibin, L. Jun, D. Dashang, and F. Xinyan, "Stochastic reactive power optimization based on normal vector of voltage stability limit surface for distribution network with wind power," *Electric Power Automation Equipment*, vol. 35, no. 10, pp. 95–100, 2015.

[67] W. Bei, Z. Yan, and C. Minjiang, "Probabilistic evaluation of voltage stability based on load fuzzy clustering," *Automation of Electric Power Systems*, vol. 04, pp. 23–27, 2007.

[68] S. Lei, L. Zhenkun, and Z. Zhiquan, "A coordinated operation strategy for integrated energy microgrid clusters based on chance-constrained programming," *Power System Protection and Control*, vol. 49, no. 14, pp. 123–131, 2021.

[69] L. Huan, C. Minyou, and C. Tingli, "Adaptive time-intervalled reactive power optimization for distribution network containing wind power generation," *Power System Technology*, vol. 38, no. 08, pp. 2207–2212, 2014.

[70] Z. Bo, X. Fu-qiang, L. Yu, G. Dun-wei, and Z. Xi, "Multi-objective interval optimization approach for energy hub planning with consideration of renewable energy and demand response synergies," *Proceedings of the CSEE*, vol. 40, no. 17, pp. 1–16, 2021.

[71] C. Ruijie, L. Zongxiang, and Q. Ying, "Optimal dispatch based on multi-scene ambiguity set and modified second-order cone algorithm for distribution network," *Power System Technology*, pp. 1–9, 2021, https://kns.cnki.net/kcms/detail/11.2410.TM.20211020.1039.001.html.

[72] S. Naouali, S. B. Salem, and Z. Chtourou, "Uncertainty mode selection in categorical clustering using the rough set theory," *Expert Systems with Applications*, vol. 158, Article ID 113555, 2020.

[73] H. Bagheri Tolabi, M. H. Ali, and M. Rizwan, "Simultaneous reconfiguration, optimal placement of dstatcom, and photovoltaic array in a distribution system based on fuzzy-aco approach," *IEEE Transactions on Sustainable Energy*, vol. 6, no. 1, pp. 210–218, 2015.

[74] C. Yong, Y. Li, Z. Zeng, Z. Zhang, Z. Zhang, and Y. Liu, "Coordinated active and reactive power optimization considering load characteristics for active distribution network," *Chinese Journal of Electrical Engineering*, vol. 6, no. 4, pp. 97–105, 2020.

[75] Z. Wei-guo and W. Hui-qiao, "Research on photovoltaic power capacity optimization in microgrid," *Journal of North China Electric Power University*, vol. 41, no. 02, pp. 51–54+88, 2014.

[76] H. Zhou, J. Guo, R. Zhou, K. Gu, and L. Qian, "Interior point method based reactive power optimization of active distribution network," in *Proceedings of the 2016 China International Conference on Electricity Distribution (CICED)*, pp. 1–6, Tianjin, China, September 2016.

[77] H. Zhen, "Control and application of reactive power optimization in regional power grid," Shangdong University, Shangdong, China, 2014.

[78] Z. Wang, Y. Wang, G. Liu, Y. Zhao, Q. Cheng, and C. Wang, "Fast distributed voltage control for pv generation clusters based on approximate Newton method," *IEEE Transactions on Sustainable Energy*, vol. 12, no. 1, pp. 612–622, 2021.

[79] Y. Tami, K. Sebaa, M. Lahdeb, and H. Nouri, "Mixed-integer quadratic constrained programming versus quadratic programming methods for distribution network reconfiguration," in *Proceedings of the 2019 International Conference on Advanced Electrical Engineering (ICAEE)*, pp. 1–5, Algiers, Algeria, November 2019.

[80] Z. Deng, M. Liu, Y. Ouyang, S. Lin, and M. Xie, "Multi-objective mixed-integer dynamic optimization method

applied to optimal allocation of dynamic var sources of power systems," *IEEE Transactions on Power Systems*, vol. 33, no. 2, pp. 1683–1697, 2018.

[81] S. García-Martínez, E. Espinosa-Juárez, and C. Pérez-Rojas, "Improvement of voltage sags rates by applying optimal reconfiguration of electrical networks in presence of dg by using tabu search," in *Proceedings of the 2017 International Conference on Computational Science and Computational Intelligence (CSCI)*, pp. 202–206, Jakarta, Indonesia, December 2017.

[82] Z. Qian, D. Jinjin, Z. Daonong, W. Qunjing, and M. Jinhui, "Reactive power optimization of high- penetration distributed generation system based on clusters partition," *Automation of Electric Power Systems*, vol. 43, no. 03, pp. 130–137, 2019.

[83] F. R. Alonso, D. Q. Oliveira, and A. C. Zambroni de Souza, "Artificial immune systems optimization approach for multiobjective distribution system reconfiguration," *IEEE Transactions on Power Systems*, vol. 30, no. 2, pp. 840–847, 2015.

[84] L. Jia, L. Tianqi, and L. Xingyuan, "Application of improved particle swarm-tabu search algorithm in multi-objective reactive power optimization," *Electric Power Automation Equipment*, vol. 34, no. 08, pp. 71–77, 2014.

[85] C. Guowei, L. Xu, Z. Wang, M. Tao, and Z. Tianyu, "Optimal configuration of distributed generation based on improved grey optimization algorithm," *Acta Energiae Solaris Sinica*, vol. 40, no. 01, pp. 134–141, 2019.

[86] S. Qi, Y. Yongjin, W. Yubin, and G. Haishu, "Comprehensive optimization of distribution network using improved whale optimization algorithm," *Proceedings of the CSU-EPSA*, vol. 33, no. 05, pp. 22–29, 2021.

[87] C. Ming and Z. Kaoshe, "Research on capacity optimization of hybrid energy storage system in wind-pv- storage power generation system based on improved cuckoo search algorithm," *Power System and Clean Energy*, vol. 32, no. 08, pp. 141–147, 2016.

[88] W. Ying, Z. Yuan, and Z. Shu, "Optimization model of line reconstruction for voltage sag governance of distribution network," *Electric Power Automation Equipment*, vol. 41, no. 01, pp. 9–23, 2021.

[89] C. S. G. Rajan and K. Ravi, "Optimal placement and sizing of dstatcom using ant lion optimization algorithm," in *Proceedings of the 2019 International Conference on Computation of Power, Energy, Information and Communication (ICCPEIC)*, pp. 1–4, Melmaruvathur, Chennai, March 2019.

[90] L. Wenxue, L. Jun, Y. Zhihao, N. Rui, and C. Zhuangzhuang, "Multi-objective fuzzy chance constrained optimal reactive power flow based on credility theory," *Transactions of China Electrotechnical Society*, vol. 30, no. 21, pp. 82–89, 2015.

[91] C. Peng, G. Shaoyun, and L. Hong, "Intelligent planning of medium voltage distribution network based on triangle-shaped power supply model with single contact," *Power System Technology*, vol. 37, no. 04, pp. 947–953, 2013.

[92] P. Huan, X. Chen, and Y. Li, "Multiple objective planning of distribution network with multiple distributed generations," *Journal of System Simulation*, vol. 30, no. 10, pp. 3826–3834, 2018.

[93] G. Jie, M. Lu, Z. Tongtong, L. Shuqi, and J. Zhijian, "Data-driven optimization for reactive power operation in source distribution network without accurate modeling," *Electric Power Automation Equipment*, vol. 41, no. 01, pp. 1–11, 2021.

[94] Z. Tao, X. Xueqin, S. Suyi, and S. Xiaowei, "Optimal location and parameter setting of statcom based on improved multiple population quantum particle swarm optimization algorithm," *Proceedings of the CSEE*, vol. 35, no. S1, pp. 75–81, 2015.

[95] L. Yuan, L. Dichen, D. Xiinwel, and H. Yonq, "Application of hybrid genetic algorithm in power system parameter measurement," *Automation of Electric Power Systems*, vol. 31, no. 12, pp. 86–91, 2007.

[96] Z. Ji'ang, P. Wang, and C. Ze, "Multi-objective dispatching adopting chaos particle swarm optimization cooperated with interior point method," *Power System Technology*, vol. 45, no. 02, pp. 613–621, 2021.

[97] S. Mugemanyi, Z. Qu, F. X. Rugema, Y. Dong, C. Bananeza, and L. Wang, "Optimal reactive power dispatch using chaotic bat algorithm," *IEEE Access*, vol. 8, pp. 65830–65867, 2020.